UNIVERSITY OF CALIFORNIA,
IRVINE

Jet Atomization for Real Liquids at High Pressures

DISSERTATION

submitted in partial satisfaction of the requirements
for the degree of

DOCTOR OF PHILOSOPHY

in Mechanical and Aerospace Engineering

by

Jordi Poblador Ibanez

Dissertation Committee:
Professor William A. Sirignano, Chair
Professor Said E. Elghobashi
Professor Roger H. Rangel

2022

DEDICATION

To my loved ones, friends and family.

TABLE OF CONTENTS

LIST OF FIGURES

LIST OF TABLES

LIST OF ACRONYMS

AMR	Adaptive Mesh Refinement
BWR	Benedict-Webb-Rubin
CFL	Courant-Friedrichs-Lewy
CIR	Courant-Isaacson-Rees
CSF	Continuum Surface Force
EA	Eulerian Algebraic
EI	Eulerian Implicit
ELVIRA	Efficient Least squares Volume-of-fluid Interface Reconstruction Algorithm
ENO	Essential Non-Oscillatory
FFT	Fast Fourier Transform
FMM	Fast-Marching Method
GALS	Gradient Augmented Level Set
GFM	Ghost Fluid Method
HF	Height Function
KH	Kelvin-Helmholtz
LE	Lagrangian Explicit
LoCLiD	Lobe-Corrugation-Ligament-Droplet
LoHBrLiD	Lobe-Hole-Bridge-Ligament-Droplet
LoLiD	Lobe-Ligament-Droplet
LS	Level Set
LTE	Local Thermodynamic Equilibrium
MYC	Mixed-Youngs-Centered
NIST	National Institute of Standards and Technology
PLIC	Piecewise Linear Interface Construction
PPE	Pressure Poisson Equation
PR	Peng-Robinson
RK	Redlich-Kwong
RT	Rayleigh-Taylor
SIMPLE(C)	Semi-Implicit Method for Pressure-Linked Equations (Consistent)
SMART	Sharp and Monotonic Algorithm for Realistic Transport
SRK	Soave-Redlich-Kwong
VdW	Van der Waals
VOF	Volume Of Fluid
WENO	Weighted Essentially Non-Oscillatory

ACKNOWLEDGMENTS

All the people and institutions mentioned on this page deserve my deepest gratitude. Without their support and assistance, this work would not have been possible.

I would like to start by thanking my research advisor, mentor, and chair of my dissertation committee, Prof. William A. Sirignano, for his endless support and dedication to my research. He offered me the opportunity to tackle a very challenging problem, with which I have learned a great deal over the past few years. Without his guidance, I would not be the researcher I am today.

Next, I would like to thank the other members of my dissertation committee, Prof. Said E. Elghobashi and Prof. Roger H. Rangel. Besides their help and advice in writing this dissertation, they have had vital roles in my personal and professional growth at UC Irvine. Prof. Elghobashi has guided me over the years, and our insightful discussions have contributed to achieving the research goals of this dissertation. Also, I probably would not have been able to pursue a Ph.D. degree in the United States without the vote of confidence from Prof. Rangel, who awarded me with a Balsells Graduate Fellowship.

I would also like to thank Prof. Antonino Ferrante and his student Pablo Trefftz Posada, from the Unversity of Washington, for the helpful discussions and contributions in developing the numerical framework of this dissertation.

And although late in my Ph.D. years, a special thank you to Prof. Fazle Hussain, from Texas Tech University, for his endless patience in our discussions and kind encouraging words, and to Prof. Perry Johnson for embracing me as a peer and providing a final energy boost to finish my dissertation.

This research has been funded by the NSF grant with Award Number 1803833 and Dr. Ron Joslin as Scientific Officer. Additional funding and support have been provided by the Balsells Fellowship program, the Graduate Division Completion Fellowship, and the William and Ida Melucci Space Exploration & Technology Endowed Fellowship. This work utilized the infrastructure for high-performance and high-throughput computing, research data storage and analysis, and scientific software tool integration built, operated, and updated by the Research Cyberinfrastructure Center (RCIC) at the University of California, Irvine. Other computational resources were provided by the startup allocation MCH210008 in the XSEDE network, supported by the NSF grant number ACI-1548562.

Permission was obtained from Elsevier, AIP Publishing and Cambridge University Press to reuse figures from other works, with proper citation in the figure captions. Additionally, permission was obtained from Elsevier and AIP Publishing to reuse and adapt previously published material from works by the author of this dissertation. The main co-author of these publications is William A. Sirignano, who directed and supervised this dissertation. Only fair use was made of any reused figures and adapted material from previously published works.

To all my friends and colleagues, thank you for being by my side, not necessarily physically, during the past few years. Without your support, I would not have had the energy to complete this project. I have enjoyed the company and expertise of Dr. Arash Zandian, Dr. Zeinab Shadram, and Dr. Tuan Nguyen. I have grown as a person and researcher, along with my friends and soon-to-be doctors Andres Adam, David Morata, Zihao Zhu, and Jingyi Zeng. I have learned with future doctor Branson Davis what a great research collaboration looks like. I have realized that friends can be a family with Marina, Kristen, Marc, Mireia, Clara, and hairy Amber. And I can be the happiest person on Earth knowing that no matter the distance, some friendships are meant to be forever. Thank you, Didac, Alex, Efren, Gerard, Joan, Oriol, and many more.

Irene, soon-to-be Dr. Martinez, you are Irvine, you are these years, this thesis, you are me, we are us. Thank you for your constant support, constant understanding, and constant company. There is no stronger pillar than you.

And last but not least, I want to acknowledge my loving parents, sister, and family for their unconditional love and support. We have made it through the distance and the time difference. I am proud of us. Thank you.

Let there be light for all of us. Fiat Lux.

VITA

Jordi Poblador Ibanez

EDUCATION

Ph.D. in Mechanical and Aerospace Engineering **2022**
University of California Irvine *Irvine, CA, USA*

M.S. in Mechanical and Aerospace Engineering **2018**
University of California Irvine *Irvine, CA, USA*

M.S. in Aeronautical Engineering **2018**
ESEIAAT, Universitat Politècnica de Catalunya *Terrassa, Spain*

B.S. in Aerospace Technology Engineering **2015**
ESEIAAT, Universitat Politècnica de Catalunya *Terrassa, Spain*

RESEARCH EXPERIENCE

Graduate Student Researcher **2017–2022**
University of California, Irvine *Irvine, CA, USA*

Collaboration Fellowship **2015–2016**
CTTC, Universitat Politècnica de Catalunya *Terrassa, Spain*

TEACHING EXPERIENCE

Teaching Assistant **2018–2022**
ENGRMAE 91: Introduction to Thermodynamics F19
ENGRMAE 112: Propulsion F18, F20
ENGRMAE 130A: Introduction to Fluid Mechanics W18, W19, W22
University of California, Irvine *Irvine, CA, USA*

REFEREED JOURNAL PUBLICATIONS

Poblador-Ibanez, J. and Sirignano, W. A., *"Temporal atomization of a transcritical liquid n-decane jet into oxygen"* **2022**
International Journal of Multiphase Flow *in press*

Poblador-Ibanez, J. and Sirignano, W. A., *"A Volume-of-Fluid method for variable-density, two-phase flows at supercritical pressure"* **2022**
Physics of Fluids *in press*

Poblador-Ibanez, J. and Sirignano, W. A., *"Liquid-jet instability at high pressures with real-fluid interface thermodynamics"* **2021**
Physics of Fluids Vol. 33 (8) pp. 083308

Poblador-Ibanez, J., Davis, B. W., and Sirignano, W. A., *"Self-similar solution of a supercritical two-phase laminar mixing layer"* **2021**
International Journal of Multiphase Flow Vol. 135 pp. 103465

Davis, B. W., Poblador-Ibanez, J., and Sirignano, W. A., *"Two-phase developing laminar mixing layer at supercritical pressures"* **2021**
International Journal of Heat and Mass Transfer Vol. 167 pp. 120687

Poblador-Ibanez, J. and Sirignano, W. A., *"Transient behavior near liquid-gas interface at supercritical pressure"* **2018**
International Journal of Heat and Mass Transfer Vol. 126 pp. 457 – 473

PEER-REVIEWED CONFERENCE PROCEEDINGS

Poblador-Ibanez, J. and Sirignano, W. A., *"Temporal liquid decane jet flow through oxygen at transcritical conditions"* **May 2022**
ILASS-Americas 32nd Annual Conference on Liquid Atomization and Spray Systems, Madison, WI, USA

Poblador-Ibanez, J., Sirignano, W. A., and Hussain, F., *"Vortex dynamics in the early deformation of a transcritical liquid jet"* **May 2022**
ILASS-Americas 32nd Annual Conference on Liquid Atomization and Spray Systems, Madison, WI, USA

Poblador-Ibanez, J. and Sirignano, W. A., ***"Volume of Fluid method for low-Mach-number compressible supercritical liquid jet"*** **Sep 2021**
15th Triennial International Conference on Liquid Atomization and Spray Systems, Edinburgh, UK (Virtual Conference)

Poblador-Ibanez, J. and Sirignano, W. A., ***"Early deformation and interface thermodynamics of real liquid jets at high pressures"*** **May 2021**
ILASS-Americas 31st Annual Conference on Liquid Atomization and Spray Systems (Virtual Conference)

Poblador-Ibanez, J. and Sirignano, W. A., ***"Analysis of an axisymmetric liquid jet at supercritical pressures"*** **May 2019**
ILASS-Americas 30th Annual Conference on Liquid Atomization and Spray Systems, Tempe, AZ, USA

Poblador-Ibanez, J. and Sirignano, W. A., ***"Liquid-gas equilibrium and interface dynamics at supercritical pressure"*** **Jul 2018**
14th Triennial International Conference on Liquid Atomization and Spray Systems, Chicago, IL, USA

PUBLISHED THESIS

Poblador-Ibanez, J., ***"Liquid-Gas Heat and Mass Transfer at Supercritical Pressures"*** **Jan 2018**
M.S. thesis, University of California Irvine, Irvine, CA, USA

Poblador-Ibanez, J., ***"Study for the numerical resolution of conservation equations of mass, momentum and energy to be applied in different engineering problems"*** **Sep 2015**
B.S. thesis, ESEIAAT, Universitat Politècnica de Catalunya, Terrassa, Spain

HONORS, FELLOWSHIPS AND AWARDS

William and Ida Melucci Space Exploration & Technology Endowed Fellowship **2022**
Henry Samueli School of Engineering, University of California, Irvine

Graduate Division Completion Fellowship **2021**
Graduate Division, University of California, Irvine

Best Academic Record of all M.S. in engineering **2018**
ESEIAAT, Universitat Politècnica de Catalunya

Best Academic Record for M.S. Aeronautical Engineering **2018**
ESEIAAT, Universitat Politècnica de Catalunya

ICLASS 2018 Student Travel Award **2018**
Institute for Liquid Atomization and Spray Systems

Balsells Graduate Fellowship **2016-2017**
Henry Samueli School of Engineering, University of California, Irvine

Collaboration Fellowship **2015**
MECD, Gobierno de España, and CTTC, Universitat Politècnica de Catalunya

Honors received for the B.S. thesis **2015**
ESEIAAT, Universitat Politècnica de Catalunya

MOBINT grant **2015**
Generalitat de Catalunya

Erasmus.es grant **2015**
MECD, Gobierno de España

ABSTRACT OF THE DISSERTATION

Jet Atomization for Real Liquids at High Pressures

By

Jordi Poblador Ibanez

Doctor of Philosophy in Mechanical and Aerospace Engineering

University of California, Irvine, 2022

Professor William A. Sirignano, Chair

The injection of liquid fuel at supercritical pressures is a necessary but overlooked topic in combustion. Under the premise that the liquid will swiftly transition to a supercritical state, the role of two-phase dynamics is typically ignored. Nevertheless, a transcritical domain exists for which a sharp interface prevails before substantial heating occurs. This transcritical scenario may persist, for example, during the early deformation of liquid hydrocarbon fuels injected into high-pressure combustion chambers. Local thermodynamic phase equilibrium (LTE) enhances the dissolution of the oxidizing species into the liquid phase, and vaporization or condensation may occur simultaneously in several regions along with the interface. Following species and thermal mixing, fluid properties vary greatly, with liquid- and gas-mixture properties being more comparable near the interface. Small surface instabilities emerge early due to the combination of low, variable surface-tension force and gas-like liquid viscosities.

The mixing process, interface thermodynamics, and early deformation of a cool liquid n-decane jet submerged into a hotter moving gas initially composed of pure oxygen are studied under different ambient pressures and gas velocities. For this purpose, a two-phase, low-Mach-number flow solver for variable-density fluids is proposed. Since the jet flow evolution corresponds to transitional turbulence, no turbulence models are considered. The interface

is captured using a split Volume-of-Fluid method, generalized for a non-divergence-free liquid velocity. Both phases exchange mass across the interface. Numerical challenges emerge compared to incompressible two-phase algorithms, which are successfully addressed for the first time in this type of flow. The importance of transcritical mixing effects for increasing pressures is demonstrated. At first, local deformation features emerge, which differ significantly from earlier incompressible works. Then, instead of the traditional atomization into droplets, the minimal surface-tension force is responsible for the folding and layering of liquid sheets. Thus, rather than spray formation, surface-area increase at transcritical conditions is primarily the result of gas-like deformations under shear. Moreover, the interface may be easily perturbed in hotter regions submerged in the faster oxidizer stream under specific triggers. The net mass exchange limits the liquid-phase vaporization to the small liquid structures at high pressures. Then, the dynamical vortex identification method λ_ρ is used to identify the interaction between vortical structures and the liquid surface, explaining various deformation mechanisms. Details on the evolution of vortex structures are provided, showing that layering traps and weakens the vortices.

Chapter 1

Introduction

This introductory chapter provides details on the structure of this dissertation in Section 1.1. The motivation behind this work and the importance of the thesis topic are discussed in Section 1.2. Many features or real liquids at high pressures are introduced, and the reader is referred to Chapter 2 for a more detailed discussion. Lastly, Section 1.3 provides a clear list of goals or milestones this dissertation has been able to address.

1.1 Dissertation Structure

This dissertation is structured as follows. First, Chapter 1, this chapter, introduces the topic of this dissertation, describes the motivation behind the study of the atomization of real liquids at high pressures, and provides a few research goals that have been achieved with this study. The dissertation's topic is mainly centered around the injection of liquid fuels into combustion chambers operating at elevated pressures, well above the critical pressure of the liquid fuel.

Chapter 2 is a comprehensive literature review of previous studies involving the atomization of incompressible liquid jets and the thermodynamic transition that liquid fuels experience as they enter a transcritical regime. Moreover, simpler studies involving a fully-coupled model between the governing equations and a non-ideal thermodynamic model are presented in order to provide valuable insight for the study performed in this dissertation. Then, Chapter 3 describes the full physical model and the thermodynamic domain of applicability or validity of the approach. Next, Chapter 4 addresses the numerical methods used to solve the governing equations and the interface evolution for low-Mach-number two-phase flows, as well as details on the implementation approach and algorithm.

The following chapters describe the temporal evolution of planar liquid jets when submerged in a faster oxidizer stream. Chapter 5 discusses two-dimensional results, which simplify the visualization of diffusive mixing effects within each phase, while Chapters 6 and 7 present a parametric three-dimensional study involving various ambient pressures and relative velocities between the liquid and gaseous streams. Details on the surface deformation, droplet formation, and role of vortex dynamics are provided. Lastly, Chapter 8 summarizes and concludes this dissertation. Note, supporting material is available in the appendices attached to this document and in the online submission.

1.2 Motivation

From vehicles to power units, many engineering applications require energy sources involving combustion processes. The performance and design of combustion chambers depend on what type of fuel is used (e.g., gas, liquid or solid) and how it mixes with the surrounding oxidizer. The breakup of the central liquid core into droplets for liquid fuels determines how fast the fuel evaporates and mixes with the oxidizer before the chemical reaction starts. This process is called atomization, and understanding the physics behind it helps design better

the combustion chamber (e.g., size, injector shape, and distribution) and improve the quality and controllability of the combustion reaction.

Combustion chemical reactions at typical operating conditions result in high dissociation of species and reduced temperature. These issues reduce the efficiency and specific energy conversion per unit mass of fuel of the reaction. However, higher pressures mitigate this problem. Also, heat addition at higher pressure results in the more efficient process of heat addition at higher temperature. Therefore, there is an interest in moving towards a high-pressure combustion chamber regime, which is often supercritical for the liquid fuel. Hydrocarbon-based fuels (e.g., diesel fuel, Jet A, RP-1) are widely used and have critical pressures around 20 bar, while injection in diesel engines or gas turbines may occur at pressures between 25-40 bar and chamber pressures in rocket engines range between 70 to 300 bar. For instance, the Saturn's V F-1 engine operated at a chamber pressure of 70 bar using RP-1 as fuel[1]. Newer engines reach even higher pressures. The Merlin 1D engine used in the Falcon 9 rocket also uses RP-1 as fuel and operates at a chamber pressure of 97 bar[2]. An extreme case is the Raptor engine that will power the Starship rocket. It uses liquid methane as fuel and operates with a chamber pressure around 300 bar[3].

A clear jump in fluid properties across the phase interface at subcritical pressures allows a clear distinction between the liquid and gas phases. Moreover, variations of fluid properties in both phases are minimal. Therefore, extensive studies analyzing breakup mechanisms at these conditions have been done numerically and experimentally. For chamber pressures at near-critical or supercritical conditions, the thermodynamic behavior of the liquid-gas interface changes, and the liquid injection resembles a turbulent gas jet. The fluid properties of both phases look more alike in the vicinity of the interface, which is suddenly immersed in

[1] https://en.wikipedia.org/wiki/Rocketdyne_F-1
[2] https://en.wikipedia.org/wiki/SpaceX_Merlin
[3] https://en.wikipedia.org/wiki/SpaceX_Raptor

a variable-density layer that is much easily affected by aerodynamic forces (i.e., turbulence), becoming difficult to identify [1–7].

This diffusive behavior has been described in the past as a rapid transition of the liquid to a gas-like supercritical state under the assumption that two clear, distinct phases cannot coexist in this thermodynamic regime [8, 9]. Nevertheless, evidence of a two-phase behavior at supercritical pressures exists in multi-component configurations [10–15]. At supercritical pressures for the liquid fuel, the gas species is easily dissolved into the liquid phase based on requirements that liquid and gas should be in local thermodynamic phase equilibrium (LTE) at the interface. Diffusion layers of the order of micrometers evolve on each side of the interface, where fluid properties change considerably [15–17]. The newly formed mixture in the liquid phase near the interface presents a higher critical pressure than the original liquid, usually above the chamber pressure. In some situations, the estimated liquid mixture critical pressure may still be slightly below the chamber pressure while phase equilibrium still supports a two-phase behavior [15]. Under these considerations, surface tension and heat of vaporization persist, albeit they are weakened.

The experimental observations at supercritical pressures are consistent with fast atomization caused by a sharp reduction of surface-tension forces as liquid and gas become similar. Moreover, liquid viscosities drop and present gas-like values near the interface [18, 19]. Therefore, the interface may be subject to the rapid growth of small surface instabilities and fast distortion, causing an early breakup of tiny droplets. Under this extreme environment where a cloud of tiny droplets is immersed in a variable-density fluid, traditional visualization techniques (e.g., shadowgraphy or ballistic imaging) might suffer from scattering and refraction issues that can diffuse the two-phase behavior. Some new experimental techniques are being developed to capture the two-phase behavior in supercritical pressure environments [20–23]. Numerical results of incompressible liquid round jets and planar sheets under conditions similar to those found at supercritical pressures also support this reasoning [24–28]. Con-

figurations with high Weber number at moderate Reynolds number show a rapid breakup process dominated by early droplet formation and enhanced radial development of the two-phase mixture. That is, scenarios where inertia forces dominate over surface-tension and viscous forces.

The interface temperature is another parameter that must be considered. Although cold studies show similar features as experiments injecting liquid fuel at supercritical pressures and high temperatures, heating can cause a transition from a two-phase interface to a diffusive mixing where the liquid-gas interface cannot be identified [7]. That is, the interface temperature is eventually larger than the mixture critical temperature at a given pressure if the surrounding gas is hot enough, causing a transition to a diffuse mixing between both phases where surface tension and heat of vaporization have vanished completely.

Moreover, very high pressures reduce the molecular mean free path considerably while higher interface temperatures, but still below the mixture critical temperature, increase the thickness of the phase "non-equilibrium" transition region. This trend results in the transition region entering the continuum regime once the molecular mean free path is substantially smaller than the relevant characteristic length [29–32], which happens as the interface region approaches the mixture critical temperature. Then, phase equilibrium with equal temperatures on both phases may no longer be the proper modeling choice for the liquid-gas interface. The phase "non-equilibrium" transition region must be modeled to define the proper liquid and gas interface state. That is, similar to the supercritical mixing behavior once finite sharp gradients of fluid properties define the transition from one side of the interface to the other. At lower pressures, the molecular mean free path is comparable to (albeit smaller than) the interface thickness and phase equilibrium correctly represents the liquid-gas interface in the temperature range of two-phase coexistence. The transition layer is described as a phase "non-equilibrium" domain following Dahms and Oefelein [29–32]. However, it must be understood that the thermodynamic equilibrium of the continuous fluid is maintained

throughout the thicker transition layer; there is no question about the equation of state. The distinction between the two phases has disappeared and thereby disallowed the use of the phase-equilibrium law. The "non-equilibrium" terminology arises from the use of non-equilibrium molecular dynamics to model and study the thickening of the phase transition layer. Therefore, the existing semantics in the literature is not optimal. Nonetheless, the phase "non-equilibrium" terminology used in the literature to describe the interface behavior appears throughout this dissertation.

The use of the word "transcritical" to describe such conditions where two phases coexist because the pressure is supercritical for the fuel, but the interface temperature is subcritical was pioneered by Delplanque and Sirignano [11, 13, 14]. These works performed studies on droplet vaporization at supercritical pressures and the effects on fuel combustion. Other researchers followed with similar works, such as that of Yang and Shuen [12]. It is noted that a two-phase interface can be sustained until enough heating causes an increase in the droplet temperature, with the liquid surface reaching the mixture critical point and transitioning to a diffusive-controlled phase mixing. Therefore, because critical pressure depends on composition, a region in a field where a supercritical domain neighbors a subcritical domain with near-uniform pressure throughout both domains can easily exist.

At this point, it is clear that previous studies of liquid atomization have avoided a deeper insight into real-life scenarios found in combustion applications. It is necessary to analyze if phase equilibrium can be established (i.e., clear diffusion layers evolve on each side of the interface) before substantial disruption and heating of the liquid-gas interface occur. If so, the early stages of transcritical liquid fuel injection are still dominated by a two-phase problem, albeit more aggressive and complex. The coupling between fluid dynamics and thermodynamics must be analyzed (e.g., how variable fluid properties affect the liquid deformation cascade) and the role of vortex dynamics in the generation of distinct breakup mechanisms.

Since experimentalists still have trouble analyzing this thermodynamic regime (e.g., low-cost high-pressure vessels are scarce and there is considerable scattering in current imaging techniques), a physically-sound numerical methodology is needed to understand it. This numerical method must handle two-phase flows with heat and mass transfer across the phase interface and must be consistent with high-pressure non-ideal thermodynamics. Inherent challenges appear: the interface defining two distinct regions must be captured with precision during the simulation and the discontinuity in fluid properties across the interface is difficult to address numerically. An equation of state and other models and correlations able to predict both gas and liquid non-ideal states must be used, ensuring that non-idealities representative of dense or compressed fluids are captured [18, 33, 34]. Lastly, note that liquid atomization is a problem involving transitional turbulence (i.e., a transition from laminar to turbulent flow) as smaller liquid structures and flow scales are generated. Nonetheless, the early times of the deformation of a liquid jet can be studied accurately with direct numerical approaches without the need for turbulence models as long as the mesh is fine enough to capture the quasi-laminar flow [24–28, 35, 36].

1.3 Research Goals

Section 1.2 provides a clear background to define research goals for this dissertation. The following points summarize the milestones that have been achieved in this work.

- Develop a consistent thermodynamic model able to predict with sufficient accuracy high-pressure fluid states, both for pure fluids and mixtures, and phase equilibrium at the interface.
- Develop a weakly-compressible numerical code that handles complex two-phase flows with variable mass, momentum, and energy transfer across the interface. This code

should include a proper interface capturing method and a correct coupling with the thermodynamic model. Turbulence models are not necessary since the goal is to represent a transitional turbulence flow type.

- Analyze the breakup process of the liquid phase: instability growth, the scale of the perturbations, and generation of liquid structures during the process. Determine whether the results are similar or not to those seen in incompressible studies.

- Analyze how high-pressure thermodynamics affect the breakup process and the behavior of the liquid-gas interface. Consider various issues: the establishment of phase equilibrium before substantial growth of surface instabilities, analyzing the impact of phase equilibrium on the interface properties, and describing the impact on the surface deformation caused by species and thermal diffusion on both sides of the liquid-gas interface.

- Analyze the generation and evolution of vortex structures in the high-pressure flow. Determine their role in the deformation patterns observed across the analyzed configurations.

Chapter 2

Background

This chapter provides a literature review of relevant topics related to this dissertation. Section 2.1 introduces previous work on the breakup and atomization of incompressible liquid jets, focusing on the classification of various atomization regimes based on distinct deformation mechanisms that have been explained with vorticity dynamics. Then, Section 2.2 presents experimental and theoretical work on the thermodynamic transition that liquid fuels undergo as the thermodynamic pressure increases beyond the critical pressure of the fuel. The mixture critical temperature is also highlighted to discuss whether two phases may coexist or not. To complement this chapter, Sections 2.3, 2.4 and 2.5 discuss preliminary work on simplified one-dimensional and two-dimensional configurations involving a fully-coupled approach between the governing equations and a thermodynamic model able to capture the real-fluid properties and the phase-equilibrium solution at the liquid-gas interface. These works provide valuable insights on certain physical features relevant for this dissertation (e.g., diffusive mixing at high pressures, thermodynamic behavior of the interface).

2.1 Incompressible Liquid Breakup

The injection of liquid fuels into a combustion chamber is a complex problem. The injector supplies the liquid into the combustion chamber. The liquid going through may be affected by upstream phenomena, such as cavitation inside the injector, or downstream phenomena, such as the development of turbulent flow or acoustic perturbations related to combustion. Then, a region where the liquid-gas interface starts to deform in a wave-like behavior, eventually yielding to a breakup of the liquid core and the formation of droplets [37].

The primary driving mechanism for the liquid breakup of a round jet can be inferred from the Reynolds and Weber numbers of the liquid jet [38]. The Reynolds number is the ratio between inertia and viscous forces, while the Weber number is the ratio between inertia and surface-tension forces. Figure 2.1 shows four different domains depending on the magnitude of these two non-dimensional numbers. When inertia forces are weak compared to viscous forces or surface tension (e.g., low-speed flows), the Rayleigh mechanism or capillary instabilities are responsible for breaking up the liquid jet. These instabilities are related to the surface-tension force, which always minimizes surface energy. That is, surface area per unit volume is minimized. This effect is destabilizing for round jets (i.e., a spherical droplet presents a smaller surface area per unit volume than a cylindrical jet) but stabilizing for ideally infinite liquid sheets. As the relative importance of inertia forces increases, aerodynamic effects become the main drivers of the liquid breakup, eventually atomizing the liquid into tiny droplets. In the atomization domain, capillary effects are only meaningful in the late stages of the breakup process, where smaller liquid structures are subject to a stronger influence of the surface-tension force.

The hydrodynamic instabilities disrupting the liquid-gas interface within the atomization domain are the Kelvin-Helmholtz instability (KH) and the Rayleigh-Taylor instability (RT). The classical KH instability is related to a discontinuity in the tangential velocity at the

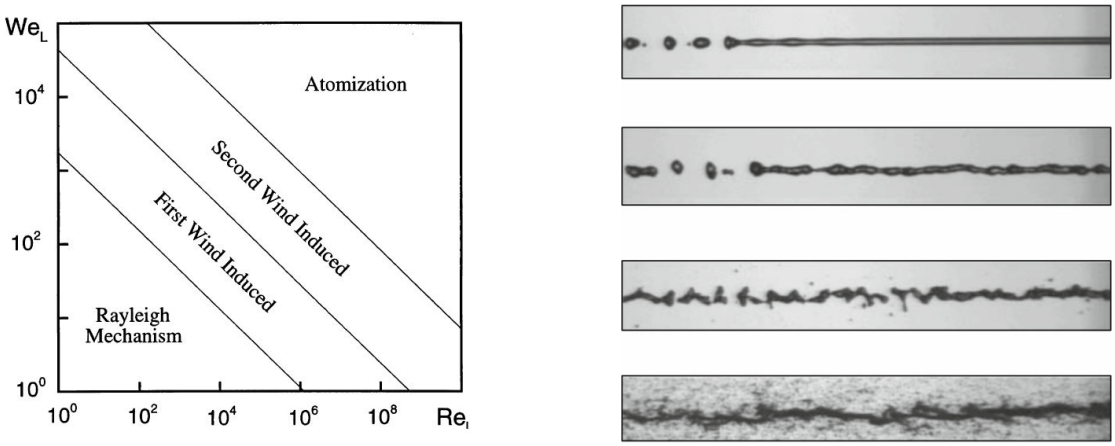

(a) (b)

Figure 2.1: Breakup modes of a liquid round jet. (a) Diagram showing the breakup modes as a function of the liquid Reynolds and Weber numbers [38]; (b) experimental studies showing the breakup transition from Rayleigh mechanism (top) to atomization (bottom) [39].

interface. This discontinuity generates a vortex sheet that may tend to grow the amplitude of a given perturbation [40]. On the other hand, RT instabilities are linked to a component of acceleration parallel to the interface (e.g., gravity), causing a pressure gradient that contributes to the baroclinic torque. The combined effect of these instabilities generates a cascade of liquid structures (i.e., lobes, holes, ligaments, bridges) prior to forming droplets. KH instabilities are responsible for growing the amplitude of surface perturbations while RT instabilities deform the liquid surface, generating the aforementioned liquid structures.

Jarrahbashi and Sirignano [24], Jarrahbashi et al. [25] and Zandian et al. [26–28, 35, 36] have analyzed in detail the breakup process and generation of liquid structures in the atomization regime for various incompressible configurations (e.g., round jet, planar sheet, round jet with a co-flowing gas) using direct numerical simulations. The early deformation of liquid jets is a problem involving a transition to turbulence as smaller liquid structures and flow scales are generated. Moreover, the analyzed configurations present liquid Reynolds numbers below 10,000 (see Figure 2.3). Examples of observed liquid structures and the cascade process are seen in Figure 2.2. The novelty introduced by these authors in the analysis is the approach to the problem from the point of view of vorticity dynamics. They show that the

generation of liquid structures is a consequence of interactions of hairpin vortices with KH vortices. Furthermore, different atomization domains are identified according to their flow characteristics (i.e., Reynolds and Weber numbers and density and viscosity ratios) and the breakup cascade type.

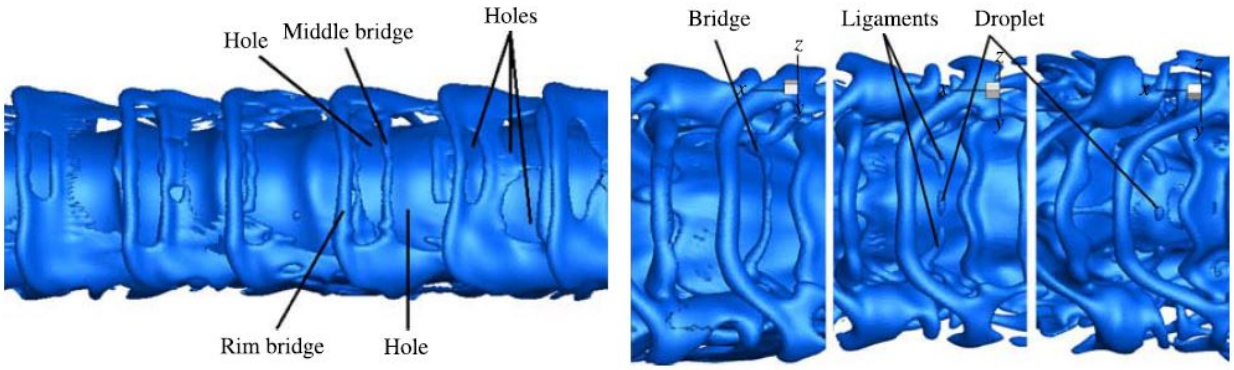

Figure 2.2: Generation of various liquid structures during the breakup cascade process of a round jet with $Re_l = 1.6 \times 10^3$, $We_l = 2.3 \times 10^5$ and $\rho_g/\rho_l = 0.5$ [25].

Jarrahbashi et al. [25] classifies the liquid breakup mechanisms for a round liquid jet using the liquid Reynolds number and the density ratio between gas and liquid phases. It is observed that domains where inertia forces become stronger at the liquid-gas interface (i.e., high Reynolds number and/or high density ratio) present different breakup characteristics than flows with lower inertia. However, Zandian et al. [26–28] use the liquid Reynolds number and the gas Weber number to identify three atomization domains with different formation of liquid structures prior to the liquid breakup into droplets (see Figure 2.3). The gas Weber number is used instead of the liquid Weber number to include density ratio effects in the classification. Otherwise, the transitional zone between the different atomization domains would move significantly in the diagram shown in Figure 2.3. Although the analysis is performed for the atomization of a planar liquid sheet, the identified domains can be generalized to other configurations [26]. As a reference for the reader, the categorization shown in Figure 2.1 would correspond to a very small region at the bottom-left corner of the diagram shown in Figure 2.3.

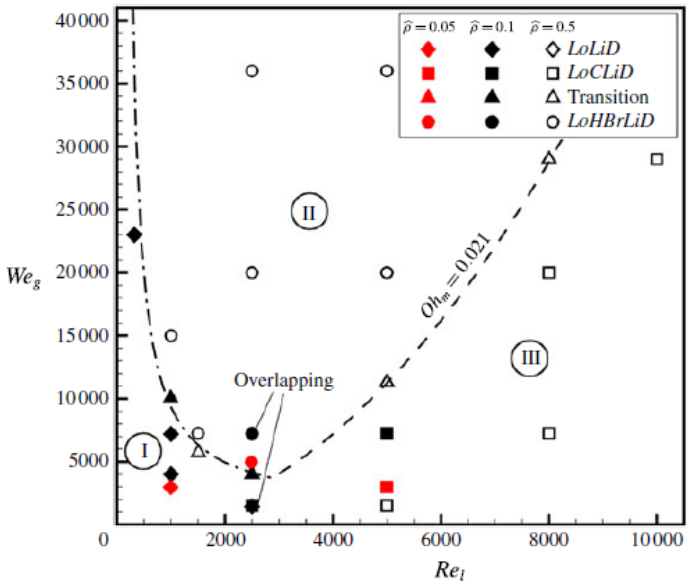

Figure 2.3: Diagram showing atomization domains I (LoLiD or Lobe-Ligament-Droplet), II (LoHBrLiD or Lobe-Hole-Bridge-Ligament-Droplet) and III (LoCLiD or Lobe-Corrugation-Ligament-Droplet) based on the liquid Reynolds number and the gas Weber number [26–28].

A sketch of the formation of liquid structures in each atomization domain is shown in Figure 2.4. Domain I (LoLiD or Lobe-Ligament-Droplet) is characterized by low liquid Reynolds numbers and low gas Weber numbers. That is, surface-tension forces are still important compared to inertia forces. The breakup process follows the formation and stretching of lobes, which eventually break up into large droplets due to capillary instabilities. The second domain, domain II (LoHBrLiD or Lobe-Hole-Bridge-Ligament-Droplet), has different behavior. As the lobes form, the increased inertia of the gas phase perforates the lobes. These perforations or holes increase in size, forming thin bridges that break up into ligaments. The ligaments end up separating from the liquid stream and breaking up into tiny droplets. Lastly, domain III (LoCLiD or Lobe-Corrugation-Ligament-Droplet) is similar to domain I but with enhanced inertia effects on the liquid-gas interface. In this case, the lobes present corrugations that are stretched into ligaments. Like in domain II, these smaller structures separate from the liquid surface and end up breaking up into smaller droplets than domain I.

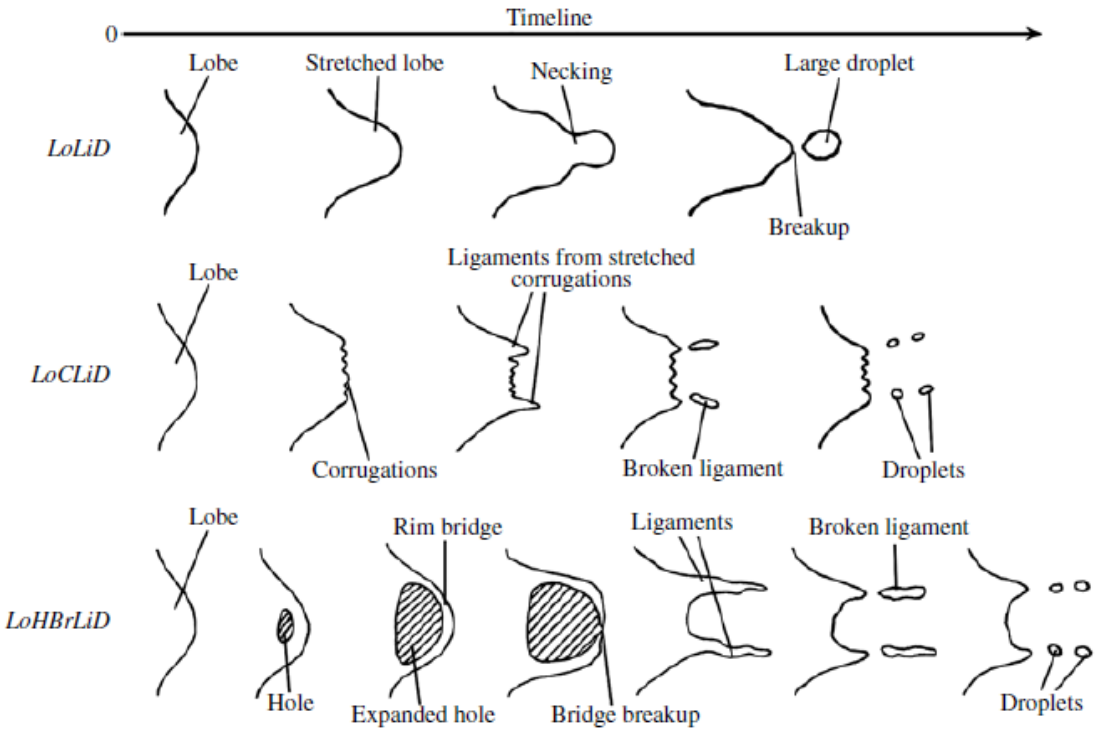

Figure 2.4: Cascade of liquid structures in the atomization domains I (LoLiD or Lobe-Ligament-Droplet), II (LoHBrLiD or Lobe-Hole-Bridge-Ligament-Droplet) and III (LoCLiD or Lobe-Corrugation-Ligament-Droplet) [26–28].

Although these works solve the incompressible Navier-Stokes equations, conditions reminiscent of high-pressure environments are analyzed (e.g., high density ratios due to a compressed gas phase, reduced surface tension, or high Weber numbers). In these situations, the inertia of the gas phase increases, and interfacial forces on the liquid-gas interface become weaker. Vortical structures concentrate closer to the rim of the lobes, and the liquid stream's hole formation rate or perforation increases (domain II). The combined effect results in a rapid formation of thinner bridges and ligaments, which are quickly stretched away from the liquid core and eventually break up into tiny droplets due to capillary instabilities (see Figure 2.5). Thus, the radial development of the two-phase mixture is enhanced with an early formation of tiny droplets.

These incompressible results already suggest that real-engine configurations are dominated by very fast atomization of the liquid fuel. Nonetheless, high-pressure effects must be de-

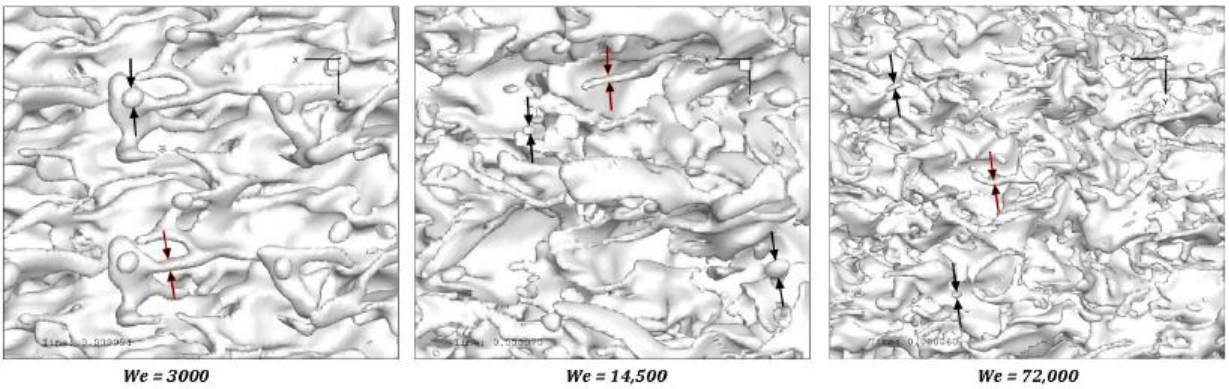

Figure 2.5: Formation of ligaments and droplets in a planar liquid sheet varying We_l fixing all other parameters [35].

scribed in detail to fully understand the physics involved in the injection process in real engines.

2.1.1 Vortex dynamics

The breakup mechanisms shown in Jarrahbashi and Sirignano [24], Jarrahbashi et al. [25], and Zandian et al. [26, 27, 35, 36] can be explained via vortex dynamics. These studies determine topology changes during the breakup process of the liquid surface from the information of the local rotation of fluid particles (i.e., linked to flow vorticity $\vec{\omega} = \nabla \times \vec{u}$) and the interaction of vortex structures. Particularly revealing are the results presented in Zandian et al. [27] where vortex structures are identified using the λ_2 method from Jeong and Hussain [41] and their detailed interactions are shown to be responsible for the cascade of liquid structures summarized in Figure 2.4.

The λ_2 method identifies a vortex based on searching for a local pressure minimum in a plane crossing the vortex. An equation for the pressure Hessian is obtained by taking the gradient of the momentum equation and by removing the terms related to unsteady straining of the fluid and viscous effects since they might generate pressure minima without a vortex being present. After these simplifications, the negative pressure Hessian is approximated

by the sum of the strain-rate tensor squared, $\bar{\bar{S}}^2$, and the vorticity tensor squared, $\bar{\bar{\Omega}}^2$. A local pressure minimum in a plane is identified if the pressure Hessian tensor must have two positive eigenvalues or, in other words, a vortex is defined as a connected region with two negative eigenvalues of $\bar{\bar{S}}^2 + \bar{\bar{\Omega}}^2$. If, in general, the eigenvalues of a 3x3 matrix are ordered as $\lambda_1 \geq \lambda_2 \geq \lambda_3$, two negative eigenvalues exist when $\lambda_2 < 0$.

Although a local pressure minimum is not a necessary nor sufficient condition for the existence of a vortex [42], the method is more suitable for the type of flows this dissertation aims to solve. Moreover, a compressible formulation based on the λ_2 method exists, called the dynamical vortex identification method or λ_ρ [43], which is indicated for the non-ideal compressible fluid behavior observed at high pressures. Another widely-used vortex identification method is the Q-criterion [44]. However, this method may be inconsistent for vortices subject to strong external strain, such as in atomization studies, and have an ambiguous extension to compressible flows [42].

Figure 2.6 describes how the interaction of vortex structures is responsible for the different breakup mechanisms shown in Figure 2.4 and detailed in the works by Zandian et al. [26–28]. The different atomization domains can be explained by understanding how hairpin vortices generated along the liquid surface interact with the primary KH vortex or roller vortex. The KH vortex is generated due to the velocity gradient normal to the liquid-gas interface or velocity shear and is located downstream of the wave crest. The velocity field induced by the KH vortex is responsible for the elongation of lobes on the liquid surface. Then, the hairpin vortices intertwine with the primary KH vortex in different manners, causing different breakup mechanisms to occur.

The LoLiD domain (see Figure 2.6a) shows vortex interactions that do not affect the lobe's shape significantly; thus, the lobe extends until capillary forces can generate lobe thinning and neck formation that yields to droplet formation. On the other hand, vortex interactions in the LoCLiD and LoHBrLiD domains (see Figures 2.6b and 2.6c, respectively) occur right

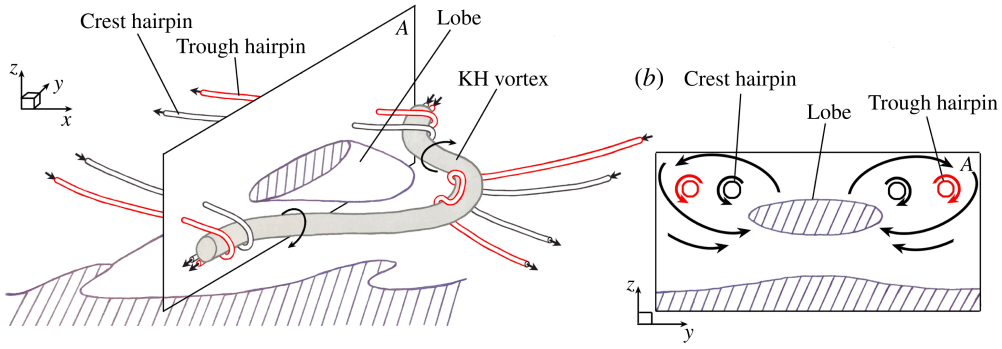

(a) LoLiD domain

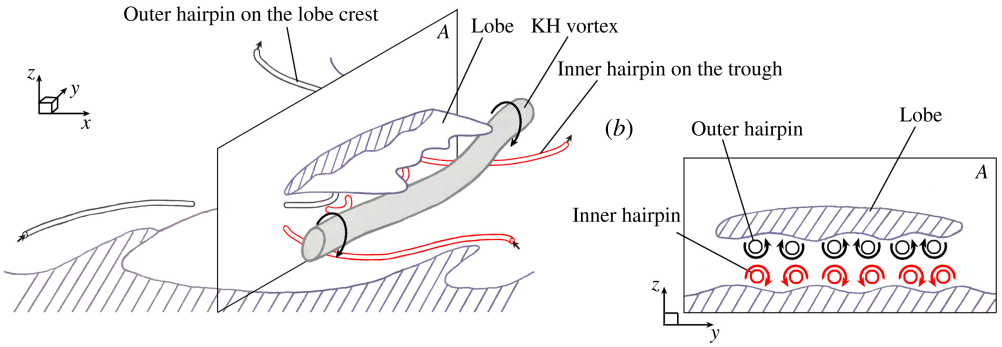

(b) LoCLiD domain

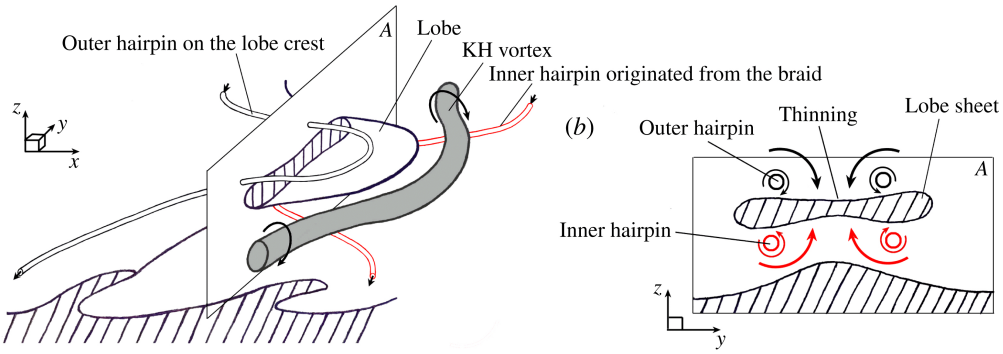

(c) LoHBrLiD domain

Figure 2.6: Interaction of vortex structures responsible for the breakup mechanisms defining the atomization domains identified in the works by Zandian et al. [26–28]. (a) LoLiD domain; (b) LoCLiD domain; (c) LoHBrLiD domain [27].

above and/or below the lobe. In both cases, the inner hairpin vortex located at the wave's trough displaces below the lobe, aided by the induced motion from the KH vortex. For the LoCLiD domain, the outer hairpin vortex located near the wave's crest moves below the lobe and interacts with the inner hairpin vortex. These interactions corrugate the vortices themselves, which induce corrugations on the edge of the liquid lobe, eventually stretching

small ligaments and forming droplets. For the LoHBrLiD domain, the outer hairpin vortex remains above the lobe's surface. The inner and outer vortices bend, inducing flow motion that directly pushes gas toward the liquid surface. This effect thins the lobe locally and eventually causes perforation of the liquid (i.e., hole formation). Later, the hole expands and forms bridges that eventually break up into small ligaments and droplets.

2.2 Transition to High-Pressure Injection

This section presents a qualitative and theoretical description of the thermodynamic transition typical liquid fuels experience as they are injected into high-pressure combustion chambers above the fuel's critical pressure.

Table 2.1 shows the critical properties (i.e., critical pressure, p_c; critical temperature, T_c; and critical density, ρ_c) of the species of interest in these applications and that are reviewed in the following pages. The focus is on heavy liquid hydrocarbons (e.g., n-decane) that can be used as pure fuels but also exist in large quantities in typical hydrocarbon-based fuels such as kerosene or diesel fuel. Moreover, these fuels are injected into an oxidizer, such as pure oxygen or air. Thus, gases such as oxygen or nitrogen are dominant inside the combustion chamber.

Table 2.1: Molecular weight (W), critical properties and acentric factor, ω, of n-octane, n-decane, n-dodecane, oxygen and nitrogen. Source: NIST.

Species	W (kg/mol)	p_c (bar)	T_c (K)	ρ_c (kg/m^3)	ω
C_8H_{18}	0.114230	24.97	569.32	234.90	0.3950
$C_{10}H_{22}$	0.142280	21.03	617.70	233.34	0.4884
$C_{12}H_{26}$	0.170330	18.20	658.00	226.55	0.5740
O_2	0.031999	50.43	154.58	436.14	0.0222
N_2	0.028013	33.98	126.19	313.19	0.0372

Subsection 2.2.1 presents experimental works that have dealt with high-pressure liquid injection in single-component and multi-component configurations, and Subsection 2.2.2 presents a review about the high-pressure thermodynamics that define the two-phase problem.

2.2.1 Experimental work

The atomization of a liquid jet changes drastically as pressure increases. Low-pressure atomization presents clear structures developing on the liquid surface that eventually break up into droplets. However, at operating pressures for many combustion applications, the full picture of the injection of liquid fuels resembles a turbulent gas jet. As discussed in Section 1.2, these pressures are often above the critical pressure of the liquid fuel. Therefore, this behavior has been wrongly described as a very rapid transition of the liquid phase to a supercritical gas-like state dominated by diffusive mixing [8, 9].

The complexity of liquid atomization at high pressures requires a review of the classical breakup mechanisms coupled with non-ideal thermodynamics. Experimental works show a clear change in behavior as pressure increases up to supercritical values. Cold-flow studies (i.e., low temperature with no chemical reactions) of injection of cryogenic propellants at different pressure conditions are shown in Mayer et al. [2]. Similar studies are those of Mayer and Tamura [1], Mayer et al. [3], Chehroudi et al. [45, 46], Oschwald et al. [4] and Chehroudi [5].

Figure 2.7 shows a full-scale experiment where a cold stream of liquid nitrogen is injected into a chamber filled with gaseous nitrogen at a higher temperature. Pressure varies from subcritical values to supercritical values, while all other conditions remain fixed. Nitrogen has approximately a critical pressure of $p_c = 34$ bar and a critical temperature of $T_c = 126.2$ K. At low pressures, the formation of lobes and capillary instabilities can be identified. As pressure nears the critical value and the surface-tension coefficient weakens, faster atomization is

observed. Thin ligaments form and tiny droplets are ejected from the liquid core. This observation is consistent with the results from the numerical studies discussed in Section 2.1 where inertia forces become dominant. Once the pressure is supercritical, no clear liquid structures nor droplets are observed, and the injection process is dominated by turbulent mixing.

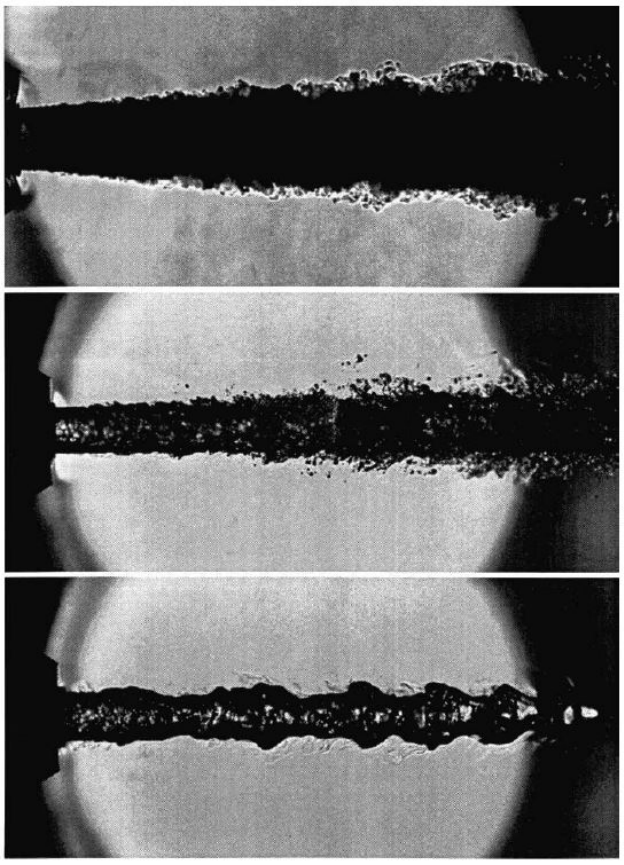

Figure 2.7: Injection of liquid nitrogen into gaseous nitrogen at a supercritical pressure of 4 MPa (top image), a near-critical pressure of 3 MPa (center image) and a subcritical pressure of 2 MPa (bottom image) [2].

This experiment is a simplified approach to supercritical liquid injection since both liquid and gas are the same pure component (i.e., nitrogen). In this specific case, the liquid phase will eventually transition to a supercritical state provided that the gaseous nitrogen is at a sufficiently high temperature. Nevertheless, no information is known a priori about the characteristic times of each physical process. For example, is the phase transition faster than

the liquid disruption in a dense and reduced surface-tension environment? Therefore, it might be misleading to state that atomization is no longer a relevant mechanism at supercritical pressures because of a fast transition to a supercritical state.

This observation is even more relevant in combustion applications where fuel and oxidizer have different components (e.g., a mixture of hydrocarbons as fuel and air as oxidizer). The mixing process occurring near the liquid-gas interface modifies the critical fluid properties of the mixtures, generating a more complex situation. In this scenario, it is common for the mixture critical pressure to be above the chamber pressure. These changes allow the liquid-gas interface to appear and disappear (i.e., diffuse) as the local mixture composition varies (see Figure 2.8). Further discussion about conditions driving phase separation is provided in Subsection 2.2.2.

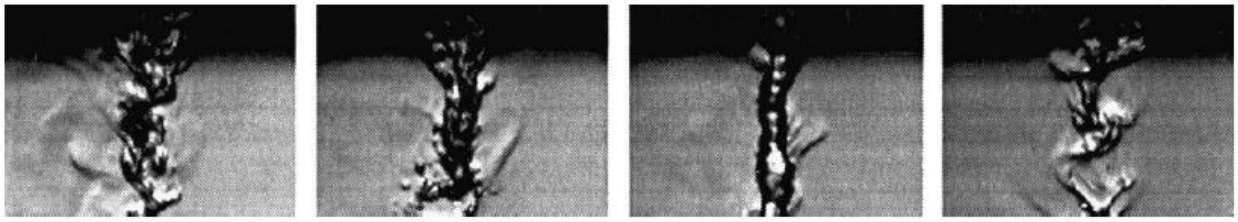

Figure 2.8: Injection of liquid nitrogen into gaseous helium at a supercritical pressure of 5.5 MPa. At a fixed position, the liquid-gas interface is seen to appear and disappear (i.e., diffuse) as both species mix [2].

Falgout et al. [6] performed experiments injecting pure hydrocarbons and diesel fuel into air at supercritical pressures. A similar turbulent-like structure as in Figure 2.7 is observed, although now there is multi-component mixing. Figure 2.9 shows ballistic images and shadow images of diesel fuel injected at different conditions. In all cases, the diesel fuel is approximately injected at 400K. The critical properties of n-dodecane, $C_{12}H_{26}$, are used to estimate the critical properties of diesel fuel (i.e., $p_c = 18.2$ bar and $T_c = 658$ K). n-dodecane is a major component of diesel fuel, whose average formula is $C_{12}H_{23}$.

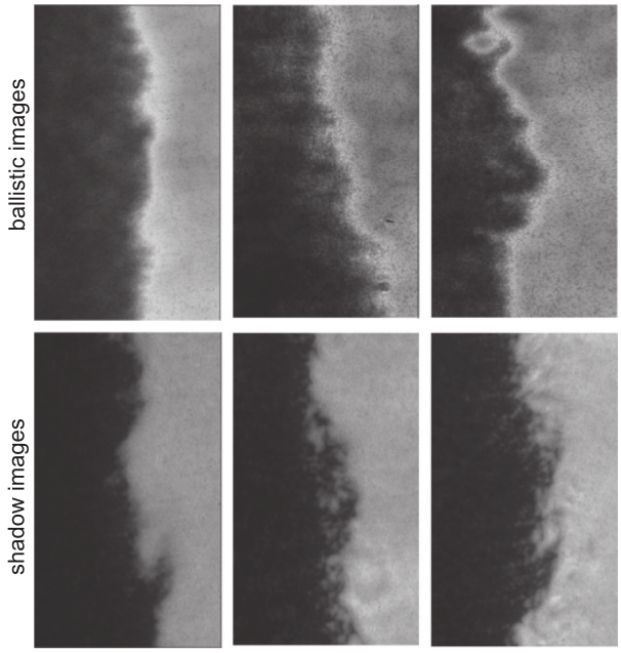

Figure 2.9: Injection of diesel fuel into air at supercritical pressures. Case 1 at 450 K and 30 bar (left); Case 2 at 675 K and 45 bar (center); and Case 3 at 900 K and 60 bar (right) [6].

In Figure 2.9, Case 1 belongs to a slightly supercritical pressure for the diesel fuel (i.e., a reduced pressure of $p_r = p/p_c \approx 1.65$) while the ambient temperature is well below the critical temperature. Under these conditions, ballistic images look fuzzy, and no liquid-gas interface can be identified. However, shadow images indicate classical spray structures and droplet clouds. Here, a two-phase behavior can be maintained near the interface at supercritical pressures because phase equilibrium enhances the dissolution of air into the liquid, which causes a change in mixture critical properties [15]. Moreover, the low-temperature environment ensures that the liquid-gas interface cannot transition to a supercritical state.

A diffusive behavior can be observed in Case 2 and Case 3. The diesel fuel is subject to moderate supercritical pressure in Case 2 (i.e., $p_r \approx 2.47$) while the ambient temperature is close to the critical temperature. The interface becomes more challenging to identify, and shadow images do not show clear spray structures, but some Schlieren structures are distinctive of more significant density gradients around the injected fuel. At these conditions, a two-phase interface can still exist. However, higher interface temperatures will reduce

the magnitude of the sharp discontinuities across the interface (i.e., density), and enough heating might cause a transition of the interface from a two-phase behavior under local thermodynamic equilibrium to a supercritical diffuse mixing between fluids.

Lastly, Case 3 presents a higher supercritical pressure with $p_r \approx 3.30$ with the ambient temperature well above the critical temperature of the diesel fuel. Under this configuration, ballistic images nor shadow images show clear indications of a two-phase behavior. Moreover, shadow images present similarities with Case 2, where a higher presence of Schlieren structures is observed, indicating that diffusive mixing at such high pressures has a more substantial impact on the fluid density. These results might indicate that the interface has been heated enough to transition to a supercritical diffuse mixing state. Nevertheless, there is no information on the actual interface temperature. The liquid fuel is still being injected at a relatively low temperature, absorbing substantial amounts of heat. Therefore, the interface temperature of the liquid core can still be substantially low, while smaller ligaments and droplets detaching from the main jet can be heated faster and transition to a supercritical state.

Current imaging techniques have difficulties penetrating dense sprays [20]. A large number of small droplets generate a lot of scattering or noise, which is hard to filter out. The presence of diffusion layers with variable fluid properties adds to the complexity of the problem since wave refractions will occur in a changing medium, affecting the propagation of light or laser beams used in the experiment. The high-pressure regime may induce very fast atomization following the trend shown in incompressible simulations (see Section 2.1). The atomization might still be driven by two-phase interactions, while tiny droplets form a cloud. The picture here gets complicated as non-ideal thermodynamics and phase equilibrium are involved: some droplets might transition to a supercritical state and some might vaporize, while species diffuse and change mixture fluid properties all around. Therefore, the main liquid core may be hidden underneath a cloud of tiny droplets inside a diffusive environment,

and the proper imaging technique is yet to be proposed. Some new experimental techniques are being developed to capture this type of flows [20–23].

Further evidence of this transcritical behavior is presented in Crua et al. [7]. Various fuels are injected at diesel-engine relevant conditions and show the existence of two-phase atomization and droplets in hot environments at supercritical pressures for the fuel. Figure 2.10 shows the behavior of isolated droplets formed during the injection of n-dodecane into an ambient gas composed of hot combustion products of a previous premixed combustion reaction (i.e., nitrogen, carbon dioxide, and water).

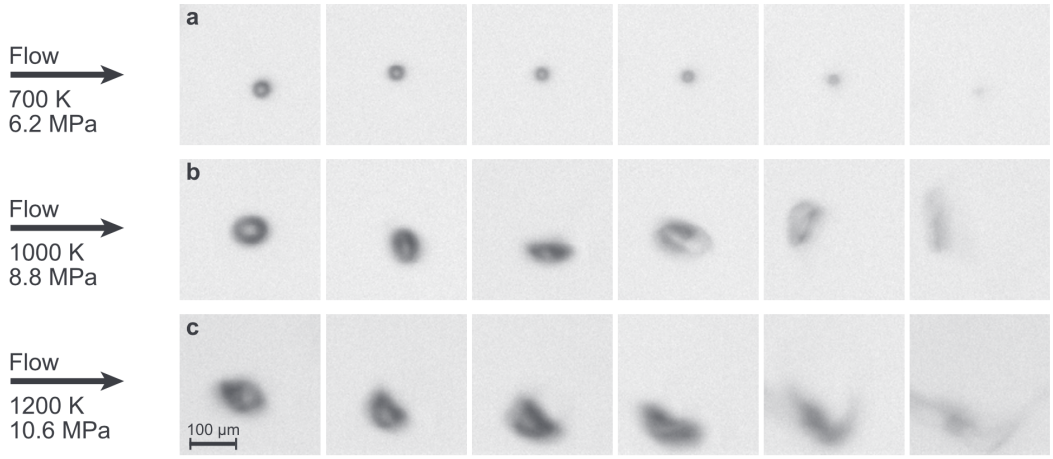

Figure 2.10: Droplet behavior after the injection of n-dodecane fuel into a hot mixture of reaction products at supercritical pressures. Case (a) at 700 K and 62 bar (top); Case (b) at 1000 K and 88 bar (middle); and Case (c) at 1200 K and 106 bar (bottom) [7].

Case (a) shows the classical evaporation of a spherical droplet where surface-tension forces are apparent. At these temperatures slightly above the critical temperature of the fuel (i.e., a reduced temperature of $T_r = T/T_c \approx 1.06$), a two-phase problem exists. Only at the late stages of the droplet evaporation, once the liquid mixture has been heated closer to the ambient gas temperature, the liquid mixture might experience a diffuse transition to a supercritical state. In Cases (b) and (c), higher pressures translate into an enhanced dissolution of the ambient gas into the liquid [15]. Thus, liquid and gas have similar properties near the interface, reducing surface-tension forces. The fluid motion strongly affects the droplets, and

they quickly lose their spherical shape. Because of the higher ambient temperatures, the liquid phase heats faster than in Case (a), and eventually, the interface reaches a supercritical state where liquid and gas mix in a diffuse manner.

2.2.2 High-pressure thermodynamics

The experimental results discussed in Subsection 2.2.1 highlight the physical complexity of liquid fuel injection at supercritical pressures and hot environments (e.g., in a combustion chamber). Jofre and Urzay [47] present a comprehensive analysis of this type of flow and address both flow dynamics and thermodynamic considerations. Figure 2.11 shows a schematic of the various thermodynamic regimes that are reached during the injection of liquid fuels in combustion chambers at supercritical pressures for the fuel.

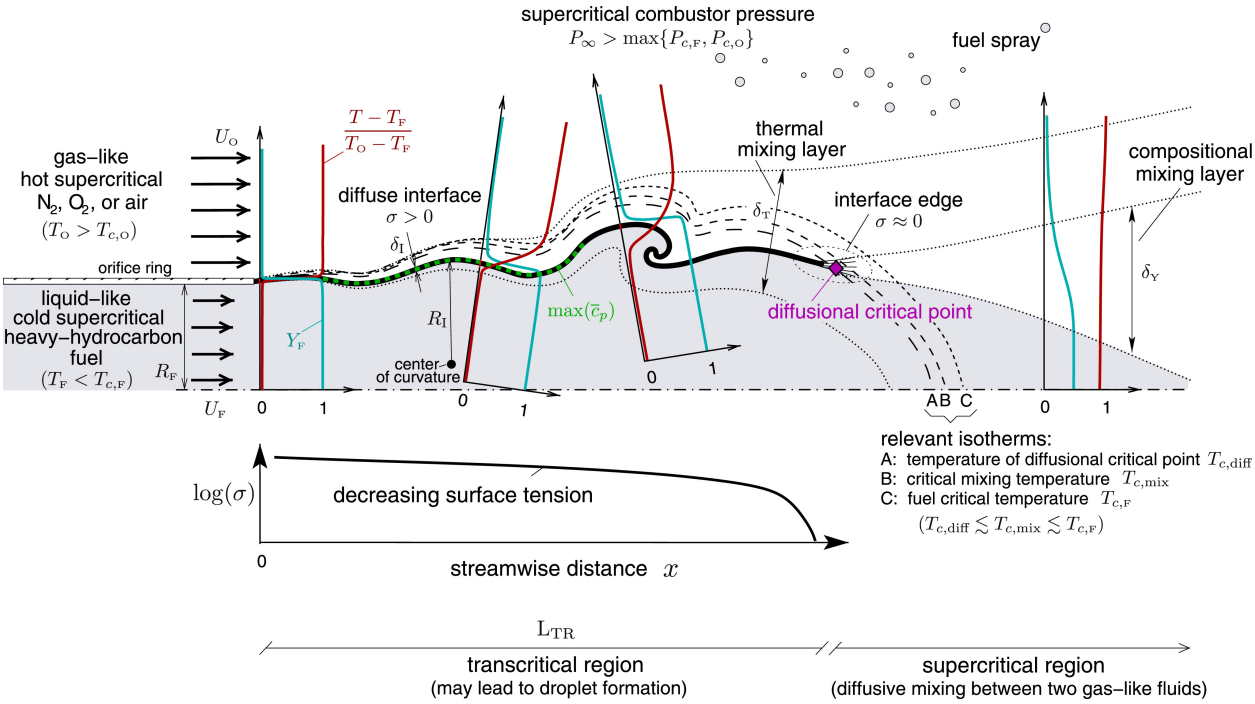

Figure 2.11: Schematic showing the thermodynamic transition of a liquid fuel injected into a chamber with a supercritical ambient pressure and high ambient temperature able to heat up the liquid mixture beyond its critical temperature [47].

Initially, the liquid is injected at relatively low temperatures, well below the fuel critical temperature. Local thermodynamic phase equilibrium or LTE prevails, and a two-phase problem exists with heat and mass exchange across the liquid-gas interface. At this point, the liquid fuel is experiencing a transcritical environment characteristic of the early stages of the injection process, where the surface-tension coefficient and the heat of vaporization remain within finite values. Both real fluids are compressible at these high pressure and do not behave ideally. Therefore, a proper equation of state and other models and correlations must be used to represent the non-ideal fluid [18, 33, 34].

Phase-equilibrium diagrams are shown in Figure 2.12 for binary mixtures of n-octane/oxygen and n-decane/oxygen. These diagrams are obtained using the Soave-Redlich-Kwong (SRK) equation of state [48] (see Subsection 3.3.1 for more details) and show the fuel mole fraction at the interface, both for the liquid side and the gas side, as a function of the interface temperature and pressure. The reduced pressure based on the critical pressure of the fuel is used. Note that a maximum temperature exists for a given pressure beyond which two phases cannot be sustained. That is, a mixture critical temperature can be identified as a function of pressure. For a formal definition of local thermodynamic phase equilibrium, see Subsection 3.3.4.

At low pressures (i.e., below the fuel critical pressure), oxygen dissolution into the liquid phase is negligible. Therefore, mixture properties are little changed. However, oxygen dissolution is enhanced as pressure increases beyond the fuel critical pressure, and the mixture critical properties near the interface change considerably. In this case, the critical pressure of the liquid mixture may be above the ambient pressure, and a distinct two-phase environment is maintained. If the critical pressure of the liquid mixture at equilibrium is lower than the ambient pressure, the fluid should be better described as a compressed liquid that can still maintain a two-phase behavior under the interface balance provided by phase equilibrium [15].

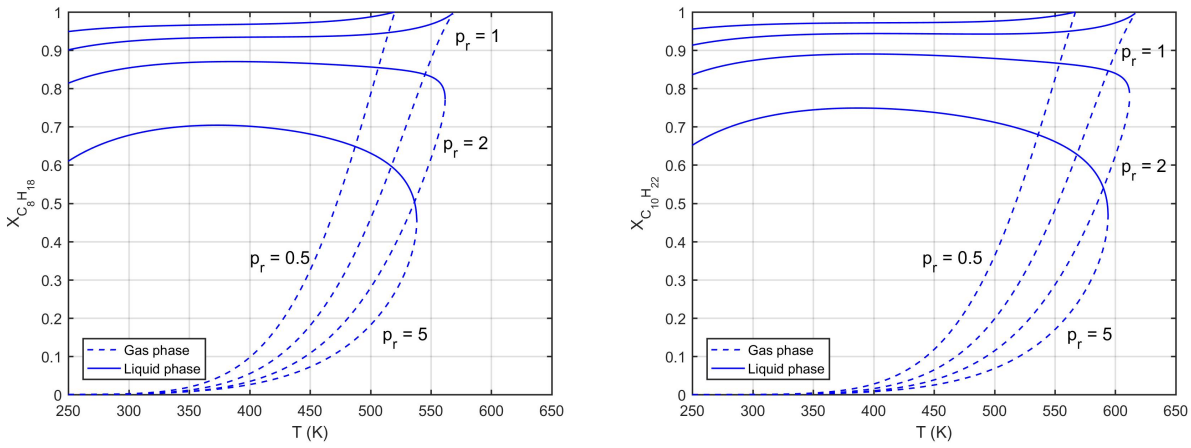

(a) (b)

Figure 2.12: Phase-equilibrium diagrams obtained with the Soave-Redlich-Kwong equation of state. Diagrams show the mole fraction of the fuel as a function of temperature and reduced pressure, $p_r = p/p_{c,\text{fuel}}$. (a) n-octane/oxygen; (b) n-decane/oxygen [15].

Poblador-Ibanez and Sirignano [15] provide estimates of the mixture critical properties of the binary pairs n-octane/oxygen and n-decane/oxygen based on the methodology proposed by Chueh and Prausnitz [49] and a methodology based on analyzing phase-equilibrium diagrams in search for the mixture critical point. The shape of these diagrams depends on the specific equation of state used in the model (i.e., the SRK equation of state in this work), which affects the predicted mixture critical point. The latter method is a graphical interpretation of the analytical approach used to evaluate mixture critical points [50].

Figure 2.13 shows the mixture critical pressure and temperature as a function of the oxygen mole fraction predicted from Chueh and Prausnitz [49]. The critical temperature decreases monotonically from the fuel critical temperature to the oxygen critical temperature as the concentration of oxygen in the mixture increases. Therefore, the temperature range where two distinct phases coexist is reduced as pressure increases. On the other hand, the mixture critical pressure follows a different trend. It increases as more oxygen is present in the mixture, but instead of following a monotonic increase, it peaks around $X_{O_2} = 0.9$ (not shown in Figure 2.13a for the sake of a good y-axis scale). The model by Chueh and

Prausnitz [49] might not be accurate enough, especially at higher oxygen concentrations where critical pressures well above 500 bar are predicted. Instead, the methodology based on the phase-equilibrium diagram presented in Poblador-Ibanez and Sirignano [15] predicts more reasonable critical pressures for the mixtures with higher oxygen concentration.

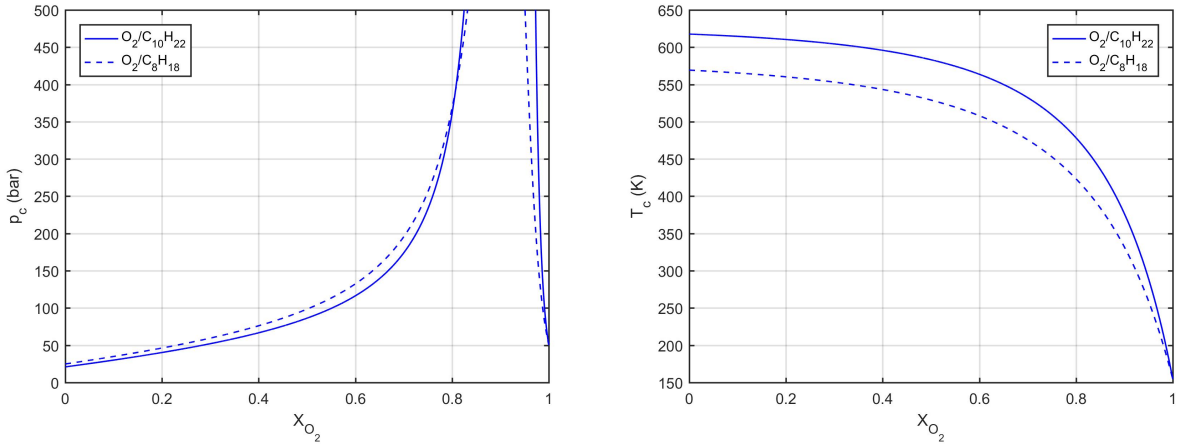

(a) (b)

Figure 2.13: Mixture critical properties of binary mixtures composed of n-octane/oxygen and n-decane/oxygen as a function of mixture composition obtained using the methodology by Chueh and Prausnitz [49]. (a) critical pressure; (b) critical temperature [15].

The issues in accurately predicting mixture critical points highlight the importance of certain aspects of non-ideal fluid modeling. Questions about what equation of state to use, what mixing rules need to be implemented in the equation of state, or how to estimate binary interaction coefficients if experimental data is scarce become important. Moreover, the answers to these questions can also affect the prediction of more essential fluid properties such as density.

This transcritical regime is sustained if the interface temperature is below the mixture critical temperature at the given chamber pressure. For example, Figure 2.12b shows that the SRK equation of state predicts a mixture critical temperature for n-decane/oxygen around 590 K for a reduced pressure of $p_r = 5$, which is equivalent to a pressure of 105.15 bar. The hot ambient gas heats the liquid phase during this stage, and the interface temperature

rises. Thermal and mass diffusion layers grow on both sides of the interface, where mixing also affects the fluid properties of each phase. Two-phase dynamics still play a role in the evolution of the liquid jet, generating typical liquid structures and droplets.

As shown in Figure 2.11, the continuous heating of the interface causes the already reduced surface-tension coefficient to drop even further and eventually disappear once the interface has reached the mixture critical temperature. Following a phase-equilibrium diagram at high pressure, such as the case with $p_r = 5$ in Figure 2.12b, the increase in temperature toward the mixture critical temperature enhances the dissolution of oxygen into the liquid phase and the vaporization of n-decane. This trend results in liquid and gas looking more alike (e.g., similar composition and similar density), effectively reducing the surface-tension forces at the liquid-gas interface. This variation in the surface-tension coefficient of transcritical jets is an important feature that needs to be analyzed in detail. The magnitude of the surface-tension coefficient and its variations will define the relative importance of inertia forces over capillary forces and how violently the liquid jet can atomize under these conditions.

Once the interface reaches the mixture critical temperature, two phases cannot be identified, and a diffuse mixing transition with sharp gradients of fluid properties exists. Here, surface-tension forces and the heat of vaporization have entirely vanished, and the fluid has become supercritical.

Jofre and Urzay [47] discuss stability concerns for the multi-component mixture. Three different criteria for the stability of the mixture can be defined in terms of thermal stability (i.e., molar heat at constant volume must be positive), mechanical stability (i.e., isothermal compressibility must be positive), and diffusional stability. If a system is diffusional stable, it is also mechanically and thermally stable [47].

The criteria to determine if a mixture is diffusional stable is directly related to the non-ideal thermodynamic factor, Γ_{11} for a binary mixture, that must be included when evaluating

the mass diffusion coefficient (see Subsection 3.3.3). For $\Gamma_{11} > 0$, the system is diffusional stable, and diffusion of a species occurs in the direction of decreasing concentration. If $\Gamma_{11} < 0$, diffusion would occur in the direction of increasing concentration. This situation of phase instability leads to phase separation and the appearance of transcritical interfaces at a given pressure, temperature, and composition. As shown in Figure 2.11, this stability criterion can be used to define a diffusional critical point beyond which phase separation does not happen due to reversed diffusion. That is, the diffusional critical temperature, $T_{c,\text{diff}}$, is the maximum temperature of the diffusional unstable region at a given pressure. Jofre and Urzay [47] show that the difference between the diffusional critical temperature and the mixture critical temperature is at most 5 K for n-dodecane/nitrogen mixtures in the range of 50-200 bar.

Below the mixture critical temperature (or the diffusional critical temperature) at a given pressure, the phase-equilibrium envelope is unconditionally stable, as well as any other thermodynamic state outside this enclosed space [47]. Therefore, the establishment of a liquid-gas interface at equilibrium and the subsequent mixing occurring in both phases provides diffusional stable mixtures as long as there are no substantial disturbances in the flow (e.g., chemical reactions that modify the local temperature or composition, significant pressure variations). In other words, the interface acts as a limiting boundary for the liquid mixture and gas mixture compositions.

Other considerations that might limit the applicability of phase equilibrium at the interface relate to the time scales of the physical processes and the internal structure of the phase non-equilibrium transition region between both phases. The first issue might be problematic if the relaxation time required for the interface to reach an equilibrium state is of the same order (or more) than the dynamical time scales (e.g., how fast the interface deforms). The results presented in Poblador-Ibanez and Sirignano [15] for one-dimensional transient flow around a liquid-gas interface at high pressures show that interface properties under phase equilibrium

reach a quasi-steady-state solution very fast in time (see Subsection 2.3.2). Starting from harsh initial conditions, interface values such as the interface temperature reach a steady value in less than 10 μs. Nonetheless, the temperature rate of change over time becomes negligible after 0.2 μs to 0.7 μs while diffusion mixing layers grow on both sides of the interface. Other interface properties follow a similar behavior. This observation suggests that the interface can reach an equilibrium solution as it deforms under the influence of the fluid dynamics, as long as small perturbations of the equilibrium state are induced from an instant of time to the following.

The structure of the phase non-equilibrium transition region between liquid and gas is described in detail in Dahms and Oefelein [29–31] and Dahms [32]. In these works, the linear gradient theory is used to estimate the thickness of the phase non-equilibrium region and compare it to the molecular mean free path of the vapor phase. Using the Knudsen number, the ratio between the molecular mean free path and the interface thickness, a criterion where $Kn < 0.1$ is established to determine when the interface enters a continuum domain where phase-equilibrium is no longer able to represent the interface state.

At transcritical conditions where pressure is supercritical for the pure liquid, but the temperature is below the mixture critical temperature (i.e., subcritical), the interface non-equilibrium region has a thickness of a few nanometers. Values no larger than 8 nm are shown for typical hydrocarbon/nitrogen mixtures such as n-dodecane/nitrogen [29–32]. As shown in Figure 2.14, the interface thickness increases exponentially as it approaches the mixture critical temperature (i.e., it increases with temperature). Notice that, in Figure 2.14, the reduced temperature is provided in terms of the liquid mixture critical temperature, which is a function of pressure as described in previous lines and seen in Figure 2.12.

On the other hand, the molecular mean free path of the vapor phase at the interface increases with temperature [29] and, as seen in Dahms and Oefelein [29], Poblador-Ibanez and Sirignano [15], Davis et al. [16], and Poblador-Ibanez et al. [17], the interface equilib-

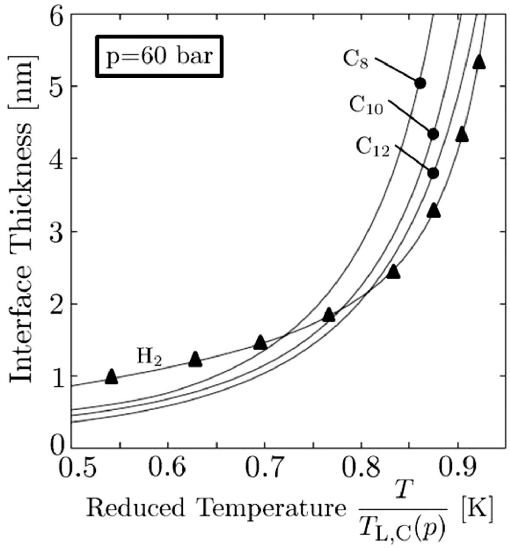

Figure 2.14: Estimated interface thickness at 60 bar as a function of interface temperature for different binary configurations. The interface temperature is expressed as a reduced temperature using the mixture critical temperature. H_2 corresponds to the hydrogen/LOX mixture; C_8 corresponds to the n-octane/nitrogen mixture; C_{10} corresponds to the n-decane/nitrogen mixture; and C_{12} corresponds to the n-dodecane/nitrogen mixture [30].

rium temperature increases with pressure. However, higher pressures can compress the fluid and present a dominant effect where the molecular mean free path is reduced considerably. Therefore, it becomes more likely that the interface might enter a continuum domain near the mixture critical point as pressure increases. In this case, the interface thickness might be orders of magnitude larger than the molecular mean free path and a diffuse variation of fluid properties across the interface is possible, albeit with sharp gradients, even before reaching the mixture critical state. Following this non-equilibrium transition, assumptions made under the phase-equilibrium model, such as liquid and gas having the same temperature at the interface, are no longer valid. At lower interface temperatures, phase equilibrium is well established.

Nonetheless, making an analogy with compressible flows, the non-equilibrium layer thickness across a shock wave is at least an order of magnitude greater than the thickness of the phase non-equilibrium layer. For practical purposes, it is treated as a discontinuity. Therefore, even if the interface enters a continuum, the liquid-gas interface could still be treated as

a discontinuity with a different set of boundary conditions given by phase non-equilibrium before diffusive mixing enlarges the phase-transition region.

Another issue to consider is the interface heat transfer efficiency or thermal resistivity as discussed in Stierle et al. [51]. If the internal interface structure presents a poor heat transfer efficiency, a non-negligible temperature jump across the phase non-equilibrium transition region exists, which needs to be accounted for. Thus, LTE is no longer a valid assumption, and the non-equilibrium transition region has to be modeled. Note that this condition does not imply that the transition layer has entered the continuum as in the works by Dahms and Oefelein [29–31] and Dahms [32]. The fluids of interest for this dissertation present relatively small thermal conductivities at the interface. Nevertheless, an estimation of the temperature jump across the interface discussed in Davis et al. [16] shows that the temperature jump can be neglected when compared to the magnitude of the expected interface equilibrium temperatures. Further details on the validity of the two-phase LTE interface model for the problems analyzed in this dissertation are provided in Section 3.1.

The temperature range of two-phase coexistence at real-engine conditions decreases considerably as pressure increases beyond the critical pressure of the injected fuel. Suppose the interface temperature is close to or above the mixture critical temperature. In that case, the phase transition will be driven by diffusive mixing, either because the interface becomes supercritical or because the molecular mean free path of the gas phase is substantially smaller than the non-equilibrium interface thickness. Other discussed issues also play a role in identifying the two-phase behavior (e.g., diffusional stability). These features must be considered and analyzed before using a two-phase model to study liquid fuel injection at high pressures. That is, a clear domain of application and its limitations must be defined appropriately.

Given the complexity of transcritical flows, other works have focused on analyzing the injection of liquid fuels at conditions well above the thermodynamic domain of two-phase coexistence. For instance, Zhang et al. [52] and Wang et al. [53] analyze the injection of

liquid kerosene into hotter gaseous oxygen at supercritical pressures without identifying a phase interface. Chamber pressure is set well above the critical pressure of the analyzed fuel at 253 bar, and the lower temperature is range-bound by the injection temperature of the liquid of 492 K. Thus, two phases cannot coexist for this specific configuration.

2.3 One-Dimensional Liquid-Gas Interface at Supercritical Pressures

A transient study of a one-dimensional liquid-gas interface at supercritical pressures for the pure liquid is performed in Poblador-Ibanez and Sirignano [15]. The one-dimensional configuration does not consider interface instabilities and focuses the study on the diffusive mixing process that occurs at high pressures. The interface location remains fixed for simplicity, and the diffusion-driven problem is solved relative to the interface location. Pressure is assumed to be constant everywhere in the domain. Thus, the velocity field can be obtained directly from the continuity equation, and there is no need to solve the momentum equation. Only binary configurations are considered where the pure liquid fuel is either n-octane or n-decane and the pure gas is oxygen. A schematic of the problem and its configuration is shown in Figure 2.15. Similar work is that of He and Ghoniem [54], where a sharp interface method is presented to solve multiphase flows with heat and mass transfer across the interface in a one-dimensional spherical configuration. The momentum equation is also omitted as pressure is almost constant throughout the domain.

Initially, the liquid starts at 450 K and is composed of pure hydrocarbon, while the gas starts at 550 K and is composed of pure oxygen. The analyzed pressures range from subcritical to supercritical values for the fuel (i.e., 10, 50, 100, and 150 bar). Critical properties of the involved species are shown in Table 2.1. The thermodynamic modeling for the real fluid

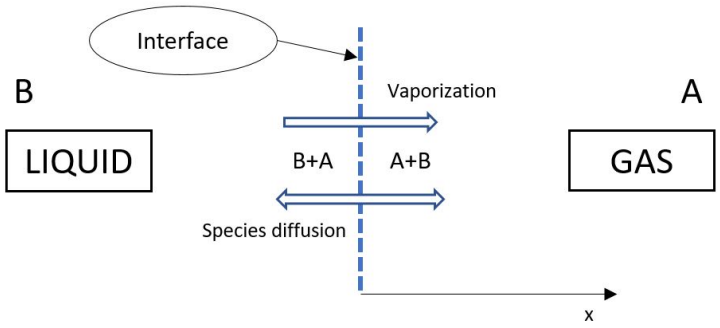

Figure 2.15: Sketch of the transient one-dimensional interface problem configuration. A and B relate to the pure gas species (i.e., oxygen) and the pure liquid species (i.e., hydrocarbon), respectively. The vaporization of the fuel is emphasized [15].

follows the same guidelines shown later in Section 3.3, but where the original SRK equation of state is used without the volume-correction term. That is, properties of the dense fluid (i.e., liquid), such as density, might be underestimated.

The study's goal is to confirm the coexistence of two phases at these high pressures and analyze how fast diffusion layers grow on either side of the interface. The importance of establishing characteristic times for the diffusion processes and the interface relaxation to thermodynamic equilibrium is already explained in Section 2.2. If phase equilibrium is well established before substantial disruption and heating of the liquid-gas interface, it is conceivable that high-pressure atomization is still a two-phase problem with a sharp interface immersed in a diffusive environment. Furthermore, a deep insight into the thermodynamic behavior of the interface and the diffusive region is provided.

2.3.1 Diffusive behavior near the interface

Phase-equilibrium diagrams for the analyzed mixtures are shown in Figure 2.12. As previously discussed, the dissolution of oxygen (or gas species) into the liquid phase is enhanced at supercritical pressures for the pure liquid species. A two-phase coexistence is verified for a given pressure up to a specific interface temperature (i.e., mixture critical temperature).

Therefore, mass diffusion of each species is relevant not only in the gas phase but also in the liquid phase.

Mixing or diffusion layers with clear variations in fluid properties are seen in Figure 2.16, where density profiles are plotted. As pressure increases, the liquid density drops considerably near the interface due to a combined effect of the enhanced dissolution of the lighter gas species and the interface temperature increase at higher pressures (see Subsection 2.3.2). The behavior of viscosity under this diffusive mixing is shown in Subsection 2.4.2. Higher pressures also cause an increase in pure liquid and gas densities, especially significant in the gas phase. At 10 bar and 550 K, the density of pure oxygen is only 6.98 kg/m^3, whereas it increases to 100.14 kg/m^3 at 150 bar. Thus, large density ratios (i.e., ρ_g/ρ_l) are an important feature of high-pressure injection. Moreover, the magnitude of the density variations across the mixing layers increases with pressure.

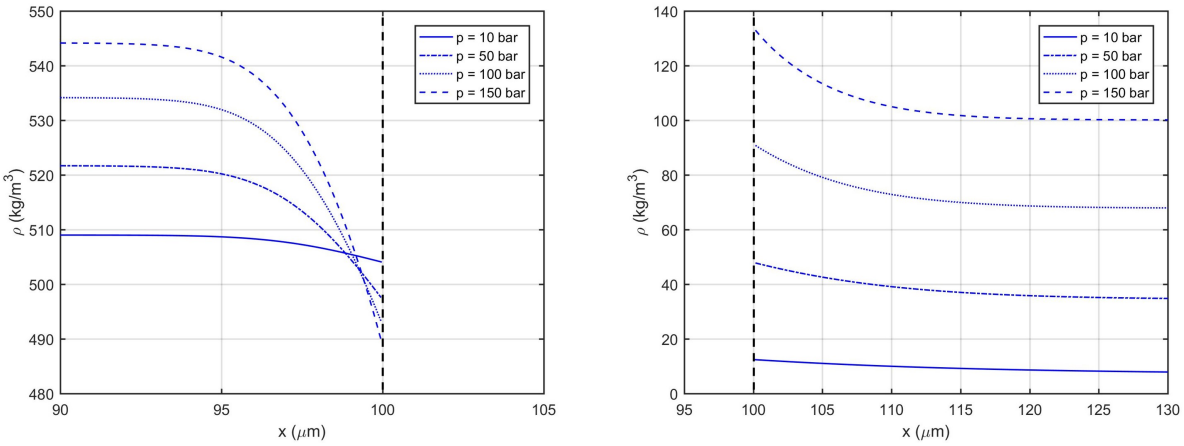

Figure 2.16: Effects of pressure on the density variation across the diffusion layers in the transient, one-dimensional flow problem at high pressures. The interface is located at $x = 100$ μm, with the liquid on the left side and the gas on the right side. Profiles correspond to $t = 100$ μs. (a) liquid density; (b) gas density [15].

Diffusion of mass and energy around the interface occurs relatively fast and generates mixing layers with variable fluid properties across them. As shown in Figure 2.17, the thickness of the mixing layers is of the order of micrometers at very high pressures (i.e., 150 bar). After

10 μs, diffusion layers have a thickness of $\sim$ 3 μm in the liquid phase and $\sim$ 10 μm in the gas phase. These values increase later in time, where the liquid phase presents a diffusion layer thickness of $\sim$ 10 μm at 100 μs, while the gas-phase diffusion-layer thickness is around $\sim$ 30 μm.

According to the incompressible simulations from Jarrahbashi et al. [24, 25] and Zandian et al. [26–28], high-pressure environments could present unstable perturbations with wavelengths between 80-120 μm and growth rates around 20-100 μs. Therefore, the results shown in Poblador-Ibanez and Sirignano [15] suggest that sufficiently thick diffusion layers will exist around the interface with a well-defined phase equilibrium before substantial growth of the instabilities. Nevertheless, the impact of high-pressure thermodynamics is not assessed.

2.3.2 Thermodynamic behavior of the one-dimensional interface

Figure 2.18 shows the pressure effects on some interface properties. As pressure increases, the temperature of the equilibrium solution also increases. This trend is discussed in Dahms and Oefelein [29]. It shows that for a given initial configuration (i.e., ambient pressure and gas and liquid temperatures), the interface equilibrium solution gets closer to the mixture critical temperature because the critical temperature is reduced at higher pressures and because the interface temperature increases. Other issues related to whether the interface enters the continuum domain or not might become a problem sooner as the interface temperature rises. Nevertheless, the problem configuration and results are shown in Poblador-Ibanez and Sirignano [15] fall within the domain where two phases coexist as the interface temperature is far away from the mixture critical temperature at the various pressures. An extended discussion about this verification is provided in Section 3.1.

The immediate effect that higher temperatures have relates to more oxygen dissolution into the liquid phase at a given pressure. However, the main contributor to the dissolution of

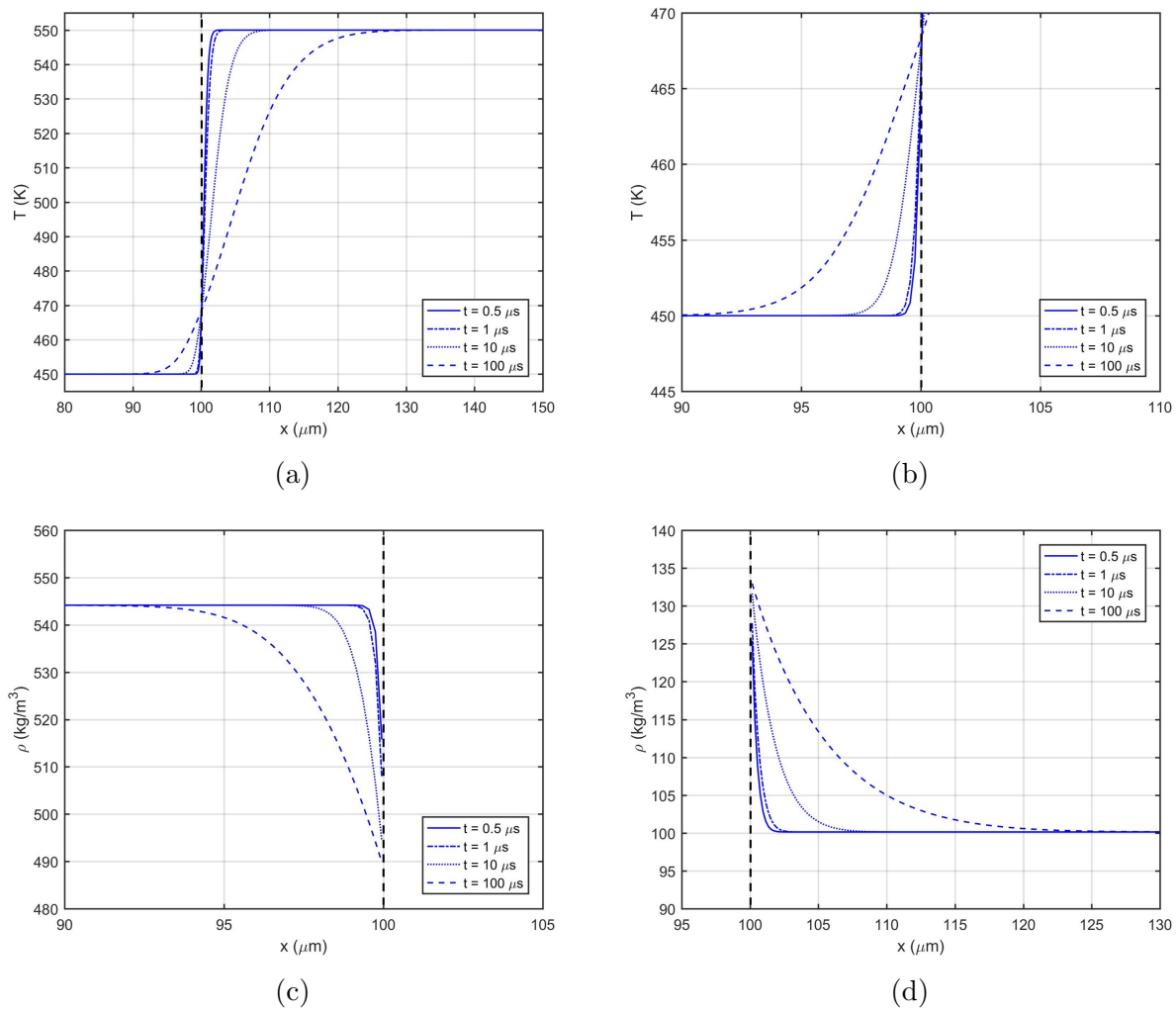

Figure 2.17: Temporal evolution of the temperature profile and the fluid density profile for the n-decane/oxygen mixture at 150 bar in the transient, one-dimensional flow problem at high pressures. The interface is located at $x = 100$ μm, with the liquid on the left side and the gas on the right side. (a) temperature; (b) liquid temperature near the interface; (c) liquid density; (d) gas density [15].

oxygen is the high-pressure interface, as discussed in Subsection 2.2.2. Because of this trend, the liquid density reduces as pressure increases (see Figure 2.18c). On the other hand, higher pressures compress the gas phase (see Figure 2.18d). Thus, as liquid and gas densities become more similar (i.e., both fluids become more similar), the surface-tension force at the interface is reduced.

A preliminary analysis of the most unstable wavelengths is done in Poblador-Ibanez and Sirignano [15] based on the evaluated interface properties and a linearized KH problem that includes normal viscous stress [40]. A comparison between low-pressure and high-pressure injection conditions shows a significant drop in the magnitude of the most unstable wavelengths with an increased growth rate. Even though the results should be taken qualitatively (since shear stress or viscous damping is not considered), they show a clear trend to very rapid atomization.

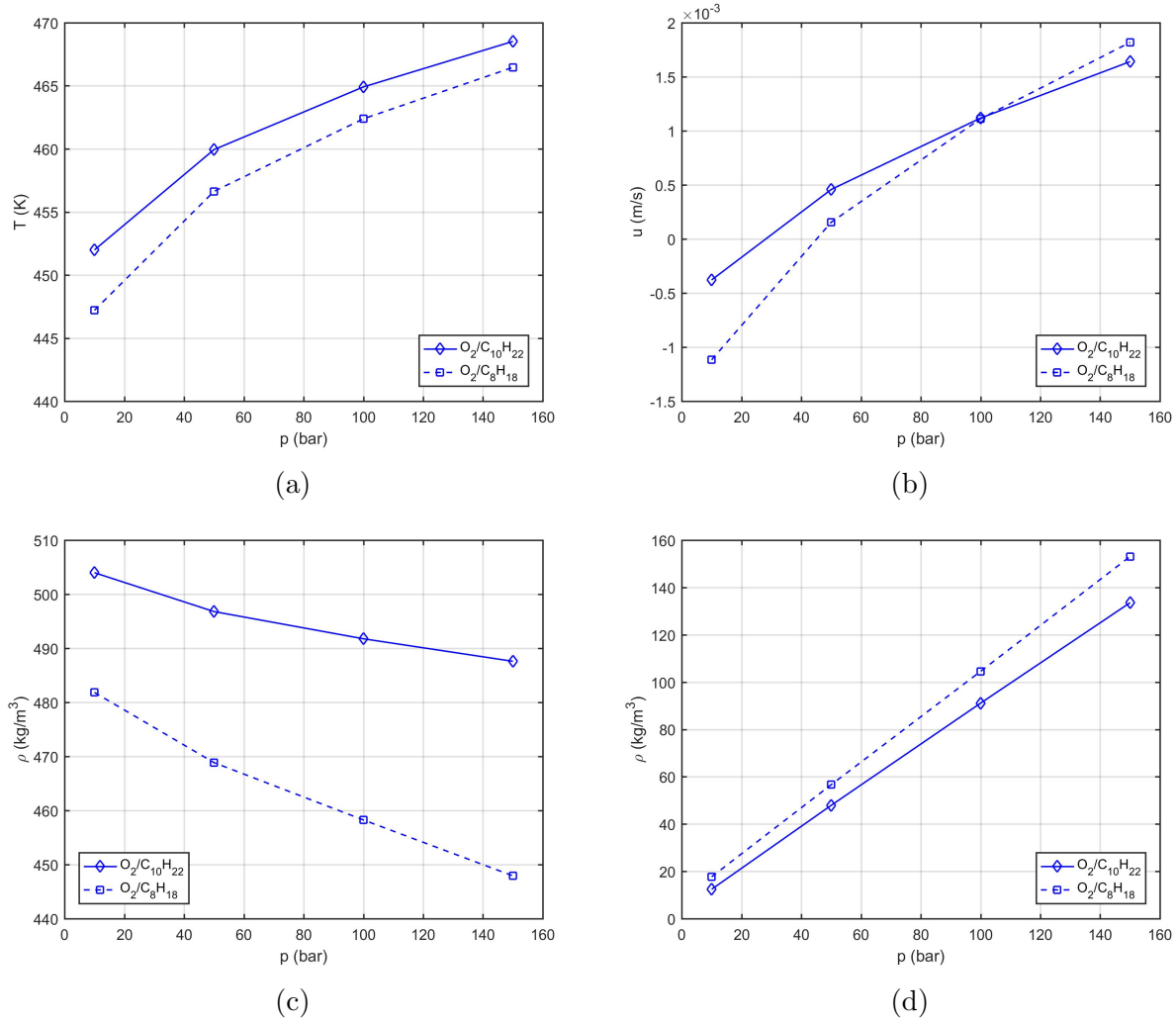

Figure 2.18: Effects of pressure on interface temperature, velocity and densities at $t = 100$ μs in the transient, one-dimensional flow problem at high pressures. (a) temperature; (b) interface velocity; (c) liquid density; (d) gas density [15].

Although the interface location remains fixed in this analysis, it is possible to estimate the actual interface velocity by displacing the velocity field as if the liquid end of the numerical domain were sitting on a wall with zero velocity. The results are plotted in Figure 2.18b. In a low-pressure environment, the heat flux from the gas phase into the interface vaporizes the liquid, and the interface recedes (i.e., $u < 0$). That is, the liquid volume is reduced even though heating should expand it somewhat. As pressure increases and the dissolution of the lighter species is enhanced, the liquid volume near the interface expands, causing the interface to advance (i.e., $u > 0$) while the liquid is still vaporizing. However, at sufficiently large pressures (e.g., ~ 50 bar for n-decane/oxygen or ~ 100 bar for n-octane/oxygen), a phase-change reversal occurs and the energy balance across the interface causes net condensation instead of vaporization [15]. Together with volume expansion near the interface, condensation also contributes to expanding the liquid phase. In summary, the liquid volume expansion near the interface is a result of the interaction of three mechanisms: thermal expansion due to heating of the liquid, which is more relevant for higher interface temperatures (i.e., higher pressures); volume expansion due to the dissolution of a lighter species; and the volume addition or subtraction due to mass exchange at the interface.

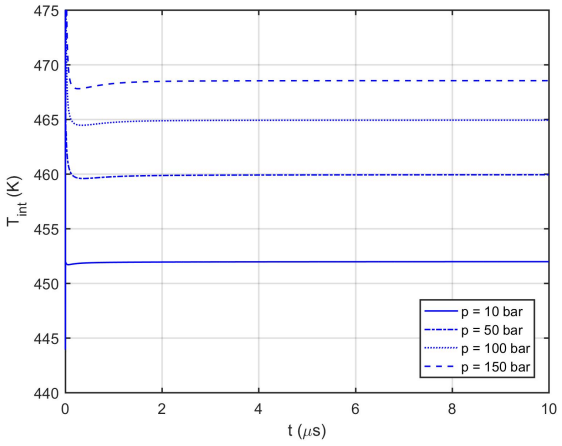

Figure 2.19: Interface temperature evolution for the n-decane/oxygen mixture at different pressures in the transient, one-dimensional flow problem at high pressures [15].

Due to the problem setup, the interface reaches a steady solution as diffusion processes occur around it. Figure 2.19 shows the interface temperature for the binary mixture of n-decane and oxygen at the different analyzed pressures. The interface temperature, as well as other properties, reach steady values very early in time. The temperature change becomes negligible in less than 10 μs coming from a sharp initial condition; but, more importantly, the temperature rate of change becomes negligible earlier, between 0.2 μs and 0.7 μs. That is, the interface can reach its equilibrium state quickly.

The establishment of local thermodynamic phase equilibrium shows a short characteristic time. This result suggests that an interface subject to perturbations can quickly adapt from equilibrium state to equilibrium state. That is, as the interface deforms in atomization problems and the flow characteristics around it change, it can be assumed to remain under a phase-equilibrium state that must be determined at all times.

A careful thermodynamic analysis is performed in Poblador-Ibanez and Sirignano [15] to understand and verify these results. The First Law of thermodynamics is validated for a control mass which includes the diffusion layers. Entropy is seen to increase in time mainly due to the irreversibility of the mixing process. The phase-change reversal at the interface occurs even though heat conducts from the hot gas to the cool liquid. The gas-mixture enthalpy is higher than the liquid-phase enthalpy for all analyzed pressures. However, the gas phase's internal energy drops below the liquid phase's internal energy as the pressure term in $h = e + p/\rho$ becomes more critical. Therefore, net condensation is achieved by increasing pressure. Closer to the transition point, weak vaporization can still occur, although the gas phase's internal energy is already below the internal energy of the liquid phase. In all situations, the hydrocarbon vaporizes, and oxygen condenses.

The vaporization/condensation across the interface is further discussed in Subsection 2.5.2 where results of an axisymmetric liquid jet injected at high pressures are shown. The wave

dynamics around the perturbed interface provide more insights into the thermodynamic behavior of the interface and allow a better interpretation of the problem.

2.4 Two-Dimensional Two-Phase Laminar Mixing Layer at Supercritical Pressures

A two-dimensional, two-phase laminar mixing layer is analyzed in Davis et al. [16], and Poblador-Ibanez et al. [17]. Instead of analyzing a one-dimensional transient problem, the steady-state solution of the two-dimensional laminar mixing layer equations for a two-phase configuration is presented here. However, due to the nature of the problem, the solution method resembles that of Poblador-Ibanez and Sirignano [15]. Liquid and gas are initially separated by a splitter plate and injected into the domain at different velocities, as shown in Figure 2.20. For the laminar mixing layer case, the solution of the governing equations marches downstream, whereas, in the one-dimensional transient problem presented in Section 2.3, the solution marches over time.

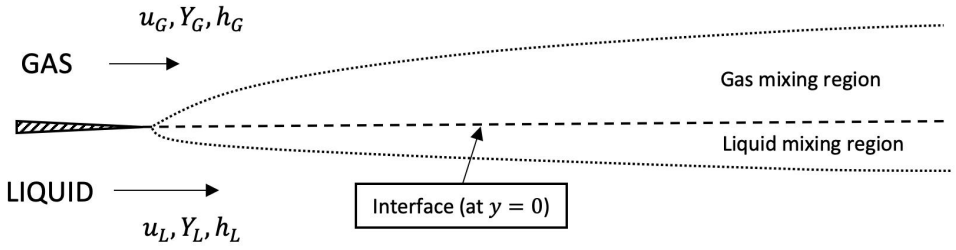

Figure 2.20: Sketch of the two-dimensional laminar mixing layer between a liquid stream and a gas stream. As reported in Davis et al. [16], the dividing streamline or interface between the liquid and the gas is assumed to be fixed at $y = 0$ m [17].

The binary mixtures analyzed in Davis et al. [16] and Poblador-Ibanez et al. [17] are very similar to those shown in the one-dimensional transient problem in Section 2.3. The liquid phase starts as a pure hydrocarbon (i.e., n-decane), whereas the gas phase is initially

composed of pure oxygen. Various subcritical and supercritical pressures are analyzed, and different initial temperatures are considered within the thermodynamic domain of two-phase coexistence. Again, local thermodynamic phase equilibrium represents the interface state, and pressure is uniform in the computational domain. The freestream velocities of each phase are selected such that the laminar flow assumption remains valid in the computational setup. Compared to Poblador-Ibanez and Sirignano [15], here, the thermodynamic model based on the volume-corrected SRK equation of state presented in Section 3.3 is used.

2.4.1 Interface temperature under different configurations

As discussed in Subsection 2.3.2, an increase in ambient pressure results in an increase of the interface equilibrium temperature if all other parameters remain the same (i.e., liquid and gas temperatures remain the same). Additional analysis of the interface behavior is performed in Davis et al. [16] where different initial temperatures for each phase are also considered. In summary, the analyzed cases include an ambient pressure range between 10 bar and 150 bar, an initial liquid temperature between 400 K and 490 K, and an initial gas temperature between 510 K and 600 K. In all cases, the interface equilibrium temperature is closer to the bulk liquid temperature than the bulk gas temperature. Approximately, the interface temperature satisfies $T_{\text{int}} < T_L + 0.15(T_G - T_L)$, where T_L is the initial liquid temperature, and T_G is the initial gas temperature.

This observation suggests that the liquid phase can absorb significant amounts of heat from high-temperature gas at supercritical pressures. The implications for transcritical injection are clear. Even if the surrounding gas is above the mixture's critical temperature (e.g., because of the initial injection temperature or downstream combustion), it will take time to heat enough the liquid phase to raise the interface temperature beyond the critical point. Nevertheless, the complete picture at high temperatures may show features of both two-phase

flows and supercritical fluids. It is expected that a large amount of small liquid structures (i.e., droplets) are generated at high pressures due to the reduction of surface-tension forces and the enhanced mixing effects in the liquid phase. Therefore, these small structures can be heated faster and may show an interface transition to diffusive mixing between phases while the cooler liquid core still shows evident two-phase characteristics.

These findings highlight the complexity of modeling transcritical flows. If a full-scale analysis is desired, covering the wide range of thermodynamic states (e.g., interface transition to a supercritical state) is necessary. Techniques to model the transition from a two-phase interface to a diffusive interface based on thermodynamic theory are needed, similar to the approach from Aggarwal et al. [55].

2.4.2 Self-similar behavior

The results presented in Davis et al. [16] show that the laminar mixing-layer problem at high pressures can be described under a self-similar behavior. Even though the mixing layer equations involve non-ideal terms and are coupled to a thermodynamic model developed from a real-gas equation of state and other high-pressure principles and correlations, similarity is apparent. Poblador-Ibanez et al. [17] prove it by transforming the two-phase, laminar mixing layer equations into a system of ODEs described in terms of a similarity variable, η. Then, mixture composition and mixture enthalpy (i.e., temperature) only depend on η, which describes the fluid state in any location in the (x, y) space. As long as the fluid properties obtained with the thermodynamic model also behave in a self-similar manner, similarity is achieved. That is, the thermodynamic model must ultimately depend only on the ambient pressure, temperature, and composition. The detailed transformation steps are shown in Poblador-Ibanez et al. [17], and a successful comparison with the results from Davis et al. [16] is provided.

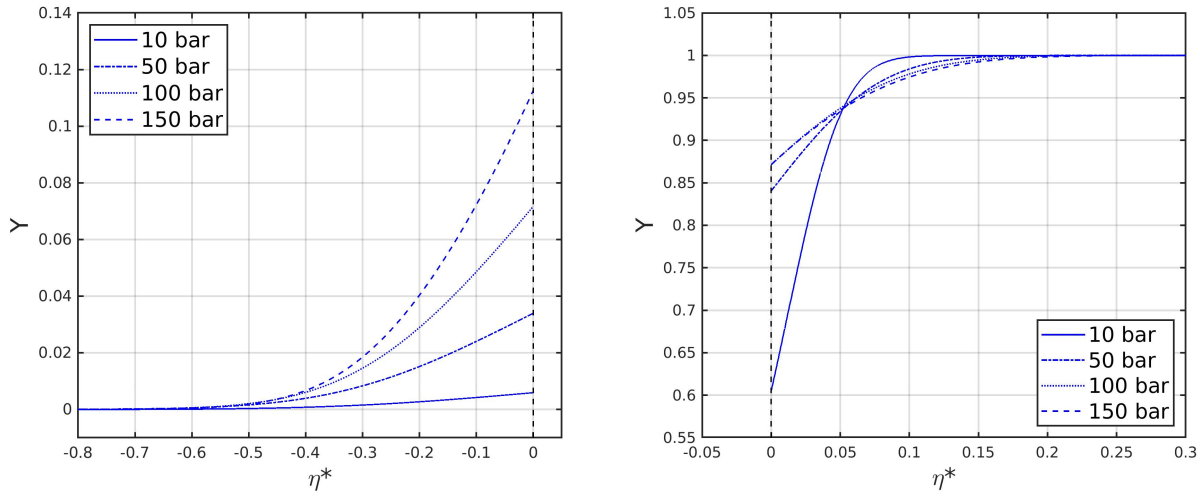

Figure 2.21: Self-similar solution of oxygen mass fraction, Y, for the n-decane/oxygen mixture under the two-phase laminar mixing layer configuration at high pressures. (a) Y in the liquid phase; (b) Y in the gas phase [17].

Some of the self-similar results across the mixing layers are shown in Figures 2.21, 2.22 and 2.23 in terms of normalized variables using liquid freestream properties. The self-similar variable is normalized as $\eta^* = \eta/\sqrt{\rho_L \mu_L / u_L}$, where ρ_L is the pure liquid density, μ_L is the pure liquid viscosity and u_L is the liquid freestream velocity. Other variables follow $h^* = h/h_L$, where h_L is the pure liquid enthalpy, $\rho^* = \rho/\rho_L$ and $\mu^* = \mu/\mu_L$. The gas phase mixing layer is defined by $\eta^* > 0$ while the liquid phase mixing layer is defined by $\eta^* < 0$. The interface is located at $\eta^* = 0$. Notice that mass fraction is already a non-dimensional number. Thus, no normalized variable has been identified.

The effects of high-pressure thermodynamics discussed in previous sections are also observed. As pressure increases above the pure liquid critical pressure, the dissolution of oxygen is enhanced (see Figure 2.21a). The trend whereby liquid and gas densities become more similar at high pressures and present more significant variations within the mixing region is shown in Figure 2.23a. More importantly, the liquid viscosity experiences a sharp decrease toward gas-like values as pressure increases well above the pure liquid critical pressure (see Figure 2.23b); also, the viscosity of the gas mixture shows a slight decrease below the pure

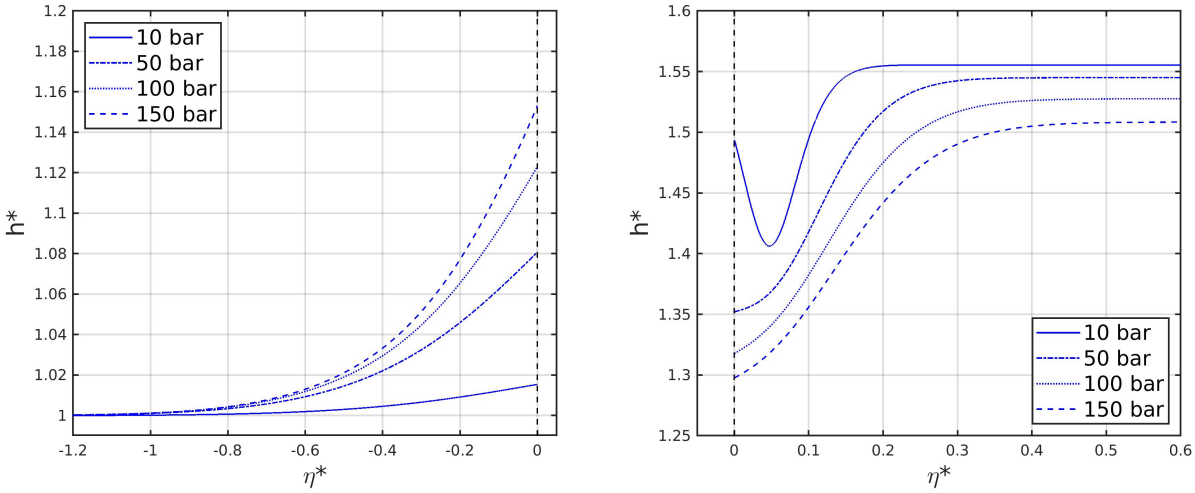

Figure 2.22: Self-similar solution of the normalized mixture enthalpy, h^*, for the n-decane/oxygen mixture under the two-phase laminar mixing layer configuration at high pressures. (a) h^* in the liquid phase; (b) h^* in the gas phase [17].

gas viscosity. In general, both higher temperatures and higher densities increase the fluid's viscosity. In the gas phase, the effect of a local increase in density is overcome by the sharp decrease in temperature in the vicinity of the interface, similar to what is observed in Figure 2.17a. Thus, the viscosity in the gas phase drops slightly. On the other hand, the liquid phase experiences the opposite. The temperature increase across the mixing layer is minimal, and the dissolution of oxygen causes a substantial drop in liquid density, which, in turn, causes a large drop in liquid viscosity.

The gas-like viscosity of the liquid phase near the interface may contribute to faster and more violent atomization at high pressures than initially expected. A reduction of surface-tension forces is not the only cause that triggers the growth of short-wavelength perturbations. That is, the smaller liquid viscosity near the interface reduces the viscous damping that helps stabilize surface perturbations.

Figure 2.22 shows the specific mixture enthalpy distribution, which is consistent with the increase of temperature in the liquid phase and the decrease of temperature in the gas

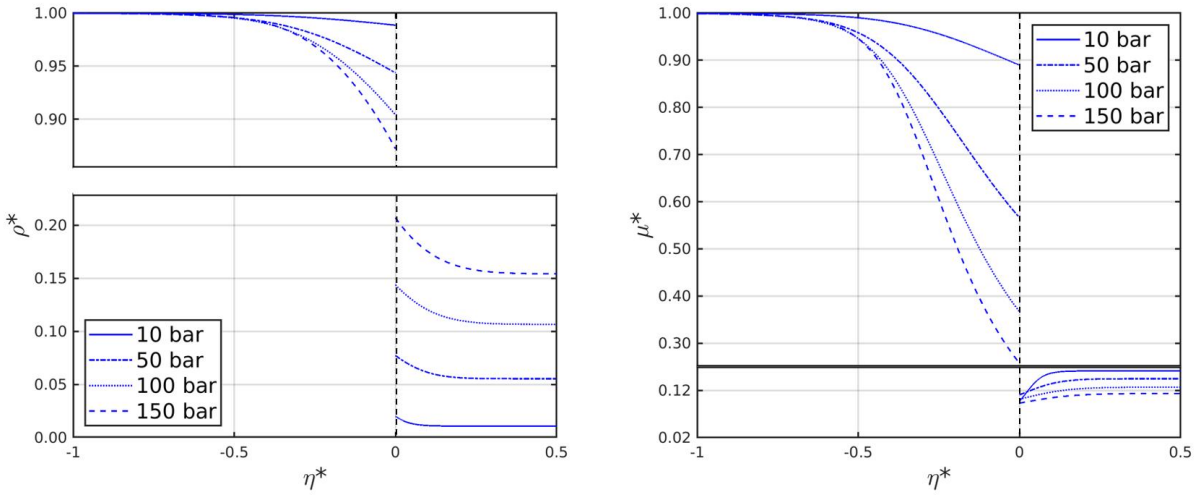

(a) (b)

Figure 2.23: Self-similar solution of the normalized mixture density, ρ^*, and mixture viscosity, μ^*, for the n-decane/oxygen mixture under the two-phase laminar mixing layer configuration at high pressures. (a) normalized density, ρ^*; (b) normalized viscosity, μ^* [17].

phase. At 10 bar, the specific mixture enthalpy distribution in the gas phase shows a trough inside the mixing layer. The reason for this trend is explained in Poblador-Ibanez and Sirignano [15]. The mixing process is internal in a mass element containing the mixing layers of both phases. The heat flux, Q, across the boundaries of this mass element is negligible and, for a constant pressure process, the enthalpy change of a mass element is related to the heat flux into it as $\Delta H = Q|_p = 0$. Thus, the enthalpy increase in the liquid phase has to be compensated by an enthalpy decrease in the gas phase. However, this requirement cannot satisfy a monotonic enthalpy distribution in the gas phase at 10 bar. As seen in Figure 2.22b, the gas mixture enthalpy at the interface for the 10-bar case is too high.

The insights gained with the works by Davis et al. [16] and Poblador-Ibanez et al. [17] about the self-similar behavior of mixing around the liquid-gas interface at high pressures under certain conditions can be helpful for future modeling of more complex flow simulations. For example, the self-similar approach could be used to implement realistic initial conditions or develop a reduced-order model to establish the interface phase equilibrium solution and the surrounding mixing in under-resolved regions.

2.5 Two-Dimensional Axisymmetric Jet at Supercritical Pressures

A transcritical axisymmetric liquid jet injected into a gas is analyzed for a binary system (i.e., only two species are involved) in Poblador-Ibanez and Sirignano [19]. This work represents an extension of the previous works by Poblador-Ibanez and Sirignano [15], Davis et al. [16] and Poblador-Ibanez et al. [17] to a real liquid jet where the interface deforms. Then, the thermodynamic modeling at high pressures coupled with fluid dynamics can be tested. Even though liquid injection is a three-dimensional phenomenon, the axisymmetric study already shows the initial development of instabilities on the liquid-gas interface and provides insight into the high-pressure liquid injection problem. The two main goals of this study are to test a numerical methodology able to handle the transcritical liquid injection problem and show that, in this thermodynamic regime, the atomization of the liquid jet is still a two-phase problem. That is, phase equilibrium is well established before the substantial disruption of the interface. For the full set of governing equations, the reader is referred to Chapter 3 and Appendix A for axisymmetric considerations.

A few comments need to be provided regarding this study. The thermodynamic model is based on the original SRK equation of state without the volume correction term. Nevertheless, the development of thermodynamic relations follows the same steps shown in Section 3.3. The governing equations are solved by extending the numerical methods used in Jarrahbashi and Sirignano [24], Jarrahbashi et al. [25], and Zandian et al. [26, 27, 35, 36] to real fluids with variable fluid properties. Instead of the Semi-Implicit Method for Pressure-Linked Equations (SIMPLE) [56] used in these works, the SIMPLEC method [57] is implemented since it works better for highly-coupled flows and, in general, shows better performance than SIMPLE. Both methods can handle weakly compressible flows. The interface is captured and advected with the original Level-Set (LS) method [58–60] discussed in Subsection 4.1.1,

which treats the advection of a distance function, θ, with the interface location given by the isosurface where $\theta = 0$.

The connection between both phases (i.e., the inclusion of the interfacial jumps) is performed on a point-to-point basis. The solution of the LS is provided within a discretized domain; therefore, the exact location of the interface may not coincide with a grid node. Interface nodes are found by interpolating known LS values at grid nodes to the zero level-set value. This approach identifies and uses interface nodes at a grid-level resolution to connect liquid and gas phases. The matching conditions between the different governing equations are obtained following the guidelines provided in Subsections 3.3.4 and 4.1.3. Once a solution for the interface is known, an extrapolation technique is used to impose boundary conditions that capture interfacial jumps at the grid nodes neighboring the interface [19].

Lastly, due to the uncertainty about how to evaluate the interface velocity in level-set methods, this study assumes that the interface material line moves with the fluid; thus, neglecting phase-change effects. Some comments regarding this assumption are given in Subsection 2.5.3. More details regarding the problem setup and modeling can be found in Poblador-Ibanez and Sirignano [19].

2.5.1 Instability analysis

A temporal study with periodic boundary conditions in the axial direction has been performed to analyze the growth of imposed perturbations in the liquid-gas interface [19]. Similar to previous works [15–17], the liquid is initially composed of pure n-decane at 450 K, and the gas phase contains pure oxygen at 550 K. The jet has a radius of 20 μm and is moving at 30 m/s while the gas is initially at rest. Three different chamber pressures have been analyzed (i.e., 50, 100, and 150 bar), all of them supercritical for the fuel being injected (see Table 2.1).

The imposed perturbation wavelength is obtained from a preliminary test where a numerical perturbation is initially introduced near the inlet of the jet. A wave develops after some time, providing an estimate of the most unstable wavelength (e.g., approximately 20 μm at 150 bar). As pressure decreases, longer wavelengths and slower growth rates are obtained as expected, since the equilibrium solution at the interface moves further away from the mixture critical point and surface-tension forces become increasingly stronger [15]. Based on these results, an initial sinusoidal perturbation with a wavelength of 20 μm and an amplitude of 0.5 nm is imposed for all pressures in the temporal study. This initial configuration represents a perturbation of 0.0025 % the jet radius. The axial length of the numerical domain is set to 100 μm to capture five waves, and the outer radial boundary is treated as an open boundary located 80 μm away from the centerline of the jet. That is, it is sufficiently far away from the liquid-gas interface to make sure all the relevant features of the flow development stay within the domain boundaries.

Assuming an initial behavior of the perturbation amplitude given by $A(t) = A_0 e^{c_R t}$, where c_R is the growth rate and A_0 the initial amplitude, approximate instability growth rates can be obtained. This assumption is reasonable as long as the liquid-gas interface presents a sinusoidal-like shape.

Table 2.2: Surface tension and estimated instability growth rates as a function of chamber pressure for the axisymmetric jet with an initial perturbation with a 20 μm wavelength at $t = 5$ μs. The Reynolds number based on the liquid properties and the Weber number based on the gas properties are also shown [19].

p (bar)	σ (mN/m)	c_R (μs^{-1})	Re_L	We_G
50	3.560	0.4037	5355	349
100	2.461	1.0294	5062	993
150	1.628	1.4112	4830	2214

Table 2.2 reports representative values for surface-tension coefficient, perturbation growth rate, Reynolds number based on the liquid phase, and Weber number based on the gas phase

at different pressures. The Reynolds and Weber numbers are defined, respectively, as

$$Re_L = \frac{\rho_L U D_{\text{jet}}}{\mu_L} \quad ; \quad We_G = \frac{\rho_G U^2 D_{\text{jet}}}{\sigma} \tag{2.1}$$

where U is the jet velocity, ρ_L is the pure liquid density, μ_L is the pure liquid viscosity, ρ_G is the pure gas density, D_{jet} is the jet diameter and σ is a representative surface-tension coefficient.

The perturbation presents an N-shape after only 5 μs for the most extreme case at 150 bar. Nevertheless, phase equilibrium is well established, and clear diffusion layers are seen growing on either side of the interface. As reported in Poblador-Ibanez and Sirignano [19], these results differ considerably from other works aiming to represent conditions reminiscent of high-pressure liquid injection with an incompressible Navier-Stokes solver [24–28]. For similar density ratios and Reynolds numbers, the expected instability wavelength is in the range of 80-120 μm with a slower instability growth. Even though Weber numbers are smaller in the present study, the model predicts a much faster atomization process. These results are consistent with experimental observations (see Subsection 2.2.1), but some deeper insight is needed.

As explained in detail in Subsection 3.3.1, the original SRK equation of state underestimates the density of dense fluids (i.e., liquids). Furthermore, models to predict the viscosity coefficient correlate directly with the density of the fluid [61]. Therefore, a more realistic configuration should be expected if an equation of state is used that predicts better the liquid density (i.e., the volume-corrected SRK equation of state presented in Subsection 3.3.1). That is, higher densities in the liquid phase will increase the surface-tension forces holding the liquid interface together and will also result in a higher liquid viscosity, which will mitigate the perturbation growth even further under viscous dissipation or damping.

The change in fluid properties across the mixing region on each phase is quantified in Tables 2.3 and 2.4. A comprehensive summary of pure-fluid density and viscosity compared against density and viscosity evaluated at the interface for each phase is presented. The interface is defined with the symbol Γ, and pure-fluid properties are identified for the gas phase (G) and the liquid phase (L). The fluid phase is identified at any other location with the subscripts g for the gas phase and l for the liquid phase. As shown in Subsection 2.4.2, liquid viscosity near the interface drops to gas-like values. Therefore, the liquid phase near the interface presents a mixing layer with lower density and much lower viscosity than the pure liquid region. This change in fluid properties can affect the development of instabilities at the interface, influenced by the surrounding diffusive environment with low surface tension and gas-like viscosities. Deviations of density and viscosity ratios between the pure substances and the interface become more relevant as pressure increases, with liquid and gas properties becoming alike. This feature resulting from enhanced mixing in the liquid phase is not captured in the incompressible simulations [24–28] and might explain the rapid growth of smaller perturbations in the present study.

Table 2.3: Pure fluid densities and interface densities at 50, 100 and 150 bar for the axisymmetric jet [19].

p (bar)	ρ_G (kg/m^3)	ρ_L (kg/m^3)	ρ_G/ρ_L	$(\rho_g)_\Gamma$ (kg/m^3)	$(\rho_l)_\Gamma$ (kg/m^3)	$(\rho_g/\rho_l)_\Gamma$
50	34.47	521.70	0.0661	48.13	492.80	0.0977
100	67.87	534.16	0.1271	91.19	488.18	0.1869
150	100.14	544.17	0.1840	133.57	483.71	0.2765

Table 2.4: Pure fluid viscosities and interface viscosities at 50, 100 and 150 bar for the axisymmetric jet [19].

p (bar)	μ_G (mPa·s)	μ_L (mPa·s)	μ_G/μ_L	$(\mu_g)_\Gamma$ (mPa·s)	$(\mu_l)_\Gamma$ (mPa·s)	$(\mu_g/\mu_l)_\Gamma$
50	0.03277	0.1169	0.2803	0.02477	0.07837	0.3162
100	0.03332	0.1266	0.2631	0.02649	0.06436	0.4122
150	0.03402	0.1352	0.2517	0.02765	0.05513	0.5047

2.5.2 Thermodynamic behavior of the multidimensional interface

Subsection 2.3.2 shows the results obtained in Poblador-Ibanez and Sirignano [15], where net condensation may provide the proper energy balance at the interface as pressure is increased. However, the simplicity of the one-dimensional study is overwhelmed in two- and three-dimensional studies where wave dynamics play an essential role in the thermodynamic behavior of the interface.

As seen in Figure 2.24, the phase change across the interface varies along the interface, with a more substantial condensation rate near the wave trough and a weaker condensation or even weaker vaporization near the wave crest. Both reported pressures (i.e., 100 and 150 bar) presented net condensation in the one-dimensional study with the gas enthalpy being higher than the liquid enthalpy and the gas internal energy being lower than the liquid internal energy [15]. The axisymmetric study still presents the same behavior for the enthalpy and the internal energy for each phase, but once the interface starts to deform, vaporization can appear again for lower high-pressure cases (e.g., 100 bar). Therefore, a rephrasing of the discussion provided in Poblador-Ibanez and Sirignano [15] on the condensation/vaporization processes happening at the interface is necessary to understand the inherent difficulties caused by compressions and expansions around the growing perturbation (see Figure 2.25).

For a constant pressure process across the interface (in our case $p_l \approx p_g \approx p_\Gamma$) the relation between internal energy and enthalpy is $\Delta e = \Delta h - p\Delta v$ with $\Delta e = e_g - e_l$, $\Delta h = h_g - h_l$ and $\Delta v = v_g - v_l > 0$. Low-pressure thermodynamics dictate that the change in internal energy and the change in enthalpy across an interface go in the same direction. That is, if $\Delta h > 0$, then $\Delta e > 0$. Therefore, in situations where the gas is at a higher temperature than the liquid, $\Delta h > 0$ and $\Delta e > 0$ dictates a vaporizing process. This relation between the change in enthalpy and the change in internal energy is related to the $p\Delta v$ term being small at low pressures compared to Δh.

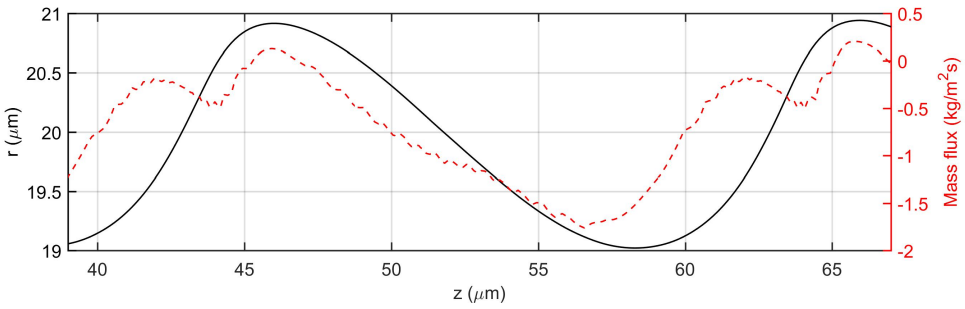

(a)

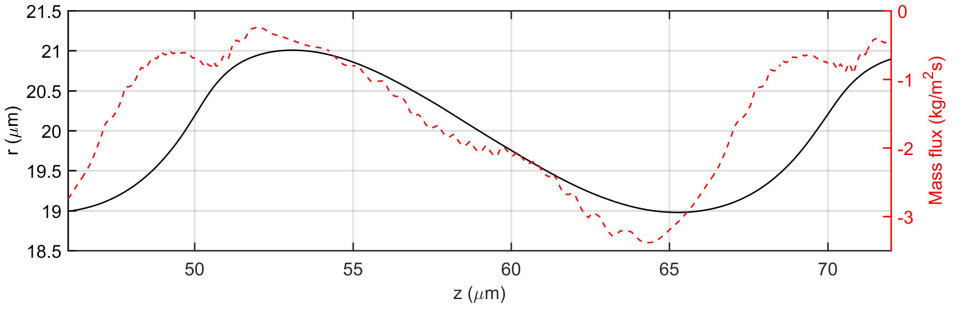

(b)

Figure 2.24: Distribution of the mass flux crossing the interface (red dashed line) vs the interface position (black solid line) for the axisymmetric jet. (a) 100 bar at $t = 8$ μs; (b) 150 bar at $t = 5.5$ μs [19].

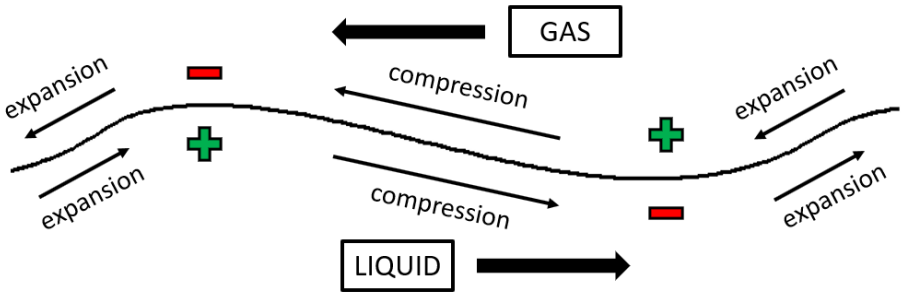

Figure 2.25: Fluid compression and expansion around a wavy liquid-gas interface.

On the other hand, very high pressures can create a reversal of the classical low-pressure point of view. When the $p\Delta v$ term becomes very large, its magnitude can be larger than Δh. In this situation, $\Delta h > 0$ can be associated to $\Delta e < 0$ and no clear direction for vaporization or condensation can be established. This means vaporization of a cool liquid caused by a hotter gas may exist with $\Delta h > 0$ and $\Delta e < 0$ or condensation of a cool liquid surrounded by a hotter gas may exist with $\Delta e < 0$ and $\Delta h > 0$.

With wave dynamics involved, compression of the gas phase and expansion of the liquid phase are experienced near the wave crest, while expansion of the gas phase and compression of the liquid phase occurs near the wave trough. Therefore, for a given pressure, $p\Delta v$ is larger near the wave trough, and the thermodynamic reversal occurs first in this region as pressure is increased, allowing condensation to be a possible solution of the energy balance at the interface. For vaporization or condensation to occur at very high pressures, it is necessary that $p\Delta v > \Delta h$ since Δh and Δe have opposite signs. Thus, the energy balance, together with the compression and expansion processes around the interface, determines whether net vaporization or net condensation exists.

2.5.3 Guidelines for a proper numerical approach

This study is helpful to identify the main features of high-pressure atomization and weaknesses of a particular numerical approach. This section summarizes these weaknesses and proposes solutions, some of them already commented throughout the text, that define the numerical modeling presented in this thesis.

The thermodynamic model based on the original SRK equation of state underestimates the density of dense fluids. This issue may induce faster liquid jet atomization, which is not related to an actual physical feature. Therefore, to be consistent with the actual properties of the species involved in the simulations, the volume-corrected SRK equation of state shown in Subsection 3.3.1 is used in the results presented in this thesis. It should be noted that the new equation of state dramatically improves the accuracy for the analyzed pure species. It is expected that similar hydrocarbons or gases will behave accordingly. However, the quadratic mixing rules may not be the best choice for mixtures, especially near the critical point of the mixture. It might become necessary in future works (but out of the scope of this thesis) to analyze what mixing rules better suit the transcritical domain. As long as

the thermodynamic environment is sufficiently far away from the mixture critical point, the results obtained with quadratic mixing rules are consistent and show good agreement with available experimental data.

Some comments have to be provided about the level-set method as well. The uncertainty of evaluating the interface velocity from a discrete point of view to advect the distance function θ in a consistent physical manner is worrisome. Some works define a constant normal-wise extrapolation of the mass flux across the interface into each phase and use it to evaluate the interface velocity as a field variable [62]. This approach seems correct for incompressible two-phase problems, but its implementation is unclear once density variations exist near the interface. Neglecting the phase change effect in evaluating the interface velocity as suggested in this preliminary study is not a good approach. The reasoning behind the simplification was that the interface velocity would depend strongly on the fluid velocity compared to any influence from phase change. However, there are regions along the interface where the fluid velocity is negligible, and the movement of the interface is linked mainly to the change in phase.

Also, level-set methods are known to lose mass as numerical errors related to the discretization of the advection equation and the reinitialization to keep θ a distance function accumulate. This numerical behavior is not desired if phase change is an essential feature of high-pressure liquid injection. That is, the numerical mass loss might be of the same order of mass generation or loss due to phase change; therefore, the physical process would not be adequately captured. The Gradient Augmented Level-Set (GALS) method described in Subsection 4.1.1 has been tested, proving to be more accurate than the original level set. However, it still presents some degree of mass loss. Moreover, the level-set method implemented in this preliminary study diffuses the sharp interface within a region of the order of 3-to-5 times the mesh size. Therefore, numerical diffusion overlaps with the actual diffusion around the interface, affecting the solution of the local phase equilibrium. The Volume-of-

Fluid method described in Subsection 4.1.2 is used in this thesis to mitigate these problems, following the guidelines from Baraldi et al. [63] and Dodd and Ferrante [64] and including liquid compressibility and phase-change effects in the evaluation of the volume fraction, C.

Lastly, the method to relate both phases in this preliminary study proved problematic once the interface deformation became sufficiently large. The SIMPLEC method could not march further in time with oscillations in the curvature computations. Full convergence of the implicit system of equations defined under the SIMPLEC framework is not guaranteed. Coupling the SIMPLEC method with a simplified version of the Ghost Fluid Method (GFM) described in Subsection 4.1.1 has also been unsuccessful. The algorithm did not show consistency when imposing jump conditions across the interface due to the additional complexity of the real fluid. Further testing of the SIMPLEC method using incompressible two-phase benchmark problems (e.g., two-dimensional standing wave [65]) has cast some doubts about the validity of the method in all possible scenarios. Therefore, an explicit treatment of the governing equations may ease some of the numerical difficulties associated with highly-coupled, two-phase problems.

Chapter 3

Modeling of the Real-Fluid, Two-Phase Configuration

This chapter presents the modeling details implemented in this work to analyze the early deformation and atomization of transcritical liquid jets. Section 3.1 briefly describes the model applicability and its limitations toward simulating a wider range of expected thermodynamic states in a complete combustor simulation environment. The set of governing equations and the matching relations or jump conditions connecting the solutions of both phases across the interface are presented in Section 3.2. Here, a low-Mach-number formulation has been considered where fluid compression results from mass and thermal mixing rather than pressure variations. Lastly, a description of the thermodynamic model (e.g., equation of state) used to evaluate fluid and transport properties, as well as the interface phase equilibrium state, is provided in Section 3.3. More details are available in Appendix B and Appendix C.

3.1 Model Description and Physical Limitations

The theoretical model and numerical approach proposed in this study aim to solve two-phase flows in a high-pressure thermodynamic environment (i.e., supercritical for the liquid) but below the mixture critical point. That is, the interface between the two fluids is sufficiently cold compared to the mixture critical temperature. As previously stated in Chapter 2, two phases can be maintained under local thermodynamic phase equilibrium, and enhanced mixing in the liquid phase changes the mixture critical properties, resulting, generally, in a subcritical liquid interface. Jofre and Urzay [47] present a comprehensive examination of the thermodynamic complexity that liquid fuels face in such environments. A two-phase configuration with reduced surface-tension force and finite energy of vaporization exists near the injector before the interface temperature approaches the mixture critical point or diffusional critical point [47]. The interface undergoes a non-equilibrium diffuse transition from the liquid to the gas phase near the mixture critical point, with steep gradients limited to the nanoscale (i.e., works by Dahms and Oefelein [29–32]). No further differentiation between liquid and gas can be made beyond the mixture critical point, and diffusive mixing between the two fluids occurs. These features or fluid transitions are outlined in Figure 2.11, which has been extracted from Jofre and Urzay [47].

The model proposed in this study cannot address the interface transition to a supercritical state nor phase non-equilibrium for interface temperatures close to the mixture critical point. Moreover, it does not consider a combustion chemical reaction between fuel and oxidizer. Instead, it focuses on the early stages of the fuel injection process when two phases arguably coexist. While conventional liquid hydrocarbon fuels are injected at relatively low temperatures, previous studies have indicated that the interface equilibrium temperature is relatively close to the liquid bulk temperature [15–17], as discussed in Subsection 2.4.1. Because heavy hydrocarbon mixtures have high critical temperatures (e.g., $T_c = 617.7$ K for n-decane), the interface can remain away from the mixture critical point before significant mixing and

heating occur, either due to a sufficiently hot oxidizer stream like in the sketch from Jofre and Urzay [47] (i.e., Figure 2.11) or due to downstream combustion. Under this scenario, the mixing between the fuel and the oxidizer at high pressures can be driven by two-phase atomization before the liquid-gas interface transitions to a supercritical state. Therefore, a resolved two-phase model is a powerful tool for analyzing the physical phenomena driving the liquid fuel early mixing stage at engine-relevant conditions and better understanding the physical setup of downstream phenomena.

The thermodynamic range of two-phase coexistence is a unique feature of a given fuel-oxidizer mixture, and careful individual analysis is required to determine whether a two-phase solver can accurately represent reality and under what conditions. Figure 3.1 provides additional justification for the proposed two-phase technique in studying the type of mixtures considered in this work. Phase-equilibrium diagrams for the binary mixture of n-decane/oxygen are shown in Figure 3.1a, where the fuel mole fraction in the liquid and gas phases at the interface is plotted as a function of interface temperature and thermodynamic pressure. The thermodynamic model described in Section 3.3 has been used to obtain these results. The n-decane/oxygen mixture is chosen as a reference of hydrocarbon-based liquid fuels used in a variety of engineering applications, and other fuel-oxidizer configurations should behave similarly (e.g., diesel-air). From Figure 3.1a, it is noted that the mixture critical temperature, which is a function of pressure, is very similar to the hydrocarbon critical temperature (i.e., about 580 K at 150 bar). The mixture critical temperature decreases significantly below the hydrocarbon value only for extremely high pressures (i.e., 150 bar and above). In this work, the bulk temperature of each phase limits the interface equilibrium temperature range in the absence of energy sources or chemical reactions. As shown in the following chapters, this dissertation investigates the binary mixture of n-decane/oxygen with a liquid n-decane bulk temperature of 450 K and a gaseous oxygen bulk temperature of 550 K. As a result, the interface equilibrium temperature is projected to remain close to 450 K. In contrast, the

temperature upper bound is limited by the gas bulk temperature in conditions of strong, diffusive mixing. The interface cannot reach a supercritical state in any situation.

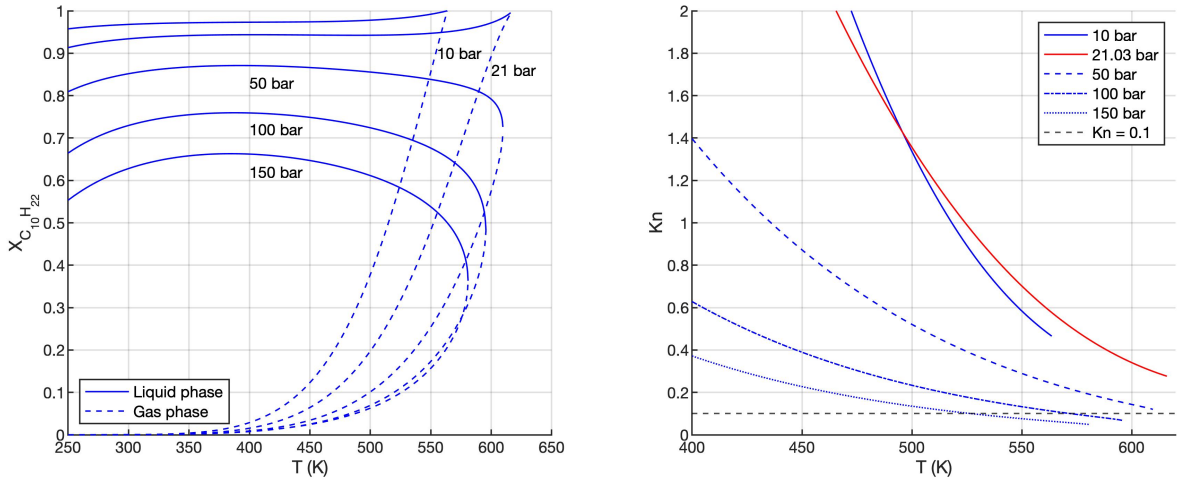

(a) (b)

Figure 3.1: Phase-equilibrium diagrams for the binary mixture of n-decane/oxygen as a function of interface temperature and ambient pressure. (a) n-decane mole fraction at the interface; (b) estimated Knudsen number at the interface using the vapor equilibrium composition [66].

Additionally, the interface thickness has to be analyzed to infer whether the phase non-equilibrium transition region enters the continuum domain or not. As detailed in the works by Dahms and Oefelein [29–32], the Knudsen number criterion, $\mathrm{Kn} = \Lambda / l_\Gamma < 0.1$, is considered for that purpose. The interface thickness, l_Γ, is estimated as a function of temperature by assuming an exponential growth similar to Figure 6 from Dahms and Oefelein [30]. Then, the molecular mean free path of the vapor phase is estimated from Dahms and Oefelein [29] as $\Lambda = \left(k_B T\right) / \left(\sqrt{2}\pi p d^2\right)$ where k_B is the Boltzmann constant, T the interface temperature, p the interface pressure and $d = \sum_{i=1}^{N=2} X_i d_i$ the average molecule kinetic diameter. Because its definition is closely related to the molecular mean free path, the kinetic diameter is chosen as the representative molecule diameter. For oxygen, $d_{O_2} = 0.346$ nm [67] and, for n-decane, $d_{C_{10}H_{22}} = 0.485$ nm [68].

Figure 3.1b presents the Knudsen number as a function of the interface equilibrium state at different pressures and temperatures. The continuum criteria established in Dahms and Oefelein [29] is only problematic for the 150-bar scenario, where calculations indicate that the interface may enter the continuum domain at temperatures over 525 K. Nonetheless, in the results shown in the following chapters, the interface equilibrium temperature remains substantially below this threshold, and the phase-equilibrium interface model can be justified. Figures 6.3a and 6.23 only show a few interface regions at 150 bar that appear to be close to the theoretical limit at which a continuous interface should be considered.

Other considerations for non-ideal mixtures at high pressures discussed in Subsection 2.2.2 have been examined, such as mixture stability (e.g., diffusional stability) which is responsible for phase separation and the reappearance of a two-phase interface [47]. During the various analyzed cases, no anomalies were identified, implying that the composition obtained from the LTE interface model offers a stable boundary for the mixing in both phases when no energy source or thermodynamic pressure oscillations exist. Furthermore, a low-Mach-number environment is considered, with density variations tied to mass and thermal mixing rather than pressure variations. The compressible terms emerging in a compressible, wave-like pressure equation can be safely omitted for gas velocities up to 100 m/s. The estimated gas-phase speed of sound at high pressures is around 450 m/s (i.e., an oxygen-dominant mixture in this study). The compressible terms in the compressible pressure equation scale with the Mach number squared, M^2, and are on the order of $M^2 \sim \mathcal{O}(10^{-2} - 10^{-3})$ for the range of injection velocities analyzed in this work. The speed of sound can be obtained from the thermodynamic model as shown in Appendix B.1.

Finally, as stated throughout this dissertation, different encountered difficulties should be addressed in future works to improve the model's performance and broaden the thermodynamic region in which it can be utilized. For example, under the Volume-of-Fluid framework, one should deal with the spurious currents generated around the interface, find ways to reduce the

added computational cost and handle higher interface temperatures with a non-equilibrium model near the mixture critical point or a transition to a supercritical diffuse interface. As an example, Zhu and Aggarwal [69] and Aggarwal et al. [55] address the transition from a two-phase interface to a supercritical interface in transcritical droplet studies. Despite these challenges, the dissertation's purpose is to establish a clear framework for studying two-phase flows at supercritical pressures and the early atomization of liquid fuels at engine-relevant conditions.

3.2 Governing Equations

The governing equations of fluid motion for compressible, two-phase flows are the continuity equation, Eq. (3.1), the momentum equation, Eq. (3.2), the species continuity equation, Eq. (3.6), and the energy equation, Eq. (3.8). Since both fluids are compressible, the velocity field is not necessarily divergence-free (i.e., $\nabla \cdot \vec{u} \neq 0$).

In a three-dimensional Cartesian coordinate system, the continuity equation is expressed as

$$\frac{\partial \rho}{\partial t} + \nabla \cdot (\rho \vec{u}) = 0 \tag{3.1}$$

and the momentum equation becomes, without body forces (e.g., gravity),

$$\frac{\partial}{\partial t}(\rho \vec{u}) + \nabla \cdot (\rho \vec{u}\vec{u}) = -\nabla p + \nabla \cdot \bar{\bar{\tau}} \tag{3.2}$$

where ρ and $\vec{u} = (u, v, w)$ are the fluid density and velocity vector, respectively, and p is the pressure. The viscous stress dyadic tensor, $\bar{\bar{\tau}}$, can be expressed as $\bar{\bar{\tau}} = \mu[\nabla\vec{u} + \nabla\vec{u}^{\mathrm{T}} - \frac{2}{3}(\nabla \cdot \vec{u})\bar{\bar{I}}]$, where μ is the dynamic viscosity of the fluid and $\bar{\bar{I}}$ represents the identity dyadic tensor. For simplicity, a Newtonian fluid under Stokes' hypothesis is assumed. The components of the

viscous stress tensor are

$$\bar{\bar{\tau}} = \begin{pmatrix} \tau_{xx} & \tau_{xy} & \tau_{xz} \\ \tau_{yx} & \tau_{yy} & \tau_{yz} \\ \tau_{zx} & \tau_{zy} & \tau_{zz} \end{pmatrix} \tag{3.3}$$

where

$$\tau_{xx} = \mu\left(2\frac{\partial u}{\partial x} - \frac{2}{3}\nabla\cdot\vec{u}\right) \quad ; \quad \tau_{yy} = \mu\left(2\frac{\partial v}{\partial y} - \frac{2}{3}\nabla\cdot\vec{u}\right) \quad ; \quad \tau_{zz} = \mu\left(2\frac{\partial w}{\partial z} - \frac{2}{3}\nabla\cdot\vec{u}\right) \tag{3.4}$$

$$\tau_{xy} = \tau_{yx} = \mu\left(\frac{\partial u}{\partial y} + \frac{\partial v}{\partial x}\right) \quad ; \quad \tau_{xz} = \tau_{zx} = \mu\left(\frac{\partial u}{\partial z} + \frac{\partial w}{\partial x}\right) \quad ; \quad \tau_{yz} = \tau_{zy} = \mu\left(\frac{\partial v}{\partial z} + \frac{\partial w}{\partial y}\right) \tag{3.5}$$

Notice that the symmetry of the viscous stress tensor has been emphasized.

Stokes' hypothesis might need to be revised in future works. The fluid does not behave ideally at high pressures, where both liquid and gas are dense and compressible fluids. Therefore, future works should compare the current modeling of the fluid with a new model that includes the bulk viscosity or second coefficient of viscosity and determine if the differences between both approaches are substantial. For reference, Jaeger et al. [70] provide a methodology to evaluate the bulk viscosity for the fluid mixtures this dissertation analyzes.

The equations that describe mass and momentum conservation, Eqs. (3.1) and (3.2), are known as the Navier-Stokes equations. Their solution only represents the dynamic behavior of the fluid motion, and many studies regarding liquid atomization have not analyzed further coupling with thermodynamics. The transport of various species composing either liquid

or gas phases has to be considered and the transport of energy to study a more realistic configuration.

A species continuity equation is defined for each species i as

$$\frac{\partial}{\partial t}(\rho Y_i) + \nabla \cdot (\rho Y_i \vec{u} + \vec{J_i}) = 0 \tag{3.6}$$

where Y_i is the mass fraction of species i and $\vec{J_i}$ represents the mass flux due to diffusion of species i. Only binary mixtures are analyzed in this work and, from now on, the relevant equations are simplified for two-component mixtures. That is, for mixtures with N components where $N = 2$. Nevertheless, the modeling and numerical framework can easily be extended to multi-component mixtures.

The liquid phase starts as a pure hydrocarbon (i.e., $Y_2 = Y_F = 1$) while the gas phase begins as pure oxygen (i.e., $Y_1 = Y_O = 1$). The subscript F stands for fuel and the subscript O stands for oxidizer. For a binary mixture, only one species continuity equation has to be solved since $\sum_{i=1}^{N=2} Y_i = Y_O + Y_F = 1$. The mass diffusion flux is modeled using mass-based Fickian diffusion (i.e., $\vec{J_O} = -\rho D_m \nabla Y_O$). Although a non-ideal model is used to evaluate the transport coefficient D_m (see Subsection 3.3.3), the use of more complex models to evaluate mass diffusion has to be investigated in the future (e.g., generalized Maxwell-Stefan formulation for multi-component mixtures, thermo-diffusion or Soret effect). Choosing the oxidizer species, its transport equation is

$$\frac{\partial}{\partial t}(\rho Y_O) + \nabla \cdot (\rho Y_O \vec{u}) = \nabla \cdot (\rho D_m \nabla Y_O) \tag{3.7}$$

The energy equation is expressed as a transport equation for the mixture specific enthalpy, h, as

$$\frac{\partial}{\partial t}(\rho h) + \nabla \cdot (\rho h \vec{u}) = \frac{Dp}{Dt} + \nabla \cdot (k \nabla T) + \sum_{i=1}^{N=2} \nabla \cdot (\rho D_m h_i \nabla Y_i) + \Phi_d \tag{3.8}$$

where T is the temperature, k is the thermal conductivity, c_p is the specific heat at constant pressure and Φ_d is the viscous dissipation term. Notice that Fickian diffusion is again considered for the energy transport via mass diffusion.

To simplify the coupling between the governing equations, pressure terms and viscous dissipation are neglected in this work based on the assumption that, for relatively low-speed flows at very high pressures, their contribution to the total energy is negligible (see Eq. (3.9)). Therefore, a low-Mach-number formulation is assumed where the thermodynamic pressure is held constant everywhere for open-boundary flows. Under these assumptions, the term $k\nabla T$ in Eq. (3.8) is substituted as $k\nabla T = (k/c_p)\nabla h - \sum_{i=1}^{N=2}(k/c_p)h_i \nabla Y_i$ in Eq. (3.9).

$$\frac{\partial}{\partial t}(\rho h) + \nabla \cdot (\rho h \vec{u}) = \sum_{i=1}^{N=2} \nabla \cdot \left(\left[\rho D_m - \frac{k}{c_p} \right] h_i \nabla Y_i \right) + \nabla \cdot \left(\frac{k}{c_p} \nabla h \right) \tag{3.9}$$

The partial derivative of mixture enthalpy with respect to mass fraction is required in the energy equation to determine the contribution of the species' concentration gradients in the energy transport. This partial derivative is defined as $h_i \equiv \partial h / \partial Y_i$, which must not be confused with the standard definition of partial enthalpy. The derivative is taken at constant pressure, temperature, and composition for any other mixture component. Under non-ideal conditions, the weighted sum of each species' enthalpy at a given temperature and pressure does not provide the correct mixture enthalpy. This often-used mixing rule is only valid for the ideal case, where the definition of h_i also corresponds with the standard definition of partial enthalpy as the species' enthalpy at the same pressure and temperature

as the mixture. For the convection and conduction terms, the proper formulation for mixture enthalpy at high pressures is used (see Subsection 3.3.2).

Note that turbulence models are not considered. Even though liquid atomization involves a transition to a turbulent flow, the early times can be modeled with reasonable accuracy following a direct numerical approach. The scale of the domain is described in Sections 5.1 and 6.1, and representative Reynolds numbers for the analyzed cases are provided in Table 6.2. For all configurations, liquid and gas Reynolds numbers based on the jet thickness as characteristic length are of the order of $\mathcal{O}(10^3)$. The mesh size used in this work, $\Delta x \sim \mathcal{O}(10^{-8}\text{m})$, is sufficiently small to consider the effect of under-resolved dissipation scales negligible, if not fully resolved, during the time frame analyzed here.

3.2.1 Interface matching relations

The governing equations are valid, and their solutions are continuous within each phase. However, a discontinuity in thermodynamic and transport properties exists across the liquid-gas interface, denoted by the subscript Γ. To relate both liquid and gas phases, mass, momentum, and energy conservation relations are defined and imposed in the solution process of the governing equations. These relations are often referred to as jump conditions or matching conditions.

In a frame of reference moving with the interface, the mass flux, Eqs. (3.10) and (3.15), and energy flux, Eq. (3.16), crossing the interface must be continuous (i.e., fluxes normal to the interface). The normal and tangential unit vectors at any interface location are represented by $\vec{n}$ and $\vec{t}$, respectively, with $\vec{n}$ defined positive pointing toward the gas phase. The liquid side of the interface is referred to with the subscript l, whereas the gas phase at the interface is represented by the subscript g.

The vaporization or condensation rate is computed from

$$\dot{m}' = \rho_l(\vec{u}_l - \vec{u}_\Gamma) \cdot \vec{n} = \rho_g(\vec{u}_g - \vec{u}_\Gamma) \cdot \vec{n} \tag{3.10}$$

where $\dot{m}'$ is the mass flux per unit area across the interface. For $\dot{m}' > 0$, net vaporization occurs. On the other hand, $\dot{m}' < 0$ represents net condensation. The energy balance across the interface (i.e., Eq. (3.16)) determines whether net vaporization or net condensation occurs.

The interface moves with respect to the material (i.e., the fluid) for a non-zero value of $\dot{m}'$. Under this circumstance, the normal component of the velocity field is discontinuous across the interface, and the tangential component is continuous for a no-slip condition between at the liquid-gas interface. The normal velocity jump and the tangential velocity relations are given by

$$(\vec{u}_g - \vec{u}_l) \cdot \vec{n} = \left(\frac{1}{\rho_g} - \frac{1}{\rho_l}\right)\dot{m}' \quad ; \quad \vec{u}_g \cdot \vec{t} = \vec{u}_l \cdot \vec{t} \tag{3.11}$$

The momentum balance across the two-phase interface includes surface-tension forces. In problem configurations analyzing real fluids, interface matching conditions will change depending on the interface location. Therefore, interface temperature and composition changes will generate a surface gradient of the surface-tension coefficient. The surface-tension force per unit area at the liquid-gas interface is given by

$$\vec{f_s} = -\sigma\kappa\vec{n} + \nabla_s\sigma \tag{3.12}$$

where σ is the surface-tension coefficient, κ is the interface curvature defined positive with a convex liquid shape (i.e., $\kappa = \nabla \cdot \vec{n}$) and $\nabla_s = \nabla - \vec{n}(\vec{n} \cdot \nabla)$ is the surface-gradient operator.

The momentum balance normal to the interface yields a relation for the pressure jump across the interface. This pressure jump is caused by a combination of surface-tension forces, mass transfer, and a mismatch in the normal viscous stresses, as seen in Eq. (3.13). Similarly, a momentum balance in the tangential direction provides a relation for the tangential stress at the interface, given in Eq. (3.14).

$$p_l - p_g = \sigma\kappa + (\bar{\bar{\tau}}_l \cdot \vec{n}) \cdot \vec{n} - (\bar{\bar{\tau}}_g \cdot \vec{n}) \cdot \vec{n} + \left(\frac{1}{\rho_g} - \frac{1}{\rho_l}\right)(\dot{m}')^2 \tag{3.13}$$

$$(\bar{\bar{\tau}}_g \cdot \vec{n}) \cdot \vec{t} - (\bar{\bar{\tau}}_l \cdot \vec{n}) \cdot \vec{t} = \nabla_s \sigma \cdot \vec{t} \tag{3.14}$$

The normal force $\sigma\kappa$ is responsible for minimizing surface area per unit volume. The surface-tension force tends to smooth the liquid surface for two-dimensional structures. Although smoothing also occurs in three-dimensional structures, surface tension is responsible for ligament thinning and neck formation, which eventually promotes liquid breakup due to capillary forces. On the other hand, the gradient of the surface-tension coefficient along the interface drives the flow toward regions of higher surface-tension coefficient.

The matching relations for the species continuity equation and the energy equation under the simplified low-Mach-number, binary configuration become, respectively,

$$\dot{m}'(Y_{O,g} - Y_{O,l}) = (\rho D_m \nabla Y_O)_g \cdot \vec{n} - (\rho D_m \nabla Y_O)_l \cdot \vec{n} \tag{3.15}$$

and

$$\begin{aligned}\dot{m}'(h_g - h_l) =& \left(\frac{k}{c_p}\nabla h\right)_g \cdot \vec{n} - \left(\frac{k}{c_p}\nabla h\right)_l \cdot \vec{n} \\ &+ \left[\left(\rho D_m - \frac{k}{c_p}\right)(h_O - h_F)\nabla Y_O\right]_g \cdot \vec{n} \\ &- \left[\left(\rho D_m - \frac{k}{c_p}\right)(h_O - h_F)\nabla Y_O\right]_l \cdot \vec{n}\end{aligned} \tag{3.16}$$

where $\Delta h_{\text{vap}} = h_g - h_l$ is the heat or enthalpy of vaporization.

Lastly, the interface matching relations presented in this section are coupled to local thermodynamic phase equilibrium, which is formally defined in Subsection 3.3.4. Altogether, the solution of the system of equations defined by the interface jump conditions and phase equilibrium defines the local interface state (e.g., temperature and composition).

3.3 Thermodynamic Modeling

The governing equations require accurate thermodynamic and transport properties in a wide range of thermodynamic states to capture physical processes at high pressures adequately. A real-gas equation of state is used to evaluate density, enthalpy, and other thermodynamic parameters given a state point in the thermodynamic space (i.e., p, T and Y_i). Transport properties are obtained from various models and correlations developed for high-pressure or high-dense fluids.

3.3.1 Equation of state for the real fluid

The Soave-Redlich-Kwong (SRK) cubic equation of state is used in this work. It was initially developed by Soave [48] as an improved Redlich-Kwong (RK) equation of state [71]. This

family of cubic equations of state originates from the Van der Waals (VdW) equation of state [72], which was the first attempt to modify the ideal gas equation of state to account for high-density, real-gas effects. A constant attractive parameter between the fluid's molecules and a constant volumetric parameter related to the volume occupied by the fluid's molecules was considered. However, the VdW equation of state only proves to be helpful to represent real gases. Thus, Redlich and Kwong [71] and later Soave [48] proposed modifications to the VdW equation of state and a temperature-dependent attractive parameter that improve the fluid's density predictions in a broader range of fluid states, including the liquid phase.

Other non-cubic equations of state exist, which might prove more accurate. For instance, the Benedict-Webb-Rubin (BWR) equation of state [73, 74] uses extensive experimental data to estimate up to eight parameters of the proposed equation of state. Such detail provides an accurate but also component-specific equation of state. From a computational perspective, a cubic equation of state, such as the SRK equation of state, is more efficient to implement while still providing reasonable accuracy in predicting liquid and gas states. Analytical solutions exist that do not require a lot of computational resources.

However, the density predictions of dense fluids (i.e., the liquid phase or gases under very high pressures) obtained with the original SRK equation of state might still deviate considerably from experimental values with errors up to 20% [18, 75]. To improve the accuracy of the SRK equation of state, a volume correction is implemented following the work by Lin et al. [76] instead of pursuing the implementation of other cubic equations of state, such as the more complex Peng-Robinson (PR) equation of state [77] which is arguably more accurate in this aspect. This volume correction acts as a volume translation in the thermodynamic space which recovers the experimental critical molar volume, $\bar{v}_c^{\text{exp}}$, at the critical point T_c and p_c. This method also increases the accuracy of density predictions for different temperatures and pressures. A clear benefit of this improvement is obtained when evaluating transport properties (e.g., viscosity) using models and correlations that rely on the fluid density as an

input parameter. Better fluid density predictions relate to better transport properties and a more realistic simulation with physical relevance.

The volume-corrected SRK equation of state becomes

$$p = \frac{R_u T}{\left[\bar{v} - b + c(T)\right]} - \frac{a(T)}{\left[\bar{v} + c(T)\right]\left[\bar{v} + b + c(T)\right]} \tag{3.17}$$

where $a(T)$ represents a temperature-dependent cohesive energy parameter, b represents the volumetric parameter and $c(T)$ is a temperature-dependent volume correction. R_u is the universal gas constant (i.e., $R_u = 8.314$ J/(mol·K)) and v is the molar volume. The cohesive parameter is evaluated as

$$a(T) = a_c \alpha(T) \quad ; \quad a_c = \frac{1}{9(2^{1/3} - 1)} \frac{R_u^2 T_c^2}{p_c} \tag{3.18}$$

$$\alpha(T) = [1 + m(1 - T_r^{0.5})]^2 \quad ; \quad m = 0.48508 + 1.55171\omega - 0.15613\omega^2 \tag{3.19}$$

where $T_r = T/T_c$ stands for the reduced temperature and the coefficient m is computed according to the modification proposed by Graboski and Daubert [78, 79]. ω represents the acentric factor of the molecule. The volumetric parameter and its correction are obtained from

$$b = b_c = \frac{2^{1/3} - 1}{3} \frac{R_u T_c}{p_c} \quad ; \quad c(T) = c_c f(T_r) \quad ; \quad c_c = \bar{v}_c^{\mathrm{SRK}} - \bar{v}_c^{\mathrm{exp}} = \left(\frac{1}{3} - Z_c^{\mathrm{exp}}\right) \frac{R_u T_c}{p_c} \tag{3.20}$$

with $\bar{v}_c^{\mathrm{SRK}}$ being the critical molar volume predicted from the original SRK equation of state, Z_c^{exp} the experimental compressibility factor of the critical point, and $f(T_r)$ a temperature-dependent function which becomes $f(T_r) = 1$ at the critical point (i.e., $T_r = 1$). This

function is obtained from Lin et al. [76] and is given by

$$f(T_r) = \beta + (1 - \beta) \exp\left(\eta |1 - T_r|\right) \tag{3.21}$$

In Eq. (3.21), β and η are experimentally fitted parameters for each species. To avoid isotherm crossing near the critical temperature at very high pressures, the volume correction should be temperature-independent if $p > p_c$. Then, Eq. (3.21) is modified as in Lin et al. [76]

$$f(T_r) = \beta + (1 - \beta) \exp\left(0.5\eta\right) \tag{3.22}$$

Figure 3.2 shows a comparison between the predicted densities with the original SRK equation of state and the volume-corrected or improved SRK equation of state against reference data from the National Institute of Standards and Technology (NIST). The results presented in this dissertation have been obtained using oxygen as the oxidizer or pure gas species and a hydrocarbon (i.e., *n*-decane) as the fuel or pure liquid species. The volumetric correction has a minor influence on the density prediction of oxygen at high pressures, and the original SRK equation of state displays reasonable accuracy. However, the importance of adding the volumetric correction is highlighted in the *n*-decane density predictions, where the volume-corrected SRK equation of state outperforms the original SRK model and matches better with the reference data from NIST.

For mixtures, quadratic mixing rules are used based on the mixture composition in terms of the mole fractions, X_i. These mixing rules presented in Eq. (3.23) follow the original guidelines provided by Soave [48] and also implemented in Lin et al. [76]. Other mixing rules could be considered, but the analysis of their performance is out of the scope of the present work, and satisfactory matching with experimental data has been obtained with the present

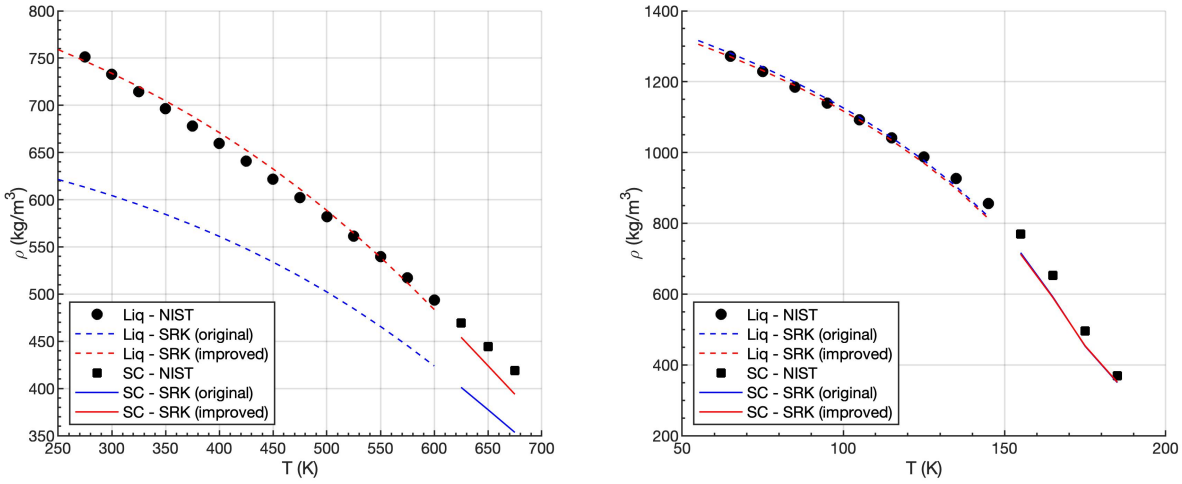

(a) (b)

Figure 3.2: Comparison of density predictions at 100 bar and different temperatures using the original SRK equation of state [48] and the volume-corrected or improved SRK equation of state [76]. The improved model predicts the density with higher accuracy when compared to reference data available at NIST as it transitions from the liquid state (Liq) to the supercritical state (SC) with increasing temperature. (a) density of *n*-decane; (b) density of oxygen.

model. Note that the dependence on temperature for the terms related to a and c is not explicitly written for nomenclature convenience.

$$a = \sum_{i=1}^{N}\sum_{j=1}^{N} X_i X_j (a_i a_j)^{0.5}(1-k_{ij}) \quad ; \quad b = \sum_{i=1}^{N} X_i b_i \quad ; \quad c = \sum_{i=1}^{N} X_i c_i \tag{3.23}$$

The binary interaction parameter, k_{ij}, is obtained from vapor-liquid equilibrium experimental data and depends on the equation of state. For instance, correlations specific for the SRK equation of state and different mixtures (e.g., nitrogen-alkane pairs) are found in Soave et al. [80]. If data is not available, the interaction coefficients are usually neglected. However, it must be justified. Data is scarce or not available for oxygen-alkane mixtures, but this is not the case for nitrogen-alkane mixtures. For the latter, $k_{ij} \approx 0$ and, under the assumption that nitrogen and oxygen are similar components, setting $k_{ij} = 0$ for oxygen-alkane mixtures can be accepted.

Validation of the thermodynamic model presented in this chapter is shown in Appendix D. Results for pure oxygen and pure n-decane are obtained for various fluid properties and transport properties at different pressures relevant for this dissertation. The estimates are successfully compared against reference data from NIST and do not include mixture properties due to few data points being available. Note in Appendix D that the improved SRK equation of state is referred to as SRK-L-M (or the SRK equation from the Lin et al. [76] model).

3.3.2 Evaluation of fluid properties from departure functions

It is useful to recast Eq. (3.17) in terms of the compressibility factor, Z, to develop equations for the fluid properties. Therefore, Eq. (3.17) is rewritten as

$$Z^3+(3B_*-1)Z^2+\left[B_*(3B_*-2)+A-B-B^2\right]Z+B_*(B_*^2-B_*+A-B-B^2)-AB=0 \quad (3.24)$$

with

$$Z=\frac{\bar{v}p}{R_uT} \quad ; \quad A=\frac{ap}{R_u^2T^2} \quad ; \quad B=\frac{bp}{R_uT} \quad ; \quad B_*=\frac{cp}{R_uT} \tag{3.25}$$

Again, the dependence on temperature for the terms related to a and c is not explicitly written. Eq. (3.24) is a cubic equation for Z, which can be solved to obtain the molar volume or the density ($\rho = W/\bar{v}$) of the mixture for a given pressure, temperature and composition. Notice that Z can be rewritten as $Z = p/(\rho RT)$, where $R = R_u/W$ is the specific gas constant.

Expressions for the mixture specific enthalpy, h, the mixture specific internal energy, e, the mixture specific entropy, s, and the fugacity coefficient of species i, Φ_i, are given in Eqs. (3.26), (3.27), (3.28) and (3.29), respectively. They are derived from fundamental

thermodynamic principles, whereby deviations from the ideal gas state (denoted by *) are introduced by means of a departure function [81].

$$h = h^*(T) + \frac{1}{W}\left[R_u T(Z-1) + R_u T \int_\infty^{\bar{v}} \left(T\left(\frac{\partial Z}{\partial T}\right)_{\bar{v},X_i}\right)\frac{d\bar{v}}{\bar{v}}\right] \tag{3.26}$$

$$e = e^*(T) + \frac{R_u T}{W}\int_\infty^{\bar{v}} \left(T\left(\frac{\partial Z}{\partial T}\right)_{\bar{v},X_i}\right)\frac{d\bar{v}}{\bar{v}} \tag{3.27}$$

$$\begin{aligned} s =& s^*(T,p_0) + \frac{1}{W}\left[- R_u \ln\left(\frac{p}{p_0}\right) - R_u \sum_{i=1}^{N} X_i \ln(X_i)\right] \\ &+ \frac{1}{W}\left[R_u \ln(Z) + R_u \int_\infty^{\bar{v}} \left(T\left(\frac{\partial Z}{\partial T}\right)_{\bar{v},X_i} - 1 + Z\right)\frac{d\bar{v}}{\bar{v}}\right] \end{aligned} \tag{3.28}$$

$$\ln(\Phi_i) = \int_\infty^{\bar{v}} \left[\frac{1}{\bar{v}} - \frac{1}{R_u T}\left(\frac{\partial p}{\partial X_i}\right)_{T,\bar{v},X_{j\neq i}}\right] d\bar{v} - \ln Z \tag{3.29}$$

Notice that Eq. (3.28) also includes terms to account for deviations from the reference pressure, p_0, of the ideal gas mixture entropy and the entropy of mixing caused by the irreversible mixing process between different species [82–84]. Combining the previous expressions with the volume-corrected SRK equation of state, the following relations are obtained

$$\begin{aligned} h = h^*(T) &+ \frac{1}{W}\left[R_u T(Z-1) + \frac{T(\partial a/\partial T)_{\bar{v},X_i} - a}{b}\ln\left(1 + \frac{B}{Z + B_*}\right)\right] \\ &+ \frac{1}{W}\left[R_u T^2 \left(\frac{Z}{\bar{v}}\right)\left(\frac{\partial c}{\partial T}\right)_{\bar{v},X_i}\right] \end{aligned} \tag{3.30}$$

$$e = e^*(T) + \frac{1}{W}\left[\frac{T(\partial a/\partial T)_{\bar{v},X_i} - a}{b}\ln\left(1+\frac{B}{Z+B_*}\right) + R_u T^2\left(\frac{Z}{\bar{v}}\right)\left(\frac{\partial c}{\partial T}\right)_{\bar{v},X_i}\right] \tag{3.31}$$

$$\begin{aligned} s = s^*(T,p_0) &+ \frac{1}{W}\left[- R_u \ln\left(\frac{p}{p_0}\right) - R_u \sum_{i=1}^{N} X_i \ln(X_i)\right] \\ &+ \frac{1}{W}\left[\frac{1}{b}\left(\frac{\partial a}{\partial T}\right)_{\bar{v},X_i}\ln\left(1+\frac{B}{Z+B_*}\right) + R_u \ln(Z+B_*-B)\right] \\ &+ \frac{1}{W}\left[R_u T\left(\frac{Z}{\bar{v}}\right)\left(\frac{\partial c}{\partial T}\right)_{\bar{v},X_i}\right] \end{aligned} \tag{3.32}$$

$$\begin{aligned} \ln(\Phi_i) =& \frac{Z+B_*-1}{b}\frac{\partial b}{\partial X_i} - \frac{B_*}{c}\frac{\partial c}{\partial X_i} - \ln(Z+B_*-B) \\ &- \frac{A}{B}\left(\frac{1}{a}\frac{\partial a}{\partial X_i} - \frac{1}{b}\frac{\partial b}{\partial X_i}\right)\ln\left(1+\frac{B}{Z+B_*}\right) \end{aligned} \tag{3.33}$$

Furthermore, expressions for the mixture specific heat at constant pressure, c_p, and the partial derivative of mixture specific enthalpy with respect to species i, h_i, are needed. They are obtained by applying the respective thermodynamic definitions. The specific heat at constant pressure becomes

$$\begin{aligned} c_p = \left(\frac{\partial h}{\partial T}\right)_{p,X_i} = c_p^*(T) &+ \frac{1}{W}\left[\frac{T}{b}\left(\frac{\partial^2 a}{\partial T^2}\right)_{p,X_i}\ln\left(1+\frac{B}{Z+B_*}\right) - R_u\right] \\ &+ \frac{1}{W}\left[\left(p - \frac{T(\partial a/\partial T)_{\bar{v},X_i} - a}{(\bar{v}+c)(\bar{v}+c+b)}\right)\left(\left(\frac{\partial \bar{v}}{\partial T}\right)_{p,X_i} + \left(\frac{\partial c}{\partial T}\right)_{p,X_i}\right)\right] \\ &+ \frac{1}{W}\left[R_u T^2\left(\frac{Z}{\bar{v}}\right)\left(\frac{\partial^2 c}{\partial T^2}\right)_{p,X_i}\right] \end{aligned} \tag{3.34}$$

and the partial derivative of the mixture molar enthalpy with respect to species i, $\bar{h}_i$, is

$$\begin{aligned}\bar{h}_i = \left(\frac{\partial \bar{h}}{\partial X_i}\right)_{p,T,X_{j\neq i}} &= \bar{h}_i^*(T) + p\left(\frac{\partial \bar{v}}{\partial X_i}\right)_{p,T,X_{j\neq i}} - R_u T \\ &+ \frac{aA_1}{\bar{v}+c+b}\left[A_2 - \frac{1}{\bar{v}+c}\left(\left(\frac{\partial \bar{v}}{\partial X_i}\right)_{p,T,X_{j\neq i}} + \left(\frac{\partial c}{\partial X_i}\right)_{p,T,X_{j\neq i}}\right)\right] \\ &+ \frac{1}{b}\left(T\left(\frac{\partial^2 a}{\partial X_i \partial T}\right)_{p,T,X_{j\neq i}} - \left(\frac{\partial a}{\partial X_i}\right)_{p,T,X_{j\neq i}} - aA_1A_2\right)\ln\left(\frac{\bar{v}+c+b}{\bar{v}+c}\right) \\ &+ R_u T^2\left(\frac{Z}{\bar{v}}\right)\left(\frac{\partial^2 c}{\partial X_i \partial T}\right)_{p,T,X_{j\neq i}}\end{aligned} \tag{3.35}$$

where A_1 and A_2 are defined as

$$A_1 \equiv \frac{T}{a}\left(\frac{\partial a}{\partial T}\right)_{\bar{v},X_i} - 1 \quad ; \quad A_2 \equiv \frac{1}{b}\left(\frac{\partial b}{\partial X_i}\right)_{\bar{v},X_i} \tag{3.36}$$

Once $\bar{h}_i$ is known, the partial derivative of the mixture specific enthalpy with respect to species i needed in Eq. (3.8) is obtained as $h_i = \bar{h}_i / W_i$.

All partial derivatives involved in the previous expressions can be found in Appendix B. Notice that in the supercritical pressure domain, the volume-correction term, c, is no longer a function of temperature (see Eqs. (3.20) and (3.22)). Therefore, all partial derivatives of c with respect to temperature become zero. Ideal-gas enthalpy, internal energy, entropy, and specific heat at constant pressure are obtained from the correlations by Passut and Danner [85] and ideal gas mixing rules as

$$h^*(T) = \sum_{i=1}^{N} Y_i h_i^*(T) \quad ; \quad e^*(T) = h^*(T) - p/\rho^* \tag{3.37}$$

$$s^*(T, p_0) = \sum_{i=1}^{N} Y_i s_i^*(T, p_0) \quad ; \quad c_p^*(T) = \sum_{i=1}^{N} Y_i c_{p_i}^*(T) \tag{3.38}$$

with

$$h_i^*(T) = \hat{A} + \hat{B}T + \hat{C}T^2 + \hat{D}T^3 + \hat{E}T^4 + \hat{F}T^5 \tag{3.39}$$

$$s_i^*(T, p_0) = \hat{B}\ln T + 2\hat{C}T + \frac{3}{2}\hat{D}T^2 + \frac{4}{3}\hat{E}T^3 + \frac{5}{4}\hat{F}T^4 + \hat{G} \tag{3.40}$$

$$c_{p,i}^*(T) = \hat{B} + 2\hat{C}T + 3\hat{D}T^2 + 4\hat{E}T^3 + 5\hat{F}T^4 \tag{3.41}$$

where ρ^* is the ideal gas density evaluated using the ideal gas law (i.e., $\rho^* = p/(RT)$), p_0 is the reference pressure for entropy calculations set at 1 atm and $\hat{A}$-$\hat{G}$ are correlation constants given in Passut and Danner [85]. For more details about the ideal-gas correlations, the reader is referred to the original work or to Appendix C.

3.3.3 Evaluation of transport properties from high-pressure correlations

The thermodynamic modeling based on the volume-corrected SRK equation of state is coupled with the evaluation of transport properties from high-pressure correlations that require information of the thermodynamic state of the mixture (i.e., pressure, temperature, composition, and density). Viscosity and thermal conductivity are obtained from the generalized multiparameter correlation from Chung et al. [61], which is widely used in the literature. Then, the surface-tension coefficient is estimated as a function of the properties and composition of each phase at the interface from the Macleod-Sugden correlation, as suggested by Poling et al. [81].

The mass-based diffusion coefficient, D_m, is obtained from the model developed by Leahy-Dios and Firoozabadi [86]. This work uses the Maxwell-Stefan equations, Eq. (3.42), to obtain generalized diffusion fluxes for each species in a mixture. Some of the variables appearing in Eq. (3.42) are the binary diffusion coefficient between species i and j, D_{ij}, which is obtained from a correlation developed in Leahy-Dios and Firoozabadi [86] that takes into account non-ideal effects such as high-pressure environments; D_i^T is a thermo-diffusion coefficient related to the Soret effect; d_i is the diffusion driving force; c in the context of Eq. (3.42) is the molar density; and J_i^M is a molar-based diffusion flux.

$$\sum_{j\neq i} \frac{X_i X_j}{D_{ij}} \left(\frac{J_j^M}{cX_j} - \frac{J_i^M}{cX_i} \right) = d_i - \sum_{j\neq i} \frac{X_i X_j}{D_{ij}} \left(\frac{D_j^T}{\rho Y_j} - \frac{D_i^T}{\rho Y_i} \right) \nabla \ln T \tag{3.42}$$

In the present work, thermal diffusion effects are neglected and, for a binary mixture, the Maxwell-Stefan equations are solved and recast in Fickian form in a mass-based frame of reference [86, 87] as $\vec{J}_1 = -\vec{J}_2 = -\rho D_m \nabla Y_1$ where $D_m = D_{12}\Gamma_{11}$. Here, D_{12} represents the mass-based binary diffusion coefficient between species 1 and 2 (i.e., species indexing) while Γ_{11} represents the thermodynamic factor associated with an element of the Fickian diffusion matrix (i.e., matrix indexing). For a binary mixture, the diffusion matrix only has one element defined by a row index 1 and a column index 1. Thus, D_m is actually $D_{m,11}$. Recall that, in Section 3.2, species 1 has been identified as the oxidizer species, O, and species 2 has been identified as the fuel species, F.

The thermodynamic factor Γ_{11} is obtained from

$$\Gamma_{11} = 1 + X_1 \left[\left(\frac{\partial \ln \Phi_1}{\partial X_1} \right)\bigg|_{p,T} - \left(\frac{\partial \ln \Phi_1}{\partial X_2} \right)\bigg|_{p,T} \right] \tag{3.43}$$

and it represents non-idealities in the diffusion process, which are included in the diffusion driving force, d_i [34, 54, 86]. The mathematical definition of the thermodynamic factor and

the unconstrained derivation of Eq. (3.43) are shown in Liu et al. [88]. Partial derivatives of the fugacity coefficient based on the SRK equation of state are shown in Appendix B.

The thermodynamic factor tends to $\Gamma_{11} \to 1$ as the mixture gets closer to the ideal state and it is identically $\Gamma_{11} = 1$ for a pure substance. However, there is no mathematical restriction for the value of this coefficient, and it may become negative for a given composition range, pressure, and temperature. As other authors report, this situation of negative or reversed diffusion is associated to phase instability of the mixture, driving phase separation and the creation of a two-phase interface [47, 89].

Further details about these models and correlations can be found in each respective work and in Appendix C.

3.3.4 Local thermodynamic phase equilibrium

A thermodynamic closure for the interface matching conditions is obtained from phase-equilibrium relations. LTE is imposed through an equality in the chemical potential for each species on both sides of the interface. This condition can be expressed in terms of an equality in fugacity [48, 81] as

$$f_{li}(T_l, p_l, X_{li}) = f_{gi}(T_g, p_g, X_{gi}) \tag{3.44}$$

where the species' fugacity, f_i, is a function of temperature, pressure and mixture composition.

For phase-equilibrium purposes, the pressure jump across the interface is neglected (see Eq. (3.13)), and pressure is assumed constant across the interface. Moreover, large pressure variations are not expected in low-Mach-number compressible flows. Therefore, the pressure can be split into a thermodynamic pressure that remains constant and equal to the chamber

pressure and a dynamic pressure whose variations are responsible for the fluid motion but have a negligible effect on the fluid properties. Under this assumption, pressure is treated constant and equal to the chamber pressure, p_{ch}, to evaluate LTE at the interface (i.e., $p_l \approx p_g \approx p_{\text{ch}}$) and other fluid and transport properties everywhere in the computational domain. Then, phase equilibrium can be expressed using the fugacity coefficient, defined as $\Phi_i \equiv f_i/pX_i$. For equal pressure on both sides of the interface, Eq. (3.44) is reduced to $X_{li}\Phi_{li} = X_{gi}\Phi_{gi}$.

The thickness of the interface is of the order of nanometers [29, 30, 32] while mass, momentum, and energy diffusion layers quickly grow to the order of micrometers around the interface [15–17]. Therefore, the present work neglects the interface thickness and temperature is assumed continuous across the interface (i.e., $T_g = T_l = T_\Gamma$), which simplifies the solution of LTE and the matching conditions at the interface and a mixture composition is readily available on each side of the interface.

The phase-equilibrium model for the interface is a valid assumption as long as the interface temperature is far from the mixture critical point at a given pressure [31]. A detailed discussion about the various issues affecting the interface modeling has been provided in Subsection 2.2.2. The thermodynamic states expected in the studies presented in this dissertation fall within the domain of two-phase coexistence under LTE as discussed in Section 3.1.

Chapter 4

Numerical Methods

This chapter introduces the numerical methods implemented to solve the two-phase, high-pressure problem. In Section 4.1, the interface capturing approach, which is based on a Volume-of-Fluid method, is discussed. Another widely-used interface capturing method, called the Level-Set method, is reviewed to highlight the intrinsic numerical difficulties that would prevent its proper implementation for the type of flows this work addresses. Also, the methodology used to capture the local interface state at every interface cell is presented. Then, in Section 4.2, the solution of the governing equations for the scalar variables (i.e., species and energy transport equations) is presented, followed by the solution method of the continuity and momentum equations in Section 4.3, where a low-Mach-number Poisson equation for the pressure field is proposed using a split pressure-gradient technique. Section 4.4 has the evaluation of fluid compressibilities, as well as the extrapolation methodologies used to get phase-wise compressibilities and velocities. Finally, Section 4.5 contains the detailed solution algorithm, information about the time step criteria, and details on the numerical implementation.

The methodologies and numerical techniques discussed in this chapter are implemented on a computational domain discretized with a Cartesian uniform mesh and control volumes or cells for the reader's reference. The proposed methodologies could be extended to non-uniform meshes or orthogonal meshes. Nonetheless, this work has been performed with a uniform mesh to focus on the intrinsic modeling difficulties of high-pressure, two-phase flows rather than specific numerical details linked to more complex mesh configurations. Moreover, a staggered configuration is used where velocity nodes are located at the center of the cell faces, and all other variables (e.g., pressure, fluid properties, volume fraction occupied by the liquid phase) are evaluated at the cell center.

4.1 Interface Capturing Model

The accurate tracking and capturing of the liquid-gas interface are essential in a two-phase fluid solver. Various interface-capturing and interface-tracking methods exist, which are summarized in Elghobashi [90]. The most popular approaches in the interface-capturing category are the Level-Set (LS) method developed by Sussman et al. [58, 59] and Osher and Fedkiw [60] and the Volume-of-Fluid (VOF) method [91, 92]. A method in the interface-tracking family is the Front-Tracking method by Tryggvason et al. [93].

A review of the classic LS method and some improvements to the approach is presented in Subsection 4.1.1. However, the LS method has some intrinsic issues that make it unsuitable for analyzing atomization of liquid jets at supercritical pressures (e.g., difficulties in maintaining a sharp interface, numerical mass loss). On the other hand, mass conservation to machine-error precision can be achieved with VOF methods [63]. Moreover, VOF methods handle vaporization or condensation naturally, and the governing equations are solved with a sharp interface approach that only diffuses the interface in a region of the order of $\mathcal{O}(\Delta x)$ by volume-averaging fluid properties at the interface cells [64, 94].

VOF methods like those developed by Baraldi et al. [63], Dodd and Ferrante [64] and Dodd et al. [94] are good starting points to develop numerical tools for transcritical atomization. Despite being intended for incompressible liquids with or without phase change, the method is computationally efficient and satisfies mass conservation while maintaining a sharp interface. Recently, the methodology presented in Baraldi et al. [63], Dodd and Ferrante [64] and Dodd et al. [94] has been extended to two-phase flows with phase change where the gas phase is compressible [95].

Few studies address the application of VOF methods to compressible liquids (e.g., see [96–98]), let alone non-ideal thermodynamics at high pressures. As a result, there is a clear gap in the literature that needs to be filled. Extending the methodologies presented in Baraldi et al. [63], Dodd and Ferrante [64] and Dodd et al. [94, 95] to handle compressible two-phase flows in combination with real-fluid thermodynamics and phase change provides an efficient numerical tool for studying supercritical liquid injection while maintaining a sharp interface.

The VOF method is extended in Subsection 4.1.2 to a compressible formulation and it is used to advect and capture the interface and its geometrical properties. Without loss of generality, the method applies to compressible flows where density variations do not necessarily need to be linked to pressure variations. That is, it can also be applied to low-Mach-number flows where density is mainly a function of mixture composition and temperature. Moreover, both liquid and gas phases are considered to be compressible.

4.1.1 A review on the Level-Set method

The level-set method was originally developed by Sussman et al. [58, 59] and Osher and Fedkiw [60]. The method consists of the advection of a scalar, $\theta(\vec{x}, t)$, defined as the shortest distance to the interface at a given location. One side of the interface (e.g., gas phase) is represented by positive values of θ while the other side (e.g., liquid phase) is represented by

negative values of θ. Therefore, the interface is located where $\theta(\vec{x}_\Gamma, t) = 0$. The level-set scalar is transported by the interface velocity, $\vec{u}_\Gamma$, as

$$\frac{\partial \theta}{\partial t} + \vec{u}_\Gamma \cdot \nabla \theta = 0 \tag{4.1}$$

which may not be the fluid velocity in the presence of phase change. The interface velocity is obtained from Eq. (3.10) as

$$\vec{u}_\Gamma = \vec{u}_l - \frac{\dot{m}'}{\rho_l}\vec{n} = \vec{u}_g - \frac{\dot{m}'}{\rho_g}\vec{n} \tag{4.2}$$

and, physically, it is only valid at the interface.

When a non-uniform velocity field advects the level set, its value may no longer represent the shortest distance to the interface. Therefore, a reinitialization technique is needed to re-distance the level-set function. The most common solution to this problem is to solve Eq. (4.3), until steady-state is reached (i.e., $|\nabla \theta'| = 1$) over a pseudo-time, t^* [58, 59].

$$\frac{\partial \theta'}{\partial t^*} = \text{sign}(\theta)(1 - |\nabla \theta'|) \tag{4.3}$$

where θ' is the re-distanced level-set scalar.

However, the classical treatment of the LS method generates a numerical mass loss, which is not desirable in atomization problems involving phase change. Apart from numerical errors associated with the discretization of Eq. (4.1), the leading cause of mass loss is the anchoring of the zero-level or interface location when performing the reinitialization of the level-set function. If not done correctly, the interface moves during the reinitialization process. Most numerical schemes such as ENO or WENO cannot handle this issue properly, and some degree of mass loss is present, even for high-order approaches [99].

To mitigate this problem, the gradient-augmented level-set method (GALS) [99] is proposed instead of the classical level-set approach. The level-set function and its gradient, $\vec{\psi}$, are advected by solving Eq. (4.1) and Eq. (4.4) with a generalization of the CIR method [100] coupled with cell-based Hermite interpolants or bicubic interpolations.

$$\frac{\partial \vec{\psi}}{\partial t} + \vec{u}_\Gamma \cdot \nabla \vec{\psi} = -\nabla \vec{u}_\Gamma \cdot \vec{\psi} \tag{4.4}$$

The advection of the level-set gradient is significant since gradient information is needed to construct the interpolants for the correct advection of the level-set function. Evaluation of the gradient of θ from high-order, finite-difference methods is another option if one does not want to solve a new equation and may avoid inaccuracies in the value of the gradient of θ under prolonged advection. Overall, the GALS method without reinitialization presents similar conservation properties as the classical LS method solved using 5th order WENO schemes with reinitialization [99]. Additionally, the bicubic interpolations allow to capture and advect subgrid structures.

To further improve the performance of the GALS method, a hybrid reinitialization technique can be implemented. It combines a geometrical re-distancing of the level-set function at grid nodes adjacent to the interface with a CIR-based reinitialization for the other nodes [101]. This approach improves the anchoring of the interface location and avoids problems arising from possible singularities in the characteristic form of Eq. (4.3), which is a Hamilton-Jacobi type of equation. To alleviate the computational costs of the reinitialization, the CIR-based method is performed only in a narrow band of a few cells around the interface. For the rest of the domain, a fast solution of Eq. (4.3) is performed, as suggested by Anumolu and Trujillo [62]. The hybrid reinitialization is seen to improve the mass conservation of the method, except in situations where the local radius of curvature is of the order of the mesh size [102].

Although the LS method cannot conserve mass to machine-error precision, its main advantage is a straightforward and smoother calculation of the interface geometry compared to VOF methods. The normal unit vector and the curvature are obtained from the level-set field [59] as

$$\vec{n} = \frac{\nabla\theta}{|\nabla\theta|} \quad ; \quad \kappa = \nabla \cdot \vec{n} = \nabla \cdot \left(\frac{\nabla\theta}{|\nabla\theta|} \right) \tag{4.5}$$

Then, information about the tangential unit vector, $\vec{t}$, can be readily found from orthogonality with $\vec{n}$.

Since the level-set method provides distance information to the interface location, a redistribution of the discontinuities as a function of θ can be done to avoid inconsistent numerical stencils near the interface [26, 27]. Using a smooth Heaviside function, $H(\theta)$, a given fluid property ϕ (e.g., density, viscosity) can be defined across the interface as

$$\phi(\theta) = \phi_l + (\phi_g - \phi_l)H(\theta) \tag{4.6}$$

where ϕ_g and ϕ_l are the values of the given fluid property in the gas phase and the liquid phase, respectively. The smooth Heaviside function tends to $H(\theta) = 1$ in the gas phase and $H(\theta) = 0$ in the liquid phase.

Similarly, a smooth Dirac delta function can be obtained as $\delta(\theta) = dH(\theta)/d\theta$. This function includes jump conditions in the governing equations as source terms active within some thin region around the interface location. In the case of the momentum equation, Eq. (3.2), surface tension is included as

$$\frac{\partial}{\partial t}(\rho\vec{u}) + \nabla \cdot (\rho\vec{u}\vec{u}) = -\nabla p + \nabla \cdot \bar{\bar{\tau}} - \sigma\kappa\delta(\theta)\vec{n} \tag{4.7}$$

and similar source terms can be added to other governing equations based on $\delta(\theta)$ [103, 104].

The previous approach presents issues that make it unfit to analyze high-pressure, two-phase flows. The redistribution of the discontinuities across the interface is performed within a region of the order of $3 - 5 \sim \Delta x$, which generates an artificially diffuse interface that may not capture the thermodynamic behavior of the interface properly for more complex simulations (e.g., with phase change) and which overlaps with actual mixing layers. Moreover, the formulation is only suitable for incompressible flows with constant fluid properties. If $\phi \neq$ constant, the smooth Heaviside distribution in Eq. (4.6) may not connect properly the diffusion layers evolving on either side of the interface for more realistic configurations. Another problem is related to the matching conditions at the interface. Because of the phase-equilibrium formulation coupled with the relations between each governing equation, interface properties can vary along the interface (e.g., temperature, composition, surface tension). Therefore, a different approach is needed to capture the sharp interface better and deal with variable fluid properties and interface matching conditions.

An accepted approach to defining a smooth numerical stencil across the interface while keeping it sharp is the Ghost Fluid Method (GFM) [105]. The method aims to extend each phase across the interface. That is, a ghost gas phase coexists with the liquid phase, and a ghost liquid is defined in the gas phase. For non-regressive interfaces, continuous variables across the interface are copied node-by-node from the actual phase to the ghost phase (e.g., velocity components). On the other hand, discontinuous variables are usually obtained from one-sided extrapolations. A different approach is used for a regressive interface (e.g., with phase change across the interface). A solution for the ghost fluid is obtained such that conservation of mass, momentum, and energy is imposed in a frame of reference with a continuous flux across the interface [106]. That is, relative to the interface velocity in the normal direction. In this case, the ghost fluid presents the same mass, momentum, and energy flux as the actual fluid at a given location. The ghost fluid solution can be found by

solving an algebraic system of equations, including the various flux-matching conditions and an equation of state.

This approach has been successfully implemented in inviscid flows [106, 107] and viscous flows [108], but without the intrinsic difficulties of real-fluid modeling. Other authors have used simplified approaches of the method for incompressible flows with phase change [62, 109], where density is not a variable to solve for, and compressible flows under perfect-gas law [110].

Theoretically, the ghost fluid solution is unique. However, solving the exact ghost fluid becomes too complex for the real-fluid modeling used in this work and the governing equations, which include many viscous-like terms and time- and space-varying variables. The highly-coupled non-linear system causes the solver performance to depend strongly on the initial solution guess. Moreover, different solutions are obtained depending on the accuracy in evaluating some terms near the interface, such as concentration gradients or temperature gradients, and simplifying the system of equations might generate many different valid solutions for the ghost fluid.

Given the intrinsic difficulties of obtaining an accurate interface modeling using the level-set method, a different path is needed. The following section presents a Volume-of-Fluid method for compressible flows with phase change. This VOF method is developed and implemented in this work and presents many advantages compared to the LS method: mass-conservation properties and physics capturing properties.

4.1.2 A Volume-of-Fluid method for compressible flows with phase change

The VOF method [91, 92] advects a characteristic function, $\chi(\vec{x}, t)$, with the fluid velocity, $\vec{u}$, following Eq. (4.8). This characteristic function becomes $\chi = 1$ in the reference phase (i.e., liquid phase in the present work) and $\chi = 0$ in the other phase (i.e., gas phase). The volume fraction, C, represents the volume occupied by the reference fluid in a cell with respect to the total cell volume, V_0. That is, $C = \frac{1}{V_0} \iiint_{V_0} \chi dV$.

$$\frac{D\chi}{Dt} = \frac{\partial \chi}{\partial t} + \vec{u} \cdot \nabla \chi = 0 \tag{4.8}$$

Baraldi et al. [63] propose the following algorithm and VOF tools to advect the volume fraction of the reference phase. A three-step split advection algorithm with Eulerian Implicit, Eulerian Algebraic, and Lagrangian Explicit steps is implemented (EI-EA-LE algorithm). Compared to the original EI-EA-LE method by Scardovelli et al. [111], the algorithm presented in Baraldi et al. [63] is wisp-free and mass-conserving to machine-error precision for incompressible flows. However, numerical errors exist and are limited by the accuracy with which $\nabla \cdot \vec{u} = 0$ is satisfied and other errors introduced by the geometrical operations of the VOF method, which are expected to increase when the liquid structure is under-resolved.

The interface is geometrically reconstructed between advection steps using the PLIC method by Youngs [112]. Even though the reconstruction algorithm is computationally expensive, the method presented in Baraldi et al. [63] is more efficient than other higher-order VOF methods (e.g., 3D-ELVIRA [113]). Further, it guarantees that the volume of the reference phase is conserved. That is, mass is conserved for a constant-density liquid. According to Haghshenas et al. [114], this volume-preserving property is only possible with low-order convective schemes such as that used in Baraldi et al. [63]. The smearing of the solution

around the interface caused by this low-order advection scheme may introduce geometrical errors as the fluid velocity advects the interface. Nonetheless, volume-conservation properties are preferred over higher-order advection schemes in this work, and a sufficiently low CFL condition is used to limit the magnitude of these errors.

To address high-pressure, two-phase flows, the VOF method proposed in Baraldi et al. [63] must be extended to compressible liquids undergoing phase change. Eq. (4.8), can be rewritten in conservative form as

$$\frac{\partial \chi}{\partial t} + \nabla \cdot (\chi \vec{u}_l) = \chi \nabla \cdot \vec{u}_l - \frac{\dot{m}}{\rho_l} \tag{4.9}$$

where the compressible term $\nabla \cdot \vec{u}_l$ appears naturally and mass exchange becomes an additional source term. $\dot{m}$ is the mass flux per unit volume added to (condensation with $\dot{m} < 0$) or subtracted from (vaporization with $\dot{m} > 0$) the liquid phase, which is only non-zero at interface. $\dot{m}$ is evaluated as $\dot{m} = \dot{m}' \delta_\Gamma$, where $\dot{m}'$ is the mass flux per unit area across the interface and δ_Γ is a delta function that activates the phase-change term only at the interface cells. The value of $\dot{m}'$ is obtained by solving the system of interface matching conditions discussed in Subsection 3.2.1 and Subsection 4.1.3. Here, δ_Γ is obtained from the concept of interfacial surface area density as presented in Palmore and Desjardins [115]. In a given region Ω of the domain, $\delta_\Gamma = \int_{\Gamma \cap \Omega} dS / \int_\Omega dV$. This term is non-zero only at interface cells, where $\delta_\Gamma = A_\Gamma / V_0$, with V_0 being the cell volume and A_Γ the area of the interface plane crossing the cell (i.e., obtained from the PLIC).

Note that a liquid density, ρ_l, and a liquid phase velocity, $\vec{u}_l$ are used in Eq. (4.9). The use of these variables is necessary because the liquid and gas phases have different fluid compressibilities and there exists a normal velocity jump across the interface when both phases exchange mass (see Subsection 3.2.1). Thus, the advection of the liquid phase must be performed with a velocity representative of the liquid. Otherwise, physical and numerical

inconsistencies would appear. The extrapolation techniques used to address this issue are explained later in Section 4.4. For the compressible liquid, ρ_l is the interface liquid density.

The EI-EA-LE algorithm from Baraldi et al. [63] is extended as follows. Eq. (4.9) is integrated over the volume of the cell and with a first-order forward Euler scheme in time, which results in the following equation to update the volume fraction of a given cell

$$C^{n+1} = C^n - \sum_{i=1}^{N_{\text{faces}}} F_i + \tilde{C}(\nabla \cdot \vec{u}_l)\Delta t - \frac{\dot{m}}{\rho_l}\Delta t \tag{4.10}$$

The sum of the signed fluxes of the reference phase in and out of the cell is represented by the term $\sum_{i=1}^{N_{\text{faces}}} F_i$. The signed fluxes take into account the direction of the cell face normal unit vector pointing outwards. These fluxes are evaluated geometrically within the EI-EA-LE split advection algorithm coupled with PLIC [63]. $\tilde{C}$ is the cell's volume fraction, which could be evaluated implicitly ($\tilde{C} = C^{n+1}$) or explicitly ($\tilde{C} = C^n$). Nonetheless, given the split advection method utilized here, only the implicit formulation, $\tilde{C} = C^{n+1}$ has been proven to provide consistent results. In conclusion, Eq. (4.10) takes into account the variations of the cell volume fraction caused by the flux of the reference phase across the cell faces, the local volume expansion of the reference phase, and the addition or subtraction of liquid volume caused by phase change. Therefore, the proposed approach differs from previous methods that studied incompressible liquids with or without mass exchange.

The EI-EA-LE consecutive steps update the volume fraction following $C^n \rightarrow C^{EI} \rightarrow C^{EA} \rightarrow C^{LE} = C^{n+1}$ (or $C^n \rightarrow C^{EI} \rightarrow C^{LE} = C^{n+1}$ in two dimensions). The split method is constructed such that $C^{n+1} = C^n - \sum_{i=1}^{N_{\text{faces}}} F_i$ from Eq. (4.10) is recovered for an incompressible fluid without phase change. The EI and LE steps alone satisfy this recovery condition in two dimensions. Nonetheless, a non-zero one-dimensional divergence (e.g., $\partial u/\partial x$) is considered in the EI and LE steps. The EA step is only utilized to satisfy the incompressible three-dimensional version of Eq. (4.10).

As a reference for the reader, the next lines use the following nomenclature. u, v and w represent the liquid velocity components in x-, y- and z-directions and E, W, N, S, T and B define the East-West (x-direction), North-South (y-direction) and Top-Bottom (z-direction) cell faces, respectively.

For a two-dimensional compressible liquid without phase change ($\dot{m} = 0$), the EI-LE steps yield, with the EI step in the x-direction and the LE step in the y-direction,

$$C^{EI} = \frac{C^n + F_W^u - F_E^u}{1 - \frac{u_E - u_W}{\Delta x}\Delta t} \tag{4.11a}$$

$$C^{LE} = C^{EI}\left(1 + \frac{v_N - v_S}{\Delta y}\Delta t\right) + F_S^v - F_N^v = C^n - \sum_{i=1}^{N_{\text{faces}}} F_i + C^{EI}(\nabla \cdot \vec{u}_l)\Delta t \neq C^{n+1} \tag{4.11b}$$

which does not immediately satisfy the form of Eq. (4.10). Therefore, a correction step is required after performing the EI-LE split advection to match Eq. (4.10), which is given by

$$C^{n+1} = C^{LE} + (\tilde{C} - C^{EI})(\nabla \cdot \vec{u}_l)\Delta t \tag{4.12}$$

In a three-dimensional compressible flow, the EA step is designed such that Eq. (4.11) and the necessary correction are still valid.

Before advecting the interface, the current approach implements the volume addition or subtraction induced by the mass exchange. The EI-EA-LE advection steps now follow Eq. (4.13) with the EI step in the x-direction, the EA step in the y-direction, and the LE step in the z-direction. Eq. (4.13) includes the preliminary step to address mass exchange and the final correction step to match the form of Eq. (4.10). The solution algorithm alternates the direction of the EI-EA-LE steps for each time step to reduce directional bias. The VOF method has been implemented for a uniform Cartesian mesh, but extensions to non-uniform meshes

or orthogonal meshes could be implemented.

$$C^{PC} = C^n - \frac{\dot{m}}{\rho_l}\Delta t \tag{4.13a}$$

$$C^{EI} = \frac{C^{PC} + F_W^u - F_E^u}{1 - \frac{u_E - u_W}{\Delta x}\Delta t} \tag{4.13b}$$

$$C^{EA} = \frac{C^{EI}\left[1 - \frac{u_E - u_W}{\Delta x}\Delta t + (\nabla \cdot \vec{u}_l)\Delta t\right] + F_S^v - F_N^v}{1 + \frac{w_T - w_B}{\Delta z}\Delta t} \tag{4.13c}$$

$$C^{LE} = C^{EA}\left(1 + \frac{w_T - w_B}{\Delta z}\Delta t\right) + F_B^w - F_T^w \tag{4.13d}$$

$$C^{n+1} = C^{LE} + (\tilde{C} - C^{EI})(\nabla \cdot \vec{u}_l)\Delta t \tag{4.13e}$$

The advection steps presented in Eq. (4.13) usually provide a consistent volume-fraction field. That is, the volume fraction stays bounded (i.e., $0 \leq C \leq 1$) and advection within the compressible reference phase provides $C = 1$. Nevertheless, small errors may be introduced by the finite precision of the geometrical fluxes and the accuracy with which $\vec{u}_l$ satisfies the divergence constraint $\nabla \cdot \vec{u}_l$. These errors may cause wisps or residual values of C to appear in the gas phase (i.e., $C << 1$). The wisp-suppression algorithm from Baraldi et al. [63] is applied to limit the number of wisps left in the domain.

Other advection errors relate to undershoots (i.e., $C < 0$) and overshoots (i.e., $C > 1$), which may be introduced by the EA advection step, the phase change correction or the compressibility term in Eq. (4.12) or Eq. (4.13e). Such errors tend to appear in interface cells whose volume is filled almost completely by liquid or interface cells that have almost no liquid. These errors are corrected with a redistribution algorithm [63, 116], which in this work has been modified to include the direction of the interface normal unit vector in the redistribution. Because most of the undershoots and overshoots are caused by phase change and volume change perpendicular to the interface, directionality preserves the interface shape better.

This VOF approach is not mass-conserving to machine error for compressible flows. When density is not constant, using a volume-preserving technique does not guarantee mass conservation. However, as the mesh is refined and a smaller time step is used, mass conservation improves (see Appendix F). This issue is also apparent in other available VOF methods for compressible flows [96–98]. Nonetheless, the proposed approach is advantageous because it maintains a sharp interface and simplifies to the mass-conserving VOF method from Baraldi et al. [63] in the limit of incompressible flow without phase change.

Geometrical information of the interface is obtained from VOF-based methods. The Mixed-Youngs-Centered (MYC) method [117] is used to determine the interface normal unit vector, $\vec{n}$, and the improved Height Function (HF) method from López et al. [118] is used to compute the interface curvature, κ. The HF method is second-order accurate, but it has significant curvature errors when the interface normal unit vector is not aligned with the coordinate axes [63]. These errors are responsible for the generation of spurious currents around the interface, among other causes discussed in Section 4.3, due to a lack of an exact interfacial pressure balance. Mesh refinement limits the magnitude of the curvature errors and the generation of spurious currents.

Various works address methodologies to improve the accuracy of the interface geometrical description under the VOF framework. They have not been pursued in this work, but these approaches could be considered for future code development. Popinet [119] describes an adaptative scheme to improve the accuracy of curvature computations for under-resolved interfaces using the HF method, while other works propose a combination of the VOF and LS methods [120, 121]. The latter approach takes advantage of the smooth LS field to obtain better estimates of the interface geometry using Eq. (4.5). However, a critical step in which the LS function is re-distanced with respect to the PLIC interface does not guarantee a mesh-converging curvature. The HF method is preferred to evaluate curvature in this work due to the inherent complexity of combining the VOF and LS methods.

4.1.3 Determination of the spatially-varying interface equilibrium state

The local matching relations that define the interface state under thermodynamic phase equilibrium (i.e., LTE) have been presented in Subsections 3.2.1 and 3.3.4. At each interface cell, the system of equations is solved using the normal-probe technique discussed in other works (e.g., [15, 19, 104]). A line perpendicular to the interface plane is drawn, extending into both the liquid and gas phases. The centroid of the interface plane at a given cell is chosen as the probe's starting point. In each phase, two nodes are created on the line where the mass fraction and enthalpy values are linearly interpolated (i.e., bilinear interpolation in two dimensions and trilinear in three dimensions). Then, the gradients perpendicular to the interface that are needed in Eqs. (3.15) and (3.16) can be computed.

The nodes on the probe should ideally be equally spaced with Δx. However, in some cases, larger spacing is required to avoid using grid nodes in opposite phases when interpolating mass fraction or enthalpy values (see Figure 4.1). This situation must be avoided because

there is a sharp jump in these variables across the interface that could considerably distort the average value.

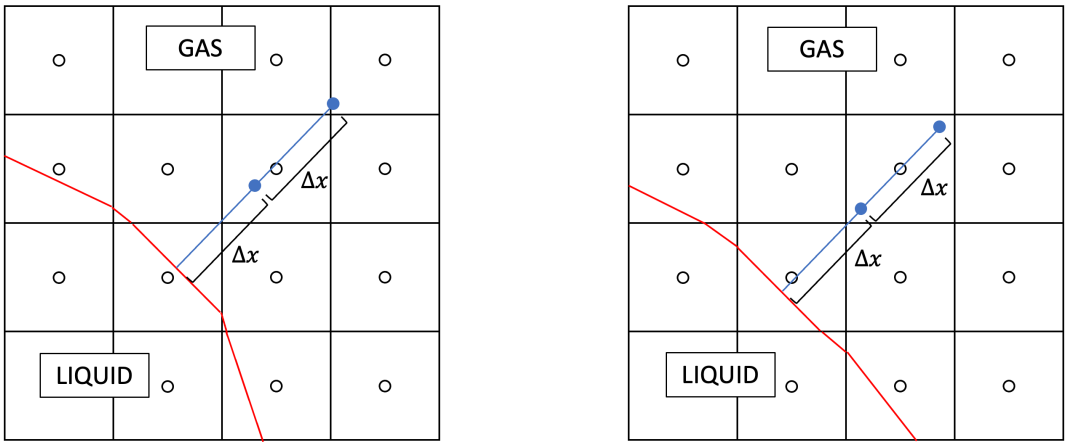

(a) (b)

Figure 4.1: Sketch of the construction of the normal probe used to evaluate perpendicular gradients to the interface needed to solve matching conditions and LTE. Only the probe extending into the gas phase is shown in a two-dimensional setup. The extension of the liquid-phase normal probe and the extension to three dimensions are straightforward. (a) Constant spacing of Δx results in the averaging on the probe node nearest to the interface being defined by grid nodes belonging to different phases; (b) Constant spacing of Δx results in a well-defined probe [66].

In general, the perpendicular gradient at each side of the interface can be calculated using a second-order, one-sided finite-difference method. The values of each variable in the two probe nodes and the interface value are used. It is important to note that the entire interface plane is assumed to have the same equilibrium solution. The deformation and breakup of the liquid surface in atomization problems generates small and thin structures that eventually become under-resolved by the mesh. Thus, the normal probe might cross the interface. In this situation, a first-order, one-sided finite difference method is used to evaluate the perpendicular gradient of a mass fraction or enthalpy. Nevertheless, the interface geometry and equilibrium state in such under-resolved situations may already be poorly defined.

The interface solution is unknown, and the equations formed by the matching relations and LTE must be solved iteratively. Due to the modeling simplifications discussed in Section 3.2

(e.g., binary mixture, low-Mach-number flows), the momentum jump conditions, Eqs. (3.13) and (3.14), are decoupled from phase equilibrium, Eq. (3.44), the species continuity matching condition, Eq. (3.15), and the energy balance across the interface, Eq. (3.16). To find the interface solution at each interface cell, the same iterative solver outlined in Poblador-Ibanez and Sirignano [15] can be used. The system solution defines the properties of the interface plane located in a given interface cell: mass and heat fluxes across the interface, temperature, surface-tension coefficient, composition, and fluid properties on each side of the interface and, as a result, the pressure jump to be imposed in the momentum equation.

4.2 Solution of the Species and Energy Transport Equations

The species transport equation, Eq. (3.7), and the enthalpy transport equation, Eq. (3.9), are solved in non-conservative form using finite differences, as opposed to traditional fluid-dynamics solvers. This discretization method is chosen because it improves numerical stability and allows the interface solution to be directly included in the discrete numerical stencils. That is, the interface solution for enthalpy and composition is imposed as a phase boundary condition. As a result, these equations are solved independently in each phase using phase-wise variables.

Other researchers use finite-volume techniques to solve the conservative form of the energy equation in terms of fluid temperature [104, 122]. In these works, a one-fluid method is used where fluid properties are volume-averaged at interface cells, and the energy jump across the interface is imposed via a localized source term. This one-fluid approach is appropriate because the temperature is constant across the interface. To obtain the correct temperature gradients numerically for each phase, one would still need to extrapolate the temperature

field on both sides of the interface or utilize one-sided stencils. A similar approach is used to handle the solution of the continuity and momentum equations, as seen in Section 4.3.

The method provided here covers the mixture composition and enthalpy solution, both of which have severe discontinuities across the interface unless the interface equilibrium state is very close to the mixture critical point. A phase-wise technique in which the interface solution is integrated into the discretization is preferred to prevent further costly extrapolations. Other two-phase works have also employed the finite-difference method to solve these transport equations [62, 94, 95].

The non-conservative forms of Eqs. (3.7) and (3.9) are integrated in time using an explicit first-order step, with convective and diffusive terms evaluated explicitly, as

$$\frac{DY_O}{Dt}^{n+1} = \frac{Y_O^{n+1} - Y_O^n}{\Delta t} + (\vec{u}_f \cdot \nabla Y_O)^n = \frac{1}{\rho^n}\left[\nabla \cdot (\rho D_m \nabla Y_O)^n\right] \tag{4.14}$$

$$\frac{Dh}{Dt}^{n+1} = \frac{h^{n+1} - h^n}{\Delta t} + (\vec{u}_f \cdot \nabla h)^n = \frac{1}{\rho^n}\left[\nabla \cdot \left(\frac{\lambda}{c_p}\nabla h\right)^n + \sum_{i=1}^{N=2} \nabla \cdot \left(\left[\rho D_m - \frac{\lambda}{c_p}\right] h_i \nabla Y_i\right)^n\right] \tag{4.15}$$

where $\vec{u}_f$ represents a phase-wise velocity. That is, $f = g$ refers to the gas-phase velocity and $f = l$ identifies the liquid-phase velocity. The phase-wise velocity is obtained as explained in Section 4.4. The term $\vec{u}_f$ in Eqs. (4.14) and (4.15) is obtained by averaging face values at the center of the cell using a linear interpolation.

The VOF split-advection algorithm's low-order temporal scheme is considered when choosing a first-order integration in time. To ensure a numerically stable solution of the species and enthalpy transport equations, the time-step value is already conservatively chosen using proper CFL conditions (see Section 4.5). Thus, geometrical errors introduced when advecting the volume fraction are minimized, and any influence of a low-order temporal integration in

the mixture composition and mixture enthalpy solution. Although a higher-order temporal integration may be implemented in the governing equations, this is not done to keep the algorithm simple. This issue may be addressed in future developments based on this code.

The inclusion of the interface solution in the numerical stencils is represented in Figure 4.2. A two-dimensional sketch shows the interface located between cells i and i-1 and focus is given to the numerical stencils in the x-direction for the discretization of the species transport equation. However, the following discussion can easily be extrapolated to other directions and to the enthalpy transport equation. The interface can intersect the numerical stencil used to evaluate $\partial Y_O/\partial x$ or $\partial(\rho D_m[\partial Y_O/\partial x])/\partial x$ depending on the cell and discretization order. Thus, $\Delta x_1 < \Delta x$ must be determined. Note $\Delta x_2 = \Delta x_3 = \Delta x$ in the sketch, being Δx the mesh size.

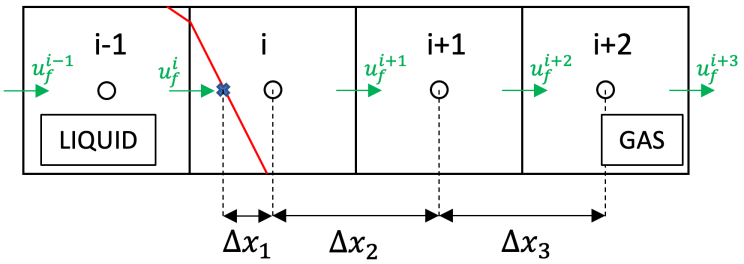

Figure 4.2: Sketch showing how the interface intersects the numerical stencil in the x-direction and how its location is determined [66].

The determination of Δx_1 could be done by using the PLIC interface at cell i, but the method proposed in Dodd et al. [94] provides a faster and more stable estimate of Δx_1. A staggered volume fraction, $C^{i-1/2}$, is calculated from the volume fractions at cells C^{i-1} and C^i and the respective PLIC interface reconstructions. That is, the liquid volume of a staggered cell between node i and $i-1$ is determined. This method becomes exact depending on the interface distribution (i.e., equivalent to using the location obtained from the PLIC interface). $\Delta x_1 \neq \Delta x$ is only evaluated if nodes i and i-1 belong to different phases, even if $C^{i-1/2} > 0$. Otherwise, $\Delta x_1 \equiv \Delta x$. Under the example provided in Figure 4.2, the staggered volume fraction is used to evaluate $\Delta x_1 \approx (1 - C^{i-1/2})\Delta x$.

The convective terms are discretized using an adaptive first-/second-order upwinding technique to preserve numerical stability and boundedness (i.e., $Y_O \leq 1$). The diffusive and non-reactive nature of the analyzed problem imposes a limiting boundary for the temperature field. Also, the species mass fraction cannot become negative or be above one. A first-order upwind discretization of the convective term satisfies such requirements as it is unconditionally bounded within the limits of the CFL conditions [123]. On the other hand, a second-order upwinding scheme might cause undershoots or overshoots if the mesh does not resolve the variable field satisfactorily. For instance, when a sharp gradient is not well captured. Moreover, the inclusion of the interface in the numerical stencil may reduce spatial accuracy, especially when its location approaches a grid node. Similarly, diffusive terms are discretized using second-order central differences, albeit the spatial resolution around the interface may be lower when the interface is too close to a grid node. Specific details and examples regarding the discretization of convective and diffusive terms are provided in Appendix E.

The suggested discretization is at best second-order accurate in space and may drop to first-order near the interface or when boundedness issues arise. Boundedness issues should only appear around sharp-gradient regions, and the spatial accuracy drop related to the interface proximity to the grid nodes will only affect specific cells at each time step. Nonetheless, the use of these low-order schemes is motivated by concerns about the numerical stability of the sharp-interface method in a highly-coupled and non-linear problem. Furthermore, the proposed mesh has been substantially refined to obtain a smooth interface and improve the performance of the phase-wise extrapolations discussed in Section 4.4 over a wider interface region as it deforms. As a result, a localized low-order spatial discretization of the scalar transport equations is not a concern.

Other considerations must be made to ensure a stable and physically accurate solution as a result of two extreme discretization scenarios: when the interface plane is almost overlapping

with a grid node, defined as $\Delta x_1 < 0.01\Delta x$, and when the interface cell changes phase in the time interval provided by the time step (i.e., $C^n < 0.5$ and $C^{n+1} \geq 0.5$ or $C^n \geq 0.5$ and $C^{n+1} < 0.5$). In both cases, we assign the interface value of the species mass fraction or mixture enthalpy of the corresponding phase due to the proximity between the interface and the grid node. It becomes a reasonable approximation for a sufficiently small Δt. Furthermore, under-resolved regions (i.e., droplets or thin structures of the order of the mesh size) may produce inaccurate solutions. To circumvent this issue, if a nonphysical solution is found, the values for oxidizer mass fraction or enthalpy assigned to the problematic cell are calculated as an average of the surrounding physically-correct values of the same fluid phase. Such discretization errors are very localized, and the proposed solutions have a negligible impact on the overall evolution of the two-phase flow. The goal is to prioritize a stable algorithm where no numerical issues will prevent the time marching.

4.3 Solution of the Continuity and Momentum Equations

The two-phase continuity and momentum equations, Eqs. (3.1) and (3.2), are solved in conservative form using the one-fluid method. The velocity field presents a discontinuity normal to the interface in the presence of phase change. Nonetheless, the one-fluid approach is an accepted method since the normal jump in the velocity field is mild compared to the magnitude of the velocity field around the interface. However, phase-wise velocity field values must be employed in specific parts of the momentum equation, as indicated in the following lines. This methodology was chosen since it is a conventional approach used in the literature [64, 95, 122] and we favor a conservative approach for global mass and momentum.

Fluid properties are volume-averaged at interface cells using the local volume fraction as $\phi = \phi_g + (\phi_l - \phi_g)C$, where ϕ is any fluid property such as density or viscosity. The Continuum Surface Force (CSF) method from Brackbill et al. [124] extended to flows with variable surface tension [125, 126] is used to include the normal and tangential momentum jumps across the interface, Eqs. (3.13) and (3.14), into the one-fluid momentum equation. The surface-tension force is modeled as a body force only active at the interface, $\vec{F_\sigma} = \vec{f_\sigma}\delta_\sigma(\vec{x} - \vec{x}_\Gamma)$, which is then replaced under the CSF framework by $\vec{f_\sigma} = -\sigma\kappa\vec{n} + \nabla_s\sigma$ with the Dirac δ-function as $\delta_\sigma(\vec{x} - \vec{x}_\Gamma) = |\nabla C|$. $\nabla_s\sigma = \frac{\partial\sigma}{\partial s_1}\vec{t_1} + \frac{\partial\sigma}{\partial s_2}\vec{t_2}$ is calculated using the HF-based approach described in Seric et al. [126]. That is, a similar method based on the height functions used to calculate the curvature (see Subsection 4.1.2). In three dimensions, the gradient is evaluated along two orthogonal tangential directions, s_1 and s_2, while the simplification to a two-dimensional configuration is straightforward. Because the method is based on the HF approach, a minimum mesh resolution is required to obtain an accurate representation of $\nabla_s\sigma$ [126].

The MYC method estimates the interface normal unit vector within the VOF framework. However, the CSF method takes the approximation $\vec{n} = -\nabla C/|\nabla C|$ in modeling the added source term in the momentum equation. The tangential unit vectors at the interface are also determined using this definition. As a result, the volume fraction gradient is used to give directionality and locality to the surface-tension force. Additionally, a density scaling is applied to get a body force per unit volume that is independent of the fluid density [124, 125]. This adjustment produces an evenly distributed surface-tension force, which improves the CSF approach's performance and minimizes the magnitude of the spurious currents introduced by the term.

The resulting momentum equation becomes

$$\frac{\partial}{\partial t}(\rho\vec{u}) + \nabla\cdot(\rho\vec{u}\vec{u}) = -\nabla p + \nabla\cdot\bar{\bar{\tau}} + \frac{\rho}{\langle\rho\rangle}\Big(\sigma\kappa\nabla C + \nabla_s\sigma|\nabla C|\Big) \tag{4.16}$$

with $\langle\rho\rangle = \frac{1}{2}(\rho_G + \rho_L)$, where ρ_G and ρ_L are the freestream gas and liquid densities, respectively. Similar to the normal force term $\sigma\kappa\nabla C$, the tangential force term $\nabla_s\sigma|\nabla C|$ is further simplified once the tangential unit vectors, $\vec{t}_1$ and $\vec{t}_2$, are evaluated from the normal unit vector, $\vec{n}$.

The predictor-projection method by Chorin [127] is used to solve the pressure-velocity coupling in the momentum equation. A semi-explicit temporal integration of Eq. (4.16) without the pressure gradient term yields the predictor step as

$$\vec{u}^p = \frac{\rho^n\vec{u}^n}{\rho^{n+1}} + \frac{\Delta t}{\rho^{n+1}}\left[-\nabla\cdot\left(\rho\vec{u}\vec{u}\right)^n + \nabla\cdot\bar{\bar{\tau}}^n + \frac{\rho^{n+1}}{\langle\rho\rangle}\left(\sigma^{n+1}\kappa^{n+1}\nabla C^{n+1} + \nabla_s\sigma^{n+1}|\nabla C^{n+1}|\right)\right] \quad (4.17)$$

where $\vec{u}^p$ is the predicted velocity field, which does not satisfy continuity. Note that the surface-tension term is evaluated implicitly and that an implicit update of the density is also available. That is, the momentum equation is solved after advecting the interface and updating the fluid properties, as shown in Figure 4.4.

A higher-order temporal scheme could have been implemented (e.g., Adams-Bashforth or Runge-Kutta). Nonetheless, the global temporal accuracy of $\vec{u}$ and p is bounded by the first-order time integration in the VOF method [63, 64]. Therefore, the time step Δt is already chosen small, and using a higher-order method in the momentum equation might not provide any significant advantage, as discussed in Section 4.3. Future development of the code may include an improvement of these integration schemes.

Once the predicted velocity has been evaluated, the projection step involving the pressure gradient term is used to obtain the correct velocity field at the new time step, $\vec{u}^{n+1}$, which satisfies the continuity equation constraint. This step is given by

$$\vec{u}^{n+1} = \vec{u}^p - \Delta t\frac{\nabla p^{n+1}}{\rho^{n+1}} \quad (4.18)$$

which is used to obtain an equation for the pressure field by taking the divergence operator on both sides of the equation as

$$\nabla \cdot \left(\frac{\nabla p^{n+1}}{\rho^{n+1}} \right) = \frac{1}{\Delta t} \left(\nabla \cdot \vec{u}^{p} - \nabla \cdot \vec{u}^{n+1} \right) \tag{4.19}$$

The pressure field that results fulfills the continuity constraint implicit in the term $\nabla \cdot \vec{u}^{n+1}$. This term is evaluated for the one-fluid velocity following the steps outlined in Duret et al. [97]. A mass conservation equation is obtained for each phase and, addressing the one-fluid density as $\rho = \rho_g(1 - C) + \rho_l C$ in the one-fluid continuity equations (i.e., Eq. (3.1)), the following relation is obtained

$$\nabla \cdot \vec{u}^{n+1} = -(1 - C)\frac{1}{\rho_g}\frac{D\rho_g}{Dt} - C\frac{1}{\rho_l}\frac{D\rho_l}{Dt} + \dot{m}\left(\frac{1}{\rho_g} - \frac{1}{\rho_l} \right) \tag{4.20}$$

where the implicit notation has been dropped on the right hand side.

The form of Eq. (4.20) captures the interfacial physics. The global fluid compressibility at interface cells is obtained as a volume average of the compressibility of each fluid. Additionally, the volume expansion or compression caused by phase change is included. In single-phase cells, Eq. (4.20) recovers the compressibility term $-\frac{1}{\rho}\frac{D\rho}{Dt}$ of the particular phase, which is another way of rewriting the continuity equation, Eq. (3.1). The evaluation of $\frac{1}{\rho_g}\frac{D\rho_g}{Dt}$ and $\frac{1}{\rho_l}\frac{D\rho_l}{Dt}$ is presented in Section 4.4. These terms are assumed to be independent of pressure for low-Mach-number flows since density becomes a function of temperature, mixture composition, and thermodynamic pressure only. Moreover, for open-boundary flows, the thermodynamic pressure remains constant.

Eqs. (4.18) and (4.19) are solved using the split pressure-gradient method for two-phase flows by Dodd and Ferrante [64] and Dodd et al. [94]. The pressure gradient term divided by the

fluid density is substituted as

$$\frac{1}{\rho^{n+1}}\nabla p^{n+1} \rightarrow \frac{1}{\rho_0}\nabla p^{n+1} + \left(\frac{1}{\rho^{n+1}} - \frac{1}{\rho_0}\right)\nabla \hat{p} \tag{4.21}$$

where $\hat{p} = 2p^n - p^{n-1}$ is a linear extrapolation in time of the pressure field and $\rho_0 = \min(\rho) \equiv \rho_G$. For the type of problems analyzed here (i.e., non-reactive and diffusive in nature), the minimum density in the computational domain always coincides with the freestream gas density, ρ_G. Implementing this substitution into Eqs. (4.18) and (4.19), they are rewritten as

$$\vec{u}^{n+1} = \vec{u}^{p} - \Delta t\left[\frac{1}{\rho_0}\nabla p^{n+1} + \left(\frac{1}{\rho^{n+1}} - \frac{1}{\rho_0}\right)\nabla \hat{p}\right] \tag{4.22}$$

and

$$\nabla^2 p^{n+1} = \nabla \cdot \left[\left(1 - \frac{\rho_0}{\rho^{n+1}}\right)\nabla \hat{p}\right] + \frac{\rho_0}{\Delta t}\left(\nabla \cdot \vec{u}^{p} - \nabla \cdot \vec{u}^{n+1}\right) \tag{4.23}$$

As long as the pressure remains smooth in time (i.e., incompressible or low-Mach-number compressible flows), this method is quite accurate in predicting the pressure field as $\nabla \hat{p} \approx \nabla p^{n+1}$ [64]. In the case where $\nabla \hat{p} \equiv \nabla p^{n+1}$, the substitution is exact, and the resulting pressure field matches the solution obtained with an unsplit method (e.g., multi-grid iterative solver). Across the interface, the existing pressure jump may be problematic in situations of combined high curvature, high surface-tension coefficient, and high density ratio or ρ_l/ρ_g. Under such a scenario, the linear extrapolation of the pressure field may not be smooth in time and can cause numerical oscillations and an unstable pressure solver. Thus, the time step has to be reduced considerably to achieve enough temporal smoothness [64], defeating the purpose of the split pressure-gradient as explained in later paragraphs. Dodd and Ferrante [64] report these issues in configurations with density ratios $\rho_l/\rho_g \geq 1000$ (e.g., water-air at ambient pressure). However, we start reporting issues with the pressure solver

for much lower density ratios around $\rho_l/\rho_g \approx 86$. Nevertheless, this issue is unlikely to significantly influence the kind of flows that this model is designed to analyze since high pressures increase the density of the gas phase substantially, decreasing the density ratio at the interface. For future development of the code, the works from Cifani [128] and Turnquist and Owkes [129] can be considered to improve the performance of the split pressure-gradient method in configurations with a high density ratio.

The essential benefit of the split pressure-gradient technique is that, under the low-Mach-number assumption, Eq. (4.23) becomes a constant-coefficient pressure Poisson equation (PPE). This equation, when combined with a uniform mesh, can be solved using a rapid Poisson solver based on a series of Discrete Fourier Transforms or FFT [64, 130], which can be adapted to different sets of boundary conditions relevant to the type of problems we aim to analyze (e.g., periodic or homogeneous Neumann boundary conditions). The FFT method achieves computational speed-up orders of magnitude greater than other solvers such as Gauss elimination (i.e., $\mathcal{O}(10^2)$) or multi-grid solvers (i.e., $\mathcal{O}(10)$) due to its non-iterative nature. As stated earlier, this computational advantage may disappear in some problem configurations if the time step has to be reduced substantially to achieve numerical stability. Nonetheless, this method is pursued as it greatly improves the computational efficiency of one part of the two-phase solver and compensates for the computational cost added by the thermodynamic model and the necessary phase-wise extrapolations across the interface (see Section 4.4).

The one-fluid method to solve the continuity and momentum equations generates spurious currents around the interface. These spurious currents appear due to a lack of an exact interfacial pressure balance, and various factors contribute to it: (a) the non-smooth curvature field and surface-tension gradient obtained from the HF technique; (b) the sharp volume-averaging of fluid properties; (c) the localized source terms linked to mass exchange; and (d) the non-smooth extrapolation of fluid compressibilities and phase-wise velocities. Further, it

is necessary to analyze how these challenges affect other sections of the computational model, such as the energy and species transport equation solution or the extrapolation of phase-wise velocities. Appendix F shows mesh-convergence studies of the entire model applied to some verification tests. This numerical issue is a cause for caution in liquid injection problems when the emergence of instabilities along the liquid-gas interface must be purely physical. At supercritical pressures, where the liquid and gas phases are more similar near the interface, this problem becomes more concerning since the surface-tension force that would typically stabilize surface perturbations is reduced.

Eqs. (4.17) and (4.23) are discretized using finite-volume techniques [131]. The viscous term is discretized with second-order central differences, but phase-wise velocities are used. As described in Dodd et al. [94], if the one-fluid velocity were utilized in this term, an artificial pressure spike would exist across the interface due to the velocity discontinuity in the presence of mass exchange. On the other hand, the convective term is discretized with the SMART algorithm by Gaskell and Lau [132]. This numerical scheme is up to third-order accurate in space and ensures numerical stability and boundedness. However, depending on the cell Peclet number, a hybrid technique is applied at interface cells, which alternates between second-order central differences and first-order upwinding (i.e., central differences for $Pe < 2$). For this term, the one-fluid velocity must be used to capture the momentum jump caused by vaporization or condensation given in Eq. (3.13).

The volume-averaging of fluid properties is only relevant for interface cells where $0 < C < 1$. In a compressible framework, the node of an interface cell will have the fluid properties of the phase that occupies more than 50% of the cell. Thus, the other phase's fluid properties are undefined at a node level. Here, we choose to circumvent this issue by using the fluid properties of the interface equilibrium solution as representative values for the volume average. Similarly, the terms ρ_g and ρ_l that appear in the phase change term in Eq. (4.20) are

also defined from the local interface solution, as well as the mass flux, $\dot{m}'$, used to evaluate $\dot{m}$.

The staggered-mesh approach requires that any interface property be evaluated at cell faces. However, these properties are only evaluated at interface cells, and two consecutive interface cells might not be available to average the variable. Thus, the averaging method proposed in Dodd and Ferrante [64] is implemented, where any given interface property ϕ (e.g., curvature) is averaged at the velocity nodes or cell faces as

$$\phi_{i+1/2,j,k} = \begin{cases} \phi_{i+1,j,k} & \text{if } \phi_{i,j,k} = 0 \\ \phi_{i,j,k} & \text{if } \phi_{i+1,j,k} = 0 \\ \frac{1}{2}(\phi_{i+1,j,k} + \phi_{i,j,k}) & \text{otherwise} \end{cases} \tag{4.24}$$

Here, the location of a u-node is addressed. The same technique can be used in all the other velocity nodes. Eq. (4.24) is used to calculate σ, κ, $\frac{\partial \sigma}{\partial s_1}$ and $\frac{\partial \sigma}{\partial s_2}$, which will only have a non-zero value at interface cells. Additionally, it may be used to obtain interface values for the interface-capturing numerical stencils described in Section 4.2 and Appendix E.

4.4 Determination of Fluid Compressibilities and Phase-Wise Velocities

The compressibility of the liquid and gas phases has to be determined to evaluate $\nabla \cdot \vec{u}^{n+1}$ and solve the pressure field (i.e., Eqs. (4.20) and (4.23)). Moreover, it is a necessary preliminary step to obtain phase-wise velocities used in various parts of the model, as described in Subsection 4.1.2 and Sections 4.2 and 4.3.

The thermodynamic pressure remains constant under the low-Mach-number constraint and the unconfined flow this work addresses. Therefore, the compressibility of the fluid, related to the material change in its density, is only a function of changes in mixture composition and temperature or, equivalently, mixture enthalpy. An equation based on fundamental thermodynamic relations is given by

$$\frac{D\rho}{Dt} = \frac{\left.\frac{\partial\rho}{\partial T}\right|_{Y_i}}{\left.\frac{\partial h}{\partial T}\right|_{Y_i}} \frac{Dh}{Dt} + \sum_{i=1}^{N} \left(\left.\frac{\partial\rho}{\partial Y_i}\right|_{T,Y_{j\neq i}} - \frac{\left.\frac{\partial\rho}{\partial T}\right|_{Y_i}}{\left.\frac{\partial h}{\partial T}\right|_{Y_i}} \left.\frac{\partial h}{\partial Y_i}\right|_{T,Y_{j\neq i}} \right) \frac{DY_i}{Dt} \tag{4.25}$$

which relates the material or total derivative of the fluid density to the solution of the governing equations for species transport, Eq. (4.14), and enthalpy transport, Eq. (4.15).

For a binary mixture, Eq. (4.25) simplifies to

$$-\frac{1}{\rho}\frac{D\rho}{Dt} = \frac{1}{c_p\bar{v}} \left.\frac{\partial\bar{v}}{\partial T}\right|_{Y_i} \frac{Dh}{Dt} + \left(\left.\frac{\rho}{W_O}\frac{\partial\bar{v}}{\partial X_O}\right|_{T,X_{j\neq i}} - \left.\frac{\rho}{W_F}\frac{\partial\bar{v}}{\partial X_F}\right|_{T,X_{j\neq i}} - \frac{h_O - h_F}{c_p\bar{v}} \left.\frac{\partial\bar{v}}{\partial T}\right|_{Y_i} \right) \frac{DY_O}{Dt} \tag{4.26}$$

with all terms on the right hand side of the equation evaluated at time $n+1$, which is not shown to simplify the notation. $\bar{v}$ is the mixture molar volume and W_O and W_F are the molecular weights of the oxidizer species and the fuel species, respectively. The thermodynamic partial derivatives are derived from the thermodynamic model based on the volume-corrected SRK equation of state presented in Section 3.3. Detailed expressions for $\partial\bar{v}/\partial X_i$ and $\partial\bar{v}/\partial T$ are available in Davis et al. [16] and also provided in Appendix B. The material derivatives Dh/Dt and DY_O/Dt are obtained from the solution of the respective non-conservative governing equations, Eqs. (4.14) and (4.15). The fluid compressibility can only be evaluated in single-phase cells, but its value is also required at interface cells and in a narrow band of cells across the interface, as it is needed to evaluate the phase-wise velocities $\vec{u}_g$ and $\vec{u}_l$ (i.e., $\nabla\cdot\vec{u}_g = -\frac{1}{\rho_g}\frac{D\rho_g}{Dt}$ and $\nabla\cdot\vec{u}_l = -\frac{1}{\rho_l}\frac{D\rho_l}{Dt}$) and the one-fluid velocity divergence, Eq. (4.20).

The multidimensional extrapolations by Aslam [133] are used to obtain distinct values of each fluid's compressibility in this narrow band of cells. Although the technique was originally conceived for LS methods, it can easily be adapted to a VOF framework, as explained in the following lines. Figure 4.3 presents the extrapolation region for liquid values in a two-dimensional configuration. The definition of extrapolation regions for the gas phase is analogous and extends to three-dimensional configurations.

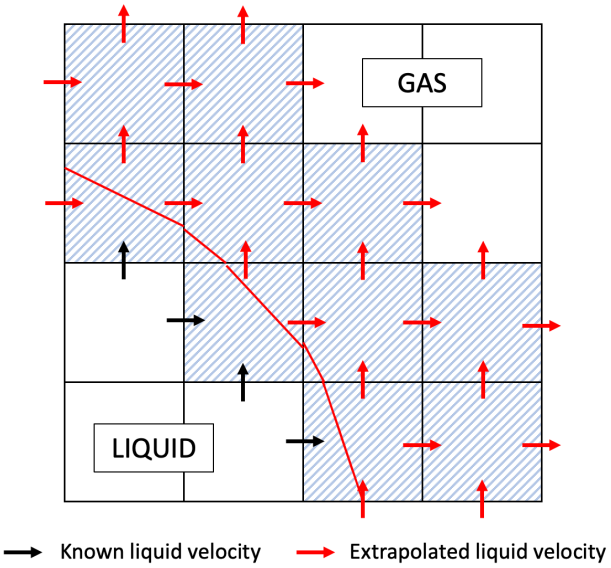

Figure 4.3: Extrapolation region (dashed cells) for the liquid compressibility and location of phase-wise velocity components in a two-dimensional mesh [66].

For a linear extrapolation, the following two-step extrapolation equation has to be solved

$$\frac{\partial g_n}{\partial \tau} + H(C)\big(\vec{n}\cdot\nabla g_n\big) = 0 \quad ; \quad \frac{\partial g}{\partial \tau} + H(C)\big(\vec{n}\cdot\nabla g - g_n\big) = 0 \tag{4.27}$$

where, if looking at the extrapolation of liquid-phase values, $g = \nabla\cdot\vec{u}_l = -\frac{1}{\rho_l}\frac{D\rho_l}{Dt}$, $g_n = \vec{n}\cdot\nabla g$ and $\vec{n}$ points toward the gas phase. The extrapolation of the gas-phase fluid compressibility follows the same approach. The first step performs a constant extrapolation of the normal gradient of g (or g_n) and, then, the velocity divergence implicit in g is extrapolated in a linear fashion following the direction given by g_n. The extrapolation of liquid-phase values is only performed in the region defined by $H(C)$, where $H(C) = 0$ if $C = 1$ and $H(C) = 1$

otherwise. That is, the extrapolation is done only at interface cells (i.e., $0 < C < 1$) and gas cells (i.e., $C = 0$). When extrapolating gas-phase values, $H(C) = 0$ if $C = 0$ and $H(C) = 1$ otherwise.

The normal unit vector is defined exclusively at interface cells in the VOF framework. Therefore, we need to provide an estimate of $\vec{n}$ in the extrapolation region to solve Eq. (4.27). Here, an inverse-distance weighted average is proposed to obtain each component n_m (i.e., $m = x, y, z$) of $\vec{n}$ at non-interface cells following $n_m = (\sum_i \frac{n_{m,i}}{d_i})/(\sum_i \frac{1}{d_i})$. Only the information from the closest set of i interface cells in the neighborhood of the node of interest is used to calculate this average. d_i is defined as the distance between the node and the centroid of the interface plane in cell i. After obtaining each component n_m, the vector is re-normalized to have $|\vec{n}| = 1$.

A constant extrapolation might be required for numerical stability purposes [115]. In other words, a linear extrapolation may overestimate or underestimate the fluid compressibility inside the extrapolation zone, particularly when initialized with harsh initial conditions. This issue may lead to the development of an unstable or unrealistic solution. A constant extrapolation of the fluid's compressibility is achieved by addressing only the second step of Eq. (4.27) by setting $g_n = 0$. Since the extrapolation band is very thin, a constant extrapolation does not introduce significant accuracy issues.

Eq. (4.27) is solved to steady-state in a fictitious time, τ, which does not necessarily have units of time. For practical purposes, reaching a steady-state inside the extrapolation region defined in Figure 4.3 is enough. However, another faster method to extrapolate fluid compressibilities is presented in McCaslin et al. [134]. The same extrapolation equations from Aslam [133] are solved directly at a steady-state with a fast-marching method (FMM). The FMM approach has the advantage since it does not require time-consuming iterations on a pseudo-time despite having a lower spatial accuracy in high-order extrapolations. Neverthe-

less, both the FMM method and the iterative method present the same level of accuracy in the case of a constant extrapolation.

Once the fluid compressibilities have been extrapolated, the phase-wise velocities are calculated with the extrapolation technique presented in Dodd et al. [94] extended to compressible flows as

$$\frac{\partial \vec{u}_l}{\partial \tau} + \nabla(\nabla \cdot \vec{u}_l) = \nabla g \rightarrow \nabla(\nabla \cdot \vec{u}_l) = \nabla g \tag{4.28}$$

which is solved directly at steady-state conditions of a fictitious time-like variable, τ, that does not have units of time, similar to Eq. (4.27). Nevertheless, the nature of this equation requires an iterative approach until the desired tolerance is achieved. That is, how well the phase-wise velocity satisfies the extrapolated divergence field or fluid compressibility. Eq. (4.28) uses liquid-phase value, but the extrapolation of gas-phase velocities follows the same approach.

Two boundary conditions have to be imposed in Eq. (4.28). Phase-wise velocity components must match the real velocity of the fluid (i.e., one-fluid velocity) along the boundary of the extrapolation region that falls inside the fluid phase that is being extrapolated. That is, $\vec{u}_l = \vec{u}$ in the example shown in Figure 4.3. Then, the phase-wise velocity components along the extrapolation boundary in the ghost region must satisfy the discrete velocity divergence of the boundary cell (i.e., the extrapolated $\nabla \cdot \vec{u}_l$). Second-order finite differences are used to discretize Eq. (4.28) within the extrapolation region. The staggered phase-wise velocities satisfy the phase-wise velocity divergence field or fluid compressibility with this extrapolation method.

The proposed extrapolation techniques might become problematic in under-resolved areas where the extrapolated fields are not smooth enough and are also affected by poor interface geometrical information (see Subsection 4.1.2). Convergence might not be achieved, which

may jeopardize the code's performance. One option is to perform Adaptive Mesh Refinement (AMR) around under-resolved regions. However, the reduced surface-tension force at high pressures will inevitably promote the formation of small structures that might still be under-resolved with AMR without penalizing the computational performance. Therefore, we propose another solution that will keep the simulation advancing in time.

A "block" of nodes is defined around under-resolved interface points. The phase-wise fluid compressibility and velocity extrapolations omit nodes inside these under-resolved regions. The extrapolation zone is assumed to be incompressible within these locations, and the one-fluid velocity is used as phase-wise velocity. To keep the pressure solver consistent, under-resolved interface cells have $\nabla \cdot \vec{u}^{n+1} = 0$. Nonetheless, the mass exchange is still considered during the advection of the volume fraction.

Under-resolved regions are identified based on various criteria. For instance, high-curvature regions relative to the mesh size are problematic. In two dimensions, the threshold $1/\kappa < 3\Delta x$ is used, whereas three different curvatures are considered in three dimensions: the curvature of the surface with $1/\kappa < 6\Delta x$ and the curvatures in the two principal directions, κ_1 and κ_2, used to determine the three-dimensional curvature with $1/\kappa_1 < 3\Delta x$ and $1/\kappa_2 < 3\Delta x$. That is, we have to adjust the threshold based on the fact that the three-dimensional curvature may be twice the curvature of a two-dimensional surface with the same radii of curvature (e.g., a circle and a sphere with the same diameter), and it may also be zero if the two radii of curvature in the principal directions cancel each other locally. Under-resolved zones are also identified around thin liquid structures or gas pockets where two opposing extrapolations from two separate interfaces would conflict.

In areas where geometry errors already exist and may be prevalent, the inaccuracies added by this approach are expected to be limited. However, mass conservation properties are penalized since the interface advection around such under-resolved areas does not account for volume expansion or contraction. The error introduced in assuming an incompressible

one-fluid at the interface cells should be small for the type of flows analyzed in this work. For instance, the velocity jump caused by mass exchange, $(\vec{u}_g - \vec{u}_l) \cdot \vec{n}$, may be of the order of $\mathcal{O}(10^{-1} - 10^{-2}$ m/s) and the velocity field is of the order of $\mathcal{O}(10^{1}$ m/s).

4.5 Algorithm and Implementation Details

Figure 4.4 presents a flowchart schematic of the solution algorithm for every time step. The simulation is started by setting initial conditions for each variable in the solution process.

The bulk of the interface capturing model (i.e., VOF) is employed first, including the interface advection, the MYC method to evaluate the interface normal unit vector, the PLIC interface reconstruction, and the HF method to evaluate the interface curvature. Then, the governing equations for species continuity and energy are solved once the interface location has been updated at time t^{n+1}.

The LTE and jump conditions are solved at each interface cell after the entire domain has an updated solution for the interface position and geometry and the mass fraction and enthalpy in both phases. Simultaneously, because the thermodynamic model for low-Mach-number flows only depends on the thermodynamic pressure, temperature, and composition, the fluid characteristics can be updated everywhere (e.g., ρ^{n+1}).

The new fluid compressibilities are determined and extrapolated before solving the continuity and momentum equations. Following that, the estimated fluid compressibilities across the interface are used to calculate phase-wise velocities. The phase-wise velocities obtained at time t^{n+1} are used in the following time step. The momentum equation is then solved using the predictor-projection approach with the split pressure-gradient technique to solve the low-Mach-number PPE using an FFT-based solver.

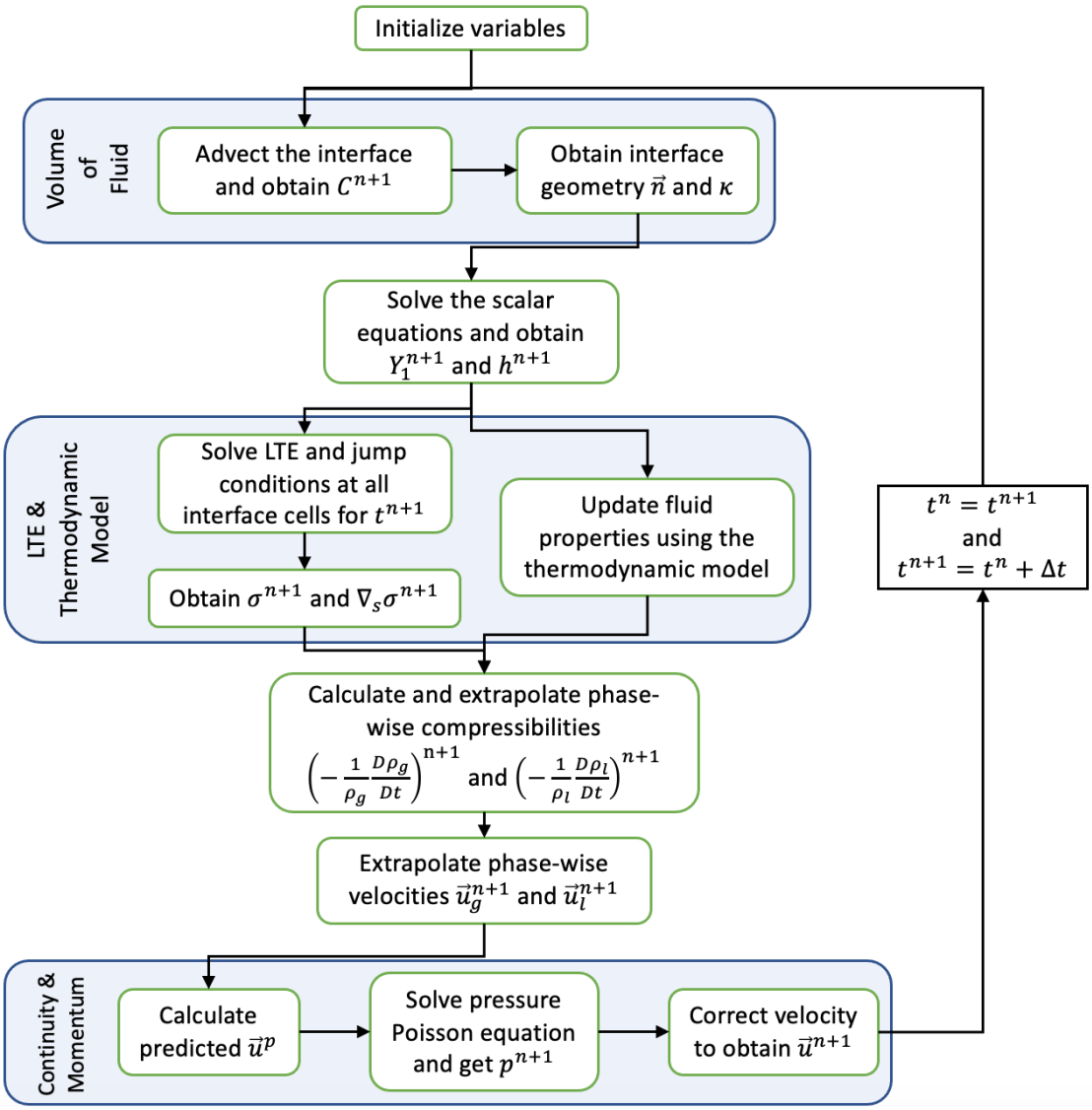

Figure 4.4: Flowchart of the solution algorithm with the steps taken at every time step to solve low-Mach-number, transcritical two-phase flows [66].

The time step, Δt, is updated before proceeding to the following time iteration. CFL conditions have to be satisfied to ensure numerical stability in the explicit solver. Here, the CFL conditions presented in Kang et al. [135] are used, which have also been applied in other

two-phase works [62, 97]. The following relations are determined

$$\begin{cases} \tau_{\vec{u}} = \frac{|u|_{\max}}{\Delta x} + \frac{|v|_{\max}}{\Delta y} + \frac{|w|_{\max}}{\Delta z} \\ \tau_{\mu} = \left(\frac{2}{\Delta x^2} + \frac{2}{\Delta y^2} + \frac{2}{\Delta z^2} \right) \left(\frac{\mu}{\rho} \right)_{\max} \\ \tau_{\sigma} = \sqrt{\frac{\sigma_{\max}\kappa_{\max}}{\rho_{\min}\min(\Delta x^2, \Delta y^2, \Delta z^2)}} \end{cases} \quad \text{and} \quad \begin{cases} \Delta t_{\vec{u}} = \frac{2}{\tau_{\vec{u}} + \tau_{\mu} + \sqrt{(\tau_{\vec{u}} + \tau_{\mu})^2 + 4\tau_{\sigma}^2}} \\ \Delta t_h = \frac{\min(\Delta x^2, \Delta y^2, \Delta z^2)}{2\alpha_{\max}} \\ \Delta t_Y = \frac{\min(\Delta x^2, \Delta y^2, \Delta z^2)}{2(D_m)_{\max}} \end{cases} \tag{4.29}$$

where $\alpha = \lambda/(\rho c_p)$. Then, these relations are used to evaluate the time step as

$$\Delta t = C_{\text{CFL}} \min(\Delta t_{\vec{u}}, \Delta t_h, \Delta t_Y) \tag{4.30}$$

The choice of $C_{\text{CFL}} = 0.1 - 0.2$ is a conservative numerical compromise between numerical stability and computational cost. As explained in Section 4.3, this coefficient might need to be reduced to achieve a stable solver if the density ratio, the curvature, or the surface-tension coefficient causes a significant pressure jump across the interface.

This algorithm has a higher computational cost than equivalent algorithms for incompressible flows with no phase change. The pressure solver is typically the most expensive component of a fluid dynamics simulation. Thus, using the split pressure-gradient strategy is advantageous as it is particularly computationally efficient. However, the solution of LTE at all interface cells, the update of fluid properties using the thermodynamic model, and the extrapolation of phase-wise fluid compressibilities and velocities account for at least 40% of the computational cost every time step before substantial surface deformation occurs.

There is a scalability problem in configurations where the interface deforms significantly, such as studying liquid jet atomization. As the interface deforms and the surface area grows, additional interface nodes are created, increasing the interface's thermodynamic and topology complexity. Furthermore, the convergence rate of phase-wise extrapolations may

be lower if the surface becomes under-resolved. As a result, the computational cost may rise significantly over time at each time step.

The code is written in Fortran 90 and uses the message-passing interface (MPI) and OpenMP for multi-processor computing. The computational domain is partitioned in a pencil-like distribution with the contiguous memory along the jet's transverse direction. Following this decomposition, the computational resources are better utilized to capture the interface surface area and perform the various operations that scale with it (e.g., local equilibrium state, extrapolations). External open-source libraries have been linked to the code: 2DECOMP&FFT [136] to perform the domain decomposition and FFTW3 [137] to solve the pressure field via Eq. (4.23) using Discrete Fourier Transforms. The simulations were carried out on the University of California Irvine's local HPC3 cluster and different supercomputers from the XSEDE network [138].

The validation and verification of the numerical method are presented in Appendix F. Previous works following a similar two-phase method have been validated and verified in simpler scenarios such as incompressible flows with or without phase change [63, 64, 94, 95, 115]. Therefore, Appendix F only presents a handful of tests under such conditions and focuses on the verification of the fully-coupled model that captures the high-pressure physics. At these later conditions, no analytical solutions are available, and the thermodynamic model employed impacts the final results. Furthermore, experiments under these conditions are limited. They either focus on the full-scale injection problem or the evaporation of isolated droplets, so there is a lack of detailed data showing surface topology, perturbation wavelengths, and growth rates or details on the enhanced mixing occurring at high pressures. Therefore, we focus on verifying the numerical consistency of the proposed model and addressing the impact of known issues such as the effect of spurious numerical currents around the interface or mass conservation. Despite the difficulties in adequately validat-

ing the numerical method, each part of the code has been validated independently (e.g., thermodynamic model, advection algorithm).

Chapter 5

Two-Dimensional Planar Jet: High-Pressure Physics for Real Jets

The temporal analysis of the early deformation of a two-dimensional planar liquid jet injected into oxygen at supercritical pressures is presented in this chapter. Although the surface-tension force acts differently in two dimensions (i.e., surface-area minimization in two dimensions hinders ligament thinning, neck formation, and droplet breakup), it serves to illustrate the critical mixing features and interface thermodynamics that arise at supercritical pressures.

This chapter must be understood as introductory material for Chapters 6 and 7. An overview of the main physics in three-dimensional planar jet atomization at transcritical conditions is presented with better detail due to the simpler two-dimensional configuration. Section 5.1 describes the problem considered here and the computational setup, while Sections 5.2, 5.3 and 5.5 show, respectively, the main features of intraphase molecular mixing (e.g., diffusive mixing), the evolution of the interface local equilibrium state, and a first look at the role of vorticity dynamics in the deformation of the liquid jet.

5.1 Analyzed Configuration

Following the binary mixture of n-decane/oxygen used in previous works [15–17, 19] and described in Chapter 2 and Section 3.1, a planar liquid jet initially composed of pure n-decane at 450 K immersed into a hotter gas stream initially composed of pure oxygen at 550 K is considered. The ambient thermodynamic pressure is 150 bar, which is supercritical for both species (see Table 2.1). However, as detailed in Sections 2.2 and 3.1, a two-phase problem at the liquid-gas interface can be sustained for this binary mixture in the selected thermodynamic space. Other similar mixture configurations (e.g., diesel/air or RP-1/oxygen) are expected to behave similarly within each respective thermodynamic domain of two-phase coexistence, which should not differ much from that of n-decane/oxygen.

Practical physical parameters are chosen for the temperature of each fluid and the chamber pressure. The thickness of the jet is chosen to be 20 μm, and its surface is initially perturbed with a sinusoidal wave in the streamwise direction with an amplitude of 0.5 μm and a wavelength of 30 μm. The perturbation amplitude is sufficiently small to let the instability grow naturally in a short amount of time, and the perturbation wavelength chosen here is consistent with those previously reported as the fastest-growing perturbations in a similar study involving the same binary mixture in an axisymmetric configuration [19]. This study has been discussed in Section 2.5. Then, following a hyperbolic tangent profile, a velocity distribution is imposed in the streamwise direction ranging from 0 m/s in the center of the liquid to the gas freestream velocity of 30 m/s within a thin layer of a few micrometers or about 6 μm. The equation describing the initial velocity profile is $u(y) = (u_G/2)\big(\tanh\big[6.5\times10^5(y-H')\big]+1\big)$, where $u_G = 30$ m/s is the gas freestream velocity, $H' = 10$ μm is the jet half-thickness and y is the coordinate transverse to the jet center plane. Note H' and y must be in units of meters [m] to obtain a velocity in meters per second [m/s]. The transverse component of the velocity is initially set at zero. As shown

in Section 3.1, this configuration satisfies the low-Mach-number methodology developed in this dissertation.

The computational domain has symmetry boundary conditions in the center plane of the jet (i.e., only half the jet is considered) and includes only one wavelength of the perturbed liquid surface. For the temporal study, periodic boundary conditions are imposed in the streamwise direction, and outflow boundary conditions are imposed along the gas-phase top boundary, sufficiently far away from the interface location. These restrictions are necessary to limit the computational cost, especially in a three-dimensional configuration, since a fine mesh is needed to properly capture the physics of the atomization cascade process toward smaller structures. However, larger domains may be explored in the future since significant deformation may deviate from periodicity and an antisymmetric mode may develop [27]. The resulting domain size has 30 μm length in the streamwise direction and 30 μm in the transverse direction, which is large enough to include the liquid phase and the mixing layers during the analyzed times. The domain is uniformly discretized with 600^2 cells or, equivalently, a uniform mesh size of $\Delta = \Delta x = \Delta y = 0.5$ μm. As shown in Appendix F.3, this mesh size gives sufficient resolution to capture the liquid structures without entering into the non-continuum region or the phase non-equilibrium region across both fluids.

The initial domain setup for the two-dimensional planar jet is equivalent to the view provided in Figure 6.1b. Moreover, for the jet analyzed in this chapter, a simplified two-dimensional analysis of one of the cases is considered in the parametric study for Chapters 6 and 7. It corresponds to case C1 in Table 6.1, with a thermodynamic pressure of 150 bar and a gas freestream velocity of 30 m/s.

5.2 Intraphase Diffusive Mixing

The temporal evolution of the molecular diffusive mixing within each phase for the two-dimensional jet, as well as the growth and deformation of the liquid surface, is shown from Figure 5.1 to Figure 5.6. These figures present the temperature field, the composition of each phase, and how their variations affect the fluid properties such as density and viscosity. The domain has been enlarged utilizing the periodic behavior in the streamwise direction to show the liquid perturbation at all times clearly.

Figures 5.1, 5.2 and 5.3 illustrate the species and energy mixing (i.e., the solution of Eqs. (3.7) and (3.9)). As observed in simpler studies where the interface does not deform [15–17], mass and thermal diffusion drive the mixing between both phases during the early times (i.e., $t < 1$ μs). As seen in Figure 5.1, the temperature decreases considerably in the gas phase as the hotter gas enters in contact with the cooler liquid. Meanwhile, heating occurs more slowly in the liquid phase. That is, the liquid-phase specific heat is larger. The study of the fuel mixing into the oxidizer stream is critical in combustion applications since it impacts combustion efficiency. n-decane vaporizes and mixes well with oxygen as the atomization cascade unfolds at these extremely high pressures, as seen in Figure 5.2. Along the interface, small discrete regions of high fuel-vapor concentration emerge in the gas phase. Furthermore, smaller liquid fuel structures form and extend into the hotter gas stream, where vaporization rates increase, and the mixing of the hydrocarbon fuel with the oxidizing species is enhanced. Changes in net mass flux per unit area across the interface are shown in Figure 5.8. Figure 5.3 shows the greater solubility of oxygen at high pressures. LTE is satisfied at the interface by a greater dissolution of oxygen at supercritical pressures compared to a negligible dissolution at subcritical pressures (i.e., see Figure 3.1a).

Such a diffusive mixing process within each phase is partially responsible for the fast and strong deformation of the liquid-gas interface. Although "fast" is always a relative term,

comparison with lower pressures proves that the intraphase mixing process is a key feature in explaining how easily and in what manner the liquid phase deforms (see Chapter 6). As observed in Figures 5.4, 5.5 and 5.6, the variations in fluid density and viscosity are considerable. Fuel mixing in the gas phase and a reduction in temperature generates localized regions within the mixing layer with densities 40% greater than the freestream value at 150 bar. On the other hand, the dissolution of oxygen in the liquid phase is responsible for a large reduction in the liquid density and a sharp drop in liquid viscosity toward gas-like values.

Even though the initial perturbation amplitude is only 1/60th of the perturbation wavelength, the interface begins to display significant deformation relatively early in time. The liquid begins to elongate and roll over itself between 1 μs and 5 μs. This rapid deformation is not unexpected. That is, compared to previous incompressible flow studies [24–28, 36], the analyzed case has a shorter wavelength, and the initial shear strain rate between both fluid streams is greater. The choice of a short perturbation wavelength is motivated by the low surface-tension environment and the significant mixing expected at very high pressures, both of which promote the growth of such perturbations. The earlier study of a supercritical axisymmetric liquid jet shown in Section 2.5 revealed a faster-than-usual interface deformation [19] with a similar configuration. The liquid deformation becomes increasingly chaotic as time passes (e.g., for $t > 5\mu$s). Nevertheless, there is an orderly process where folding or layering of liquid sheets occur, as seen in Figures 5.1 through 5.6. Different liquid zones coalesce, which can trap small gas pockets. Thin and elongated liquid structures or ligaments form, which may break into two-dimensional droplets. This layering mechanism is further explained in Subsection 6.3.4 and defines the three-dimensional liquid-phase deformation in the long term for high-pressure configurations at 100 bar and above.

The three-dimensional solution can be very different. Because surface-tension force naturally produces neck thinning and droplet breakup, a more significant presence of droplets

is expected. Furthermore, the approach utilized in this work is dependent on a sufficient mesh resolution of the liquid shape. Despite using a very fine mesh, the evolution of the liquid surface is influenced by numerical inaccuracies once very small liquid structures or high-curvature regions emerge.

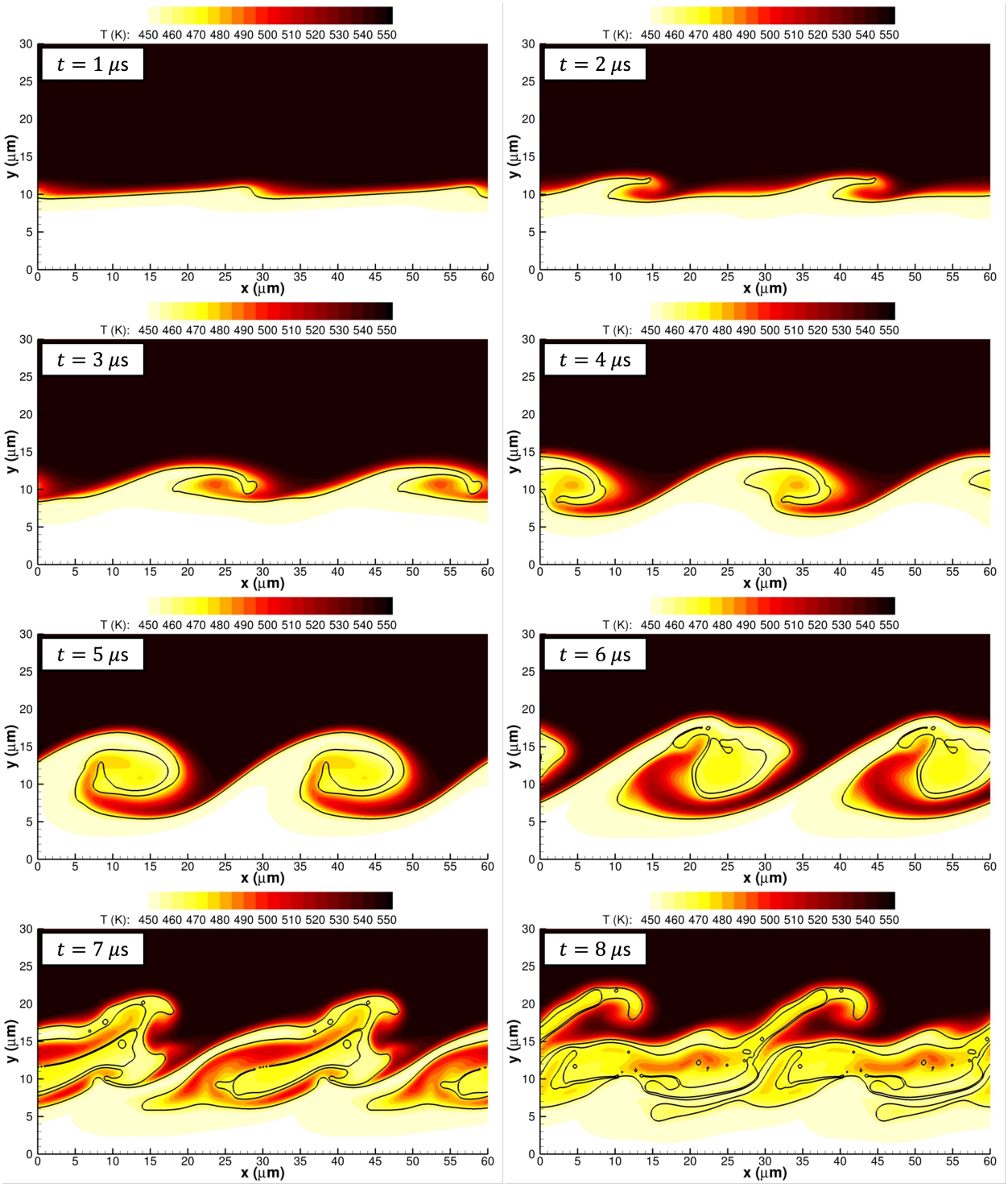

Figure 5.1: Temperature field for the two-dimensional planar jet at 150 bar with $u_G = 30$ m/s. The interface location is highlighted with a solid black curve representing the isocontour with $C = 0.5$ [139].

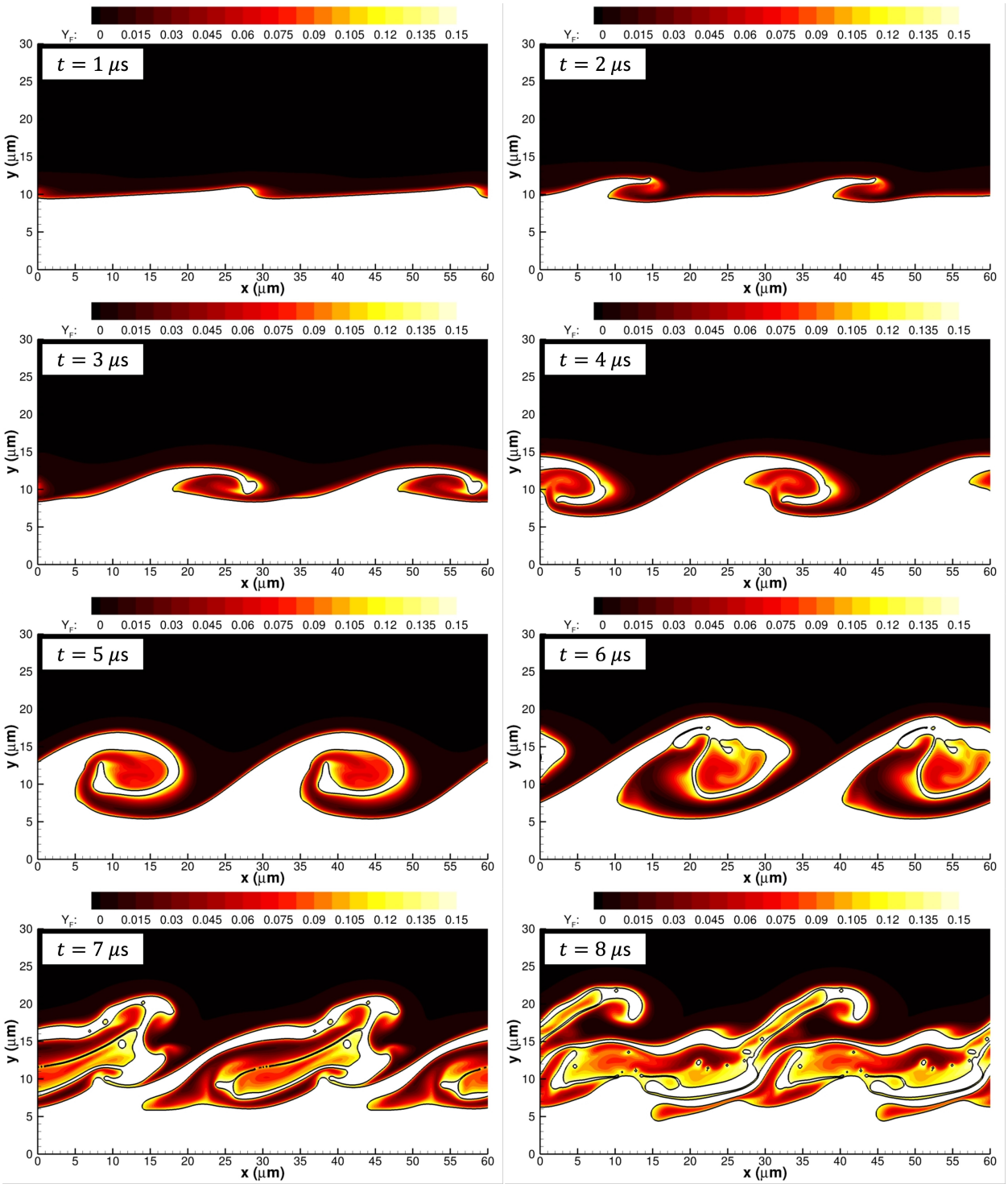

Figure 5.2: n-decane mass fraction, Y_F, in the gas phase for the two-dimensional planar jet at 150 bar with $u_G = 30$ m/s. The interface location is highlighted with a solid black curve representing the isocontour with $C = 0.5$ [139].

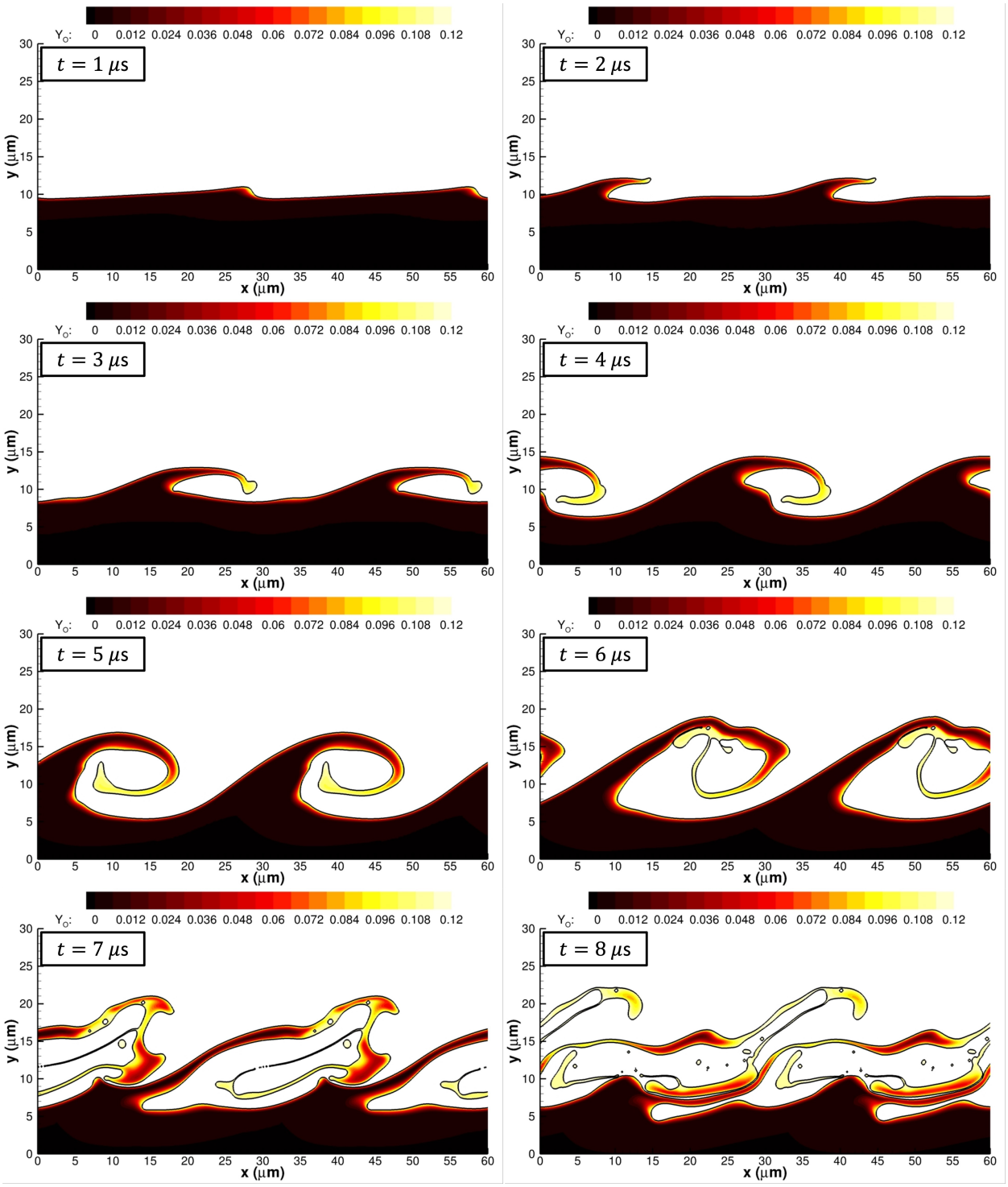

Figure 5.3: Oxygen mass fraction, Y_O, in the liquid phase for the two-dimensional planar jet at 150 bar with $u_G = 30$ m/s. The interface location is highlighted with a solid black curve representing the isocontour with $C = 0.5$ [139].

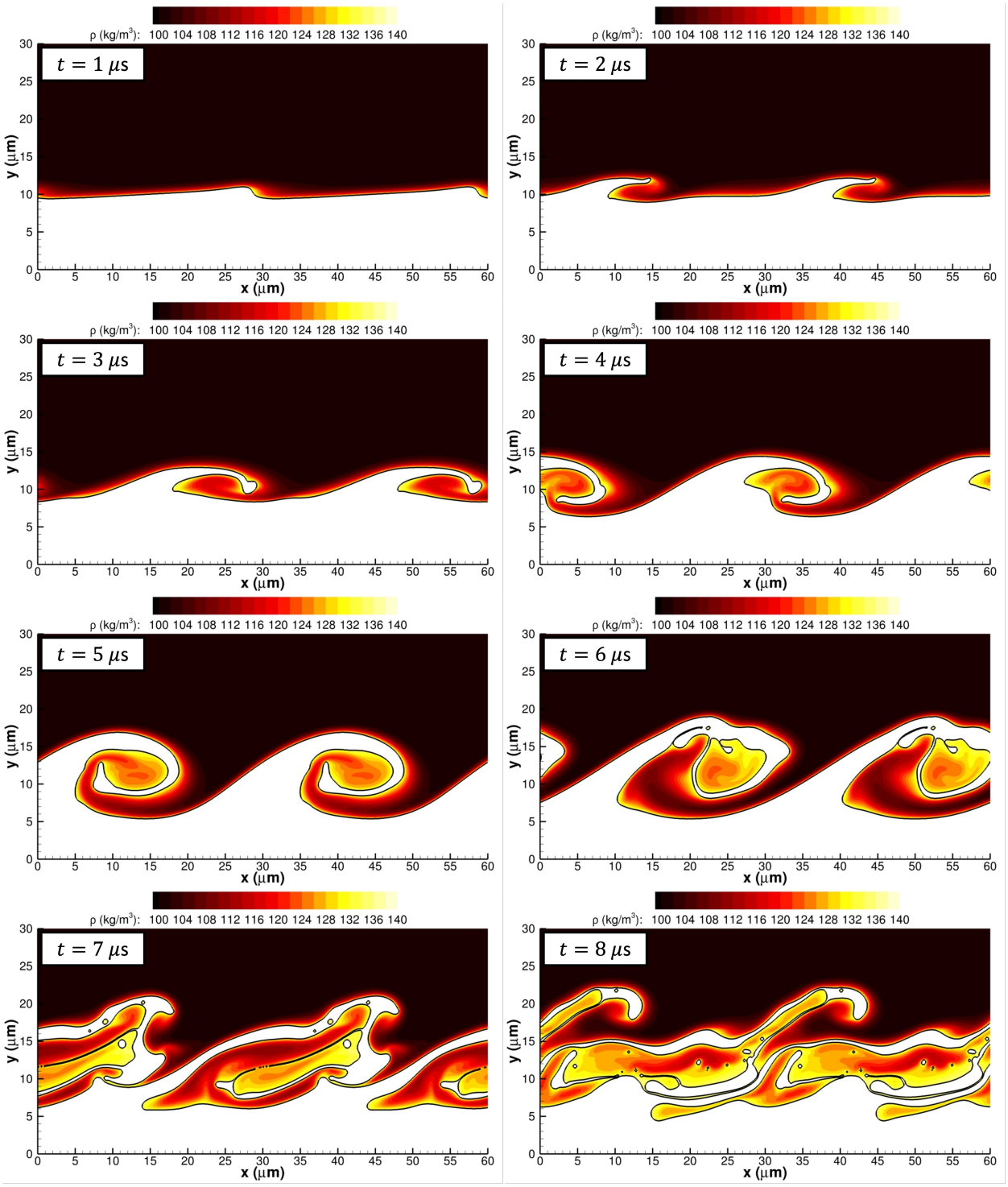

Figure 5.4: Gas density for the two-dimensional planar jet at 150 bar with $u_G = 30$ m/s. The interface location is highlighted with a solid black curve representing the isocontour with $C = 0.5$ [139].

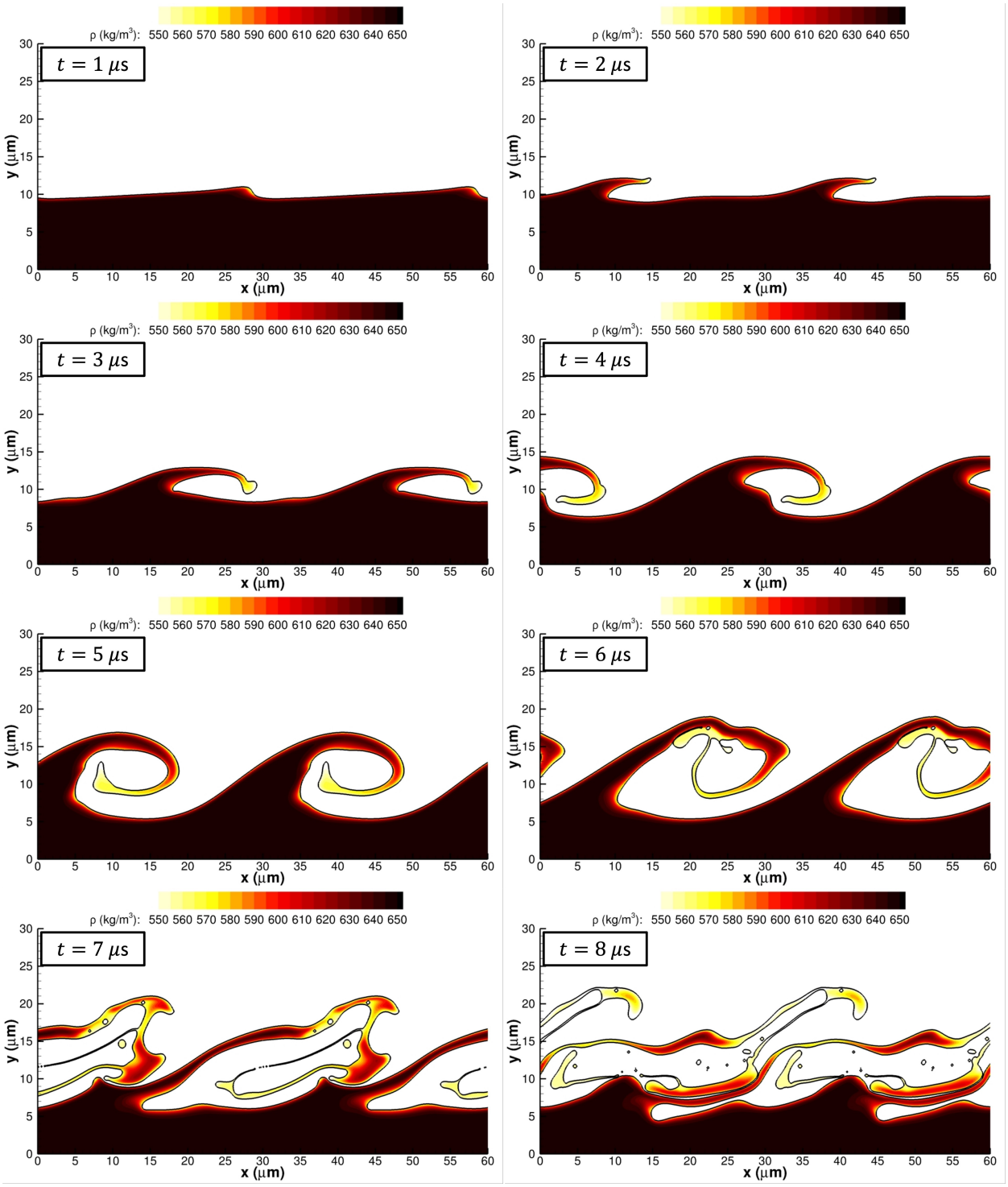

Figure 5.5: Liquid density for the two-dimensional planar jet at 150 bar with $u_G = 30$ m/s. The interface location is highlighted with a solid black curve representing the isocontour with $C = 0.5$ [139].

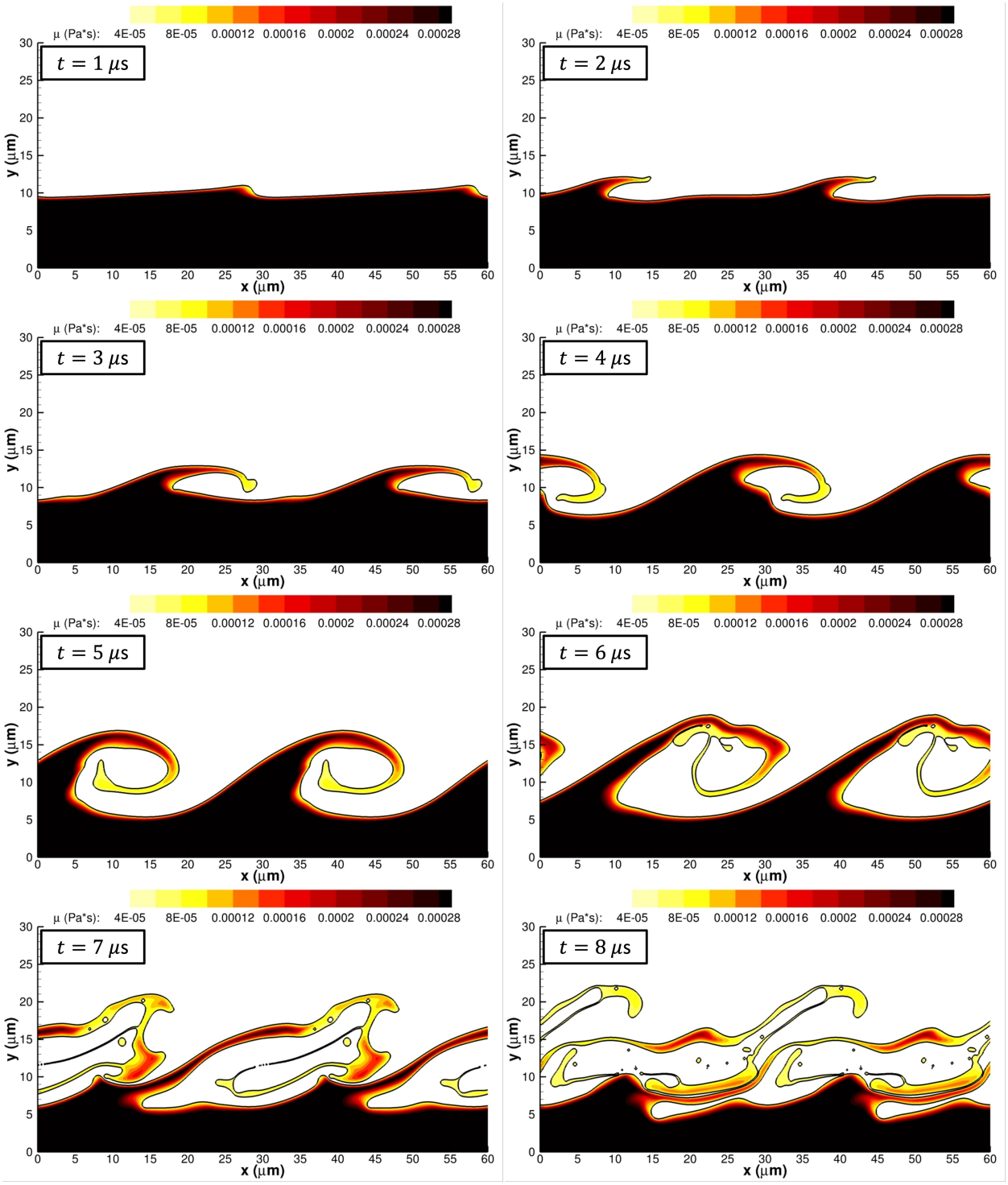

Figure 5.6: Liquid viscosity for the two-dimensional planar jet at 150 bar with $u_G = 30$ m/s. At this high pressure, the viscosity of the gas mixture remains within the range of 2.8-3.4x10^{-5} Pa*s. The interface location is highlighted with a solid black curve representing the isocontour with $C = 0.5$ [139].

5.3 Interface Thermodynamics

Fluid properties are not constant along the liquid-gas interface. At high pressures, the solution of the matching or jump conditions between both phases coupled with local thermodynamic phase equilibrium varies strongly. This feature is illustrated in Figure 5.7, which represents the magnitude of various interface parameters (e.g., temperature) along the interface for the two-dimensional jet discussed in this chapter at $t = 4$ μs. Near compressed gas regions, the surface temperature is higher (e.g., crest of the perturbation or regions of strong gas entrainment). At these elevated temperatures, phase-equilibrium requirements promote the dissolution of oxygen into the liquid phase and the vaporization of n-decane into the gas phase. Although the influence of the temperature and composition variations on the interface gas density and viscosity can be negligible, fluid properties in the liquid phase change considerably. Note that a higher temperature is associated with a slightly higher concentration of oxygen in the liquid phase and a reduction in liquid density and viscosity. Additionally, this reduction in liquid density around the high-temperature surface causes the surface-tension coefficient to decrease compared to the rest of the liquid-gas interface. Both phases have a more similar density and composition, resulting in a lower inter-molecular attraction of the liquid phase near the contact surface (i.e., the origin of the surface-tension force). The opposite effect where a higher surface-tension coefficient is observed occurs in lower temperature regions near areas of compressed liquid (e.g., wave trough) or within the rolling liquid (e.g., trapped gas phase).

The variations over time of interfacial parameters such as the surface-tension coefficient and the net mass flux per unit area across the interface are shown in Figure 5.8. The net mass exchange between the two phases varies significantly along the interface. Net condensation is observed in simpler analyses at 150 bar, where the interface does not deform [15–17]. The interface deformation and multidimensional mixing dynamics influence the mass and energy balance across the interface, and net vaporization or net condensation can occur

simultaneously at separate interface locations at such elevated pressures. This feature of transcritical atomization has been previously discussed in Section 2.5, and it is illustrated for the two-dimensional planar liquid jet in Figure 5.8. Interface regions submerged in the hotter oxidizer stream or near compressed gas show net vaporization or weaker condensation. The heat flux into the liquid is larger and, thus, the energy balance may result in a vaporizing interface. On the other hand, cooler regions and compressed-liquid regions show a stronger net condensation. This phase-change reversal depends on the thermodynamic pressure as discussed in previous works [15–17]. At 150 bar, it is easy to observe net condensation regions and net vaporization regions simultaneously during the atomization process. However, net condensation may not be achieved at lower pressures. Although the total mass exchange across the interface over the analyzed time is negligible (i.e., less than 1% of the total liquid mass for this problem setup as shown in Appendix F.3) and that phase change does not appear to have a significant impact on the interface dynamics at high pressures, it remains a crucial feature of transcritical two-phase flows due to its complex behavior.

At supercritical pressures, a reduced surface-tension environment already develops because both phases look similar near the interface. In other words, the gas density increases considerably with pressure while the dissolution of the lighter gas into the liquid decreases the liquid density. Instabilities are expected to grow faster with shorter wavelengths, but the additional weakening of the surface-tension force near the wave crest due to a higher temperature accelerates the growth of surface instabilities. Furthermore, mixing in the liquid phase significantly impacts the liquid's dynamical properties (i.e., density and viscosity) as discussed in Section 5.2. The greater interface temperature near the wave crest promotes the solubility of oxygen into the liquid at $t = 1$ μs. Then, a layer with decreased density and gas-like liquid viscosity forms (see Figures 5.5 and 5.6). These mixing effects can be seen all over the interface, but they are more pronounced towards the wave crest or other hotter interface areas. As a result of the lower liquid viscosity, the viscous dissipation that would dampen the perturbation growth is reduced, further enhancing the surface instability.

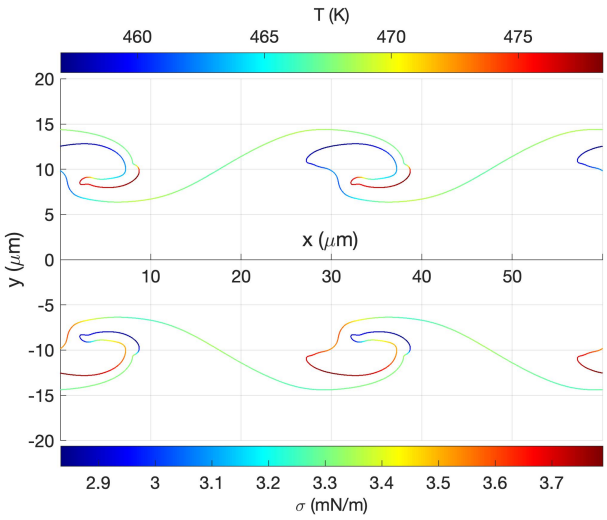

(a) Temperature and surface-tension coefficient

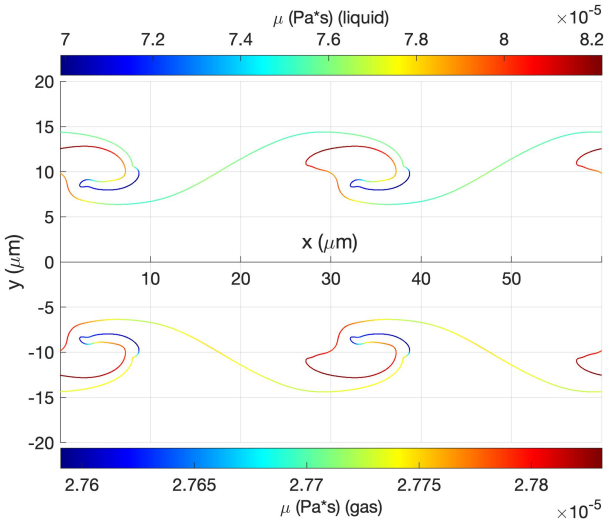

(b) Viscosity

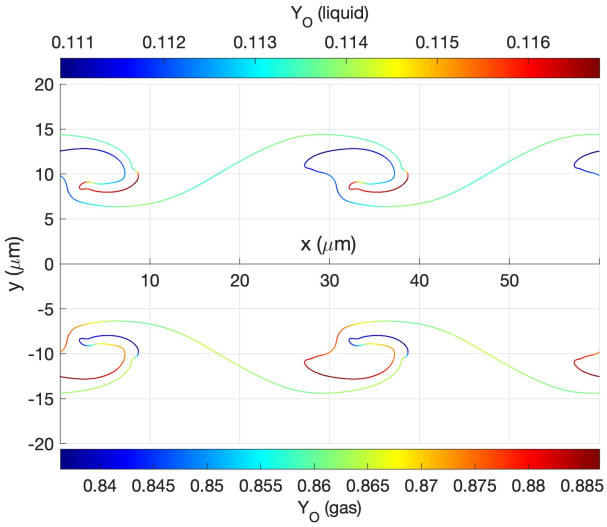

(c) Oxygen mass fraction

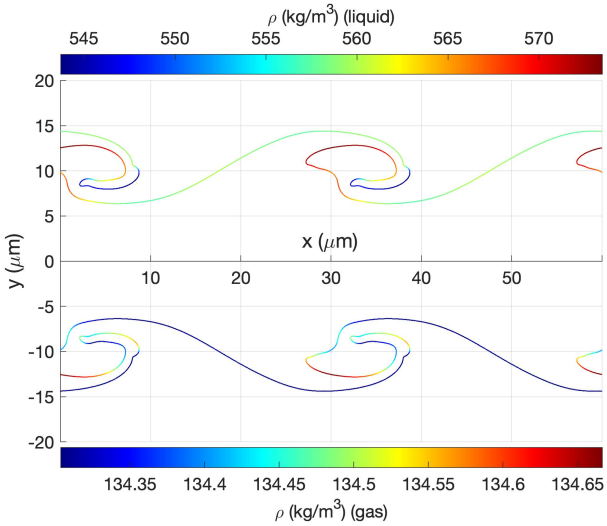

(d) Density

Figure 5.7: Interface properties variation along the interface for the two-dimensional planar jet at 150 bar with $u_G = 30$ m/s at $t = 4$ μs. The symmetry condition is used to mirror the jet and plot different variables on each side. The interface shape is colored by the value of each respective variable. (a) temperature, T, and surface-tension coefficient, σ; (b) viscosity, μ; (c) oxygen mass fraction, Y_O; and (d) density, ρ [139].

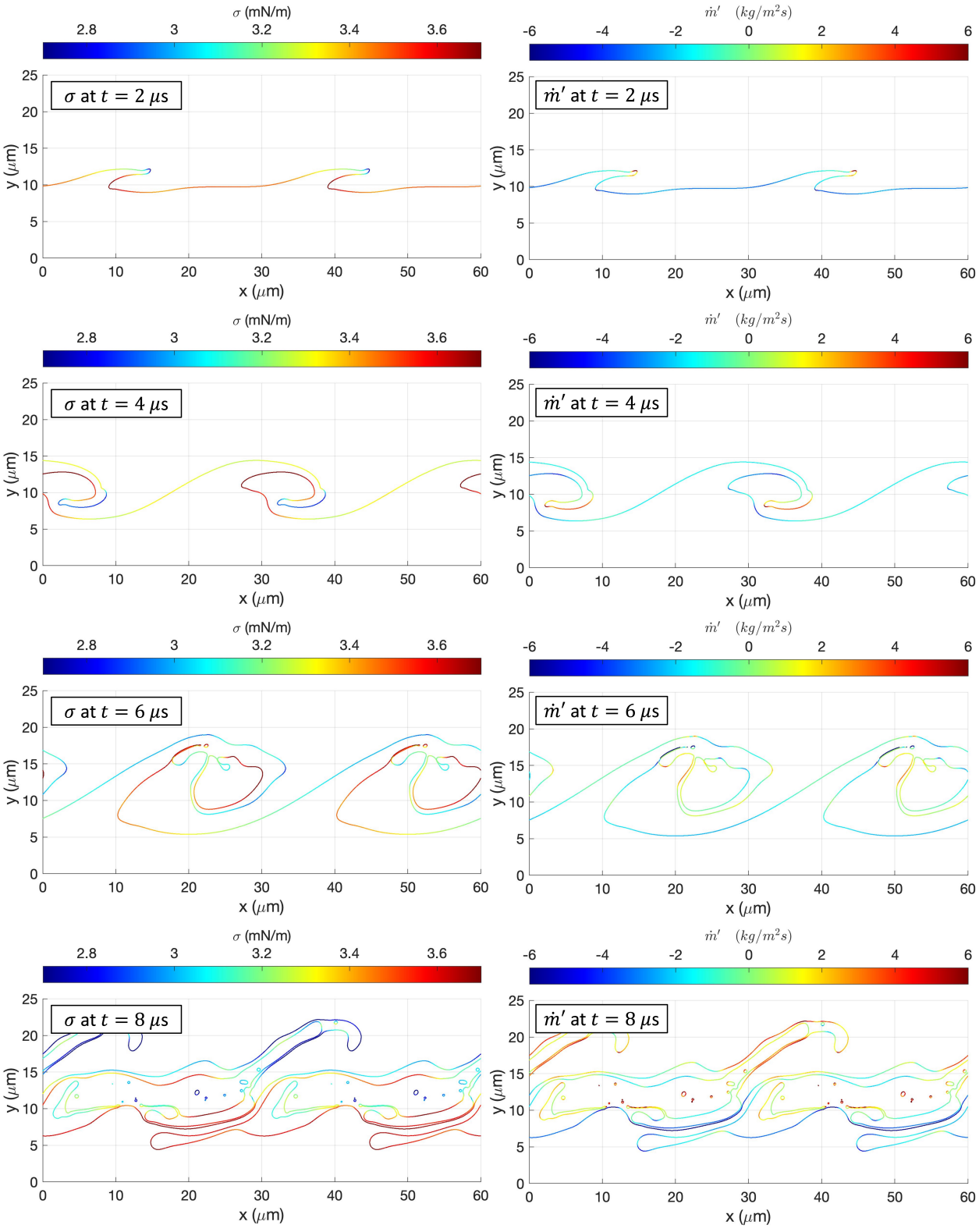

Figure 5.8: Surface-tension coefficient, σ, and net mass flux per unit area, $\dot{m}'$, along the interface for the two-dimensional planar jet at 150 bar with $u_G = 30$ m/s. The interface shape is colored by the value of each respective variable [139].

As liquid density, liquid viscosity, and surface tension decrease, the liquid becomes more vulnerable to deformation under the dense gas-phase dynamics, explaining the rapid emergence of elongated liquid structures. For example, from $t = 1$ μs to $t = 4$ μs, the deformation of the liquid at the wave crest (i.e., more substantial gas inertia and reduced liquid density and viscosity) appears as an elongated two-dimensional lobe that stretches rather quickly into the gas phase before vortical motion bends it.

The three-dimensional picture is more complex than the two-dimensional results. As shown in Section 6.4, the surface variations of interface properties substantially impact the appearance of stable and unstable regions. Coupled to local intraphase mixing, unstable interface regions may be susceptible to further growth of short-wavelength surface perturbations or ripples originating from surface corrugation or coalescence events such as a droplet impact.

5.4 Pressure Effects and Real-Fluid Considerations

The temporal deformation of the two-dimensional planar liquid jet with the gas freestream velocity of $u_G = 30$ m/s is compared for different thermodynamic pressures. Moreover, the effects of diffusive mixing within each phase and the change in fluid properties are shown for the 150-bar case. The same binary mixture of n-decane and oxygen and initial temperature conditions are considered for all cases. For further information on the range of fluid properties involved at each pressure, the reader is directed to Davis et al. [16], or Poblador-Ibanez et al. [17], both of which study the same pressures using the same thermodynamic model, or later chapters discussing the three-dimensional planar jet.

The comparison is shown in Figure 5.9, where the volume fraction field represents the liquid phase. Evidence of the rapid growth of the perturbations and deformation of the liquid surface at high pressures or engine-relevant conditions is seen. The coupled physical and

numerical models are obtained at different pressures (i.e., real-fluid considerations and with mass exchange across the interface). At low pressures (i.e., between 10 and 50 bar), the interface mainly deforms due to shear strain and the effect of higher surface-tension force. At the subcritical pressure of 10 bar, momentum transfer via mass exchange might be important during the early times as the magnitude of $\dot{m}'$ is relatively larger than at higher pressures. The gas density is relatively low (about 7 kg/m^3 at 10 bar and 34.5 kg/m^3 at 50 bar), whereas the liquid density is of the order of 600 kg/m^3. Furthermore, fluid properties stay nearly constant across the mixing layers in both phases at 10 bar. At 50 bar and above, mixing effects are more pronounced. Short-wavelength instabilities do not grow at such low pressures in the time studied here. However, at the higher pressures of 100 bar and 150 bar, a substantial perturbation growth and surface deformation is observed as the surface-tension force is reduced, the gas phase presents a higher density, and fluid properties in the liquid phase change considerably.

Because the gas density increases and the surface-tension coefficient decreases with pressure, the observed pressure effects could be interpreted as a greater impact of inertial terms on the two-phase dynamics. Nevertheless, gas Weber and liquid Reynolds numbers are still low compared to previous incompressible works [26–28] in order to justify such a chaotic deformation at 150 bar. As seen in Table 6.2, the non-dimensional parameters for the high-pressure, two-dimensional jet analyzed in this chapter are $We_G \approx 530$ and $Re_L \approx 1285$, as depicted in case C1. The importance of the thermodynamic model and the variation of fluid properties within each phase is also illustrated in Figure 5.9. The subfigures on the last row represent the same 150-bar case arrangement but without considering mass exchange across the interface nor intraphase mixing. Only the momentum equation is considered. Both phases are incompressible and remain pure gaseous oxygen and pure liquid n-decane with the density and viscosity corresponding to the initial temperatures and thermodynamic pressure considered. As a result, the surface-tension coefficient remains constant, delaying and reducing the production of elongated ligaments. At 150 bar, the increased gas inertia

deforms the liquid surface, although not as much as with the complete physical model. That is, in the absence of oxygen in the liquid mixture, the liquid phase remains denser and more viscous. This conclusion proves that liquid injection at high pressures is dominated not only by an increase in gas density and a reduction in surface tension but also by greater mixing in both phases, which has a significant impact on the fluid properties and the thermodynamic state of the interface.

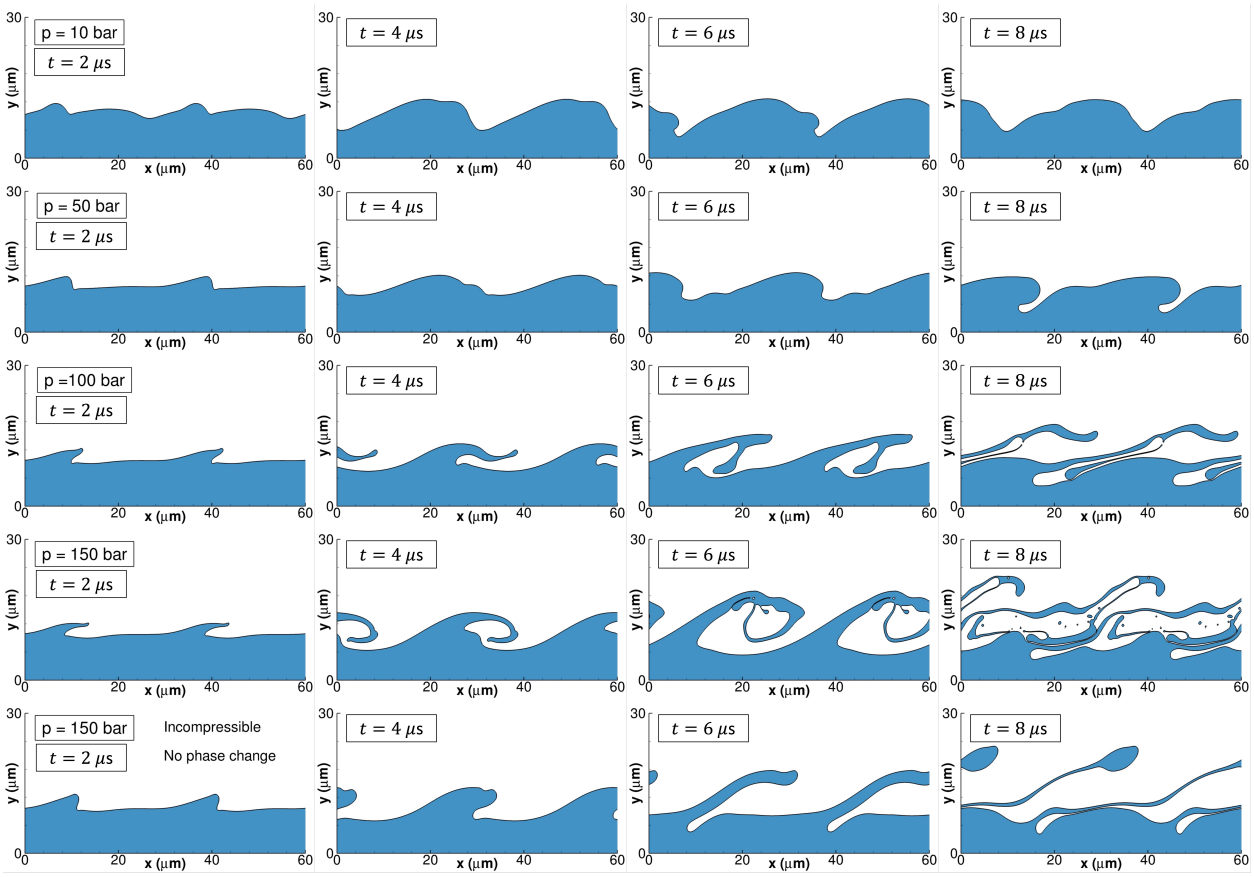

Figure 5.9: Pressure effects on the two-dimensional planar jet deformation with $u_G = 30$ m/s. The figures show the liquid phase evolution from 2 μs to 8 μs with the interface location highlighted with a solid black curve representing the isocontour with $C = 0.5$. Subfigures (a) to (d): 10 bar; subfigures (e) to (h): 50 bar; subfigures (i) to (l): 100 bar; subfigures (m) to (p): 150 bar; and subfigures (q) to (t): 150 bar without phase change and with incompressible fluids [139].

5.5 Role of Vorticity Dynamics

Liquid-jet atomization is a physical problem defined by a transition to turbulence where vorticity plays an essential role in the surface deformation and mixing processes. Previous works detailed the role of vortex dynamics in the atomization cascade process of incompressible liquid jets [24–27, 36], which have been discussed in Subsection 2.1.1. In those works, the λ_2 method from Jeong and Hussain [41] identifies vortex structures in favor of other widely-used vortex identification methods such as the Q-criterion [44]. Here, a compressible extension of the λ_2 method, called the dynamical vortex identification method or λ_ρ from Yao and Hussain [43] is used. An overview of the method's formulation is given in Section 7.1.

Vortices are identified in a compressible flow by looking for local pressure minimums in the plane of a modified pressure Hessian tensor. In other words, a vortex is a connected region with two positive eigenvalues of the pressure Hessian. However, the dynamical terms defining the negative modified pressure Hessian tensor are considered; as a result, connected regions with two negative eigenvalues constitute a vortex. This condition corresponds to detecting regions with a negative second eigenvalue of the Hessian tensor (i.e., λ_ρ or λ_2 in the incompressible formulation). Because pressure minimums can occur without a vortex, terms like the unsteady fluid straining and the dilatation part of the viscous strain are ignored. Furthermore, viscous terms are disregarded, which can remove pressure minimums in regions with vortical motion [43].

The contour plot of λ_ρ in the two-dimensional jet discussed in this chapter is shown in Figure 5.10. The time illustrated in the figure goes from $t = 1$ μs to $t = 2.7$ μs, and the location and behavior of various two-dimensional vortices are indicated. The λ_ρ methodology does not provide information on the vortex's rotation direction, and the magnitude of the eigenvalue is a measure of the strength of the vortex in a given location. The λ_ρ approach has to be combined with other data such as the velocity field or the vorticity field to understand

the flow behavior. Such analysis has been done to annotate the plots shown in Figure 5.10 with the direction of rotation of the vortices. Note that because of the sharp volume-averaging of fluid properties across the interface, some visualization noise exists along the surface that might prevent proper identification of the physical phenomena. This problem is especially troublesome in a three-dimensional visualization of λ_ρ iso-surfaces, as highlighted in Section 7.1. Thus, spatial filtering of the velocity field and proper care of the density gradient terms is necessary to dissipate the numerical noise while ensuring that the physical vortices are still well represented.

First, two clockwise vortices, one in each phase, form. Vortex 1 is a liquid-phase vortex that remains attached to the region where the inner liquid bends. This vortex forces liquid from the core into the two-dimensional lobe, reducing the angle between the lobe and the surface of the liquid core over time. On the other hand, the gas stream flowing over the liquid lobe causes the formation of Vortex 2. Vortex 2 persists in front of the lobe's tip or downstream of the growing perturbation as the gas inertia stretches it under the lobe. This vortex is a Kelvin-Helmholtz (KH) vortex or roller vortex, and the fluid motion it induces is what causes the liquid lobe to roll over itself and the observed gas-phase entrainment under the wave (e.g., see Figure 5.1). Furthermore, vortex 2 can force the lobe's tip higher (i.e., bend upward) when it stretches. Because this liquid region has a lower density and viscosity than the liquid core, it can be more easily affected by the gas-phase dynamics. Vortex 3 detaches from vortex 2 and goes immediately beneath the lobe between 2 mus and 2.2 μs. The vortex's clockwise rotation then amplifies the lobe's rolling momentum. In the three-dimensional vorticity dynamics study presented in Chapter 7, the small vortex forming at the very tip of the lobe is recognized as a "rim vortex" along the edge of the lobe, which is a result of the wake generated by the gas flowing across the lobe's edge. Note that vortex 2 and vortex 3, together with the rim vortex, belong to the same vortex sheet and what is being identified are the locations of higher vortical motion strength and how they evolve.

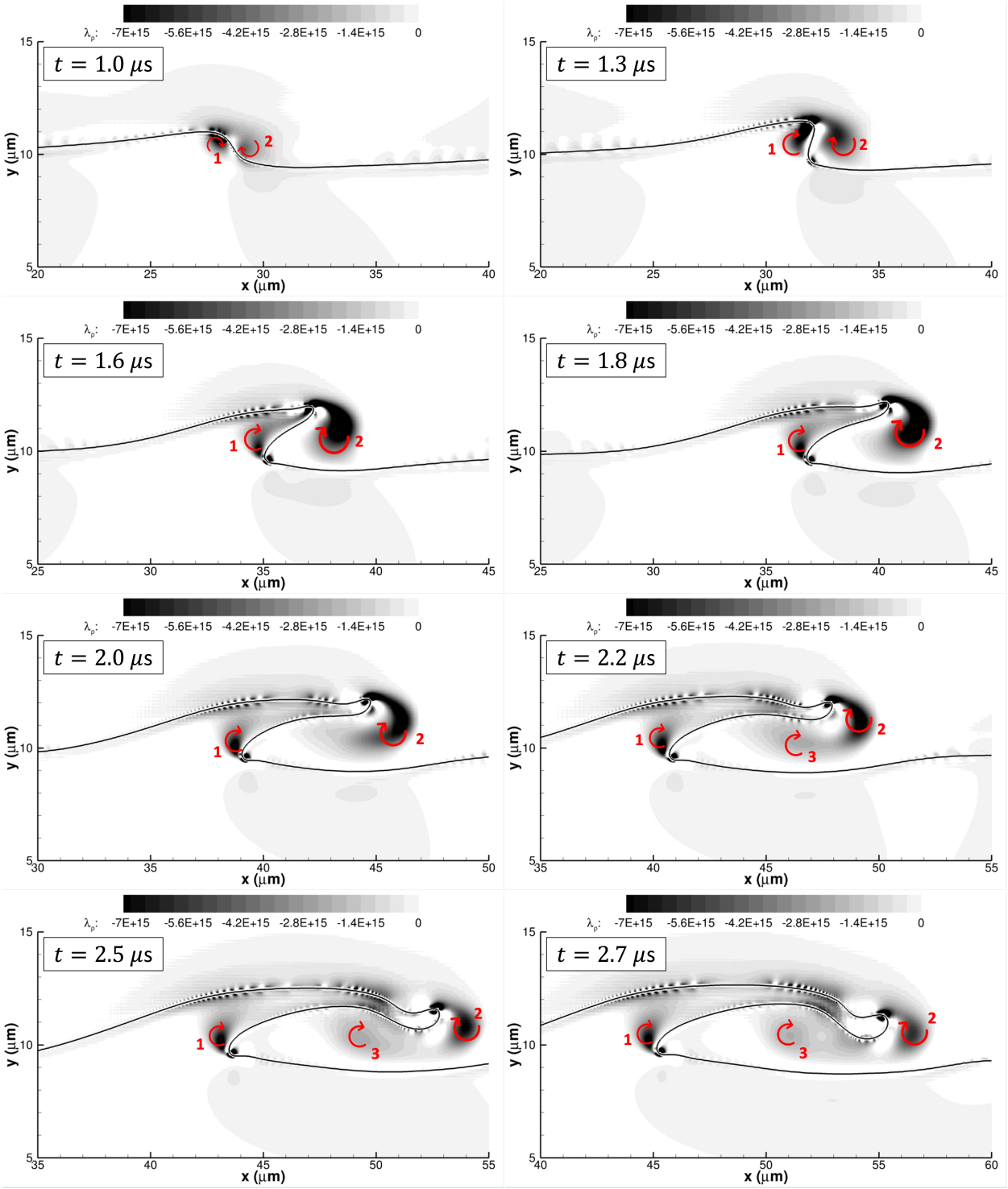

Figure 5.10: λ_ρ contours for the two-dimensional planar jet at 150 bar with $u_G = 30$ m/s. The red arrows point the rotation direction of the vortex. The interface location is highlighted with a solid black curve representing the isocontour with $C = 0.5$ [139].

Chapter 6

Three-Dimensional Planar Jet: Qualitative Description

The temporal analysis of the atomization of a three-dimensional planar liquid jet injected into oxygen at supercritical pressures is presented in this chapter. While Chapter 5 presented a preliminary study of a similar two-dimensional planar jet as an introduction to the physics and features of real liquid jets at such elevated pressures, various issues are discussed in detail here. First, an overview of the analyzed configurations is presented in Section 6.1. Thermodynamic pressure and gas freestream velocity are the main parameters changing. Then, a discussion on how the enhanced mixing and variable fluid properties affect the classification of liquid jets at high pressures is provided in Section 6.2. Early-deformation mechanisms shared by various configurations are shown in Section 6.3. The rise of further surface instabilities beyond the one imposed by the initial perturbation wavelength is discussed in Section 6.4. The formation of ligaments and droplets at these conditions is presented in Section 6.5. Lastly, full-jet characteristics such as the surface-area growth, the transverse development of the two-phase mixture, and phase-change features over time are discussed in Sections 6.6 and 6.7.

6.1 Analyzed Configurations

This dissertation emphasizes the analysis of temporal planar real-liquid jets at increased pressures and transcritical conditions. Due to the high level of resolution required to produce a sufficiently smooth interface solution and the additional coupling with a complete thermodynamic model, the computational cost of solving such two-phase flows is very high. During the breakup process, smaller liquid structures are continuously formed, and the interface surface area between the liquid and the gas grows over time. Furthermore, the required phase-wise extrapolations incur additional computational costs. These concerns become more severe in atomization simulations that include mass and thermal mixing. As a result, the additional physics scale up during the simulation, raising the computational cost exponentially compared to simpler incompressible atomization simulations.

The numerical domain has been reduced to analyze temporal planar liquid jets with a symmetry boundary condition in the centerline of the jet, periodic boundary conditions in the streamwise and spanwise directions, and outflow boundary conditions in the gas-phase top boundary, away from the liquid-gas interface. The jet thickness is $H = 20$ μm (i.e., a jet half-thickness of 10 μm), and two initial sinusoidal perturbations are superimposed in the streamwise and spanwise directions. The perturbation wavelength in the streamwise direction, defined along the x axis, is 30 μm, and the amplitude is 0.5 μm. The spanwise direction is aligned with the z axis, and the sinusoidal perturbation has a wavelength of 20 μm and an amplitude of 0.3 μm. To avoid the high computational cost, the domain size has only one wavelength in each direction.

The initial perturbation amplitude is small enough to allow unstable waves to grow freely. Moreover, the spanwise perturbation promotes the formation of three-dimensional structures early on. The wavelengths of the initial perturbations in both directions are chosen based on prior estimates for an axisymmetric jet in a similar configuration given by Poblador-Ibanez

and Sirignano [19], which showed that, in the range of 100 bar to 150 bar, surface waves naturally developed with a wavelength within 20 μm to 30 μm. At high pressures, the reduced surface-tension force and lower liquid viscosity cause waves with a substantially shorter wavelength to be unstable and grow compared to previous incompressible studies, where the most unstable wavelengths were roughly 100 μm [24–28, 36]. The domain dimensions are $L_x = L_y = 30$ μm and $L_z = 20$ μm, respectively, with a uniform spatial resolution of $\Delta = 0.0667$ μm. Such mesh size corresponds to a uniform mesh of 450 x 450 x 300 nodes, whereby enough mesh resolution may be attained to provide relevant results as shown in Chapter 4 and Appendix F.3. The time step obtained with the time-step limits described in Section 4.5 is of the order of $\Delta t \sim \mathcal{O}(10^{-11})$ s for all simulations. The time step is not constant, as it varies slightly throughout the computation based on the CFL conditions.

The relative velocity between two streams is important in this temporal analysis rather than an absolute velocity. The higher-density inner "jet" begins at rest and as pure n-decane at $T_L = 450$ K, whereas the lower-density ambient phase begins as pure oxygen at $T_G = 550$ K and moves at a freestream velocity u_G. That is, across the liquid-gas interface, there is a strong initial discontinuity. As discussed in this dissertation, both species are illustrative of engines that run on hydrocarbon fuels injected into high-pressure combustion chambers with enriched air or pure oxygen as an oxidizer (e.g., diesel engines, gas turbines, or rocket engines). Table 2.1 provides the the molecular weight and critical properties of n-decane and oxygen (i.e., critical pressure, p_c; critical temperature, T_c; and critical density, ρ_c).

A suitable temperature range has been chosen, with the oxidizer stream being hotter than the injected n-decane to provide enough energy to evaporate the fuel. However, at these high-pressure conditions, the temperature is low enough to warrant two-phase modeling under local thermodynamic phase equilibrium. Section 3.1 presents a complete discussion of the validity of this physical modeling. The internal structure of the interface phase non-equilibrium region, the transition to a mixture subcritical or supercritical state, the relevance of the two-

phase approach in the early stages of n-decane injection under real-engine conditions, and the low-Mach-number assumption are all discussed.

The high-density, compressible fluid with decane as the dominating component will be referred to be liquid in this context, regardless of whether it is subcritical or supercritical locally. Similarly, the lower-density fluid with oxygen as the primary component will be regarded as gas over the transcritical domain.

Table 6.1: List of analyzed three-dimensional cases using liquid n-decane at 450 K and gaseous oxygen at 550 K and their relevant fluid properties. The subscripts G and L refer to the values obtained using freestream conditions for the gas and the liquid phases, respectively.

Case	p (bar)	u_G (m/s)	ρ_G (kg/m^3)	ρ_L (kg/m^3)	μ_G (μPa·s)	μ_L (μPa·s)	σ (mN/m)
A1	50	50	34.47	615.18	32.77	228.01	7.10
A2	50	70	34.47	615.18	32.77	228.01	7.10
B1	100	50	67.86	632.59	33.32	265.14	5.00
B2	100	70	67.86	632.59	33.32	265.14	5.00
C1	150	30	100.14	646.67	34.02	302.43	3.40
C2	150	50	100.14	646.67	34.02	302.43	3.40
C3	150	70	100.14	646.67	34.02	302.43	3.40

Table 6.2: List of analyzed three-dimensional cases using liquid n-decane at 450 K and gaseous oxygen at 550 K and their characteristic Reynolds and Weber numbers. The subscripts G and L refer to the values obtained using freestream conditions for the gas and the liquid phases, respectively.

Case	Re_L	Re_G	We_G
A1	2698	1052	243
A2	3777	1473	476
B1	2387	2037	679
B2	3342	2852	1330
C1	1285	1766	530
C2	2141	2943	1473
C3	2998	4121	2886

Table 6.1 summarizes the studied cases by indicating the thermodynamic pressure, the gas-phase freestream velocity, u_G, and other relevant freestream parameters of each fluid (i.e.,

ρ_G, ρ_L, μ_G and μ_L). Furthermore, a representative value of the surface-tension coefficient based on the surface-averaged value at the early simulation times before significant interface deformation is provided. The thermodynamic pressure and the gas-phase freestream velocity change between cases. Because of numerical stability constraints imposed by the FFT pressure, all investigated pressures are supercritical for the pure hydrocarbon. The density ratio ρ_G/ρ_L becomes too large for the pressure solver to handle efficiently at subcritical pressures (e.g., $\rho_G/\rho_L = 86$ at 10 bar). A significant reduction in the time step postpones the development of numerical instabilities, but it becomes an unrealistic alternative as it increases the computational cost and defeats the purpose of the fast FFT pressure solver. This issue was described in Section 4.3, and it should be addressed in future studies to allow for simulation of lower pressures and better comparisons of subcritical and transcritical atomization. At this point, two incompressible configurations (A2i and C1i) have been considered in which phase change is ignored and thermal mixing and species mixing are not taken into account. As a result, the effects of mixing on the atomization process at high pressures may be evaluated. These incompressible simulations follow the approach used in the works by Jarrahbashi and Sirignano [24], Jarrahbashi et al. [25] and Zandian et al. [26–28, 35, 36] to analyze incompressible two-phase flows but using the Volume-of-Fluid method to capture the interface instead of the Level-Set method.

A hyperbolic tangent function is used to initialize the velocity field, which distributes the streamwise velocity from 0 m/s in the liquid phase to u_G within a 6 μm region around the interface. With 90 computational cells, the shear layer thickness is well resolved. The distribution follows that presented in Section 5.1 with $u(y) = (u_G/2)\big(\tanh\big[6.5 \times 10^5 (y - H')\big] + 1\big)$, where $u_G = 30$ m/s is the gas freestream velocity, $H' = 10$ μm is the jet half-thickness and y is the coordinate transverse to the jet center plane. In order to obtain a velocity in meters per second, H' and y must be in units of meters. The other velocity components are set to zero or $v = w = 0$ m/s. The domain size and initial velocity distribution for various u_G values are shown in Figure 6.1. Note that in the pages that follow, the graphical domain for

the results might be extended using the periodic boundary conditions to visualize certain liquid structures and features better.

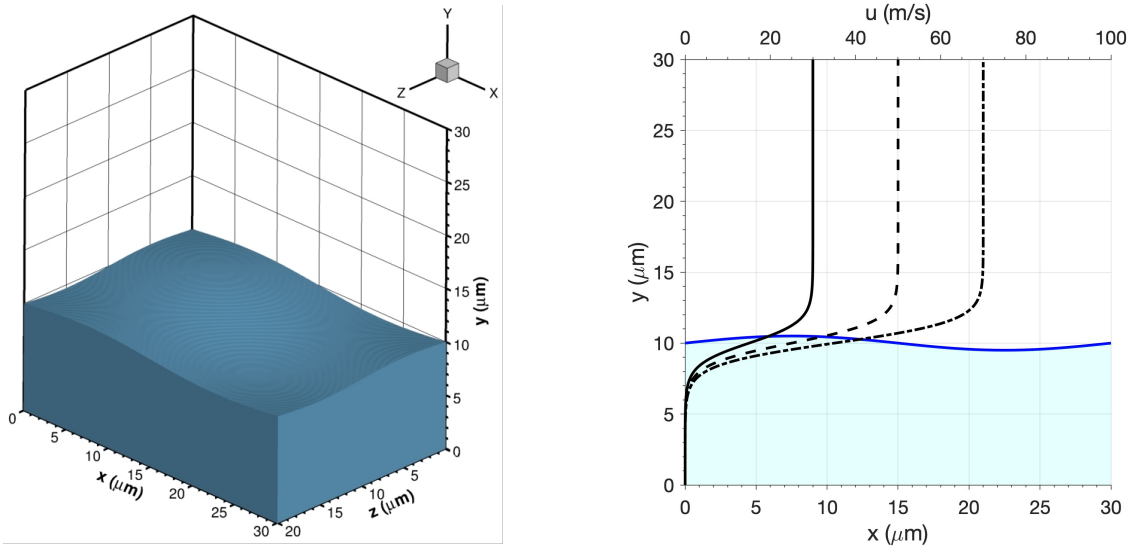

(a) (b)

Figure 6.1: Three-dimensional problem configuration. (a) size of the numerical domain and initial shape of the perturbed interface; (b) side view in the $x-y$ plane showing the interface initial perturbation in the streamwise direction and the velocity profiles imposed for each gas freestream velocity, u_G [140].

Each case can be defined in terms of a liquid Reynolds number, Re_L, and a gas Weber number, We_G, using the fluid properties shown in Table 6.1, similar to how Zandian et al. [26–28] address the classification of various incompressible jets. The density ratio ρ_G/ρ_L between both fluids is integrated into the characterization using the gas Weber number. The Reynolds number $Re_L = \rho_L u_G H/\mu_L$ is a measure of how important inertia forces are in comparison to viscous forces, whereas the Weber number is defined as $We_G = \rho_G u_G^2 H/\sigma$ and is the ratio of inertia forces to the surface-tension force. The thickness of the jet is represented by H in both equations. Table 6.2 presents Re_L, Re_G and We_G for the analyzed configurations and highlights the mild Reynolds number in both phases, which justifies the study of the early liquid injection problem without the need of implementing turbulence models. However, the classification of real jets at high pressures presents various issues

related to the strong variation of fluid properties within each phase and along the liquid-gas interface. These issues are discussed in Section 6.2.

Indeed, the chosen domain setup has some limits, as discussed in Section 5.1. Analyzing a perturbed interface with only one wavelength per direction and periodic boundary conditions may prevent longer wavelengths from appearing naturally. This issue does not appear to be significant at first glance, as all of the scenarios from Table 6.1 demonstrate a clear cascade deformation process with the appearance of smaller perturbations and the generation of smaller liquid structures. In addition, the symmetric boundary in the jet's centerline prevents antisymmetric modes from forming, which can be essential in some scenarios [27]. Despite this possibility, testing non-symmetric configurations revealed no significant growth of antisymmetric modes over the time investigated in this study. Furthermore, the gas-phase top boundary is located relatively near the initial liquid surface. As the liquid surface spreads in the transverse direction (i.e., along the y axis), the open boundary may affect the results once liquid structures and regions of perturbed flow get close. This problem restricts the maximum physical time for each examined scenario. Other constraints are related to the numerical technique and the thermodynamic two-phase modeling at high pressures, as addressed in Chapter 3 and Chapter 4.

6.2 Classification of Real Liquid Jets

The classification of the cases shown in Table 6.2 based on the gas Weber number and the liquid Reynolds number using freestream conditions is based on the approach proposed by Zandian et al. [26–28]. Figure 6.2 shows the studied scenarios in a gas Weber vs. liquid Reynolds diagram, which also shows the three atomization sub-domains identified by Zandian et al. [26] (i.e., LoLiD, LoHBrLiD and LoCLiD sub-domains described in Section 2.1). Despite using a realistic injection configuration under a high-pressure environment (e.g., jet

size, relative injection velocity), all examples have a relatively low gas Weber number. The surface-tension coefficient is already small due to the high-pressure environment, and all thermophysical properties are obtained from a detailed thermodynamic model. Meanwhile, Zandian et al. [26–28] work in the incompressible limit without mass exchange or mixing and parameterize the problem. Only the liquid density, domain size, and gas freestream velocity are realistically set, while all other fluid parameters are determined by fixing Re_L, We_G, density ratio, and viscosity ratio allowing for a wide range of Weber and Reynolds numbers to be covered.

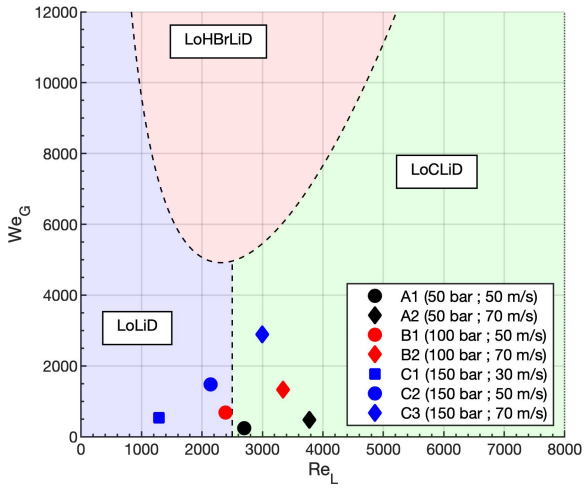

Figure 6.2: Classification on a We_G vs. Re_L diagram using freestream properties of the configurations presented in Tables 6.1 and 6.2. The dashed curves separate the atomization sub-domains identified in the incompressible work by Zandian et al. [26]. The Lobe-Ligament-Droplet (LoLiD) sub-domain is shaded in blue, the Lobe-Corrugation-Ligament-Droplet (LoCLiD) sub-domain is shaded in green and the Lobe-Hole-Bridge-Ligament-Droplet (LoHBrLiD) sub-domain is shaded in red [140].

It would be relevant to explore high-pressure examples that fall into the three atomization sub-domains for comparison purposes. According to Zandian et al. [26], the proposed scenarios only cover the LoLiD and LoCLiD sub-domains, while higher gas Weber numbers are required to cover the LoHBrLiD sub-domain. To reach the LoHBrLiD region, however, various changes would be required, such as changing the working species, increasing the initial temperatures (i.e., reducing σ by having a higher interface temperature, which relates to

more similar liquid and gas phases under phase equilibrium), or changing the jet size or gas freestream velocity. If the focus of the work remains on the injection of liquid hydrocarbon fuels into oxygen or air, a change in the mixture species might have a negligible influence on We_G. Replacing n-decane with n-dodecane and oxygen with nitrogen, for example, may not make a significant impact. Increased fluid temperatures may also lead the interface to fall into a high-temperature domain closer to or above the mixture critical temperature, contradicting the two-phase assumption. As a result, increasing the jet size or the gas freestream velocity appears to be the only option.

With all other variables held constant, an increase in the gas freestream velocity from 70 m/s to roughly 120 m/s is required to at least quadruple the gas-phase Weber number to $We_G \approx 8650$, which is above the bottom boundary of the LoHBrLiD sub-domain defined around $We_G \approx 4900$. Nonetheless, such a case would modify the liquid-phase Reynolds number to $Re_L \approx 5150$, and the new case would fall under the LoCLiD sub-domain. Such high velocities, while not implausible, could also violate the low-Mach-number assumption and be numerically troublesome, as the spurious currents generated by the numerical model would be significantly greater and could impact the interface temporal development. Its value must triple to get a similar gain in We_G varying the jet thickness. However, because both We_G and Re_L develop linearly with H, the new example would again not fall within the LoHBrLiD zone. Furthermore, there is a case to be made for using the perturbation wavelength as the characteristic length rather than the jet thickness. Despite this, the scenarios reported in Zandian et al. [26–28] use a wavelength-to-thickness ratio similar to that used in the current study. Therefore, a change in characteristic length does not explain why the real configurations are so far from the LoHBrLiD sub-domain.

Even though the investigated scenarios are far from the LoHBrLiD sub-domain described by the incompressible theory, holes and bridges are formed under certain circumstances, as illustrated in Section 6.3. As σ decreases and the Weber number rises due to higher ambient

pressure or a higher velocity, the hole formation mechanism occurs more frequently. The creation of holes can be associated with two distinct deformation mechanisms: liquid perforation caused by the surrounding gas phase and liquid sheet tearing caused by continuous stretching and thinning of the liquid sheets.

The enhanced mixing in both phases, as well as the variations in fluid properties throughout the interface and across mixing zones, are important features of high-pressure liquid injection as discussed in this dissertation (e.g., see Sections 2.3, 2.4, 2.5 and Chapter 5). The inertial effects may be underestimated since these features are not included in the definitions of Weber and Reynolds numbers based on freestream properties. As pressure rises, local thermodynamic phase equilibrium increases oxygen dissolution into the liquid phase. The reader is referred to Figure 3.1a, which depicts phase-equilibrium diagrams for the binary mixture of n-decane and oxygen at various pressures (e.g., 50, 100, and 150 bar). The mixture temperature obtained in this study is bounded between the bulk temperatures of each phase from 450 K to 550 K. The phase-equilibrium diagrams for supercritical pressures for n-decane (i.e., above 21 bar) show that as the interface temperature rises, liquid and gas become more alike. When equilibrium compositions become increasingly similar, liquid density falls, and gas density rises significantly, lowering the surface-tension coefficient. Consequently, the surface-tension coefficient in hotter interface locations may be significantly different from colder parts, as illustrated in Figure 6.3, which shows the interface local temperature and surface-tension coefficient for case C1 at 5 μs. More details about the interface thermodynamic behavior have been discussed in Section 5.3 for the two-dimensional jet, such as how composition and density change with temperature on both sides of the liquid-gas interface. This behavior is no different in three-dimensional computations.

Similar to Section 5.2, Figure 6.4 shows the variation of fluid properties across mixing regions for case C1 at 5 μs as well. A slice across the three-dimensional domain is illustrated here for an xy plane at $z = 15$ μm. Several characteristics are observed. The evaporation

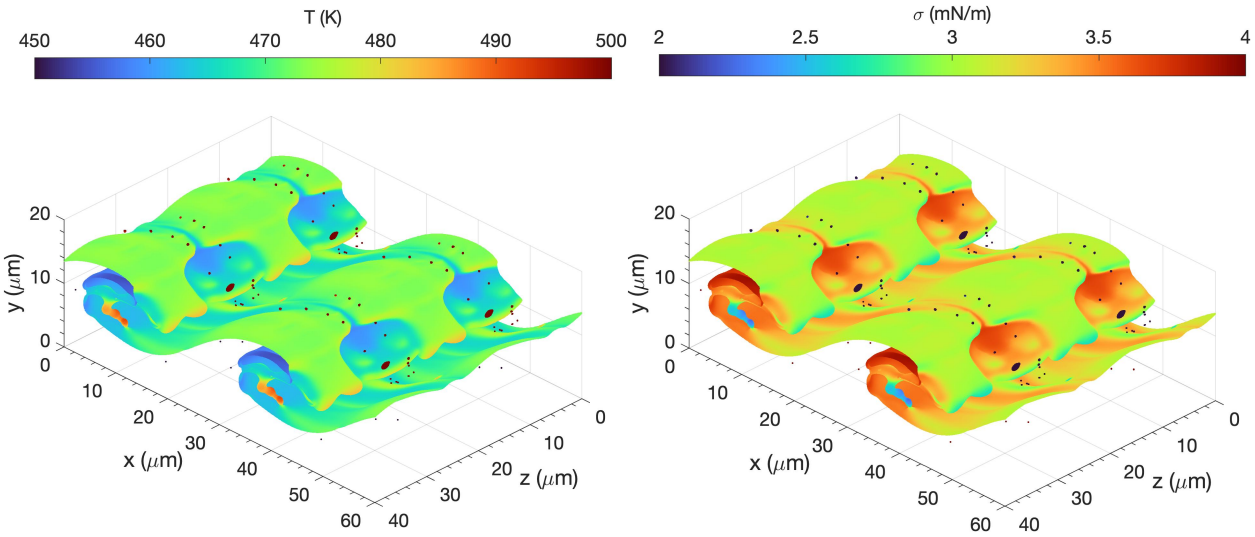

Figure 6.3: Interface equilibrium temperature and surface-tension coefficient for case C1 at $t = 5$ μs with a thermodynamic pressure of 150 bar and a gas freestream velocity of $u_G = 30$ m/s. Small droplets are seen flowing above the main surface with a larger temperature and lower surface-tension coefficient than each respective color scale. (a) interface temperature; (b) surface-tension coefficient [140].

of n-decane, combined with a significant fall in gas temperature, generates a 40 percent increase in gas density from 100.14 kg/m^3 in the freestream to roughly 140 kg/m^3 near the interface. Simultaneously, the gas viscosity decreases slightly because the increase in density cannot compensate for the sudden decrease in temperature. That is, higher densities and hotter fluids relate to higher fluid viscosity. On the other hand, oxygen dissolves in the liquid phase, which also heats near the interface. As a result, the liquid density is reduced significantly near the interface, from 646.67 kg/m^3 in the freestream to around 550 kg/m^3 near the surface. Although the reduction is approximately 15%, the absolute change is more than twice that of the gas-phase density variation. More critically, the liquid viscosity decreases by approximately an order of magnitude, resulting in regions of the liquid phase with fluid properties more closely matching those of a gaseous fluid. Furthermore, the size of a liquid structure (e.g., a droplet, a ligament, or a lobe) affects how quickly the liquid phase heats. In such a case, small or thin liquid structures submerged in a hotter gas have greater interface temperatures, stronger mixing effects, and a lower surface-tension coefficient.

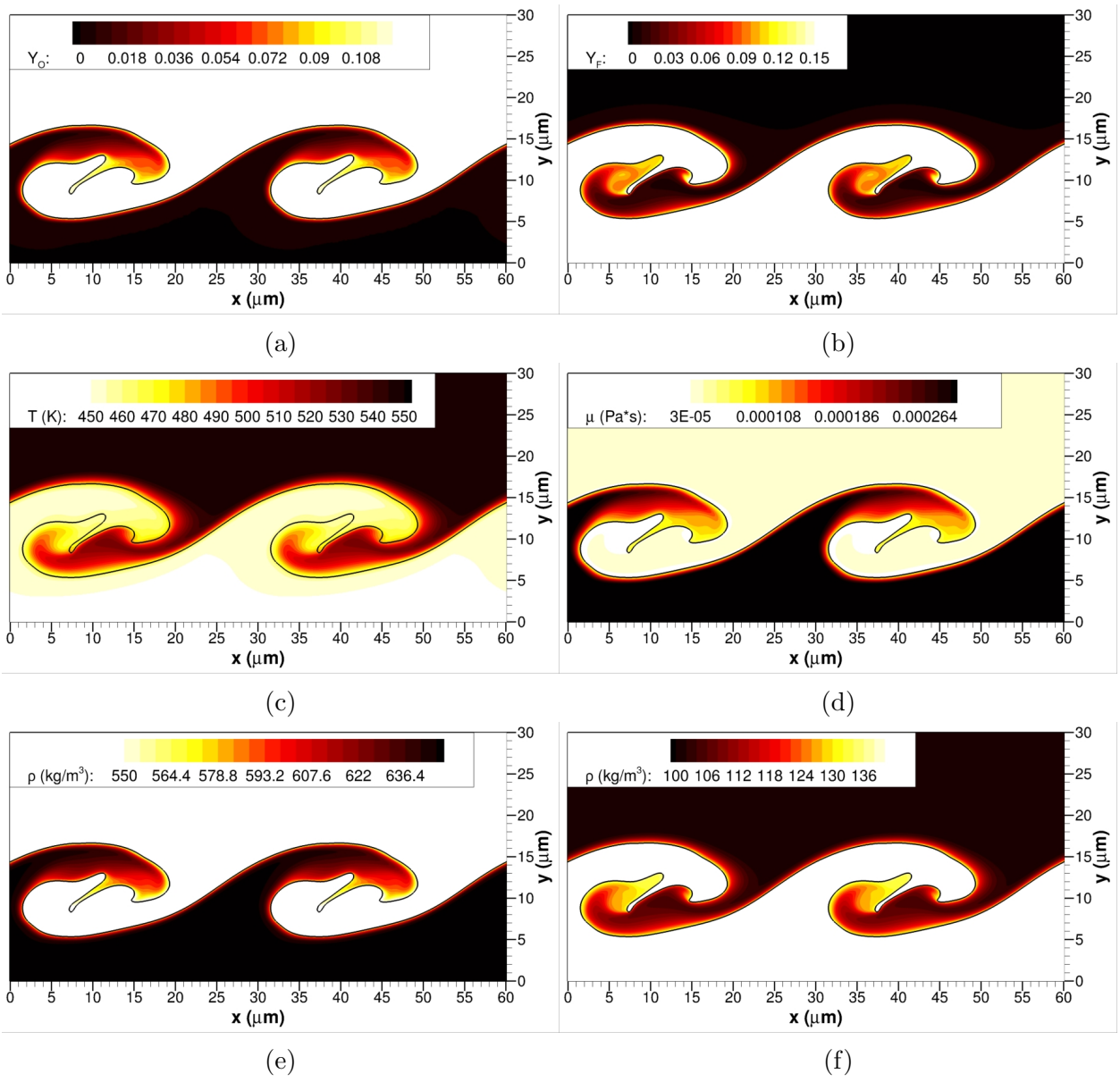

Figure 6.4: Slice across the three-dimensional domain (xy plane with $z = 15$ μm) showing the variations of mixture composition, temperature, viscosity and density across the mixing region for case C1 at $t = 5$ μs with a thermodynamic pressure of 150 bar and a gas freestream velocity of $u_G = 30$ m/s. (a) oxidizer or oxygen mass fraction in the liquid phase; (b) fuel or n-decane mass fraction in the gas phase; (c) temperature; (d) viscosity of the two-phase mixture; (e) liquid density; (f) gas density [140].

These observations provide useful information. At 150 bar, the effects of mass and thermal mixing are more intense than at lower pressures and influence how the liquid deforms locally. That is, distinct liquid regions may behave differently based on local velocity and length

scales and the local interface equilibrium state and fluid properties. Furthermore, because mixing occurs continuously throughout time, the liquid phase may exhibit very different behaviors at the beginning of the simulation (i.e., beginning of the intraphase mixing process) compared to later. The volume-averaged liquid density and viscosity for the examined configurations are shown in Figure 6.5. The average liquid properties change significantly over time, especially at very high pressures of 100 bar and above.

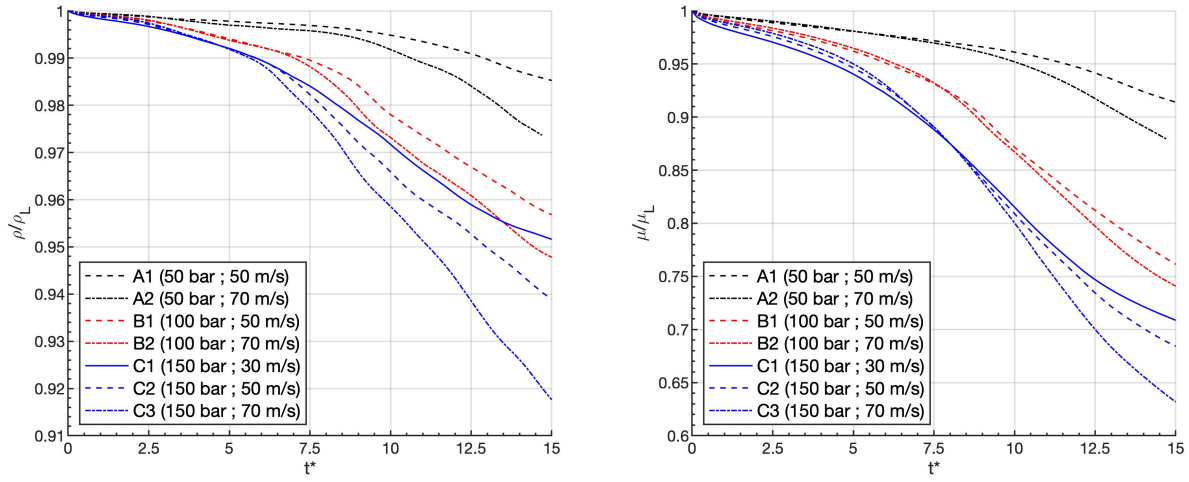

(a) (b)

Figure 6.5: Average liquid-phase density and viscosity over the liquid volume normalized by the freestream properties, ρ_L and μ_L, presented in Table 6.1. The non-dimensional time is obtained as $t^* = t/t_c = t\frac{u_G}{H}$. (a) average liquid-phase density; and (b) average liquid-phase viscosity [140].

Considering this fluid behavior, it is evident that utilizing freestream parameters to characterize each configuration may be misleading, especially as pressure increases and intraphase mixing effects dominate. Determining an effective Weber and Reynolds number is equally difficult. As previously stated, distinct fluid regions will have distinct fluid properties and will behave significantly differently. However, depending on the lower and upper thermophysical boundaries, a region in the We_g vs. Re_l diagram may be determined where the effective parameters may be situated (see Figure 6.6).

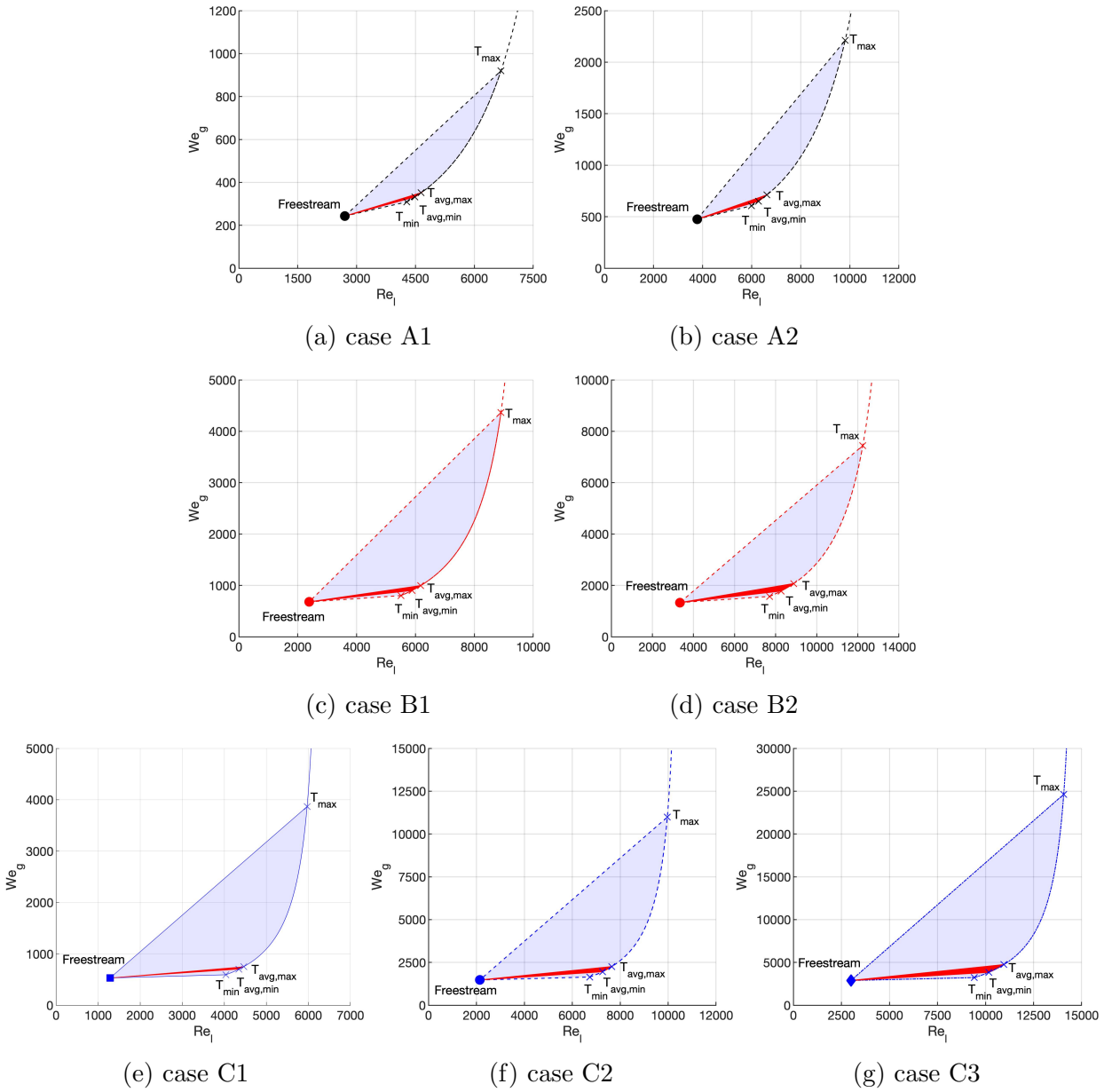

(a) case A1 (b) case A2

(c) case B1 (d) case B2

(e) case C1 (f) case C2 (g) case C3

Figure 6.6: Effects of thermal and species mixing on the classification of each case in a We_g vs. Re_l diagram. The effective We_g and Re_l describing each configuration are located somewhere in the shaded area, with a higher probability to be inside the region defined by the freestream condition and the minimum and maximum interface average temperatures (i.e., region shaded in red). The values of We_g and Re_l may change over time as both phases undergo mixing. (a) case A1; (b) case A2; (c) case B1; (d) case B2; (e) case C1; (f) case C2; and (g) case C3 [140].

The earlier definition based on the freestream fluid properties and an average value of the surface-tension coefficient, We_G and Re_L, is used to establish a lower boundary for the

effective We_g and Re_l. The characteristic length and velocity are still represented in this assessment by the jet thickness, H, and the gas freestream velocity, u_G. That is, the focus remains on a global characterization of the whole jet while taking into account changes in fluid properties. The local length scale (e.g., the radius of curvature or lobe thickness) and the local velocity affect the fluid locally.

The various possible interface equilibrium states, on the other hand, define the upper boundary for We_g and Re_l. As a function of the interface temperature, thermodynamic phase equilibrium provides the fluid properties of each phase, the composition, and the surface-tension coefficient. These interface fluid properties may be used to estimate this upper limit for We_g and Re_l, resulting in a curve represented by a locus of points that advances toward higher values of We_g and Re_l as the interface temperature increases (see any of the curves in Figure 6.6). That is, as the temperature rises and more oxygen dissolves into the liquid phase, the liquid viscosity falls faster than the liquid density, increasing Re_l. Meanwhile, an increase in the interface temperature results in a significant drop in the surface-tension coefficient as both phases look more alike, causing a sharp increase in We_g.

The effective We_g and Re_l numbers characterizing the cases specified in Table 6.2 are located somewhere inside the two shaded zones illustrated in each sub-figure from Figure 6.6. The first region shaded in red represents the most likely location of the effective We_g and Re_l. The freestream condition and the interface solution between the minimum average interface temperature, $T_{\text{avg,min}}$, and the maximum average interface temperature, $T_{\text{avg,max}}$, measured during the calculations are used to describe it. The second region shaded in blue shows a considerably less likely area where the effective global We_g and Re_l may be located, though it might represent the jet's local behavior. The freestream condition, the absolute minimum interface temperature observed throughout the simulation, T_{min}, and the absolute maximum interface temperature observed during the simulation, T_{max}, define this region.

The freestream condition better represents the jet classification early in the simulation. Each freestream condition also represents the two incompressible configurations, A2i and C1i. The effective We_g and Re_l increase with mixing, which is more noticeable at higher pressures, as seen in Figure 6.6. For example, the 150-bar case with $u_G = 50$ m/s (i.e., case C2) at average interface conditions might show We_g and Re_l 53 percent and 257 percent greater, respectively, than at the freestream condition. Both parameters could increase by up to 44 percent and 70 percent at lower pressures, such as in the 50-bar case and $u_G = 50$ m/s (i.e., case A1). Although hole formation is evident, the jet's categorization remains in the LoCLiD atomization sub-domain even when considering an effective gas-phase Weber number and an effective liquid-phase Reynolds number.

6.3 Early-Deformation Mechanisms

This section explains and categorizes some observed deformation patterns during the computations. Some similarities can be observed across the configurations presented in Table 6.1, but the main differences induced by the rising pressure are highlighted. That is, similarities are observed for situations with similar We_G and Re_L based on freestream conditions, but variations of each feature are caused by the high-pressure mixing effects that influence the effective We_g and Re_l, as stated in Section 6.2. From Subsection 6.3.1 to Subsection 6.3.4, the following features are identified: (a) lobe extension, bending, and perforation; (b) lobe and crest corrugation; (c) ligament stretching and shredding; and (d) liquid sheet folding and layering followed by liquid sheet tearing. Table 6.3 contains a summary identifying which feature appears in each studied case. In addition, the numerous deformation mechanisms are identified in Figure 6.7, which locates the deformation features in a We_G vs. Re_L diagram. For the sake of brevity, we offer the figures that are required to support our statements. The reader is directed to the Supplemental Material, where slides depicting the jet deformation

for each scenario are presented. In order to effectively compare cases, a non-dimensional time, $t^* = t/tc$, has been defined. The characteristic time is defined as $t_c = H/u_G$ based on the jet thickness as characteristic length and the gas freestream velocity as characteristic velocity. To provide some context, the quick interface deformation observed at high pressures coupled to a small computational domain limits the physical times analyzed in this work to be below 10 μs.

Table 6.3: Classification of the deformation features discussed in this section.

	A1	A2	B1	B2	C1	C2	C3	A2i	C1i
Lobe extension (a)	No	Yes	Yes	No	Yes	No	No	Yes	Yes
Lobe bending (a)	No	Yes	Yes	No	Yes	No	No	No	No
Lobe perforation (a)	No	No	Yes	No	Yes	No	No	No	No
Lobe corrugation (b)	No	No	No	Yes	No	Yes	Yes	No	No
Crest corrugation (b)	No	No	Yes	Yes	No	Yes	Yes	No	No
Ligament stretching (c)	Yes	Yes	Yes	Yes	Yes	Yes	Yes	Yes	Yes
Ligament shredding (c)	No	No	No	Yes	No	Yes	Yes	No	No
Layering and liquid sheet tearing (d)	No	No	Yes	Yes	Yes	Yes	Yes	No	Yes

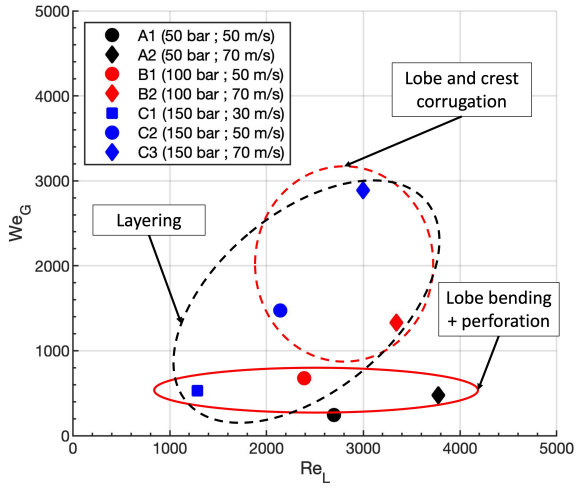

Figure 6.7: Visual classification of the identified early deformation mechanisms and the analyzed configurations in a We_G vs. Re_L diagram. The red solid curve identifies the lobe bending and perforation mechanism, the red dashed curve identifies the lobe and crest corrugation mechanism and the black dashed curve identifies the layering mechanism [140].

6.3.1 Lobe extension, bending and perforation

The initial shear layer and sinusoidal surface distribution define the formation of a lobe in the faster liquid region, which subsequently evolves in distinct ways depending on the physical parameters of each configuration. For cases A2, B1, and C1, the initial lobe stretches into the gas phase as its tip bends upward. That is, it rotates clockwise in the side view provided in Figure 6.8 following the positive z direction. Each configuration has a similar We_G between 476 and 679, but a very different Re_L between 1285 and 3777. Moreover, high-pressure features define how the lobe deformation process unfolds. For instance, the greater surface-tension force in case A1 with $We_G = 243$ is responsible for the reconnection of the initial lobe with the liquid core. On the other hand, cases B2, C2, and C3 with $We_G > 1000$ reveal a different lobe deformation mechanism, as described in Subsection 6.3.2.

Figure 6.8 shows the sequence of the deformation process, which includes lobe extension, bending, and perforation, for the case at 150 bar with $u_G = 30$ m/s (i.e., case C1). Intraphase mixing reduces the local liquid density and viscosity as the lobe stretches and thins (see Figure 6.9). As a result, the vortical motion of the denser gas in front of the lobe can bend the lobe's tip upward. Bending is a precursor of lobe perforation or hole formation. The liquid structure is perforated as the thin lobe faces the incoming gas stream with a steeper angle. The perforation process is also aided by surface-tension pinching along the edge of the lobe, which contributes to further thinning. Then, the hole expands quickly, and a bridge forms, connecting the sides of the lobe. In the process, some small droplets form, which quickly vaporize. Despite hole formation being mesh dependent in VOF methods (i.e., when the liquid structure size drops below the mesh size), the physics support the hole formation process, and mesh resolution may have little impact on the precise time when the perforation event occurs. The reader is referred to Subsection 7.2.1 where the developments discussed here are analyzed using vortex dynamics.

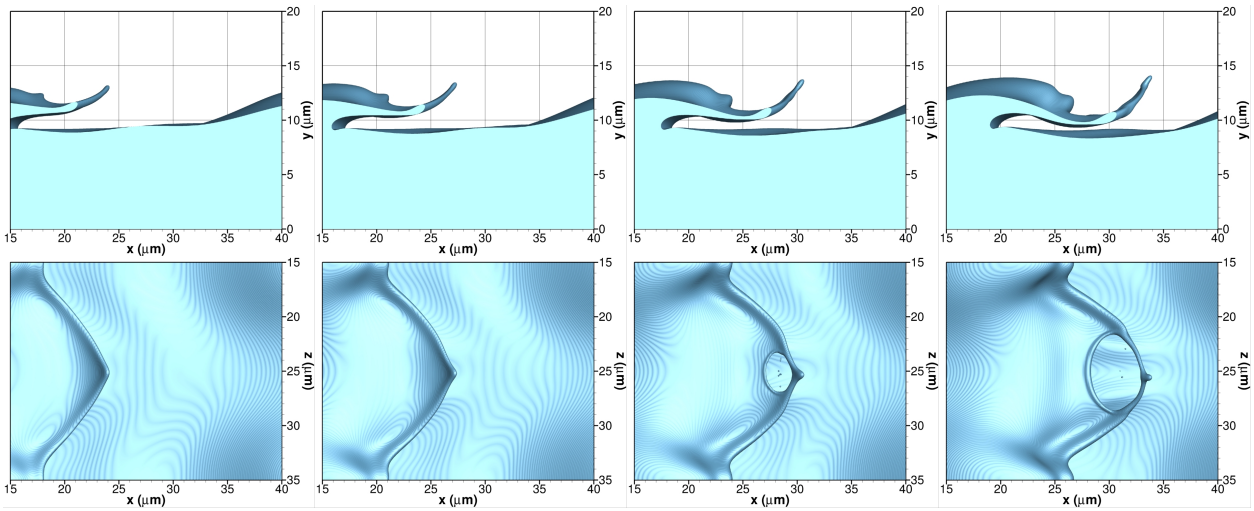

(a) $t^* = 3.75$ (b) $t^* = 4.05$ (c) $t^* = 4.35$ (d) $t^* = 4.65$

Figure 6.8: Lobe extension, bending and perforation at 150 bar with gas freestream velocity of $u_G = 30$ m/s (i.e., case C1). The top figures show the side view from an xy plane located at $z = 40$ μm and the bottom figures show the top view from an xz plane located above the liquid surface. The interface location is identified as the isosurface with $C = 0.5$. A non-dimensional time is obtained as $t^* = t/t_c = t\frac{u_G}{H}$. (a) $t^* = 3.75$; (b) $t^* = 4.05$; (c) $t^* = 4.35$; and (d) $t^* = 4.65$ [140].

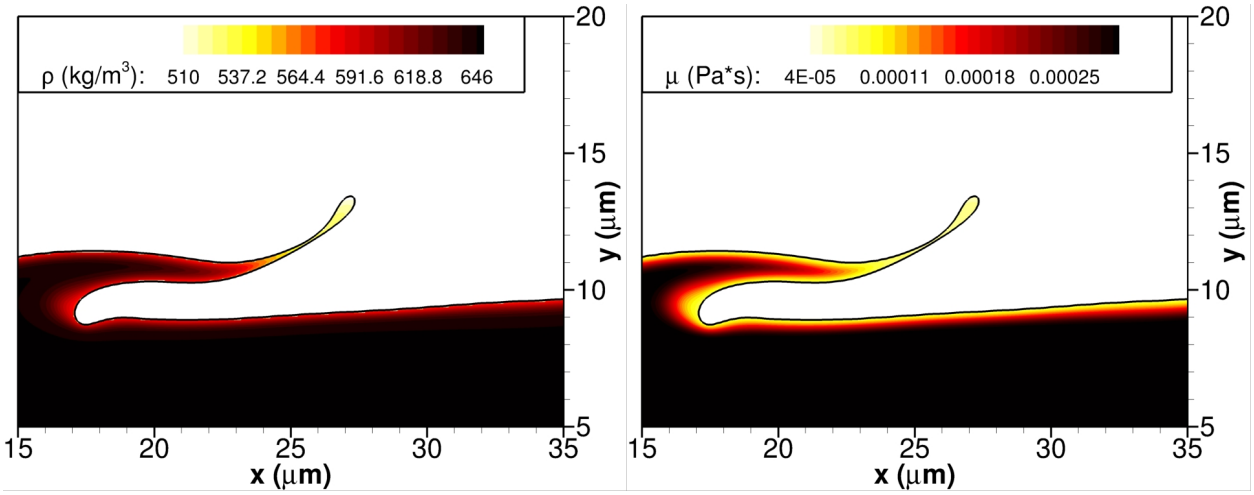

(a) (b)

Figure 6.9: Lobe extension, bending and perforation at 150 bar with gas freestream velocity of $u_G = 30$ m/s (i.e., case C1) at the non-dimensional time $t^* = t/t_c = t\frac{u_G}{H} = 4.05$. A slice through the three-dimensional domain is obtained from an xy plane located at $z = 25$ μm. The interface location is identified as the isosurface with $C = 0.5$. (a) liquid density; and (b) viscosity of the two-phase mixture [140].

The emergence of the deformation mechanism described in this section is directly related to a range of gas-phase Weber numbers. The different fluid behavior induced by the pressure rise, also reflected in the liquid-phase Reynolds number, produces different deformation processes, as shown in Figure 6.10. The larger surface-tension coefficient at lower pressures is reflected in the lobe thickness and the radius of curvature of the lobe's edge. Case A2 at 50 bar (see Figure 6.10a) shows a thicker lobe than cases B1 and C1 at 100 bar and 150 bar, respectively. The bending angle also increases noticeably. At 50 bar, the angle of the lobe with respect to the streamwise direction is about 10 degrees. Then, the bending angle increases to about 25 degrees at 100 bar and 45 degrees at 150 bar.

The described trends are a direct outcome of the changes in fluid behavior. As pressure increases, mixing in the liquid phase is enhanced, and fluid properties vary more strongly, making the liquid phase less dense and less viscous (i.e., with gas-like viscosities) near the interface. Furthermore, when pressure increases, the gas phase becomes more viscous and significantly denser, and the differences between the liquid and gas phases rapidly decrease. As a result, at 150 bar, the liquid phase is more easily altered by gas flow dynamics than at 50 bar. Furthermore, at low pressures, the examined cases have a greater Re_L than at high pressures, owing to the higher gas freestream velocities required to attain similar We_G. Overall, the greater Re_L translates into inertial terms dominating over viscous terms, which may aid the stretching of the lobe in the streamwise direction and limit bending to a certain extent.

The impact of intraphase mixing on lobe perforation is clear. For example, in cases B1 and C1 (i.e., 100 and 150 bar), a thin lobe forms and bends sufficiently toward the oxidizer stream to develop a hole around the same non-dimensional time $t^* \approx 4.3$. Case A2 at 50 bar, on the other hand, does not show hole formation on the lobe, and the lobe's tip stretches, forming a ligament as the mechanism described in Subsection 6.3.3. Figure 6.2 shows that all three examples are well below the LoHBrLiD atomization sub-domain reported by Zandian

et al. [26]; yet, hole formation occurs early in the computation in localized areas at very high pressures. The early development of holes at high pressures, followed by bridge thinning and breakup into ligaments and droplets, may contribute to further surface instabilities early in the liquid deformation process. As described in Section 6.4, the liquid surface is prone to the growth of short-wavelength perturbations at high pressures generated by impact or coalescence events and flow disturbances.

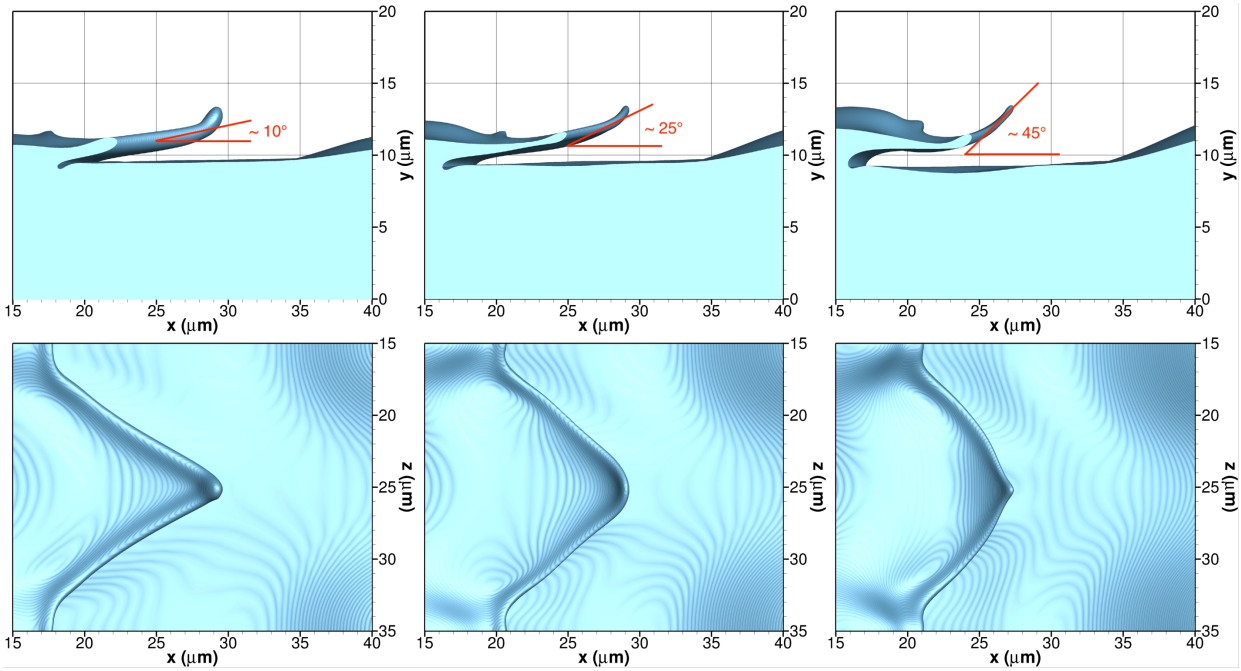

(a) case A2 at $t^* = 4.025$ (b) case B1 at $t^* = 4.00$ (c) case C1 at $t^* = 4.05$

Figure 6.10: Pressure effects on the early lobe extension comparing cases A2, B1 and C1 with similar We_G. The top figures show the side view from an xy plane located at $z = 40$ μm and the bottom figures show the top view from an xz plane located above the liquid surface. The interface location is identified as the isosurface with $C = 0.5$. A non-dimensional time is obtained as $t^* = t/t_c = t\frac{u_G}{H}$. (a) case A2 at $t^* = 4.025$; (b) case B1 at $t^* = 4.00$; and (c) case C1 at $t^* = 4.05$ [140].

Comparing examples A2 with A2i and C1 with C1i provides additional evidence of the influence of intraphase mixing and interface thermodynamics in the deformation process. Phase change is not considered in the incompressible limit, and the fluid properties of each phase remain constant and equal to the freestream conditions. The surface-tension coefficient in the incompressible simulations remains constant and equal to the values reported in Table 6.1,

which are obtained from an average of the surface-tension coefficient values observed along the interface in cases A2 and C1, respectively, at the beginning of the computations before substantial surface deformation occurs.

Because of the limited and reduced mixing process, examples A2 and A2i evolve somewhat similarly at first, with only minor differences noticed during the lobe stretching phase. The compressible scenario, for example, has a somewhat thinner lobe due to a greater interface temperature along the lobe's edge, lowering the local surface-tension coefficient below the average value used in the incompressible simulation. Cases C1 and C1i, on the other hand, show significant disparities. Lobe extension or stretching is reduced because the incompressible case has much higher density and viscosity than the compressible scenario. Furthermore, a larger surface-tension coefficient results in a thicker lobe. As a result, neither lobe bending nor hole creation occurs for an extended time throughout the computation, as shown in Figure 6.11, which is more consistent with the sub-domain classification for incompressible flows identified by Zandian et al. [26].

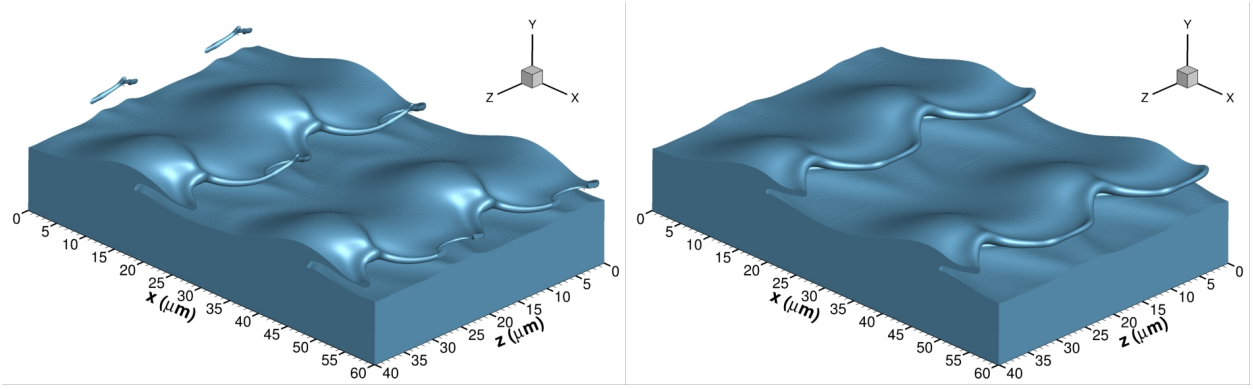

(a) (b)

Figure 6.11: Lobe extension, bending and perforation at 150 bar with gas freestream velocity of $u_G = 30$ m/s (i.e., case C1) at the non-dimensional time $t^* = t/t_c = t\frac{u_G}{H} = 4.5$. The interface location is identified as the isosurface with $C = 0.5$. (a) compressible case C1; and (b) incompressible case C1i [140].

6.3.2 Lobe and crest corrugation

A different lobe deformation mechanism is found in scenarios B2, C2, and C3. They all have a very high thermodynamic pressure of 100 bar or 150 bar, respectively, which results in a lower surface-tension coefficient than at 50 bar. The gas Weber number based on freestream conditions, We_G, is higher than 1000 in all three cases. There are no significant differences seen as Re_L and We_G vary for each specific configuration. The evolution of the lobe over time for case C2 is illustrated in Figure 6.12.

A thin lobe extends at first, like the lobe early extension described in Subsection 6.3.1. Instead of bending upward, the lobe corrugates around the streamwise direction, engulfing the gas mixture and eventually bursting into droplets, much like a bag breakup process. Ligaments form around the edge of the lobe after it bursts, which stretch into the oxidizer stream, while the remainder of the lobe flattens as the primary perturbation wave rises behind it. Mesh resolution in VOF methods determines breakup events to some extent, as acknowledged earlier in Subsection 6.3.1. If improved interface reconstruction methods were utilized, such as the two-plane reconstruction or the R2P approach [141–143], the bursting of the lobe could be delayed somewhat. Such resolution effect has been studied for bag-breakup events [143]. Nevertheless, the rate at which the lobe is corrugating and thinning undoubtedly points to a rapid bursting, as captured using the current interface reconstruction methodology (i.e., PLIC).

The crest of the rising perturbation corrugates, albeit the dynamical process causing this corrugation may be different from the one causing the lobe corrugation. This topic is examined in detail in Subsection 7.2.2, where an analysis involving vortex dynamics is used to explain the early deformation mechanisms seen in Case C2. As observed in Figure 6.12, as the perturbation crest identified along the x direction at $z = 15$ μm or $z = 35$ μm grows, a nose-shaped structure appears. As the corrugation happens, a ligament forms and is rapidly

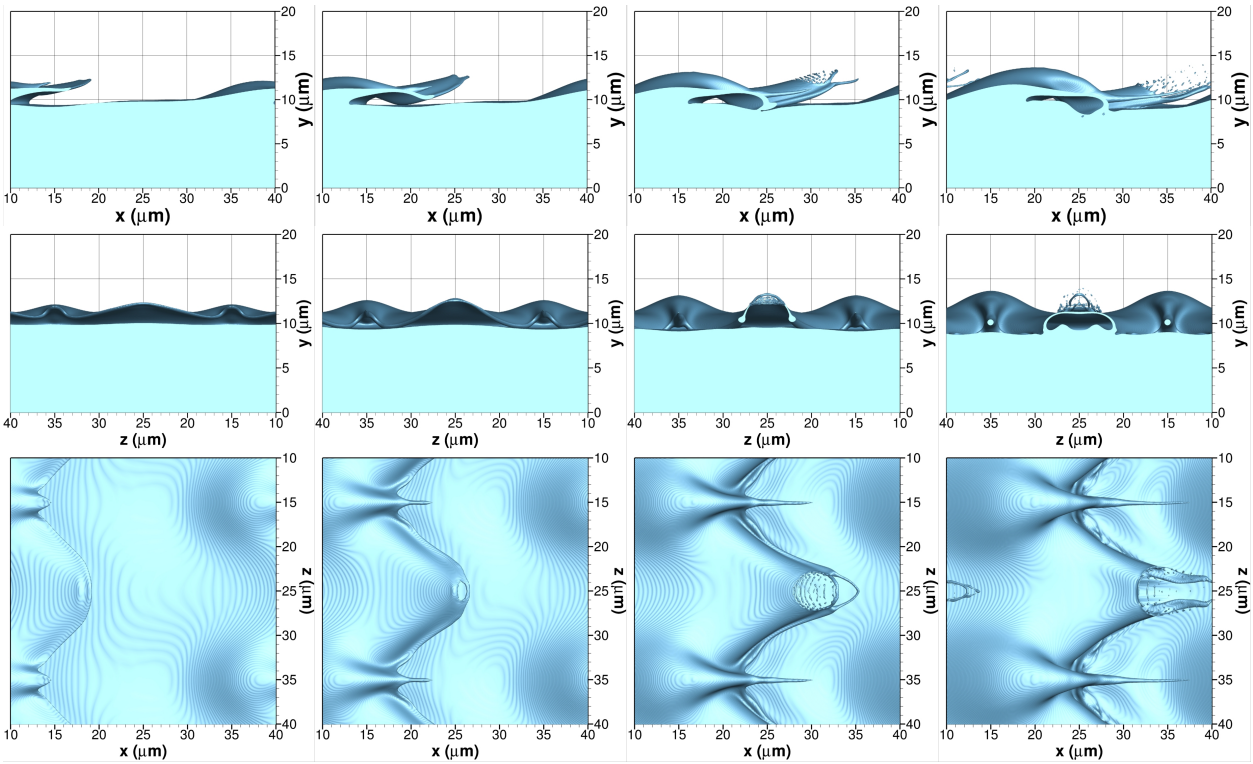

(a) $t^* = 3.0$ (b) $t^* = 3.5$ (c) $t^* = 4.0$ (d) $t^* = 4.5$

Figure 6.12: Lobe and crest corrugation at 150 bar with gas freestream velocity of $u_G = 50$ m/s (i.e., case C2). The thin lobe bursts, similar to a bag breakup. The top figures show the side view from an xy plane located at $z = 40$ μm, the middle figures show the side view from an yz plane located at $x = 30$ μm and the bottom figures show the top view from an xz plane located above the liquid surface. The interface location is identified as the isosurface with $C = 0.5$. A non-dimensional time is obtained as $t^* = t/t_c = t\frac{u_G}{H}$. (a) $t^* = 3.0$; (b) $t^* = 3.5$; (c) $t^* = 4.0$; and (d) $t^* = 4.5$ [140].

stretched into the oxidizer stream, similar to the ligaments that form following the lobe bursting described in this section or the bridge breakup in the hole formation process described in Subsection 6.3.1. Subsection 6.3.3 explains the physics behind the rapid stretching of ligaments at high pressures.

Crest corrugation is not an inherent mechanism of only high gas-phase Weber number configurations (i.e., $We_G > 1000$). It is also visible in case B1, and to a lesser extent, in cases A1, A2, and C1. Thus, this behavior may appear due to the initial shape of the liquid surface and the initial shear layer rather than any specific dynamical behavior of high-pressure flows.

Only the cases with a high gas-phase Weber number reveal the simultaneous stretching of a ligament when the corrugation occurs. Notably, as analyzed in Section 6.4, the corrugation of the liquid surface can cause surface instabilities in low surface-tension conditions. Furthermore, the burst of the lobe into droplets and the formation of thin ligaments seen in Figure 6.12 may be responsible for the formation of later surface instabilities.

6.3.3 Ligament stretching and shredding

It is not unusual that ligaments form and stretch into the oxidizing stream before breaking up into droplets or merging with the liquid. As demonstrated in Figure 6.2, all examined configurations fall inside the LoLiD, and LoCLiD atomization sub-domains identified by Zandian et al. [26], which have this deformation cascade as a distinguishing feature. Figure 6.13 highlights various precursor events prior to creating ligaments, such as crest corrugation, hole formation with bridge breakup, and lobe burst. Previous subsections identified the problem configurations under which these events occur.

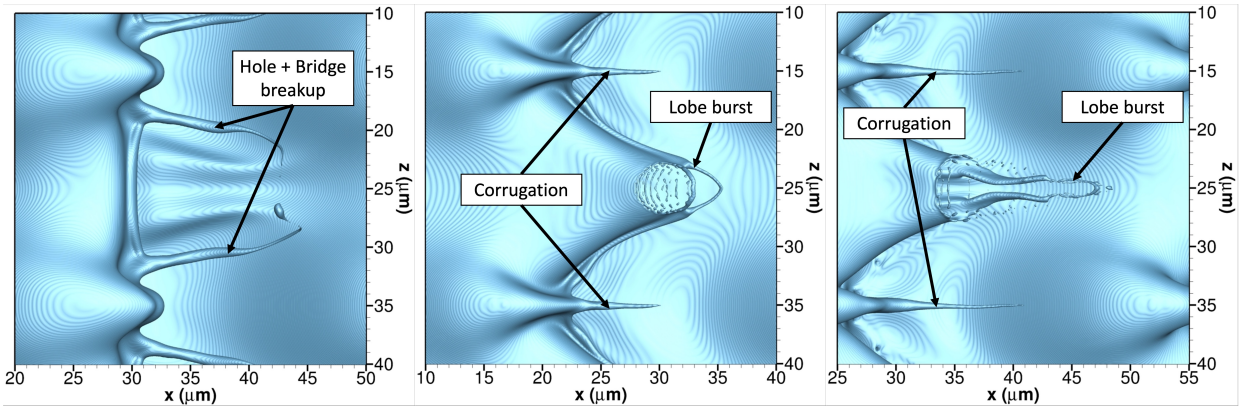

(a) case C1 at $t^* = 5.40$ (b) case C2 at $t^* = 4.00$ (c) case C2 at $t^* = 4.75$

Figure 6.13: Ligament formation and stretching from different precursor events: hole plus bridge breakup, crest corrugation and thin lobe burst. The top view is obtained from an xz plane located above the liquid surface. The interface location is identified as the isosurface with $C = 0.5$. A non-dimensional time is obtained as $t^* = t/t_c = t\frac{u_G}{H}$. (a) case C1 at $t^* = 5.40$; (b) case C2 at $t^* = 4.00$; and (c) case C2 at $t^* = 4.75$ [140].

Thin and elongated ligaments that easily stretch into the oxidizer stream are more likely to form at supercritical pressures. Smaller liquid structures develop faster, either from small protuberances on the liquid surface or at the edge of lobes (e.g., local corrugations), where the liquid-phase temperature and oxygen dissolution increase. As previously stated, the surface-tension coefficient decreases, the liquid density decreases, and the liquid viscosity approaches that of a gas. These heating and species mixing effects can also be seen in the ligaments that form due to the hole formation or the lobe bursting. These gas-like liquid regions are more easily impacted by the surrounding gas flow, similar to the lobe bending process described in Subsection 6.3.1. As a result, the local Reynolds number and Weber number rise. Therefore, any protuberance is quickly pulled away from the liquid surface when immersed in the moving gas phase, forming a rapidly stretching ligament. At 100 bar and 150 bar, this phenomenon occurs more frequently, especially at higher gas freestream velocities of 50 m/s and 70 m/s. When compared to the behavior of ligaments at moderate pressures, ligaments at high pressures can become exceedingly thin. Surface-tension forces are minimal, and capillary instabilities that encourage neck development and ligament rupture into droplets become significant only when ligaments reach very small scales. Many ligaments exhibit numerical breakup before capillary instabilities can occur. These ligaments stretch and vaporize, and eventually, their thickness falls below the mesh size.

As a result, ligament shredding is common in cases B2, C2, and C3. That is, thin ligaments are constantly formed, with some of them breaking up into a few droplets and others simply stretching and vaporizing. Section 6.5 provides a comprehensive analysis of ligament and droplet generation under real-engine conditions, as well as a discussion of the influence of mesh resolution. Figure 6.14 depicts the ligament shredding that occurs in case B2 at 100 bar with a gas freestream velocity of $u_G = 70$ m/s. As seen in Figure 6.14a, short-wavelength surface instabilities develop towards the peak of the wave, promoting ligament shredding near its edge. As discussed in Section 6.4, hotter interface locations, such as those near the wave

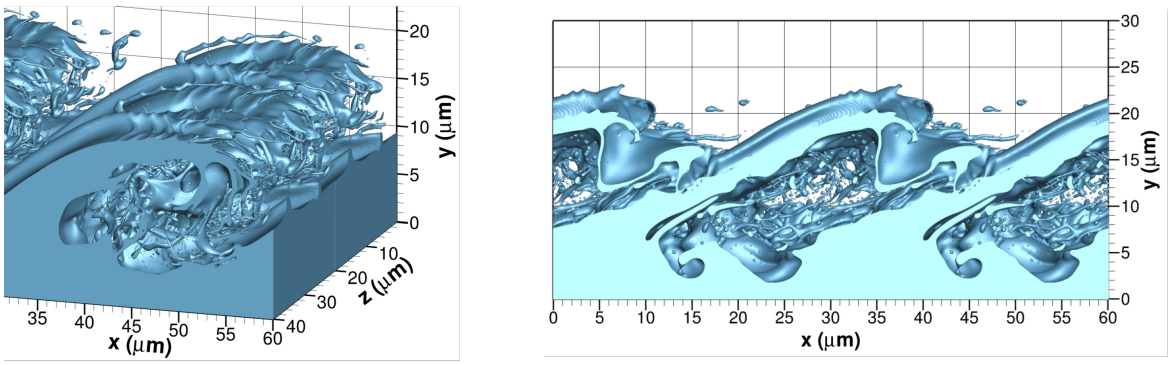

(a) $t^* = 9.625$ (b) $t^* = 11.55$

Figure 6.14: Ligament shredding at 100 bar with gas freestream velocity of $u_G = 70$ m/s (i.e., case B2). The side view in the right figure is obtained from an xy plane located at $z = 40$ μm. The interface location is identified as the isosurface with $C = 0.5$. A non-dimensional time is obtained as $t^* = t/t_c = t\frac{u_G}{H}$. (a) $t^* = 9.625$; and (b) $t^* = 11.55$ [140].

crest, may develop surface instabilities more easily as the local surface-tension coefficient and liquid viscosity fall. This surface behavior promotes mixing and the breakup of liquid structures, resulting in the liquid phase exhibiting fluid properties more comparable to gas properties sooner and a more chaotic deformation of the liquid jet. Furthermore, Figure 6.14b demonstrates how there is a predisposition to confine the shredded ligaments and droplets beneath the rising wave. The confinement of detached liquid structures is characterized by the development of liquid layers or sheets that eventually overlap each other. This mechanism is observed in all analyzed cases at 100 bar and 150 bar. Subsection 6.3.4 describes the layering process in detail.

6.3.4 Layering and liquid sheet tearing

The development of overlapping liquid layers is observed at pressures of 100 bar or above for the binary mixture considered in this work. These layers or liquid sheets can be more or less disrupted depending on the We_G and Re_L of each specific scenario, but they are regarded as a common feature with essential consequences in the atomization process.

Due to vortical motion, the perturbations growing in the high-pressure configurations can readily roll over themselves at first. Under the conditions studied in this work, wave crest rolling is less common at lower pressures (i.e., 50 bar). Later, the roller vortices that form weaken and, as shown in Figure 6.15, the liquid regions adjacent to the oxidizer stream begin to form liquid sheets that are easily stretched in the streamwise direction. Case C1 results are shown here because they have a negligible amount of shredding and droplet formation, allowing for a clear view of the layering process.

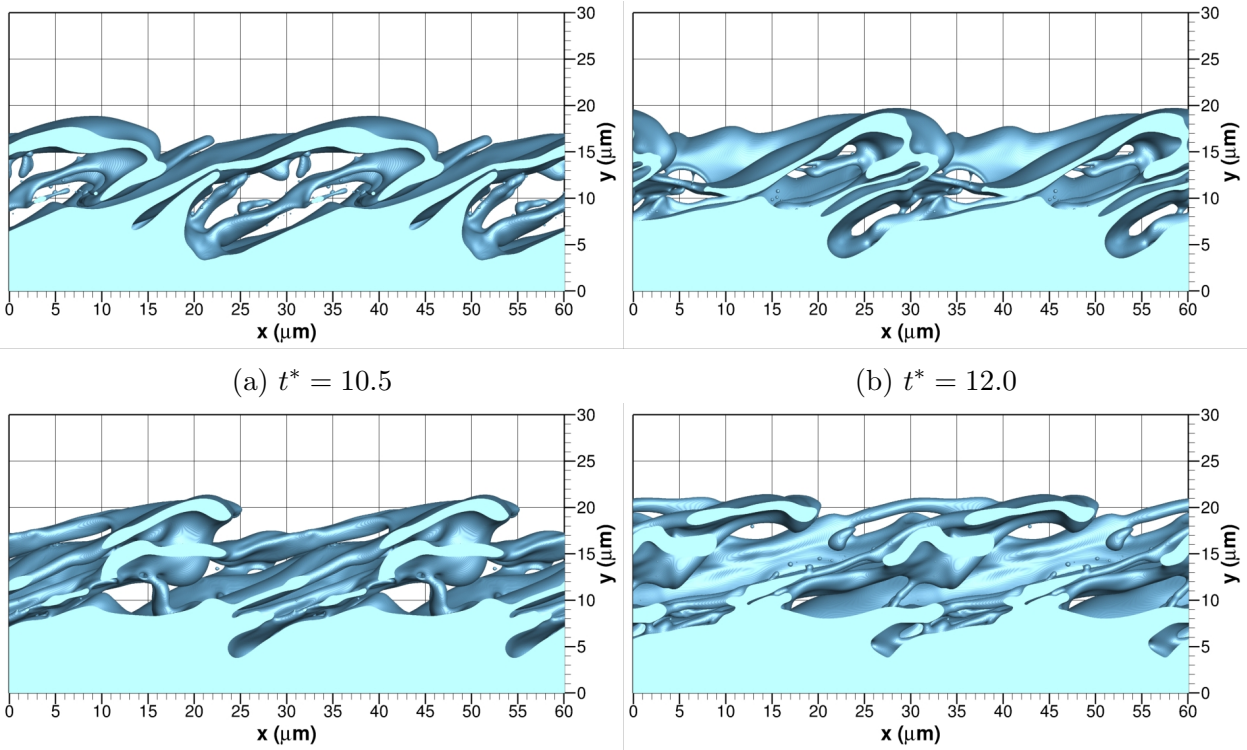

(a) $t^* = 10.5$ (b) $t^* = 12.0$

(c) $t^* = 13.5$ (d) $t^* = 15.0$

Figure 6.15: Layering or overlap of liquid sheets at 150 bar with gas freestream velocity of $u_G = 30$ m/s (i.e., case C1). The side view is obtained from an xy plane located at $z = 40$ μm. The interface location is identified as the isosurface with $C = 0.5$. A non-dimensional time is obtained as $t^* = t/t_c = t\frac{u_G}{h}$. (a) $t^* = 10.5$; (b) $t^* = 12.0$; (c) $t^* = 13.5$; and (d) $t^* = 15.0$ [140].

The layer generation or layering rate increases as the momentum mixing layer expands. When liquid regions encounter faster-moving gas streams, a liquid sheet forms quickly and flows over and past a previously created liquid sheet. Case C1, for example, depicts four

layers that overlapped at the end of the computation (see Figures 6.15 and 6.17). This cake-like overlapping of liquid sheets is referred to as "layering" in this work. However, this type of mixing mechanism is also referred to as "folding" in the literature. For instance, the experimental works by Buch and Dahm [144, 145] analyze the structures of conserved scalar mixing in turbulent shear flows. It is shown that the scalar mixing structures stretch, fold and form layers, and the mechanism is referred to as "folding". Liquid sheets are compressed during layering in two-phase flows, and the two-phase mixture's transverse development is limited. Layering, in other words, can reduce gas entrainment into the liquid jet, which normally helps push liquid structures away from the liquid core and drives the atomization of the liquid.

The rate of layer formation is quantified for case C1 using the streamwise velocity component, u. The average streamwise velocity profile is analyzed on various transverse locations. An average value for the streamwise velocity component, u_{avg}, is obtained from the data on xz planes located at $y = 5$ μm, $y = 7.5$ μm, $y = 10$ μm, $y = 12.5$ μm, $y = 15$ μm, $y = 17.5$ μm, $y = 20$ μm, $y = 22.5$ μm, and $y = 25$ μm. These average streamwise velocity profiles are presented in Figure 6.16 at the non-dimensional times of $t^* = 0$, $t^* = 3.75$, $t^* = 7.5$, $t^* = 11.25$, and $t^* = 15$. Furthermore, the standard deviation, σ_{std}, of u is used to visualize the dispersion of the streamwise velocity component on each xz plane one standard deviation around the mean value. The exact initial velocity distribution imposed in the computations (see Section 6.1) is represented discretely in Figure 6.16 at $t^* = 0$ with $\sigma_{\text{std}} = 0$.

As the sharp initial velocity profile diffuses, the momentum mixing layer expands. The buildup of the surface perturbation and the strong vortical motion dominate the first half of the computation for case C1. For example, at $t^* = 7.5$, when the streamwise component of the velocity field becomes negative just above the liquid surface between 5 μm and 10 μm, gas entrainment is strong. Aside from the skewed velocity distribution toward negative streamwise values, the greater standard deviation at $t^* = 7.5$ indicates a more chaotic velocity

field overall. On the other hand, the streamwise velocity profile is spread more evenly and smoothly after the layering becomes the primary deformation mechanism for $t^* > 10$, further suggesting the disruptive effect of layering in limiting the atomization process.

Figure 6.16 also follows the primary or first liquid layer as it stretches and deforms, as shown in Figure 6.15. Three reference locations are followed: the top of the primary layer, a halfway location for the same layer, and the surface of the liquid jet core. As expected, the transverse development of the layering mechanism follows the expansion of the momentum mixing layer. There is some streamwise acceleration, which primarily influences the layering process inside the two-phase mixture. The top layer moves at a steady velocity of around 25 m/s, while the middle layer displays a velocity increase from around 14 m/s to 18 m/s. The surface of the main liquid core, on the other hand, moves at a much lower rate of 2 m/s to 3 m/s compared to the top regions of the two-phase mixture. Because the liquid jet's core is little disrupted within the examined time frame, longer times may be required to atomize the liquid jet. The top layers may overlap the jet core approximately every 1.4 μs once layering becomes the primary deformation mechanism.

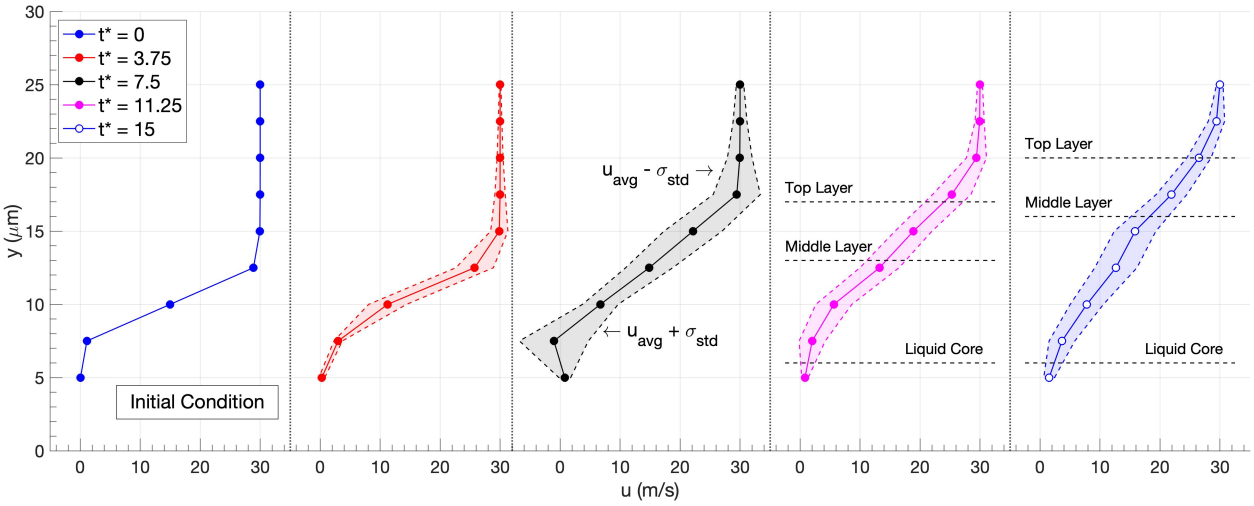

Figure 6.16: Analysis of the streamwise velocity component at 150 bar with gas freestream velocity of $u_G = 30$ m/s (i.e., case C1). Various times are analyzed and the average streamwise velocity component, u_{avg}, as well as the dispersion around one standard deviation, σ_{std}, is shown. Once the layering deformation mechanism becomes dominant (i.e., $t^* > 10$), different locations within the layers are presented [140].

Holes develop more frequently as the liquid sheets stretch and become exceedingly thin (see Figure 6.17). In other words, perforation events generated by the gas phase or other liquid structures cause the sheet to break due to constant stretching and thinning of the liquid layers. Mesh resolution, as highlighted in Subsections 6.3.1 and 6.3.2, has an impact on the exact time for perforation or sheet tearing. However, the ultimate focus here is to understand why liquid sheets develop so easily, how they may stretch and form multiple liquid layers at such high pressures, and what effect this deformation process has on liquid jet atomization and fuel mixing. Local sheet tearing can also be detected at lower pressures (e.g., cases A1 and A2 at 50 bar), but layering is not a dominant feature.

Layering occurs due to the lower surface-tension force combined with the relatively thin initial shear layer between the two fluids. Surface tension becomes relevant at larger length scales in classical subcritical atomization. Thus, liquid sheets are rarely so easily stretched by the oxidizer stream before surface tension, and capillary instabilities distort and break up the liquid. The enhanced intraphase mixing at high pressures impacts the evolution of the layering process but does not dictate whether or not layering happens. The incompressible case C1i, for example, exhibits a visible development of overlapping liquid sheets. Mixing in the liquid phase, like the lobe extension process described in Subsection 6.3.1, allows for the creation of thinner liquid structures that are more easily stretched due to the reduced density and viscosity. In the compressible scenario, this condition favors the creation of holes on the liquid sheets or sheet tearing more than with an incompressible fluid behavior (i.e., case C1 vs. case C1i). Figure 6.18 shows a comparison between the compressible case C1 and its incompressible counterpart, case C1i. Similar to the results illustrated in Figure 6.11, here, the hole formation rate during layering is reduced in the incompressible case. At $t^* = 12.75$, the liquid sheets in case C1i are still intact, whereas the liquid sheets have been perforated in many locations in the compressible case. Later at $t^* = 14.25$, hole formation is observed in the incompressible computation.

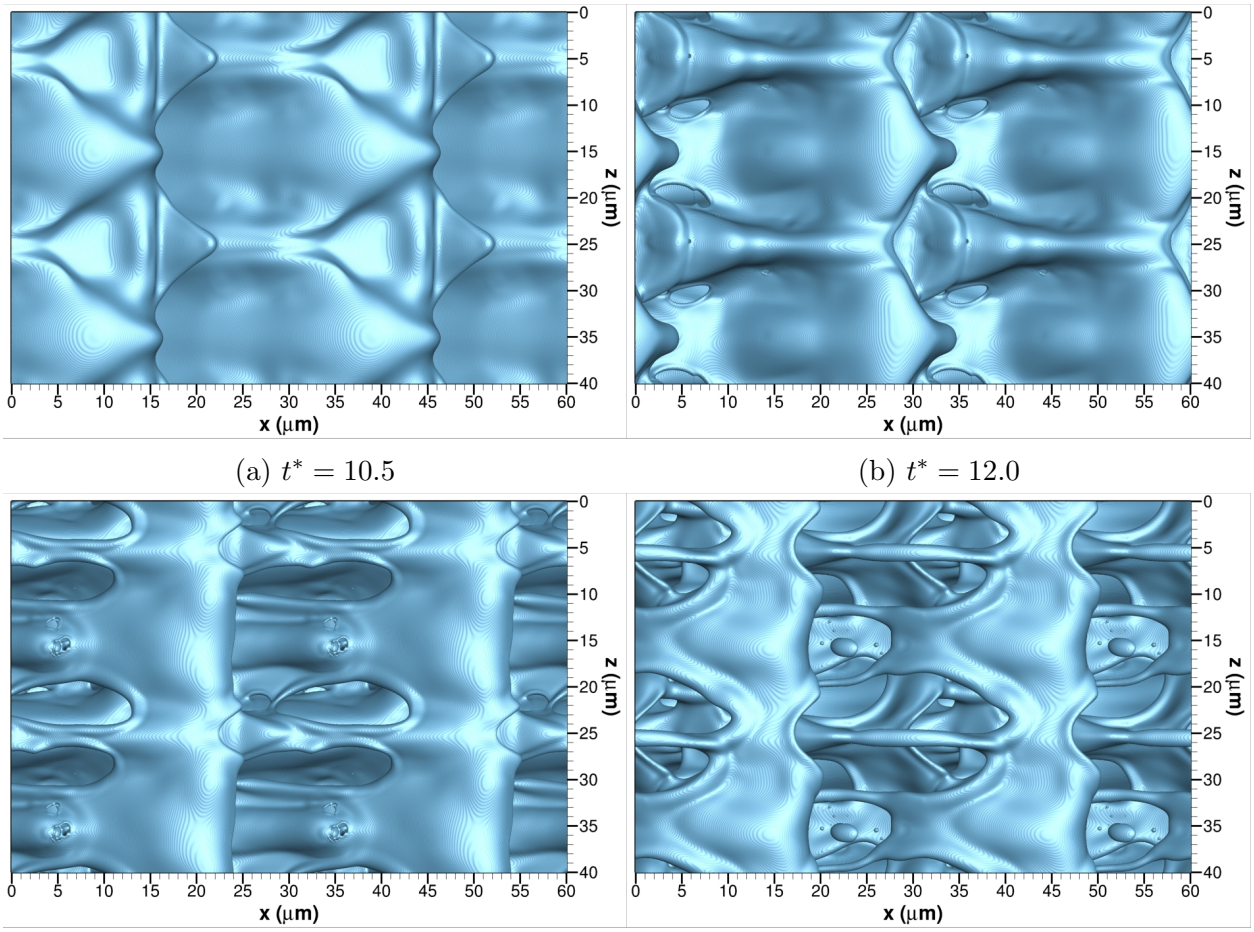

(a) $t^* = 10.5$ (b) $t^* = 12.0$

(c) $t^* = 13.5$ (d) $t^* = 15.0$

Figure 6.17: Layering or overlap of liquid sheets at 150 bar with gas freestream velocity of $u_G = 30$ m/s (i.e., case C1). The top view is obtained from an xz plane located above the liquid surface. The interface location is identified as the isosurface with $C = 0.5$. A non-dimensional time is obtained as $t^* = t/t_c = t\frac{u_G}{H}$. (a) $t^* = 10.5$; (b) $t^* = 12.0$; (c) $t^* = 13.5$; and (d) $t^* = 15.0$ [140].

The liquid density and viscosity of both liquid and gas phases are shown in Figure 6.19 for a slice of the three-dimensional domain identified as the xy plane with $z = 15$ μm for the configuration C1 at 150 bar. $t^* = 15$ is the non-dimensional time. That is, the represented slice corresponds to the snapshot presented in Figures 6.15d and 6.17d. The liquid-phase internal structure reveals that pure liquid-decane qualities only exist near the jet center. As a result of the dissolution of oxygen and the heating of the liquid phase, the liquid sheets and layers that form have a decreased liquid density and a sharp drop in liquid viscosity after some time.

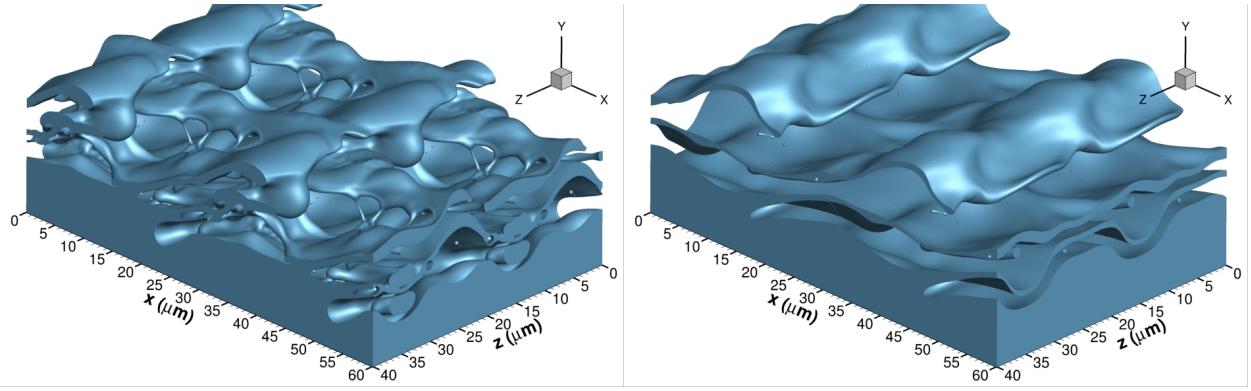

(a) case C1 at $t^* = 12.75$

(b) case C1i at $t^* = 12.75$

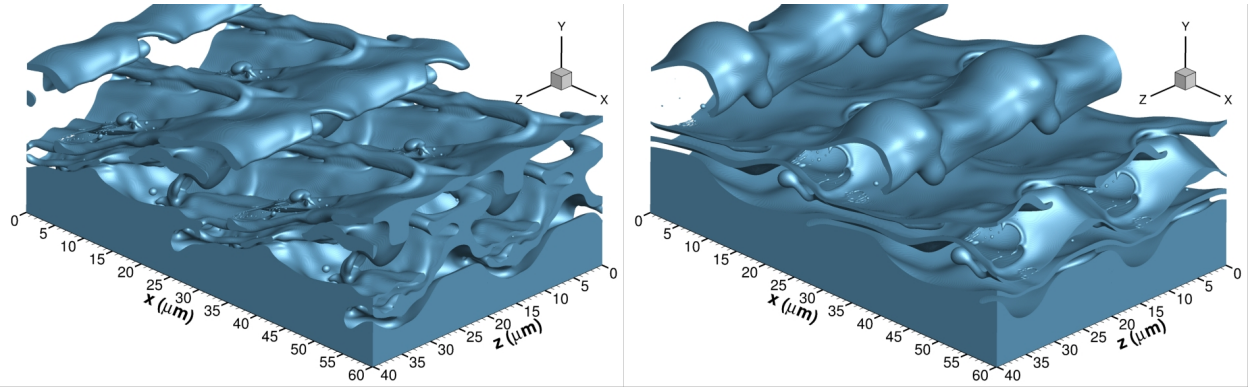

(c) case C1 at $t^* = 14.25$

(d) case C1i at $t^* = 14.25$

Figure 6.18: Layering or overlap of liquid sheets at 150 bar with gas freestream velocity of $u_G = 30$ m/s (i.e., case C1). A comparison between the compressible case and the incompressible case is provided to show the increased rate of hole formation in the compressible scenario. The interface location is identified as the isosurface with $C = 0.5$. A non-dimensional time is obtained as $t^* = t/t_c = t\frac{u_G}{H}$. (a) compressible case C1 at $t^* = 12.75$; (b) incompressible case C1i at $t^* = 12.75$; (c) compressible case C1 at $t^* = 14.25$; and (d) incompressible case C1i at $t^* = 14.25$.

The fluid properties of both phases change significantly over time as mixing occurs at these high-pressure conditions, as discussed in Section 6.2. First, only small portions of the liquid phase have higher oxygen concentrations and temperatures, localized along the liquid-gas interface (e.g., near the wave crest, where a hotter interface temperature is expected). As explained earlier, these regions are easily impacted by the dense gas-phase dynamics. The lobe deformation patterns described in Subsections 6.3.1 and 6.3.2, as well as the ligament stretching and shredding outlined in Subsection 6.3.3, are examples of this behavior. All of

these localized behaviors are caused by the high-pressure environment; yet, the majority of the liquid phase retains the fluid properties of the injected fuel.

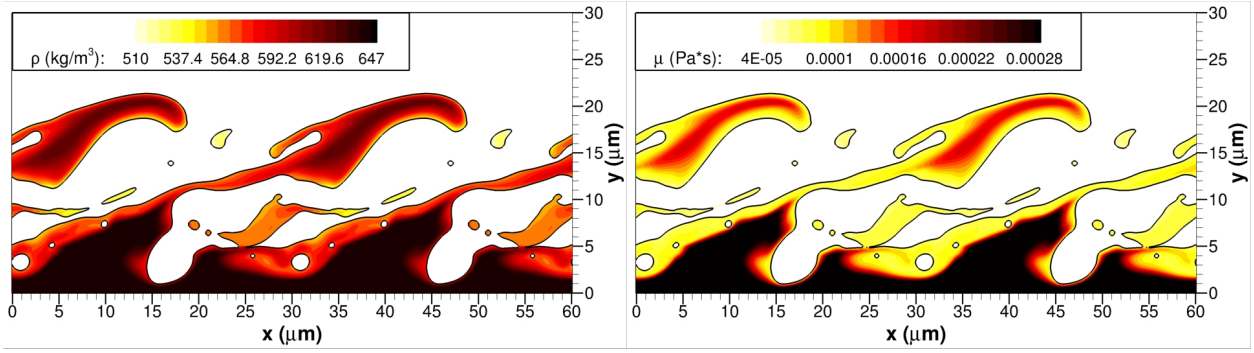

(a) (b)

Figure 6.19: Layering or overlap of liquid sheets at 150 bar with gas freestream velocity of $u_G = 30$ m/s (i.e., case C1) at the non-dimensional time $t^* = t/t_c = t\frac{u_G}{H} = 15$. A slice through the three-dimensional domain is obtained from an xy plane located at $z = 15$ μm. The interface location is identified as the isosurface with $C = 0.5$. (a) liquid density; and (b) viscosity of the two-phase mixture [140].

After a while, the mixing regions in the liquid have grown large enough that lower densities and gas-like viscosities are more characteristic of the jet's outer parts. The transition point where liquid sheets begin to form accelerates mixing as the surface area increases and the thickness of the liquid sheet decreases under prolonged stretching. As a result, more liquid sheets and layers are formed. Due to the lower surface tension at very high pressures, liquid sheets can stretch for long periods without capillary instabilities producing large-scale breakup events, as explained in Subsection 6.3.3. Local ligament and droplet production are observed in configurations with greater velocities or inertial forces surrounding the development and stretching of liquid layers.

6.4 Triggers of Unstable Surface Perturbations

This section discusses the numerous events that can cause the development of surface instabilities at high pressures. The reader is reminded of the relevance of examining the influence

of spurious currents generated by the computational approach, as highlighted in Section 4.3. Suppose spurious currents are not constrained by the mesh resolution and problem configuration. In that case, the sharp-interface approach and the pressure solver based on the FFT method may trigger the emergence of numerical instabilities around the interface or cause an unstable numerical solution. The examples discussed within this section have a physical explanation and, to the best of the author's knowledge, the numerical method's impact is effectively limited. Spurious currents are more detrimental at low density ratios ρ_G/ρ_L. Nonetheless, no indication of numerical instability is found at 50 bar, where the density ratio is the lowest. Grid testing (see Appendix F.3) demonstrates that grid resolution has little influence on the formation of the instabilities described in this section, and the current mesh size gives at least a resolution of around 20 to 30 cells per wavelength of the observed short-wavelength surface perturbations.

The lower surface-tension coefficient in transcritical two-phase flows promotes the emergence of surface instabilities produced by surface perturbations caused by impact events (e.g., droplet collision) or flow disturbances near the liquid-gas interface. These situations are not unique to high-pressure flows, but they are more common than under subcritical conditions. Stable events are also observed. Figure 6.20, for example, depicts the coalescence of ligaments and droplets for case C1 at 150 bar and a gas freestream velocity of $u_G = 30$ m/s. The ligaments and droplets that form after the bridge created during the lobe perforation seen in Figure 6.8 breaks hit the liquid surface near the perturbation's trough. The combination of low velocities, increased surface tension, and higher liquid viscosity near the trough results in a stable state in which the impact energy is dissipated, and the amplitude of the generated surface perturbation decays. For the reader's reference, Figures 6.3 and 6.4 show the interface temperature, the surface-tension coefficient and the liquid fluid properties for case C1 at $t = 5$ μs. This physical time corresponds to the non-dimensional time $t^* = 7.5$ shown in Figure 6.20e. Additional stable impact events also take place in case C1 between $t^* = 8.4$ and $t^* = 9.75$, where a one-micron droplet collides against the liquid surface close to the

perturbation crest, and in case B1 from $t^* = 7.5$ to $t^* = 9.25$ where droplets impact the liquid surface near the perturbation trough.

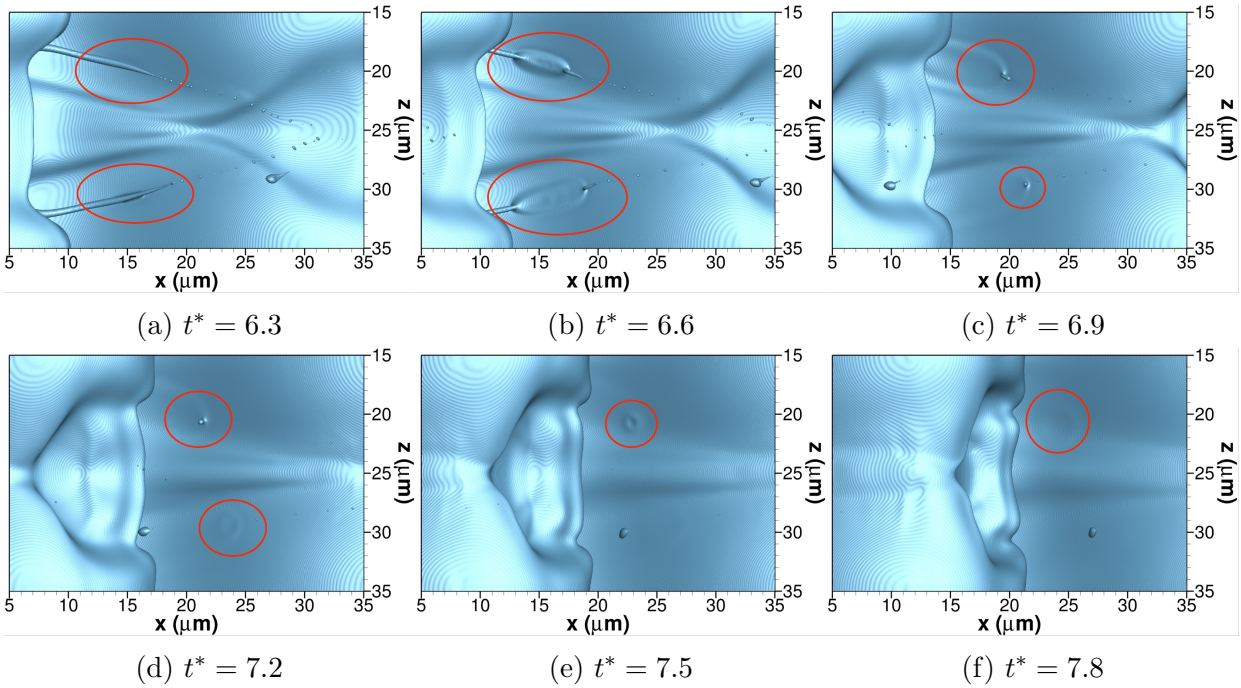

(a) $t^* = 6.3$ (b) $t^* = 6.6$ (c) $t^* = 6.9$

(d) $t^* = 7.2$ (e) $t^* = 7.5$ (f) $t^* = 7.8$

Figure 6.20: Stable collision events at 150 bar with gas freestream velocity of $u_G = 30$ m/s (i.e., case C1). Impact regions are circled in red. The top view is obtained from an xz plane located above the liquid surface. The interface location is identified as the isosurface with $C = 0.5$. A non-dimensional time is obtained as $t^* = t/t_c = t\frac{u_G}{H}$. (a) $t^* = 6.3$; (b) $t^* = 6.6$; (c) $t^* = 6.9$; (d) $t^* = 7.2$; (e) $t^* = 7.5$; and (f) $t^* = 7.8$ [140].

Many examples of unstable impact or coalescence events exist, particularly at greater gas freestream velocities. Figure 6.21 shows the formation of short-wavelength surface instabilities at 100 bar and $u_G = 70$ m/s (i.e., case B2) following the collision of a ligament near the crest of the main perturbation about $z = 15$ μm, which is also seen, for example, at 150 bar and $u_G = 50$ m/s (i.e., case C2). This collision causes a series of waves on the liquid surface, whose amplitude increases over time and dictates the formation of several lobes along the main perturbation's edge. These lobes extend into the gas phase and are the precursors to producing small thin ligaments and droplets (e.g., shredding). Remarkably, the propagation of these instabilities causes the creation of new surface waves upstream, which does not happen in lower pressure scenarios like case A1 at 50 bar with $u_G = 50$ m/s. For this

low-pressure case, a surface wave propagates from $t^* = 6.25$ to $t^* = 10$, generating a lobe at the main perturbation's edge but not causing upstream instabilities.

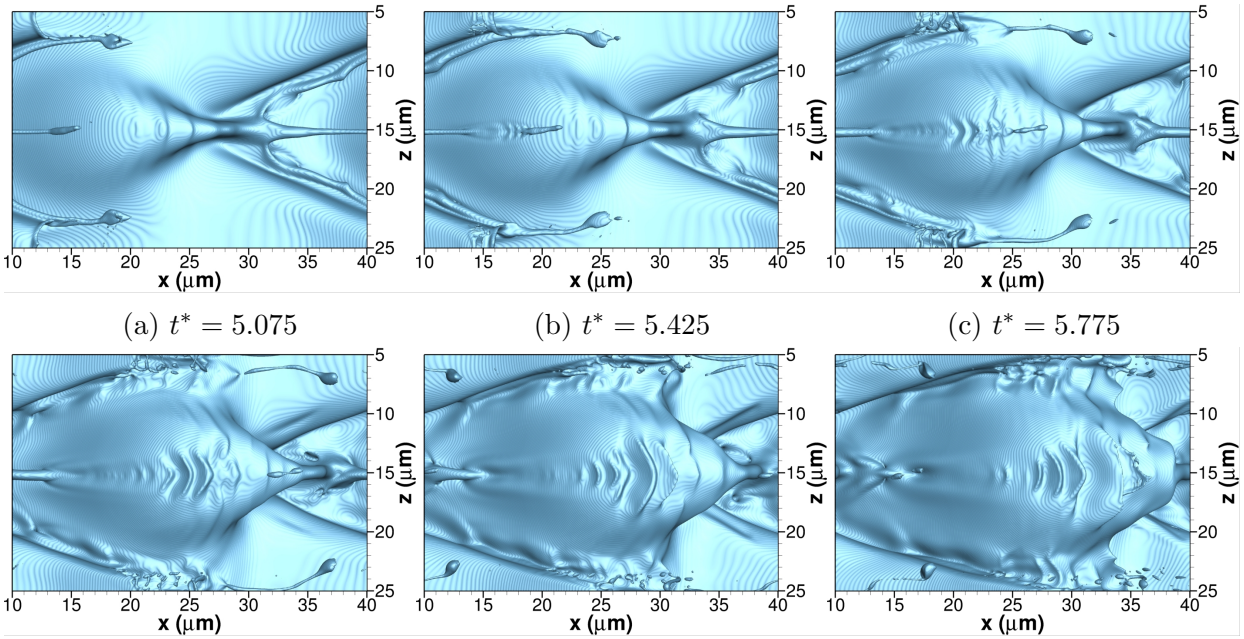

(a) $t^* = 5.075$ (b) $t^* = 5.425$ (c) $t^* = 5.775$

(d) $t^* = 6.125$ (e) $t^* = 6.475$ (f) $t^* = 6.825$

Figure 6.21: Unstable collision events at 100 bar with gas freestream velocity of $u_G = 70$ m/s (i.e., case B2). The top view is obtained from an xz plane located above the liquid surface. The interface location is identified as the isosurface with $C = 0.5$. A non-dimensional time is obtained as $t^* = t/t_c = t\frac{u_G}{H}$. (a) $t^* = 5.075$; (b) $t^* = 5.425$; (c) $t^* = 5.775$; (d) $t^* = 6.125$; (e) $t^* = 6.475$; and (f) $t^* = 6.825$ [140].

Flow disturbances induced by liquid structures flowing extremely close to the liquid surface are another event that causes the emergence of surface instabilities. These perturbations can be detected in the configurations C2 and C3 at 150 bar, for example. When the early lobe bursts into droplets and ligaments, as shown in Subsection 6.3.2, the faster gas carries a train of droplets and other liquid structures, distorting the flow field around it enough to disturb the surface below. Surface waves also develop at high pressures and high velocities around regions where the liquid surface corrugates, such as the crest corrugation described in Subsection 6.3.2. Case C2 at 150 bar shows a weak wave formation around the corrugating crest, while Case B2 at 100 bar shows a mild formation. At 150 bar and $u_G = 70$ m/s (i.e., case C3), the waves that arise as the perturbation crest corrugates from $t^* = 3.15$ to

$t^* = 5.95$ become unstable as illustrated in Figure 6.23, defining the subsequent creation of ligaments and droplets.

In real-fluid environments, the interaction of mixing effects with interface dynamics and its local thermodynamic equilibrium state may accelerate the emergence of surface instabilities beyond the observed behavior at incompressible, constant-properties conditions. Cases A2i and C1i, for example, indicate that short-wavelength surface instabilities rarely grow. Only the collision of two surface waves after $t^* > 10.15$ along $z = 15$ μm in scenario A2i causes surface instabilities around the perturbation crest, where a faster streamwise velocity exists (see Figure 6.22). Surface waves traveling near the perturbation crest in the real-fluid situation are frequently subjected to faster velocities and more shear and higher temperatures due to their proximity to the hotter oxidizer stream. The interface equilibrium solution has a lower surface-tension coefficient and liquid viscosity near it at higher temperatures. As a result, those areas are anticipated to be more vulnerable to the growth of unstable surface waves.

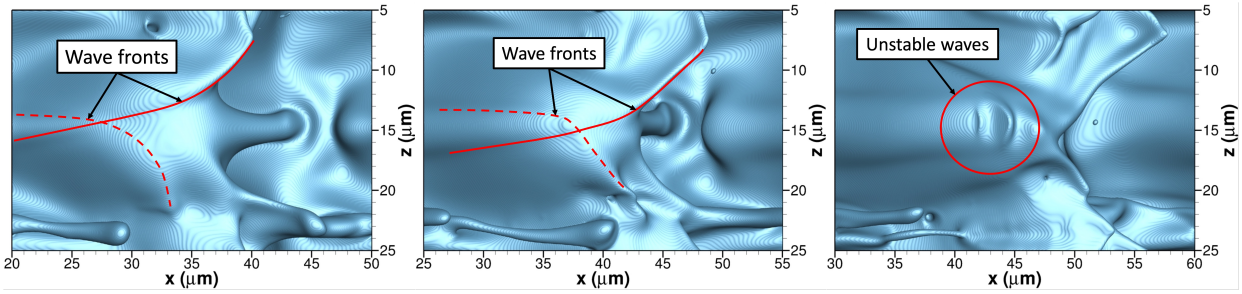

(a) $t^* = 10.15$ (b) $t^* = 11.20$ (c) $t^* = 12.25$

Figure 6.22: Unstable growth of surface waves in the incompressible case at 50 bar with gas freestream velocity of $u_G = 70$ m/s (i.e., case A2i). The top view is obtained from an xz plane located above the liquid surface. The interface location is identified as the isosurface with $C = 0.5$. A non-dimensional time is obtained as $t^* = t/t_c = t\frac{u_G}{H}$. (a) $t^* = 10.15$; (b) $t^* = 11.20$; and (c) $t^* = 12.25$.

The described feature is illustrated in Figure 6.23, which depicts the interface temperature for case C3 at various times. The creation of waves on a hotter surface produces hotter wave crests and cooler wave troughs. As a result, the wave crest's surface-tension coefficient

and liquid viscosity are lower than the wave trough's. Furthermore, small structures such as ligaments, lobes, and droplets have greater surface temperatures because the confined liquid volume heats faster.

The varying fluid properties along the wave, combined with the faster-neighboring gas stream, may result in an unstable dynamic process with rapid growth. Although collision events might enhance this behavior, as illustrated in Case C3, the surface wrinkles formed by the corrugation mechanism can become unstable on their own. As seen in Figure 6.23, once the wave's amplitude has risen considerably, the crest is rapidly stretched into the oxidizer stream, generating small lobes that precede the eventual shredding of small ligaments and breakup of droplets. Additional analysis of this coupled instability growth mechanism with variable fluid properties is required. Nonetheless, the features presented here emphasize the impact of significant variations in fluid properties on the atomization of real liquids at supercritical pressures.

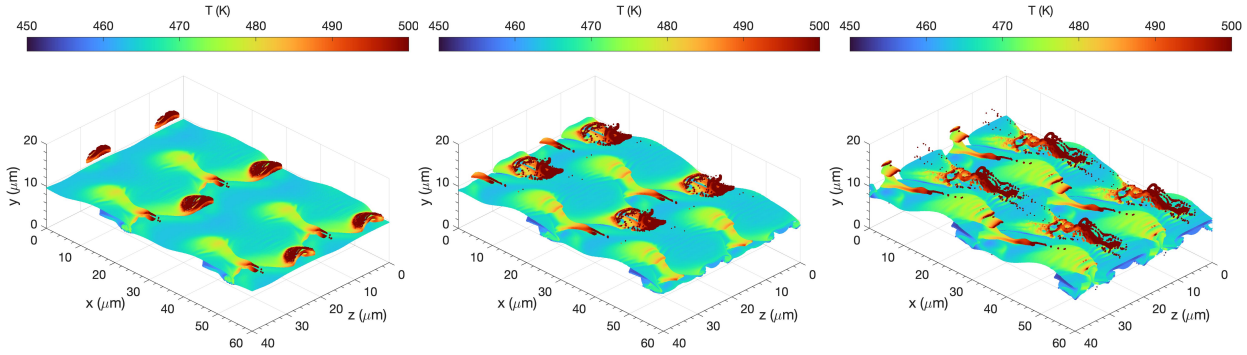

(a) $t^* = 3.85$ (b) $t^* = 4.55$ (c) $t^* = 5.25$

Figure 6.23: Interface temperature at 150 bar with gas freestream velocity of $u_G = 70$ m/s (i.e., case C3). The interface location is identified at the centroid of each local interface plane given by the PLIC method. A non-dimensional time is obtained as $t^* = t/t_c = t\frac{u_G}{H}$. (a) $t^* = 3.85$; (b) $t^* = 4.55$; and (c) $t^* = 5.25$ [140].

Lastly, linear theory may provide an approximate assessment of the most unstable wavelength for a surface instability, as well as its growth rate, based on the interface fluid properties. Assuming the Kelvin-Helmholtz instability is the cause of the identified short-wavelength perturbations, the perturbation growth rate is estimated using the linear analysis of small-

amplitude interface perturbations from Joseph et al. [40], which includes the effect of viscous normal stress, as

$$\epsilon = -i\frac{k(\rho_g u_{\infty_g} + \rho_l u_{\infty_l})}{\rho_g + \rho_l} - k^2\frac{\mu_g + \mu_l}{\rho_g + \rho_l} \pm \left[\frac{\rho_g\rho_l k^2(u_{\infty_g} - u_{\infty_l})^2}{(\rho_g + \rho_l)^2} - \right.$$
$$\left. - \frac{\sigma k^3}{\rho_g + \rho_l} + \frac{k^4(\mu_g + \mu_l)^2}{(\rho_g + \rho_l)^2} + 2ik^3\frac{(\rho_g\mu_l - \rho_l\mu_g)(u_{\infty_g} - u_{\infty_l})}{(\rho_g + \rho_l)^2}\right]^{1/2} \tag{6.1}$$

where $\epsilon = \epsilon_R + i\epsilon_I$ is the complex growth rate of a perturbation whose amplitude evolves as $\Omega(x,t) = \hat{\Omega}\exp(\epsilon t)\exp(ikx)$, and $\hat{\Omega}$ is the initial perturbation amplitude. Therefore , the real part of the growth rate, ϵ_R, defines whether or not an oscillation is stable (i.e., stable for $\epsilon_R < 0$). The wave number is represented by k, and the velocities of the gas and liquid streams are defined as $u_{\infty_g} = u_G$ and $u_{\infty_l} = 0$ for the current analysis. Furthermore, gravity is ignored in Eq. (6.1). As a limiting case, the interface densities and viscosities (i.e., ρ_g, ρ_l, μ_g and μ_l) of each phase are obtained from phase-equilibrium results as a function of interface temperature.

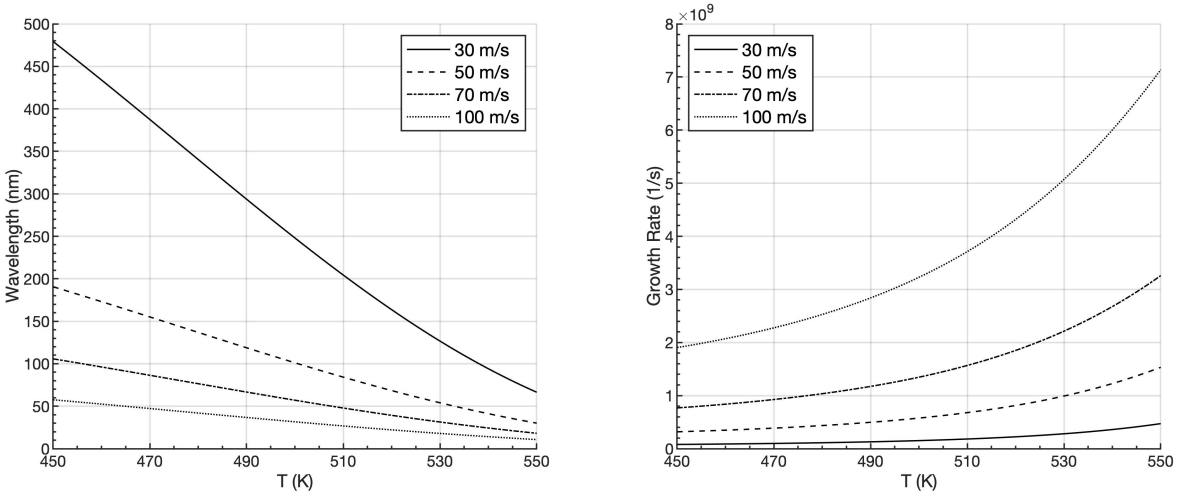

(a) (b)

Figure 6.24: Analysis of the wavelength of the most unstable wave and its amplitude growth rate using the linear theory, Eq. (6.1), for an n-decane/oxygen interface at 150 bar. Fluid properties are assumed to be the interface fluid properties obtained as a function of temperature from phase-equilibrium data. (a) wavelength; and (b) growth rate.

The wavelength of the most unstable wave and its amplitude growth rate are shown in Figure 6.24. The results calculated from Eq. (6.1) are presented as a function of the interface temperature and u_G for an interface of the binary mixture of n-decane/oxygen at 150 bar. Depending on the configuration, the magnitude of the most unstable wavelengths spans from a few nanometers to hundreds of nanometers. The linear theory estimated wavelengths are significantly smaller than the short-wavelength perturbations observed on the liquid surface, around 2 μm and 3 μm. This difference is an expected outcome because the theory is based on a viscous potential flow with only normal stresses, and hence the stabilizing shear stress is omitted. Additionally, this analysis involves the interface fluid properties, which differ somewhat from the liquid-phase and gas-phase fluid properties far from the interface, and a sharp, discontinuous shear layer between both phases. Nonetheless, the linear theory results provide insight into how much more unstable the liquid-gas interface can become as the equilibrium temperature varies and the fluid properties change while being exposed to different velocities.

The most unstable wavelengths at a given velocity difference are roughly cut by a factor of two when varying from an interface temperature of 450 K to an interface temperature of 500 K. In the same way, their growth rates increase by a factor of 1.5 from 450 K to 500 K. As a result, hotter interface regions subjected to greater velocities are expected to generate unstable surface waves that do not develop in colder regions, primarily if a catalyst exists (e.g., collision). Note that the most unstable wavelength does not scale with the interface temperature alone in the situations examined here. Because cooler interface regions are frequently near the bottom of the two-phase mixing layer, they are susceptible to considerably lower velocities. The most unstable wavelength, in this case, rapidly increases an order of magnitude when the velocity difference is reduced, as shown in Figure 6.24. Therefore, they may not develop.

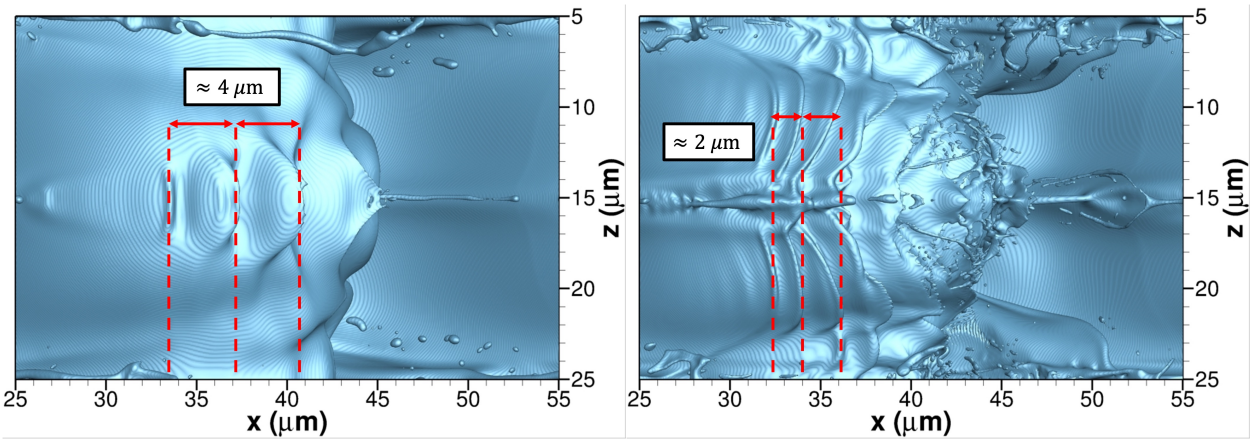

(a) case C2 (b) case C3

Figure 6.25: Estimated wavelength of unstable surface waves at 150 bar with gas freestream velocities of $u_G = 50$ m/s and $u_G = 70$ m/s (i.e., cases C2 and C3) at the non-dimensional time of $t^* = t/t_c = t\frac{u_G}{H} = 7$. Lower freestream velocities generate longer wavelengths of the surface perturbations. The top view is obtained from an xz plane located above the liquid surface. The interface location is identified as the isosurface with $C = 0.5$. (a) case C2; and (b) case C3.

Further examination of the configurations that produce short-wavelength surface instabilities reveals a tendency in which lower pressures and lower velocities produce slightly longer wavelengths, as expected from the linear theory. For instance, case C2 (i.e., 150 bar and $u_G = 50$ m/s) generates waves with wavelengths ranging from 3 μm to 4 μm, whereas Case C3 (i.e., 150 bar and $u_G = 70$ m/s), as previously noted, creates surface instabilities with wavelengths ranging from 2 μm to 3 μm. This comparison is visualized in Figure 6.25, where a view from an xz plane located above the liquid surface is used to depict the wavelength of the surface perturbations at $t^* = 7$ for cases C2 and C3.

6.5 Formation of Ligaments and Droplets

This section describes the generation of detached ligaments and droplets in each investigated configuration. Furthermore, trapped bubbles and gas pockets are considered. In contrast to the previous Sections 6.3 and 6.4, which focused on specific aspects of the liquid jet de-

formation, this section focuses on the breakup process of the whole liquid jet. Structures connected to the bulk liquid, such as connected ligaments, are not examined. The construction of an effective identification method capable of capturing such cases is complex. Nonetheless, ligaments detach from the main liquid and are captured by the identification algorithm.

Detached structures from the main liquid jet, whether liquid or gas, are determined using an interface data set with information on the thermodynamic state of the interface as well as the position of interface cells and pertinent geometrical information (e.g., temperature, mass flux per unit area). This data collection is used to plot the interface temperature in Figures 6.3a and 6.23, for example. Compared to other techniques that identify structures directly from the volume fraction field, this data set provides more information for analysis.

A structure is made up of a collection of adjacent interface cells. Two interface cells are regarded adjacent to each other in a three-dimensional domain if they fall within a cube of three cells per side centered around either interface cell. Once the structure's geometry is determined (i.e., the distribution of the interface cells that define the structure), the surface area can be calculated by adding the areas of each local interface plane (i.e., from the PLIC). If necessary, the enclosed volume can also be calculated using the volume fraction field of the interface cells and inner cells defining the structure. However, in our computations, the volume fraction field belongs to a distinct data set, which cannot be easily post-processed to calculate the volume of detached structures. Because of this issue, the "traditional" identification method involving the volume fraction field is only addressed when volume data is required for the analysis (e.g., the ligament size assessment shown in Figure 6.29).

The volume fractions, C, of the enclosed cells are not accessible to determine whether the structure constitutes a liquid body (e.g., a droplet) or a gaseous body (e.g., bubble) because the data set used here only includes information from the interface cells. The interface normal unit vector, $\hat{n}$, is utilized instead. In this study, $\hat{n}$ points into the liquid phase [63].

Consequently, a geometrical constraint can be used to determine the fluid phase of the enclosed volume. Note that $\hat{n} = -\vec{n}$ as defined in Subsection 3.2.1. A two-dimensional sketch of the technique is shown in Figure 6.26, which can readily be extended to three-dimensional configurations. A computational box is defined for every detached structure. This box contains the structure, which may touch the sides of the box at various locations. The simple example of a structure similar to an ellipse is illustrated in Figure 6.26. Given the direction of the interface normal unit vector, $\hat{n}$, a test point is obtained for each interface cell characterizing the structure. This test point is located at a distance of Δx following $\hat{n}$ from the local interface plane centroid. All test points for a liquid structure (such as a droplet or ligament) are contained within the computational box. If at least one test point falls outside the computational box, the enclosed volume is gas (i.e., bubble or gas pocket). The technique is robust because the contact points between the sides of the computational box and the structure usually touch tangentially. Only severely under-resolved structures might fail since the geometrical information of the interface might be ill-defined. Nevertheless, this issue has a small impact on the study of detached structures.

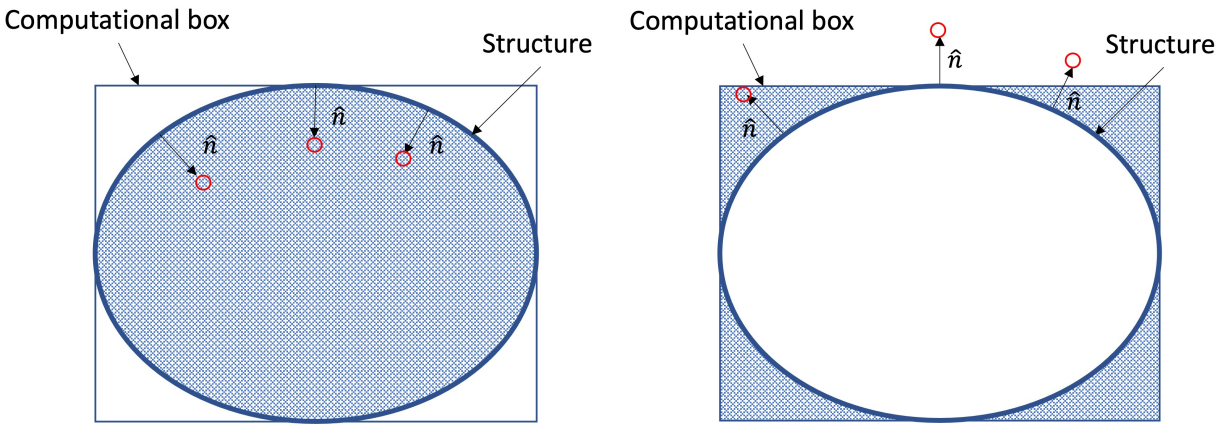

(a) liquid structure (b) gas structure

Figure 6.26: Two-dimensional sketch showing the three-dimensional methodology to determine whether a detached structure (e.g., droplet, ligament, bubble or gas pocket) encloses liquid phase or gas phase based on the geometry constraint imposed by the interface normal unit vector, $\hat{n}$. The red circles represent the test points obtained by extending a point from the local interface plane centroid a distance of Δx following $\hat{n}$. (a) liquid structure; and (b) gas structure [140].

Once the fluid phase contained by an identified structure has been determined, the structure's shape is considered to classify among discrete droplets, ligaments, bubbles and gas pockets. For this purpose, first the shape of the computational box containing the structure is analyzed. Three characteristic lengths are evaluated, one per axes: $\delta x = x_{\max} - x_{\min}$, $\delta y = y_{\max} - y_{\min}$ and $\delta z = z_{\max} - z_{\min}$. Moreover, the volume of the computational box is computed as $\delta V = \delta x \delta y \delta z$. Here, the subscripts "max" and "min" refer to the maximum and minimum locations in each direction of the interface cells defining the structure. The streamwise length, δx, is used to normalize the computational box size (i.e., $\delta \hat{x} = 1$, $\delta \hat{y} = \delta y / \delta x$ and $\delta \hat{z} = \delta z / \delta x$), and the conditions $0.8 < \delta \hat{y} < 1.2$ and $0.8 < \delta \hat{z} < 1.2$ are evaluated. If these conditions are met, the computational box is roughly cubic and may contain a spherical shape or similar. Otherwise, the computational box is larger at least in one direction, indicating that it contains an elongated structure. Note that a deviation of up to 20% in the length of $\delta \hat{y}$ and $\delta \hat{z}$ with respect to $\delta \hat{x}$ is allowed. The choice to normalize by the streamwise length might seem arbitrary, but it is done since ligaments are expected to stretch mainly in the streamwise direction. Other normalization criteria may be evaluated in future works, such as normalizing by the intermediate length (i.e., if $\delta y < \delta z < \delta x$, normalize the lengths dividing by δz).

Another criterion is used to determine whether or not a nearly cubic computational box encloses a spherical structure. A sphere has an exact ratio $S/\delta V = \pi / \delta x_c$, which represents the ratio between the structure's surface area and the volume of the computational box, $S/\delta V$, and an equivalent cube length, $\delta x_c = (\delta V)^{1/3}$. The threshold $S/\delta V = 2.5/\delta x_c$ is being used. For $S/\delta V > 2.5/\delta x_c$, the structure is characterized as a droplet or bubble regardless of the shape being slightly distorted based on whether the enclosed volume is liquid or gas. On the other hand, if $S/\delta V \leq 2.5/\delta x_c$, the structure is identified as a detached ligament or gas pocket depending on the fluid phase of the enclosed volume. For non-cubic computational boxes, the structures are only identified as detached ligaments or gas pockets depending on the fluid phase.

The reader is reminded that the analysis of ligament and droplet formation presented in this section has been performed using only one set of data per problem setup and a single mesh configuration. Therefore, it is not possible to prove statistical convergence nor mesh convergence of results such as droplet size distributions or the amount of generated droplets. Nevertheless, an assessment is made to infer whether under-resolution affects the analysis.

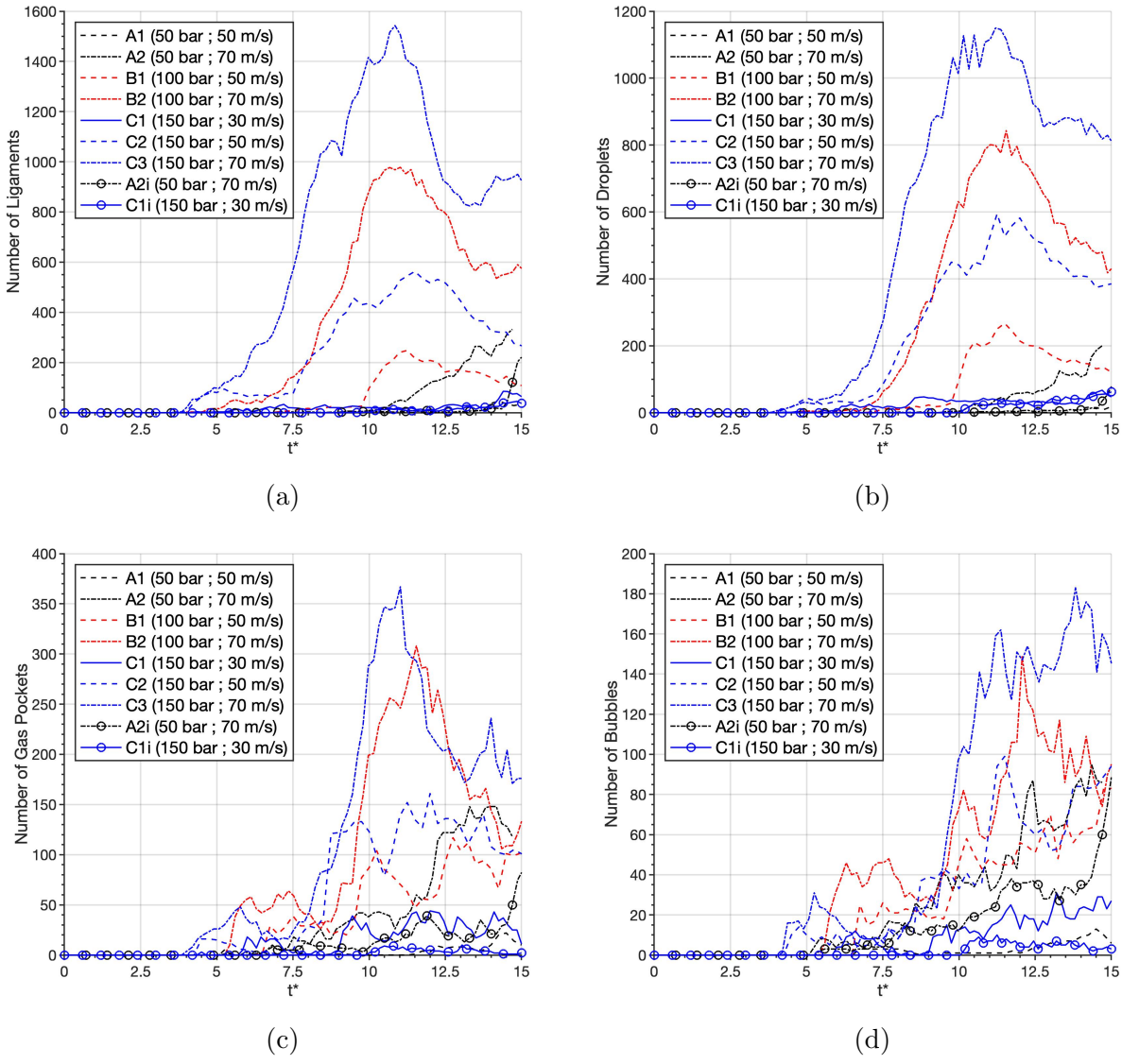

Figure 6.27: Number of detached structures over time contained inside the computational domain defined in Figure 6.1a. A non-dimensional time is obtained as $t^* = t/t_c = t\frac{u_G}{H}$. (a) number of ligaments; (b) number of droplets; (c) number of gas pockets; and (d) number of bubbles [140].

The number of ligaments, droplets, gas pockets and bubbles created over time for each investigated case are shown in Figure 6.27. The computational region defined in Figure 6.1a contains the detached structures. The data was not gathered from the larger region depicted in other figures, which used periodicity in the streamwise and spanwise directions to represent the surface development better. As the flow becomes chaotic, configurations with higher We_G and Re_L reflect the expected trend of an increased formation of ligaments and droplets. Even though the generation of trapped gas pockets and bubbles is partially determined by the initial lobe development and how it reconnects with the liquid jet, the increased generation of ligaments and droplets in configurations with stronger inertial terms promotes more collision and coalescence events. Thus, additional gaseous structures may be trapped within the liquid phase.

When examining the generation of detached liquid structures, the effect of Re_L becomes evident. Cases A2, B1, and C1 have a similar We_G, as seen in Table 6.2. However, Re_L diminishes as pressure increases. This trend results in a greater presence of ligaments and droplets at lower pressures over time. Viscous forces decrease relative to inertial terms, separating liquid structures from the main liquid jet. There are also some mixing effects detected. For example, case B1 has more droplets than case A2 until $t^* \approx 14$, while case C1 has more droplets than case A2 until $t^* \approx 11.5$. A similar pattern can be seen in the number of ligaments. As described in previous sections, this phenomenon is caused by the lower liquid density and gas-like viscosity around local regions of the liquid jet. Coupled with a denser gas at high pressures, these areas are more easily perturbed and deformed. Compared to their compressible counterparts, the incompressible configurations A2i and C1i have a lower formation of ligaments and droplets.

The analysis of the configurations C1 and B1 shows a similar scenario where the higher pressure results in the formation of droplets sooner. The disparities induced by a change in Re_L are more significant in scenarios where We_G is also higher. For instance, the gas Weber

numbers in cases B2 and C2 are similar (see Table 6.2), but the liquid Reynolds number in the 100-bar case is higher than at 150 bar. Despite the high-pressure scenario demonstrating an early production of ligaments and droplets, the lower-pressure case shows an enhanced separation of liquid structures over time, as stated in the previous lines.

The layering effect on the early atomization process is also detailed in Figure 6.27. Layering begins to form after $t^* = 10$ in all situations where layering exists (i.e., high pressures of 100 bar and 150 bar). Cases B1, B2, C2, and C3 show a peak in the development of droplets and ligaments at about the same non-dimensional time. These results match the layering features stated in Subsection 6.3.4. The development of liquid sheets disrupts vortical structures and limits gas-phase entrainment. Furthermore, as the liquid sheets overlap, they press against each other. This behavior inhibits the formation of ligaments and droplets while promoting collision and coalescence events.

The images provided in the Supplemental Material may give the impression that hundreds of liquid structures do not exist in specific configurations, as depicted in Figure 6.27. This appearance is due to the size of such structures and the restricted number of viewpoints available. Some ligaments and droplets may be hidden beneath larger liquid structures, or their size may be too small that the plotting software cannot reconstruct an isosurface with $C = 0.5$. Testing and validation of the structure identification method and the classification into liquid or gas structures have been done. Global parameters such as total surface area and total liquid volume, for example, are conserved, and each interface cell is uniquely allocated to a specific structure.

The normalized distribution of the droplet size for all analyzed cases is depicted in Figure 6.28 at two different instants of time $t^* = 11.25$ and $t^* = 14.7$, if data is available. Whenever a liquid structure has been identified as a droplet, an effective diameter, D_e, is calculated by adopting a spherical shape and using the information on the structure's surface area

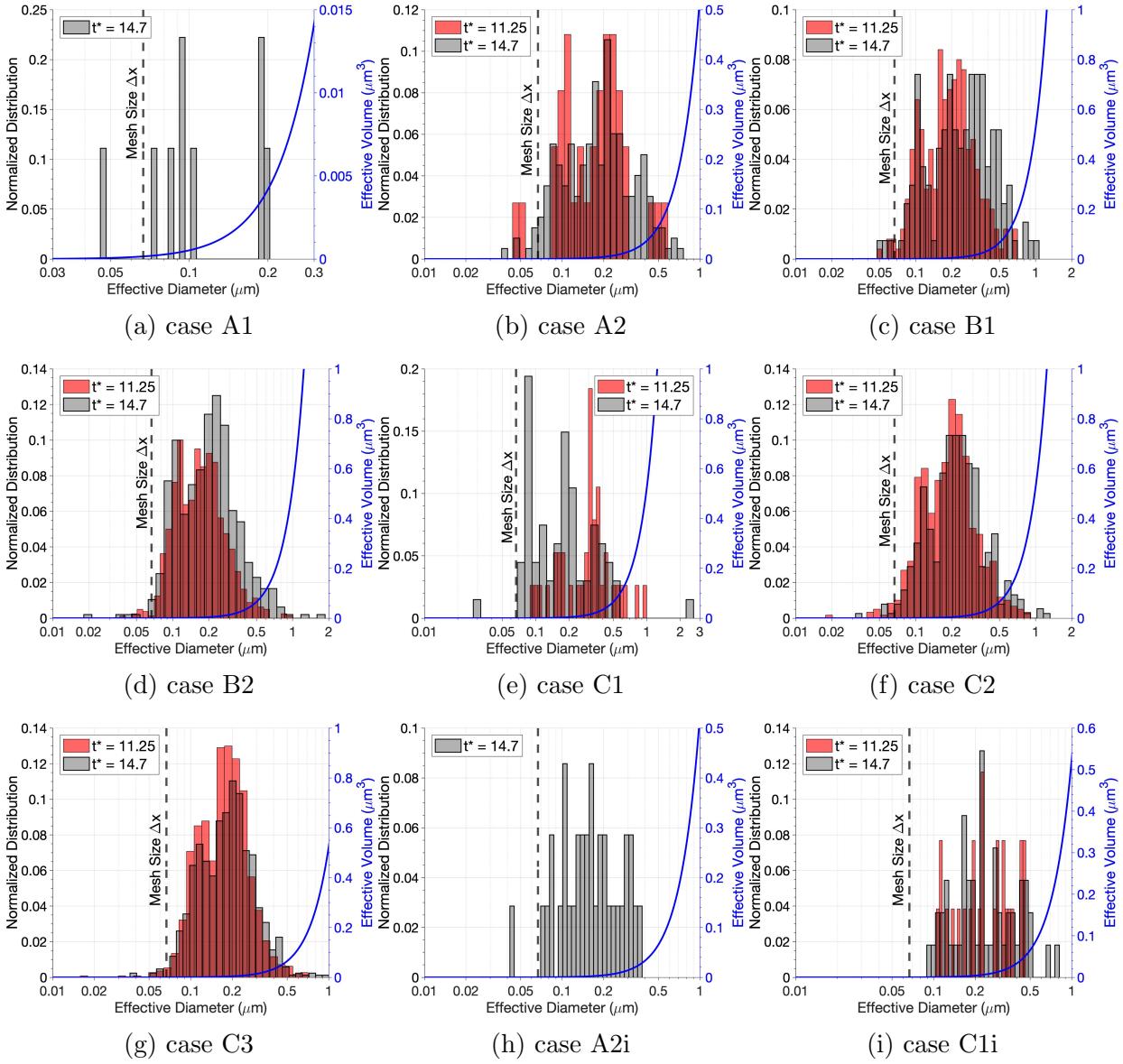

(a) case A1 (b) case A2 (c) case B1

(d) case B2 (e) case C1 (f) case C2

(g) case C3 (h) case A2i (i) case C1i

Figure 6.28: Droplet effective diameter distribution at different instants of time for all analyzed cases. A non-dimensional time is obtained as $t^* = t/t_c = t\frac{u_G}{H}$. The associated droplet effective volume is represented by the blue curve and the mesh resolution limit is represented by the vertical dashed line. Notice the logarithmic scale used in the horizontal axis. (a) case A1; (b) case A2; (c) case B1; (d) case B2; (e) case C1; (f) case C2; (g) case C3; (h) case A2i; and (i) case C1i [140].

such that $S = \pi D_e^2$. The total number of droplets at each represented time and for each configuration is used to normalize the droplet-size distribution.

The droplet effective diameter distribution reveals that practically all droplets are sub-micron in size, with only a few having effective diameters above 1 μm. This finding is consistent with the lower surface-tension force at high pressures. Droplet production caused by capillary instabilities is reduced and occurs mainly at very small scales. For example, assuming that droplets can keep a spherical shape for very small local Weber numbers (i.e., in the range of 1 to 10), approximate droplet diameters may be obtained based on the range of fluid properties observed during the computations. The droplet diameter is estimated to be on the order of a few nanometers in an extreme case with a very low surface-tension coefficient and a very high velocity of 70 m/s. This number is physically problematic because it may violate the continuum fluid mechanics inherent in the modeling used in this dissertation and because of a tiny droplet that would vaporize almost instantaneously. Expected droplet sizes are more in line with those obtained in the computations, between 0.01 μm and 1 μm, with more conservative estimates using lower velocities ranging from 5 m/s to 10 m/s. As seen in Figure 6.29c, the droplets are primarily located in slower-moving flow regions, and almost none exists in the faster gaseous stream.

A few spherical droplets are considered to provide examples of local droplet Weber number defined as $We_{\mathrm{d}} = \frac{\rho_{\mathrm{d}} \Delta U^2 D_{\mathrm{d}}}{\sigma_{\mathrm{d}}}$, where ρ_{d} is an approximate droplet density, ΔU is an approximate relative velocity between the droplet and the surrounding gas, D_{d} is an approximate droplet diameter and σ_{d} is an average surface-tension coefficient based on the droplet's surface composition and temperature. Three different spherical droplets at different pressures centered at (x_{d}, y_{d}, z_{d}) are shown in Table 6.4: a droplet from case A2 at $t^* = 14.7$ located at (11.4, 17.3, 16.4) μm, a droplet from case B2 at $t^* = 13.75$ located at (22.9, 10.0, 2.1) μm and a droplet from case C1 at $t^* = 15$ located at (17.0, 13.9, 15.0) μm. The size of these droplets ranges from 0.47 μm to 0.67 μm and the local Weber numbers are well below unity (i.e., $We_{\mathrm{d}} < 1$). Thus, surface tension is greater than inertial terms, allowing the liquid structure to maintain a spherical shape.

Table 6.4: Spherical droplets at three different thermodynamic pressures: case A2 at 50 bar and $t^* = 14.7$, case B2 at 100 bar and $t^* = 13.75$, and case C1 at 150 bar and $t^* = 15$. Their location, approximate size and properties are shown, as well as their local Weber number.

Case	x_d (μm)	y_d (μm)	z_d (μm)	ρ_d (kg/m^3)	D_d (μm)	ΔU (m/s)	σ_d (mN/m)	We_d
A2	11.4	17.3	16.4	564	0.67	3.0	6.3	0.54
B2	22.9	10.0	2.1	557	0.60	1.25	4.4	0.12
C1	17.0	13.9	15.0	510	0.47	0.50	1.8	0.033

Furthermore, the mesh resolution appears to be low enough to resolve the majority of the droplets. Only a few droplets fall into the sub-grid scale, but droplets are essentially non-existent below a certain size. This size boundary may be mesh-dependent. However, it is difficult to claim that the lifetime of such droplets is essential for the development of the two-phase flow. As previously noted, such tiny droplets evaporate quickly and may not be adequately represented by the discrete numerical methods. Moreover, resolving such tiny droplets should not be a reasonable expectation for a two-phase solver that considers phase change.

On the other hand, many droplets have only two or three cells throughout their diameter. This issue induces some under-resolution effects in the results, but it is estimated to have a minor impact on the overall development of the liquid jet. The effective volume of the droplets (i.e., $V_e = \pi D_e^3/6$) is biased toward the bigger diameters, as illustrated in Figure 6.28. As a result, better-resolved droplets with five cells per diameter or more represent nearly all of the liquid volume contained in the droplets.

The modest droplet size and generally uniform size distributions across all configurations raise the question of whether numerical breakup affects droplet formation as well. For example, it has been discussed in previous Subsections 6.3.1 and 6.3.2 that mesh resolution can influence the exact time for the hole formation or the lobe burst. Nonetheless, there are significant differences in the interface deformation patterns across all cases, indicating

that droplet size distributions obtained later are connected to two-phase flow dynamics rather than a specific numerical setup. Additionally, Table 6.4 shows that surface-tension forces can generate spherical droplets in some domain regions. In any case, because droplet formation is restricted to very small scales, the findings presented in this section underscore the critical role that ligaments may play in two-phase mixing at high pressures.

The ligament's characteristic size may also be studied. For this study, the ligament is assumed to be an exact cylinder. Because it is difficult to include other geometric parameters that may describe the geometry of the ligament, this assumption simplifies the analysis. The actual picture may be different; the flow dynamics can bend or curve several ligaments, mainly when high pressures cause considerable stretching. The diameter and length are calculated using the cylinder assumption from its surface area and volume. Unfortunately, this technique lacks the desired robustness. When the shape of a ligament deviates significantly from that of a perfect cylinder, estimated lengths may become nonphysical (e.g., negative or imaginary). As a result, a different approach is taken to achieve effective lengths that may characterize the ligament's size.

The cylinder's volume-to-surface ratio is $V/S = DL/(2D + 4L)$, where D is the diameter and L is the length. Assuming $L >> D$, the approximation $2D + 4L \approx 4L$ is accepted; consequently, $V/S \approx D_e/4$ defines an effective diameter, D_e, for the ligament. The effective length, L_e, is therefore calculated using the volume of a cylinder $V = \pi D_e^2 L_e/4$ rather than the surface area of a cylinder. In this manner, a robust technique is applied in which L_e is always positive. Using this approach, only a few ligaments present inconsistent effective lengths (e.g., too small or too large).

The normalized distribution of L_e and D_e for case C3 at $t^* = 14.7$ is shown in Figure 6.29a. The effective length can be an order of magnitude higher than its effective diameter, indicating the creation of highly elongated ligaments. On the other hand, as ligaments stretch as filaments and vaporization rates accelerate, the effective diameter of the ligaments can

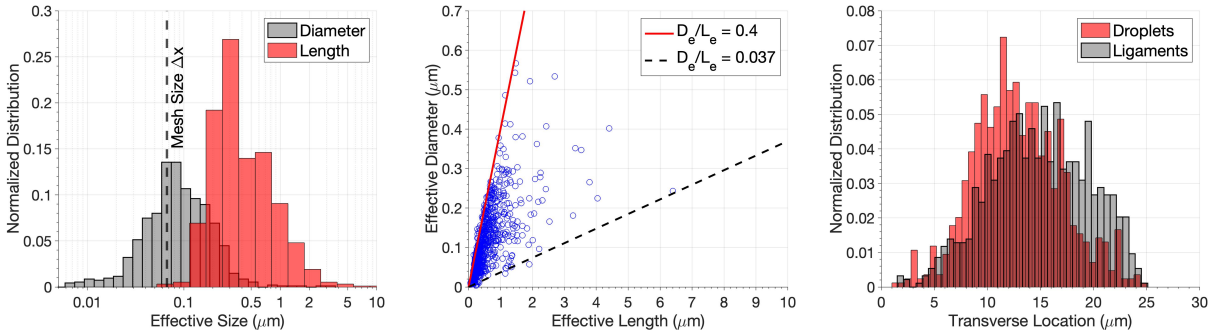

(a) (b) (c)

Figure 6.29: Effective ligament length and diameter and spatial distribution of ligaments and droplets at 150 bar and $u_G = 70$ m/s (i.e., case C3) for the non-dimensional time of $t^* = 14.7$. (a) effective diameter and effective length distribution. Notice the logarithmic scale used in the horizontal axis; (b) correlation between effective diameter and effective length; and (c) spatial distribution of ligaments and droplets [140].

easily become under-resolved. This scenario is expected in places where inertial terms have a significant role (i.e., regions with higher velocities). Like the under-resolved droplets, demanding a finer mesh to resolve the ligament thickness better as it stretches is unrealistic. The lower surface tension reduces the chance of droplets developing from ligament necking. Vaporization will rapidly reduce the liquid volume at such small scales, resulting in a limited lifetime for the thin portion of the ligament. Comparable effective lengths and diameters are achieved for all cases; however, each distribution changes slightly. Figures for all analyzed configurations depicting the size and location distributions of ligaments are provided in Appendix G.1.

An examination of the correlation between the effective length and the effective diameter for case C3 at $t^* = 14.7$ reveals a general tendency in which longer ligaments have bigger diameters (see Figure 6.29b). For all studied configurations, a boundary described by $D_e/L_e = 0.4$ emerges, and practically all ligaments have a similar D_e/L_e ratio. However, there are some exceptions, and each case has some ligaments with greater length-to-diameter ratios. For example, in the illustrated case C3, the upper limit defining elongated ligaments is represented by a trend line defined by $D_e/L_e = 0.037$. Note that the threshold defined

by $D_e/L_e = 0.4$ occurs due to the ligament and droplet classification criteria utilized in this work. For $D_e/L_e > 0.4$, every structure represented by the cylindrical ligament assumption is categorized as a droplet.

Finally, a distribution of the transverse location of each liquid structure is presented. An average transverse location determined from all interface cells defining the structure is employed for this. Figure 6.29c depicts such a distribution for case C3 at $t^* = 14.7$. It is noteworthy that both ligaments and droplets can be found throughout the two-phase mixture region. Ligaments are more concentrated in the layering region where they are created, whereas droplets are concentrated closer to the jet core underneath the growing liquid perturbation and liquid layers. The liquid phase breaks up in a well-defined zone, and no structures are found above the top layers or liquid sheets that form at 150 bar. This observation could be the result of two things. First, as discussed in Subsection 6.3.4, layering inhibits the entrainment of the gas phase. Therefore, the transverse development of the two-phase mixture is confined. Then, small droplets or ligaments released into the hotter gas stream may evaporate quickly enough that they do not get too far above the liquid layers before completely disappearing. Lower pressure scenarios (i.e., 50 bar) show a faster transverse growth later in time with the existence of a few droplets above the liquid jet, as seen in Section 6.6. Layering is not a predominant deformation mechanism at 50 bar hence the transverse development is faster.

6.6 Transverse Development and Surface-Area Growth

This section examines some of the general deformation characteristics of transcritical liquid jets. The transverse development of the liquid jet, the surface-area expansion of the jet divided by the liquid volume, and the surface area ratio between detached liquid structures and the entire liquid-phase surface area are all shown in Figure 6.30. The first sub-figure

indicates how quickly the jet expands away from the centerline, whereas the second sub-figure shows the surface-area growth and the characteristic length of the jet structure as it deforms. The two-phase mechanism that promotes surface-area expansion is highlighted in the third sub-figure.

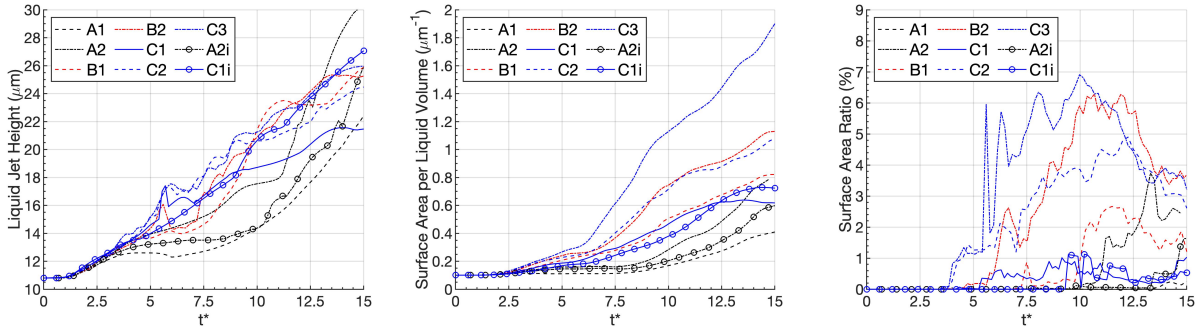

(a) (b) (c)

Figure 6.30: Temporal evolution of the transverse development or height of the liquid jet, the surface-area-to-liquid-volume ratio and the surface area ratio between detached liquid structures (i.e., ligaments and droplets) and the total liquid-phase surface area. A non-dimensional time is obtained as $t^* = t/t_c = t\frac{u_G}{H}$. (a) surface area per liquid volume; (b) liquid jet height in the transverse direction; and (c) surface area ratio of detached liquid structures [140].

The analysis of the liquid jet height evolution presented in Figure 6.30a reveals that the transverse development of the jet is similar for very high pressures of 100 bar and above. Surface-tension forces are weak and only have an impact on the smallest scales. As a result, the growth of the initial perturbation, wave rolling, and subsequent creation of liquid sheets becomes a significant feature determining the two-phase mixture's transverse development. Layering, as mentioned in Subsection 6.3.4, limits the entrainment of the gas phase, which would increase the transverse expansion of the two-phase mixture. The initial surface perturbation does not expand as quickly at 50 bar as at higher pressures. Yet, the limited layering encourages the transverse growth of the jet later in time, and case A1 eventually has the same jet height as case C1. Moreover, case A2 can expand quicker than high-pressure cases.

Although the incompressible case C1i develops quicker than its compressible equivalent or case C1, both configurations exhibit a comparable surface deformation over time. Differences

arise because the incompressible case is unaffected by mixing, and so it does not deform as much as the compressible case. That is, the liquid layers' edges do not roll as easily, and holes emerge less often. These differences are sufficient to cause the upper liquid layer to expand faster in the transverse direction in the incompressible computation. On the other hand, a comparison between case A2 and A2i shows a faster transverse development for the compressible case. Here, the formation of ligaments and droplets in case A2 explains the difference. Because of the limited layering at 50 bar, ligaments and droplets that form more frequently in the real-fluid computation are more easily ejected from the jet's core.

The absolute surface-area growth is also represented by the surface-area growth divided by the instantaneous liquid volume (see Figure 6.30b). Although it could be argued that such representation should be achieved using the initial liquid volume as a fixed parameter, the volume of the liquid phase does not change considerably during the time covered in this study, as seen in Figure 6.32a. Another benefit of representing the surface area per unit volume is that it removes the reliance on the size of the domain. The value of surface area would depend on how big the domain is and how much liquid is contained.

All configurations begin with a surface area per unit volume of about 0.1 μm^{-1}, which specifies the characteristic length of the jet, $L_{\text{jet}} = V_{\text{jet}}/S_{\text{jet}}$, to be $L_{\text{jet}} = 10$ μm or the jet half-thickness, H'. This characteristic length decreases over time as lobes, ligaments, and droplets form. The 50-bar cases have $L_{\text{jet}} = 1.27 - 2.44$ μm, the 100-bar cases have $L_{\text{jet}} = 0.89 - 1.22$ μm, and the 150-bar cases have $L_{\text{jet}} = 0.53 - 1.62$ μm at $t^* = 15$. Surface-area growth, as expected, scales with We_G. That is, as the surface-tension coefficient drops with pressure and the gas freestream velocity increases, the relative strength of the inertial forces diminishes, resulting in smaller structures and a larger surface area.

An examination of the individual influence of detached liquid structures on the total surface area reveals that the primary process for surface-area growth may not be the traditional generation of ligaments and droplets due to liquid jet atomization. The surface area ratio

between the surface area of detached ligaments and droplets and the total surface area of the liquid phase is shown in Figure 6.30c. Even when ligaments and droplets form abundantly, the surface area of detached liquid structures is never more than 7% of the total surface area. Furthermore, the liquid volume enclosed by the detached ligaments and droplets is substantially smaller than 7% of the entire liquid volume, as these small detached structures have a higher surface area per unit volume than the remainder of the liquid jet. Surface tension tends to minimize the surface area per unit volume, but continuous deformation and fragmentation of a liquid jet into smaller structures increases the available surface area per unit volume.

Figure 6.27 demonstrates that when the layering mechanism becomes dominant at pressures of 100 bar or above, the number of ligaments and droplets decreases. That is, some recombination of liquid structures occurs, but the surface area of the liquid phase continues to rise. This observation adds to the evidence that the early increase in surface area is caused by surface deformation of the liquid jet (e.g., lobe and layer formation) rather than atomization into ligaments and droplets. Given the low surface-tension environment, this outcome is not surprising. Capillary instabilities that cause liquid phase deformation and ligament breakup into droplets can only occur at very small scales. When combined with the variable fluid properties caused by species and thermal mixing at high pressures, the liquid-phase deformation displays features of a gas-like behavior rather than the typical subcritical behavior of liquid injection and spray generation.

6.7 Mass Exchange Across the Interface

The phase change is another significant factor to consider when analyzing liquid injection at transcritical conditions. When liquid fuel is injected into a hotter gas environment, the available energy causes the fuel to vaporize and the liquid volume to decrease. Similar

conditions at very high pressures (i.e., considerably over the critical pressure of the fuel) can, however, exhibit a thermodynamic reversal in which net condensation occurs while the fuel species vaporizes and mixes with the oxidizer [15–17, 19, 139]. This high-pressure feature has been discussed in various earlier sections (i.e., Subsections 2.3.2 and 2.5.2 and Section 5.3).

The energy balance across the interface, influenced by the local flow conditions near the interface (e.g., mixing layer compression and expansion, thermal and concentration gradients), is directly responsible for this thermodynamic reversal. For pressures above 50 bar, one-dimensional configurations with the same binary mixture and initial temperatures as this study reveal that net condensation can occur [15–17]. As detailed in Section 5.3, a complex picture emerges in high-pressure liquid atomization in which net vaporization and net condensation can occur simultaneously in different interface locations as illustrated in Figure 6.31a. This figure shows the local mass flux per unit area across the interface for the configuration C2 at $t^* = 12.5$, with positive values indicating a net vaporization rate and negative values indicating a net condensation rate.

Net condensation occurs in liquid regions with sufficient cool liquid volume able to absorb the heat coming from the hotter gas. As smaller structures form and less liquid volume are available in a particular liquid region, the liquid heats rapidly and, eventually, the energy input from the gas phase cannot be absorbed entirely and may evaporate the liquid mixture. Thus, net vaporization at very high pressures occurs primarily in narrow lobes and liquid layers, as well as detached liquid structures like ligaments and droplets. The temporal evolution of the total mass flow over the contiguous liquid jet and detached liquid structures for case C2 is presented in Figure 6.31b. Since the liquid jet comprises most of the interface surface area, the net contribution of mass exchange across the interface causes net condensation for a considerable amount of time. However, vaporization is particularly intense in ligaments and droplets, which may offset the net condensation from the rest of the liquid phase.

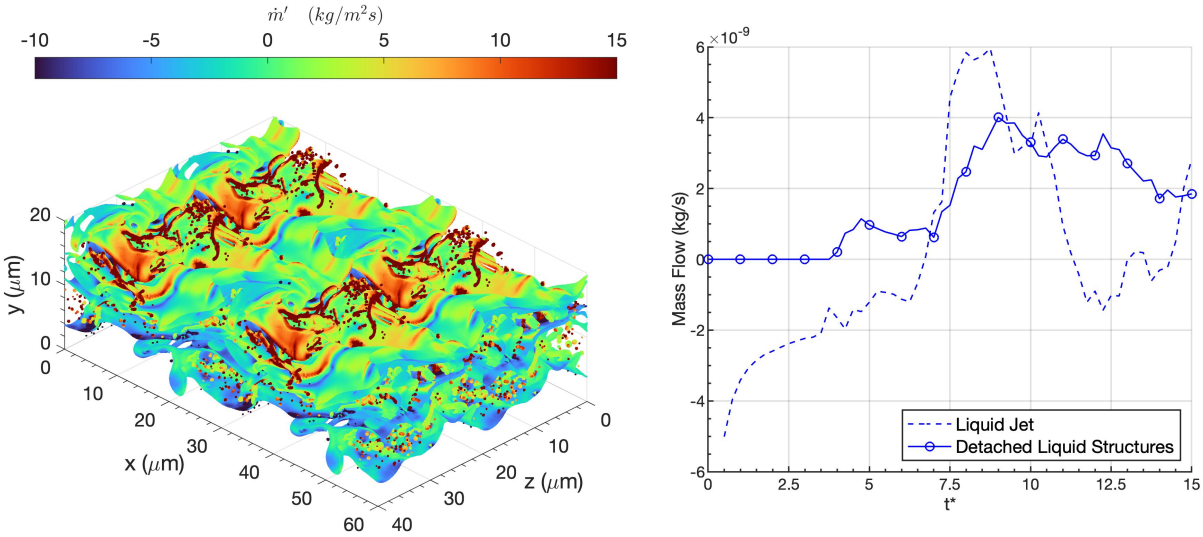

(a) (b)

Figure 6.31: Local mass flux per unit area across the interface at $t^* = 12.5$ and temporal evolution of the mass flow across the liquid surface at 150 bar and $u_G = 50$ m/s (i.e., case C2). A comparison between the mass flow across the main liquid jet and the detached liquid structures is provided. A non-dimensional time is obtained as $t^* = t/t_c = t\frac{u_G}{H}$. (a) local mass flux per unit area; and (b) mass flow across liquid structures [140].

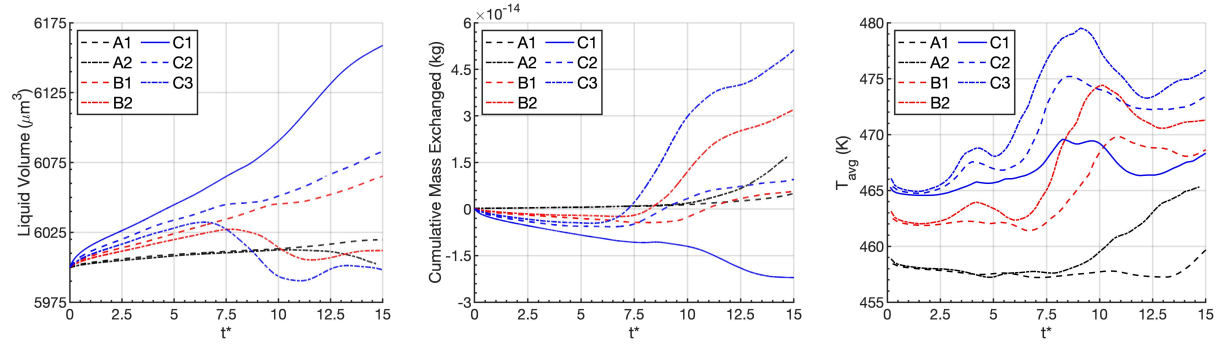

(a) (b) (c)

Figure 6.32: Temporal evolution of the volume of the liquid phase, the cumulative mass exchanged across the interface and the average interface temperature. A non-dimensional time is obtained as $t^* = t/t_c = t\frac{u_G}{H}$. (a) liquid phase volume; (b) cumulative mass exchanged across the interface; and (c) average interface temperature [140].

Although the liquid phase tends to vaporize over time due to mass exchange, the liquid volume may not decrease much. The temporal variations of the liquid-phase volume for all examined cases are shown in Figure 6.32a, and, even though case C2 indicates net evaporation about $t^* = 6.5$, the liquid volume continues to increase. That is, the heating of the liquid

phase, along with increased oxygen dissolution into the liquid as pressure rises, can generate enough local liquid volume expansion to counteract the volume reduction induced by a vaporizing interface.

The production of ligaments and droplets, which is a significant feature in cases A2, B2, C2, and C3, promotes the vaporization of the liquid phase, as seen in Figure 6.32b. In some cases, evaporation rates can be high enough to reduce the total liquid volume (e.g., cases A2, B2, and C3). Limited production of such structures, on the other hand, results in a slowly vaporizing scenario (e.g., case A1) or a continuously condensing case (e.g., case C1). The generation of smaller liquid structures is typically associated with an increase in average interface temperature, as illustrated in Figure 6.32c. The heat from the hotter gas can more quickly raise the temperature of a small liquid structure, causing it to vaporize after enough heating.

Last, the effect of layer formation at pressures more than 100 bar is visible, demonstrating how this deformation mechanism might affect mixing and vaporization. The start of the layering process at $t^* = 10$ defines a peak in the formation of ligaments and droplets, as explained in Section 6.5. Similarly, as the detached structures are sheltered from the hotter gas and their production rate slows, the average interface temperature reaches a peak and decreases. The liquid vaporization rate decreases as some residual ligaments and droplets are fully vaporized or recombine with other liquid structures. Moreover, the total liquid volume may grow again due to the expansion of local liquid volume, overcoming the surface evaporation.

Chapter 7

Three-Dimensional Planar Jet: Vortex Dynamics

The role of vortex dynamics on the surface deformation and the temporal evolution of vortex structures in the three-dimensional configurations presented in Chapter 6 and summarized in Table 6.1 is discussed in this chapter. Section 5.5 shows some preliminary results for a two-dimensional jet, illustrating how the evolution of the vortical motion in the flow field is responsible for the observed liquid surface deformation. Therefore, a similar conclusion is expected for the three-dimensional results. As presented in Subsection 2.1.1, some previous three-dimensional works that deal with incompressible liquid jets show how the evolution and interaction of vortex structures define the deformation cascade process toward atomizing the liquid.

Many aspects of vorticity dynamics can be analyzed, especially for a complex two-phase flow configuration with variable fluid properties. This chapter focuses on the high-pressure regime at 150 bar and the following issues. First, Section 7.1 introduces the vortex identification method employed here and, then, Section 7.2 shows how vortex dynamics explain some of the

early-deformation mechanisms discussed in Section 6.3. Section 7.3 explores the evolution of the vortical structures over time as the surface deforms and moves toward layering at 150 bar. Details on the generation, deformation, and breakup of vortices are given. Lastly, Section 7.4 provides some insights on various features of vortex dynamics that may be analyzed in future works, such as a detailed study of vorticity generation terms in these high-pressure flows, dynamical aspects of the vortex evolution such as helicity or flexion, and how the vortical motion defines the mixing of the fuel vapor in the gas phase.

7.1 The Dynamical Vortex Identification Method

Subsection 2.1.1 and Section 5.5 introduces the dynamical vortex identification λ_ρ method by Yao and Hussain [43] as a proper approach to identify and define vortex structures in compressible flows. The method is a compressible extension of the λ_2 method by Jeong and Hussain [41] and is presented in detail in this section.

The compressible momentum equation, Eq. (3.2), is rewritten here using tensor notation as

$$\frac{\partial}{\partial t}(\rho u_i) + (\rho u_i u_k)_{,k} = -p_{,i} + \tau_{ik,k} \tag{7.1}$$

Note that the localized body force described in Section 4.3 to account for the surface tension is not added. Despite being a source of vorticity generation, surface tension has a negligible total contribution [26]. Therefore, the term is usually neglected in vorticity studies of two-phase flows and can be safely eliminated from the vortex identification method.

Taking the gradient of Eq. (7.1) and using the total or material derivative, D/Dt, the following equation is obtained

$$\frac{D}{Dt}(\rho u_i)_{,j} + (\rho u_i)_{,k} u_{k,j} + (\rho \Theta u_i)_{,j} = -p_{,ij} + \tau_{ik,kj} \tag{7.2}$$

where $\Theta = \nabla \cdot \vec{u} = u_{k,k}$ is the divergence of the velocity field or volume dilatation rate. If we only consider the symmetric part of the previous equation, an equation for the pressure Hessian, $p_{,ij}$, follows as

$$\frac{DS^m_{ji}}{Dt} - S^\tau_{ij} + S^M_{ij} + S^\Theta_{ij} = -p_{,ij} \quad \text{where} \quad \begin{cases} S^m_{ij} = \frac{1}{2}[(\rho u_i)_{,j} + (\rho u_j)_{,i}] \\ S^\tau_{ij} = \frac{1}{2}[\tau_{ik,kj} + \tau_{jk,ki}] \\ S^M_{ij} = \frac{1}{2}[(\rho u_i)_{,k} u_{k,j} + (\rho u_j)_{,k} u_{k,i}] \\ S^\Theta_{ij} = \frac{1}{2}[(\rho \Theta u_i)_{,j} + (\rho \Theta u_j)_{,i}] \end{cases} \tag{7.3}$$

Local pressure minimums in a plane crossing a vortex can identify vortices in a compressible flow. For this, a minimum of a modified pressure Hessian tensor is considered. A vortex is, in other words, a contiguous region with two positive eigenvalues of the modified pressure Hessian. Since pressure minimums might occur in the absence of a vortex, terms such as the unsteady fluid straining and the dilatation component of viscous strain are neglected. Additionally, viscous effects are ignored, eliminating pressure minimums around regions with vortical motion. Therefore, the pressure minimum from a modified pressure Hessian, $p_{,ij} \approx -S^M_{ij} - S^\Theta_{ij}$, is considered as a better vortex identifier.

The requirement for a pressure minimum can also be inferred by analyzing the eigenvalues of $S^M_{ij} + S^\Theta_{ij}$, where two negative eigenvalues are needed. If the tensor eigenvalues are ordered as $\lambda_1 \geq \lambda_2 \geq \lambda_3$, it means $\lambda_2 < 0$. This mathematical requirement is the origin of the nomenclature for the incompressible vortex identification method λ_2, which is replaced by λ_ρ in the compressible or variable-density formulation to emphasize the dynamical analysis once density is included. As noted in Yao and Hussain [43], the term S^M_{ij} can be rewritten as

$$S^M_{ij} = \rho(S_{ik}S_{kj} + \Omega_{ik}\Omega_{kj}) + \frac{\rho_{,k}}{2}(u_i u_{k,j} + u_j u_{k,i}) \tag{7.4}$$

where the first term on the right hand side is a density-weighted λ_2 method. That is, the λ_2 method finds a negative second eigenvalue of the tensor $S_{ik}S_{kj} + \Omega_{ik}\Omega_{kj}$, where S_{ij} is the symmetric component of the gradient of the velocity field, $\nabla\vec{u}$, and Ω_{ij} is the antisymmetric component. This definition is used when post-processing the data obtained from the three-dimensional computations.

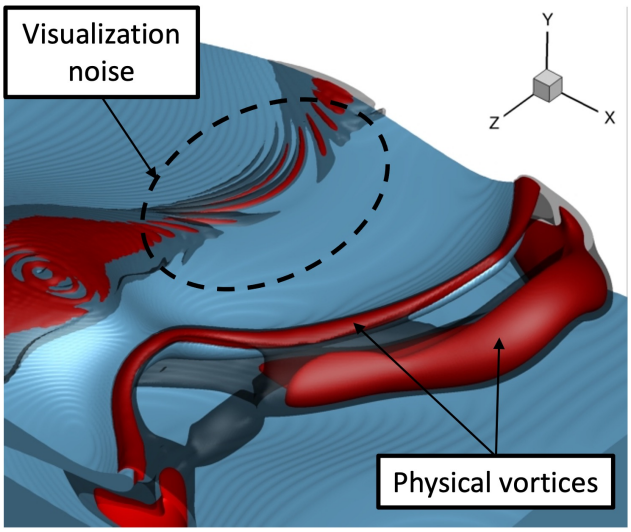

Figure 7.1: λ_ρ visualization noise generated by the sharp interface and the coupled numerical approach used in this dissertation at 150 bar with gas freestream velocity of $u_G = 30$ m/s (i.e., case C1). The interface location is identified as the blue isosurface with $C = 0.5$ and two different isosurfaces of λ_ρ are given: $\lambda_\rho = -2.5 \times 10^{15}$ kg/(m^{3}s^2) (red) and $\lambda_\rho = -1 \times 10^{15}$ kg/(m^{3}s^2) (transparent black). The non-dimensional time $t^* = t/t_c = t\frac{u_G}{H} = 3.75$ is represented.

The λ_ρ method can be applied to many different compressible flows, including two-phase flows. However, care is needed for two-phase simulations using a sharp interface, such as the approach used in this dissertation. This issue is especially problematic if many terms are included sharply (e.g., surface-tension force, mass exchange) and certain variables are extrapolated across the interface. The numerical oscillations and spurious currents have been explained in detail in Chapter 4, but their effect has been deemed negligible for the configurations analyzed in this dissertation (see Appendix F.3). Nonetheless, the spurious currents are magnified when evaluating the λ_ρ variable and can generate visualization noise along the surface, complicating the visualization of vortex structures. Thus, it is essential to

choose a proper value of λ_ρ to be represented. Moreover, as highlighted in Section 5.5, spatial filtering of the velocity field is implemented, and adequate treatment of the density gradient terms (i.e., using phase-wise densities) is also necessary to minimize the visualization noise. With all these considerations, the physical vortices are still well captured.

Figure 7.1 illustrates the visualization noise problem for a snapshot of case C1 at 150 bar at the non-dimensional time of $t^* = 3.75$. Two different λ_ρ isosurfaces are represented to highlight the importance of picking an eigenvalue that limits the visualization noise. A roller vortex or deformed Kelvin-Helmholtz vortex can be seen in front of the growing surface wave. Also, a vortex along the edge of the lobe is captured. However, some visualization noise is apparent on the liquid surface, which does not correspond to a physical vortical motion in the region. The isosurface with value $\lambda_\rho = -1 \times 10^{15}$ kg/(m^{3}s^2) (transparent black) captures a considerable amount of visualization noise, while the isosurface with $\lambda_\rho = -2.5 \times 10^{15}$ kg/(m^{3}s^2) (red) reduces it to some degree and still captures the physical vortices everywhere else.

The λ_ρ approach does not provide information about the rotation direction of the vortex, and the magnitude of the eigenvalue can be understood as a measure of the strength of the vortex in a specific position. Therefore, there is some degree of arbitrariness in choosing a specific value of λ_ρ. In this analysis, a judgment is made to use a λ_ρ value that limits the visualization noise but represents the regions of vortical motion that affect the liquid surface evolution and other physical processes (e.g., fuel mixing). The information provided by λ_ρ is complemented with the velocity and the vorticity fields to obtain more information and accurate representation of the vortices.

7.2 Early-Deformation Mechanisms Explained via Vortex Dynamics

Certain deformation patterns discussed in Section 6.3 can be described using vortex dynamics and information on the velocity field, $\vec{u}$, and the vorticity field, $\vec{\omega} = \nabla \times \vec{u}$ (i.e., $\vec{u} = (u, v, w)$ and $\vec{\omega} = (\omega_x, \omega_y, \omega_z)$, respectively). Compared to previous incompressible works that performed a similar study on the role of vortex dynamics in the deformation of the liquid jet [24–27, 36], the surface deformation in the real jet is defined by the coupling of vortex dynamics and the variation of fluid properties within each phase. Thus, such a vorticity dynamics study is more complex.

In this section, the deformation of the liquid surface is explained by connection with the evolution of the vortical structures. For instance, Subsection 7.2.1 describes the lobe extension, bending, and perforation mechanism seen in case C1, which also is representative of cases B1 and A2, and Subsection 7.2.2 describes the lobe and crest corrugation mechanism observed in cases C2, C3, and B2. These deformation mechanisms are detailed in Subsections 6.3.1 and 6.3.2, respectively. Later, Section 7.3 has the details of the vorticity field: vortex generation, deformation (i.e., stretching and tilting), and the breakup of vortical structures over time.

The reader is also referred to the Supplemental Material where slides have been provided to showcase the evolution of the vortical structures over time for various of the analyzed configurations. Similar to Chapter 6, not all snapshots nor analyzed configurations are presented in this chapter, and only the images necessary to support the discussion are included.

7.2.1 Lobe extension, bending and perforation

The lobe extension, bending and perforation mechanism is explained in this subsection using vorticity dynamics. This deformation pattern has been identified as characteristic for cases A2, B1, and C1, all of which present a similar gas freestream Weber number between $We_G = 476$ and $We_G = 679$. Case C1 is chosen for the study (i.e., thermodynamic pressure of 150 bar and gas freestream velocity of $u_G = 30$ m/s), as it is the configuration with the most significant influence of high-pressure, real-fluid thermodynamics and variable fluid properties. Cases A2 and B1 behave similarly, but the bending and perforation of the lobe are limited as the thermodynamic pressure drops.

The λ_ρ value of -2.5×10^{15} kg/(m^{3}s^2) is chosen to identify the vortex responsible of causing the lobe deformation explained in this subsection. This value minimizes the visualization noise of the λ_ρ isosurface. Figure 7.2 illustrates the evolution of the roller vortex or Kelvin-Helmholtz vortex that forms downstream of the lobe due to the initial shear between both phases. Additionally, two other main vortical structures are identified. A vortex appears along the edge or rim of the lobe or wave, and its formation is discussed in Subsection 7.3.2. This rim vortex is also identified in some configurations of the incompressible two-phase work by Zandian et al. [27], although the vortex is referred to as a hairpin vortex due to its deformation following the lobe (e.g., see Figure 10a or Figure 10b from Zandian et al. [27]). Also, a vortex is identified in the liquid phase due to the density-weighting effect of the λ_ρ method. This vortex is the reciprocal roller vortex in the liquid phase and pushes the liquid underneath the wave crest, aiding in the growth of the perturbation. The three identified vortices rotate clockwise when observed from the represented xy planes. Nonetheless, this subsection focuses on the roller vortex responsible for the stretching, bending, and hole formation of the initial lobe.

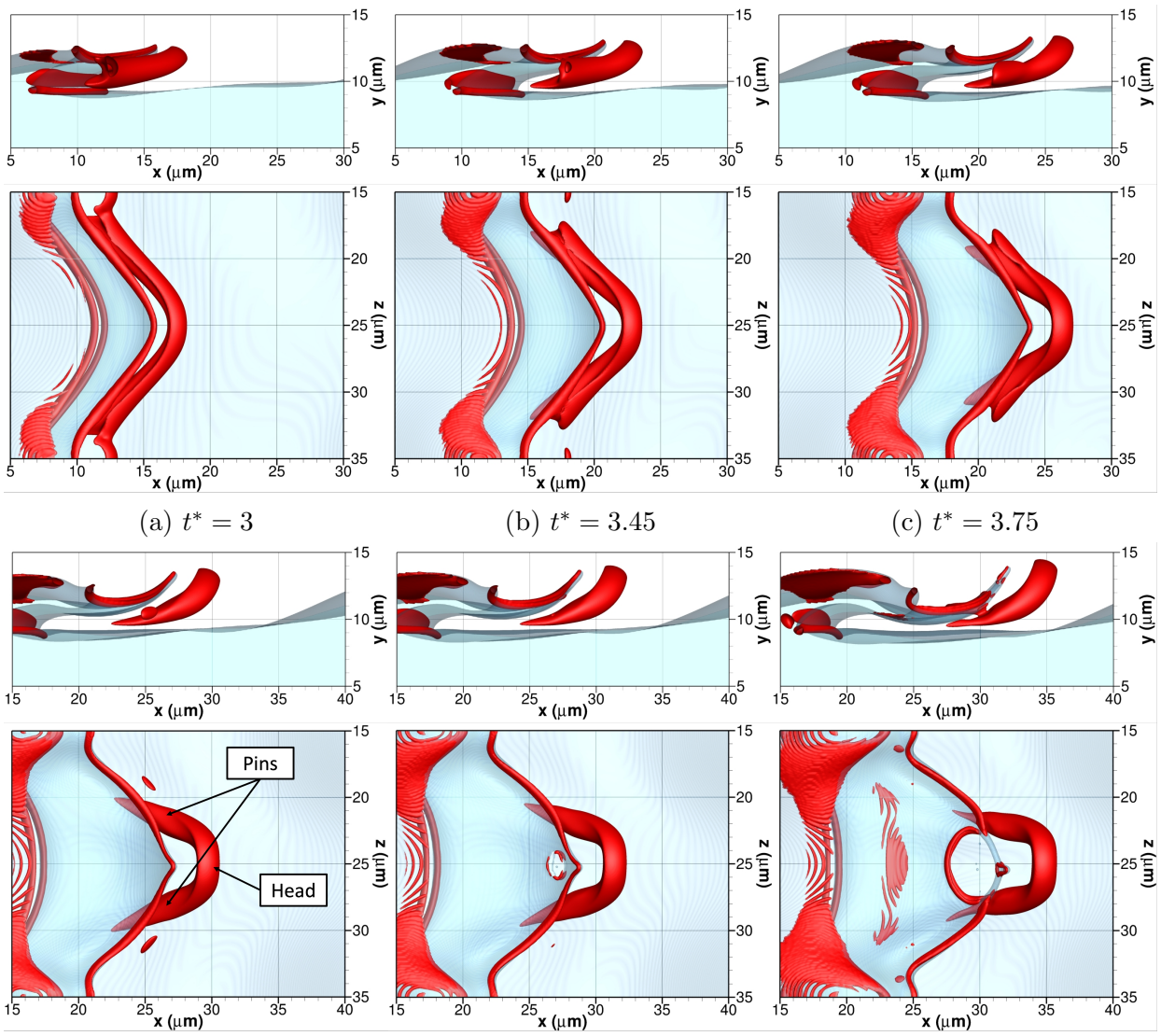

(a) $t^* = 3$ (b) $t^* = 3.45$ (c) $t^* = 3.75$

(d) $t^* = 4.05$ (e) $t^* = 4.2$ (f) $t^* = 4.5$

Figure 7.2: Vortex dynamics of the lobe extension, bending and perforation deformation mechanism at 150 bar with gas freestream velocity of $u_G = 30$ m/s (i.e., case C1). The top figures show the side view from an xy plane located at $z = 35$ μm and the bottom figures show the top view from an xz plane located above the liquid surface. The interface location is identified as the transparent blue isosurface with $C = 0.5$ and the vortex structures are identified by the red isosurface with $\lambda_\rho = -2.5 \times 10^{15}$ kg/(m^{3}s^2). A non-dimensional time is obtained as $t^* = t/t_c = t\frac{u_G}{H}$. (a) $t^* = 3$; (b) $t^* = 3.45$; (c) $t^* = 3.75$; (d) $t^* = 4.05$; (e) $t^* = 4.2$; and (f) $t^* = 4.5$.

As seen in Figure 7.2, the roller vortex downstream of the wave quickly deforms into a hairpin vortex around the coordinate $z = 25$ μm. At the same time, other regions of the roller vortex weaken and the magnitude of the λ_ρ eigenvalue falls below the threshold used

here. At $t^* = 3$, the roller vortex is located right in front of the lobe. The vortical motion in the gas phase, coupled with the denser gas phase at 150 bar and the considerable decrease in liquid-phase density and viscosity under thermal and species mixing, can stretch the lobe. The snapshots from $t^* = 3.45$ to $t^* = 4.05$ show the roller vortex deformation into a hairpin vortex. As the vortex "pins" align with the flow in the streamwise direction, the induced velocity field pushes the "head" of the vortex upward in the transverse direction toward the faster-moving gas. Then, the hairpin vortex begins to stretch along the streamwise direction.

The lobe deforms together with the hairpin vortex. As the hairpin head moves upwards, the lobe is carried by the induced velocity; it stretches and its tip bends upwards as well. In the process, the pins move under the lobe. In other words, the hairpin vortex pushes gas under itself and into the bottom surface of the lobe. The lobe stretches and curves very easily with similar fluid properties between the gas and liquid phases (i.e., see Figure 6.9), eventually facing the incoming gas stream with a steep slope. Between $t^* = 4.05$ and $t^* = 4.2$, the perforation event occurs and a hole forms, which quickly expands as seen at $t^* = 4.5$. Note that another rim vortex forms along the upstream edge of the hole.

The local velocity and vorticity fields right before the hole formation provide more insight into the deformation mechanism. Figures 7.3 and 7.4 depict the components of the velocity and vorticity fields in two planes crossing the lobe and the hairpin vortex at $t^* = 4.05$: an xy plane cutting the lobe through its center at a constant coordinate $z = 25$ μm and a yz plane cutting the lobe along the spanwise direction near its tip with a constant coordinate $x = 26$ μm. The rotation of various vortices is highlighted.

The strong vorticity associated with the head and the pins of the vortex is illustrated. Figure 7.3f shows how the vorticity vector in the vortex head is mainly aligned with the spanwise direction (i.e., z axis), while the vorticity vector in the vortex pins is predominantly aligned with the streamwise direction or the x axis, as depicted in Figure 7.4b. The vorticity around the rim vortex is also noteworthy. Such vortical motion defines the deformation

and bending of the lobe. As seen in Figures 7.3c, 7.4c and 7.4e, which show the v and w components of the velocity field in different planes, the gas phase flows underneath the hairpin vortex and is ejected upwards toward the lobe. This fluid motion is enough to bend the thin lobe as the liquid properties in that region resemble more those of a gas.

Additionally, the two cross-sections show how thin the liquid lobe becomes in the region where the hole forms later. The hole formation process is caused by the gas phase perforating such a thin liquid structure. As explained in Subsection 6.3.1, the lobe bends steeply facing the gas stream. It is easily perforated coupled with the strong gas entrainment below the lobe. Moreover, the plots of the velocity components and the vorticity field provide some more insight into the stretching of the lobe and the evolution of its thickness. The lobe is not only stretched along the streamwise direction as its tip submerges into faster gas regions (i.e., as highlighted in Figure 7.3a); it is also stretched along the spanwise direction, as clearly seen in Figure 7.4e. The pins of the hairpin vortex displace the two opposite edges of the lobe in the z direction, effectively separating them and generating a thin film in between.

The ease with which localized stretching occurs in the liquid phase can also be related to the bigger-picture deformation of high-pressure cases where liquid stretching and folding precedes the formation of liquid sheets or layers. As explained in Subsection 6.3.4, this deformation mechanism, referred to as layering, becomes dominant for low surface-tension configurations with enhanced intraphase mixing at high pressures.

The vortex structure evolution varies with pressure as well. Nonetheless, a strong coupling exists between the deformation of the vortices and the intraphase mixing responsible for the substantial variations in fluid properties, especially in the liquid phase. Although this characteristic of the atomization of real fluids needs to be studied in detail, this chapter only focuses on certain dynamical aspects and summarizes some of the observed main features.

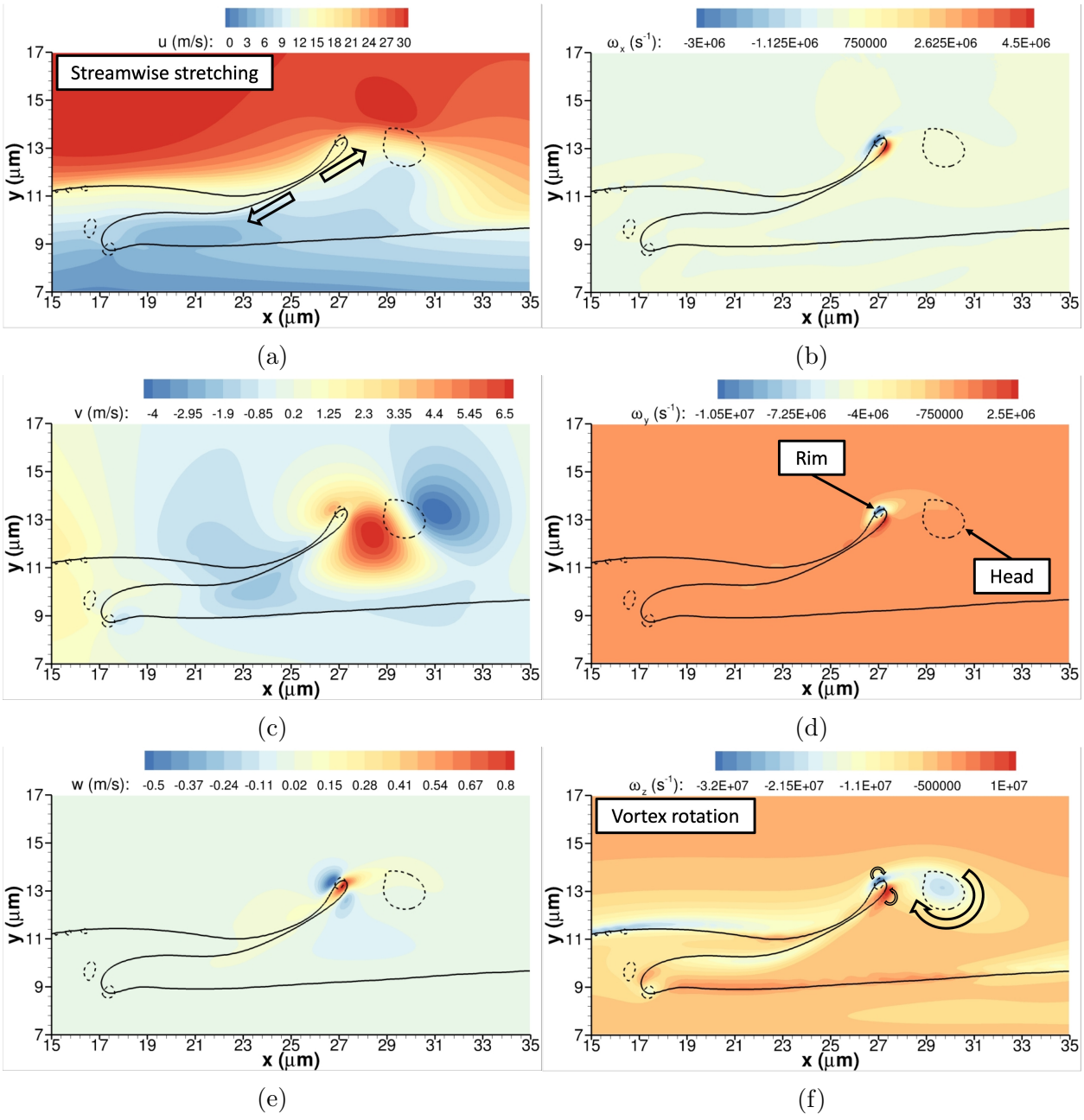

Figure 7.3: Vortex dynamics of the lobe extension, bending and perforation deformation mechanism at 150 bar with gas freestream velocity of $u_G = 30$ m/s (i.e., case C1) at the non-dimensional time $t^* = t/t_c = t\frac{u_G}{H} = 4.05$. The contours of the velocity and vorticity fields are shown on an xy plane located at $z = 25$ μm. The interface location is identified as the solid black curve representing the isocontour with $C = 0.5$ and the cut vortex structures are identified by the dashed black isocontour with $\lambda_\rho = -2.5 \times 10^{15}$ kg/(m^{3}s^2). (a) u velocity component; (b) ω_x vorticity component; (c) v velocity component; (d) ω_y vorticity component; (e) w velocity component; and (f) ω_z vorticity component.

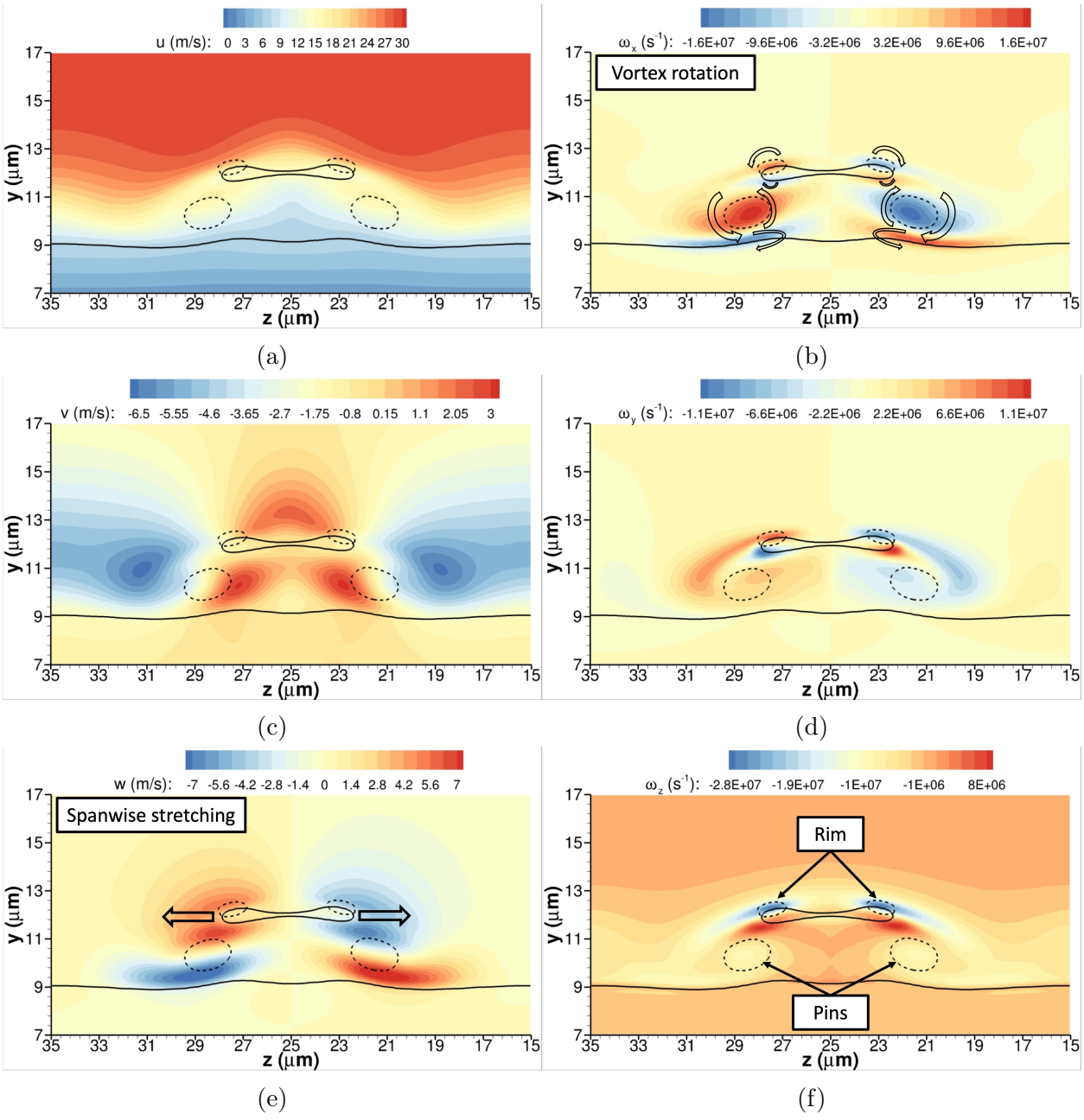

Figure 7.4: Vortex dynamics of the lobe extension, bending and perforation deformation mechanism at 150 bar with gas freestream velocity of $u_G = 30$ m/s (i.e., case C1) at the non-dimensional time $t^* = t/t_c = t\frac{u_G}{H} = 4.05$. The contours of the velocity and vorticity fields are shown on an yz plane located at $x = 26$ μm. The interface location is identified as the solid black curve representing the isocontour with $C = 0.5$ and the cut vortex structures are identified by the dashed black isocontour with $\lambda_\rho = -2.5 \times 10^{15}$ kg/(m^{3}s^2). (a) u velocity component; (b) ω_x vorticity component; (c) v velocity component; (d) ω_y vorticity component; (e) w velocity component; and (f) ω_z vorticity component.

A combination of mixing effects and the deformation of the roller vortex explains why the initial lobe in cases A2, B1, and C1 deforms differently after stretching despite having similar We_G. Additionally, the influence of mixing in the liquid phase is highlighted by case C1i. As illustrated in Figure 7.2, Figure 7.5 presents the liquid lobe and the deformed roller vortex for cases A2, B1 and C1i around the non-dimensional time of $t^* \approx 4$, right before the lobe perforation occurs in cases B1 and C1. Various features are identified and described by these figures.

The roller vortex evolves similarly for all cases. However, the deformation into a hairpin vortex is only apparent at very high pressures, regardless of the fluid being considered compressible under non-ideal thermodynamics or incompressible with constant fluid properties. At 50 bar, the roller vortex stretches faster into the oxidizer stream (i.e., it is subject to higher velocities) and breaks up quickly, resulting in the hairpin head weakening. In comparison, the head of the hairpin vortex remains strong for a long time in configurations at 100 bar and 150 bar, defining the flow patterns in the gas phase. Then, the interaction of the vortex with the liquid structure is defined by the fluid properties of each phase.

Lower ambient pressures translate into a higher surface-tension force, a thicker lobe with rounded edges and a lesser influence of species and thermal mixing in the liquid phase, with the lobe's liquid properties being more similar to the properties of the liquid core. Additionally, the gas phase becomes less dense. As explained in Subsection 6.3.1, the high-pressure lobe is more easily affected by the denser gas due to the enhanced mixing effects that cause the local liquid density and viscosity to drop sharply. Thus, the vortical motion defined by the hairpin vortex can stretch more easily the lobe in the streamwise and spanwise directions as the thermodynamic pressure increases, bending the lobe upwards and generating a thin lobe region that precedes the perforation event.

Figure 7.2d at 150 bar shows the lobe extending over the vortex pins with the tip being close to the vortex head. At 100 bar, the lobe cannot stretch so easily (see Figure 7.5b). As a

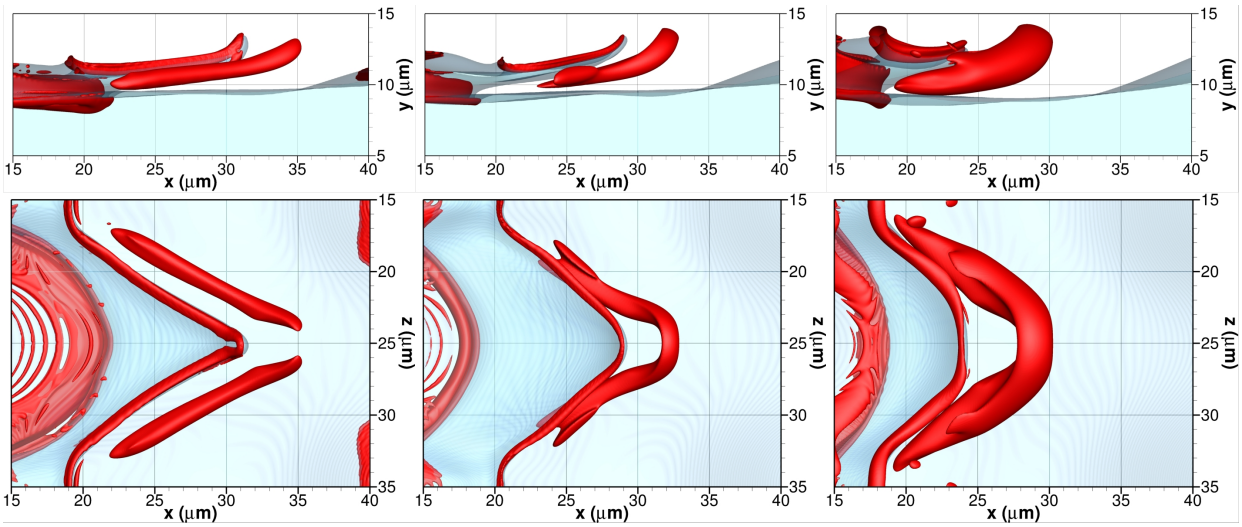

(a) case A2 at $t^* = 4.20$ (b) case B1 at $t^* = 4.00$ (c) case C1i at $t^* = 4.05$

Figure 7.5: Pressure and mixing effects on the vortex dynamics of the early lobe extension comparing cases A2, B1 and C1i with similar We_G. The reader is referred to Figure 7.2 for a comparison with case C1. The top figures show the side view from an xy plane located at $z = 35$ μm and the bottom figures show the top view from an xz plane located above the liquid surface. The interface location is identified as the transparent blue isosurface with $C = 0.5$ and the vortex structures are identified by the red isosurface of λ_ρ. A non-dimensional time is obtained as $t^* = t/t_c = t\frac{u_G}{H}$. (a) case A2 at $t^* = 4.20$ with $\lambda_\rho = -3\times10^{15}$ kg/(m^{3}s^2); (b) case B1 at $t^* = 4.00$ with $\lambda_\rho = -5 \times 10^{15}$ kg/(m^{3}s^2); and (c) case C1i at $t^* = 4.05$ with $\lambda_\rho = -1 \times 10^{15}$ kg/(m^{3}s^2).

result, the vortex head and the lobe's tip are farther apart, while the lobe barely covers the vortex pins. Nevertheless, the lobe stretching and bending are enough to cause the formation of a hole as well. In comparison, as seen in Figure 7.5a, almost no spanwise stretching occurs at 50 bar, and the vortex pins are downstream and far from the lobe's edge, which explains why it is not possible to form a hole. At 50 bar, mixing is not very strong within the lobe, and the roller vortex deforms and stretches into the oxidizer stream too quickly. The importance of fluid properties variations is also reflected in Figure 7.5c, which illustrates the incompressible case C1i (i.e., 150 bar) with constant fluid properties. Even though the hairpin vortex evolves very similar to the real-fluid problem, the denser and more viscous lobe cannot be stretched as easily as in the compressible configuration, and a hole does not develop so early.

Lastly, it may be necessary to analyze whether there is a coupled mechanism in the real-fluid configurations that tends to align the vortex pins faster with the streamwise direction; thus, contributing to the vortex pins moving under the lobe as it stretches. Comparing cases A2, B1, and C1, the alignment of the vortex pins with the streamwise direction is more pronounced for a similar non-dimensional time as pressure increases. That is, the angle between the pins and the streamwise direction slightly drops as pressure increases. Noticeably, the hairpin vortex in the incompressible case C1i shows pins with a greater angle than its real-fluid counterpart.

7.2.2 Lobe and crest corrugation

In this subsection, attention focuses on the deformation mechanism defined by the corrugation of the initial lobe and the perturbation crest detailed in Subsection 6.3.2. Similar to Subsection 7.2.1, vortex dynamics also explain the deformation of the liquid surface. The lobe and crest corrugation mechanism is visible in cases B2, C2, and C3 at pressures of 100 bar and 150 bar, where all configurations are defined by $We_G > 1000$. Crest corrugation is also visible in other cases with lower We_G but to a lesser extent. Figure 7.6 shows the evolution of the vortical structures over time for case C2 at 150 bar and with a gas freestream velocity of $u_G = 50$ m/s. As done in Subsection 7.2.1, the highest-pressure case is chosen for the analysis. Therefore, the surface deformation detailed in this subsection is possible due to the liquid phase's low local density and viscosity. The value of $\lambda_\rho = -9 \times 10^{15}$ kg/(m^{3}s^2) is chosen to represent the isosurfaces defining a vortex. For further visual aid, the reader is referred to Figure 6.12.

The evolution of the roller vortex clearly explains lobe corrugation. Compared to case C1 or the vortex behavior for the lobe extension, bending, and perforation mechanism, here the initial roller vortex remains attached to the lobe's edge as seen in Figure 7.6a at $t^* = 2.50$

and is responsible for early lobe stretching in the streamwise direction. As described in the previous subsection, the rotation of this vortex is clockwise when observed from the depicted xy planes. Moreover, the reciprocal roller vortex is also visible in the liquid phase, but the rim vortex does not appear. Initially, it may be merged with the roller vortex attached to the edge of the lobe, yet it does not form later during the corrugation process.

The roller vortex in case C2 also deforms into a hairpin vortex. However, a combined effect between the lobe stretching caused by the vortical motion and the vortex evolution itself displace the vortex pins under the lobe between $t^* = 2.50$ and $t^* = 3.50$. Starting around $t^* \approx 3.50$, the vortex pins are fully captured by the lobe along its edge while the vortex head remains attached to the lobe's tip. The trapped vortex quickly stretches the lobe in the spanwise direction while at the same time accelerates the entrainment of the gas phase underneath the lobe. Thus, the lobe turns into a thin sheet that corrugates or curves along the x axis, resembling a bag that inflates rapidly due to the gas flowing into it.

This process can be seen from Figure 7.7a to Figure 7.7c, which show the contours of the vorticity component in the streamwise direction, ω_x, in yz planes cutting the early lobe at different x coordinates over time. These figures illustrate three snapshots: a yz plane with $x = 17$ μm at $t^* = 3.00$, a yz plane with $x = 23$ μm at $t^* = 3.50$ and a yz plane with $x = 27$ μm at $t^* = 4.00$. Once the vortex moves under the lobe, the spanwise stretching curves the lobe's surface downwards, reducing the gap between the lobe and the liquid core surface. This area reduction accelerates the gas entrainment under the lobe, effectively generating a transverse jet that corrugates the lobe, bends its surface, and promotes stretching and thinning of the liquid structure. The strong gas-phase entrainment occurring with the gap reduction is highlighted in the ω_x contour plots in Figure 7.7a and Figure 7.7b. The strength of the vorticity in the streamwise direction increases as the gap closes, and some counter-rotating vorticity (i.e., with respect to the identified vortex pins) is generated right on top

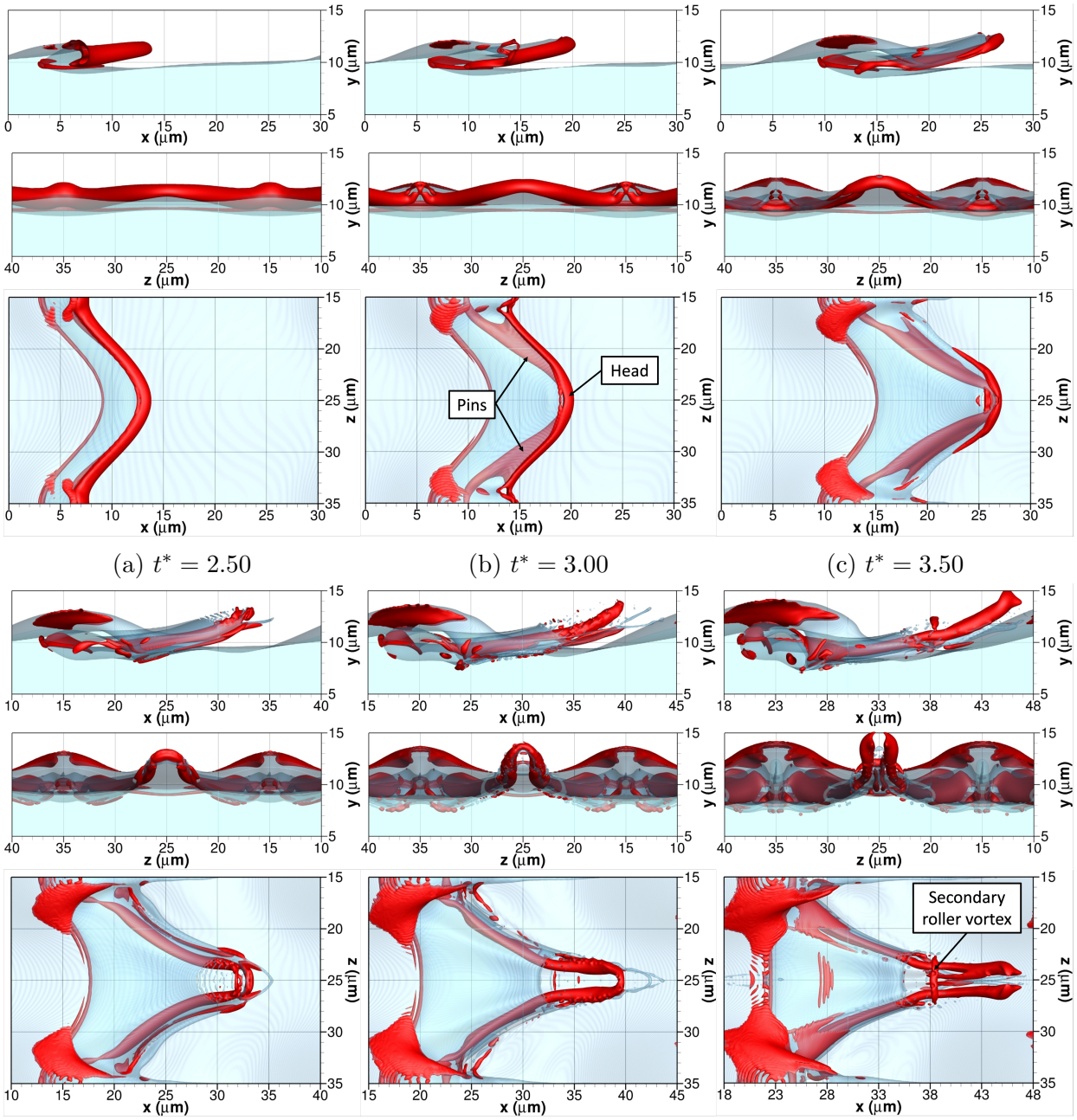

(a) $t^* = 2.50$ (b) $t^* = 3.00$ (c) $t^* = 3.50$

(d) $t^* = 4.00$ (e) $t^* = 4.50$ (f) $t^* = 5.00$

Figure 7.6: Vortex dynamics of the lobe and crest corrugation deformation mechanism at 150 bar with gas freestream velocity of $u_G = 50$ m/s (i.e., case C2). The top figures show the side view from an xy plane located at $z = 35$ μm, the middle figures show the side view from a yz plane located at each respective last x coordinate shown in the other subfigures and the bottom figures show the top view from an xz plane located above the liquid surface. The interface location is identified as the transparent blue isosurface with $C = 0.5$ and the vortex structures are identified by the red isosurface with $\lambda_\rho = -9 \times 10^{15}$ kg/(m^{3}s^2). A non-dimensional time is obtained as $t^* = t/t_c = t\frac{u_G}{H}$. (a) $t^* = 2.50$; (b) $t^* = 3.00$; (c) $t^* = 3.50$; (d) $t^* = 4.00$; (e) $t^* = 4.50$; and (f) $t^* = 5.00$.

of the liquid core surface. As a reference for the reader, $\omega_x > 0$ means counterclockwise rotation and $\omega_x < 0$ means clockwise rotation in the depicted yz planes.

This vortex capturing mechanism has not been described in previous incompressible two-phase works by Jarrahbashi et al. [25], and Zandian et al. [27]. In these incompressible studies, vortex overlapping is observed but where only one vortex flows under the lobe. That is, the hairpin vortex remains above the lobe. The results presented in this subsection differ substantially from what has been shown in earlier work, and the differences are attributed mainly to the high-pressure environment. As shown in Figure 7.5, the roller vortex separates from the early lobe as the thermodynamic pressure drops for two main reasons: higher surface-tension force and reduced mixing in the liquid phase, with the liquid fluid properties in the lobe being less similar to those of the gas phase. At very high pressures, the roller vortex downstream of the lobe stretches the liquid fast enough such that the lobe can flow past the vortex and wrap around it, effectively trapping the vortex underneath the lobe.

The thin lobe bursts into droplets near the tip, as detailed in Subsection 6.3.2. This event starts right at the lobe's tip, where the vortex head is located. The strong vortical motion coupled with the stretching of the lobe in the streamwise and spanwise directions allows for the gas phase to perforate the lobe (see Figure 7.6c). Then, the hole quickly recedes under the action of surface tension and the strong recirculation generated by the hairpin vortex. The thin liquid film is broken during the process and tiny droplets form.

Various developments occur from $t^* = 3.50$ to $t^* = 5.00$ once the lobe starts to break up. Liquid structures and vortex structures stretch rather fast into the oxidizer stream. Ligaments and droplets are seen, and the hairpin vortex extends considerably. Moreover, other vortical structures are generated due to the breakup process, as pointed out in Figure 7.6f where a secondary roller vortex forms on top of the vortex pins downstream of the lobe. Then, as the perturbation wave grows behind the lobe, the lobe is pushed downward toward the liquid surface, and, eventually, the edges of the lobe merge with the rest of the liquid jet.

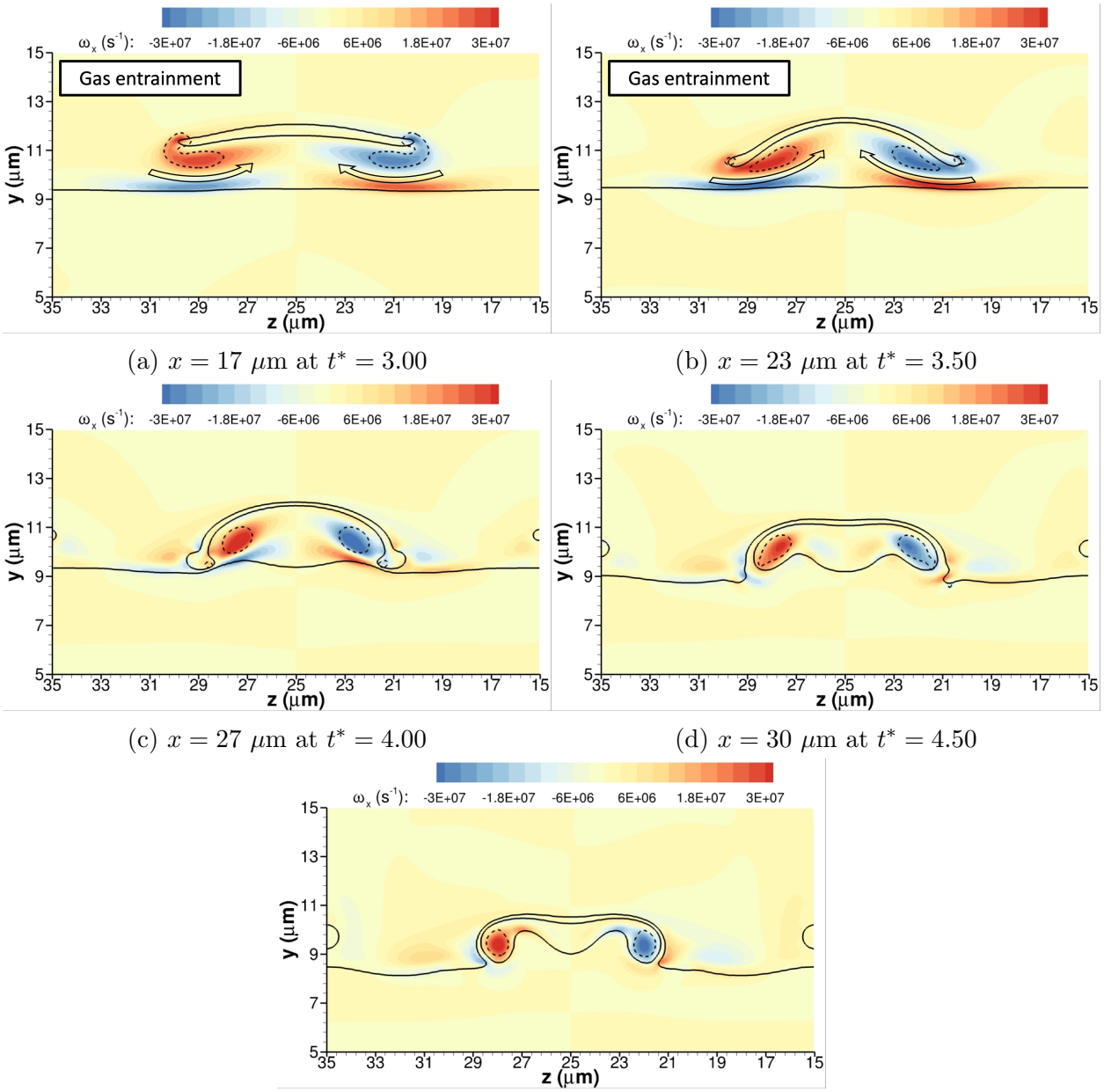

(a) $x = 17$ μm at $t^* = 3.00$

(b) $x = 23$ μm at $t^* = 3.50$

(c) $x = 27$ μm at $t^* = 4.00$

(d) $x = 30$ μm at $t^* = 4.50$

(e) $x = 33$ μm at $t^* = 5.00$

Figure 7.7: Vortex dynamics of the lobe corrugation mechanism at 150 bar with gas freestream velocity of $u_G = 50$ m/s (i.e., case C2). The contours of the horizontal component of the vorticity field, ω_x, are shown on yz planes at various x locations over time following the lobe. The interface location is identified as the solid black curve representing the isocontour with $C = 0.5$ and the cut vortex structures are identified by the dashed black isocontour with $\lambda_\rho = -9 \times 10^{15}$ kg/(m^{3}s^2). A non-dimensional time is obtained as $t^* = t/t_c = t\frac{u_G}{H}$. (a) $x = 17$ μm at $t^* = 3.00$; (b) $x = 23$ μm at $t^* = 3.50$; (c) $x = 27$ μm at $t^* = 4.00$; (d) $x = 30$ μm at $t^* = 4.50$; and (e) $x = 33$ μm at $t^* = 5.00$.

The coalescence of the liquid phase ends any gas entrainment under the lobe from the sides, but the vortex pins remain trapped inside the liquid structure. The vortical motion of these pins causes two features to emerge: (a) it lifts the liquid surface along the space between the two vortex pins; and (b) the continuous lobe stretching in the spanwise direction flattens the lobe in the absence of gas entrainment. These features are observed in Figure 7.7d and Figure 7.7e, which show the contours of ω_x in yz planes located at $x = 30$ μm at $t^* = 4.50$ and at $x = 33$ μm at $t^* = 5.00$, respectively.

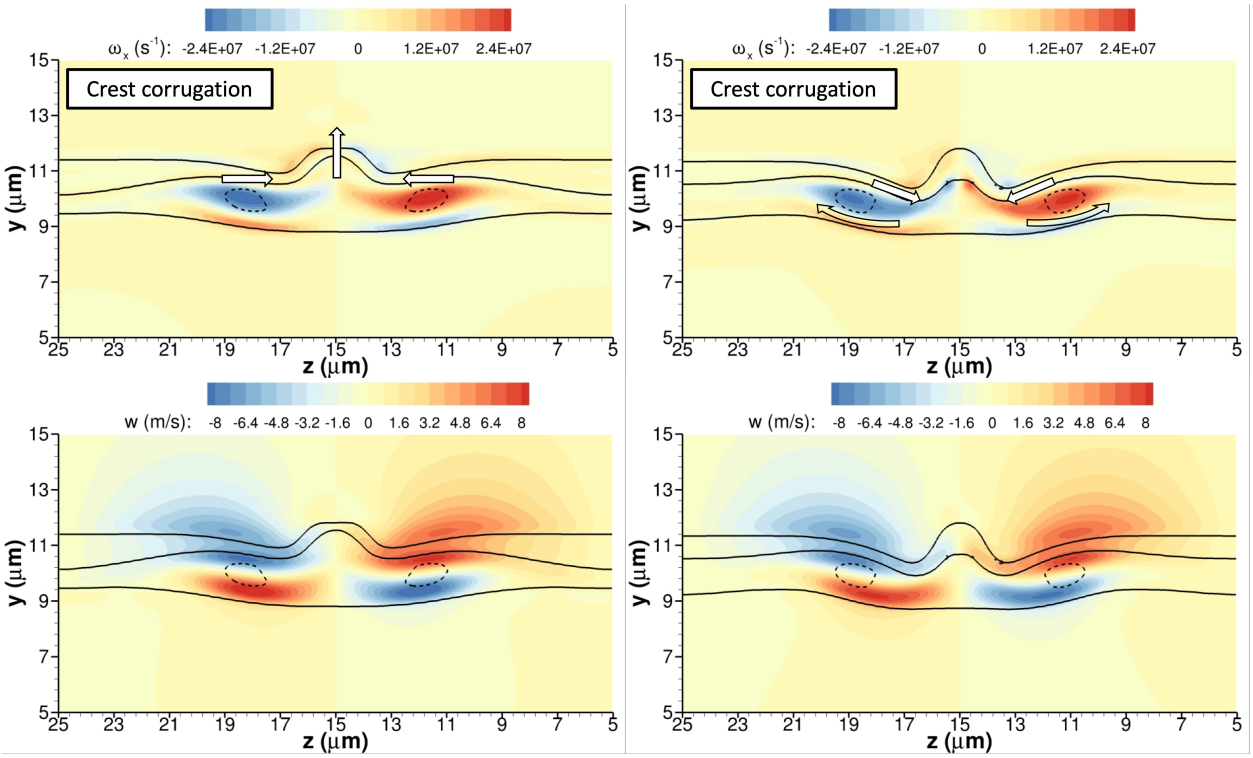

(a) $x = 12.5$ μm at $t^* = 3.00$ (b) $x = 17$ μm at $t^* = 3.50$

Figure 7.8: Vortex dynamics of the crest corrugation mechanism at 150 bar with gas freestream velocity of $u_G = 50$ m/s (i.e., case C2). The contours of the horizontal component of the vorticity field, ω_x and the spanwise component of the velocity field, w, are shown on yz planes at various x locations over time following the crest. The interface location is identified as the solid black curve representing the isocontour with $C = 0.5$ and the cut vortex structures are identified by the dashed black isocontour with $\lambda_\rho = -9 \times 10^{15}$ kg/(m^{3}s^2). A non-dimensional time is obtained as $t^* = t/t_c = t\frac{u_G}{H}$. (a) ω_x and w at $x = 12.5$ μm and $t^* = 3.00$; and (b) ω_x and w at $x = 17$ μm and $t^* = 3.50$.

The crest corrugation mechanism described in Subsection 6.3.2 is a result of the evolution of the initial roller vortex too. The crest corrugates around the streamwise direction along $z = 15$ μm or $z = 35$ μm (see Figure 6.12). As seen in Figure 7.6, the roller vortex not only deforms into a hairpin vortex with the head facing downstream, but the overall vortex structure is connected from lobe to lobe with an opposite-facing hairpin vortex submerged under the growing liquid wave. This region of the vortex can be identified, for instance, at $z = 15$ μm or $z = 35$ μm between $x = 10$ μm and $x = 15$ μm in Figure 7.6b.

Figure 7.8 presents contours of the vorticity component in the streamwise direction and the spanwise velocity component for a yz plane located at $x = 12.5$ μm and at $t^* = 3.00$ and for a yz plane located at $x = 17$ μm and at $t^* = 3.50$. As in Figure 7.7, $\omega_x > 0$ means counterclockwise rotation and $\omega_x < 0$ means clockwise rotation. The strength of the vortex under the wave is large enough to cause substantial deformation of the liquid sheet above the jet's surface. The vortical motion induces a velocity field that first pushes regions of the liquid sheet into each other, corrugating the liquid in between as illustrated in Figure 7.8a. Then, the deformation mechanism continues with the vortical motion displacing the sides of the corrugated layer downwards toward the liquid core surface and ejecting the gas phase contained within the liquid layer, the jet's surface, and the two pins of the upstream-facing hairpin vortex (see Figure 7.8b). This process amplifies the crest corrugation, giving it the nose-like shape highlighted in Figure 6.12.

As mentioned earlier, the crest corrugation mechanism is strong in cases B2, C2, and C3 and is also apparent in the other analyzed cases, but to a lesser extent. The reason why this feature emerges strongly in such high-pressure cases is related to the ability to form liquid layers. At high pressures, the growing perturbation rapidly forms an initial liquid sheet that, depending on the spanwise location, forms a lobe or a crest (i.e., related to the imposed initial surface perturbation). This liquid sheet is thinner the weaker the surface-tension force and the more the liquid fluid properties resemble those of the surrounding gas. Therefore, the

vortex mechanism discussed here affects mainly cases at 100 bar and 150 bar due to the behavior of the fluid. In other words, the corrugation of the liquid sheet is achieved more easily the thinner the liquid layer is.

7.3 Generation, Stretching and Deformation of Vortex Structures

This section presents an overview of the generation, stretching, and deformation of vortex structures observed in the computations from a qualitative and quantitative standpoint. The velocity and vorticity fields are analyzed and the terms of the vorticity equation for compressible flows (i.e., variable-density flows) to understand the vortex behavior.

The vorticity equation is derived by taking the curl of the momentum equation. After some mathematical manipulation, the compressible form of the vorticity equation reads

$$\frac{D\vec{\omega}}{Dt} = \vec{\omega}\cdot\nabla\vec{u} - \vec{\omega}(\nabla\cdot\vec{u}) + \frac{\nabla\rho\times\nabla p}{\rho^2} + \nabla\times\left(\frac{1}{\rho}\nabla\cdot\bar{\bar{\tau}}\right) + \nabla\times\vec{F}_\sigma \tag{7.5}$$

where $\vec{F}_\sigma$ is the localized body force used to model surface tension, as explained in Section 4.3. This term, together with the viscous term $\nabla\times\left(\frac{1}{\rho}\nabla\cdot\bar{\bar{\tau}}\right)$, have negligible contribution to the vorticity generation [26]. Therefore, only the vortex stretching and tilting term, $\vec{\omega}\cdot\nabla\vec{u}$, the vortex stretching due to compressibility term, $\vec{\omega}(\nabla\cdot\vec{u})$, and the baroclinic term, $\frac{\nabla\rho\times\nabla p}{\rho^2}$, are analyzed here.

Neglecting the viscous term and the surface-tension term in Eq. (7.5), an equation for each component of the vorticity field is obtained as follows

$$\frac{D\omega_x}{Dt} = \omega_x\frac{\partial u}{\partial x} + \omega_y\frac{\partial u}{\partial y} + \omega_z\frac{\partial u}{\partial z} - \omega_x(\nabla\cdot\vec{u}) + \frac{1}{\rho^2}\left(\frac{\partial\rho}{\partial y}\frac{\partial p}{\partial z} - \frac{\partial\rho}{\partial z}\frac{\partial p}{\partial y}\right) \tag{7.6}$$

$$\frac{D\omega_y}{Dt} = \omega_x \frac{\partial v}{\partial x} + \omega_y \frac{\partial v}{\partial y} + \omega_z \frac{\partial v}{\partial z} - \omega_y (\nabla \cdot \vec{u}) + \frac{1}{\rho^2}\left(\frac{\partial \rho}{\partial z}\frac{\partial p}{\partial x} - \frac{\partial \rho}{\partial x}\frac{\partial p}{\partial z}\right) \tag{7.7}$$

$$\frac{D\omega_z}{Dt} = \omega_x \frac{\partial w}{\partial x} + \omega_y \frac{\partial w}{\partial y} + \omega_z \frac{\partial w}{\partial z} - \omega_z (\nabla \cdot \vec{u}) + \frac{1}{\rho^2}\left(\frac{\partial \rho}{\partial x}\frac{\partial p}{\partial y} - \frac{\partial \rho}{\partial y}\frac{\partial p}{\partial x}\right) \tag{7.8}$$

It becomes relevant to analyze the influence of each term in the vorticity generation, especially since vortices are seen to deform and stretch substantially in Section 7.2. Additionally, the influence of compressible terms in the vortex generation might become critical. Fluid compressibility stretches the vortex, and the baroclinic term becomes essential across the liquid-gas interface and within each phase as density gradients exist under thermal and species mixing. Nevertheless, the influence of baroclinicity might be limited in high-density fluid regions due to the baroclinic term scaling with the reciprocal of density squared (i.e., ρ^{-2}), such in the liquid phase or in the gas phase at very high pressures.

In Subsection 7.3.1, an overview of the evolution of vortical structures over time demonstrates vortex generation in the atomization of liquid jets at high pressures. Then, in Subsection 7.3.2 the generation and deformation of the frequently observed rim vortices are discussed.

7.3.1 Temporal evolution of vortical structures

The evolution of vortical structures over time in liquid atomization is significant as vorticity defines the deformation of the liquid surface, changes in topology (e.g., hole formation), and breakup into ligaments and droplets. Moreover, vorticity is also a key mechanism for intraphase mixing, such as species and thermal mixing. Therefore, the evolution of vortex structures is examined here to identify regions of vortex generation and how these vortices

deform, break up and evolve toward smaller flow scales. This cascade process is expected since liquid atomization involves a transition to a turbulent flow.

Various snapshots of case C1 are presented here to highlight different features of the vortical field. As said earlier, the focus of this chapter is on the high-pressure regime at 150 bar, which presents the most extreme features observed in the non-ideal transcritical flows analyzed in this dissertation. Additionally, the case with $u_G = 30$ m/s is chosen because it has a weak formation of ligaments and droplets, allowing for better visualization of the liquid surface and vortex structures, but still displays many features observed across all cases at 100 bar and 150 bar. Nonetheless, some additional features appearing in other configurations are briefly discussed too. For detailed snapshots for various of the performed computations, the reader is referred to the Supplemental Material of this dissertation.

All configurations initially show the generation of a roller vortex or Kelvin-Helmholtz (KH) vortex caused by the imposed initial surface deformation and shear layer. This roller vortex is illustrated in Figure 7.9 and is usually accompanied by a rim vortex along the edge of the growing wave. Then, the evolution of this initial roller vortex has been shown in Section 7.2, where it becomes a hairpin vortex that defines the evolution of the initial lobe that forms on the liquid surface (i.e., the deformation mechanisms for lobe bending and perforation or for lobe corrugation). This hairpin vortex is advected by the gas phase, with its pins continuously stretching and its head curving and breaking up later. The vortex is also observed in Figure 7.10a.

As the main perturbation grows, new roller vortices appear along the wave's edge. Examples of this vortex generation are seen in Figure 7.10, where two fairly strong different roller vortices are generated downstream of the growing wave, the first one appearing around $t^* = 6.00$ and the second one appearing around $t^* = 8.40$. Compared to the initial roller vortex depicted in Figure 7.9 that deforms into a hairpin vortex as shown in Figure 7.2 and highlighted in Figure 7.10a, the new rollers remain very close to the edge of the wave. They

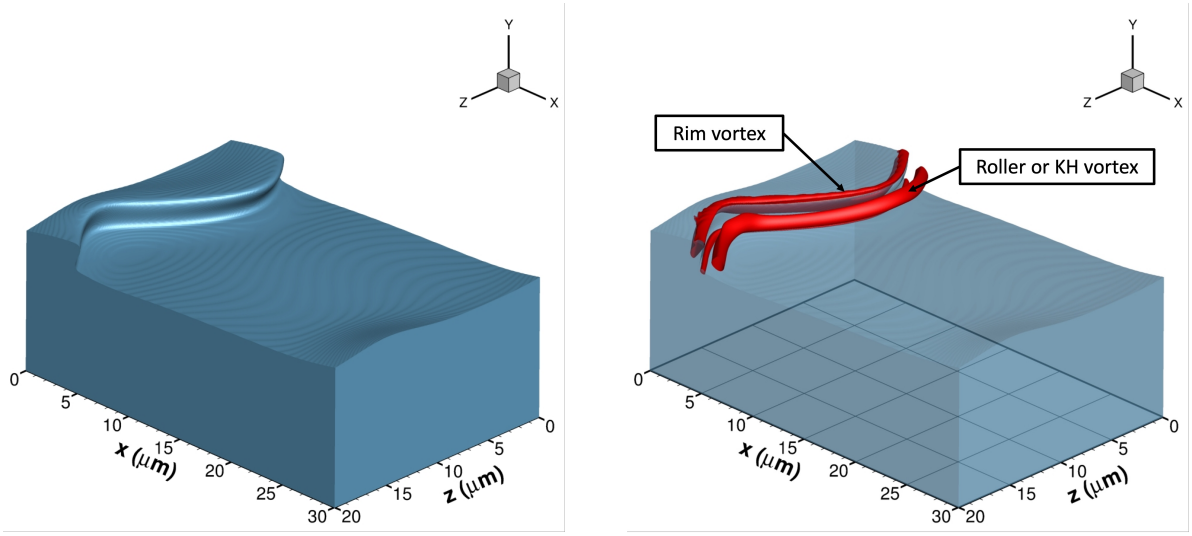

(a) (b)

Figure 7.9: Vortex structures at 150 bar with gas freestream velocity of $u_G = 30$ m/s (i.e., case C1) at the non-dimensional time of $t^* = t/t_c = t\frac{u_G}{H} = 2.25$. A three-dimensional view is provided and the interface location is identified as the blue isosurface with $C = 0.5$. (a) without vortex structures; and (b) vortex structures identified by the red isosurface with $\lambda_\rho = -2.5 \times 10^{15}$ kg/(m^{3}s^2).

contribute to the stretching of the wave that eventually leads to folding and the formation of liquid layers.

For cases at very high pressures, the generation of new roller vortices occurs when species and thermal mixing have considerably affected the fluid properties of the liquid phase in the vicinity of the growing wave. Such liquid regions have stretched and become thinner over time, increasing the available surface area such that heat and mass transfer have increased. Locally, the liquid phase has a much lower density and a gas-like viscosity. Therefore, the wave grows and rolls rapidly, generating strong gas entrainment that causes the roller vortices to be swallowed underneath the liquid wave. This vortex capture is illustrated in Figure 7.11 with a side view from an xy plane at $t^* = 8.40$ and another side view from a yz plane at $t^* = 9.90$. As discussed, most of the vortical structures are located under the wave and define the stretching of ligaments and small liquid sheets and the breakup of some droplets in the region. Furthermore, the roller vortex identified in Figure 7.10b is also depicted in

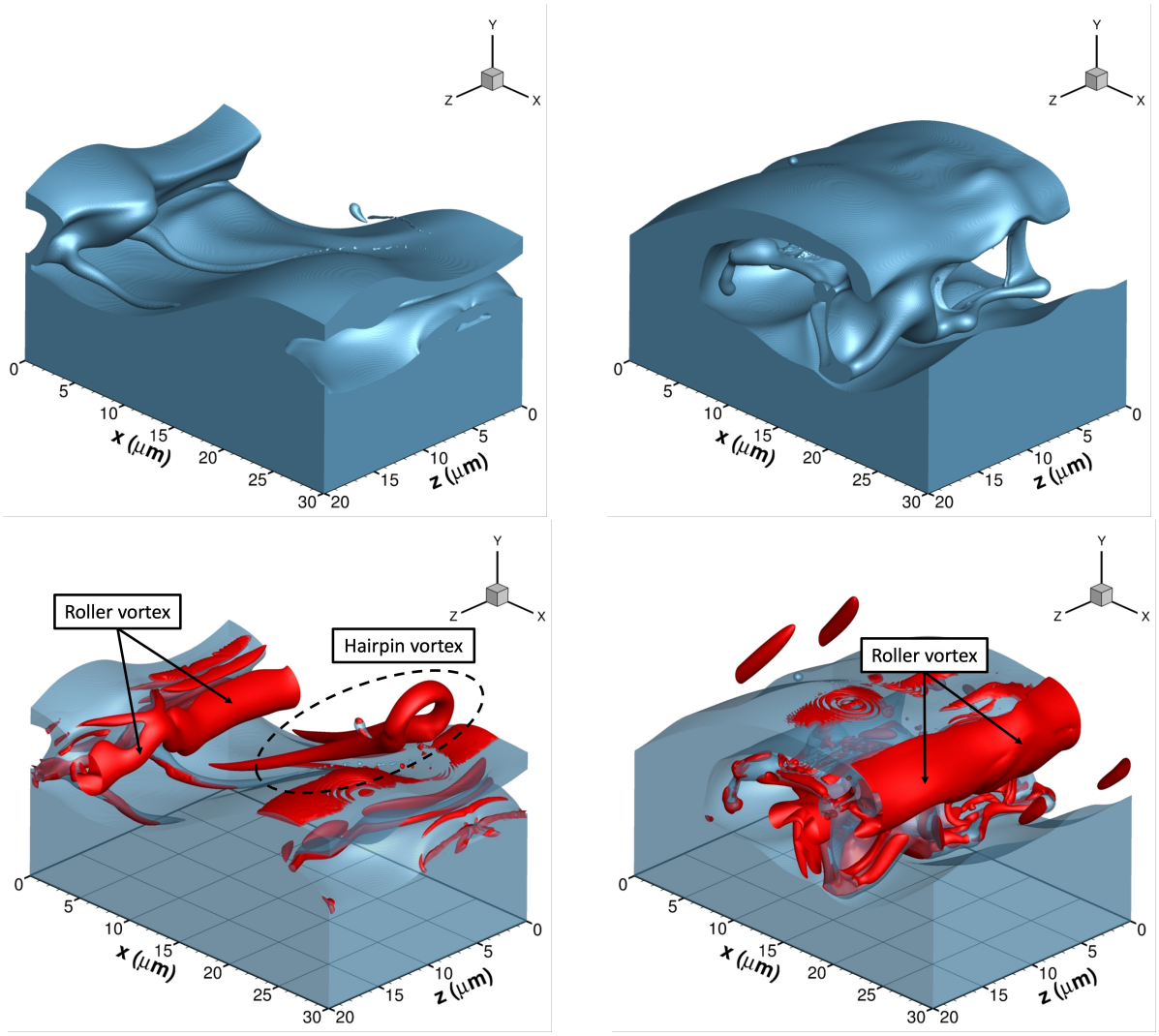

(a) $t^* = 6.00$ (b) $t^* = 8.40$

Figure 7.10: Vortex structures at 150 bar with gas freestream velocity of $u_G = 30$ m/s (i.e., case C1). A three-dimensional view is provided and the interface location is identified as the blue isosurface with $C = 0.5$ and the vortex structures are identified by the red isosurface with $\lambda_\rho = -2.5 \times 10^{15}$ kg/(m^{3}s^2). A non-dimensional time is obtained as $t^* = t/t_c = t\frac{u_G}{H}$. (a) $t^* = 6.00$; and (b) $t^* = 8.40$.

Figure 7.11a, where it is seen to be attached to the edge of the wave. Rather than a roller vortex, it could also be understood as a vortex sheet. As it forms, the strong gas entrainment stretches the vortex into the gaseous region below the liquid wave.

Once the layering mechanism becomes dominant in case C1 for $t^* > 10$, the generation of strong vortical structures is minimized. Figures 7.12 and 7.13 show that the majority of

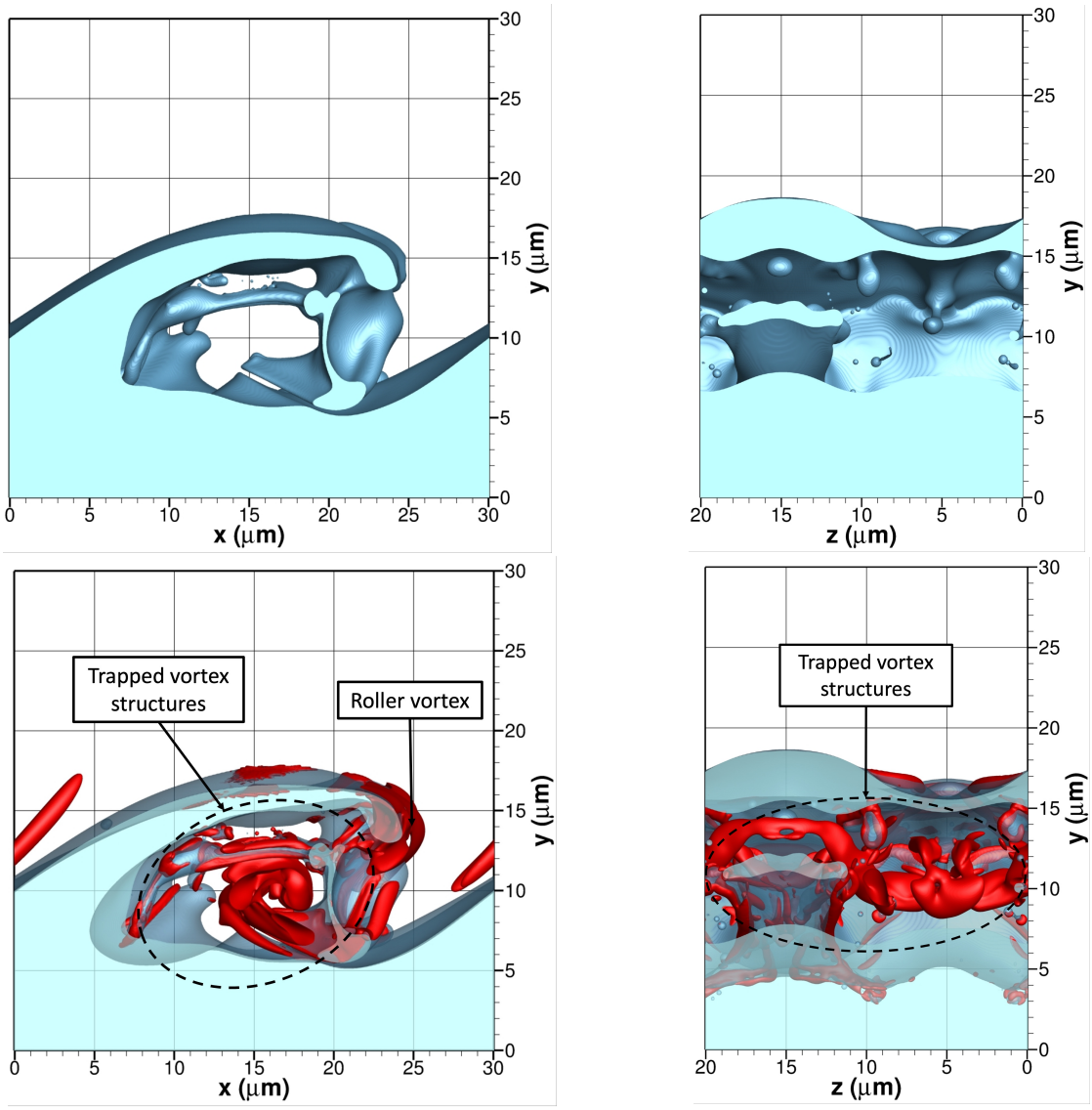

(a) $t^* = 8.40$ (b) $t^* = 9.90$

Figure 7.11: Vortex structures at 150 bar with gas freestream velocity of $u_G = 30$ m/s (i.e., case C1). The left figures show the side view from an xy plane located at $z = 20$ μm and the right figures show the side view from a yz plane located at $x = 30$ μm. The interface location is identified as the blue isosurface with $C = 0.5$ and the vortex structures are identified by the red isosurface with $\lambda_\rho = -2.5 \times 10^{15}$ kg/(m^{3}s^2). A non-dimensional time is obtained as $t^* = t/t_c = t\frac{u_G}{H}$. (a) $t^* = 8.40$; and (b) $t^* = 9.90$.

vortex structures identified by $\lambda_\rho = -2.5 \times 10^{15}$ kg/(m^{3}s^2) are confined within the two-phase mixture or the various liquid layers. Some common patterns are observed defining the evolution of vortex structures, which are detailed in the following lines.

As the liquid sheets tear under the continuous stretching and thinning, holes are frequently formed and accompanied by the generation of rim vortices along the hole's edge. An example of such vortex structure generation is shown in Figure 7.12b and Subsection 7.3.2 presents another case of rim vortex generation. These vortices are similar to the rim vortex appearing along the edge of the initial lobe discussed in Subsection 7.2.1. With the hole's expansion, the rim vortex tends to disappear or weaken.

Roller vortices are generated occasionally, albeit their strength and importance to the overall flow patterns is lower compared to the initial roller vortex or the roller vortices shown in Figures 7.9 and 7.10. The layering mechanism limits gas entrainment and recirculation overall, reducing the generation of spanwise vortical motion in the top layers of the two-phase mixture. Additionally, vortex structures within the layers tend to break up and align with the streamwise direction. Figure 6.16 shows that the average velocity profile evolves uniformly across the two-phase mixture when layering dominates. Thus, the streamwise velocity increases uniformly along the transverse direction. Such velocity distribution facilitates the streamwise stretching of vortical structures partially submerged in fluid layers with different streamwise velocities, reorienting the vortex with the fluid.

The streamwise vorticity generation is crucial to understanding and explaining the growth of three-dimensional instabilities in liquid atomization problems. Initially, a spanwise sinusoidal perturbation is imposed in each configuration with a wavelength equal to the domain size in the spanwise direction (i.e., 20 μm). Later, two or more wavelengths may be detected in the spanwise direction as observed in Figure 7.12 or Figure 7.13, for example. That is, streamwise vorticity perturbs the surface and promotes the growth of surface perturbations with a shorter wavelength than initially imposed. In fact, such a mechanism is shown

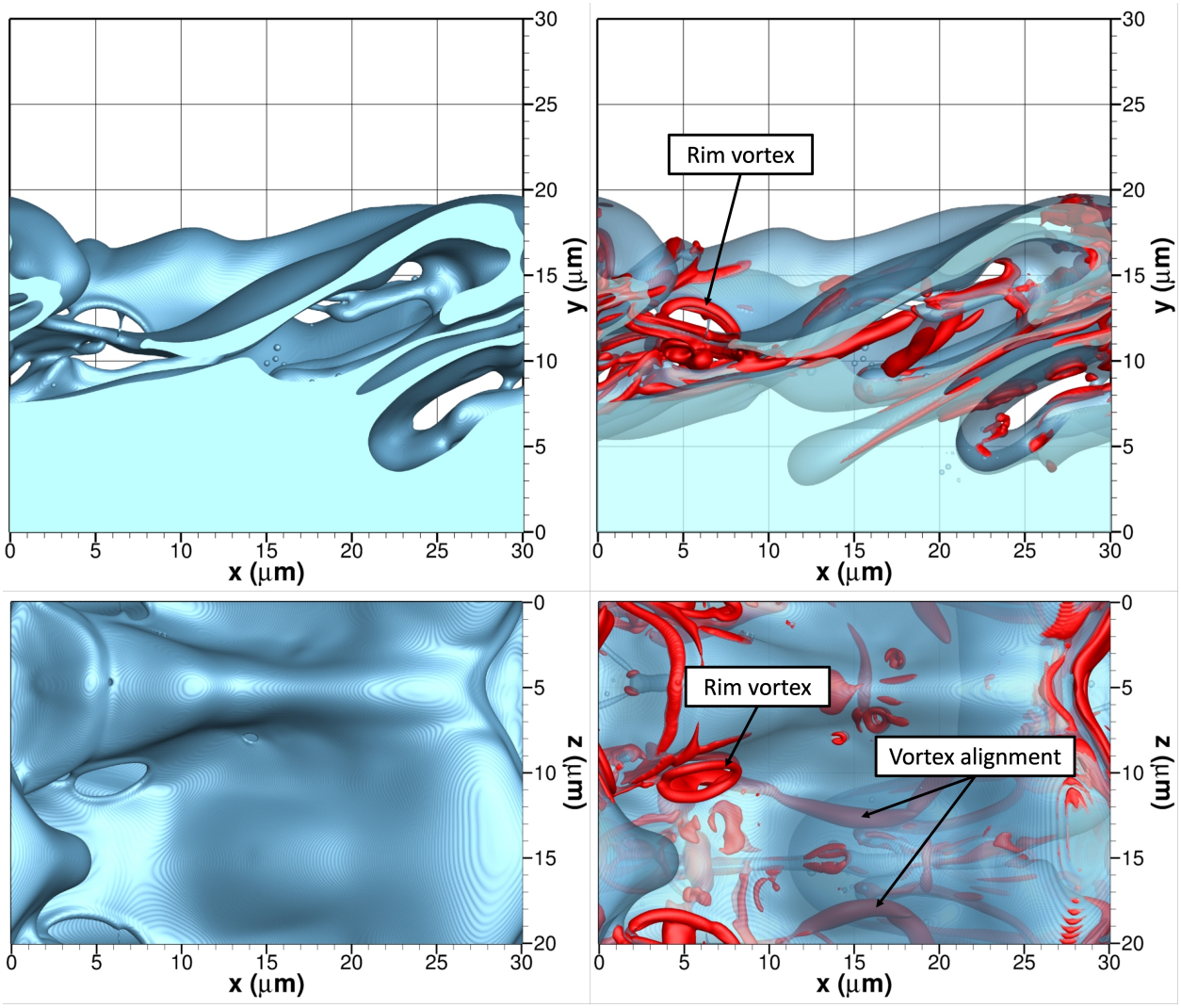

(a) (b)

Figure 7.12: Vortex structures at 150 bar with gas freestream velocity of $u_G = 30$ m/s (i.e., case C1) at the non-dimensional time of $t^* = t/t_c = t\frac{u_G}{H} = 12.00$. The top figures show the side view from an xy plane located at $z = 20$ μm and the bottom figures show the top view from an xz plane located above the liquid surface. The interface location is identified as the blue isosurface with $C = 0.5$. (a) without vortex structures; and (b) vortex structures identified by the red isosurface with $\lambda_\rho = -2.5 \times 10^{15}$ kg/(m^{3}s^2).

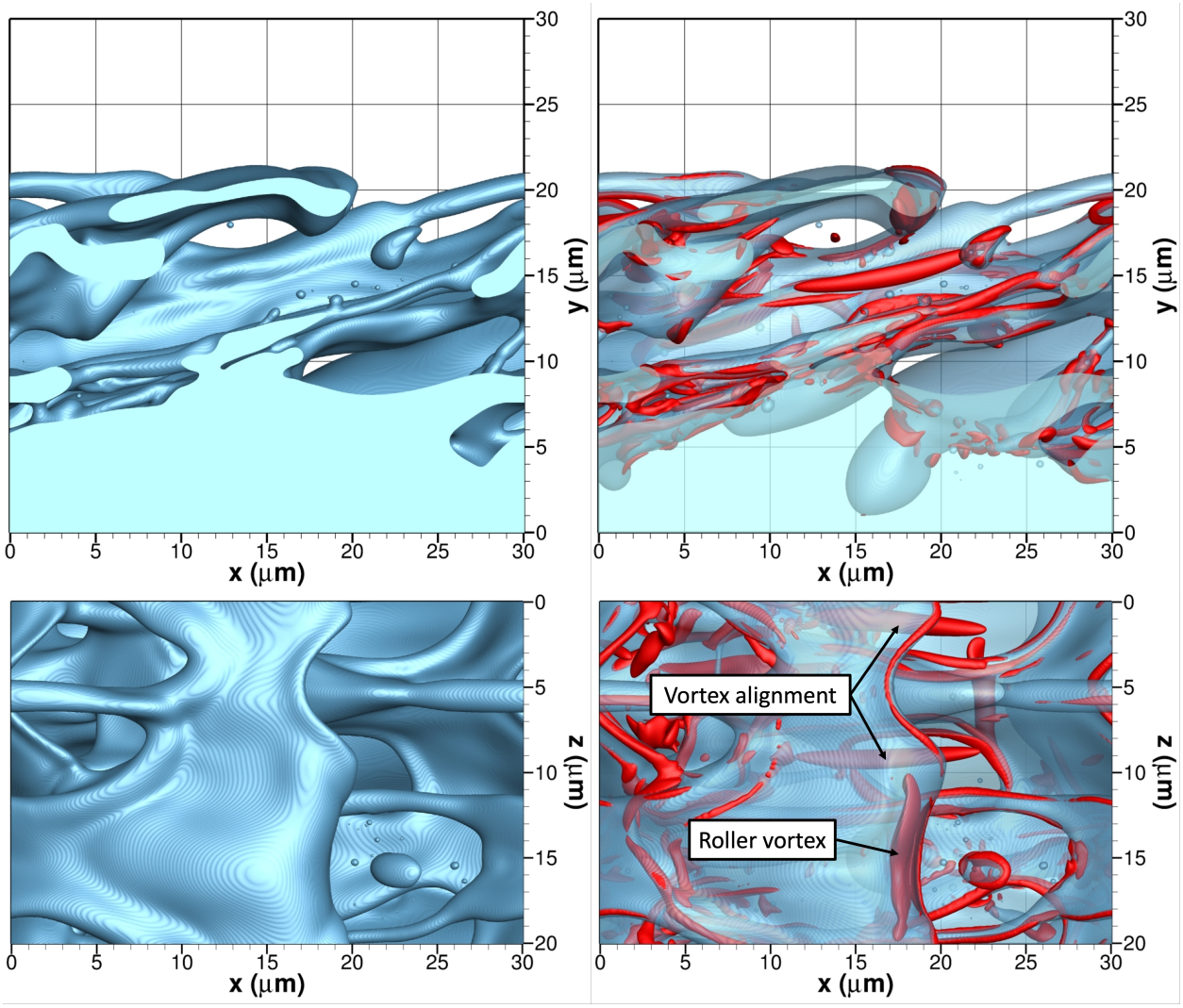

(a) (b)

Figure 7.13: Vortex structures at 150 bar with gas freestream velocity of $u_G = 30$ m/s (i.e., case C1) at the non-dimensional time of $t^* = t/t_c = t\frac{u_G}{H} = 15.00$. The top figures show the side view from an xy plane located at $z = 20$ μm and the bottom figures show the top view from an xz plane located above the liquid surface. The interface location is identified as the blue isosurface with $C = 0.5$. (a) without vortex structures; and (b) vortex structures identified by the red isosurface with $\lambda_\rho = -2.5 \times 10^{15}$ kg/(m^{3}s^2).

in Figure 7.8. Moreover, streamwise vortices influence the local deformation of the liquid surface, as discussed in Section 7.2. The generation of streamwise vorticity may be related to vortex tilting and realignment, as suggested by the figures presented in this subsection. Nevertheless, a deeper study on this issue may be required.

The qualitative picture does not change considerably for all analyzed configurations at 100 bar and 150 bar. Roller vortices and hairpin vortices define the early vortical motion, which eventually is captured underneath the liquid wave and the liquid layers. Rim vortices appear around recently formed holes, and the vortex structures tend to align with the streamwise direction. Depending on the configuration, the interface is easily perturbed, and short-wavelength perturbations grow, as detailed in Section 6.4. This scenario is seen especially in cases B2, C2, and C3. The growth of these new instabilities generates new smaller roller vortices, as shown in Figure 7.14, which aid in the deformation and stretching of small lobes on the surface of the primary perturbation wave.

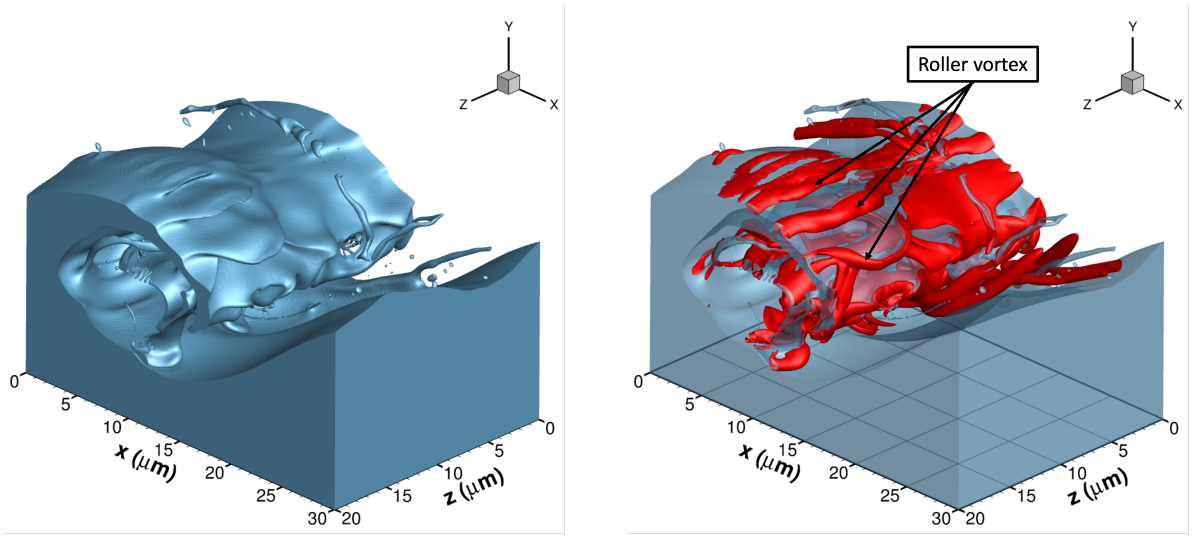

(a) (b)

Figure 7.14: Vortex structures at 150 bar with gas freestream velocity of $u_G = 50$ m/s (i.e., case C2) at the non-dimensional time of $t^* = t/t_c = t\frac{u_G}{H} = 7.50$. A three-dimensional view is provided and the interface location is identified as the blue isosurface with $C = 0.5$. (a) without vortex structures; and (b) vortex structures identified by the red isosurface with $\lambda_\rho = -9 \times 10^{15}$ kg/(m^{3}s^2).

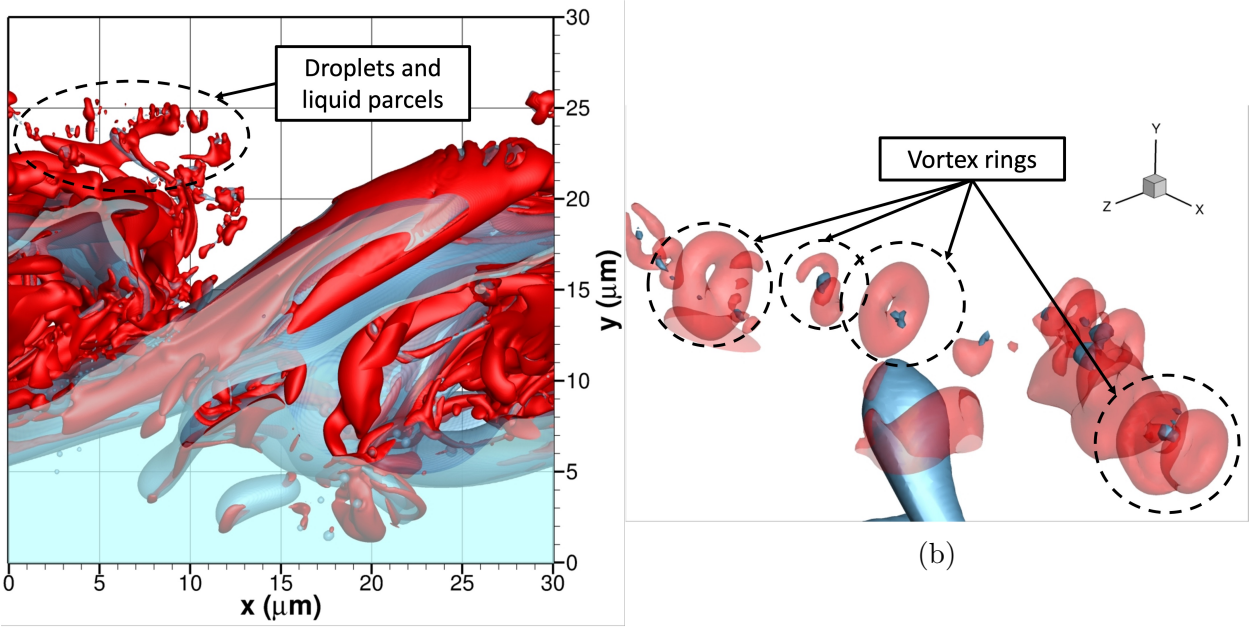

(a) (b)

Figure 7.15: Vortex structures at 50 bar with gas freestream velocity of $u_G = 70$ m/s (i.e., case A2) at the non-dimensional time of $t^* = t/t_c = t\frac{u_G}{H} = 13.30$. The interface location is identified as the blue isosurface with $C = 0.5$ and the vortex structures are identified by the red isosurface of λ_ρ. (a) side view from an xy plane located at $z = 20$ μm with $\lambda_\rho = -3 \times 10^{15}$ kg/(m^{3}s^2); and (b) vortex rings around isolated droplets and liquid parcels with $\lambda_\rho = -4 \times 10^{15}$ kg/(m^{3}s^2).

At 50 bar, however, layering is not a dominant feature, and the temporal evolution of vortex structures differs from that at higher pressures. Precisely, the initial roller vortex evolution is slightly different as highlighted in Figure 7.5a for case A2 and vortex structures are observed everywhere within the two-phase mixture at all times. That is, the overall picture resembles more that of subcritical atomization (i.e., higher surface-tension force, less mixing effects, limited layering). Because the value of λ_ρ is arbitrarily chosen to represent vortex structures, possibly the specific value chosen for case A2 is sufficiently low to capture vortex structures later in time, compared to the case C1 depicted in earlier pictures. Nonetheless, the value of $\lambda_\rho = -3 \times 10^{15}$ kg/(m^{3}s^2) used in case A2 is chosen so that the initial roller vortex is represented in a similar way as in higher-pressure configurations. Therefore, the breakup cascade of vortical structures should be observed similarly among all cases. The fact that the 50-bar case does not show such weakening of the vortex strength as the flow becomes

more chaotic points to various features: (a) the importance of layering in reducing vorticity generation is highlighted; (b) the lower-density and lower-viscosity gas at 50 bar reduces viscous dissipation; and (c) some other mechanism for vorticity generation may exist and is stronger at 50 bar than at 100 bar or 150 bar.

Another feature not observed at very high pressures is the emergence of vortex rings around fast-moving droplets and liquid parcels. Figure 7.15 illustrates this feature for case A2. Above the liquid jet, a cluster of droplets and liquid parcels is advected by the oxidizer stream. A closer look reveals that vortex rings are generated around these liquid structures. The generation of these vortices and their influence on the overall mixing should be analyzed in future works.

7.3.2 A case study: the rim vortex

The generation of vortices along the edge or rim of lobes and holes is a common feature observed in all configurations, including the incompressible computations without diffusive mixing. It may occur early in the deformation process or later, for instance, when the layering mechanism dominates and holes form from sheet tearing in the high-pressure configurations of 100 bar and 150 bar. The evolution and generation of other vortices may be considered in future works. Section 7.2 and Subsection 7.3.1 have shown various distinctive vortices in the computations whose generation and temporal evolution is intriguing or has a significant role in the deformation of the liquid surface or the mixing processes. For instance, the deformation of the initial roller vortex or KH vortex into a hairpin and its evolution is worth studying, as such a vortex is commonly observed in many computations. Other vortices that could be considered are the roller vortex forming after the lobe bursts in the corrugation mechanism (see Figure 7.6f) or the vortex rings observed at lower pressures around droplets and other liquid structures (see Figure 7.15b).

This subsection analyzes two different rim vortices forming in case C1 (i.e., 150 bar and $u_G = 30$ m/s). First, the hole resulting from the perforation of the initial lobe illustrated in Figures 6.8 and 7.2 is considered. As seen in Figure 7.2f, a rim vortex forms along the edge of the hole as it expands. A slice of the three-dimensional domain at $t^* = 4.5$ is analyzed, corresponding to an xy plane at $z = 25$ μm. On this plane, the vorticity vector defining the rim vortex is predominantly aligned with the spanwise direction. As seen in Figure 7.16, two rim vortices are generated: an upper rim vortex and a lower rim vortex.

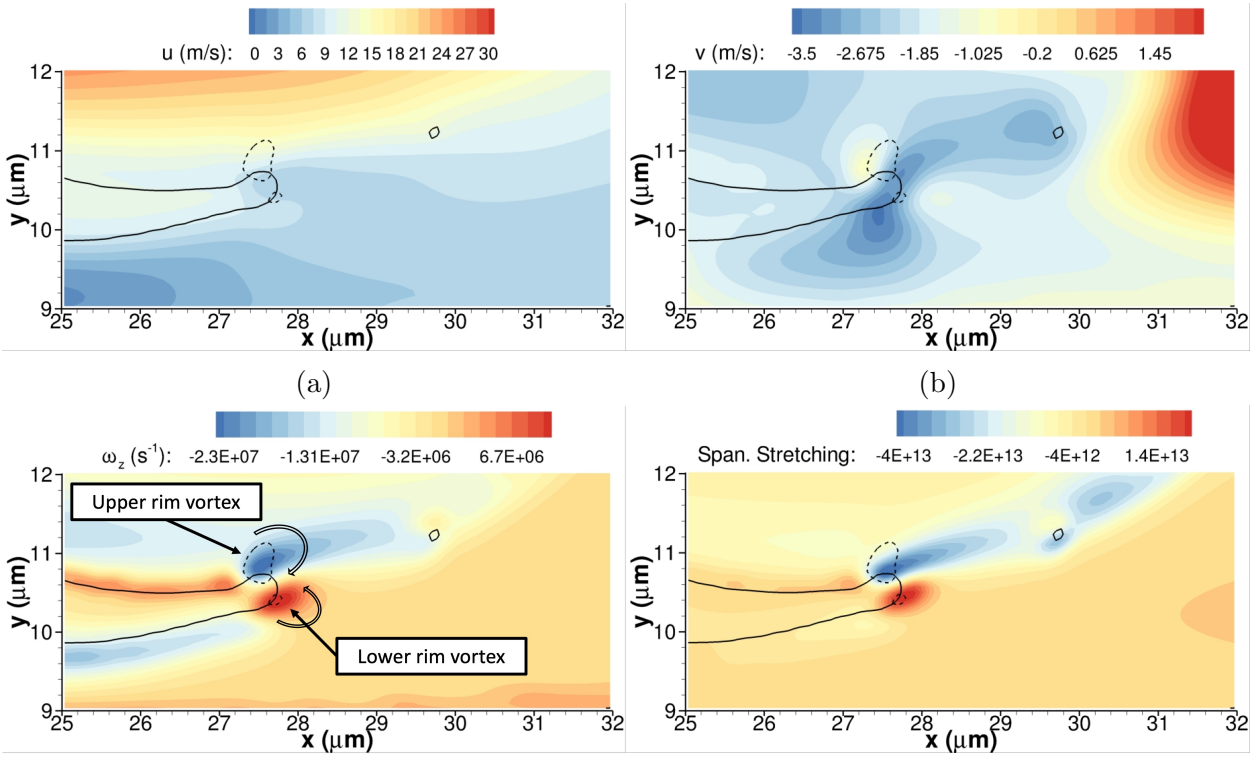

Figure 7.16: Rim vortices along the edge of a hole at 150 bar with gas freestream velocity of $u_G = 30$ m/s (i.e., case C1) at the non-dimensional time of $t^* = t/t_c = t\frac{u_G}{H} = 4.5$. The contours of various terms are shown on an xy plane located at $z = 25$ μm. The interface location is identified as the solid black curve representing the isocontour with $C = 0.5$ and the cut vortex structures are identified by the dashed black isocontour with $\lambda_\rho = -2.5 \times 10^{15}$ kg/(m^{3}s^2). (a) u velocity component; (b) v velocity component; (c) ω_z vorticity component; and (d) $\omega_z \frac{\partial w}{\partial z}$ or spanwise vortex stretching (units of s^{-2}).

The upper rim vortex can be understood as a vortex generated by the wake above the edge of the liquid sheet. Gas flows faster in the upper layers and the rounder edge of the liquid

sheet resulting from the surface-tension force bends the flow. Thus, a clockwise recirculating motion is induced. The formation of the lower rim vortex might not be apparent at first glance, but its origin is similar to the upper rim vortex. The downward motion of the liquid edge induces a weaker wake at the bottom end of the liquid and a region of counterclockwise recirculation develops. That is, locally the liquid sheet is squeezing the gas phase below, which moves out from underneath the liquid. This scenario is the common cause of most rim vortices observed throughout the computations.

A look at the spanwise vorticity generation reveals that from the terms in Eq. (7.8), the spanwise vortex stretching term, $\omega_z \frac{\partial w}{\partial z}$, dominates over the rest by at least an order of magnitude. As shown in Figure 7.16d, the spanwise vortex stretching tends to increase the spanwise vorticity magnitude of each respective rim vortex over time. This result is consistent with the hole expansion process illustrated in Figures 6.8 and 7.2 and suggests that the perforation event is a source of vorticity that aligns quickly with the edge of the hole. Despite it being lower in magnitude, the vortex stretching term due to the fluid compressibility in the upper rim vortex has the opposite effect of the spanwise vortex stretching term and tends to decrease the magnitude of ω_z in the region (i.e., $-\omega_z(\nabla \cdot \vec{u}) > 0$). For the lower rim vortex, the compressible term is negligible.

Another way of understanding the simultaneous generation of an upper and a lower rim vortex may be related to the receding liquid edge with respect to the surrounding gas. As the hole forms, it quickly expands under the action of surface tension; thus, the liquid phase moves relative to the gas phase, creating an extra space next to the liquid's edge that is quickly filled with gas from both sides of the liquid sheet. In the case depicted in Figure 7.16, the edge of the liquid sheet moves upstream with respect to the surrounding gas flow and two counter-rotating vortices appear. This discussion has relevance to the following example of a rim vortex.

The other rim vortex discussed in this subsection is generated as a result of the liquid sheet tearing occurring during the layering mechanism. Figure 7.17 presents this process for the hole forming at the upper-most liquid sheet at $t^* = 10.95$ in case C1, which is seen to quickly expand under the stretching of the liquid sheets and the action of surface tension. A closer look at the vortex structures generated during this hole formation and expansion process reveals a similar vortical picture as described in previous lines where two rim vortices form (i.e., an upper and a lower rim vortex). In this case, the rim vortices form around the entire hole's edge on both sides of the liquid sheet until the flow configuration around the hole is modified. Moreover, a third vortex appears inside the hole due to the pairing between the two counter-rotating rim vortices and is referred to as the "pairing" vortex from now on. Eventually, the upstream edge of the hole catches up with this pairing vortex, and the vortical structures merge.

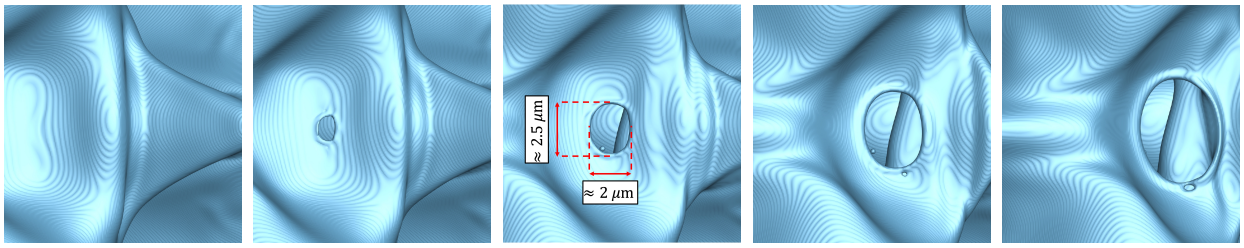

(a) $t^* = 10.80$ (b) $t^* = 10.95$ (c) $t^* = 11.10$ (d) $t^* = 11.25$ (e) $t^* = 11.40$

Figure 7.17: Hole formation from sheet tearing during layering at 150 bar with gas freestream velocity of $u_G = 30$ m/s (i.e., case C1). The top view from an xz plane located above the liquid surface is shown. The interface location is identified as the blue isosurface with $C = 0.5$. A non-dimensional time is obtained as $t^* = t/t_c = t\frac{u_G}{H}$. (a) $t^* = 10.80$; (b) $t^* = 10.95$; (c) $t^* = 11.10$; (d) $t^* = 11.25$; and (e) $t^* = 11.40$.

Here, a remark regarding the arbitrary choice of a value of λ_ρ to identify and represent vortex structures is required. This issue is also discussed in Section 7.1. The pairing vortex is identified with $\lambda_\rho = -2.5 \times 10^{15}$ kg/(m^{3}s^2). However, slightly greater magnitudes of λ_ρ do not show the vortex despite similarly capturing the rest of the vortex structures. Therefore, some vortices may be missed during the data analysis, but it is unrealistic to demand a search for an optimal λ_ρ value beyond what is done here. For this reason, we complement

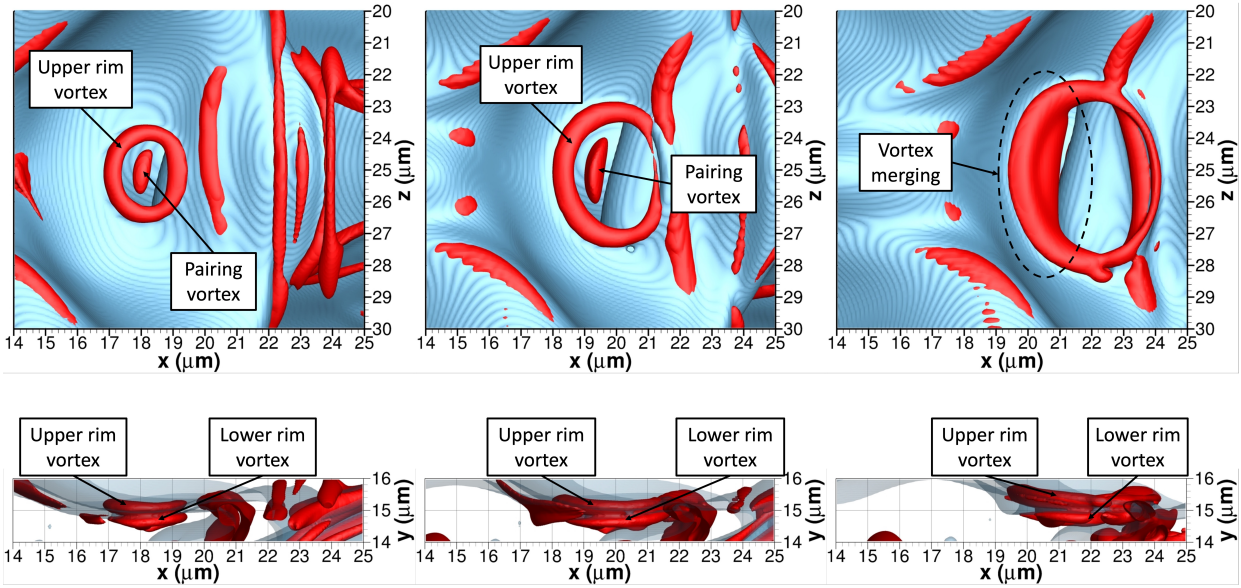

(a) $t^* = 11.10$ (b) $t^* = 11.25$ (c) $t^* = 11.40$

Figure 7.18: Vortex structures appearing after hole formation from sheet tearing during layering at 150 bar with gas freestream velocity of $u_G = 30$ m/s (i.e., case C1). The top figures show a view from an xz plane located above the liquid surface and the bottom figures show a side view from an xy plane located at $z = 29$ μm. The interface location is identified as the blue isosurface with $C = 0.5$ and the vortex structures are identified by the red isosurface with $\lambda_\rho = -2.5 \times 10^{15}$ kg/(m^{3}s^2). A non-dimensional time is obtained as $t^* = t/t_c = t\frac{u_G}{H}$. (a) $t^* = 11.10$; (b) $t^* = 11.25$; and (c) $t^* = 11.40$.

the information provided by the dynamical vortex identification method with information from the velocity and vorticity fields to improve the study of vorticity dynamics.

Similar to the rim vortex analyzed at $t^* = 4.5$, a slice through the three-dimensional domain is studied, corresponding to an xy plane located at $z = 25$ μm. Across this plane, the vorticity vector associated with each of the three vortices is mainly aligned with the spanwise direction. Therefore, we also examine the spanwise vorticity generation terms in Eq. (7.8) to understand how this vorticity is being generated. In Figure 7.19, the contours of the transverse velocity component, v, and the spanwise vorticity component, ω_z, are presented on the analyzed slice at $t^* = 11.10$, $t^* = 11.25$ and $t^* = 11.40$. The vortices of interest are depicted.

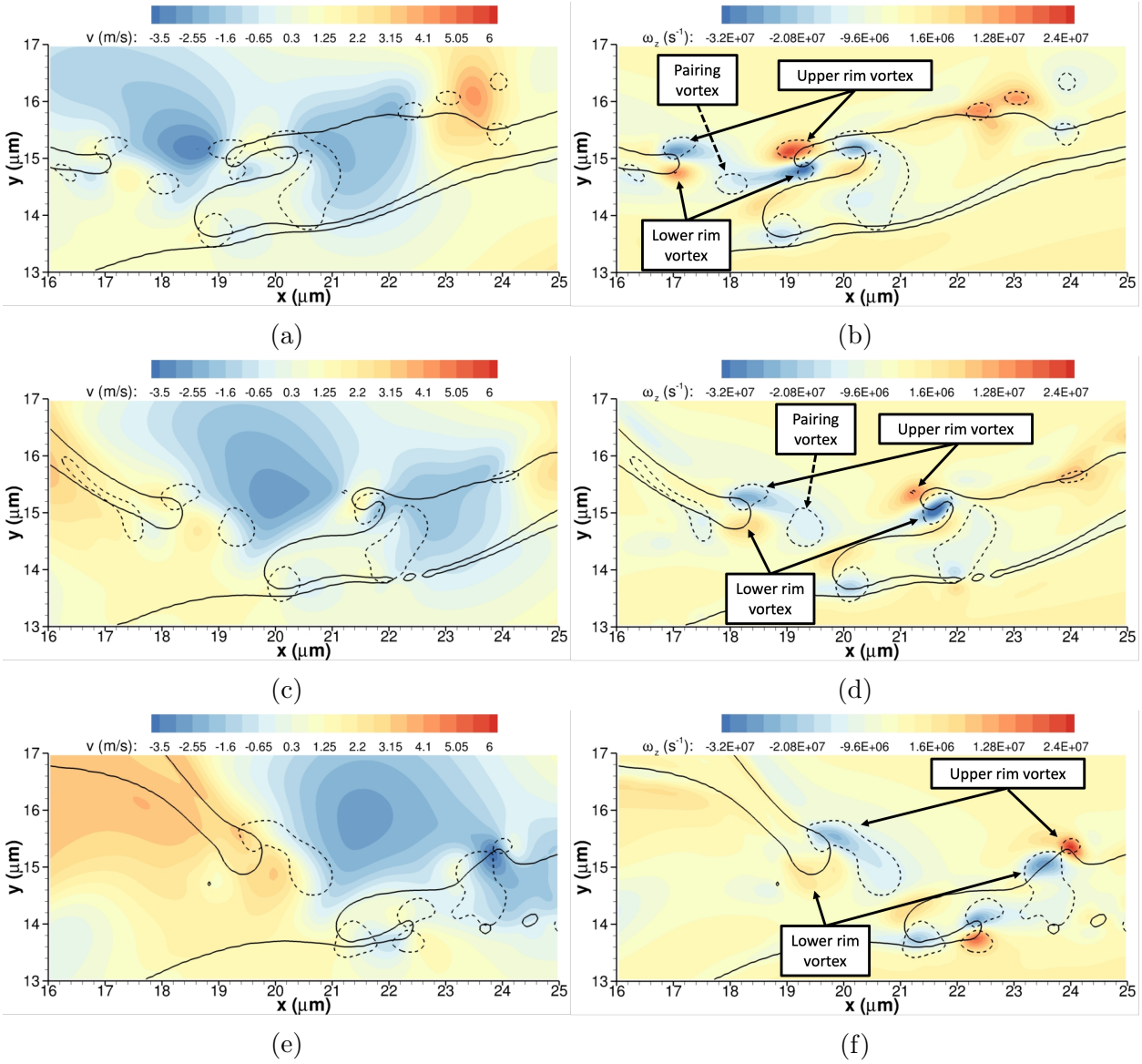

Figure 7.19: Vortex structures appearing after hole formation from sheet tearing during layering at 150 bar with gas freestream velocity of $u_G = 30$ m/s (i.e., case C1). The contours of the transverse component of the velocity field, v, and the spanwise component of the vorticity field, ω_z, are shown on an xy plane located at $z = 25$ μm. The interface location is identified as the solid black curve representing the isocontour with $C = 0.5$ and the cut vortex structures are identified by the dashed black isocontour with $\lambda_\rho = -2.5 \times 10^{15}$ kg/(m^{3}s^2). A non-dimensional time is obtained as $t^* = t/t_c = t\frac{u_G}{H}$. (a) v velocity component at $t^* = 11.10$; (b) ω_z vorticity component at $t^* = 11.10$; (c) v velocity component at $t^* = 11.25$; (d) ω_z vorticity component at $t^* = 11.25$; (e) v velocity component at $t^* = 11.40$; and (f) ω_z vorticity component at $t^* = 11.40$.

The vortex formation follows the tearing of the liquid sheet. As the hole forms and expands, gas flows from the freestream region into the hole. This fluid motion, coupled with the hole expansion under the liquid sheet stretching mechanism and the surface-tension force, generates two counter-rotating vortices along the upper and lower edges of the hole, similar to the rim vortex analyzed at $t^* = 4.5$. Note that the upper rim vortex rotates clockwise (i.e., $\omega_z < 0$) upstream of the hole and it rotates counterclockwise on the downstream side. On the other hand, the lower rim vortex rotates counterclockwise on the upstream side and clockwise downstream.

Although the vorticity associated with the pairing vortex is lower in magnitude, the vorticity vector is mainly aligned in the spanwise direction and rotates clockwise. This vortex forms due to a combined effect between the gas entrainment through the hole and the lower rim vortex. As illustrated in Figure 7.19, the gas flows into the hole on the downstream side of the pairing vortex while at the same time the lower rim vortex is inducing an upwards motion on the upstream side of the pairing vortex. As a result, the flow rotates clockwise. In addition, the pairing vortex may be understood as forming part of a connected region of negative spanwise vorticity between the upstream side of the upper rim vortex and the downstream side of the lower rim vortex. As the hole expands and the vortices deform, the pairing vortex eventually merges with the upper rim vortex along the upstream side of the hole.

Further evidence of the origin of the upper and lower rim vortices is provided in Figure 7.20 where the contours of the spanwise velocity component, w, and the streamwise vorticity component, ω_x, are shown on a slice of the three-dimensional domain at $x = 18.2$ μm and $t^* = 11.10$. The yz plane cuts the hole approximately at its midpoint. Therefore, the vorticity vector of the upper and lower rim vortices is mainly aligned in the streamwise direction. This view eliminates any influence of the streamwise velocity in highlighting the displacement of the hole's edge with respect to the surrounding gas. It clearly shows that,

in the absence of spanwise shear, the thin edge of the liquid sheet becomes rounder under the effect of surface tension and recedes as the hole expands. Therefore, the displacement of the liquid generates the two counter-rotating rim vortices as the gas phase quickly fills up the space previously occupied by the liquid.

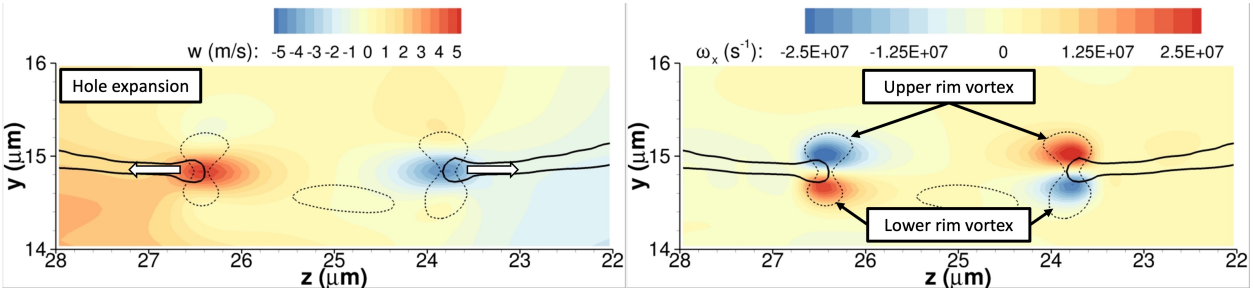

(a) (b)

Figure 7.20: Vortex structures appearing after hole formation from sheet tearing during layering at 150 bar with gas freestream velocity of $u_G = 30$ m/s (i.e., case C1) at the non-dimensional time of $t^* = t/t_c = t\frac{u_G}{H} = 11.10$. The contours of the spanwise component of the velocity field, w, and the streamwise component of the vorticity field, ω_x, are shown on a yz plane located at $x = 18.2$ μm. The interface location is identified as the solid black curve representing the isocontour with $C = 0.5$ and the cut vortex structures are identified by the dashed black isocontour with $\lambda_\rho = -2.5 \times 10^{15}$ kg/(m^{3}s^2). . (a) w velocity component; and (b) ω_x vorticity component.

From the terms in the spanwise vorticity equation, the spanwise stretching is the dominant term responsible for the vorticity generation in the rim vortices. Streamwise tilting or normal tilting have a lower magnitude and mainly affect other vortices. Figures 7.21a and 7.21c show the contours of the spanwise stretching of ω_z on the same xy slice depicted on Figure 7.19. At $t^* = 11.10$, the spanwise stretching contributes to increasing the magnitude of each respective rim vortex. However, this term weakens as the hole expands, especially in the upstream region, as shown at $t^* = 11.25$. Therefore, other terms in the vorticity equation may have a stronger influence over time, which may explain why the vorticity magnitude of the lower rim vortex decays upstream of the hole.

Although lower in magnitude, the compressible stretching term in Eq. (7.8) is deserving of attention since this term, as well as the baroclinic term, might become relevant for the

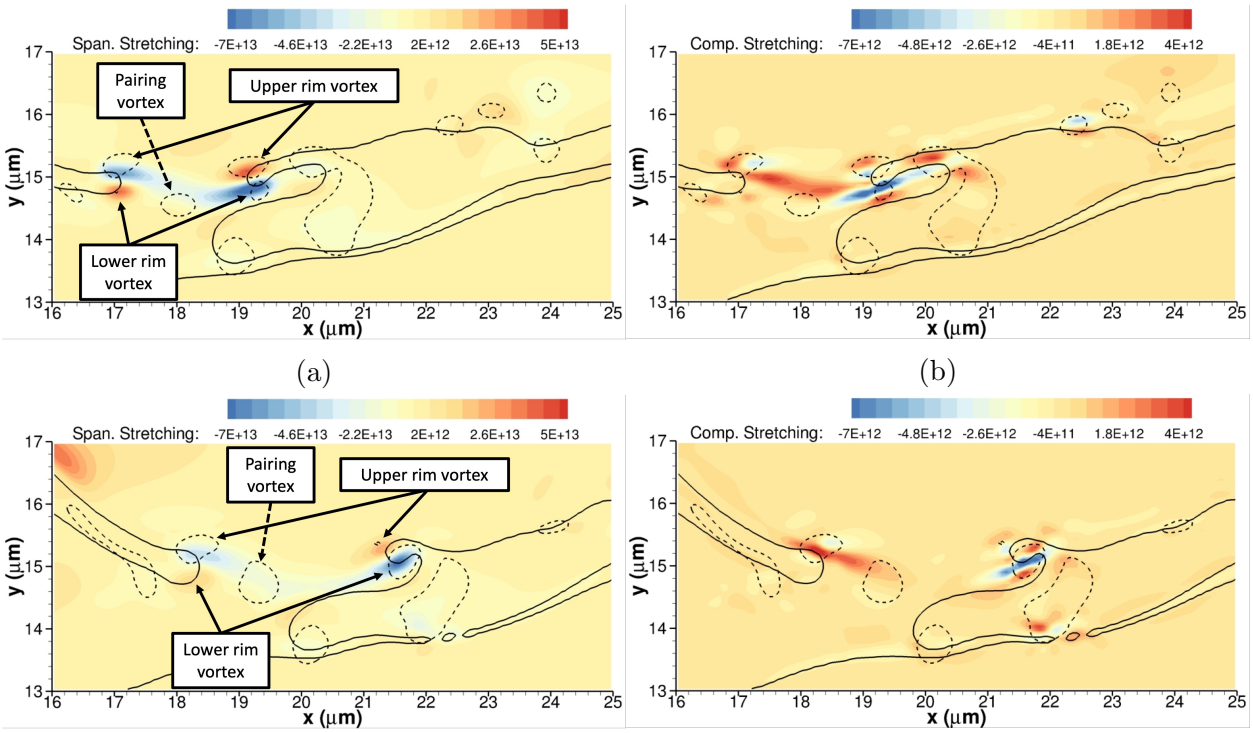

Figure 7.21: Vortex structures appearing after hole formation from sheet tearing during layering at 150 bar with gas freestream velocity of $u_G = 30$ m/s (i.e., case C1). The contours of the spanwise stretching and the compressible stretching of the spanwise vorticity, $\omega_z \frac{\partial w}{\partial z}$ and $-\omega_z(\nabla \cdot \vec{u})$, respectively, are shown on an xy plane located at $z = 25$ μm. Both variables have units of s^{-2}. The interface location is identified as the solid black curve representing the isocontour with $C = 0.5$ and the cut vortex structures are identified by the dashed black isocontour with $\lambda_\rho = -2.5 \times 10^{15}$ kg/(m^{3}s^2). A non-dimensional time is obtained as $t^* = t/t_c = t\frac{u_G}{H}$. (a) $\omega_z \frac{\partial w}{\partial z}$ at $t^* = 11.10$; (b) $-\omega_z(\nabla \cdot \vec{u})$ at $t^* = 11.10$; (c) $\omega_z \frac{\partial w}{\partial z}$ at $t^* = 11.25$; and (d) $-\omega_z(\nabla \cdot \vec{u})$ at $t^* = 11.25$.

vorticity generation within each phase in this low-Mach-number compressible flow. Note how the compressible term may have opposite effects depending on the location of the vortex. For the upper rim vortex upstream of the hole, the compressible stretching will decrease the magnitude of the streamwise vorticity there. A similar effect occurs in the region of negative streamwise vorticity near and above the pairing vortex. On the other hand, the downstream side of the hole shows different behavior. There, the compressible stretching term aligns with the vorticity vector and will tend to increase the magnitude of the upper and lower rim vortices.

The baroclinic term has not been deemed relevant to explain the rim vortex. Since it scales with the reciprocal of the density squared, baroclinicity is relatively negligible within each phase compared to other terms at 150 bar. Nonetheless, it possibly becomes relevant for other vortex structures. Moreover, a proper representation is problematic. The sharp density gradient across the liquid-gas interface, coupled to the spurious currents affecting the local pressure field, generates noise-driven contours in the vicinity of the interface that cannot be easily represented.

7.4 Insights for Future Studies

As mentioned at the beginning of this chapter, the amount of information available from the computations performed for this dissertation is immense. Thus, both Chapter 6 and the present Chapter 7 have focused on some features deemed important by the author. The inclusion of vortex dynamics in the study of high-pressure, two-phase flows opens a wide range of features and physical aspects that may be analyzed in future works. This section aims to provide some insights for this purpose.

The role of vortex dynamics in the atomization of a liquid jet and the mixing processes within each phase (e.g., mass and energy) is crucial. Sections 7.2 and 7.3 have shown the role of vortex dynamics in two deformation mechanisms observed early in the simulation and how the vortex structures evolve at high pressures from a global perspective. Additionally, a characteristic vortex formation occurring after a hole forms or along the edge of a liquid lobe/sheet (i.e., the rim vortex) has been described in more detail. Subsection 7.3.2 provides some examples of other relevant vortical structures that can be analyzed in the future, such as the hairpin vortex forming from the initial shear between both phases, the roller vortex appearing after the lobe bursts into droplets and ligaments during the lobe corrugation mechanism, or the vortex rings appearing around droplets and ligaments in case A2 at 50

bar. Similar to what has been done in Subsection 7.3.2 for the rim vortex, the sources of vorticity detailed in Eq. (7.5) should be analyzed for other vortical structures, and special consideration must be given to the compressible vortex stretching, $-\vec{\omega}(\nabla \cdot \vec{u})$, and the baroclinic term, $(\nabla\rho \times \nabla p)/\rho^2$. These two physical contributions to vorticity are significant in high-pressure flows with variable density.

Other dynamical aspects of the vorticity field may be analyzed as well. Apart from displaying the vortex structures, the vorticity field, and some terms contributing to the vorticity generation, features like the vortex lines, helicity, or flexion may provide further information on the vorticity field and the evolution of the vortex structures and their overall impact on the flow. The vortex lines (i.e., lines tangent to the vorticity vector everywhere) may show a representation of closed vortex tubes, helicity or $H = \int_V \vec{u} \cdot \vec{\omega} dV$ will provide information on the linkage of vortex lines in the flow and flexion or $\chi = \nabla \times \vec{\omega}$ will provide information on the rotation of the vorticity field or, in other words, the second derivatives of the velocity field. Note that $\chi = \nabla \times \vec{\omega} = \nabla \times (\nabla \times \vec{u}) = \nabla(\nabla \cdot \vec{u}) - \nabla^2\vec{u}$; thus, flexion is minus the Laplacian of the velocity field for an incompressible flow.

Lastly, the fuel vapor mixing in the gas phase is relevant for combustion applications. As shown in Chapters 5 and 6, fuel mixing is not only linked to two-phase mixing of droplets and ligaments. The mixing of the fuel vapor within the gas phase is also important. High-pressure regimes show a limited formation of droplets due to the reduced surface-tension force, and the mixing between liquid and gas resembles the mixing of scalar properties in turbulent gaseous flows (i.e., layering). Although molecular diffusion plays an important role in mass and energy mixing, it is expected that intraphase mixing patterns will be closely related to the evolution of vortical structures. Therefore, regions of high fuel vapor concentration will form as a result of vortical motion.

Figures 7.22 and 7.23 show isosurface of the fuel vapor mass fraction, Y_F, for case C1 (i.e., 150 bar and gas freestream velocity of $u_G = 30$ m/s) as an example of the impact of vortex

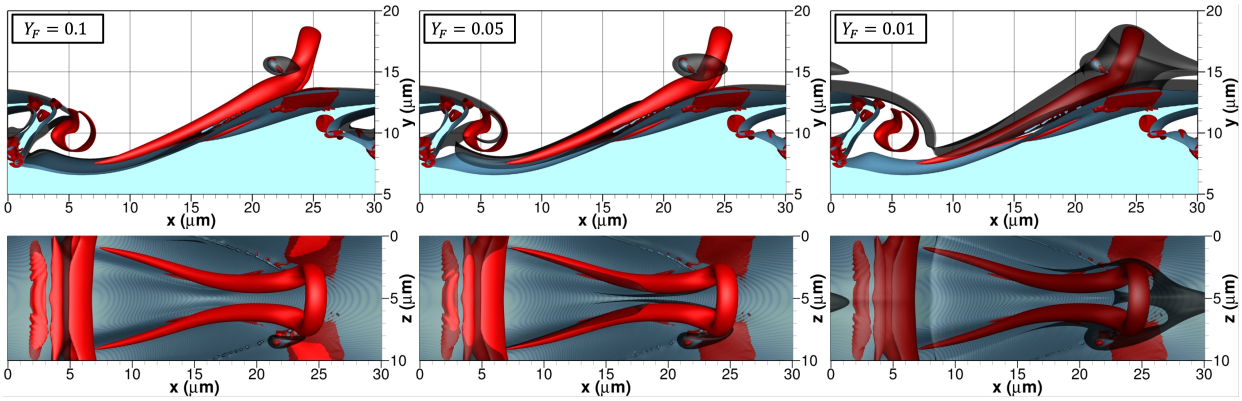

(a) (b) (c)

Figure 7.22: Fuel vapor isosurfaces at 150 bar with gas freestream velocity of $u_G = 30$ m/s (i.e., case C1) at the non-dimensional time of $t^* = t/t_c = t\frac{u_G}{H} = 6.00$. The top figures show the side view from an xy plane located at $z = 10$ μm and the bottom figures show the top view from an xz plane located above the liquid surface. The interface location is identified as the blue isosurface with $C = 0.5$ and the vortex structures are identified by the red isosurface with $\lambda_\rho = -2.5 \times 10^{15}$ kg/(m^{3}s^2). The transparent black isosurface represents various levels of fuel vapor mass fraction. (a) $Y_F = 0.1$; (b) $Y_F = 0.05$; and (c) $Y_F = 0.01$.

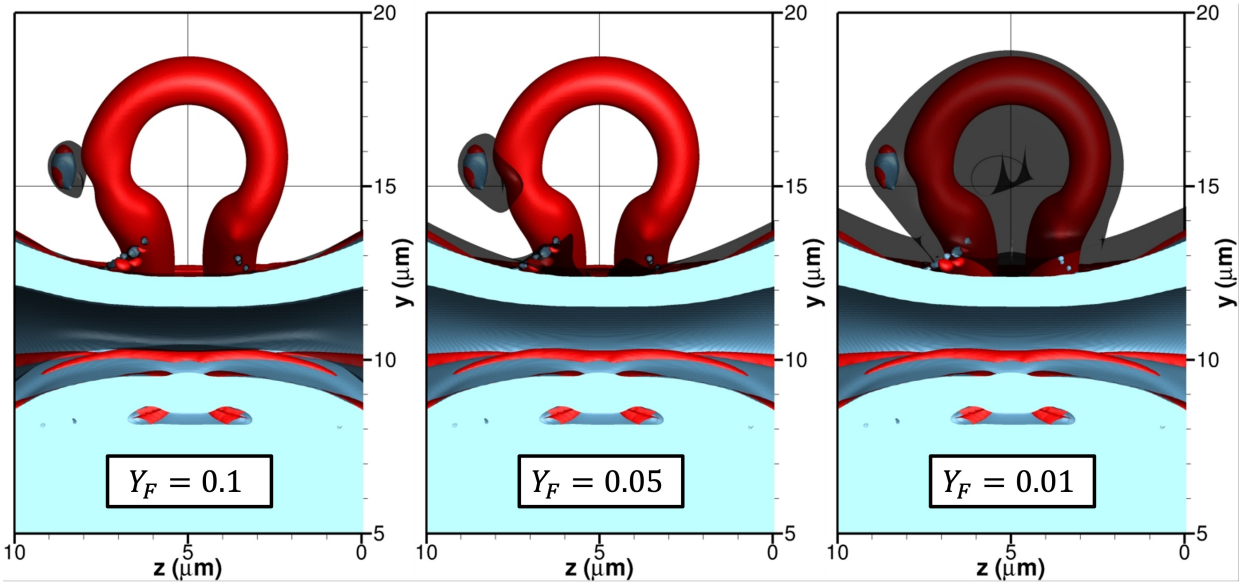

(a) (b) (c)

Figure 7.23: Fuel vapor isosurfaces at 150 bar with gas freestream velocity of $u_G = 30$ m/s (i.e., case C1) at the non-dimensional time of $t^* = t/t_c = t\frac{u_G}{H} = 6.00$. The side view from a yz plane located at $x = 30$ μm is shown. The interface location is identified as the blue isosurface with $C = 0.5$ and the vortex structures are identified by the red isosurface with $\lambda_\rho = -2.5 \times 10^{15}$ kg/(m^{3}s^2). The transparent black isosurface represents various levels of fuel vapor mass fraction. (a) $Y_F = 0.1$; (b) $Y_F = 0.05$; and (c) $Y_F = 0.01$.

dynamics in the regions of high fuel vapor concentration. Three different values of Y_F are shown at $t^* = 6.00$: 0.1, 0.05 and 0.01. For $Y_F = 0.1$, it is observed that a region of high fuel vapor concentration exists around the big droplet flowing near the hairpin vortex. Then, the isosurface is very close to the liquid surface everywhere, but between the edge of the liquid wave and the roller vortex in front, the isosurface with $Y_F = 0.1$ is stretched in the streamwise direction. This remark suggests that the vortical motion downstream of the wave's edge promotes rapid evaporation of the liquid fuel and locally higher fuel concentrations in the gas phase. As isosurface with lower values of Y_F are represented, the effect of the hairpin vortex is highlighted. For $Y_F = 0.05$, the fuel-rich region around the droplet wraps around one of the sides of the vortex head. Similarly, fuel-rich regions start to wrap around the vortex pins as well. With the lower value of $Y_F = 0.01$, the entire hairpin vortex is surrounded by a fuel-rich region compared to the rest of the gas phase.

Chapter 8

Summary and Conclusions

This dissertation has introduced a new conceptual and numerical methodology to solve low-Mach-number compressible two-phase flows with phase change. The methodology applies to compressible liquids undergoing a phase change. It is a suitable approach to study non-reactive two-phase flows in the transcritical domain where the ambient pressure is supercritical for the injected fuel, but the temperature near the liquid-gas interface is still below the mixture critical temperature. This thermodynamic state is relevant near the fuel injectors of high-pressure combustion chambers operating with liquid hydrocarbon fuels, such as those found in diesel engines, gas turbines, and rocket engines. The model cannot capture downstream phenomena affected by localized heating (e.g., chemical energy release, flame front) that may cause a transition of the liquid-gas interface to a supercritical state driven by diffusive mixing. Nonetheless, it can represent all the relevant physics involved in the early stages of the injection process. The features describing the early liquid atomization and fuel-oxidizer mixing can be studied (e.g., the role of two-phase dynamics, thermodynamic behavior of the interface, intraphase diffusive mixing).

The liquid phase is advected using a compressible extension of the VOF approach developed by Baraldi et al. [63] for compressible liquids with mass exchange across the interface (see Subsection 4.1.2). Furthermore, a non-ideal thermodynamic model based on a volume-corrected SRK equation of state [76] is integrated into the governing equations, as well as their interface balancing. This thermodynamic model has been described in Section 3.3. No turbulence model is considered. The early times of the liquid injection are described by transitional turbulence as the liquid jet atomizes. Thus, a fully-turbulent state occurs for later times than those covered in this dissertation. Table 6.2 shows that mild Reynolds numbers (i.e., $\mathcal{O}(10^3)$) are obtained in both phases based on the jet thickness and freestream properties.

The sophistication of non-ideal physics at high pressures increases the computational burden. Jump conditions and local thermodynamic phase equilibrium must be solved at each interface cell to accurately capture the interface attributes and its movement, while extrapolations of phase-wise fluid compressibilities and the associated phase-wise velocity field must be performed. This interface-resolved technique thoroughly characterizes the variations in interface properties inherent to transcritical environments and how they affect liquid deformation. The increase in computational cost is mitigated by developing a constant-coefficient PPE for low-Mach-number flows based on Dodd et al. [64, 94]. An efficient FFT algorithm is used to solve this PPE.

Several tests demonstrate the viability and correctness of the numerical model described in this dissertation (see Appendix F). A fine enough mesh is required to offer a sufficiently smooth interface solution while minimizing numerical inaccuracies and mass errors. The model recovers the mass-conserving features of Baraldi et al. [63] in the limit of incompressible liquid without phase change. The highly-coupled strategy causes the formation of spurious currents around the interface, which must be addressed to avoid an unrealistic or numerically-unstable interface development. The VOF approach alone has been shown

to generate spurious currents; the HF method used to estimate curvature and the volume-averaging of fluid properties at interface cells while solving the one-fluid momentum equation presented in Section 4.3 are sources of numerical oscillations near the interface. Also, further spurious currents are generated by localized source terms due to mass exchange and differing fluid compressibilities at the interface when accounting for the full real-fluid model.

The early atomization features of a transcritical liquid n-decane planar jet injected into oxygen have been investigated in a variety of configurations with differing ambient thermodynamic pressures (i.e., 50 bar, 100 bar, and 150 bar) and gas freestream velocities (i.e., 30 m/s, 50 m/s, and 70 m/s). The deformation of the liquid jet develops quite rapidly, particularly at very high pressures of 100 bar and above. For all cases, the studied physical times are less than 10 μs. The jet's behavior is explained by the lower surface tension and the influence of species and thermal mixing on the fluid properties in both the liquid and gas phases. To provide some context, the reduced pressure, defined as $p_r = p/p_{c,fuel}$, is 4.75 at 100 bar and 7.15 at 150 bar. The surface-tension coefficient decreases significantly at high pressures as oxygen dissolution into the liquid phase increases. Furthermore, the gas becomes denser, and the dissolution of a lighter species into the liquid phase results in a significant drop in liquid density and liquid viscosity, the latter falling to gas-like values. Consequently, perturbations with shorter wavelengths than those observed in typical subcritical or incompressible analyses might emerge quickly.

It has been demonstrated that these mixing effects play a substantial role in the local deformation of the jet as well, particularly at 100 and 150 bar. Localized mixing produces thin liquid structures that are easily stretched and deformed by the flow, such as the vortical motion in the gas phase. Eventually, these structures develop holes and may break up into ligaments and droplets. Depending on the initial problem configuration, various common deformation mechanisms have been characterized in Section 6.3 (e.g., lobe extension, bending and perforation, or lobe corrugation). Moreover, depending on the surface location,

the changing interface state (e.g., temperature, composition, surface-tension coefficient) may cause an unstable surface behavior as detailed in Section 6.4. Parts of the liquid surface submerged into the hotter and faster oxidizer stream tend to have higher surface temperatures and lower surface-tension coefficient; thus, being susceptible to unstable short-wavelength perturbations caused by trigger events such as droplet or ligament impacts. Minor lobes form on the liquid surface as a result of these small perturbations, which eventually break up into small and elongated ligaments. Following that, ligament shredding is detected.

These local features overlap with a significant deformation mechanism defined by continuous folding or layering of liquid sheets at 100 bar and 150 bar, as described in Subsection 6.3.4. This mechanism occurs due to the low overall surface-tension forces and the imposed shear layer from the initial velocity profile. In contrast to subcritical environments where surface-tension forces dominate at larger length scales, the primary surface-area growth driver at high pressures is surface deformation and layer formation rather than atomization into ligaments and droplets. According to the configurations and time frames studied in this dissertation, the surface area represented by detached ligaments and droplets is never more than 7% of the liquid-phase surface area (see Figure 6.30c).

The local production of ligaments and droplets and mass exchange are all influenced by the formation of these layers. Layering has the effect of insulating a portion of the two-phase mixing zone from the oxidizer stream. For example, it prevents the hotter gas from being entrained. As a result, the creation of ligaments and droplets is minimized, the average interface temperature decreases, and the vaporization rate decreases. These effects are significant because net condensation may occur at very high pressures (i.e., over 50 bar for the binary configuration under consideration in this dissertation), limiting the vaporization of the liquid phase. The temperature of small detached liquid structures increases rapidly to the point where the heat from the gas phase causes net evaporation in these structures. Nonetheless, the fuel species constantly vaporizes and mixes with the gas phase. Despite the

varying phase change and the possibility of opposite behaviors in different interface regions, the enhanced dissolution of oxygen and the heating of the liquid generate localized volume expansion near the interface, limiting the volume reduction of the liquid phase in vaporizing regions (see Section 6.7).

The reported characteristics, which mainly affect very high-pressure scenarios, indicate that rather than traditional two-phase mixing or spray production, the mixing of fuel and oxidizer is driven by diffusion and convective transport in each phase. Also, they help explain why tests of supercritical liquid injection utilizing conventional imaging techniques (e.g., shadowgraphy or ballistic imaging) have problems detecting any two-phase phenomena. Variable fluid properties across mixing zones, combined with the formation of small structures and micro-scale droplets, can cause scattering and refraction, concealing any evidence of two-phase flows behind a hazy structure that looks like a turbulent gas jet.

Five charts summarizing the behavior of transcritical liquid jet are shown from Figures 8.1 through 8.5. The main findings from Sections 6.3 to 6.7 are presented, which involve the features discussed in previous lines (e.g., deformation mechanisms, instability triggers, formation of ligaments and droplets, surface-area growth, and phase change at the liquid-gas interface).

The analysis involving vortex dynamics discussed in Section 7.2 reveals that the interaction between deforming vortical structures and the liquid surface explains the identified deformation patterns, such as the lobe extension, bending and perforation mechanism, or the lobe and crest corrugation mechanism. Moreover, the strong vortices formed during the growth of the surface wave at 100 bar and 150 bar deform, align with the streamwise direction, and break up toward smaller and weaker structures that tend to be trapped under the liquid layers that form at very high pressures. This process limits the formation of ligaments and droplets above the two-phase mixture, which tends to uniformize the flow as illustrated by

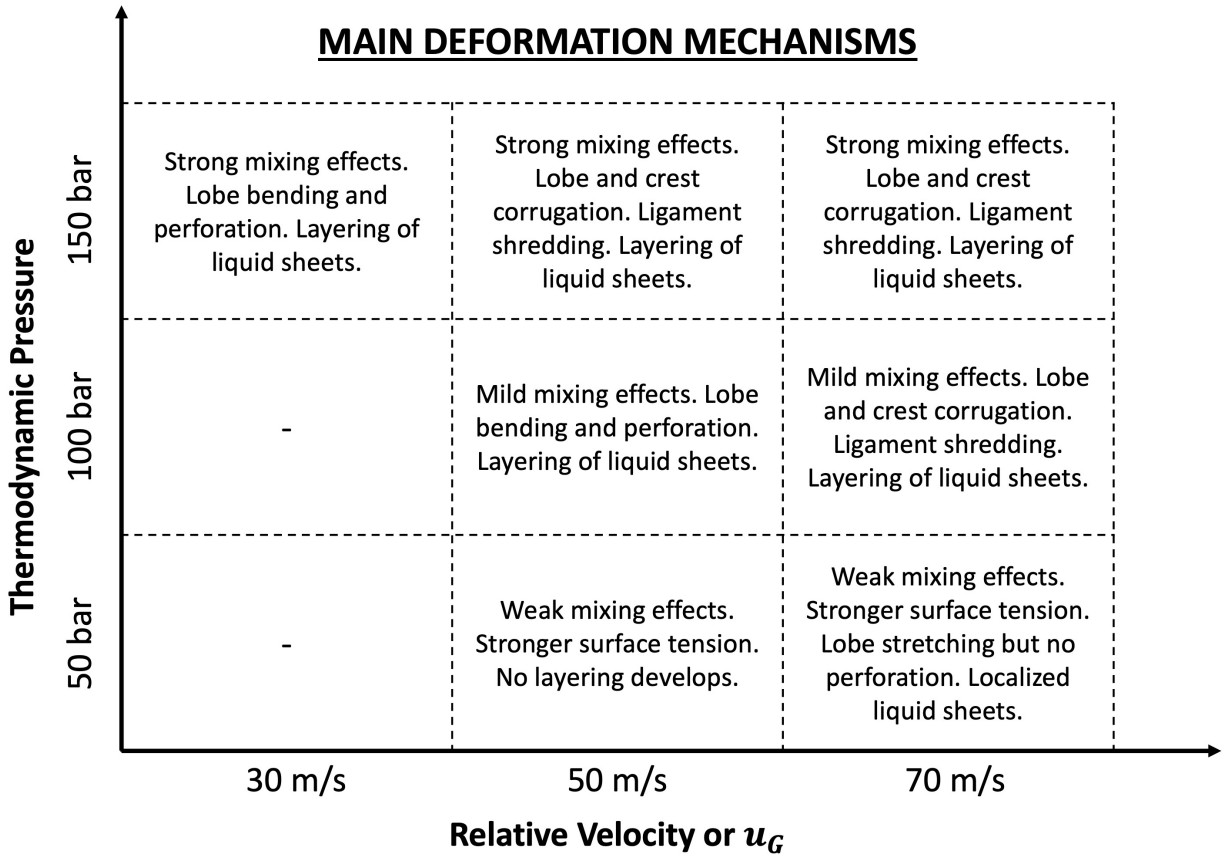

Figure 8.1: Summary of the main deformation mechanisms as a function of thermodynamic pressure and relative velocity between the gaseous and liquid streams (i.e., u_G since $u_L = 0$).

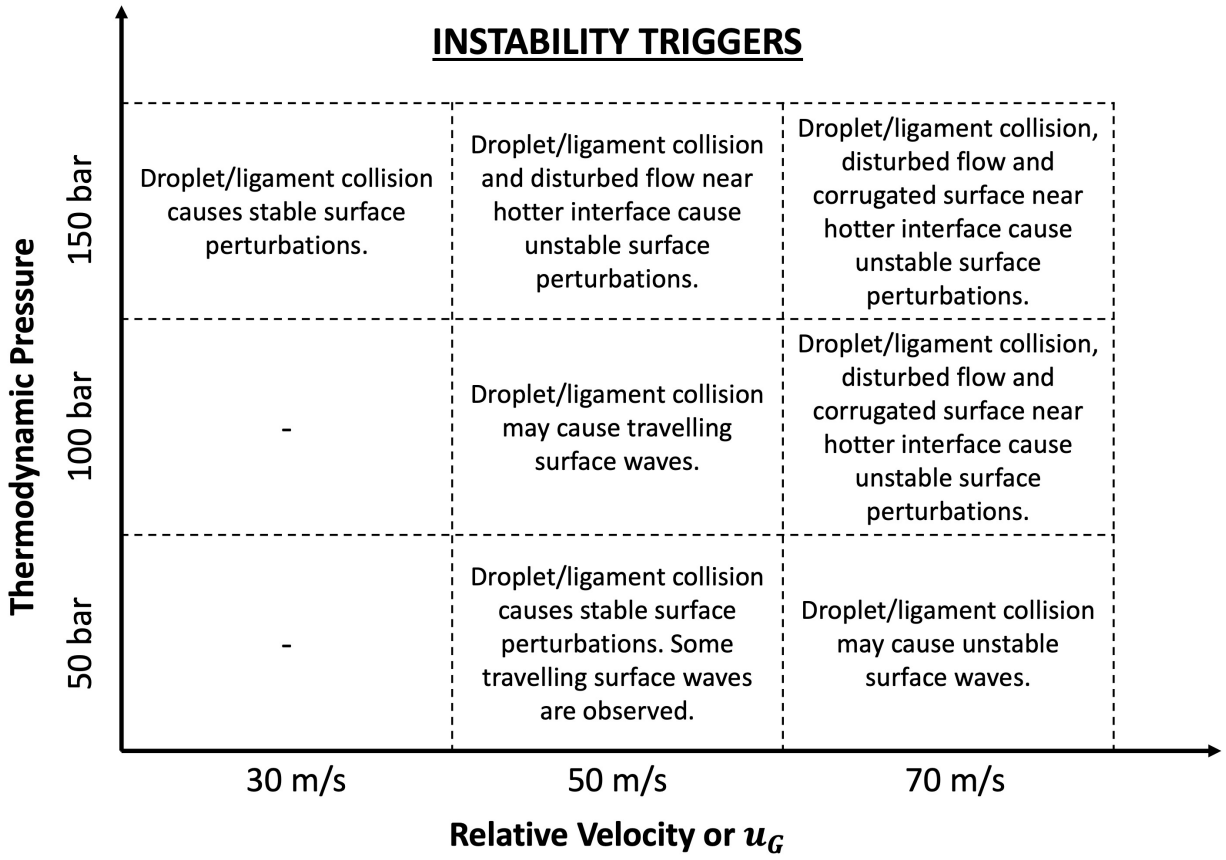

Figure 8.2: Summary of the instability triggers as a function of thermodynamic pressure and relative velocity between the gaseous and liquid streams (i.e., u_G since $u_L = 0$).

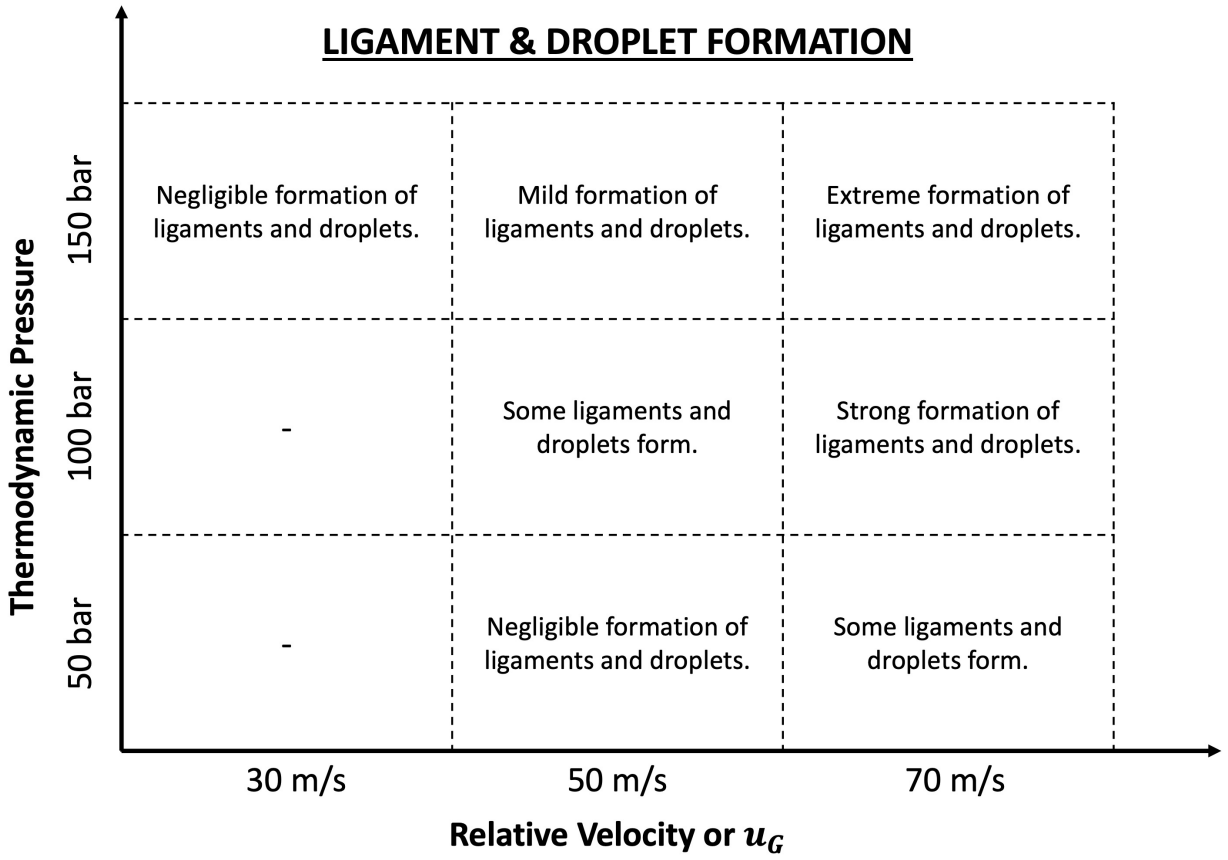

Figure 8.3: Summary of the ligament and droplet formation as a function of thermodynamic pressure and relative velocity between the gaseous and liquid streams (i.e., u_G since $u_L = 0$).

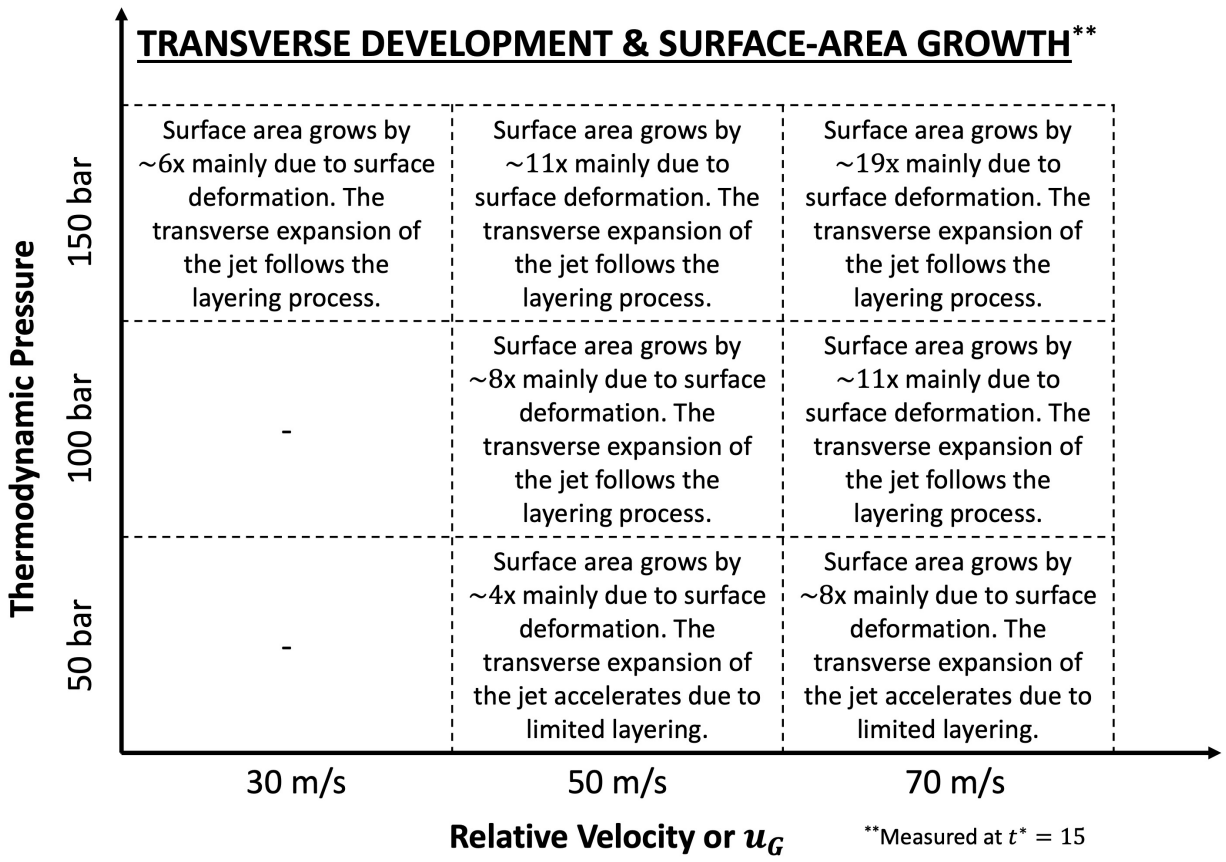

Figure 8.4: Summary of the transverse development and the surface-area growth of the liquid jet as a function of thermodynamic pressure and relative velocity between the gaseous and liquid streams (i.e., u_G since $u_L = 0$).

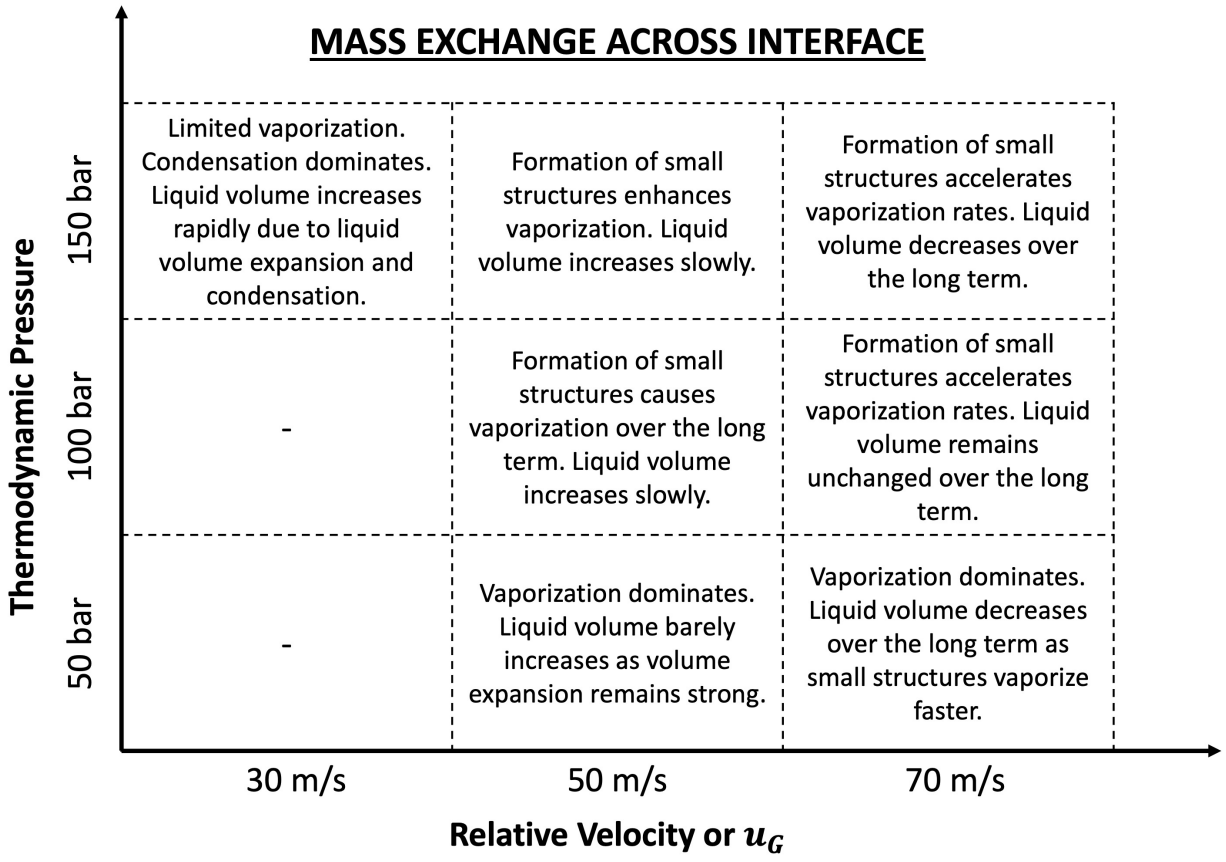

Figure 8.5: Summary of the mass exchange across the interface as a function of thermodynamic pressure and relative velocity between the gaseous and liquid streams (i.e., u_G since $u_L = 0$).

Figure 6.16. Instead, the 50 bar cases show stronger vortical structures everywhere in the two-phase mixture since layering does not become a significant feature.

Details on the rim vortex are provided in Subsection 7.3.2, which forms in the gas phase along the edge of lobes and holes and is a common feature observed in most of the configurations. Although compressible stretching and baroclinicity may be essential sources of vorticity in transcritical flows where density varies, the rim vortex is defined by vortex generation due to vortex stretching as holes and lobes expand. Additionally, the denser gas at very high pressures limits the magnitude of the baroclinic term, which scales with the reciprocal of ρ^2 or, in other terms, ρ^{-2}.

The configurations reported in this dissertation reflect only a small subset of possible configurations of the broader picture of liquid fuel injection at transcritical conditions. Only a portion of the thermodynamic space has been studied. Furthermore, various multi-component systems may exhibit similar or completely distinct behavior at different pressures and temperatures. However, to the best of the author's knowledge, this is the first work to show in-depth the physical mechanisms involved in transcritical injection and their effect on the early deformation features of the liquid jet.

In terms of future research, it is still unclear what mixing patterns arise between the fuel and the oxidizer. Because mixing is primarily driven by diffusion and convective transport in each phase, vortex dynamics have been shown to explain the causes of liquid surface deformation and are predicted to be essential for phase-wise mixing patterns as well. Simultaneously, the variable fluid properties may affect the formation of vortical structures that requires further study. Besides that, simulation capabilities should include modeling the transition from a sharp two-phase interface to a diffuse single-phase transition between the compressible liquid and the dense gas to capture scenarios where phase equilibrium is no longer valid (i.e., near and beyond the mixture critical point).

Finally, the resolution level presented in this work may not be a feasible option for full-scale simulations of spatially developing jets for many years to come. Nonetheless, the knowledge provided by this type of study is critical in developing reduced-order models or sub-grid models for use in full-scale simulations of transcritical liquid fuel injection into combustion chambers. Models that measure the formation of droplets, the increase in surface area per unit volume, and vaporization rates below the mesh size, for example, could be devised.

Bibliography

[1] W. O. H. Mayer, H. Tamura, Propellant injection in a liquid oxygen/gaseous hydrogen rocket engine, Journal of Propulsion and Power 12 (6) (1996) 1137–1147.

[2] W. O. H. Mayer, A. H. A. Schik, B. Vielle, C. Chauveau, I. Gökalp, D. G. Talley, R. D. Woodward, Atomization and breakup of cryogenic propellants under high-pressure subcritical and supercritical conditions, Journal of Propulsion and Power 14 (5) (1998) 835–842.

[3] W. O. H. Mayer, A. H. A. Schik, M. Schaffler, H. Tamura, Injection and mixing processes in high-pressure liquid oxygen/gaseous hydrogen rocket combustors, Journal of Propulsion and Power 16 (5) (2000) 823–828.

[4] M. Oschwald, J. Smith, R. Branam, J. Hussong, A. H. A. Schik, B. Chehroudi, D. G. Talley, Injection of fluids into supercritical environments, Combustion Science and Technology 178 (1-3) (2006) 49–100.

[5] B. Chehroudi, Recent experimental efforts on high-pressure supercritical injection for liquid rockets and their implications, International Journal of Aerospace Engineering 2012 (2012) 1–30.

[6] Z. Falgout, M. Rahm, D. Sedarsky, M. Linne, Gas/fuel jet interfaces under high pressures and temperatures, Fuel 168 (2016) 14–21.

[7] C. Crua, J. Manin, L. M. Pickett, On the transcritical mixing of fuels at diesel engine conditions, Fuel 208 (2017) 535–548.

[8] D. B. Spalding, Theory of particle combustion at high pressures, ARS Journal 29 (11) (1959) 828–835.

[9] D. E. Rosner, On liquid droplet combustion at high pressures., AIAA Journal 5 (1) (1967) 163–166.

[10] K. C. Hsieh, J. S. Shuen, V. Yang, Droplet vaporization in high-pressure environments I: Near critical conditions, Combustion Science and Technology 76 (1-3) (1991) 111–132.

[11] J.-P. Delplanque, W. A. Sirignano, Numerical study of the transient vaporization of an oxygen droplet at sub- and supercritical conditions, International Journal of Heat and Mass Transfer 36 (2) (1993) 303–314.

[12] V. Yang, J.-S. Shuen, Vaporization of liquid oxygen (LOX) droplets in supercritical hydrogen environments, Combustion Science and Technology 97 (4-6) (1994) 247–270.

[13] J.-P. Delplanque, W. A. Sirignano, Transcritical vaporization and combustion of LOX droplet arrays in a convective environment, Combustion Science and Technology 105 (4-6) (1995) 327–344.

[14] J.-P. Delplanque, W. A. Sirignano, Transcritical liquid oxygen droplet vaporization-effect on rocket combustion instability, Journal of Propulsion and Power 12 (2) (1996) 349–357.

[15] J. Poblador-Ibanez, W. A. Sirignano, Transient behavior near liquid-gas interface at supercritical pressure, International Journal of Heat and Mass Transfer 126 (2018) 457–473.

[16] B. W. Davis, J. Poblador-Ibanez, W. A. Sirignano, Two-phase developing laminar mixing layer at supercritical pressures, International Journal of Heat and Mass Transfer 167 (2021) 120687.

[17] J. Poblador-Ibanez, B. W. Davis, W. A. Sirignano, Self-similar solution of a supercritical two-phase laminar mixing layer, International Journal of Multiphase Flow 135 (2021) 103465.

[18] V. Yang, Modeling of supercritical vaporization, mixing, and combustion processes in liquid-fueled propulsion systems, Proceedings of the Combustion Institute 28 (1) (2000) 925–942.

[19] J. Poblador-Ibanez, W. A. Sirignano, Analysis of an axisymmetric liquid jet at supercritical pressures, in: Proceedings of the ILASS-Americas 30th Annual Conference on Liquid Atomization and Spray Systems, Tempe, AZ, 2019.

[20] M. Minniti, A. Ziaee, J. Trolinger, D. Dunn-Rankin, Ultrashort pulse off-axis digital holography for imaging the core structure of transient sprays, Atomization and Sprays 28 (6).

[21] M. Minniti, A. Ziaee, D. Curran, J. Porter, T. Parker, D. Dunn-Rankin, Femtosecond digital holography in the near-nozzle region of a dodecane spray, Atomization and Sprays 29 (3) (2019) 251–267.

[22] C. Traxinger, M. Pfitzner, S. Baab, G. Lamanna, B. Weigand, Experimental and numerical investigation of phase separation due to multicomponent mixing at high-pressure conditions, Physical Review Fluids 4 (7) (2019) 074303.

[23] T. C. Klima, A. Peter, S. Riess, M. Wensing, A. S. Braeuer, Quantification of mixture composition, liquid-phase fraction and temperature in transcritical sprays, The Journal of Supercritical Fluids 159 (2020) 104777.

[24] D. Jarrahbashi, W. A. Sirignano, Vorticity dynamics for transient high-pressure liquid injection, Physics of Fluids 26 (10) (2014) 73.

[25] D. Jarrahbashi, W. A. Sirignano, P. P. Popov, F. Hussain, Early spray development at high gas density: hole, ligament and bridge formations, Journal of Fluid Mechanics 792 (2016) 186–231.

[26] A. Zandian, W. A. Sirignano, F. Hussain, Planar liquid jet: Early deformation and atomization cascades, Physics of Fluids 29 (6) (2017) 062109.

[27] A. Zandian, W. A. Sirignano, F. Hussain, Understanding liquid-jet atomization cascades via vortex dynamics, Journal of Fluid Mechanics 843 (2018) 293–354.

[28] A. Zandian, W. A. Sirignano, F. Hussain, Length-scale cascade and spread rate of atomizing planar liquid jets, International Journal of Multiphase Flow 113 (2019) 117–141.

[29] R. N. Dahms, J. C. Oefelein, On the transition between two-phase and single-phase interface dynamics in multicomponent fluids at supercritical pressures, Physics of Fluids 25 (9) (2013) 092103.

[30] R. N. Dahms, J. C. Oefelein, Liquid jet breakup regimes at supercritical pressures, Combustion and Flame 162 (10) (2015) 3648–3657.

[31] R. N. Dahms, J. C. Oefelein, Non-equilibrium gas-liquid interface dynamics in high-pressure liquid injection systems, Proceedings of the Combustion Institute 35 (2) (2015) 1587–1594.

[32] R. N. Dahms, Understanding the breakdown of classic two-phase theory and spray atomization at engine-relevant conditions, Physics of Fluids 28 (4) (2016) 042108.

[33] J. Bellan, Supercritical (and subcritical) fluid behavior and modeling: drops, streams, shear and mixing layers, jets and sprays, Progress in Energy and Combustion Science 26 (4-6) (2000) 329–366.

[34] P. He, A. Raghavan, A. F. Ghoniem, Impact of non-ideality on mixing of hydrocarbons and water at supercritical or near-critical conditions, The Journal of Supercritical Fluids 102 (2015) 50–65.

[35] A. Zandian, W. A. Sirignano, F. Hussain, Three-dimensional liquid sheet breakup: vorticity dynamics, in: 54th AIAA aerospace sciences meeting, 2016, p. 1593.

[36] A. Zandian, W. A. Sirignano, F. Hussain, Vorticity dynamics in a spatially developing liquid jet inside a co-flowing gas, Journal of Fluid Mechanics 877 (2019) 429–470.

[37] W. A. Sirignano, Fluid dynamics and transport of droplets and sprays, Cambridge University Press, 2010.

[38] W. A. Sirignano, C. Mehring, Review of theory of distortion and disintegration of liquid streams, Progress in Energy and Combustion Science 26 (4-6) (2000) 609–655.

[39] S. Leroux, Stabilité d'un jet liquide cylindrique. Influence de fortes pressions ambiantes, Ph.D. thesis, Université de Rouen (1996).

[40] D. Joseph, J. Wang, T. Funada, Potential flows of viscous and viscoelastic liquids, Cambridge Univ. Press, 2007.

[41] J. Jeong, F. Hussain, On the identification of a vortex, Journal of Fluid Mechanics 285 (1995) 69–94.

[42] V. Kolář, Vortex identification: New requirements and limitations, International Journal of Heat and Fluid Flow 28 (4) (2007) 638–652.

[43] J. Yao, F. Hussain, Toward vortex identification based on local pressure-minimum criterion in compressible and variable density flows, Journal of Fluid Mechanics 850 (2018) 5–17.

[44] J. C. R. Hunt, A. A. Wray, P. Moin, Eddies, stream, and convergence zones in turbulent flows, Center for Turbulence Research Report CTR-S88 (1988) 193–208.

[45] B. Chehroudi, D. G. Talley, E. Coy, Visual characteristics and initial growth rates of round cryogenic jets at subcritical and supercritical pressures, Physics of Fluids 14 (2) (2002) 850–861.

[46] B. Chehroudi, R. Cohn, D. G. Talley, Cryogenic shear layers: experiments and phenomenological modeling of the initial growth rate under subcritical and supercritical conditions, International Journal of Heat and Fluid Flow 23 (5) (2002) 554–563.

[47] L. Jofre, J. Urzay, Transcritical diffuse-interface hydrodynamics of propellants in high-pressure combustors of chemical propulsion systems, Progress in Energy and Combustion Science 82 (2021) 100877.

[48] G. Soave, Equilibrium constants from a modified Redlich-Kwong equation of state, Chemical Engineering Science 27 (6) (1972) 1197–1203.

[49] P. L. Chueh, J. M. Prausnitz, Vapor-liquid equilibria at high pressures: Calculation of critical temperatures, volumes, and pressures of nonpolar mixtures, AIChE Journal 13 (6) (1967) 1107–1113.

[50] B. A. Stradi, J. F. Brennecke, P. Kohn, M. A. Stadtherr, Reliable computation of mixture critical points, AIChE Journal 47 (1) (2001) 212–221.

[51] R. Stierle, C. Waibel, J. Gross, C. Steinhausen, B. Weigand, G. Lamanna, On the selection of boundary conditions for droplet evaporation and condensation at high pressure and temperature conditions from interfacial transport resistivities, International Journal of Heat and Mass Transfer 151 (2020) 119450.

[52] L. Zhang, X. Wang, Y. Li, S.-T. Yeh, V. Yang, Supercritical fluid flow dynamics and mixing in gas-centered liquid-swirl coaxial injectors, Physics of Fluids 30 (7) (2018) 075106.

[53] X. Wang, Y. Wang, V. Yang, Three-dimensional flow dynamics and mixing in a gas-centered liquid-swirl coaxial injector at supercritical pressure, Physics of Fluids 31 (6) (2019) 065109.

[54] P. He, A. F. Ghoniem, A sharp interface method for coupling multiphase flow, heat transfer and multicomponent mass transfer with interphase diffusion, Journal of Computational Physics 332 (2017) 316–332.

[55] S. K. Aggarwal, C. Yan, G. Zhu, Transcritical vaporization of a liquid fuel droplet in a supercritical ambient, Combustion Science and Technology 174 (9) (2002) 103–130.

[56] S. V. Patankar, D. B. Spalding, A calculation procedure for heat, mass and momentum transfer in three-dimensional parabolic flows, International Journal of Heat and Mass Transfer (1972) 1787–1806.

[57] J. Van Doormaal, G. Raithby, Enhancements of the SIMPLE method for predicting incompressible fluid flows, Numerical Heat Transfer 7 (2) (1984) 147–163.

[58] M. Sussman, P. Smereka, S. Osher, A level set approach for computing solutions to incompressible two-phase flow, Journal of Computational Physics 114 (1) (1994) 146–159.

[59] M. Sussman, E. Fatemi, P. Smereka, S. Osher, An improved level set method for incompressible two-phase flows, Computers & Fluids 27 (5-6) (1998) 663–680.

[60] S. Osher, R. P. Fedkiw, Level set methods: an overview and some recent results, Journal of Computational Physics 169 (2) (2001) 463–502.

[61] T. H. Chung, M. Ajlan, L. L. Lee, K. E. Starling, Generalized multiparameter correlation for nonpolar and polar fluid transport properties, Industrial & Engineering Chemistry Research 27 (4) (1988) 671–679.

[62] L. Anumolu, M. F. Trujillo, Gradient augmented level set method for phase change simulations, Journal of Computational Physics 353 (2018) 377–406.

[63] A. Baraldi, M. S. Dodd, A. Ferrante, A mass-conserving volume-of-fluid method: volume tracking and droplet surface-tension in incompressible isotropic turbulence, Computers & Fluids 96 (2014) 322–337.

[64] M. S. Dodd, A. Ferrante, A fast pressure-correction method for incompressible two-fluid flows, Journal of Computational Physics 273 (2014) 416–434.

[65] A. Prosperetti, Motion of two superposed viscous fluids, The Physics of Fluids 24 (7) (1981) 1217–1223.

[66] J. Poblador-Ibanez, W. A. Sirignano, A Volume-of-Fluid method for variable-density, two-phase flows at supercritical pressure. Physics of Fluids *in press*. (2022). `arXiv: 2103.01874`.

[67] A. F. Ismail, K. C. Khulbe, T. Matsuura, Gas Separation Membranes: Polymeric and Inorganic, Vol. 10, Springer, 2015.

[68] F. Pazzona, B. Borah, P. Demontis, G. Suffritti, S. Yashonath, A comparative molecular dynamics study of diffusion of n-decane and 3-methyl pentane in y zeolite, Journal of Chemical Sciences 121 (5) (2009) 921.

[69] G. S. Zhu, S. K. Aggarwal, Transient supercritical droplet evaporation with emphasis on the effects of equation of state, International Journal of Heat and Mass Transfer 43 (7) (2000) 1157–1171.

[70] F. Jaeger, O. K. Matar, E. A. Müller, Bulk viscosity of molecular fluids, The Journal of Chemical Physics 148 (17) (2018) 174504.

[71] O. Redlich, J. N. S. Kwong, On the thermodynamics of solutions. V. An equation of state. Fugacities of gaseous solutions., Chemical Reviews 44 (1) (1949) 233–244.

[72] H. B. Callen, Thermodynamics and an Introduction to Thermostatistics, American Association of Physics Teachers, 1998.

[73] M. Benedict, G. B. Webb, L. C. Rubin, An empirical equation for thermodynamic properties of light hydrocarbons and their mixtures I. Methane, ethane, propane and n-butane, The Journal of Chemical Physics 8 (4) (1940) 334–345.

[74] M. Benedict, G. B. Webb, L. C. Rubin, An empirical equation for thermodynamic properties of light hydrocarbons and their mixtures II. Mixtures of methane, ethane, propane, and n-butane, The Journal of Chemical Physics 10 (12) (1942) 747–758.

[75] J. M. Prausnitz, F. W. Tavares, Thermodynamics of fluid-phase equilibria for standard chemical engineering operations, AIChE Journal 50 (4) (2004) 739–761.

[76] H. Lin, Y.-Y. Duan, T. Zhang, Z.-M. Huang, Volumetric Property Improvement for the Soave-Redlich-Kwong Equation of State, Industrial & Engineering Chemistry Research 45 (5) (2006) 1829–1839.

[77] D.-Y. Peng, D. B. Robinson, A new two-constant equation of state, Industrial & Engineering Chemistry Fundamentals 15 (1) (1976) 59–64.

[78] M. S. Graboski, T. E. Daubert, A modified Soave equation of state for phase equilibrium calculations. 1. Hydrocarbon systems, Industrial & Engineering Chemistry Process Design and Development 17 (4) (1978) 443–448.

[79] M. S. Graboski, T. E. Daubert, A modified Soave equation of state for phase equilibrium calculations. 2. Systems containing CO2, H2S, N2, and CO, Industrial & Engineering Chemistry Process Design and Development 17 (4) (1978) 448–454.

[80] G. Soave, S. Gamba, L. A. Pellegrini, SRK equation of state: Predicting binary interaction parameters of hydrocarbons and related compounds, Fluid Phase Equilibria 299 (2) (2010) 285–293.

[81] B. E. Poling, J. M. Prausnitz, J. P. O'Connell, R. C. Reid, The Properties of Gases and Liquids, Vol. 5, McGraw-Hill New York, 2001.

[82] S. R. Turns, An Introduction to Combustion, Vol. 499, McGraw-Hill, 1996.

[83] R. Tillner-Roth, D. G. Friend, A Helmholtz free energy formulation of the thermodynamic properties of the mixture {water+ ammonia}, Journal of Physical and Chemical Reference Data 27 (1) (1998) 63–96.

[84] M. A. M. Neto, J. R. Barbosa Jr, A departure-function approach to calculate thermodynamic properties of refrigerant-oil mixtures, International Journal of Refrigeration 36 (3) (2013) 972–979.

[85] C. A. Passut, R. P. Danner, Correlation of ideal gas enthalpy, heat capacity and entropy, Industrial & Engineering Chemistry Process Design and Development 11 (4) (1972) 543–546.

[86] A. Leahy-Dios, A. Firoozabadi, Unified model for nonideal multicomponent molecular diffusion coefficients, AIChE Journal 53 (11) (2007) 2932–2939.

[87] J. W. Mutoru, A. Firoozabadi, Form of multicomponent Fickian diffusion coefficients matrix, The Journal of Chemical Thermodynamics 43 (8) (2011) 1192–1203.

[88] X. Liu, A. Martín-Calvo, E. McGarrity, S. K. Schnell, S. Calero, J.-M. Simon, D. Bedeaux, S. Kjelstrup, A. Bardow, T. J. Vlugt, Fick diffusion coefficients in ternary liquid systems from equilibrium molecular dynamics simulations, Industrial & Engineering Chemistry Research 51 (30) (2012) 10247–10258.

[89] R. Krishna, J. M. van Baten, Describing diffusion in fluid mixtures at elevated pressures by combining the Maxwell–Stefan formulation with an equation of state, Chemical Engineering Science 153 (2016) 174–187.

[90] S. Elghobashi, Direct numerical simulation of turbulent flows laden with droplets or bubbles, Annual Review of Fluid Mechanics 51 (2019) 217–244.

[91] C. W. Hirt, B. D. Nichols, Volume of fluid (VOF) method for the dynamics of free boundaries, Journal of Computational Physics 39 (1) (1981) 201–225.

[92] R. Scardovelli, S. Zaleski, Direct numerical simulation of free-surface and interfacial flow, Annual Review of Fluid Mechanics 31 (1) (1999) 567–603.

[93] G. Tryggvason, B. Bunner, A. Esmaeeli, D. Juric, N. Al-Rawahi, W. Tauber, J. Han, S. Nas, Y.-J. Jan, A front-tracking method for the computations of multiphase flow, Journal of Computational Physics 169 (2) (2001) 708–759.

[94] M. S. Dodd, P. Trefftz-Posada, A. Ferrante, A coupled volume-of-fluid and pressure-correction method for gas-liquid flows with phase change: I. Incompressible formulation, (In Preparation).

[95] M. S. Dodd, D. Mohaddes, A. Ferrante, M. Ihme, Analysis of droplet evaporation in isotropic turbulence through droplet-resolved dns, International Journal of Heat and Mass Transfer 172 (2021) 121157.

[96] W. Bo, J. W. Grove, A volume of fluid method based ghost fluid method for compressible multi-fluid flows, Computers & Fluids 90 (2014) 113–122.

[97] B. Duret, R. Canu, J. Reveillon, F. Demoulin, A pressure based method for vaporizing compressible two-phase flows with interface capturing approach, International Journal of Multiphase Flow 108 (2018) 42–50.

[98] F. Denner, C.-N. Xiao, B. G. van Wachem, Pressure-based algorithm for compressible interfacial flows with acoustically-conservative interface discretisation, Journal of Computational Physics 367 (2018) 192–234.

[99] J.-C. Nave, R. R. Rosales, B. Seibold, A gradient-augmented level set method with an optimally local, coherent advection scheme, Journal of Computational Physics 229 (10) (2010) 3802–3827.

[100] R. Courant, E. Isaacson, M. Rees, On the solution of nonlinear hyperbolic differential equations by finite differences, Communications on Pure and Applied Mathematics 5 (3) (1952) 243–255.

[101] L. Anumolu, M. F. Trujillo, Gradient augmented reinitialization scheme for the level set method, International Journal for Numerical Methods in Fluids 73 (12) (2013) 1011–1041.

[102] M. F. Trujillo, L. Anumolu, D. Ryddner, The distortion of the level set gradient under advection, Journal of Computational Physics 334 (2017) 81–101.

[103] A. Esmaeeli, G. Tryggvason, Computations of film boiling. Part I: numerical method, International Journal of Heat and Mass Transfer 47 (25) (2004) 5451–5461.

[104] G. Tryggvason, J. Lu, Direct numerical simulations of flows with phase change, Procedia IUTAM 15 (2015) 2–13.

[105] R. P. Fedkiw, T. D. Aslam, B. Merriman, S. Osher, A non-oscillatory Eulerian approach to interfaces in multimaterial flows (the ghost fluid method), Journal of Computational Physics 152 (2) (1999) 457–492.

[106] R. P. Fedkiw, T. D. Aslam, S. Xu, The ghost fluid method for deflagration and detonation discontinuities, Journal of Computational Physics 154 (2) (1999) 393–427.

[107] D. Nguyen, F. Gibou, R. Fedkiw, A fully conservative ghost fluid method and stiff detonation waves, in: 12th Int. Detonation Symposium, San Diego, CA, 2002.

[108] R. P. Fedkiw, X.-D. Liu, The ghost fluid method for viscous flows, in: Innovative methods for numerical solution of partial differential equations, World Scientific, 2002, pp. 111–143.

[109] M. S. Lee, A. Riaz, V. Aute, Direct numerical simulation of incompressible multiphase flow with phase change, Journal of Computational Physics 344 (2017) 381–418.

[110] J. Lee, G. Son, A sharp-interface level-set method for compressible bubble growth with phase change, International Communications in Heat and Mass Transfer 86 (2017) 1–11.

[111] R. Scardovelli, E. Aulisa, S. Manservisi, V. Marra, A marker-VOF algorithm for incompressible flows with interfaces, in: ASME 2002 Joint US-European Fluids Engineering Division Conference, American Society of Mechanical Engineers, 2002, pp. 905–910.

[112] D. L. Youngs, Time-dependent multi-material flow with large fluid distortion, Numerical Methods for Fluid Dynamics 1 (1982) 41–51.

[113] G. Miller, P. Colella, A conservative three-dimensional Eulerian method for coupled solid–fluid shock capturing, Journal of Computational Physics 183 (1) (2002) 26–82.

[114] M. Haghshenas, J. A. Wilson, R. Kumar, Algebraic coupled level set-volume of fluid method for surface tension dominant two-phase flows, International Journal of Multiphase Flow 90 (2017) 13–28.

[115] J. Palmore Jr, O. Desjardins, A volume of fluid framework for interface-resolved simulations of vaporizing liquid-gas flows, Journal of Computational Physics 399 (2019) 108954.

[116] D. J. Harvie, D. F. Fletcher, A new volume of fluid advection algorithm: the stream scheme, Journal of Computational Physics 162 (1) (2000) 1–32.

[117] E. Aulisa, S. Manservisi, R. Scardovelli, S. Zaleski, Interface reconstruction with least-squares fit and split advection in three-dimensional Cartesian geometry, Journal of Computational Physics 225 (2) (2007) 2301–2319.

[118] J. López, C. Zanzi, P. Gómez, R. Zamora, F. Faura, J. Hernández, An improved height function technique for computing interface curvature from volume fractions, Computer Methods in Applied Mechanics and Engineering 198 (33-36) (2009) 2555–2564.

[119] S. Popinet, An accurate adaptive solver for surface-tension-driven interfacial flows, Journal of Computational Physics 228 (16) (2009) 5838–5866.

[120] M. Sussman, E. G. Puckett, A coupled level set and volume-of-fluid method for computing 3D and axisymmetric incompressible two-phase flows, Journal of Computational Physics 162 (2) (2000) 301–337.

[121] M. Sussman, A second order coupled level set and volume-of-fluid method for computing growth and collapse of vapor bubbles, Journal of Computational Physics 187 (1) (2003) 110–136.

[122] D. Juric, G. Tryggvason, Computations of boiling flows, International Journal of Multiphase Flow 24 (3) (1998) 387–410.

[123] M. Herrmann, G. Blanquart, V. Raman, Flux corrected finite volume scheme for preserving scalar boundedness in reacting large-eddy simulations, AIAA Journal 44 (12) (2006) 2879–2886.

[124] J. U. Brackbill, D. B. Kothe, C. Zemach, A continuum method for modeling surface tension, Journal of Computational Physics 100 (2) (1992) 335–354.

[125] D. B. Kothe, W. Rider, S. Mosso, J. Brock, J. Hochstein, Volume tracking of interfaces having surface tension in two and three dimensions, in: 34th Aerospace Sciences Meeting and Exhibit, 1996, p. 859.

[126] I. Seric, S. Afkhami, L. Kondic, Direct numerical simulation of variable surface tension flows using a volume-of-fluid method, Journal of Computational Physics 352 (2018) 615–636.

[127] A. J. Chorin, A numerical method for solving incompressible viscous flow problems, Journal of Computational Physics 2 (1) (1967) 12–26.

[128] P. Cifani, Analysis of a constant-coefficient pressure equation method for fast computations of two-phase flows at high density ratios, Journal of Computational Physics 398 (2019) 108904.

[129] B. Turnquist, M. Owkes, A fast, decomposed pressure correction method for an intrusive stochastic multiphase flow solver, Computers & Fluids 221 (2021) 104930.

[130] P. Costa, A FFT-based finite-difference solver for massively-parallel direct numerical simulations of turbulent flows, Computers & Mathematics with Applications 76 (8) (2018) 1853–1862.

[131] H. K. Versteeg, W. Malalasekera, An introduction to Computational Fluid Dynamics: the finite volume method, Pearson Education, 2007.

[132] P. Gaskell, A. Lau, Curvature-compensated convective transport: SMART, a new boundedness-preserving transport algorithm, International Journal for Numerical Methods in Fluids 8 (6) (1988) 617–641.

[133] T. D. Aslam, A partial differential equation approach to multidimensional extrapolation, Journal of Computational Physics 193 (1) (2004) 349–355.

[134] J. O. McCaslin, É. Courtine, O. Desjardins, A fast marching approach to multidimensional extrapolation, Journal of Computational Physics 274 (2014) 393–412.

[135] M. Kang, R. P. Fedkiw, X.-D. Liu, A boundary condition capturing method for multiphase incompressible flow, Journal of Scientific Computing 15 (3) (2000) 323–360.

[136] N. Li, S. Laizet, 2DECOMP & FFT - A highly scalable 2D decomposition library and FFT interface, in: Cray User Group 2010 conference, 2010, pp. 1–13.

[137] M. Frigo, S. G. Johnson, The design and implementation of FFTW3, Proceedings of the IEEE 93 (2) (2005) 216–231.

[138] J. Towns, T. Cockerill, M. Dahan, I. Foster, K. Gaither, A. Grimshaw, V. Hazlewood, S. Lathrop, D. Lifka, G. D. Peterson, et al., XSEDE: accelerating scientific discovery, Computing in Science & Engineering 16 (5) (2014) 62–74.

[139] J. Poblador-Ibanez, W. A. Sirignano, Liquid-jet instability at high pressures with real-fluid interface thermodynamics, Physics of Fluids 33 (8) (2021) 083308.

[140] J. Poblador-Ibanez, W. A. Sirignano, Temporal atomization of a transcritical liquid n-decane jet into oxygen. International Journal of Multiphase Flow *in press* (2022). `arXiv:2201.05639`.

[141] R. M. Chiodi, O. Desjardins, A two-plane interface reconstruction strategy to enable thin-films in VOF simulations, in: Proc. of 14th Triennial Int. Conf. on Liquid Atomization and Spray Systems, Chicago, IL, 2018.

[142] R. M. Chiodi, Advancement of numerical methods for simulating primary atomization, Cornell University, 2020.

[143] A. Han, O. Desjardins, Liquid structure classification towards topology change modeling, in: International Conference on Liquid Atomization and Spray Systems (ICLASS), 2021.

[144] K. A. Buch, W. J. A. Dahm, Experimental study of the fine-scale structure of conserved scalar mixing in turbulent shear flows. Part 1. Sc $>$ 1, Journal of Fluid Mechanics 317 (1996) 21–71.

[145] K. A. Buch, W. J. A. Dahm, Experimental study of the fine-scale structure of conserved scalar mixing in turbulent shear flows. Part 2. Sc $\approx$ 1, Journal of Fluid Mechanics 364 (1998) 1–29.

[146] W. A. Sirignano, Normal shocks with high upstream pressure, Physical Review Fluids 3 (9) (2018) 093401.

[147] F. M. White, I. Corfield, Viscous Fluid Flow, Vol. 3, McGraw-Hill New York, 2006.

[148] U. Ghia, K. N. Ghia, C. Shin, High-Re solutions for incompressible flow using the Navier-Stokes equations and a multigrid method, Journal of Computational Physics 48 (3) (1982) 387–411.

[149] E. Erturk, T. C. Corke, C. Gökçöl, Numerical solutions of 2-D steady incompressible driven cavity flow at high Reynolds numbers, International Journal for Numerical Methods in Fluids 48 (7) (2005) 747–774.

Appendices

A Momentum equation for the axisymmetric jet

The axisymmetric governing equations are the same as those presented in Section 3.2, with the exception that vector operators should consider the axisymmetric coordinates system and the momentum equation, Eq. (3.2), needs some adjustments. The radial and axial momentum equations are, respectively,

$$\frac{\partial}{\partial t}(\rho u_r) + \nabla \cdot (\rho u_r \vec{u}) = -\frac{\partial p}{\partial r} + \frac{1}{r}\frac{\partial}{\partial r}(r\tau_{rr}) + \frac{\partial \tau_{rz}}{\partial z} - \frac{\tau_{\theta\theta}}{r} \tag{A.1}$$

and

$$\frac{\partial}{\partial t}(\rho u_z) + \nabla \cdot (\rho u_z \vec{u}) = -\frac{\partial p}{\partial z} + \frac{1}{r}\frac{\partial}{\partial r}(r\tau_{rz}) + \frac{\partial \tau_{zz}}{\partial z} \tag{A.2}$$

The viscous stress tensor terms involved in the axisymmetric problem are

$$\tau_{rr} = \mu\left(2\frac{\partial u_r}{\partial r} - \frac{2}{3}\nabla \cdot \vec{u}\right) \quad ; \quad \tau_{zz} = \mu\left(2\frac{\partial u_z}{\partial z} - \frac{2}{3}\nabla \cdot \vec{u}\right) \tag{A.3}$$

$$\tau_{\theta\theta} = \mu\left(2\frac{u_r}{r} - \frac{2}{3}\nabla \cdot \vec{u}\right) \quad ; \quad \tau_{rz} = \mu\left(\frac{\partial u_z}{\partial r} + \frac{\partial u_r}{\partial z}\right) \tag{A.4}$$

Each component of the momentum equation can be formulated properly for implementation in a finite-volume solver by substituting the viscous stress tensor terms into Eqs. (A.1) and

(A.2) and rearranging the equations as

$$\begin{aligned}\frac{\partial}{\partial t}(\rho u_r) + \nabla\cdot(\rho u_r \vec{u}) = &-\frac{\partial p}{\partial r} + \nabla\cdot(\mu\nabla u_r) \\ &- \mu\frac{u_r}{r^2} + \frac{1}{3}\mu\frac{\partial}{\partial r}\big(\nabla\cdot\vec{u}\big) \\ &+ \frac{\partial\mu}{\partial r}\left(\frac{\partial u_r}{\partial r} - \frac{2}{3}\nabla\cdot\vec{u}\right) \\ &+ \frac{\partial\mu}{\partial z}\frac{\partial u_z}{\partial r}\end{aligned} \tag{A.5}$$

and

$$\begin{aligned}\frac{\partial}{\partial t}(\rho u_z) + \nabla\cdot(\rho u_z \vec{u}) = &-\frac{\partial p}{\partial z} + \nabla\cdot(\mu\nabla u_z) \\ &+ \frac{1}{3}\mu\frac{\partial}{\partial z}\big(\nabla\cdot\vec{u}\big) + \frac{\partial\mu}{\partial r}\frac{\partial u_r}{\partial z} \\ &+ \frac{\partial\mu}{\partial z}\left(\frac{\partial u_z}{\partial z} - \frac{2}{3}\nabla\cdot\vec{u}\right)\end{aligned} \tag{A.6}$$

B Speed of sound and thermodynamic derivatives based on the volume-corrected SRK equation of state

B.1 Speed of sound

The speed of sound is obtained from the volume-corrected SRK equation of state following the guidelines shown in Sirignano [146]. Pressure is differentiated as a function of density and entropy

$$dp = \left(\frac{\partial p}{\partial \rho}\right) d\rho + \left(\frac{\partial p}{\partial s}\right) ds \tag{B.1}$$

where the speed of sound is defined as

$$c_s^2 = \left(\frac{\partial p}{\partial \rho}\right)_s = \left(f_s - g_s \frac{l_s}{h_s}\right) \frac{p}{\rho} \tag{B.2}$$

with

$$f_s = \frac{3Z^3 + (6B_* - 1)Z^2 + (A - B - B^2 + 3B_*^2 - B_*)Z}{3(Z^3 + B_*^3) + (9B_* - 2)Z^2 + (9B_*^2 - 4B_*)Z + (2A - 2B - 3B^2)(Z + B_*) - 2AB} \tag{B.3}$$

$$g_s = 1 + \frac{\left(Z + B_* - B - \frac{T}{a}\frac{da}{dT}\right)A}{3(Z^3 + B_*^3) + (9B_* - 2)Z^2 + (9B_*^2 - 4B_*)Z + (2A - 2B - 3B^2)(Z + B_*) - 2AB} \tag{B.4}$$

$$h_s = c_p + \frac{1}{W}\left[\frac{T}{b}\frac{d^2a}{dT^2}\ln\left(\frac{Z+B_*+B}{Z+B_*}\right) - R_u\right] \tag{B.5}$$

$$l_s = \frac{1}{W}\left[\frac{B}{b}\frac{da}{dT}\frac{Z}{(Z+B_*+B)(Z+B_*)} - \frac{R_u Z}{Z+B_*-B}\right] \tag{B.6}$$

For an ideal gas (i.e., $Z = 1$ and $A = B = B_* = 0$), it follows that $c_s^2 = \gamma R_u T/W$. To obtain the speed of sound of an ideal gas, it is necessary to use $\gamma = c_p/c_v$ as the specific heat ratio and the relation between the specific gas constant and the specific heats at constant pressure and constant volume, $R = R_u/W = c_p - c_v$.

B.2 "a" derivatives

$$\left(\frac{\partial a}{\partial X_i}\right)_{T,\bar{v},X_{j\neq i}} = 2\sum_{j=1}^{N} X_j (a_i a_j)^{0.5}(1-k_{ij}) \tag{B.7}$$

$$\left(\frac{\partial^2 a}{\partial X_j \partial X_i}\right)_{p,T} = 2(a_i a_j)^{0.5}(1-k_{ij}) \tag{B.8}$$

$$\left(\frac{\partial^2 a}{\partial X_i \partial T}\right)_{p,T,X_{j\neq i}} = \sum_{J=1}^{N} X_j \left[\left(\frac{a_i}{a_j}\right)^{0.5}\frac{da_j}{dT} + \left(\frac{a_j}{a_i}\right)^{0.5}\frac{da_i}{dT}\right](1-k_{ij}) \tag{B.9}$$

$$\left(\frac{\partial a}{\partial T}\right)_{\bar{v},X_i} = \frac{1}{2}\sum_{i=1}^{N}\sum_{j=1}^{N} X_i X_j \left[\left(\frac{a_i}{a_j}\right)^{0.5}\frac{da_j}{dT} + \left(\frac{a_j}{a_i}\right)^{0.5}\frac{da_i}{dT}\right](1-k_{ij}) \tag{B.10}$$

$$\left(\frac{\partial^2 a}{\partial T^2}\right)_{p,X_i} = \frac{1}{2}\sum_{i=1}^{N}\sum_{j=1}^{N} X_i X_j \left[\left(\frac{a_i}{a_j}\right)^{0.5}\frac{d^2 a_j}{dT^2} + \left(\frac{a_j}{a_i}\right)^{0.5}\frac{d^2 a_i}{dT^2} + \left(\frac{1}{a_i a_j}\right)^{0.5}\frac{da_i}{dT}\frac{da_j}{dT}\right](1-k_{ij}) - \frac{1}{4}\sum_{i=1}^{N}\sum_{j=1}^{N} X_i X_j \left[\left(\frac{a_i}{a_j}\right)^{0.5}\frac{1}{a_j}\left(\frac{da_j}{dT}\right)^2 + \left(\frac{a_j}{a_i}\right)^{0.5}\frac{1}{a_i}\left(\frac{da_i}{dT}\right)^2\right](1-k_{ij}) \tag{B.11}$$

$$\frac{da_i}{dT} = a_{c_i}\frac{d\alpha_i}{dT} = \frac{a_i}{\alpha_i}\frac{d\alpha_i}{dT} \tag{B.12}$$

$$\frac{d^2 a_i}{dT^2} = a_{c_i}\frac{d^2\alpha_i}{dT^2} = \frac{a_i}{\alpha_i}\frac{d^2\alpha_i}{dT^2} \tag{B.13}$$

$$\frac{d^2\alpha_i}{dT^2} = \frac{1}{2}\left[\frac{1}{\alpha_i}\left(\frac{d\alpha_i}{dT}\right)^2 - \frac{1}{T}\frac{d\alpha_i}{dT}\right] \tag{B.14}$$

B.3 "b" derivatives

$$\left(\frac{\partial b}{\partial X_i}\right)_{T,\bar{v},X_{j\neq i}} = b_i \tag{B.15}$$

B.4 "c" derivatives

$$\left(\frac{\partial c}{\partial X_i}\right)_{T,\bar{v},X_{j\neq i}} = c_i \tag{B.16}$$

$$\left(\frac{\partial^2 c}{\partial X_i \partial T}\right)_{p,T,X_{j\neq i}} = \left(\frac{\partial c_i}{\partial T}\right)_{\bar{v},X_i} = \frac{c_{c_i}}{T_{c_i}} f'(T_{r_i}) \tag{B.17}$$

$$\left(\frac{\partial c}{\partial T}\right)_{\bar{v},X_i} = \sum_{i=1}^{N} X_i \left(\frac{\partial c_i}{\partial T}\right)_{\bar{v},X_i} = \sum_{i=1}^{N} X_i \frac{c_{c_i}}{T_{c_i}} f'(T_{r_i}) \tag{B.18}$$

$$\left(\frac{\partial^2 c}{\partial T^2}\right)_{p,X_i} = \sum_{i=1}^{N} X_i \left(\frac{\partial^2 c_i}{\partial T^2}\right)_{\bar{v},X_i} = \sum_{i=1}^{N} X_i \frac{c_{c_i}}{T_{c_i}^2} f''(T_{r_i}) \tag{B.19}$$

B.5 "v" derivatives

$$\begin{aligned}\left(\frac{\partial \bar{v}}{\partial X_i}\right)_{p,T,X_{j\neq i}} &= \frac{R_u T}{p}\left(Z + B_* - \frac{B_*}{c}\left(\frac{\partial c}{\partial X_i}\right)_{p,T,X_{j\neq i}}\right) \\ &+ \frac{R_u T}{p}\left(\frac{(B - Z - B_*)\left[\frac{A}{a}\left(\frac{\partial a}{\partial X_i}\right)_{p,T,X_{j\neq i}} - 2A\right]}{3Z^2 + 2(3B_* - 1)Z + 3B_*^2 - 2B_* + A - B - B^2}\right) \\ &+ \frac{R_u T}{p}\left(\frac{(Z + B_* + 2B[Z + B_*] + A)\left[\frac{B}{b}\left(\frac{\partial b}{\partial X_i}\right)_{p,T,X_{j\neq i}} - B\right]}{3Z^2 + 2(3B_* - 1)Z + 3B_*^2 - 2B_* + A - B - B^2}\right)\end{aligned} \tag{B.20}$$

$$\begin{aligned}\left(\frac{\partial \bar{v}}{\partial T}\right)_{p,X_i} &= -\left(\frac{\partial c}{\partial T}\right)_{p,X_i} + \frac{R_u T}{p}\left(\frac{Z + B_*}{T}\right) \\ &- \frac{R_u T}{p}\left(\frac{(Z + B_* - B)\left(\frac{A}{a}\left(\frac{\partial a}{\partial T}\right)_{p,X_i} - 2\frac{A}{T}\right) + (Z + B_* + 2B[Z + B_*] + A)\frac{B}{T}}{3Z^2 + 2(3B_* - 1)Z + 3B_*^2 - 2B_* + A - B - B^2}\right)\end{aligned} \tag{B.21}$$

B.6 "Φ" derivatives

$$
\begin{aligned}
\left(\frac{\partial \ln(\Phi_i)}{\partial X_j}\right)_{p,T,X_{i\neq j}} &= \frac{B}{Z+B_*-B}\frac{1}{b}\frac{\partial b}{\partial X_j} - \frac{Z+B_*-1}{b^2}\frac{\partial b}{\partial X_i}\frac{\partial b}{\partial X_j} \\
&- (Z+B_*)\frac{1}{b}\frac{\partial b}{\partial X_i} + \frac{B_*}{c}\frac{\partial c}{\partial X_i} + 1 \\
&+ \frac{A}{Z+B_*+B}\frac{1}{b^2}\frac{\partial b}{\partial X_i}\frac{\partial b}{\partial X_j} - \frac{A}{Z+B_*+B}\frac{1}{ab}\frac{\partial a}{\partial X_i}\frac{\partial b}{\partial X_j} \\
&+ \frac{A}{B}\left(\frac{1}{ab}\frac{\partial a}{\partial X_i}\frac{\partial b}{\partial X_j} + \frac{1}{ab}\frac{\partial a}{\partial X_j}\frac{\partial b}{\partial X_i}\right)\ln\left(1+\frac{B}{Z+B_*}\right) \\
&- \frac{A}{B}\left(\frac{2}{b^2}\frac{\partial b}{\partial X_i}\frac{\partial b}{\partial X_j} + \frac{1}{a}\frac{\partial^2 a}{\partial X_j \partial X_i}\right)\ln\left(1+\frac{B}{Z+B_*}\right) \\
&+ \frac{A}{B}\left(\frac{1}{a}\frac{\partial a}{\partial X_i} - \frac{1}{b}\frac{\partial b}{\partial X_i}\right)\ln\left(1+\frac{B}{Z+B_*}\right) \\
&+ \left(\frac{1}{b}\frac{\partial b}{\partial X_i} - \frac{1}{Z+B_*-B}\right)\left(\frac{Z}{\bar{v}}\frac{\partial \bar{v}}{\partial X_j} + \frac{B_*}{c}\frac{\partial c}{\partial X_j}\right) \\
&+ \frac{A}{Z+B_*+B}\left(\frac{1}{a}\frac{\partial a}{\partial X_i} - \frac{1}{b}\frac{\partial b}{\partial X_i}\right)\frac{1}{\bar{v}+c}\left(\frac{\partial \bar{v}}{\partial X_j} + \frac{\partial c}{\partial X_j}\right)
\end{aligned}
\tag{B.22}
$$

$$
\begin{aligned}
\left(\frac{\partial \ln(\Phi_i)}{\partial T}\right)_{p,X_i} &= \left(1 - \frac{Z+B_*}{b}\frac{\partial b}{\partial X_i}\right)\frac{1}{T} + \frac{B_*}{c}\left(\frac{1}{T}\frac{\partial c}{\partial X_i} - \frac{\partial^2 c}{\partial T \partial X_i}\right) \\
&+ \frac{A}{B}\left(\frac{1}{a^2}\frac{\partial a}{\partial T}\frac{\partial a}{\partial X_i} - \frac{1}{a}\frac{\partial^2 a}{\partial T \partial X_i}\right)\ln\left(1+\frac{B}{Z+B_*}\right) \\
&+ \frac{A}{B}\left(\frac{1}{T} - \frac{1}{a}\frac{\partial a}{\partial T}\right)\left(\frac{1}{a}\frac{\partial a}{\partial X_i} - \frac{1}{b}\frac{\partial b}{\partial X_i}\right)\ln\left(1+\frac{B}{Z+B_*}\right) \\
&+ \left(\frac{1}{b}\frac{\partial b}{\partial X_i} - \frac{1}{Z+B_*-B}\right)\left(\frac{Z}{\bar{v}}\frac{\partial \bar{v}}{\partial T} + \frac{B_*}{c}\frac{\partial c}{\partial T}\right) \\
&+ \frac{A}{Z+B_*+B}\left(\frac{1}{a}\frac{\partial a}{\partial X_i} - \frac{1}{b}\frac{\partial b}{\partial X_i}\right)\frac{1}{\bar{v}+c}\left(\frac{\partial \bar{v}}{\partial T} + \frac{\partial c}{\partial T}\right)
\end{aligned}
\tag{B.23}
$$

C Details on the models and correlations to evaluate fluid and transport properties

C.1 Ideal-gas correlations

The model used to compute the ideal gas fluid properties is that of Passut and Danner [85]. This work offers a reliable correlation to compute the ideal gas enthalpy, heat capacity at constant pressure and entropy for a wide range of temperatures. The correlations follow Eqs. (3.39), (3.41) and (3.40). The temperature input is in Rankine degrees (^{o}R) and the resulting enthalpy has units of btu/lb and the specific heat at constant pressure and the entropy have units of btu/(lb·^{o}R). To convert from temperature in Kelvin degrees (K) to temperature in Rankine degrees (^{o}R), the conversion $T[^{o}\text{R}] = \frac{9}{5} \cdot T[\text{K}]$ is used. Then, to convert from btu/lb to J/kg, the conversion $h^*[\text{J/kg}] = 2326.0 \cdot h^*[\text{btu/lb}]$ is used. The correlations are referenced to 0 btu/lb at 0 ^{o}R for the enthalpy and 0 btu/(lb·^{o}R) at 0 ^{o}R at 1 atm pressure for the entropy. Recall that entropy must satisfy $s^* = 0$ at $T = 0$.

The following Tables C.1 and C.2 provide some values for the constants to be used in this correlation for different species relevant to this dissertation.

Table C.1: Correlation constants $\hat{A}$-$\hat{C}$ for the ideal gas model from Passut and Danner [85] ideal gas model.

Species	$\hat{A}$	$\hat{B}$	$\hat{C}$ (10^3)
Oxygen	-0.98176	0.227486	-0.037305
Nitrogen	-0.68925	0.253664	-0.014549
n-Octane	29.50114	-0.022402	0.459712
n-Decane	28.48990	-0.023837	0.461164
n-Dodecane	26.21126	-0.018522	0.453893

Table C.2: Correlation constants $\hat{D}$-$\hat{G}$ for the ideal gas model from Passut and Danner [85] ideal gas model.

Species	$\hat{D}$ (10^6)	$\hat{E}$ (10^{10})	$\hat{F}$ (10^{14})	$\hat{G}$
Oxygen	0.048302	-0.185243	0.247488	0.124314
Nitrogen	0.012544	-0.017106	-0.008239	0.050052
n-Octane	-0.098062	0.104754	-0.031355	0.664632
n-Decane	-0.099786	0.108353	-0.033074	0.611062
n-Dodecane	-0.096464	0.101393	-0.029665	0.542807

C.2 Viscosity and thermal conductivity

The correlations from Chung et al. [61] have been used to obtain the values of viscosity and thermal conductivity for the non-ideal mixture. The model first computes the dilute gas viscosity, η_0, and the thermal conductivity, λ_0, using the Chapman-Enskog theory. The dilute gas viscosity becomes

$$\eta_0 = (4.0785 \times 10^{-5}) \frac{(MT)^{0.5}}{V_c^{2/3} \Omega^*} F_c \tag{C.1}$$

where η_0 is given in P (Poise), M is the molecular weight in g/mol, T is the temperature in K and V_c is the critical volume in cm^3/mol. The parameter Ω^* is the reduced collision integral, computed as

$$\Omega^* = \frac{A}{\hat{T}^B} + \frac{C}{\exp(D\hat{T})} + \frac{E}{\exp(F\hat{T})} + G\hat{T}^B \sin(S\hat{T}^W - H) \tag{C.2}$$

In Eq. (C.2), the dimensionless temperature, $\hat{T}$, is related to the potential energy parameter, ϵ, and the Boltzmann's constant, k, by the equation

$$\hat{T} = \frac{T}{\epsilon/k} \quad ; \quad \epsilon/k = T_c/1.2593 \tag{C.3}$$

being T_c the critical temperature in K.

The constants from Eq. (C.2) are $A = 1.16145$, $B = 0.14874$, $C = 0.52487$, $D = 0.77320$, $E = 2.16178$, $F = 2.43787$, $G = -6.435 \times 10^{-4}$, $H = 7.27371$, $S = 18.0323$ and $W = -0.76830$.

The factor F_c is evaluated as

$$F_c = 1 - 0.2756\omega + 0.059035\mu_r^4 + \kappa \tag{C.4}$$

where ω is the acentric factor (see Table 2.1), κ is a correction factor related to the hydrogen-bonding effect and μ_r is a dimensionless dipole moment. The last two parameters appear when dealing with polar fluids.

The dimensionless dipole moment, if needed, can be computed as

$$\mu_r = 131.3\mu/(V_c T_c)^{1/2} \tag{C.5}$$

where μ is the dipole moment of the fluid.

Finally, the dilute gas thermal conductivity can be found from the dilute gas viscosity as seen in Eq. (C.6), where λ_0 is given in cal/(cm·s·K).

$$\lambda_0 = 7.452(\eta_0/M)\Psi \quad ; \quad \Psi = 1 + \alpha\left(\frac{0.215 + 0.28288\alpha - 1.061\beta + 0.26665Z}{0.6366 + \beta Z + 1.061\alpha\beta}\right) \tag{C.6}$$

In Eq. (C.6), $\alpha = C_v/R - 3/2$, being C_v the ideal gas heat capacity at constant volume in cal/(mol·K) and R the universal gas constant $R = 1.987$ cal/(mol·K). Moreover, $\beta = 0.7862 - 0.7109\omega + 1.3168\omega^2$ and $Z = 2.0 + 10.5T_r^2$, with T_r being the reduced temperature $T_r = T/T_c$.

The heat capacity at constant volume, C_v, can be computed from Passut and Danner [85] correlations, using the relation $R = C_p - C_v$.

After dilute gas properties have been obtained, the next step is to obtain the viscosity for dense fluids (in P again) by using the relation

$$\eta = \eta_\kappa + \eta_p \tag{C.7}$$

where the following identities apply,

$$\eta_\kappa = \eta_0 \left(\frac{1}{G_2} + A_6 Y \right) \quad ; \quad \eta_p = \left(36.344 \times 10^{-6} \frac{(MT_c)^{0.5}}{V_c^{2/3}} \right) \exp\left(A_8 + \frac{A_9}{\hat{T}} + \frac{A_{10}}{\hat{T}^2} \right) \tag{C.8}$$

being $Y = \rho V_c/6$ and $G_1 = (1.0 - 0.5Y)/(1 - Y)^3$. Moreover,

$$G_2 = \frac{A_1[1 - \exp(-A_4 Y)]/Y + A_2 G_1 \exp(A_5 Y) + A_3 G_1}{A_1 A_4 + A_2 + A_3} \tag{C.9}$$

The coefficients A_i are given by $A_i = a_0(i) + a_1(i)\omega + a_2(i)\mu_r^4 + a_3(i)\kappa$. The values for $a_0(i)$, $a_1(i)$, $a_2(i)$ and $a_3(i)$ are found in Table C.3.

Similarly, the thermal conductivity (i.e., k in the formulation of this thesis) for a dense fluid (in cal/(cm·s·K)) is obtained as,

$$k = \lambda_\kappa + \lambda_p \tag{C.10}$$

where the following identities apply,

$$\lambda_\kappa = \lambda_0 \left(\frac{1}{H_2} + B_6 Y \right) \quad ; \quad \lambda_p = \left(3.039 \times 10^{-4} \frac{(T_c/M)^{0.5}}{V_c^{2/3}} \right) B_7 Y^2 H_2 T_r^{0.5} \tag{C.11}$$

$$H_2 = \frac{B_1[1 - \exp(-B_4 Y)]/Y + B_2 G_1 \exp(B_5 Y) + B_3 G_1}{B_1 B_4 + B_2 + B_3} \tag{C.12}$$

The coefficients B_i are given by $B_i = b_0(i) + b_1(i)\omega + b_2(i)\mu_r^4 + b_3(i)\kappa$. The values for $b_0(i)$, $b_1(i)$, $b_2(i)$ and $b_3(i)$ are found in Table C.4.

Table C.3: Coefficients a_0, a_1, a_2 and a_3 for Chung et al. [61] model.

i	$a_0(i)$	$a_1(i)$	$a_2(i)$	$a_3(i)$
1	6.32402	50.41190	-51.68010	1189.02000
2	0.12101×10^{-2}	-0.11536×10^{-2}	-0.62571×10^{-2}	0.37283×10^{-1}
3	5.28346	254.20900	-168.48100	3898.27000
4	6.62263	38.09570	-8.46414	31.41780
5	19.74540	7.63034	-14.35440	31.52670
6	-1.89992	-12.53670	4.98529	-18.15070
7	24.27450	3.44945	-11.29130	69.34660
8	0.79716	1.11764	0.12348×10^{-1}	-4.11661
9	-0.23816	0.67695×10^{-1}	-0.81630	4.02528
10	0.68629×10^{-1}	0.34793	0.59256	-0.72663

Table C.4: Coefficients b_0, b_1, b_2 and b_3 for Chung et al. [61] model.

i	$b_0(i)$	$b_1(i)$	$b_2(i)$	$b_3(i)$
1	2.41657	0.74824	-0.91858	121.72100
2	-0.50924	-1.50936	-49.99120	69.98340
3	6.61069	5.62073	64.75990	27.03890
4	14.54250	-8.91387	-5.63794	74.34350
5	0.79274	0.82019	-0.69369	6.31734
6	-5.86340	12.80050	9.58926	-65.52920
7	81.17100	114.15800	-60.84100	466.77500

Finally, mixture rules have to be implemented to apply this model to mixtures. The following rules are used to compute mixture parameters,

$$\sigma_m^3 = \sum_{i=1}^{N}\sum_{j=1}^{N} X_i X_j \sigma_{ij}^3 \quad ; \quad \epsilon_m/k = \frac{\sum_{i=1}^{N}\sum_{j=1}^{N} X_i X_j (\epsilon_{ij}/k)\sigma_{ij}^3}{\sigma_m^3} \tag{C.13}$$

$$V_{cm} = (\sigma_m/0.809)^3 \quad ; \quad T_{cm} = 1.2593(\epsilon_m/k) \tag{C.14}$$

$$\omega_m = \frac{\sum_{i=1}^{N}\sum_{j=1}^{N} X_i X_j \omega_{ij} \sigma_{ij}^3}{\sigma_m^3} \quad ; \quad M_m = \left(\frac{\sum_{i=1}^{N}\sum_{j=1}^{N} X_i X_j (\epsilon_{ij}/k) \sigma_{ij}^2 M_{ij}^{0.5}}{(\epsilon_m/k)\sigma_m^2} \right)^2 \tag{C.15}$$

$$\mu_m^4 = \frac{\sum_{i=1}^{N}\sum_{j=1}^{N} X_i X_j (\mu_i^2 \mu_j^2)}{(\epsilon_{ij}/k)\sigma_{ij}^3} \sigma_m^3 (\epsilon_m/k) \quad ; \quad \kappa_m = \sum_{i=1}^{N}\sum_{j=1}^{N} X_i X_j \kappa_{ij} \tag{C.16}$$

$$\mu_{rm} = 131.3 \mu_m / (V_{cm} T_{cm})^{0.5} \tag{C.17}$$

The binary parameters are given by

$$\sigma_{ij} = \xi_{ij} (\sigma_i \sigma_j)^{0.5} \quad ; \quad \epsilon_{ij}/k = \zeta_{ij} [(\epsilon_i/k)(\epsilon_j/k)]^{0.5} \quad ; \quad \omega_{ij} = 0.5(\omega_i + \omega_j) \tag{C.18}$$

$$M_{ij} = 2 M_i M_j / (M_i + M_j) \quad ; \quad \kappa_{ij} = (\kappa_i \kappa_j)^{0.5} \tag{C.19}$$

where ξ_{ij} and ζ_{ij} are binary interaction parameters taken to be unity for most systems or when no other information is provided.

To obtain the viscosity and the thermal conductivity in SI units, the following conversions must be implemented, $\eta[\text{kg/(m·s)}] = \frac{1}{10}\eta[P]$ and $k[\text{J/(m·s·K)}] = k[\text{W/(m·K)}] = 418.4 \cdot k[\text{cal/(cm·s·K)}]$.

C.3 Mass-diffusion coefficient

The model from Leahy-Dios and Firoozabadi [86] has been used to compute the diffusion coefficients required for the evaluation of the mass-diffusion fluxes. This model combines a correlation obtained using an extensive data set to evaluate the infinite-dilution diffusion coefficients with the Vignes relation (i.e., Eq. (C.20)) to obtain the binary diffusion coefficients. Then, these coefficients can be applied in the Maxwell-Stefan relations (i.e., Eq. (3.42)).

$$D_{12} = (D_{12}^{\infty})^{X_2} (D_{21}^{\infty})^{X_1} \tag{C.20}$$

The infinite-dilution diffusion coefficients are evaluated with the following correlation, given that component 2 is infinitely diluted in component 1,

$$\frac{cD_{21}^{\infty}}{(cD)^0} = A_0 \left(\frac{T_{r,1} P_{r,2}}{T_{r,2} P_{r,1}} \right)^{A_1} \left(\frac{\mu}{\mu^0} \right)^{[A_2(\omega_1,\omega_2)+A_3(P_r,T_r)]} \tag{C.21}$$

where the constants A_i are given by

$$A_0 = \exp(a_1) \quad ; \quad A_1 = 10 a_2 \quad ; \quad A_2 = a_3(1 + 10\omega_1 - \omega_2 + 10\omega_1\omega_2) \tag{C.22}$$

$$A_3 = a_4(P_{r,1}^{3a_5} - 6P_{r,2}^{a_5} + 6T_{r,1}^{10a_6}) + a_7 T_{r,2}^{-a_6} + a_2 \left(\frac{T_{r,1} P_{r,2}}{T_{r,2} P_{r,1}} \right) \tag{C.23}$$

with $a_1 = -0.0472$, $a_2 = 0.0103$, $a_3 = -0.0147$, $a_4 = -0.0053$, $a_5 = -0.3370$, $a_6 = -0.1852$ and $a_7 = -0.1914$.

In Eq. (C.21), c is the molar density in mol/m^3, μ is the viscosity in Pa·s or kg/(m·s), ω_i is the acentric factor of component i, $T_{r,i} = T/T_{c,i}$ is the reduced temperature of component i and $P_{r,i} = P/P_{c,i}$ is the reduced pressure of component i. Moreover, $(cD)^0$ is the dilute

gas density-diffusion coefficient product in mol/(m·s) and μ^0 is the dilute gas viscosity or low-pressure viscosity in Pa·s or kg/(m·s).

The dense-fluid viscosity, μ, can be obtained from the correlations by Chung et al. [61], but the proposed methods by Leahy-Dios and Firoozabadi [86] to obtain $(cD)^0$ and μ^0 are applied here. To compute $(cD)^0$, the Fuller et al. [81] method is used (i.e., Eq. (C.24)).

$$(cD)^0 = 1.01 \times 10^{-2} T^{0.75} \frac{\left(\frac{1}{M_1} + \frac{1}{M_2}\right)^{0.5}}{R\left[(\sum \nu_1)^{1/3} + (\sum \nu_2)^{1/3}\right]^2} \tag{C.24}$$

In the previous equation, $(cD)^0$ is given in mol/(m·s), M_1 and M_2 are the molecular weights of each component in g/mol, T is the temperature in K and $\sum \nu_i$ is the diffusion volume of component i. From Poling et al. [81], Table C.5 shows typical diffusion volume increments for each atom in the molecule and some diffusion volumes for simple molecules.

Table C.5: Diffusion volumes obtained from Poling et al. [81].

Component	Diffusion volume	Component	Diffusion volume
C	15.9	O	6.11
N	4.54	H	2.31
O_2	16.3	N_2	18.5
CO_2	26.9	H_2	6.12

The low-pressure viscosity is computed according to Stiel and Thodos correlation as

$$\mu^0 = \frac{\mu_1^0 M_1^{0.5} + \mu_2^0 M_2^{0.5}}{M_1^{0.5} + M_2^{0.5}} \tag{C.25}$$

where μ_i^0 is computed as follows, for $T_{r,i} < 1.5$,

$$\mu_i^0 \xi_i = 34 \times 10^{-8} (T_{r,i})^{0.94} \tag{C.26}$$

or as follows, for $T_{r,i} \geq 1.5$,

$$\mu_i^0 \xi_i = 17.78 \times 10^{-8} (4.58 T_{r,i} - 1.67)^{5/8} \tag{C.27}$$

The following expression is used to compute ξ_i,

$$\xi_i = \frac{T_{c,i}^{1/6}}{M_i^{1/2} (0.987 \times 10^{-5} P_{c,i})^{2/3}} \tag{C.28}$$

C.4 Surface-tension coefficient

To compute the surface-tension coefficient, the Macleod-Sugden correlation has been used as suggested in Poling et al. [81]. The surface-tension coefficient is evaluated as

$$\sigma = \Big([P_L] \rho_L - [P_G] \rho_G \Big)^n \tag{C.29}$$

where the surface tension of the mixture, σ, is provided in dyn/cm or mN/m. ρ_L and ρ_G are the liquid mixture density and the gas mixture density at the interface in mol/cm^3, respectively, and $[P_L]$ and $[P_G]$ are the parachor of the liquid mixture and the parachor of the gas mixture. The exponent n is usually set at 4, but some sources recommend using 3.6 for some specific mixtures instead. In the present work, the more general value of $n = 4$ has been chosen.

The parachor of the mixtures are computed according to

$$[P_L] = \sum_i^N \sum_j^N X_{li} X_{lj} [P_{ij}] \quad ; \quad [P_G] = \sum_i^N \sum_j^N X_{gi} X_{gj} [P_{ij}] \tag{C.30}$$

where X_{gi} and X_{li} are the mole fractions of component i in the gas mixture and the liquid mixture. $[P_{ij}]$ is computed as,

$$[P_{ij}] = \lambda_{ij} \frac{[P_i] + [P_j]}{2} \tag{C.31}$$

In Eq. (C.31), λ_{ij} is a binary interaction coefficient, usually set to 1 if no experimental data is available to obtain a more reliable value. $[P_i]$ is the parachor of the pure component i.

The methodology to compute the values of the parachor of each pure component consists on an empirical method that adds the structural contributions of each atom forming the molecule and the type of bonding between them. Table C.6 shows some of the values taken for each type of contribution. As an example, the parachor of the n-decane molecule results in $P = 10 \cdot 9.0 + 22 \cdot 15.5 = 431$.

Table C.6: Parachor contributions obtained from Poling et al. [81].

Element	Contribution	Element	Contribution
C	9.0	O	20.0
N	17.5	H	15.5
Double bond	19.1	Triple bond	40.6
Single bond	0.0	Semipolar bond	0.0

D Validation of the thermodynamic model

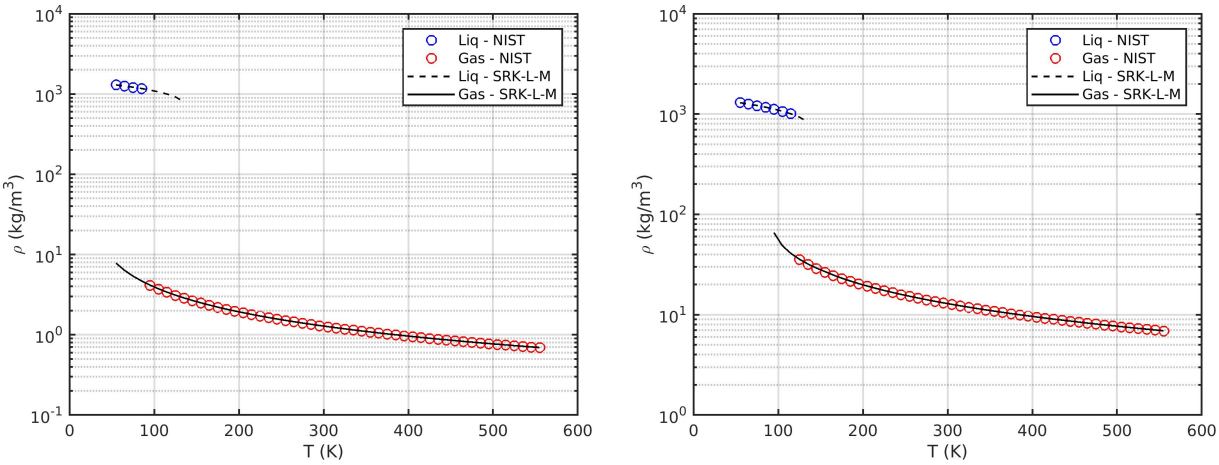

(a)

(b)

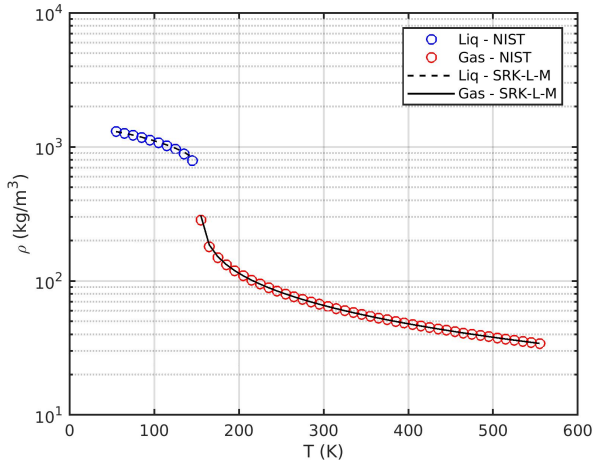

(c)

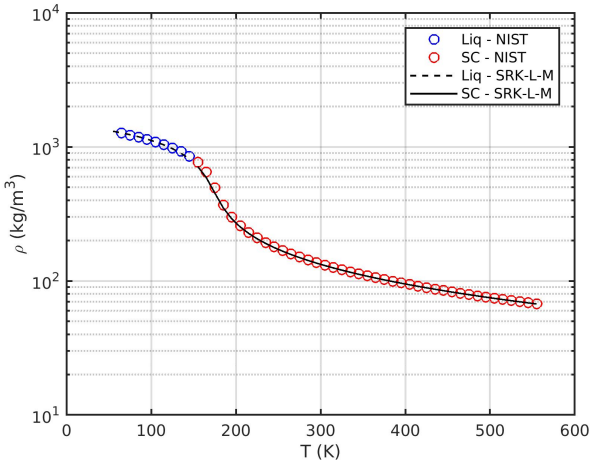

(d)

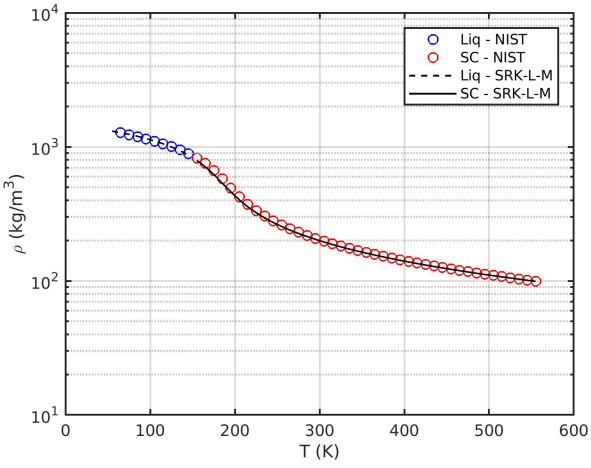

(e)

Figure D.1: Oxygen density. (a) 1 bar; (b) 10 bar; (c) 50 bar; (d) 100 bar; and (e) 150 bar.

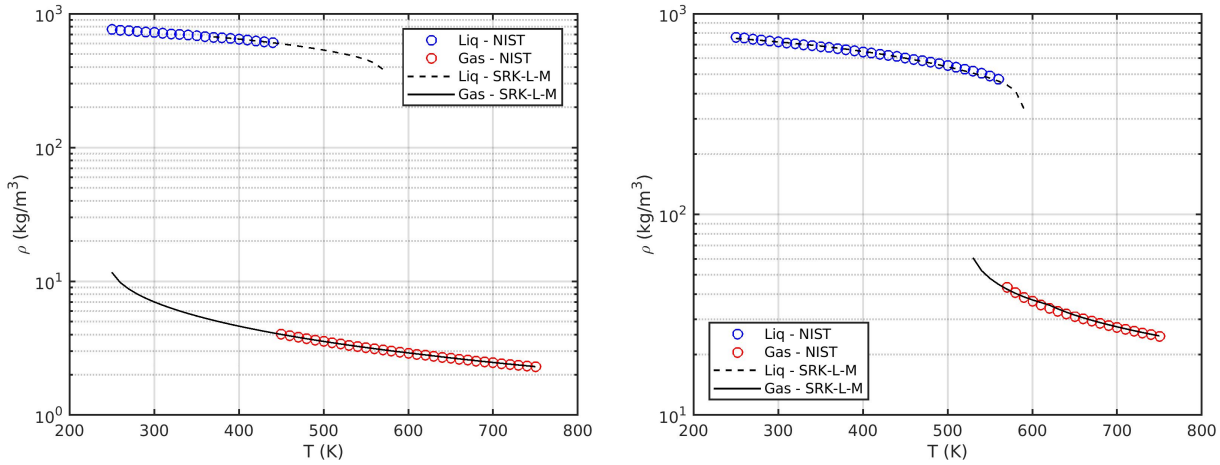

(a)

(b)

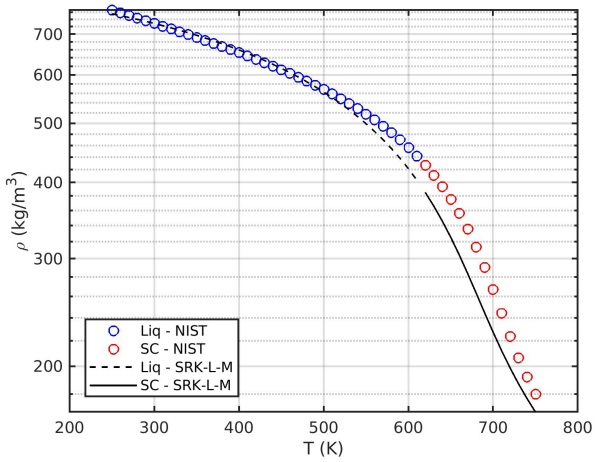

(c)

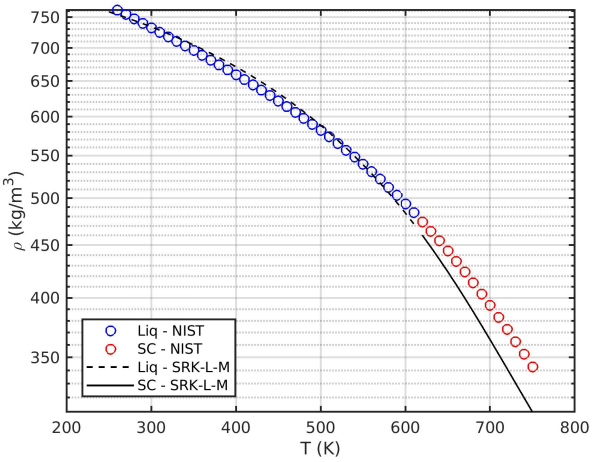

(d)

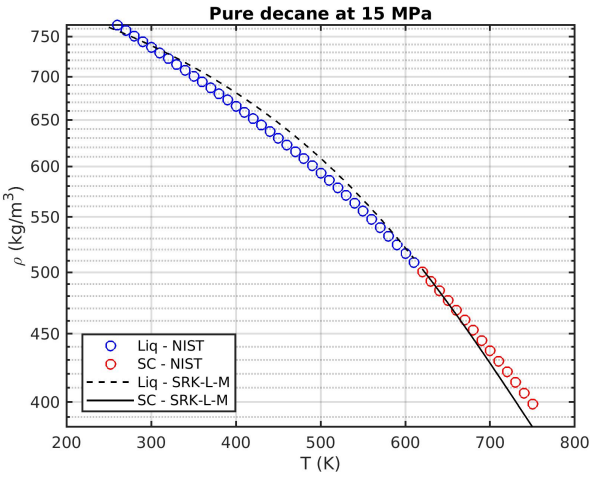

(e)

Figure D.2: *n*-decane density. (a) 1 bar; (b) 10 bar; (c) 50 bar; (d) 100 bar; and (e) 150 bar.

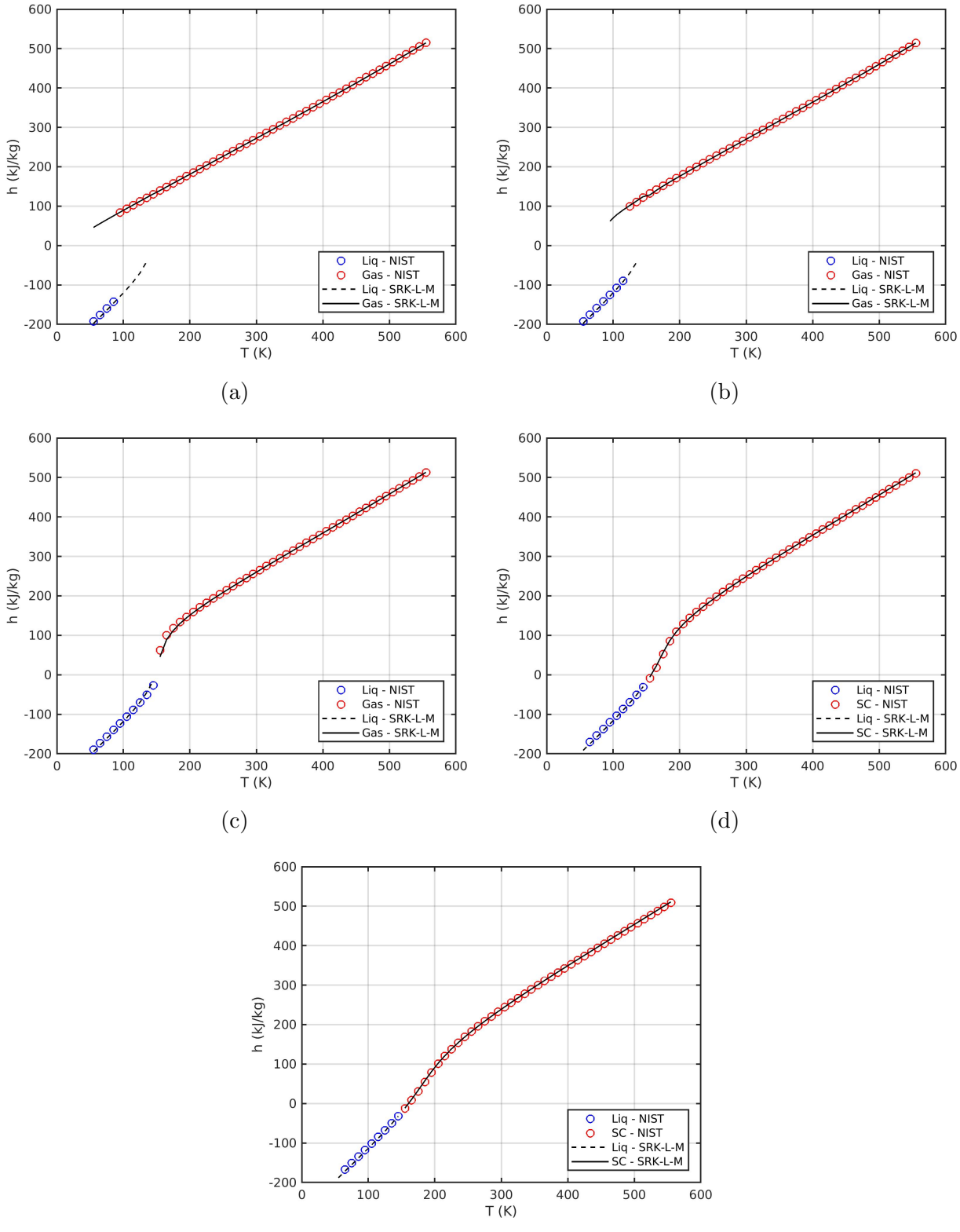

Figure D.3: Oxygen enthalpy. (a) 1 bar; (b) 10 bar; (c) 50 bar; (d) 100 bar; and (e) 150 bar.

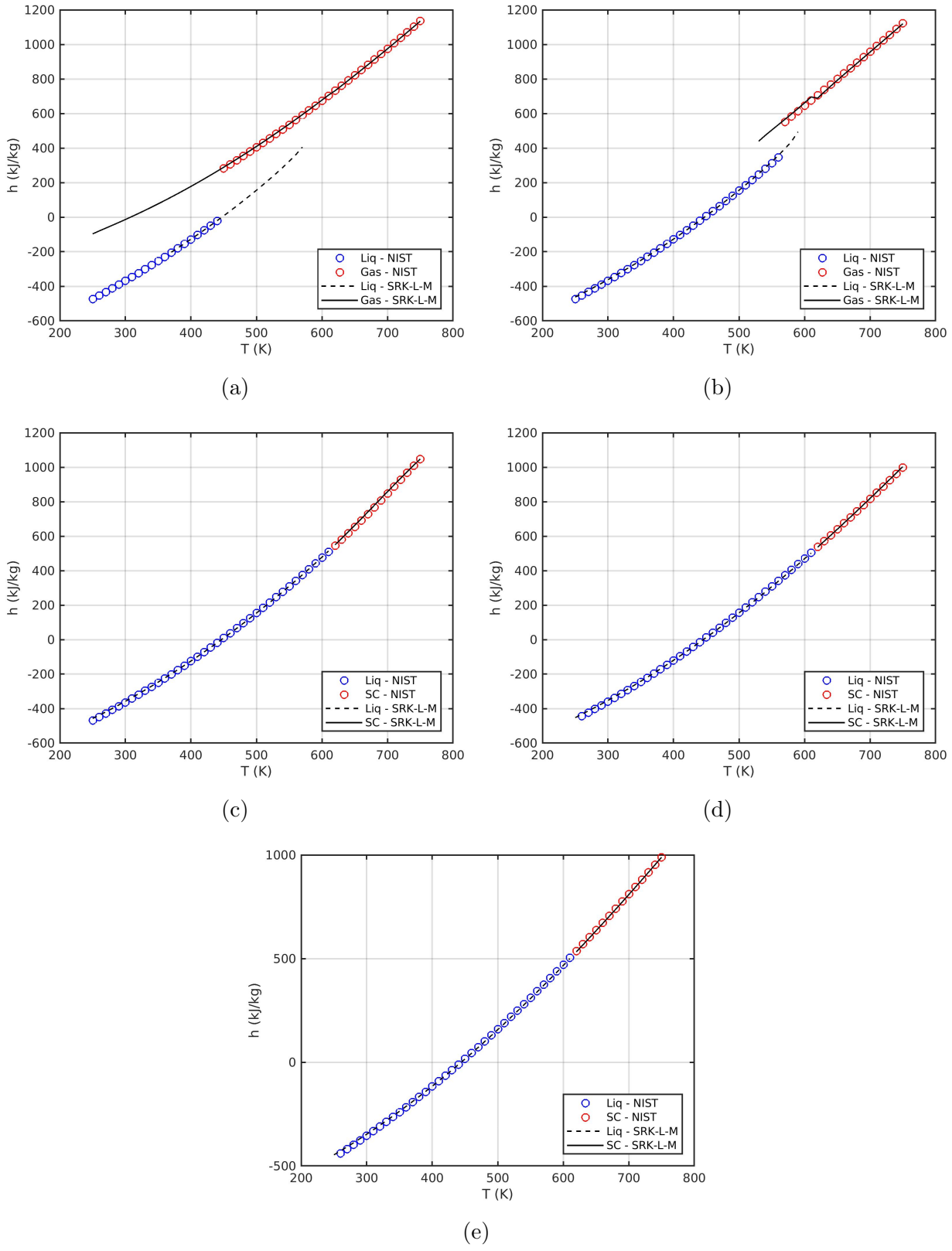

Figure D.4: n-decane enthalpy. (a) 1 bar; (b) 10 bar; (c) 50 bar; (d) 100 bar; and (e) 150 bar.

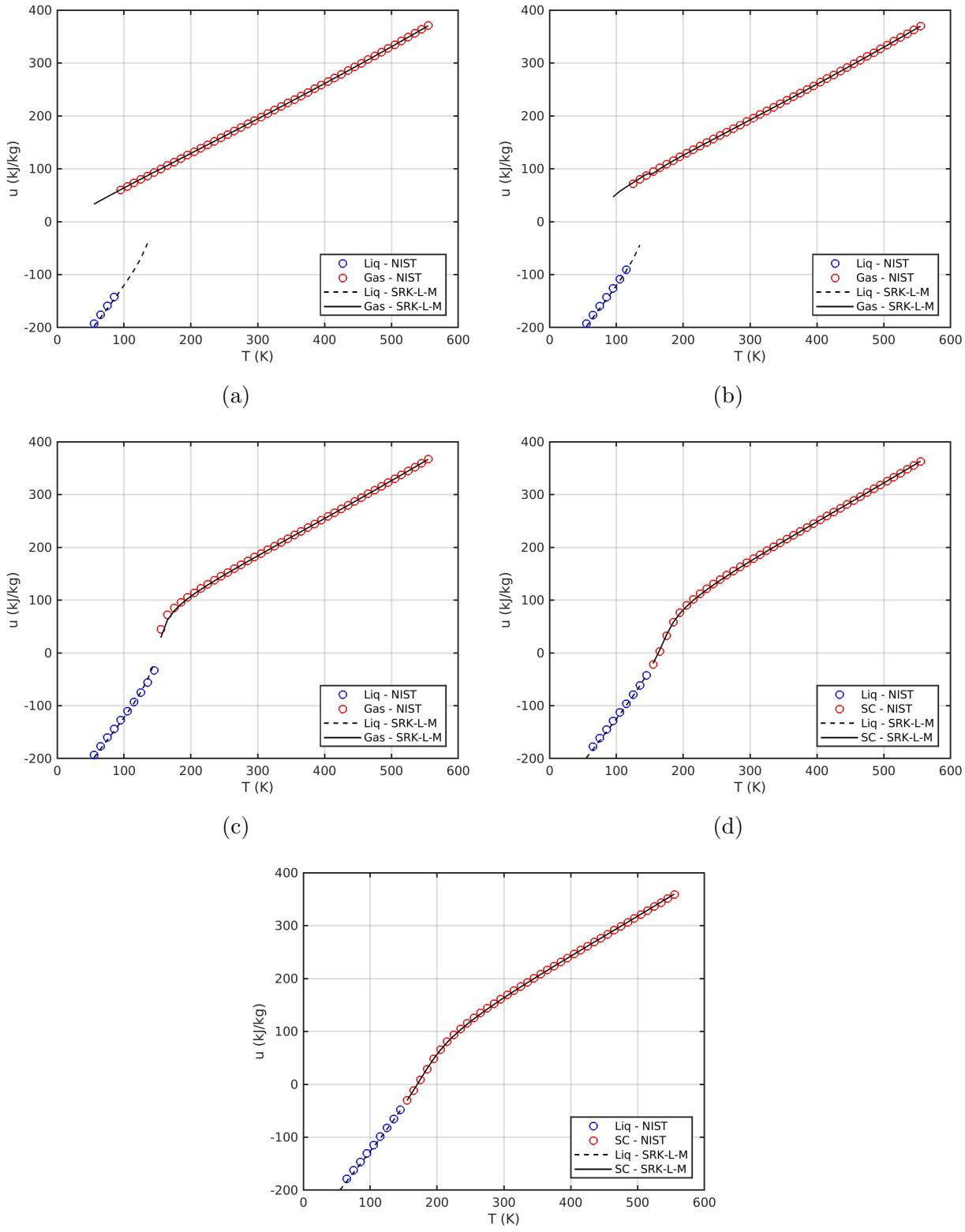

Figure D.5: Oxygen internal energy. (a) 1 bar; (b) 10 bar; (c) 50 bar; (d) 100 bar; and (e) 150 bar.

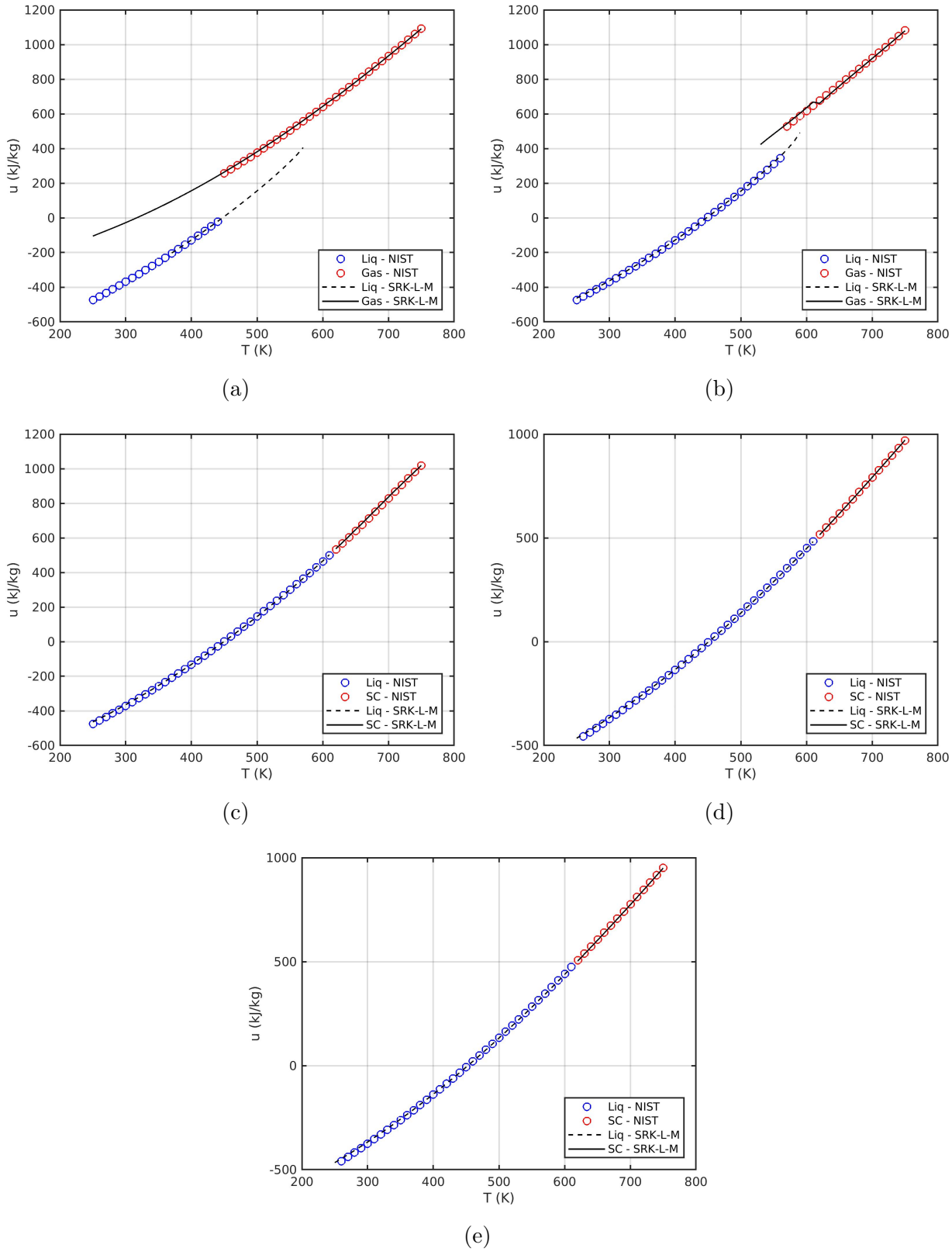

Figure D.6: n-decane internal energy. (a) 1 bar; (b) 10 bar; (c) 50 bar; (d) 100 bar; and (e) 150 bar.

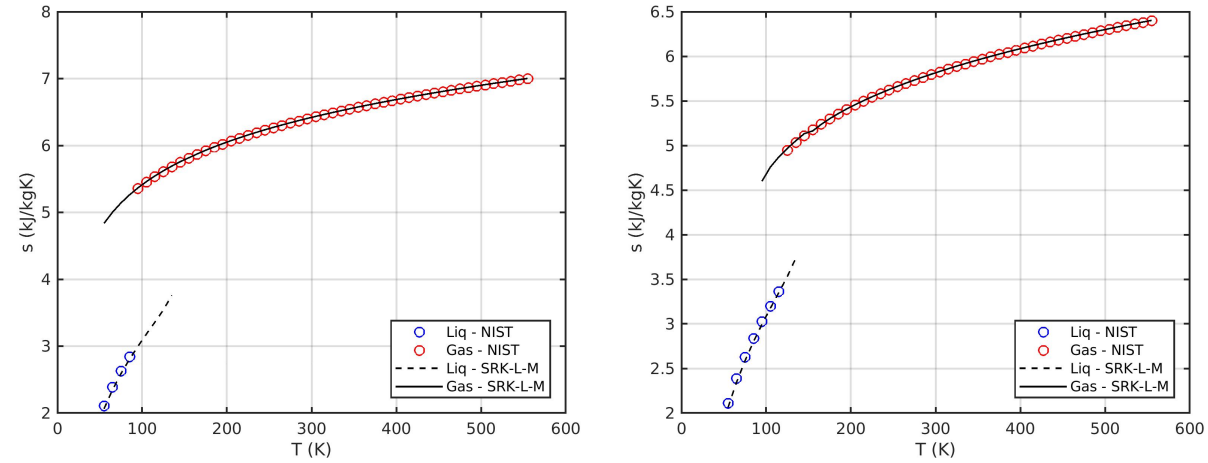

(a)

(b)

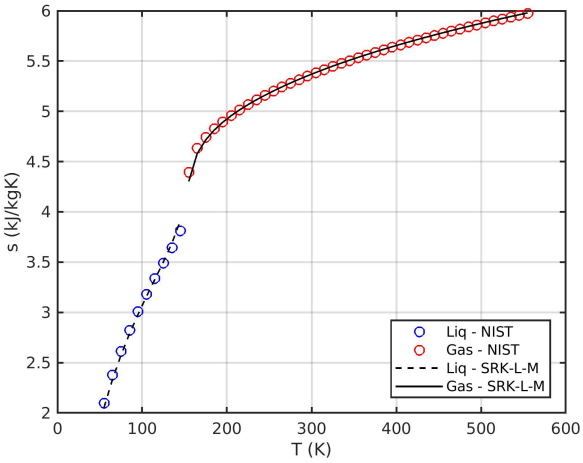

(c)

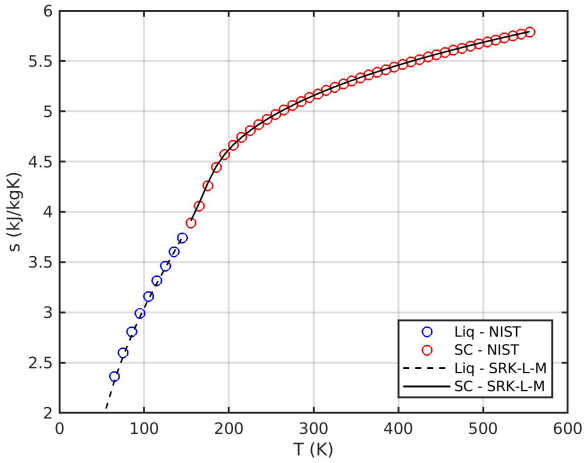

(d)

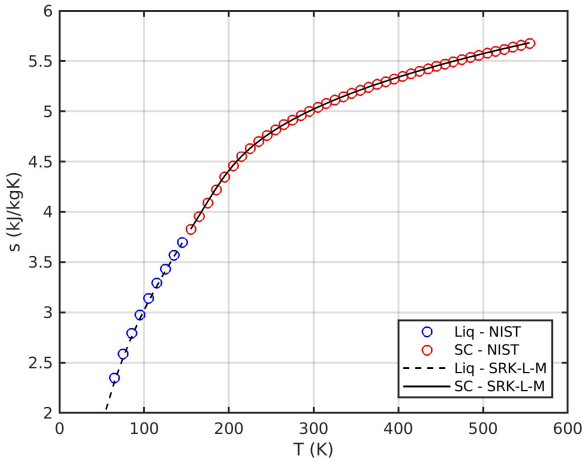

(e)

Figure D.7: Oxygen entropy. (a) 1 bar; (b) 10 bar; (c) 50 bar; (d) 100 bar; and (e) 150 bar.

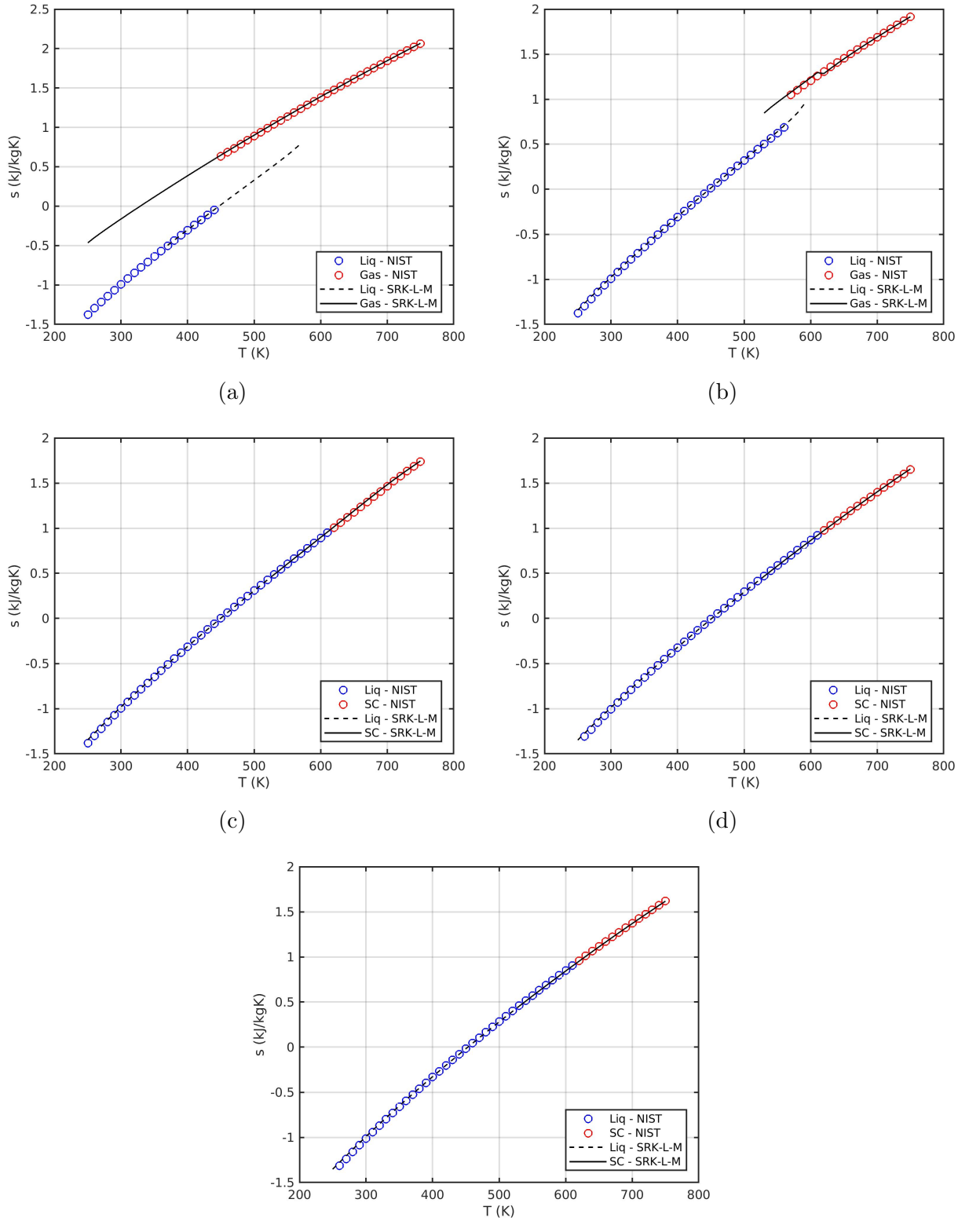

Figure D.8: *n*-decane entropy. (a) 1 bar; (b) 10 bar; (c) 50 bar; (d) 100 bar; and (e) 150 bar.

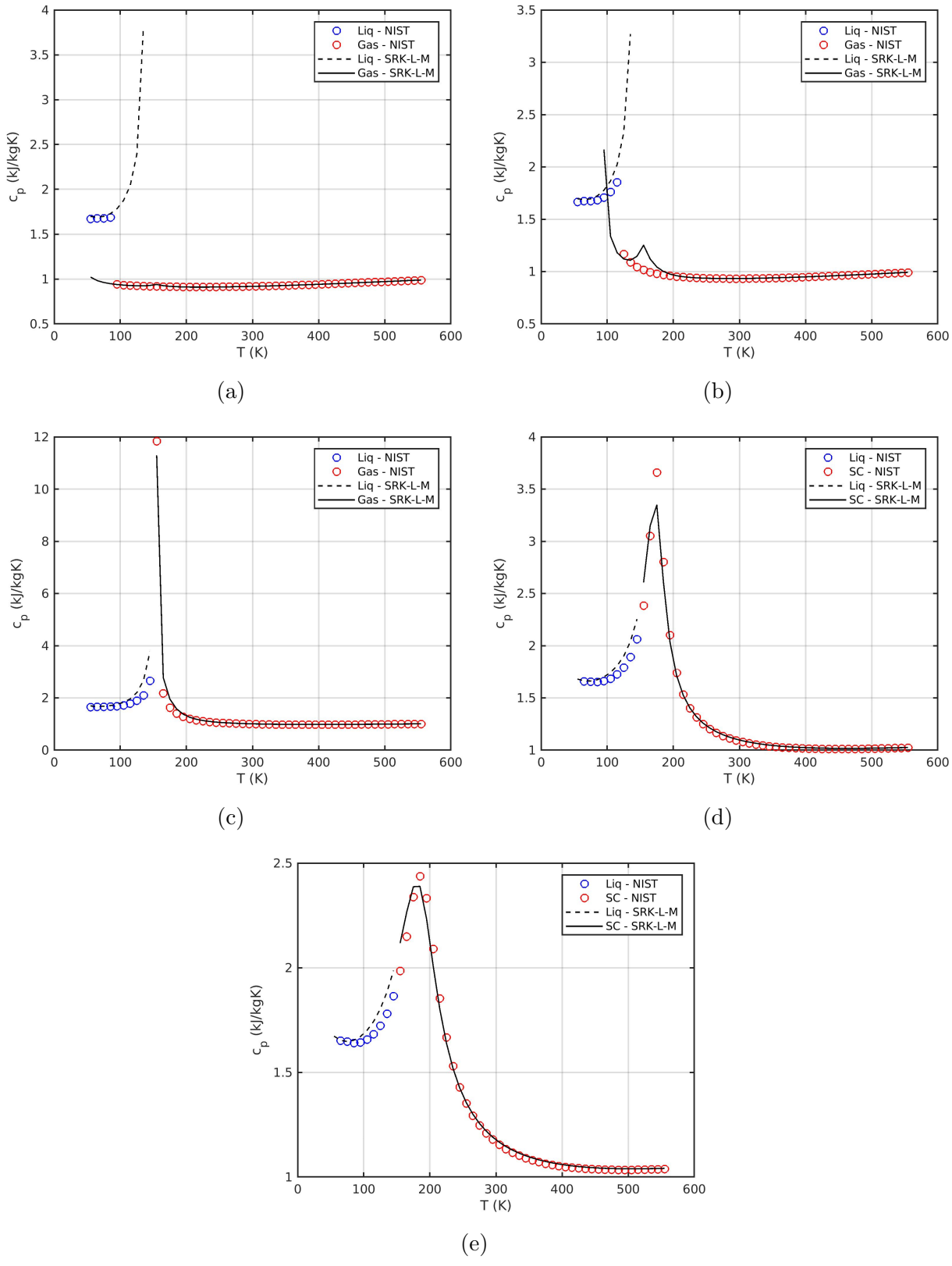

Figure D.9: Oxygen specific heat at constant pressure. (a) 1 bar; (b) 10 bar; (c) 50 bar; (d) 100 bar; and (e) 150 bar.

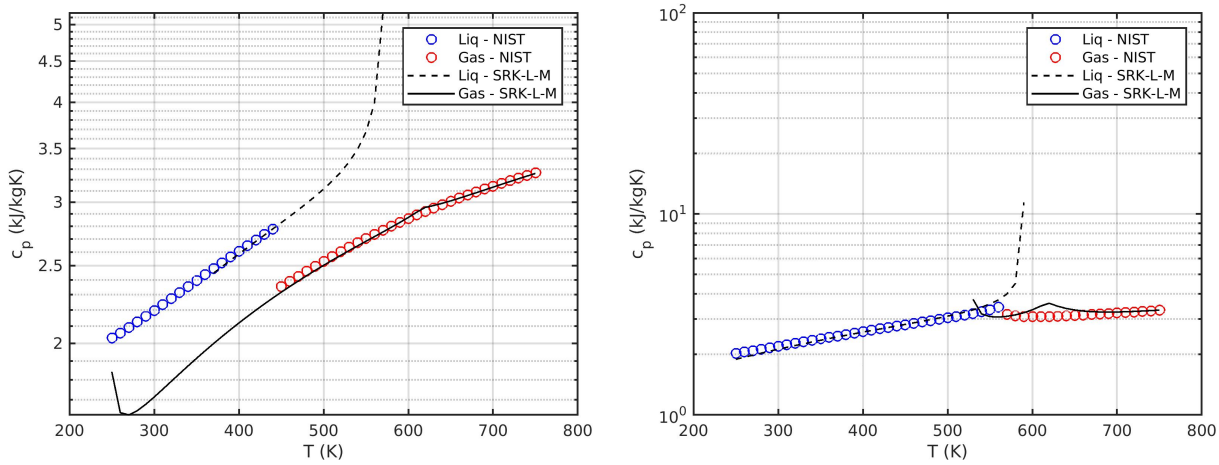

(a)

(b)

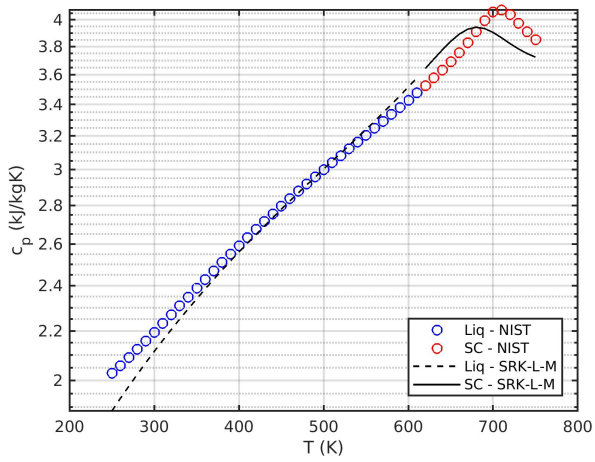

(c)

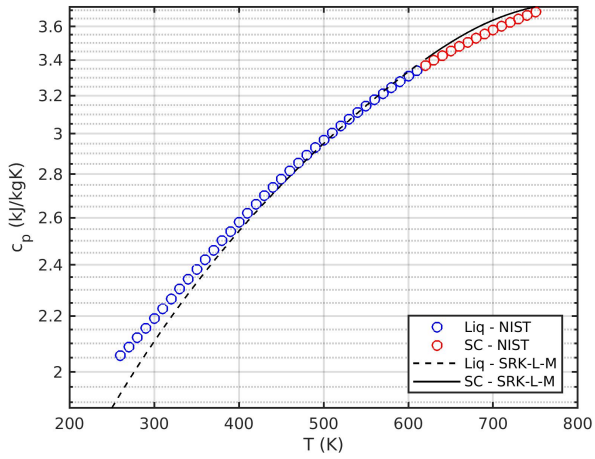

(d)

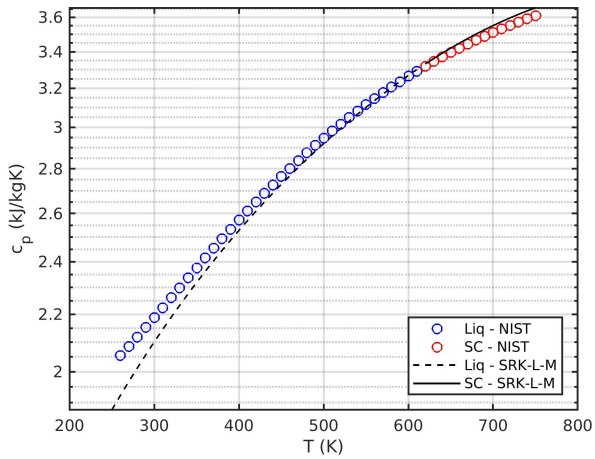

(e)

Figure D.10: *n*-decane specific heat at constant pressure. (a) 1 bar; (b) 10 bar; (c) 50 bar; (d) 100 bar; and (e) 150 bar.

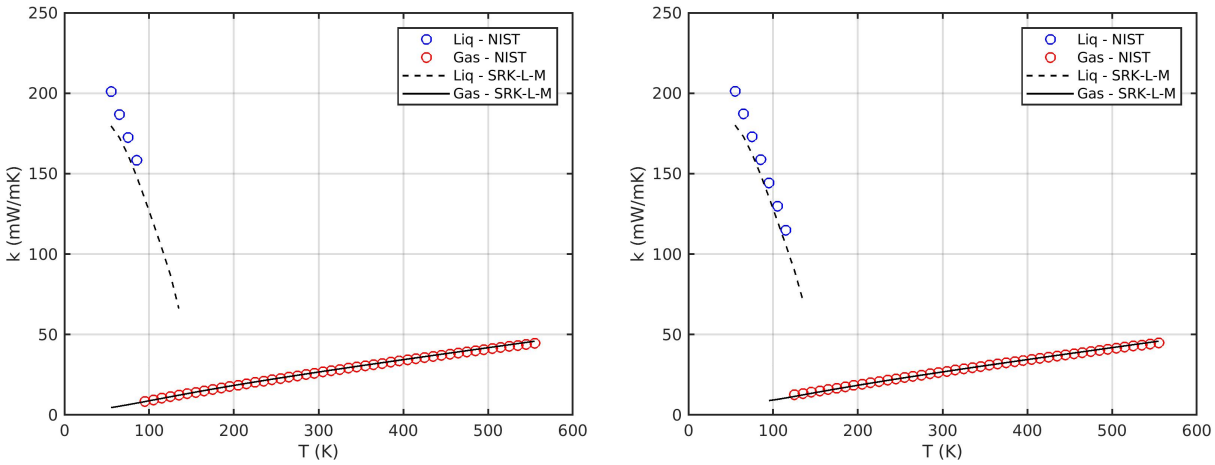

(a)

(b)

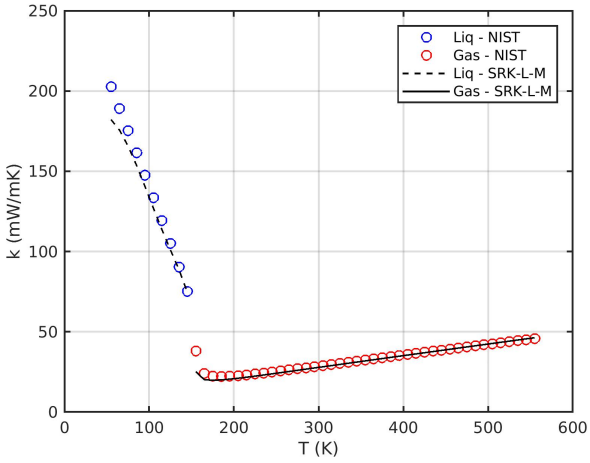

(c)

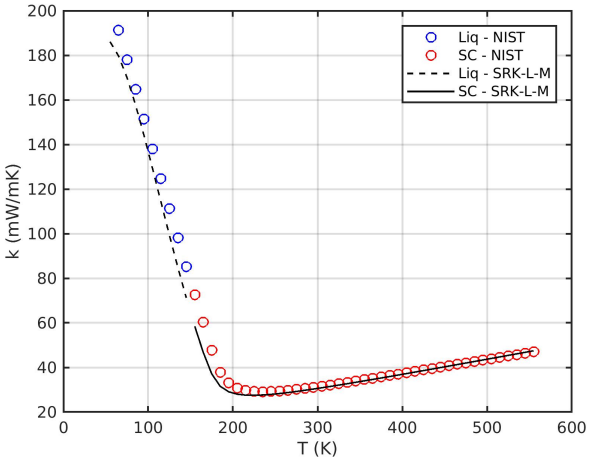

(d)

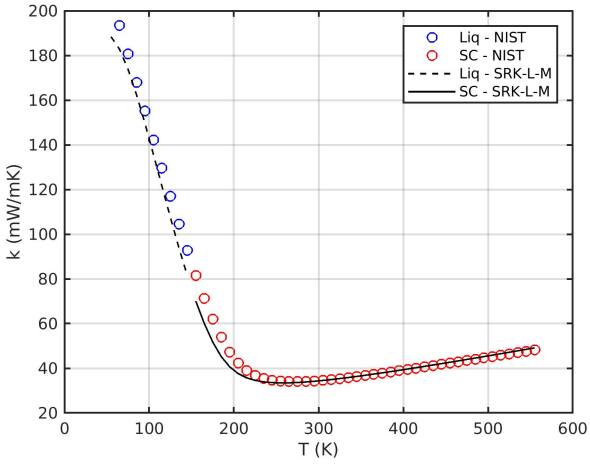

(e)

Figure D.11: Oxygen thermal conductivity. (a) 1 bar; (b) 10 bar; (c) 50 bar; (d) 100 bar; and (e) 150 bar.

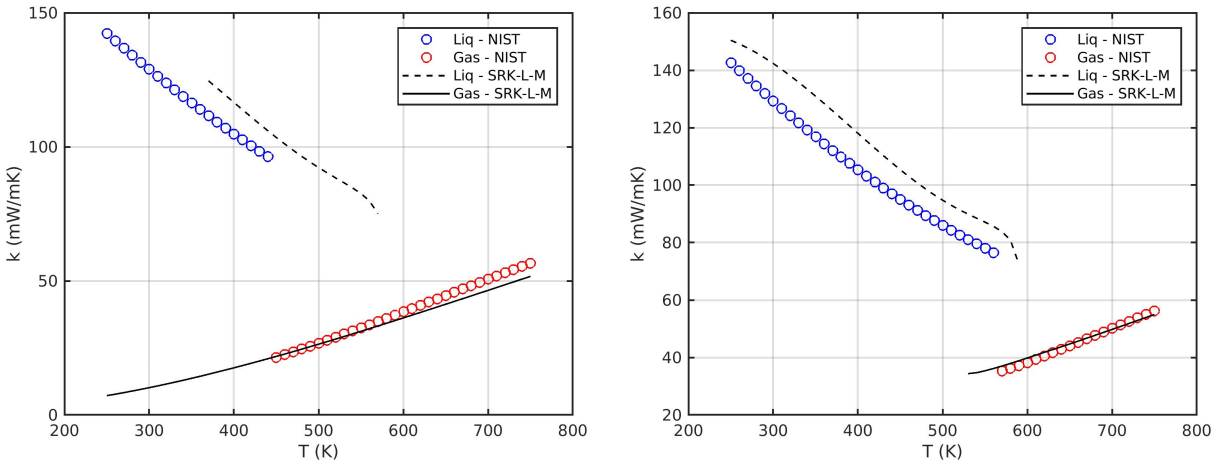

(a)

(b)

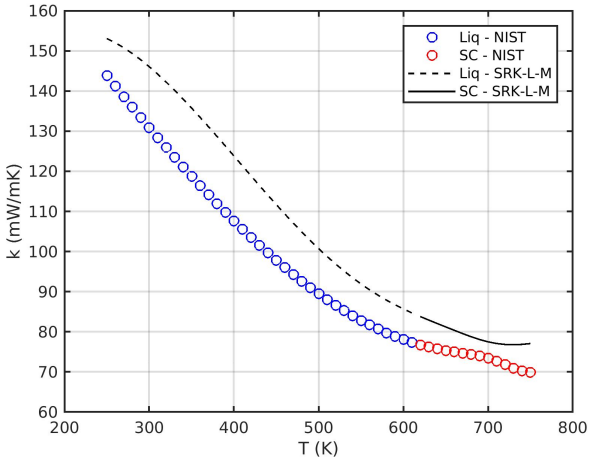

(c)

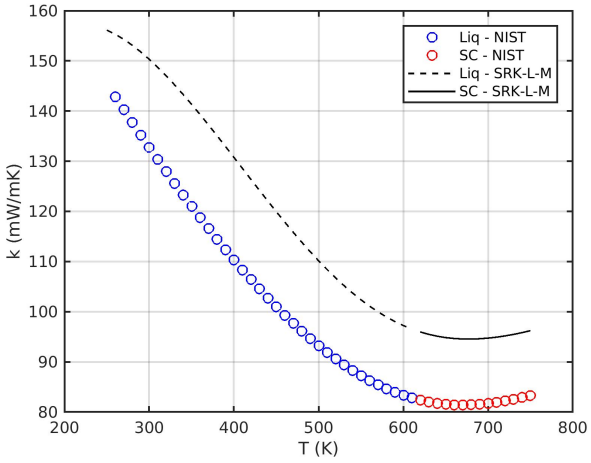

(d)

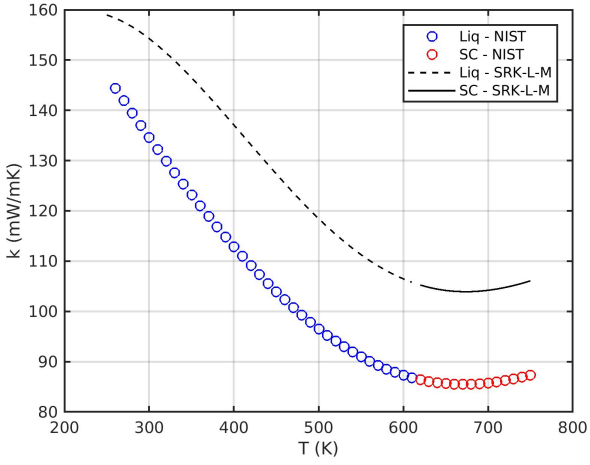

(e)

Figure D.12: n-decane thermal conductivity. (a) 1 bar; (b) 10 bar; (c) 50 bar; (d) 100 bar; and (e) 150 bar.

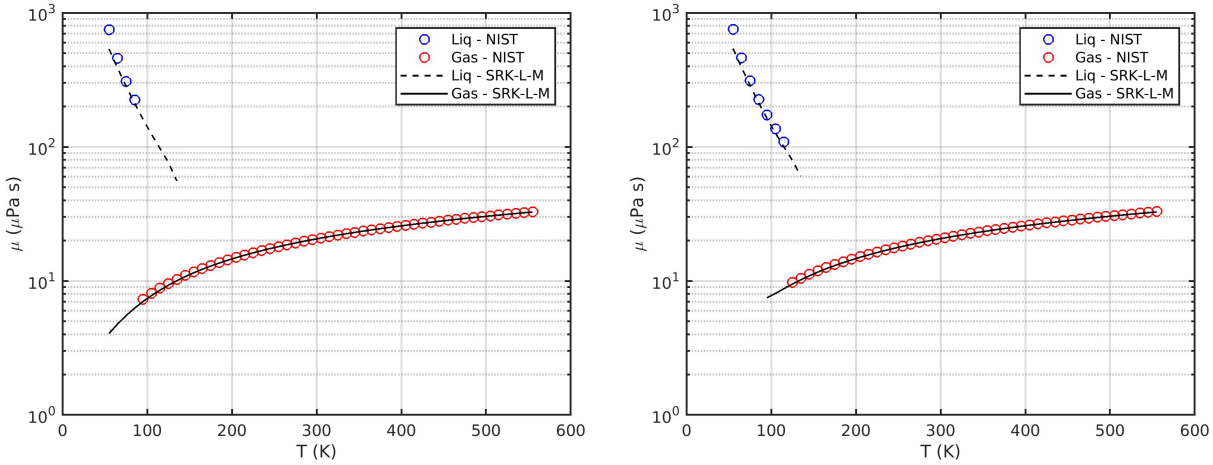

(a)

(b)

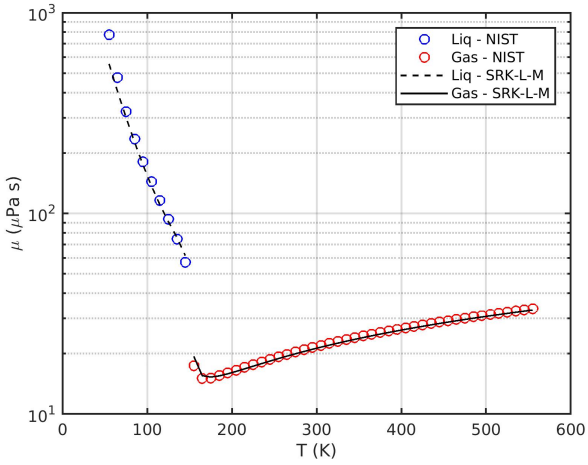

(c)

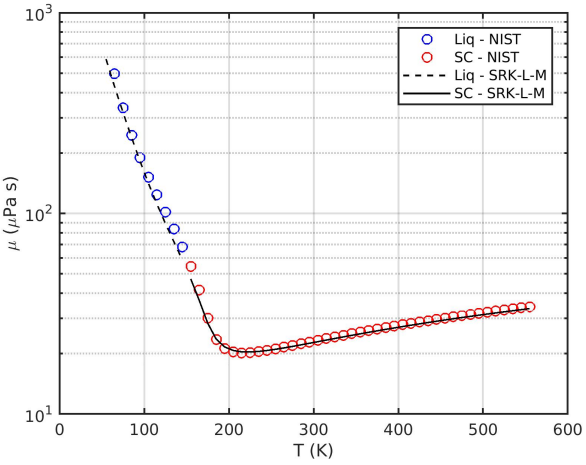

(d)

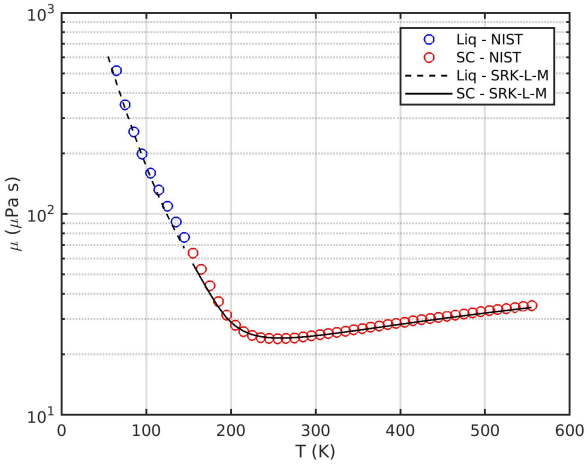

(e)

Figure D.13: Oxygen dynamic viscosity. (a) 1 bar; (b) 10 bar; (c) 50 bar; (d) 100 bar; and (e) 150 bar.

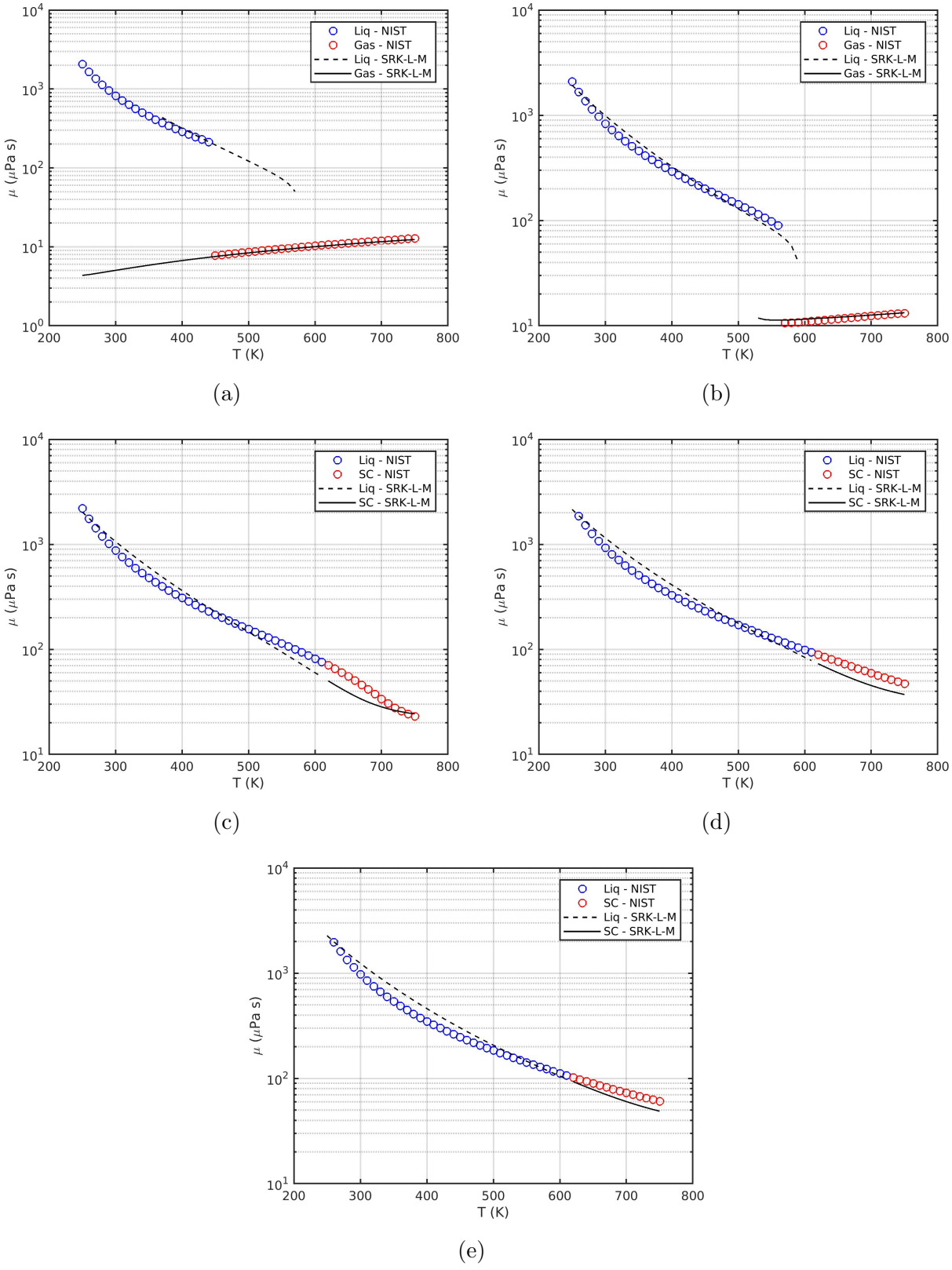

Figure D.14: *n*-decane dynamic viscosity. (a) 1 bar; (b) 10 bar; (c) 50 bar; (d) 100 bar; and (e) 150 bar.

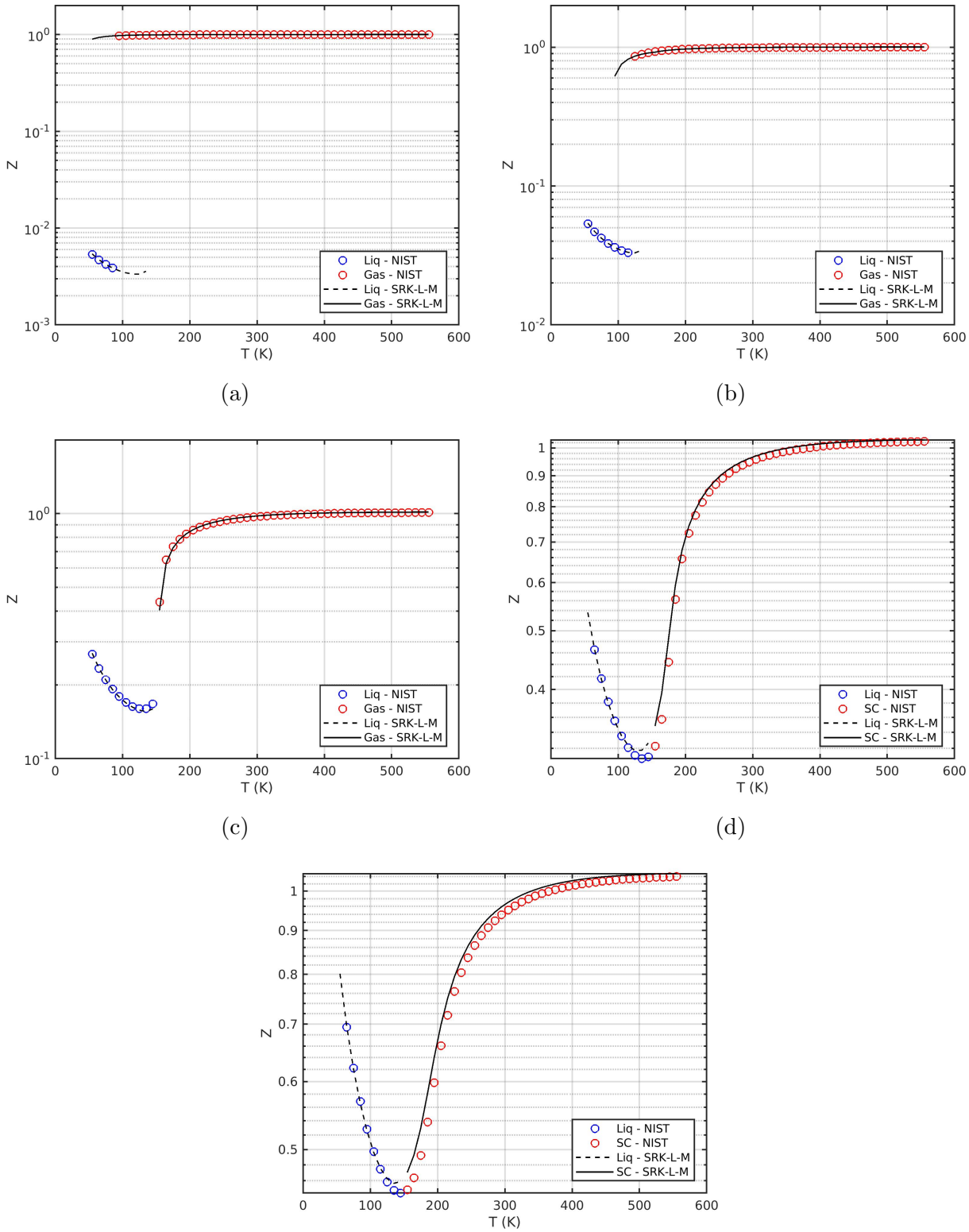

Figure D.15: Oxygen compressibility factor. (a) 1 bar; (b) 10 bar; (c) 50 bar; (d) 100 bar; and (e) 150 bar.

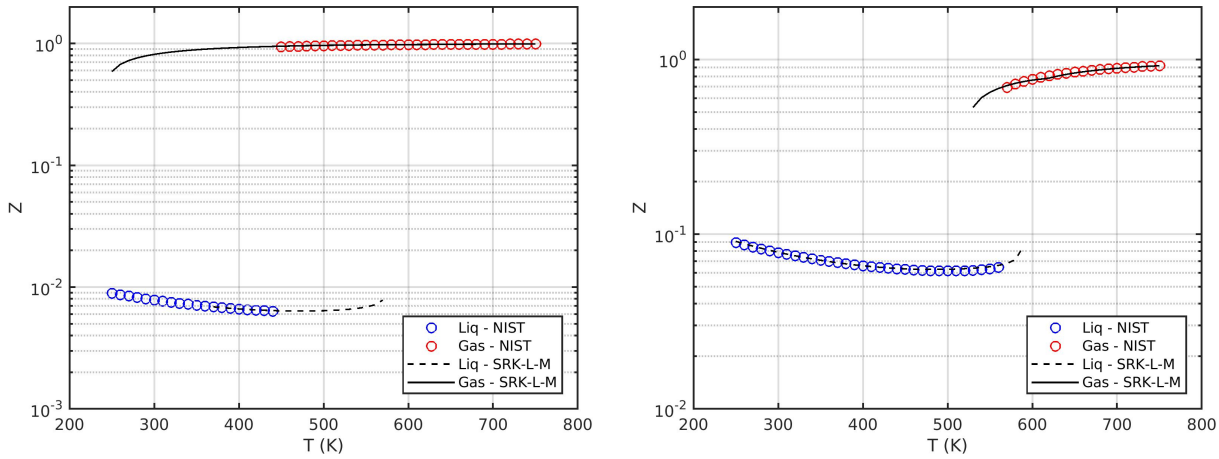

(a)

(b)

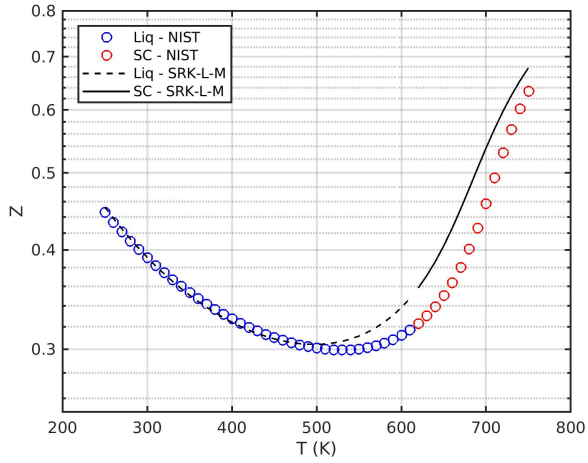

(c)

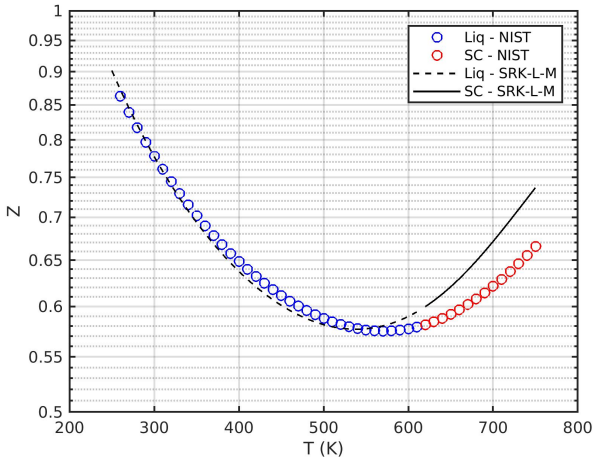

(d)

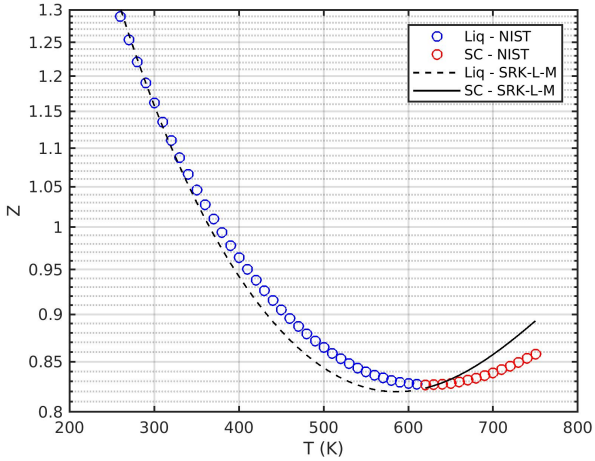

(e)

Figure D.16: *n*-decane compressibility factor. (a) 1 bar; (b) 10 bar; (c) 50 bar; (d) 100 bar; and (e) 150 bar.

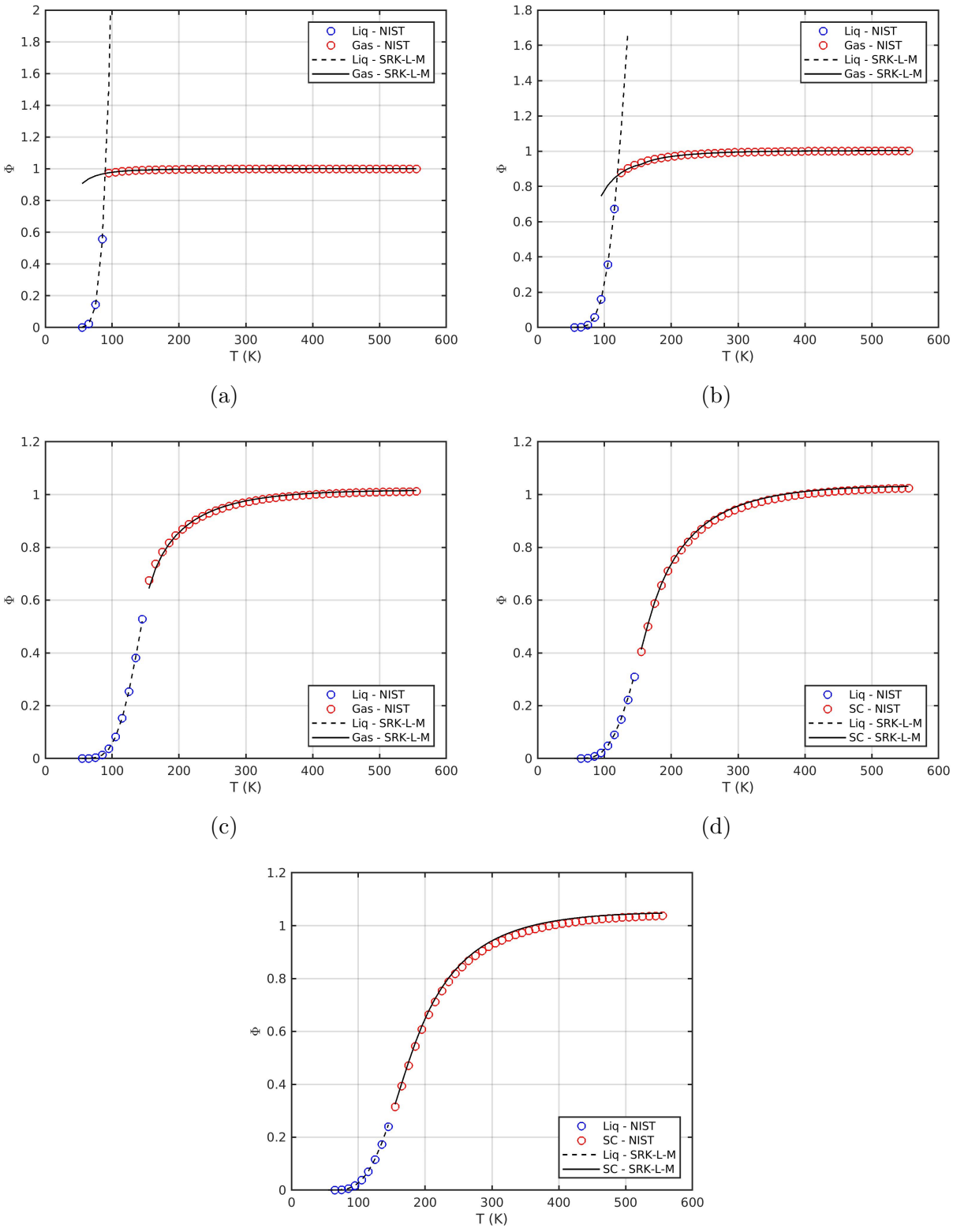

Figure D.17: Oxygen fugacity coefficient. (a) 1 bar; (b) 10 bar; (c) 50 bar; (d) 100 bar; and (e) 150 bar.

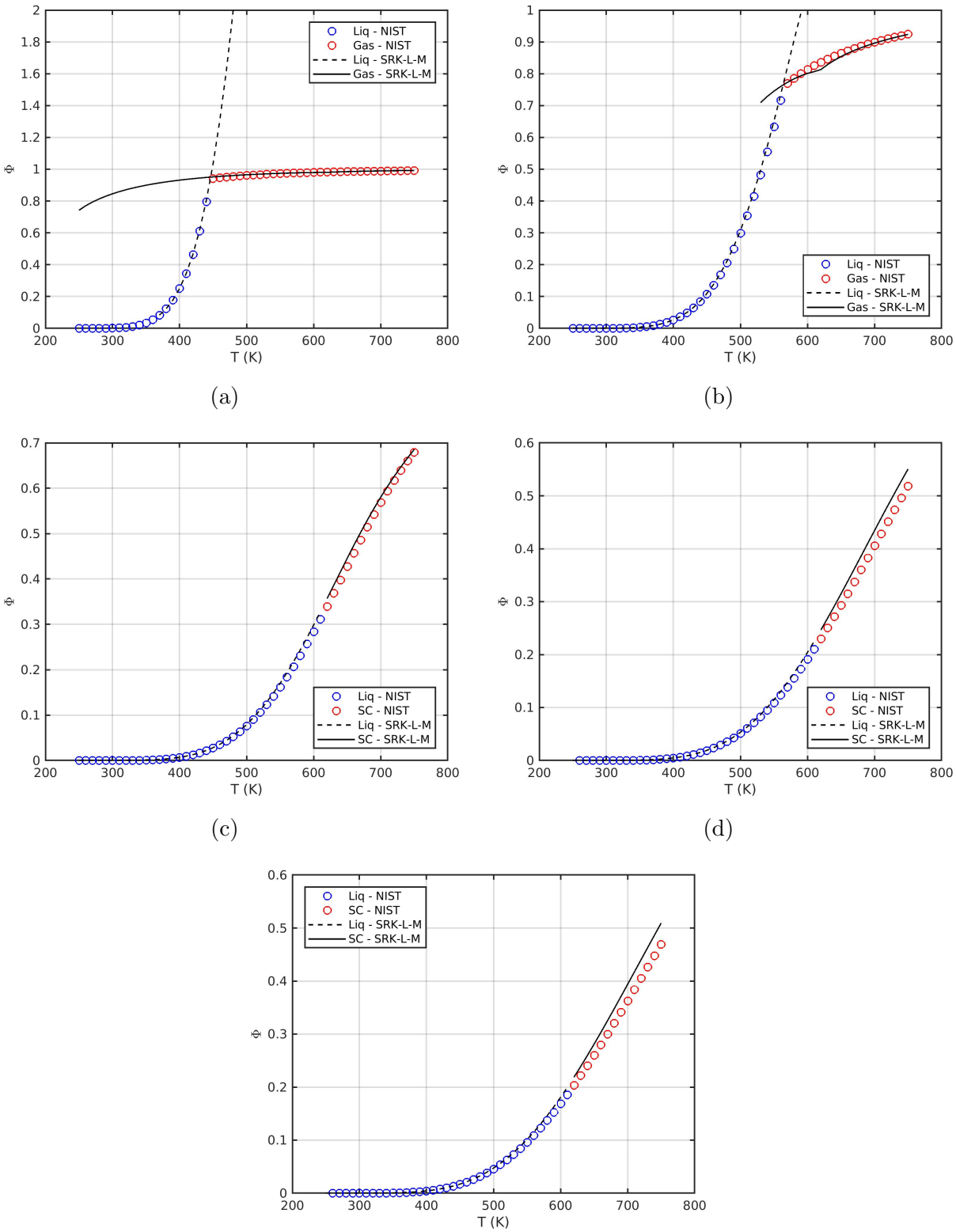

Figure D.18: n-decane fugacity coefficient. (a) 1 bar; (b) 10 bar; (c) 50 bar; (d) 100 bar; and (e) 150 bar.

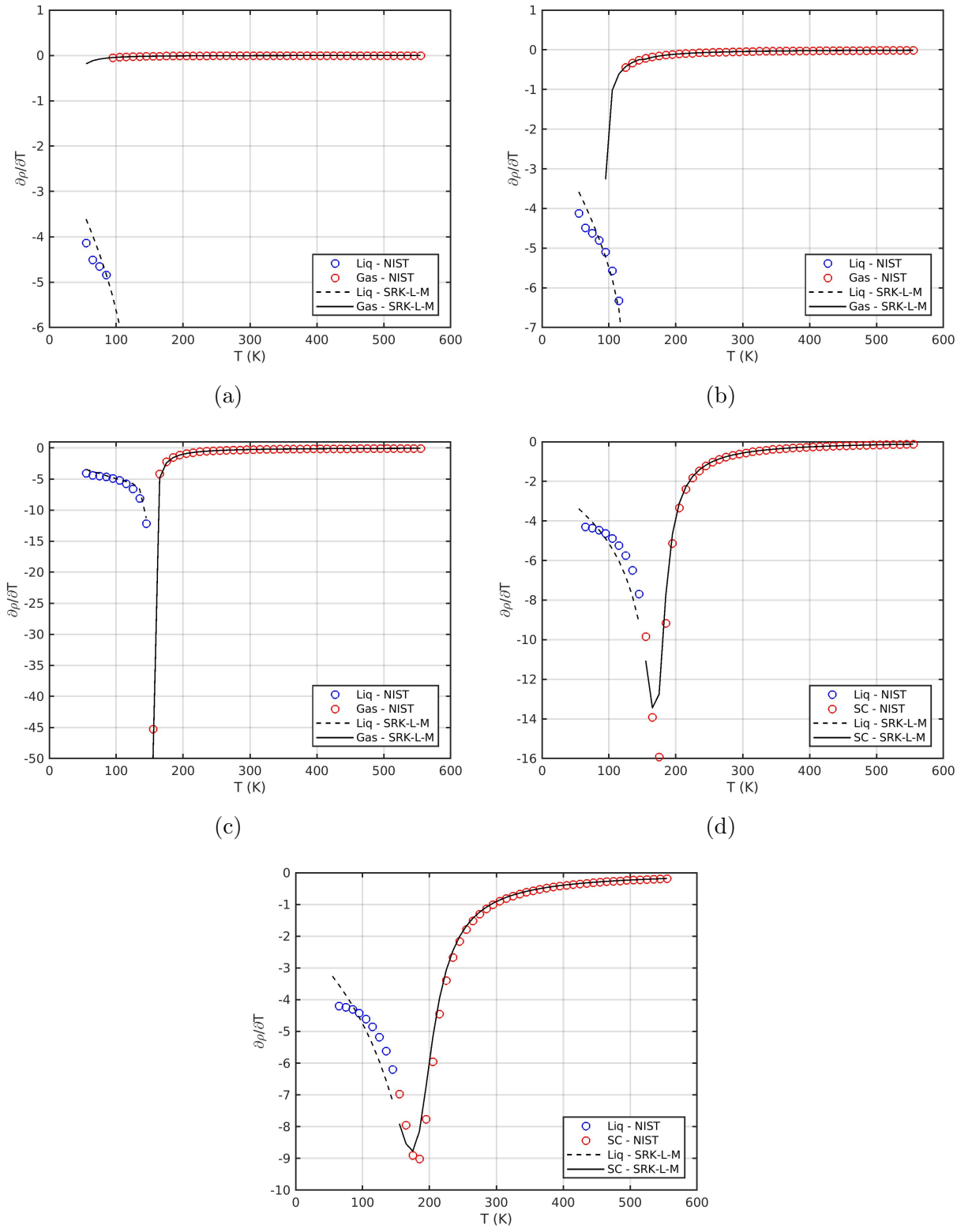

Figure D.19: Oxygen $(\partial\rho/\partial T)_{p,X_i}$. (a) 1 bar; (b) 10 bar; (c) 50 bar; (d) 100 bar; and (e) 150 bar.

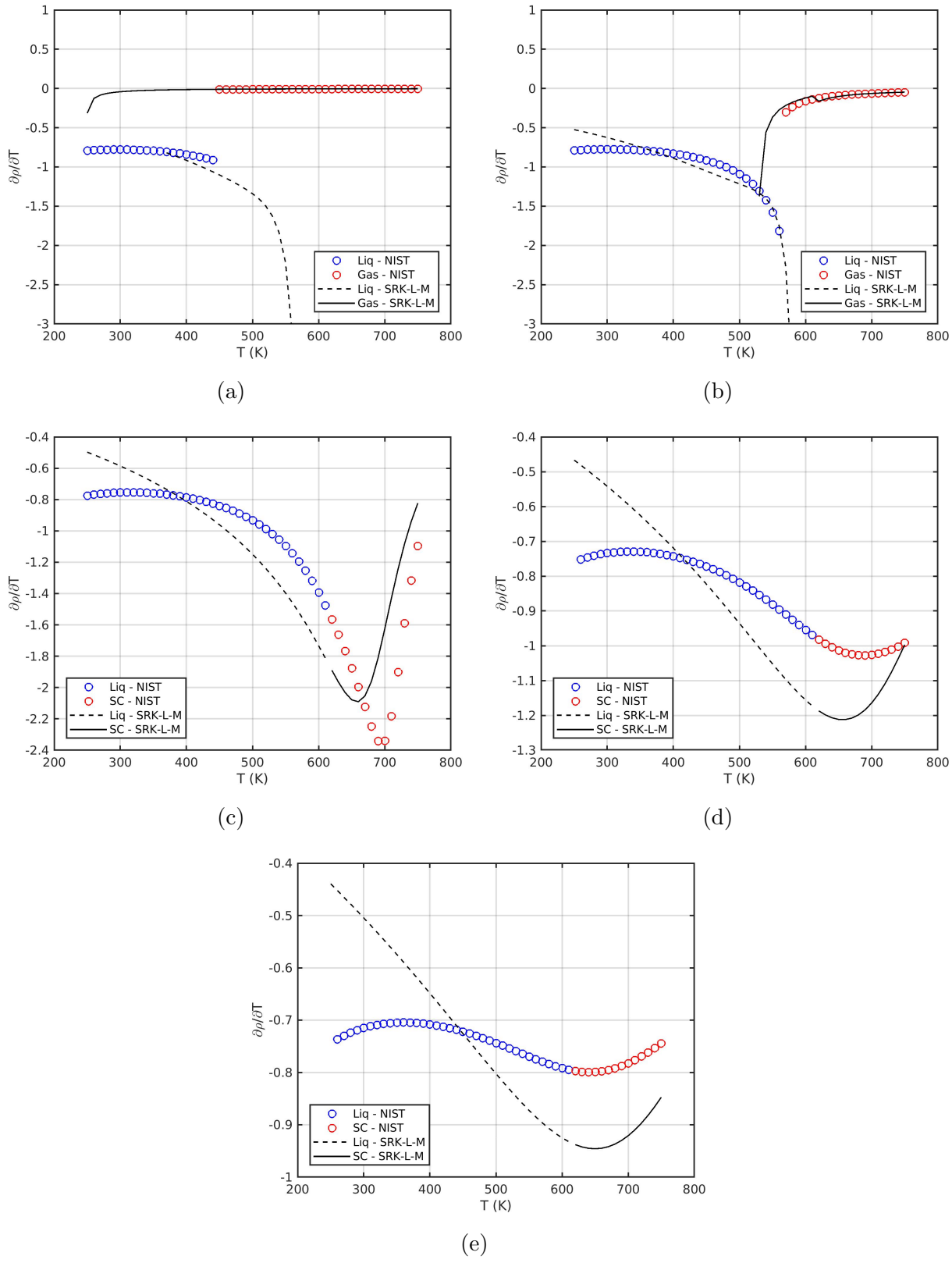

Figure D.20: n-decane $(\partial\rho/\partial T)_{p,X_i}$. (a) 1 bar; (b) 10 bar; (c) 50 bar; (d) 100 bar; and (e) 150 bar.

E Discretization of the species and enthalpy transport equations

This appendix presents the discretization of convective and diffusive terms in the transport equations for the oxidizer species mass fraction and the mixture enthalpy, Eqs. (4.14) and (4.15). The discretization of ∇Y_O in the convective term $\vec{u}_f \cdot \nabla Y_O$ of Eq. (4.14) is used as an example following the configuration presented in Figure 4.2. The method given here evaluates derivatives with respect to the x-direction and serves as a template for the derivatives with respect to y and z and can be extended to the respective term in the enthalpy transport equation. The explicit notation has been removed for clarity. This example illustrates the various scenarios encountered while evaluating $\partial Y_O/\partial x$ using an adaptive first-/second-order upwinding scheme and can be readily extended to multiple directions and interface setups.

The gradient based on gas values at cell i is found as follows. Using a uniform mesh, for $(u_f^i + u_f^{i+1})/2 < 0$ (where the phase-wise velocity is $f = g$), $\partial Y_O/\partial x$ becomes

$$\left(\frac{\partial Y_O}{\partial x}\right)^i = \begin{cases} \frac{Y_O^{i+2} - Y_O^i + (Y_O^i - Y_O^{i+1})(1+\Delta x_3/\Delta x_2)^2}{\Delta x_2 + \Delta x_3 - \frac{(\Delta x_2 + \Delta x_3)^2}{\Delta x_2}} & \text{if bounded second-order} \\ \frac{Y_O^{i+1} - Y_O^i}{\Delta x_2} & \text{if not bounded second-order} \end{cases} \tag{E.1}$$

and if $(u_f^i + u_f^{i+1})/2 \geq 0$, it becomes

$$\left(\frac{\partial Y_O}{\partial x}\right)^i = \begin{cases} \frac{Y_O^i - Y_{O,g}^\Gamma}{\Delta x_1} & \text{if } \Delta x_1 \geq 0.05\Delta x \\ \frac{Y_O^{i+1} - Y_{O,g}^\Gamma}{\Delta x_1 + \Delta x_2} & \text{if } \Delta x_1 < 0.05\Delta x \end{cases} \tag{E.2}$$

where $Y_{O,g}^\Gamma$ is the gas mass fraction of the oxidizer species at the interface. The interface value used in the discretization is averaged as in Eq. (4.24). If the distance between node i and the interface is short (i.e., defined as $\Delta x_1 < 0.05\Delta x$), node i is skipped and the gradient

is evaluated using the neighboring node i+1. This step is required to avoid a spike in the value of $\partial Y_O/\partial x$ when the interface is very close to the grid node. Otherwise, it could result in unrealistic solutions near the interface.

Another numerical stencil configuration that can be encountered is given in cell i+1 if $(u_f^{i+1} + u_f^{i+2})/2 \geq 0$. Here, $\partial Y_O/\partial x$ is evaluated as

$$\left(\frac{\partial Y_O}{\partial x}\right)^{i+1} = \begin{cases} \frac{Y_{O,g}^{\Gamma} - Y_O^{i+1} + (Y_O^{i+1} - Y_O^i)(-1-\Delta x_1/\Delta x_2)^2}{-(\Delta x_1+\Delta x_2)+\frac{(-\Delta x_1-\Delta x_2)^2}{\Delta x_2}} & \text{if bounded second-order and } \Delta x_1 \geq 0.05\Delta x \\ \frac{Y_O^{i+1}-Y_O^i}{\Delta x_2} & \text{if not bounded second-order or } \Delta x_1 < 0.05\Delta x \end{cases} \tag{E.3}$$

where any of the requirements specified in Eqs. (E.1) and (E.2) are used to preserve numerical stability and boundedness. Far from the interface, $\partial Y_O/\partial x$ is calculated with similar expressions as in Eqs. (E.1) and (E.3) just taking into account the boundedness condition.

Diffusive terms are discretized using second-order central differences, but the spatial accuracy might drop when including the interface in the numerical stencil. As done for the convective term, we look at the discretization of the $\nabla \cdot (\rho D_m \nabla Y_O)$ term in Eq. (4.14). Using the configuration presented in Figure 4.2, the discretization of $\partial(\rho D_m[\partial Y_O/\partial x])/\partial x$ is addressed. Yet, its extension to other directions or interface configurations, as well as to the diffusive terms appearing in Eq. (4.15), is straightforward. Generally, the discretization of the diffusive term follows

$$\frac{\partial}{\partial x}\left(\rho D_m \frac{\partial Y_O}{\partial x}\right) = \frac{(\rho D_m \partial Y_O/\partial x)^E - (\rho D_m \partial Y_O/\partial x)^W}{\Delta x} \tag{E.4}$$

with E and W referring to the East and West cell faces, respectively, as defined in Subsection 4.1.2.

Linear interpolation between two neighboring grid nodes is used to determine fluid characteristics at the cell face. The interface substitutes the cell face if it is placed between the grid node and its associated cell face (e.g., the West face of node i in Figure 4.2). Furthermore, if the interface is positioned after a cell face but before a neighboring node, its equilibrium solution and location are used to calculate $\partial Y_O/\partial x$ and to interpolate the fluid properties at the cell face linearly (e.g., the East face of node i-1 in Figure 4.2).

For example, the discretization of the diffusive term at cell i results in

$$\frac{\partial}{\partial x}\left(\rho D_m \frac{\partial Y_O}{\partial x}\right)^i = \frac{(\rho D_m \partial Y_O/\partial x)^E - (\rho D_m \partial Y_O/\partial x)^W}{\Delta x_1 + \Delta x_2/2} \tag{E.5}$$

with

$$\left(\rho D_m \frac{\partial Y_O}{\partial x}\right)^E = (\rho D_m)^E \left(\frac{Y_O^{i+1} - Y_O^i}{\Delta x_2}\right) \tag{E.6a}$$

$$\left(\rho D_m \frac{\partial Y_O}{\partial x}\right)^W = \begin{cases} (\rho D_m)_g^\Gamma \left(\frac{Y_O^i - Y_{O,g}^\Gamma}{\Delta x_1}\right) & \text{if } \Delta x_1 \geq 0.05\Delta x \\ (\rho D_m)_g^\Gamma \left(\frac{Y_O^{i+1} - Y_{O,g}^\Gamma}{\Delta x_1 + \Delta x_2}\right) & \text{if } \Delta x_1 < 0.05\Delta x \end{cases} \tag{E.6b}$$

where $(\rho D_m)^E$ is the product of the linear interpolations of ρ and D_m at the East face and $(\rho D_m)_g^\Gamma$ is the product of the interface gas values of ρ and D_m at equilibrium. Nonphysical spikes caused by the interface proximity to the grid node are eliminated by skipping node i when evaluating $\partial Y_O/\partial x$, as done in the discretization of the convective term.

F Validation and verification of the numerical code

F.1 Single-phase incompressible flow

Basic benchmark cases have been performed (e.g., flow between parallel plates, pipe flow, lid-driven cavity) to validate the numerical code in the laminar limit, single-phase, incompressible flow. Details about these basic configurations are given in White and Corfield [147], Ghia et al. [148] and Erturk et al. [149]. The performance in two dimensions, as well as axisymmetric or periodic configurations, is shown in Figures F.1 and F.2. The velocity profile of a periodic, three-dimensional channel flow collapses to the two-dimensional solution shown in Figure F.1a. The inclusion of species and thermal mixing is not considered here.

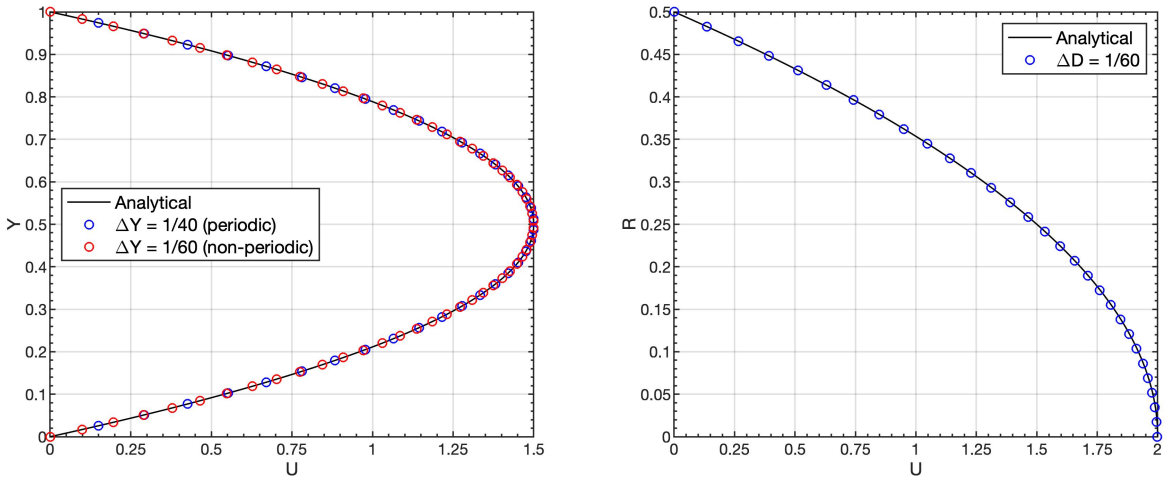

(a) (b)

Figure F.1: Benchmark case 1: channel flows. Showing normalized, fully-developed, laminar velocity profiles ($U = u/U_o$) vs. normalized height ($Y = y/h$) or radius ($R = r/D$). The mesh size is normalized as $\Delta Y = \Delta y/h$ or as $\Delta D = \Delta d/D$, respectively, which represent the mesh divisions in the transverse direction of the channel or the pipe. (a) channel flow between parallel plates. Periodic boundary conditions are tested imposing the pressure gradient from the analytical solution; (b) pipe flow. Axisymmetry is considered.

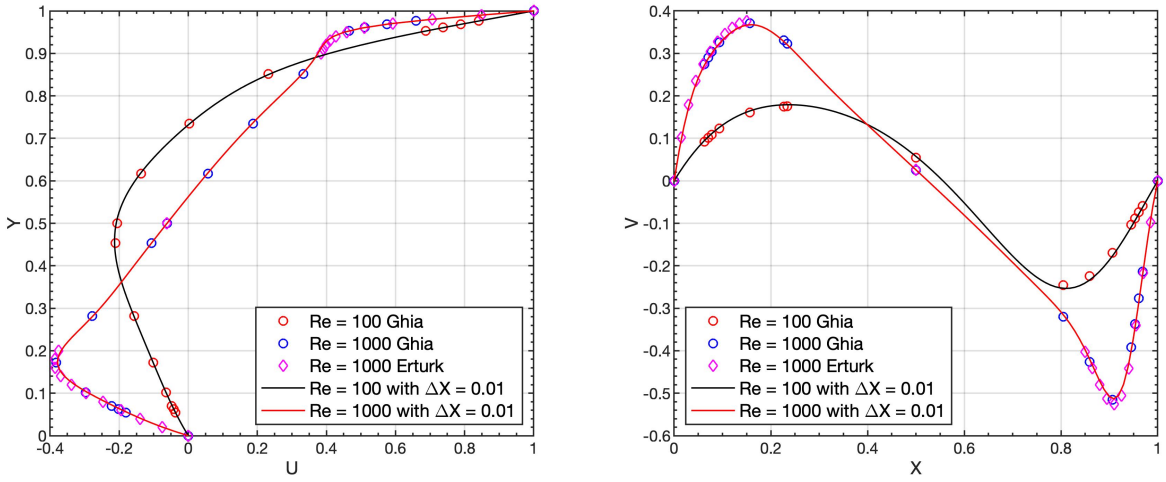

(a) (b)

Figure F.2: Benchmark case 2: lid-driven cavity at different Reynolds numbers. Showing normalized, steady-state velocity profiles ($U = u/U_{\text{lid}}$ or $V = v/U_{\text{lid}}$) vs. normalized position ($X = x/L_x$ or $Y = y/L_y$). The mesh size is normalized as $\Delta X = \Delta x/L_x$ and $\Delta Y = \Delta y/L_y$. A uniform mesh is considered where $\Delta X = \Delta Y$. (a) U vs Y at $X = 0.5$; (b) V vs X at $Y = 0.5$.

F.2 Two-phase incompressible flows

Standing capillary wave

Prosperetti [65] presents an analytical solution for the relaxation of small-amplitude, two-dimensional capillary waves that can be used to validate the dynamical behavior of the liquid surface in the presence of surface tension. The analytical solution is obtained for superposed fluids with infinite depth and lateral extent, which is solved numerically by simplifying the problem to two dimensions and using a sufficiently large domain in the surface transverse direction with open boundary conditions. Moreover, periodic boundary conditions are imposed in the wave direction. No species nor thermal mixing is considered.

The amplitude decay of an initial sinusoidal perturbation is shown in Figure F.3. A sinusoidal wave with a wavelength of 1 m and an initial amplitude of 0.01 m is considered. Each fluid has a depth of 1.5 m. The liquid density is 1000 kg/m^3 and the gas density is 100 kg/m^3,

while the liquid viscosity is 17.989 Pa·s and the gas viscosity is 1.7989 Pa·s. The surface-tension coefficient is 0.01 N/m, and gravity is considered with the lighter fluid sitting on top of the denser fluid.

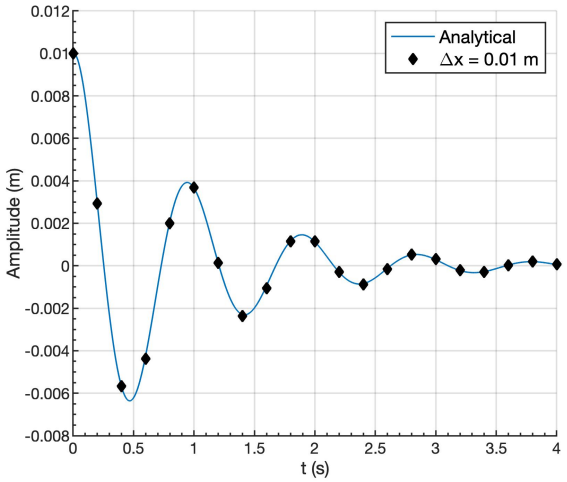

Figure F.3: Benchmark case 3: standing capillary wave. Showing wave amplitude vs. time. A uniform mesh is considered where $\Delta x = \Delta y$.

Liquid jet atomization

Furthermore, the two-phase, incompressible limit is verified by comparing the performance of the present code with previous codes used to analyze the atomization of planar liquid jets. For that purpose, the early deformation of a planar liquid jet defined in Table 1 of Zandian et al. [27] as case D3a is analyzed. Following the definition of the liquid Reynolds number, $Re_L = \rho_L u_G H/\mu_L$, and gas Weber number, $We_G = \rho_G u_G^2 H/\sigma$, this case presents $Re_L = 5000$ and $We_G = 7250$. The jet thickness is $H = 50$ μm and the freestream gas velocity is $u_G = 100$ m/s, while the liquid density is set at $\rho_L = 804$ kg/m^3 and the gas density is $\rho_G = 402$ kg/m^3. The initial perturbation wavelength is 100 μm. Further details about the problem setup are provided in Zandian et al. [27]. Again, species and thermal mixing are not considered.

The computational setup is different. The numerical model presented here is based on a Volume-of-Fluid approach, while the numerical method used in Zandian et al. [27] is based on the Level-Set method. Thus, both codes are substantially different in capturing the interface and addressing the sharp interface. Moreover, the uniform mesh size used in Zandian et al. [27] is $\Delta x = 1.25$ μm with the planar jet centered in the domain, while the results obtained with the present model use $\Delta x = 0.667$ μm with a reduced computational domain that includes fewer initial perturbations and that considers symmetry along the center plane of the jet. The time step restrictions are consistent with each numerical method.

Figures F.4 to F.8 show the comparison between both numerical approaches at different times. At 10 μs, 20 μs and 30 μs, both methods predict almost an identical surface deformation, which verifies the implemented interface capturing approach and momentum solver against a previously validated code which has been used in numerous works [24–28, 36]. Slight differences exist, which become more apparent at later times (i.e., 40 μs and 50 μs). That is, the present code maintains a sharper interface and uses a finer mesh than the results from Zandian et al. [27]. Therefore, it can better resolve the smaller structures and high-curvature regions that develop. Also, the symmetry boundary condition might affect the comparison between both simulations once the surface has deformed substantially.

The VOF data also show what appear to be surface wrinkles with a very short wavelength. These wrinkles appear in the plotting software when depicting the iso-surface of the non-smooth data set that is the volume fraction field. They do not occur in the actual computation when the right interface reconstruction techniques are applied (i.e., PLIC).

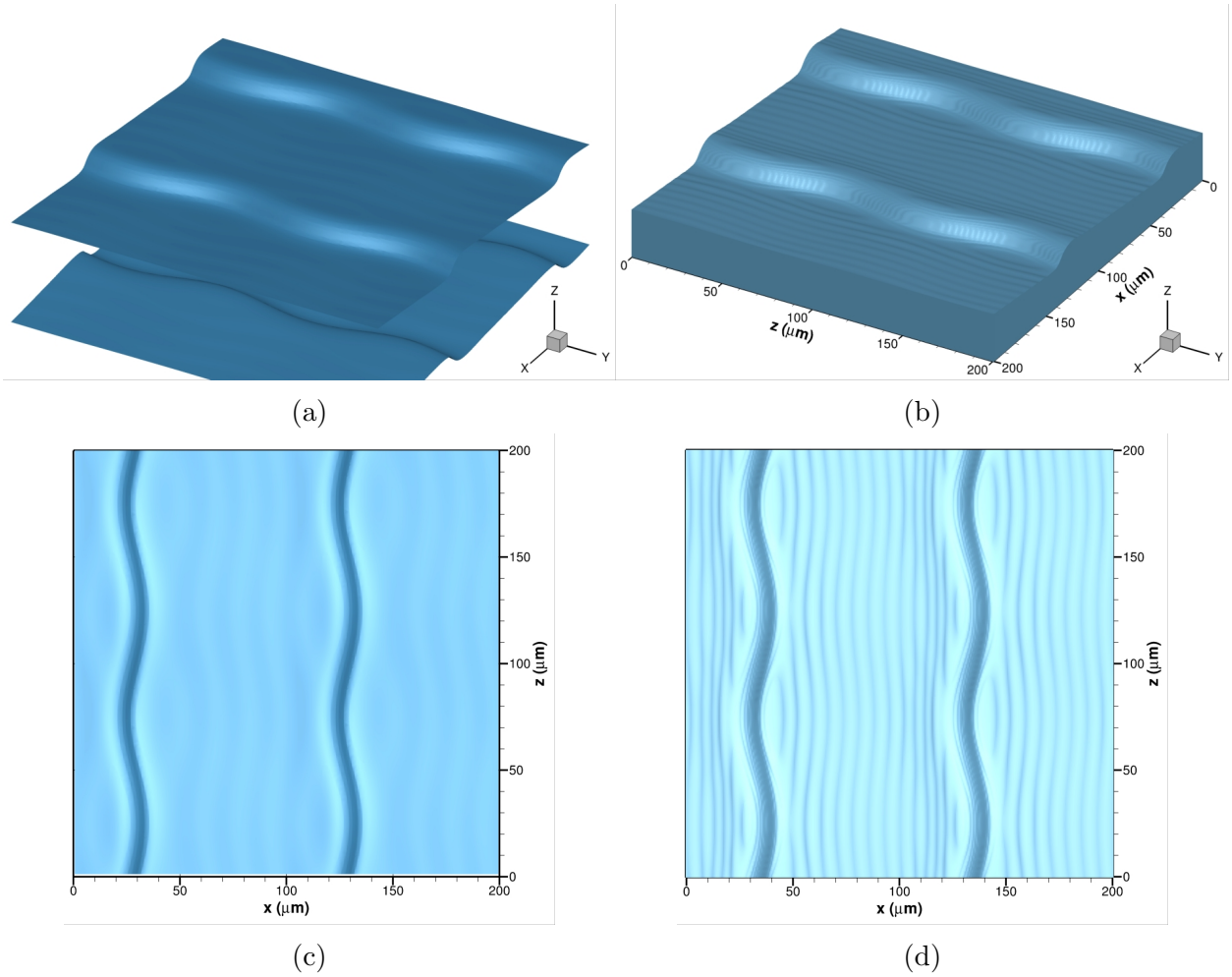

Figure F.4: Benchmark case 4(a): liquid jet injection. Surface deformation comparison at $t = 10$ μs between a numerical approach based on the Level-Set (LS) method [27] and the present numerical approach based on the Volume-of-Fluid (VOF) method. The LS method identifies the liquid surface as the iso-surface with $\theta = 0$ and the VOF method identifies the liquid surface as the iso-surface with $C = 0.5$. (a) 3D view (LS); (b) 3D view (VOF); (c) top view (LS); and (d) top view (VOF).

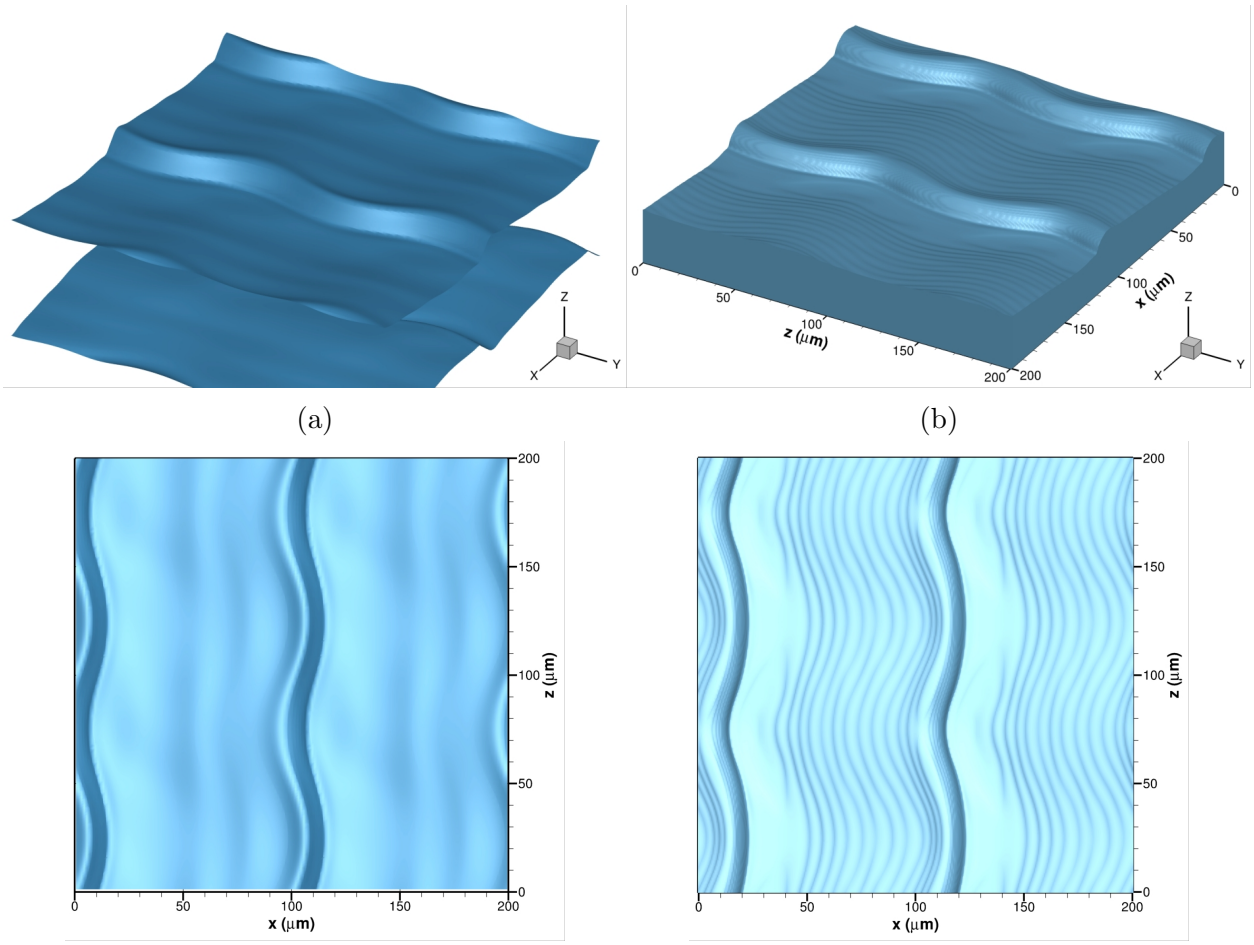

Figure F.5: Benchmark case 4(b): liquid jet injection. Surface deformation comparison at $t = 20$ μs between a numerical approach based on the Level-Set (LS) method [27] and the present numerical approach based on the Volume-of-Fluid (VOF) method. The LS method identifies the liquid surface as the iso-surface with $\theta = 0$ and the VOF method identifies the liquid surface as the iso-surface with $C = 0.5$. (a) 3D view (LS); (b) 3D view (VOF); (c) top view (LS); and (d) top view (VOF).

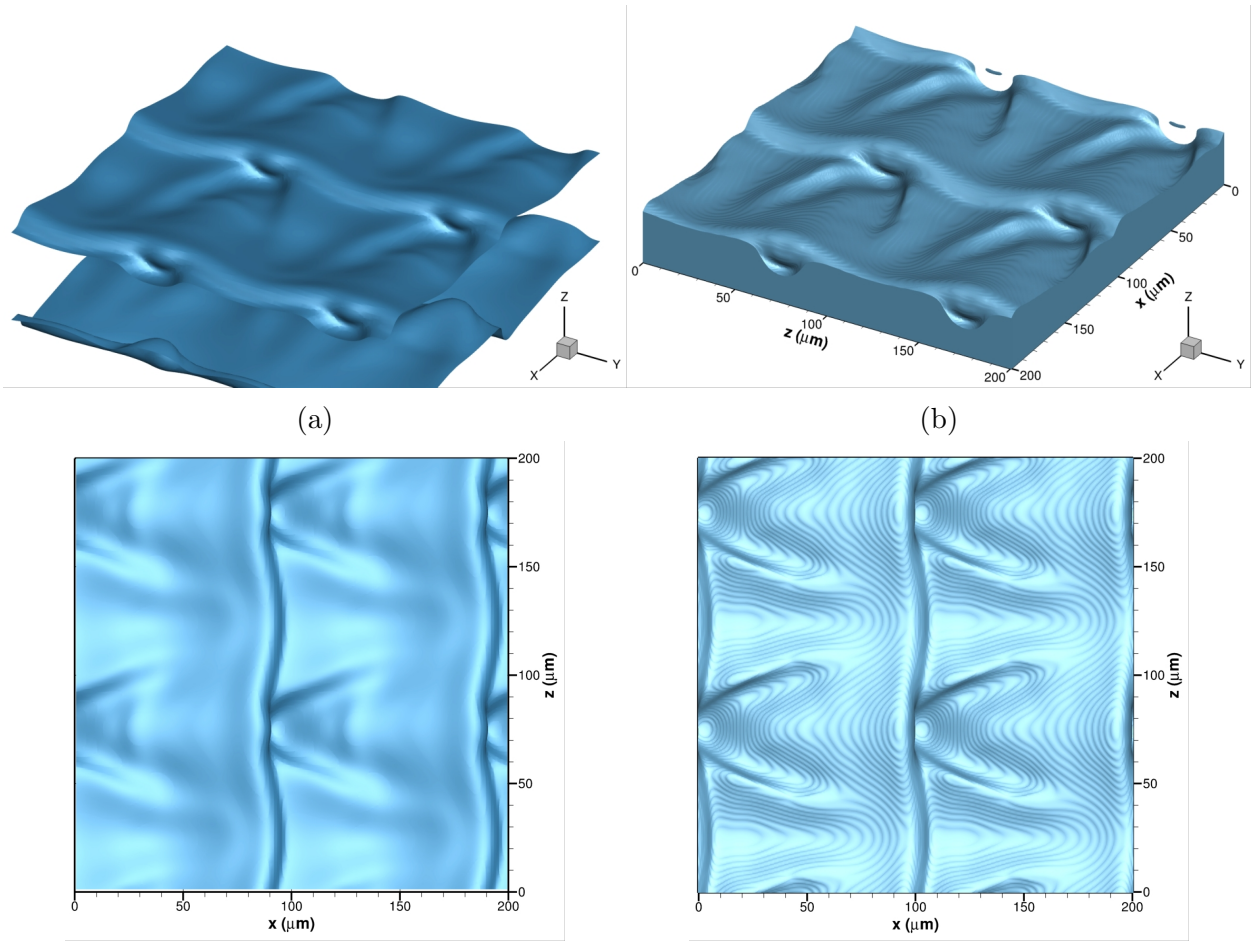

Figure F.6: Benchmark case 4(c): liquid jet injection. Surface deformation comparison at $t = 30$ μs between a numerical approach based on the Level-Set (LS) method [27] and the present numerical approach based on the Volume-of-Fluid (VOF) method. The LS method identifies the liquid surface as the iso-surface with $\theta = 0$ and the VOF method identifies the liquid surface as the iso-surface with $C = 0.5$. (a) 3D view (LS); (b) 3D view (VOF); (c) top view (LS); and (d) top view (VOF).

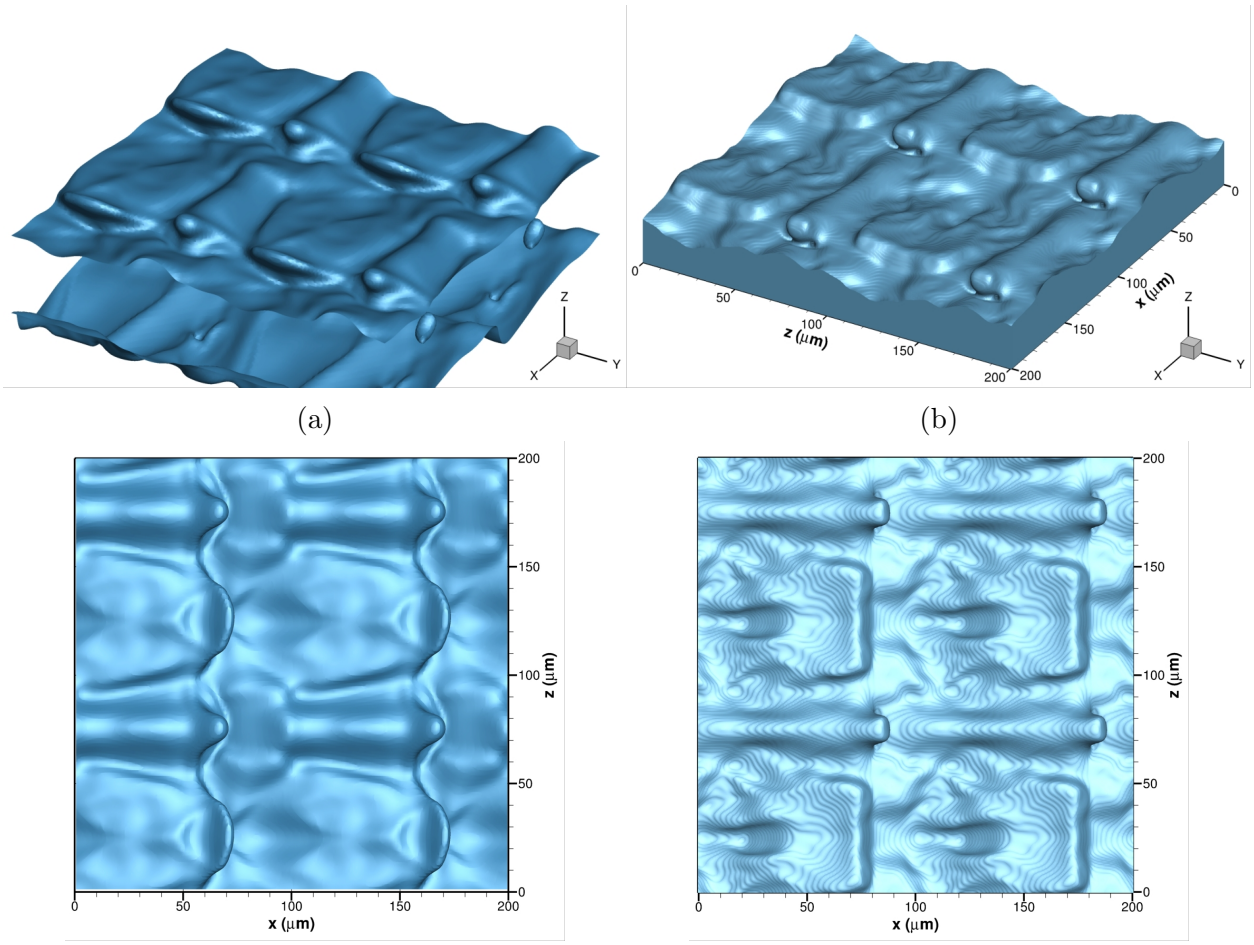

Figure F.7: Benchmark case 4(d): liquid jet injection. Surface deformation comparison at $t = 40$ μs between a numerical approach based on the Level-Set (LS) method [27] and the present numerical approach based on the Volume-of-Fluid (VOF) method. The LS method identifies the liquid surface as the iso-surface with $\theta = 0$ and the VOF method identifies the liquid surface as the iso-surface with $C = 0.5$. (a) 3D view (LS); (b) 3D view (VOF); (c) top view (LS); and (d) top view (VOF).

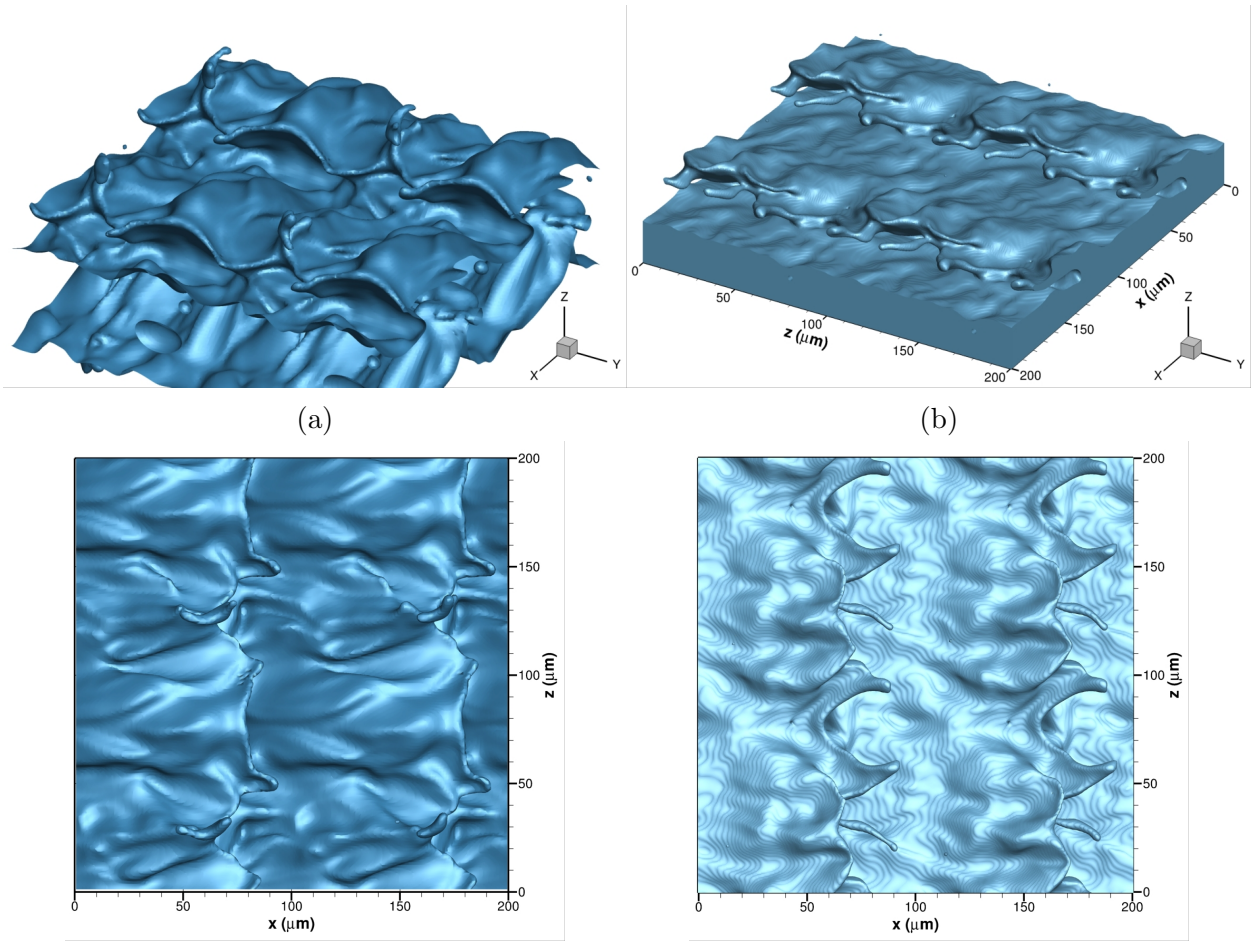

Figure F.8: Benchmark case 4(e): liquid jet injection. Surface deformation comparison at $t = 50$ μs between a numerical approach based on the Level-Set (LS) method [27] and the present numerical approach based on the Volume-of-Fluid (VOF) method. The LS method identifies the liquid surface as the iso-surface with $\theta = 0$ and the VOF method identifies the liquid surface as the iso-surface with $C = 0.5$. (a) 3D view (LS); (b) 3D view (VOF); (c) top view (LS); and (d) top view (VOF).

F.3 Two-phase transcritical flows

One-dimensional transient flow near the liquid-gas interface

A two-dimensional configuration with an initially straight interface and no shear flow has been used to study the transient behavior around a liquid-gas contact interface with zero curvature at various pressures. Poblador-Ibanez and Sirignano [15] present a complete study of this problem using a simplified one-dimensional code, which has been discussed in Section 2.3. The following are the primary distinctions between the two approaches. While in the developed model all relevant governing equations are solved, and the interface is permitted to shift as mass exchange and volume expansion occur, Poblador-Ibanez and Sirignano [15] handle the diffusion-driven problem relative to the interface by fixing its location and assuming a constant pressure across the domain. As a result, the momentum equation is disregarded, and the velocity field is derived directly from the continuity equation.

The liquid phase is initially composed of n-decane at $T_L = 450$ K. At the left boundary, the liquid is sitting on a wall, while the other extreme is in contact with hotter gaseous oxygen at $T_G = 550$ K. The highest temperature is bounded by T_G in the absence of an energy source, which is below the critical temperature of n-decane or 617.7 K. The liquid-gas interface will reach a thermodynamic equilibrium steady state as oxygen dissolves into the liquid and n-decane vaporizes when both fluids are initially at rest. The interface is initially located 50 μm apart from the wall. Volume expansion and compression caused by the mixing process and phase change produce a velocity field transverse to the interface. Periodic boundary conditions are imposed along the y-direction, no-slip wall boundary conditions are enforced at $x = 0$, and an open boundary is imposed at the right end of the domain sufficiently far away from the interface. The two-dimensional algorithm must provide a one-dimensional solution because no interface disturbance or shear flow can trigger one. Only minor numerical truncation errors show up in the solution. The critical pressure of n-decane is approximately

21.03 bar. With this consideration in mind, four pressures are analyzed: one subcritical case at 10 bar and three supercritical cases with 50, 100, and 150 bar [15]. For all pressures, a mesh size of $\Delta x = 200$ nm and a time step of $\Delta t = 2$ ns are utilized.

Because the thermodynamic models employed in both works are not identical, a direct comparison between the current work and the results given in Poblador-Ibanez and Sirignano [15] is not possible. In this work, a volume correction is used to improve the correctness of the SRK equation of state, whereas in Poblador-Ibanez and Sirignano [15], this correction is omitted. As a result, various fluid properties, particularly in the liquid phase, are expected to be somewhat different. Nonetheless, a qualitative comparison with an acceptable agreement is achievable.

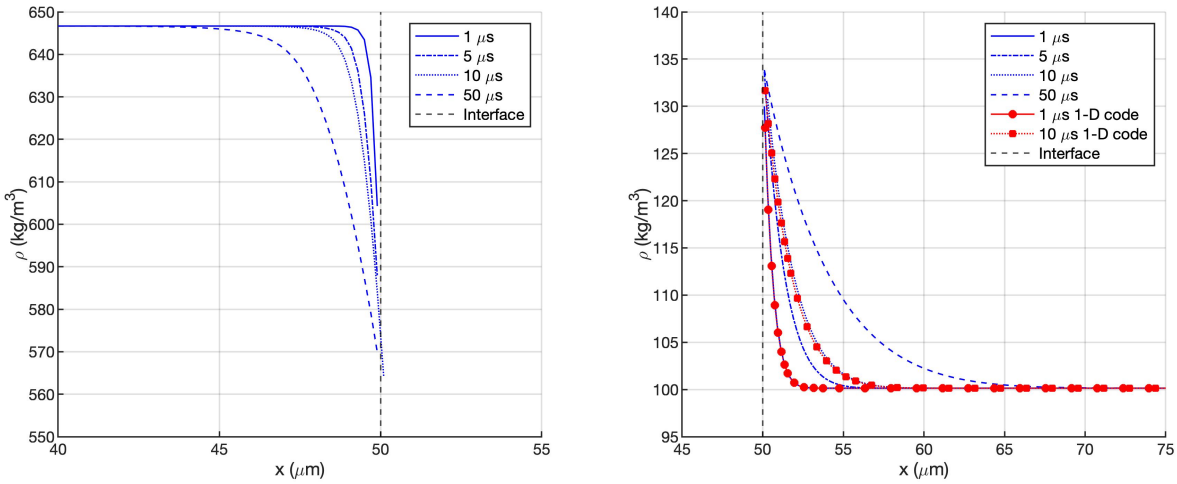

(a) (b)

Figure F.9: Benchmark case 5(a): one-dimensional transient flow near a liquid-gas interface at high pressures. Evolution of the density profiles over time for the one-dimensional unsteady flow near a liquid-gas interface with a n-decane/oxygen binary mixture at $p = 150$ bar. (a) liquid density; (b) gas density [66].

The results are one-dimensional. There is no evidence of a deviation from a one-dimensional solution or a surface instability growth. The temporal evolution of the density profiles at 150 bar is illustrated in Figure F.9. Except for slight deviations caused by the improvement in the thermodynamic model, the results in the gas phase are almost identical to those reported

in Poblador-Ibanez and Sirignano [15]. The liquid-phase solution cannot be compared as large differences exist in the predicted density using the improved SRK equation of state (i.e., liquid density is closer to 545 kg/m^3 with the original SRK equation of state). In both studies, mixing in the gas phase is very similar, with the density profile (see Figure F.9b) extending around 7-9 μm into the gas phase at $t = 10$ μs and the temperature profile extending about 10 μm in the same time. The interface tends to a steady-state solution as the mixing regions expand in size (see Figure F.10b), as reported in Poblador-Ibanez and Sirignano [15] and discussed in Section 2.3. Similar studies involving a two-dimensional laminar mixing layer exhibit the same phenomenon [16, 17] (see Section 2.4). However, in more complex configurations where the surface deforms, this behavior may not hold.

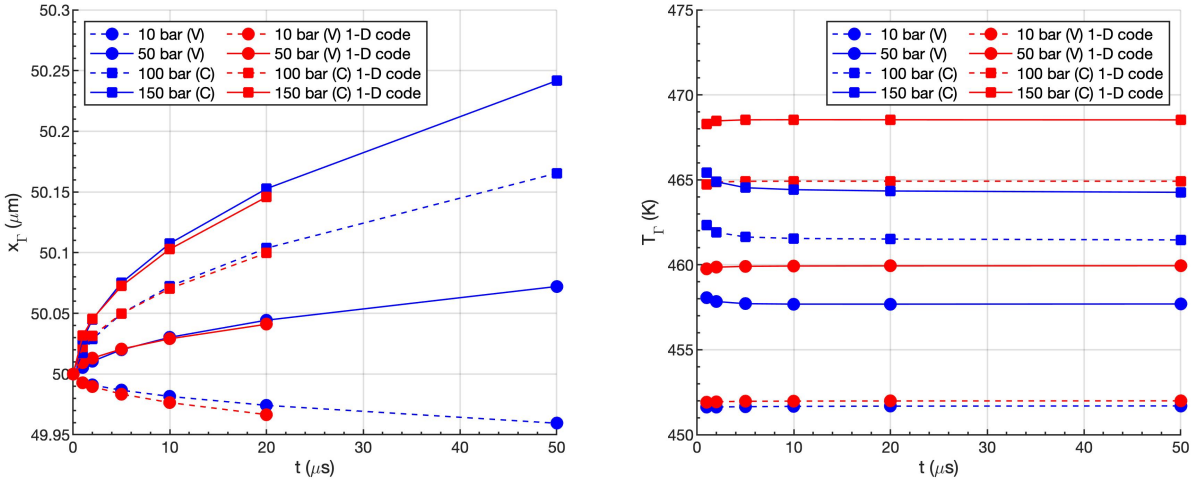

(a) (b)

Figure F.10: Benchmark case 5(b): one-dimensional transient flow near a liquid-gas interface at high pressures. Evolution of the interface location and temperature over time at different pressures for the one-dimensional unsteady flow near a liquid-gas interface with a *n*-decane/oxygen binary mixture. Depending on the ambient pressure, net vaporization (V) or net condensation (C) occurs across the interface. (a) interface location; (b) interface temperature [66].

The volume correction in the SRK equation of state has little effect in the gas phase but has a more significant impact in the liquid phase. Furthermore, when compared to Poblador-Ibanez and Sirignano [15], this improved thermodynamic model yields slightly different interface so-

lutions (e.g., lower temperatures are predicted). This shift in the interface solution generates a minor change in the evolution of the energy and species mixing, resulting in slight variations in the gas-phase density profiles that accumulate over time, as shown in Figure F.9b at 10 μs.

The two major assumptions made in Poblador-Ibanez and Sirignano [15] are verified here. The pressure remains almost constant throughout the simulation, and the velocity field is mostly driven by density variations generated by mixing. Furthermore, Figure F.10a depicts the interface location over time. The interface displacement is practically negligible because mass exchange weakens over time in this problem setup. The largest interface displacements after 50 μs are of the order of 100 nm, which is comparable to the grid spacing used in this problem and negligible compared to the diffusion layer thickness. The interface position according to Poblador-Ibanez and Sirignano [15] has been determined in Figure F.10a by integrating the interface velocity, u_Γ, over time. This velocity is calculated by shifting the velocity field obtained so that $u(x = 0) = 0$ is satisfied. The mass balance across the interface is then used to calculate u_Γ (i.e., Eq. (3.10)). On the other hand, the current approach incorporates information from the volume fraction distribution to determine the interface location at any given time. The two approaches produce slightly different results due to variations in the interface solution.

The direction of the interface displacement is also confirmed. Net vaporization is considerable at 10 bar, with very little oxygen dissolving into the liquid phase. As a result, the interface recedes and the total liquid volume drops. However, when pressure rises, so does the dissolution of oxygen into n-decane. As a result of the presence of a lighter species, local liquid volume expansion near the interface occurs. Even though the interface exhibits net vaporization at 50 bar, it is not strong enough to compensate for the liquid volume expansion. Both local volume expansion and net condensation contribute to the overall rise in liquid volume at 100 and 150 bar.

Two-dimensional capillary wave at supercritical pressures

The standing wave problem is a suitable test for determining the relaxation period of a perturbed two-phase interface driven by capillary forces. Gravity is ignored here, while the analytical solution of this problem for incompressible flows given by Prosperetti [65] may include it. In this section, a similar analysis for the relaxation of a surface perturbation at high pressures is performed for the same binary mixture of oxygen and n-decane seen in the one-dimensional transient problem. Each phase's initial temperature and composition are the same, but only one thermodynamic pressure is examined (i.e., 150 bar). The two-dimensional domain is a rectangular box with a liquid layer of 20 μm depth and a width of 30 μm. While both fluids are initially at rest, the liquid-gas interface is spatially perturbed with a sinusoidal wave of 1 μm amplitude and 30 μm wavelength. The amplitude-to-wavelength ratio of 1/30 can be considered a small interface perturbation. During the examined time frames, the height of the domain must encompass the mixing zone in both phases. A height of 60 μm is sufficient for 150 bar. Periodic boundary conditions are imposed in the x-direction along the interface, no-slip wall boundary conditions are imposed at the bottom of the liquid layer, and outflow boundary conditions are imposed at the gas-phase top boundary.

Because the interface perturbation is small and there is no shear flow, the mixing in both phases is similar to the one-dimensional configuration. The relaxation of the interface deformation induced by capillary forces pushes the whole picture even closer to a one-dimensional solution. Nonetheless, this transitory process allows us to investigate the numerical model's accuracy and consistency. The 150-bar case is chosen to investigate the numerical model's spatial convergence under surface deformation. Because of the way the equations are discretized, the temporal convergence is expected to be first order. As a result, it is not addressed here, and we rely on a sufficiently small CFL condition to reduce temporal errors. Four different uniform meshes are considered, which are presented in Table F.1. Then, the interface equilibrium solution and geometry at 19 μs is presented as a function of the

mesh resolution from Figures F.11 to F.14, once sufficient relaxation of the mixing layers has occurred.

Table F.1: Details on the meshes used in the analysis of a two-dimensional capillary wave at supercritical pressures. The number of cells per wavelength or amplitude refer to the initial configuration of the liquid-gas interface.

Mesh	M1	M2	M3	M4
Δx (μm)	3/10	2/10	1/10	1/20
Cells/Wavelength	100	150	300	600
Cells/Amplitude	3.33	5	10	20

The mesh resolution around the interface affects the solution of LTE and jump conditions along the interface. Although numerous interface properties can be represented, temperature, net mass flux per unit area, and oxygen mass fraction on both sides of the interface are illustrated in Figures F.11 and F.12. The mixing near the interface is better captured when the mesh is refined because the enthalpy and concentration gradients derived using the normal probe technique (see Subsection 4.1.3) become more precise, and the PLIC interface reconstructions tend to be more continuous. These enhancements result in a smoother distribution of fluid properties over the interface, as seen in Figures F.11, F.12, and F.14a.

The figures' scale exacerbates the perceived discrepancy between two consecutive meshes. Although the M1 mesh may appear to be an exception due to a lower resolution, particularly in the liquid phase mixing region, the normalized errors or differences in the solution between two consecutive meshes are of the order of 1% or less. A detailed study reveals that the normalized errors converge at a first-order rate or lower, which is to be expected given the complexity of the numerical approach. Similar difficulties have been reported in other studies that use simpler models to determine the interface state [94, 115]. Even while one-dimensional interfaces exhibit good grid independence behavior, limited spatial convergence occurs once multi-dimensional interfaces are considered.

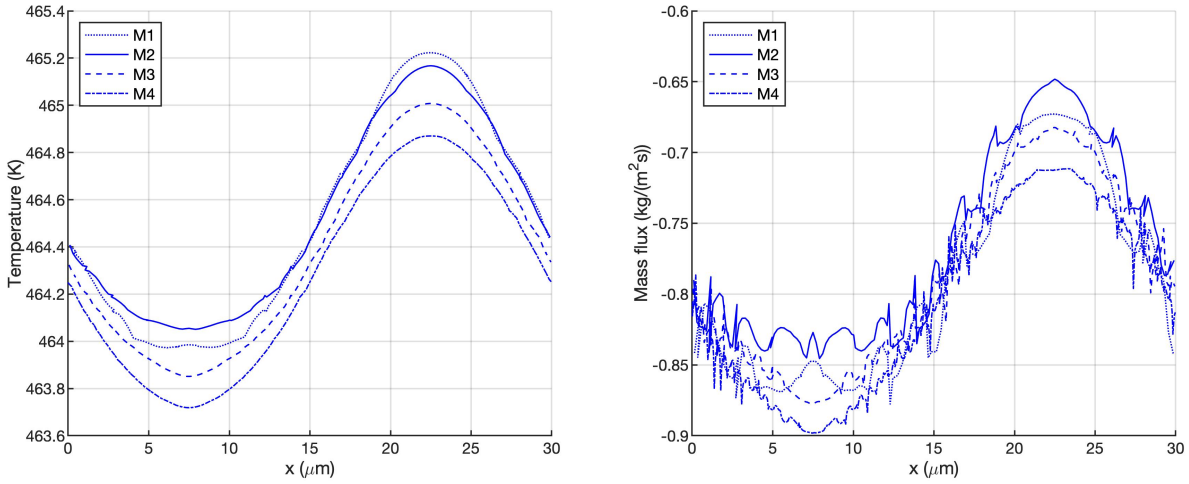

(a) (b)

Figure F.11: Benchmark case 6(a): two-dimensional capillary wave at supercritical pressures. Interface geometry and equilibrium state of the two-dimensional capillary wave at $t = 19$ μs and 150 bar. (a) temperature; (b) net mass flux [66].

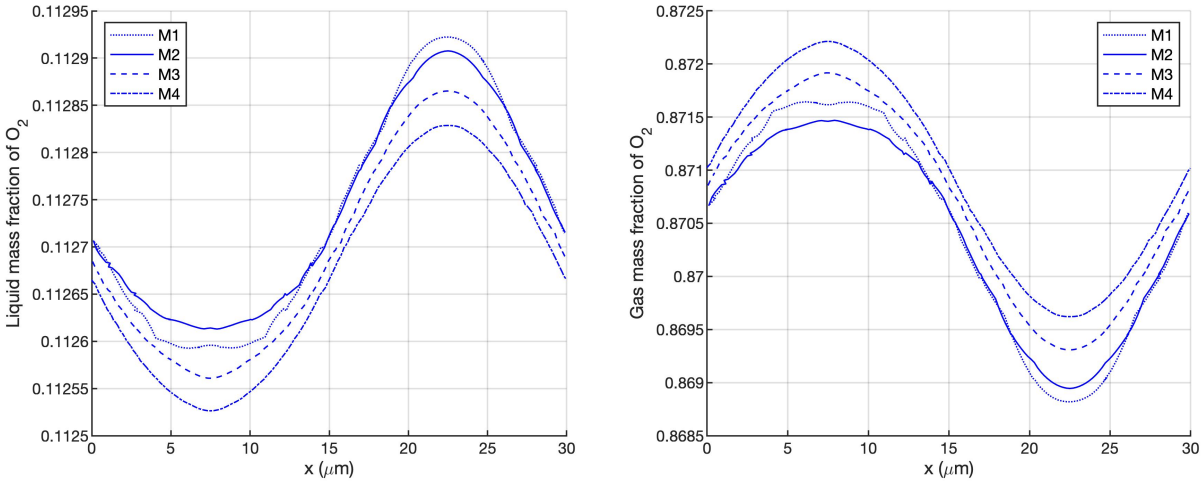

(a) (b)

Figure F.12: Benchmark case 6(b): two-dimensional capillary wave at supercritical pressures. Interface geometry and equilibrium state of the two-dimensional capillary wave at $t = 19$ μs and 150 bar. (a) oxygen mass fraction in the liquid phase; (b) oxygen mass fraction in the gas phase [66].

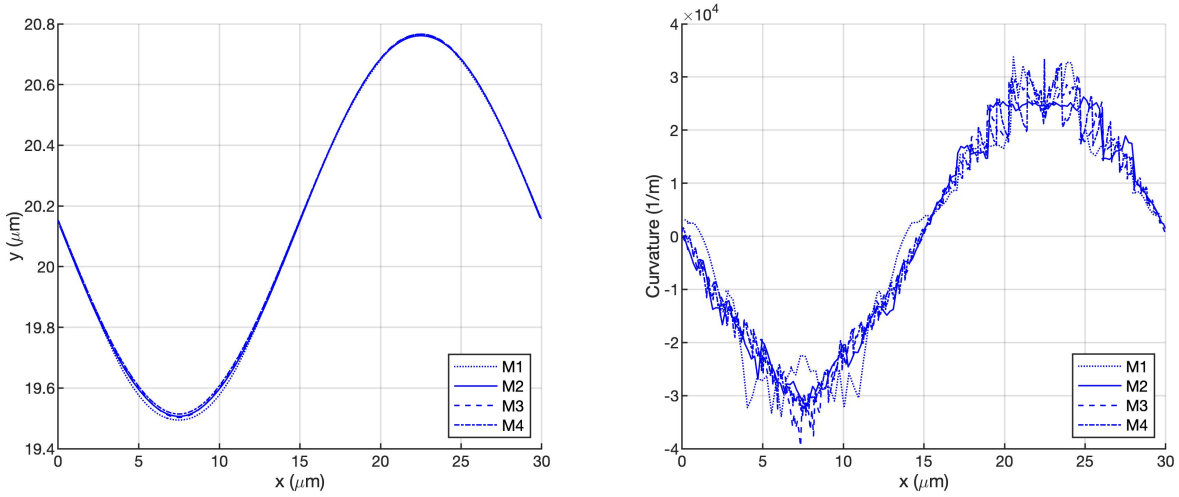

(a) (b)

Figure F.13: Benchmark case 6(c): two-dimensional capillary wave at supercritical pressures. Interface geometry and equilibrium state of the two-dimensional capillary wave at $t = 19$ μs and 150 bar. (a) interface amplitude; (b) curvature [66].

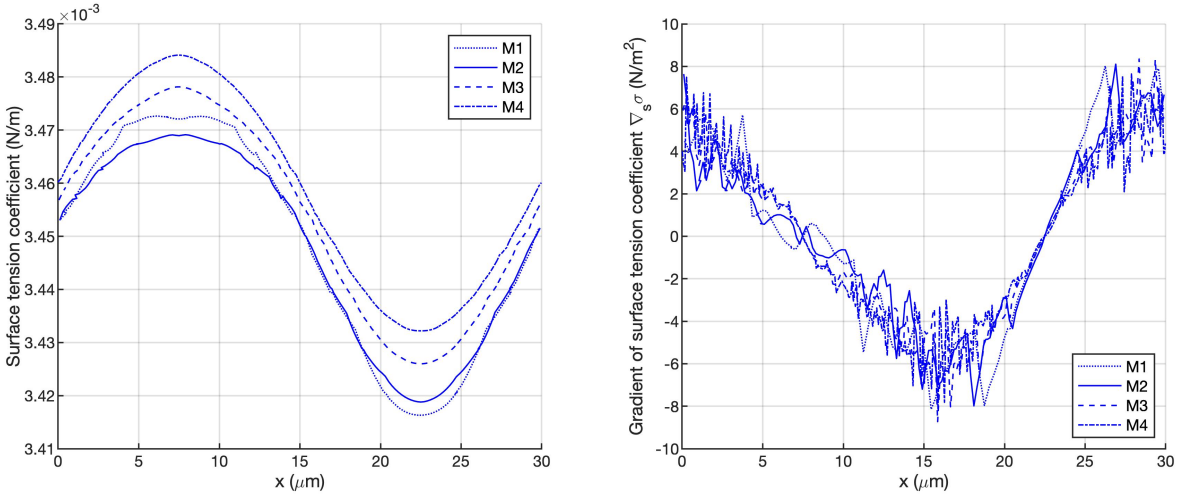

(a) (b)

Figure F.14: Benchmark case 6(d): two-dimensional capillary wave at supercritical pressures. Interface geometry and equilibrium state of the two-dimensional capillary wave at $t = 19$ μs and 150 bar. (a) surface-tension coefficient; (b) surface-tension coefficient gradient [66].

While the matching solution along the interface appears smooth as the mesh is improved, the net mass flux across the interface, $\dot{m}'$, is not (see Figure F.11b). $\dot{m}'$ is extremely sensitive to imperceptible changes in equilibrium composition or temperature, as stated in Poblador-Ibanez et al. [17]. As a result, undetectable disturbances show up in $\dot{m}'$. Furthermore, the normal-probe technique used to determine the solution of LTE and the jump conditions is constructed on the PLIC interface. It is not assured that the PLIC interface will be continuous between cells, and any information on the local interface curvature is lost (i.e., the interface is locally represented by a planar surface). Thus, the nature of the normal probe construction is consistent with the observed oscillations.

When analyzing the curvature and gradient of the surface-tension coefficient (Figures F.13b and F.14b), similar oscillations arise. Despite the fact that the interface shape and surface-tension coefficient distribution appear smooth (Figures F.13a and F.14a), κ and $\nabla_s\sigma$ are evaluated using the Height Function approach. As mentioned in Subsection 4.1.2, this approach is known to exhibit these oscillations, albeit converging with mesh refinement. Furthermore, due to the sharp volume-averaging of fluid properties, VOF methods using a one-fluid approach to solve the momentum equation show some degree of oscillations in the velocity and pressure fields near the interface, which have been presented as spurious currents in Section 4.3. In the future, the influence of these numerical perturbations on the actual development of the liquid surface should be evaluated. We accept this problem for the time being as long as it does not produce unstable numerical oscillations. The situations examined in this work show a surface deformation that corresponds to a physical mechanism. Furthermore, the magnitudes of these spurious currents are negligible compared to the jet velocity in problems involving the injection of liquid jets.

The slow spatial convergence of the interface matching solution and the modest oscillations in some of the parameters have little effect on the relaxation of the interface amplitude, as shown in Figures F.13a and F.15. Figure F.15a presents the evolution over time of the

interface vertical position at $x = 7.5$ μm, which corresponds to the initial location of the wave crest, and Figure F.15b presents the interface vertical position at the initial location of the wave trough at $x = 22.5$ μm. Figures F.13a and F.15 verify the grid convergence of the numerical model when evaluating the interface displacement.

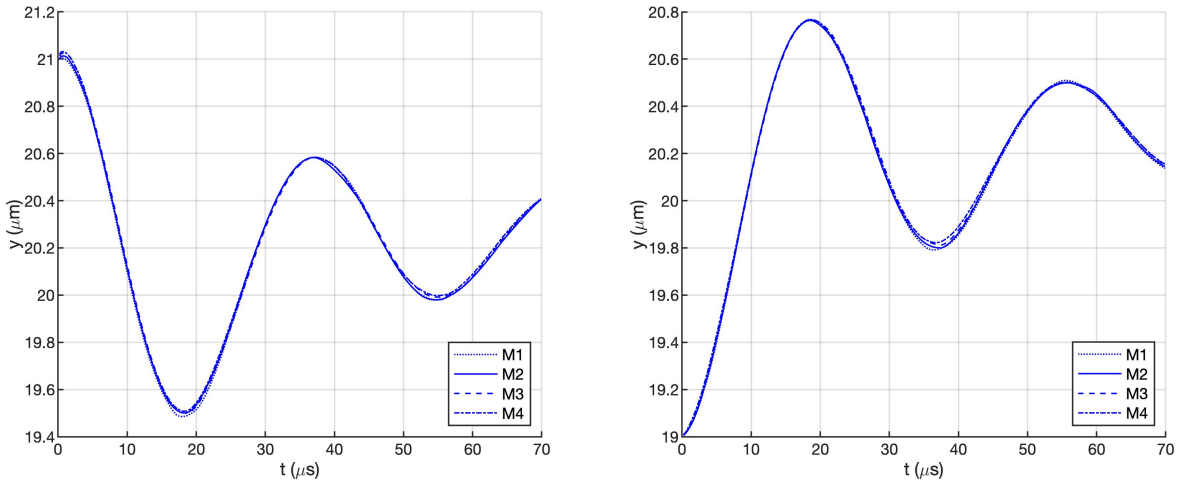

(a) (b)

Figure F.15: Benchmark case 6(e): two-dimensional capillary wave at supercritical pressures. Interface amplitude relaxation of the two-dimensional capillary wave at 150 bar. (a) at $x = 7.5$ μm (initial wave crest location); (b) at $x = 22.5$ μm (initial wave trough location) [66].

Figure F.16 shows the total change in liquid volume and mass. For this two-dimensional test a third dimension is considered with a depth of 1 m to evaluate volumes and mass. Convergence is evident with mesh refinement, particularly in the total liquid volume (see Figure F.16a). Both meshes M3 and M4 capture the strong condensation during the relaxation of the sharp initial conditions. However, as time passes, the curves deviate due to differences in predicted mass flux and the accuracy with which density variations are captured. Like the interface properties, grid convergence is possible, albeit at a first-order or lower rate.

In terms of mass errors in the liquid phase, the total amount of mass that condenses at the interface (see Figure F.17a) converges with mesh refinement and should be equal to the difference between the total liquid mass at a given time and the initial liquid mass. The total liquid mass is evaluated at every time step as $m_L = \sum_{i,j,k} \rho_{i,j,k} C_{i,j,k} \Delta x \Delta y \Delta z$, where $\rho_{i,j,k}$ at

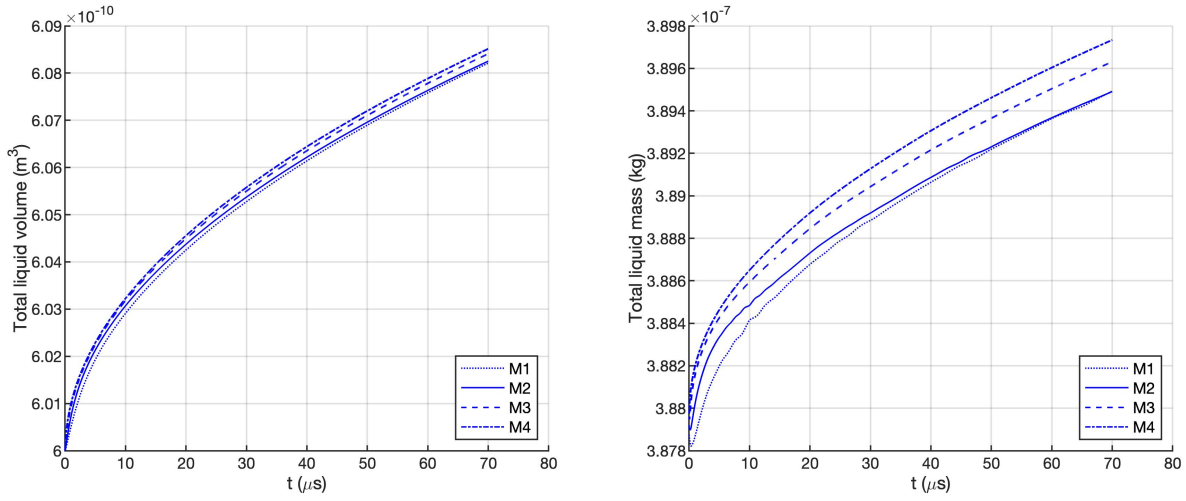

(a) (b)

Figure F.16: Benchmark case 6(f): two-dimensional capillary wave at supercritical pressures. Evolution of the total liquid volume and the total liquid mass over time for the two-dimensional capillary wave at 150 bar. (a) total liquid volume; (b) total liquid mass [66].

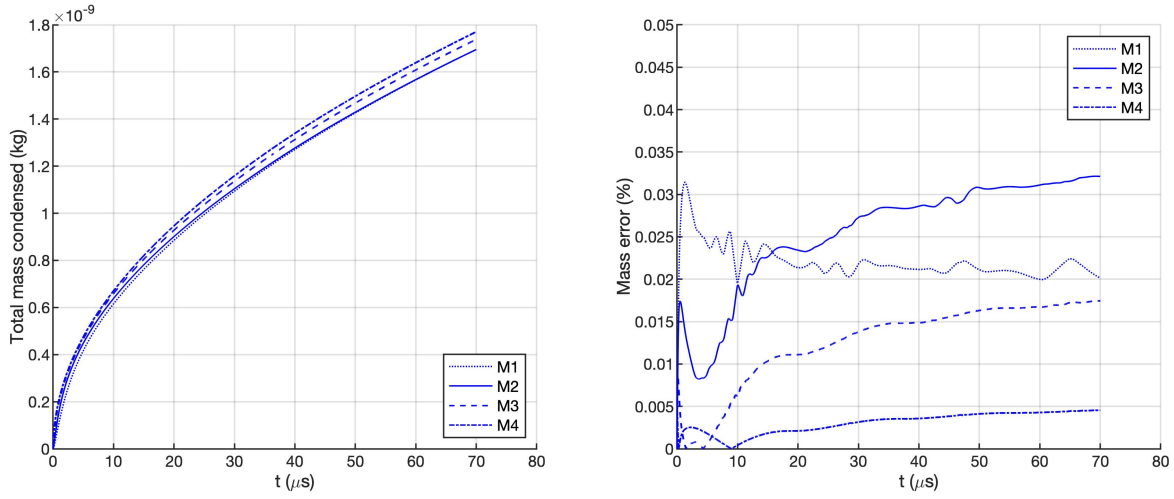

(a) (b)

Figure F.17: Benchmark case 6(g): two-dimensional capillary wave at supercritical pressures. Evolution of the total net mass exchanged across the interface and the estimated mass error over time for the two-dimensional capillary wave at 150 bar. (a) total mass condensed; (b) mass error [66].

interface cells is approximated by the liquid density at the interface. When evaluating mass conservation, this simplification at interface cells creates small error. On the other hand, the total condensed mass is obtained as $m_{\text{cond}} = -\sum_{t_{\text{initial}}}^{t_{\text{final}}} \sum_{i,j,k} \dot{m}' A_\Gamma \Delta t$. Recall $\dot{m}'$ is only

non-zero at interface cells and A_Γ represents the area of the local interface plane given by PLIC.

Even though both approaches should be equal, they exhibit mesh resolution difficulties when capturing the density field and addressing the jump conditions and LTE at the interface. Figure F.17b shows that the mass error evaluated as $E_m(\%) = 100(m_L - m_{\text{initial}} - m_{\text{cond}})/m_{\text{initial}}$ decreases with mesh refinement and after some temporal relaxation of the sharp initial condition. Although errors exist and mass conservation depends on mesh resolution, the overall thermodynamics of the interface can still be represented (e.g., identify regions of high or low mass exchange rate or whether condensation or vaporization occurs). Because continuous interface deformation produces smaller liquid structures, these errors are likely to be higher in liquid injection simulations. As a result, a fixed mesh resolution may lose accuracy in capturing the density variations and a smooth interface in certain regions. Nonetheless, the total mass exchanged across the interface constitutes only about 0.46% of the entire liquid mass in the time studied in this test.

The results reported with this test show the complexity of the numerical modeling of two-phase flows at supercritical pressures while confirming the consistency of the methods used in this work. The search for efficient and reliable approaches results in a low spatial convergence rate for several interface parameters. As a result, the mesh in atomization simulations must compromise between computational expense and interface accuracy (i.e., geometry and solution of LTE and jump conditions).

Two-dimensional planar jet at supercritical pressures

A temporal analysis of a symmetric two-dimensional planar jet is carried out to illustrate the numerical model's ability to capture interface deformation and relevant high-pressure physics

during the liquid injection. Although planar jets can exhibit antisymmetric behavior, the test problem is limited to symmetric configurations to reduce the computational cost.

The jet half-thickness is 10 μm, and the surface is initially perturbed with a sinusoidal wave of 30 μm wavelength and 0.5 μm amplitude. An initial velocity profile is imposed where the streamwise velocity varies from 0 m/s in the liquid phase to 30 m/s in the gas phase across a region of a few micrometers (i.e., around 6 μm) following a hyperbolic tangent profile. Periodic boundary conditions are imposed in the streamwise direction, and outflow boundary conditions are imposed in the gas phase along the top boundary of the numerical domain, which is far enough from the two-phase mixing zone not to affect the results. The thermodynamic pressure is 150 bar, and the initial conditions of each phase are the same as in the preceding test problems: the liquid jet is pure n-decane at 450 K, and the surrounding gas is pure oxygen at 550 K. Only one wavelength is contained within the computational domain. However, some of the results are plotted using streamwise periodicity.

Good mesh convergence and mass-conservation features have been demonstrated for configurations with minor deformations. In other words, in scenarios where the mesh can accurately resolve the liquid surface geometry. On the other hand, liquid atomization results in a cascade process in which smaller and more complex liquid structures form before they break up into droplets.

Once under-resolved areas exist, the evolution of the liquid surface with a fixed uniform mesh shows some mesh dependence (e.g., high curvature regions). Not only are the geometrical parameters that define the interface less precise, but the complex methodology presented in this work is also affected, as noted throughout this dissertation. There are other workarounds for this problem, such as applying local mesh refinement near the under-resolved areas. They are not pursued here to avoid adding to the model complexity, but they may be considered in the future. Nonetheless, the mesh cannot be refined indefinitely due to computational and physical limits.

This study looks into mesh dependence regarding both liquid surface deformation and mass conservation features. Three distinct uniform mesh sizes between M3 and M4 are investigated (see Table F.1). Their properties are shown in Table F.2.

Table F.2: Details on the meshes used in the analysis of a two-dimensional planar liquid jet at supercritical pressures. The number of cells per wavelength or amplitude refer to the initial configuration of the liquid-gas interface.

Mesh	J1	J2	J3
Δx (μm)	1/10	1/15	1/20
Cells/Wavelength	300	450	600
Cells/Amplitude	5	7.5	10

Figures F.18, F.19 and F.20 depict the evolution of the temperature field and interface deformation obtained with each mesh J1, J2, and J3. Detail close-ups of the interface perturbation are presented at the early times (i.e., $t \leq 4.5$ μs). When the liquid deformation becomes more chaotic, a bigger domain is presented using the periodic boundary in the streamwise direction. The three meshes exhibit a nearly identical evolution up to $t \approx 1.5$ μs. The coarser mesh J1 then begins to depart from J2 and J3. After 2.5 μs, deviations between J2 and J3 appear.

Even over more extended periods, the qualitative evolution of the interface is relatively similar with meshes J1, J2, and J3. Deviations become visible once under-resolved liquid structures form. These poorly-resolved regions suffer from less precise interface geometrical and thermodynamic properties and various numerical simplifications that must be incorporated to allow for extensive temporal evolution. As a result, once these mesh limitations exist, the liquid surface can evolve differently. These problems are not unique to the methodology presented in this work, and other codes dealing with simpler configurations, such as incompressible liquid atomization, also suffer from under-resolution effects. Another critical factor is the difference in fluid properties at very high pressures. Compared to grid-independence studies in two-phase incompressible flows, the resolution with which,

for example, the variable-density field is captured directly affects the liquid-phase dynamics. Thus, many additional factors influence the mesh performance.

Mass conservation is also analyzed. Mass errors are evaluated following the equations presented in the two-dimensional capillary wave problem at high pressures. It is noted that the performance is worse than that of the standing capillary wave problem. For fixed meshes, the formation of smaller liquid structures, which is typical of liquid atomization, is troublesome in dictating the evolution of the liquid surface and satisfying mass conservation. J1 is the worst performing mesh, deviating significantly from J2 and J3 early in the simulations. J2 and J3 exhibit comparable performance until the liquid-surface evolution begins to differ (see Figures F.21 and F.22). Up to 6 μs, the total liquid volume remains nearly the same for all meshes, while variations in the total liquid mass and the total net mass condensed across the interface emerge much sooner ($t \approx 3-4$ μs). Mass errors are less than 0.5% up to 4 μs, after which they increase continuously as the deformation cascade process unfolds. Compared to the overall liquid mass, these mass errors are still small. The total mass exchanged across the interface during the examined times comprises only about 0.42% of the total liquid mass.

It is worth noting that these errors are primarily due to a poorer resolution of the liquid density field and the interface, rather than the model's ability to predict condensation and vaporization rates with reasonable precision, particularly for small liquid structures. The total mass exchanged across the interface results in net condensation up to 6 μs, as shown in Figures F.21 and F.22, with the liquid shape remaining well-defined with no or negligible coalescence and breakup events. Nonetheless, when the ligaments become thinner and the density variations are less accurate across them, the estimated total liquid mass decreases when it should grow.

According to the results presented here, achieving adequate mass-conservation characteristics and grid independence in the development of the liquid surface becomes a much greater challenge than in similar VOF codes implemented for incompressible, two-phase flows. Be-

cause the computational cost and the physics limit how small the mesh may be, a trade-off must be made between numerical performance, physical coherence (e.g., avoiding mesh sizes that enter the non-equilibrium phase transition or non-continuum domains), and simulation goals. Mesh J3 is chosen if the computational expense is not an impediment in this problem setting. However, one may argue that mesh J2 should be used instead for cheaper three-dimensional computations with a similar problem setup, as discussed in the next test.

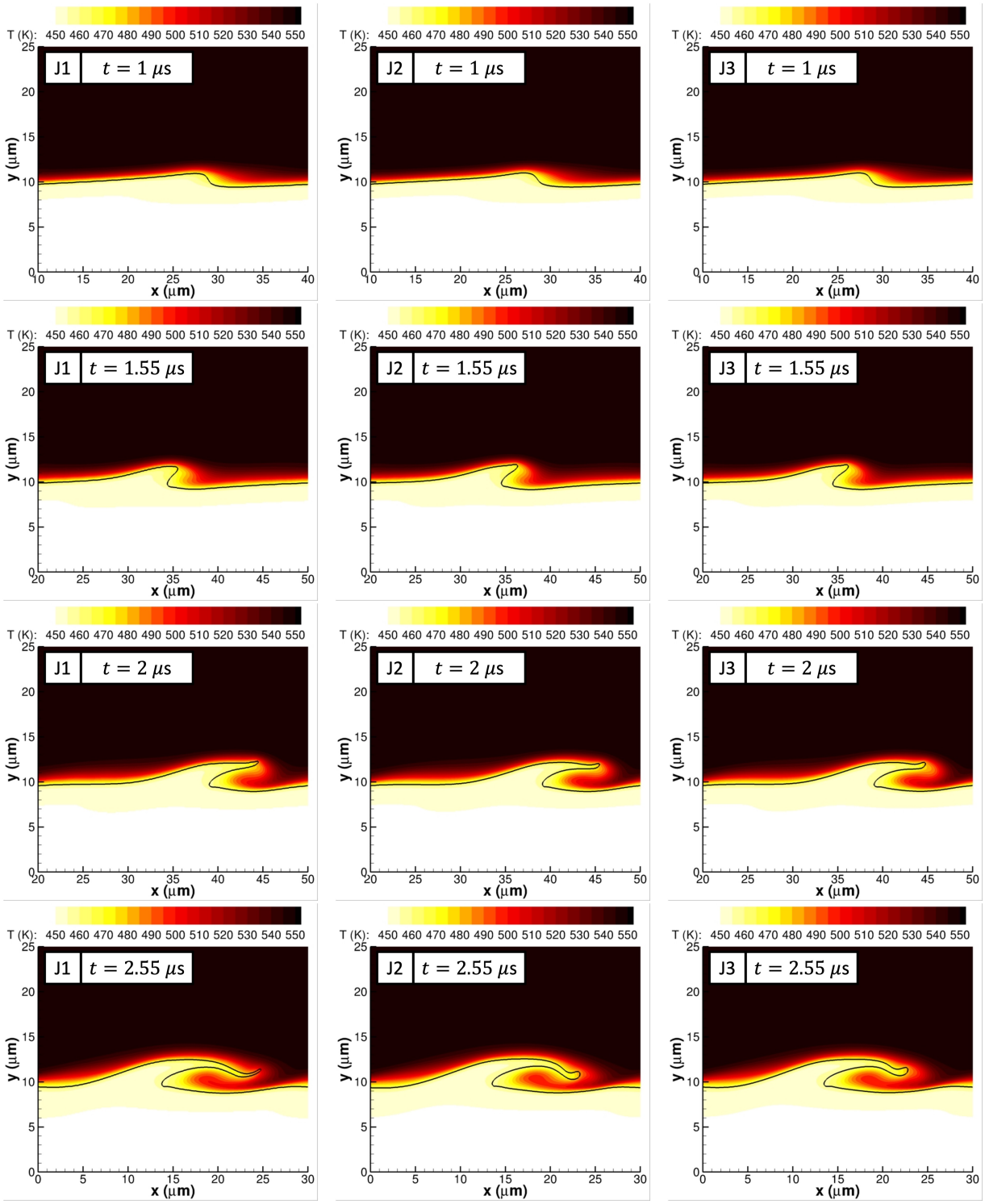

Figure F.18: Benchmark case 7(a): two-dimensional planar jet at supercritical pressures. Temperature plots and interface deformation at 150 bar for the two-dimensional planar jet with three mesh sizes J1, J2 and J3. Plotted times correspond to 1 μs, 1.55 μs, 2 μs and 2.55 μs. The interface location is highlighted with a solid black curve representing the isocontour with $C = 0.5$ [66].

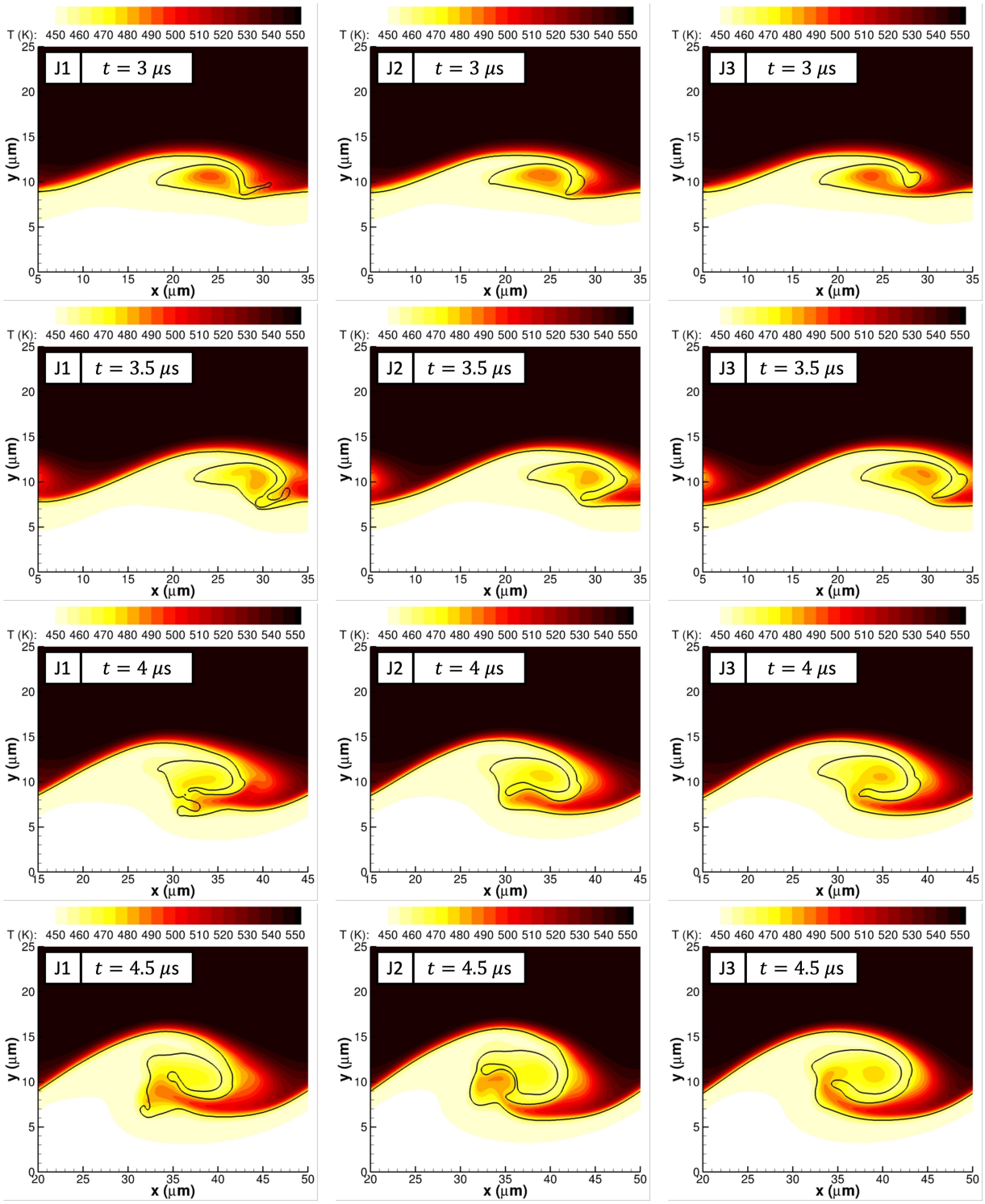

Figure F.19: Benchmark case 7(b): two-dimensional planar jet at supercritical pressures. Temperature plots and interface deformation at 150 bar for the two-dimensional planar jet with three mesh sizes J1, J2 and J3. Plotted times correspond to 3 μs, 3.5 μs, 4 μs and 4.5 μs. The interface location is highlighted with a solid black curve representing the isocontour with $C = 0.5$ [66].

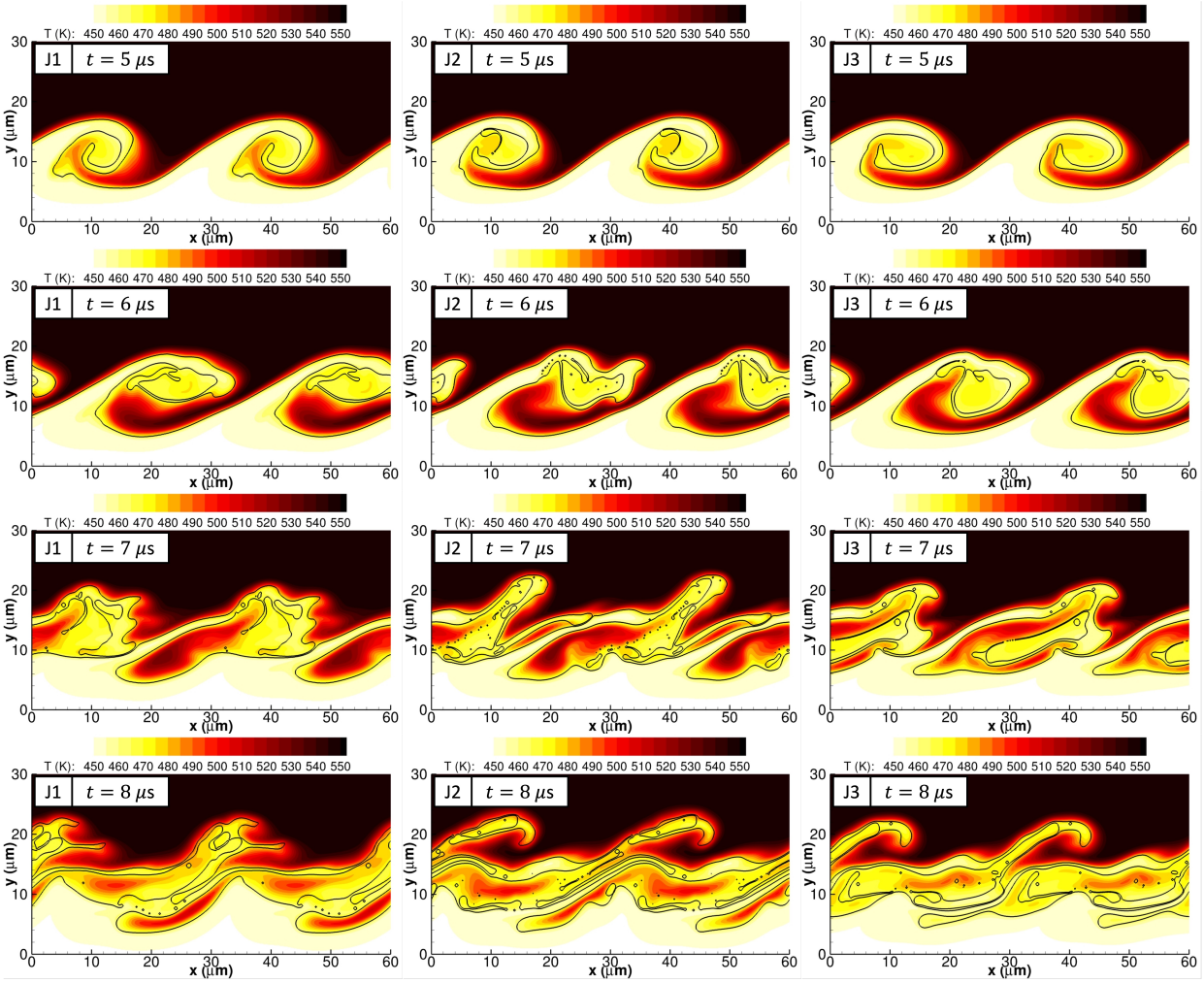

Figure F.20: Benchmark case 7(c): two-dimensional planar jet at supercritical pressures. Temperature plots and interface deformation at 150 bar for the two-dimensional planar jet with three mesh sizes J1, J2 and J3. Plotted times correspond to 5 μs, 6 μs, 7 μs and 8 μs. The interface location is highlighted with a solid black curve representing the isocontour with $C = 0.5$ [66].

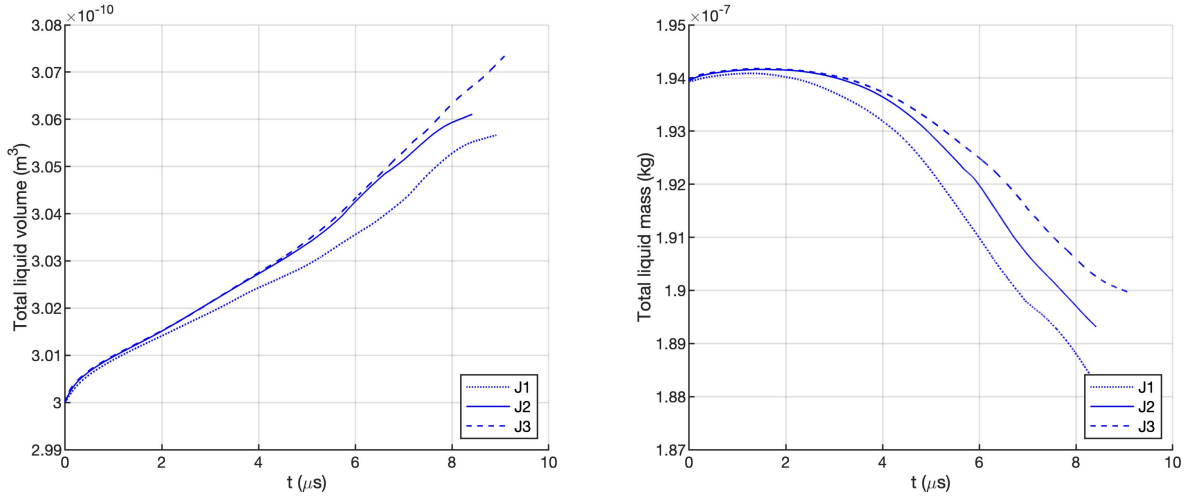

(a) (b)

Figure F.21: Benchmark case 7(d): two-dimensional planar jet at supercritical pressures. Evolution of the total liquid volume and the total liquid mass over time for the two-dimensional planar liquid jet at 150 bar. (a) total liquid volume; (b) total liquid mass [66].

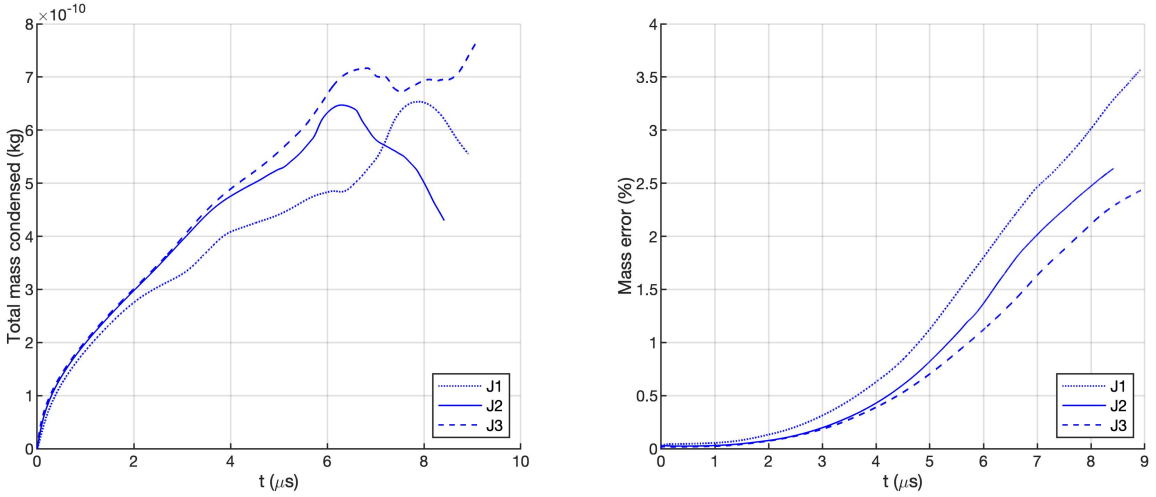

(a) (b)

Figure F.22: Benchmark case 7(e): two-dimensional planar jet at supercritical pressures. Evolution of the total net mass exchanged across the interface and the estimated mass error over time for the two-dimensional planar liquid jet at 150 bar. (a) total mass condensed; (b) mass error [66].

Three-dimensional planar jet at supercritical pressures

This test deals with a temporal and symmetric three-dimensional planar jet to further demonstrate the numerical model's capacity to handle three-dimensional configurations. The jet half-thickness is 10 μm, and the interface is initially perturbed in the streamwise direction with a sinusoidal wave of 30 μm wavelength and 0.5 μm amplitude, as in the two-dimensional case. Another sinusoidal perturbation in the spanwise direction is superimposed with a wavelength of 20 μm and an amplitude of 0.5 μm to strengthen three-dimensional effects early on. This configuration is very similar to the main problem setup used in this dissertation.

Like in previous tests, the liquid is initially composed of n-decane at 450 K, and the gaseous phase is oxygen at 550 K. The thermodynamic pressure is 150 bar, and the streamwise velocity varies from 0 m/s in the liquid to 30 m/s in the gas with the same hyperbolic tangent profile used for the two-dimensional planar jet study. Outflow boundary conditions are applied in the gas domain top boundary away from the interface, and periodic boundary conditions are imposed in the streamwise and spanwise directions. The computational domain has only one wavelength in each direction to mitigate the computational cost, and the results are plotted using periodicity in the streamwise and spanwise directions.

The early interface deformation of the three-dimensional planar jet up to 3 μs in time is shown in Figure F.23. To quantify the effect of the mesh size on the growth of three-dimensional liquid structures, two alternative meshes (J1 and J3) are used. Both mesh J1 and J3 predict a nearly identical liquid surface evolution. Some discrepancies in the elongation of the ligament stretching from the tip of the lobes that form on the liquid surface can be noticed only at 3 μs. Due to worse mesh resolution toward the ligament tip, the coarser mesh predicts a thinner and longer ligament than the finer mesh. Overall, the rest of the liquid surface appears to be relatively similar with both meshes, which may justify utilizing mesh J2 rather than mesh J3 to reduce the computational cost of three-dimensional simulations.

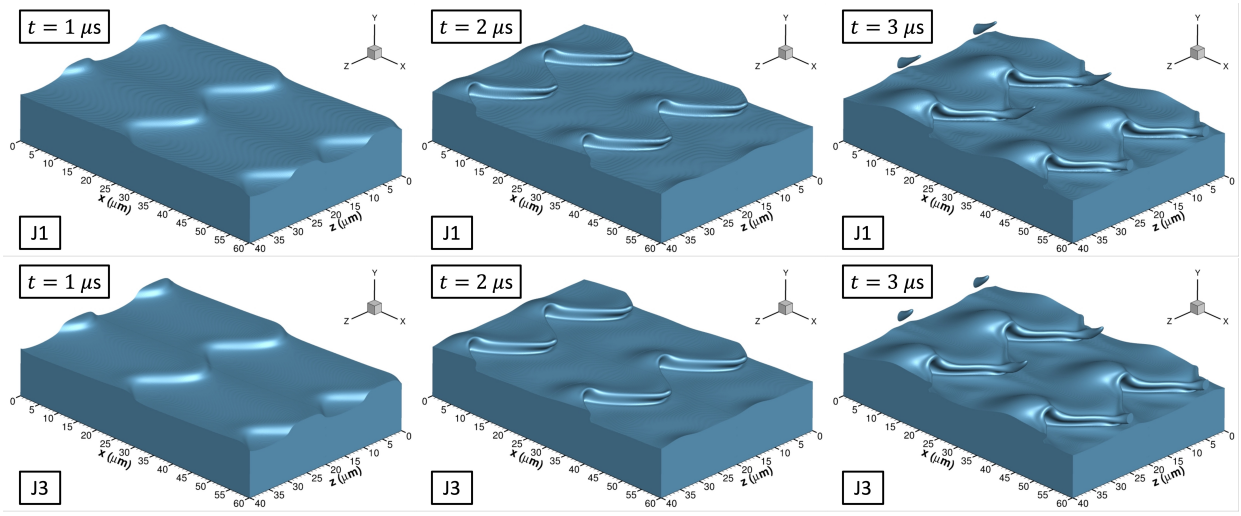

Figure F.23: Benchmark case 8: three-dimensional planar jet at supercritical pressures. Interface deformation at 150 bar for the three-dimensional planar jet with two meshes J1 and J3. The initial spanwise perturbation amplitude is 0.5 μm [66].

G Additional supporting figures

G.1 Ligament formation: size and distribution

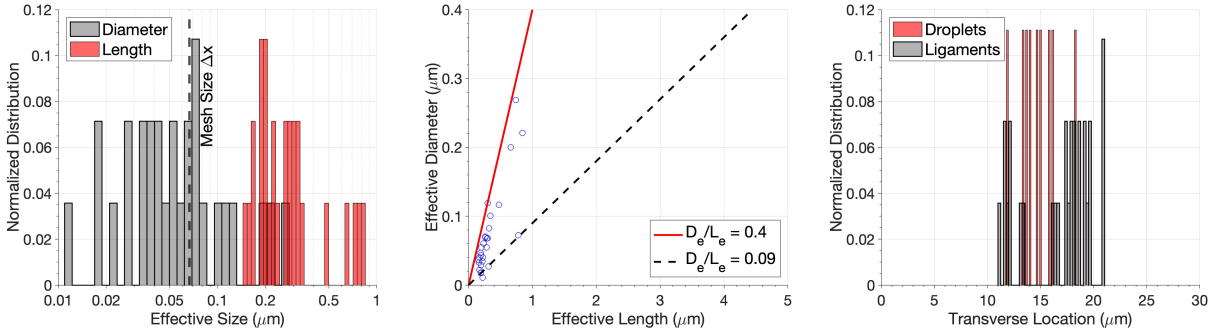

(a) (b) (c)

Figure G.1: Effective ligament length and diameter and spatial distribution of ligaments and droplets at 50 bar and $u_G = 50$ m/s (i.e., case A1) for the non-dimensional time of $t^* = 14.7$. (a) effective diameter and effective length distribution. Notice the logarithmic scale used in the horizontal axis; (b) correlation between effective diameter and effective length; and (c) spatial distribution of ligaments and droplets.

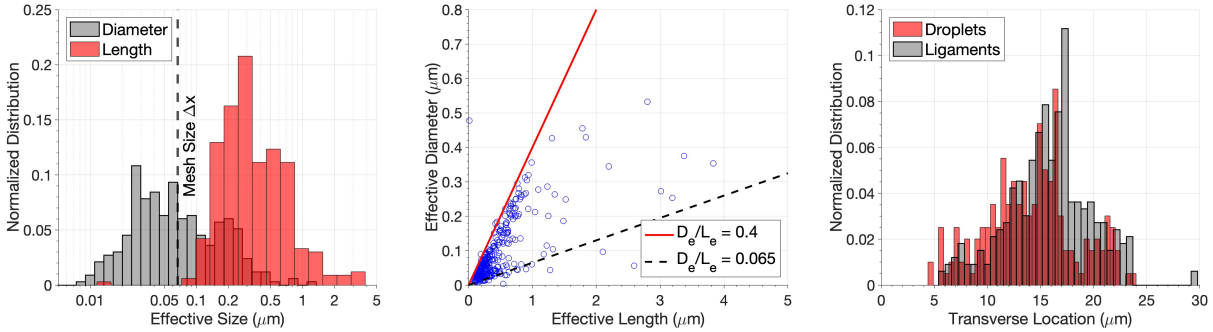

(a) (b) (c)

Figure G.2: Effective ligament length and diameter and spatial distribution of ligaments and droplets at 50 bar and $u_G = 70$ m/s (i.e., case A2) for the non-dimensional time of $t^* = 14.7$. (a) effective diameter and effective length distribution. Notice the logarithmic scale used in the horizontal axis; (b) correlation between effective diameter and effective length; and (c) spatial distribution of ligaments and droplets.

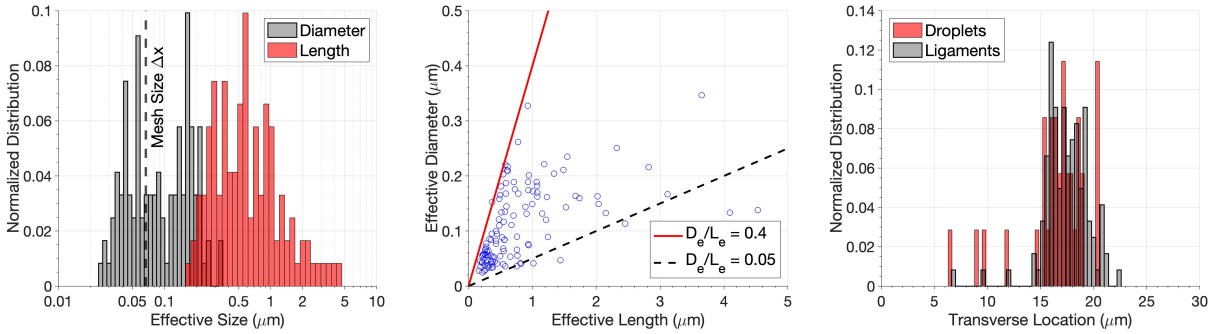

(a) (b) (c)

Figure G.3: Effective ligament length and diameter and spatial distribution of ligaments and droplets for the incompressible case at 50 bar and $u_G = 70$ m/s (i.e., case A2i) for the non-dimensional time of $t^* = 14.7$. (a) effective diameter and effective length distribution. Notice the logarithmic scale used in the horizontal axis; (b) correlation between effective diameter and effective length; and (c) spatial distribution of ligaments and droplets.

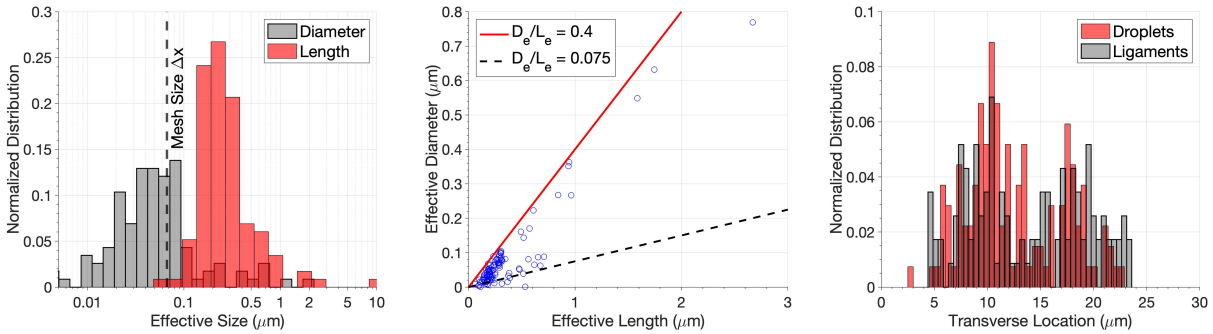

(a) (b) (c)

Figure G.4: Effective ligament length and diameter and spatial distribution of ligaments and droplets at 100 bar and $u_G = 50$ m/s (i.e., case B1) for the non-dimensional time of $t^* = 14.7$. (a) effective diameter and effective length distribution. Notice the logarithmic scale used in the horizontal axis; (b) correlation between effective diameter and effective length; and (c) spatial distribution of ligaments and droplets.

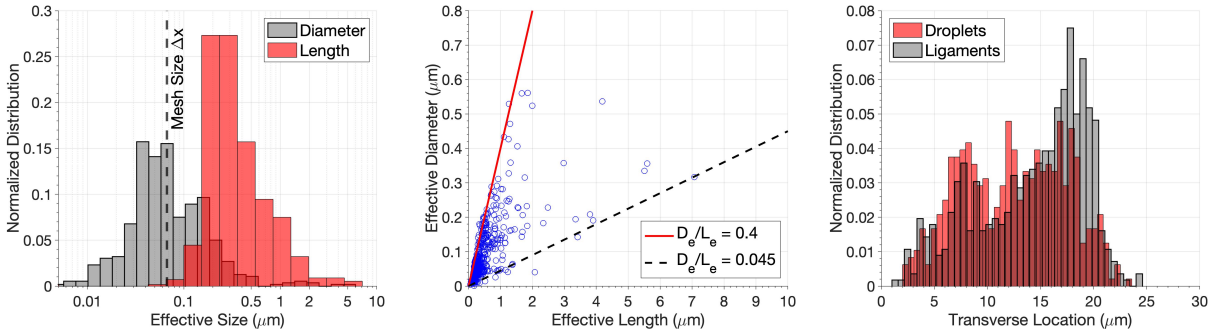

(a) (b) (c)

Figure G.5: Effective ligament length and diameter and spatial distribution of ligaments and droplets at 100 bar and $u_G = 70$ m/s (i.e., case B2) for the non-dimensional time of $t^* = 14.7$. (a) effective diameter and effective length distribution. Notice the logarithmic scale used in the horizontal axis; (b) correlation between effective diameter and effective length; and (c) spatial distribution of ligaments and droplets.

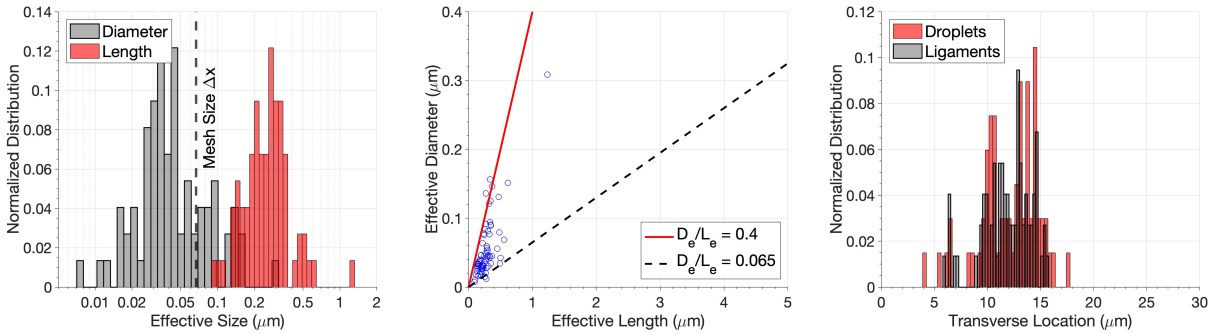

(a) (b) (c)

Figure G.6: Effective ligament length and diameter and spatial distribution of ligaments and droplets at 150 bar and $u_G = 30$ m/s (i.e., case C1) for the non-dimensional time of $t^* = 14.7$. (a) effective diameter and effective length distribution. Notice the logarithmic scale used in the horizontal axis; (b) correlation between effective diameter and effective length; and (c) spatial distribution of ligaments and droplets.

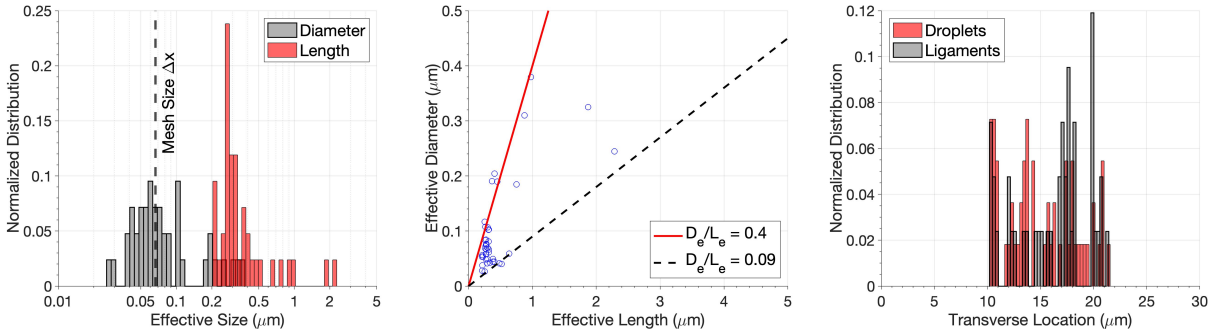

(a) (b) (c)

Figure G.7: Effective ligament length and diameter and spatial distribution of ligaments and droplets for the incompressible case at 150 bar and $u_G = 30$ m/s (i.e., case C1i) for the non-dimensional time of $t^* = 14.7$. (a) effective diameter and effective length distribution. Notice the logarithmic scale used in the horizontal axis; (b) correlation between effective diameter and effective length; and (c) spatial distribution of ligaments and droplets.

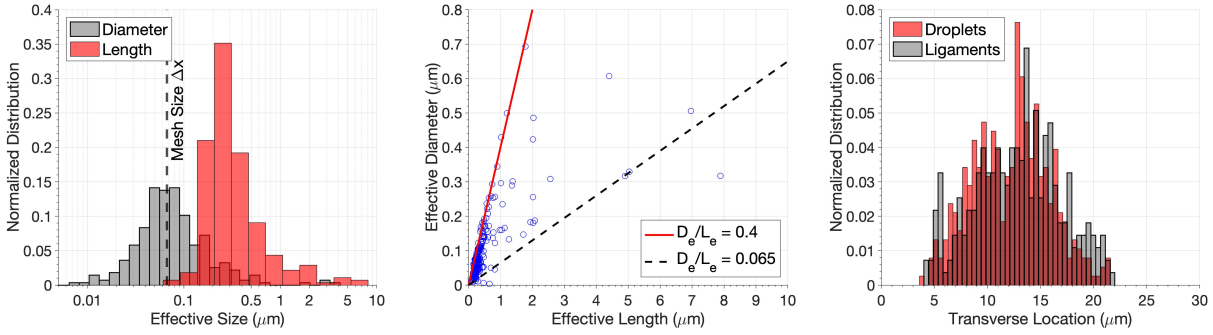

(a) (b) (c)

Figure G.8: Effective ligament length and diameter and spatial distribution of ligaments and droplets at 150 bar and $u_G = 50$ m/s (i.e., case C2) for the non-dimensional time of $t^* = 14.7$. (a) effective diameter and effective length distribution. Notice the logarithmic scale used in the horizontal axis; (b) correlation between effective diameter and effective length; and (c) spatial distribution of ligaments and droplets.